IUTAM SYMPOSIUM STUTTGART/GERMANY 1989

W. Schiehlen (Ed.)

Nonlinear Dynamics in Engineering Systems

Springer-Verlag

Nonlinear Dynamics in Engineering Systems

W. Schiehlen (Editor)
Nonlinear Dynamics in Engineering Systems
IUTAM Symposium Stuttgart/Germany 1989

International Union of Theoretical
and Applied Mechanics

W. Schiehlen (Ed.)

Nonlinear Dynamics in Engineering Systems

IUTAM Symposium, Stuttgart, Germany
August 21-25, 1989

Springer-Verlag
Berlin Heidelberg New York
London Paris Tokyo Hong Kong

Prof. Dr.-Ing. W. Schiehlen

Institute B of Mechanics
University of Stuttgart
Pfaffenwaldring 9
D-7000 Stuttgart 80
FRG

ISBN-13:978-3-642-83580-3 e-ISBN-13:978-3-642-83578-0
DOI: 10.1007/978-3-642-83578-0

2161/3020 5 4 3 2 1 0 Printed on acid-free paper

Preface

The International Union of Theoretical and Applied Mechanics (IUTAM) initiated and sponsored an International Symposium on Nonlinear Dynamics in Engineering Systems held in 1989 in Stuttgart, FRG. The Symposium was intended to bring together scientists working in different fields of dynamics to exchange ideas and to discuss new trends with special emphasis on nonlinear dynamics in engineering systems.

A Scientific Committee was appointed by the Bureau of IUTAM with the following members:

S. Arimoto (Japan),
F.L. Chernousko (USSR),
P.J. Holmes (USA),
C.S. Hsu (USA),
G. Iooss (France),
F.C. Moon (USA),
W. Schiehlen (FRG), Chairman,
G. Schmidt (GDR),
W. Szemplinska-Stupnicka (Poland),
J.M.T. Thompson (UK),
H. Troger (Austria).

This committee selected the participants to be invited and the papers to be presented at the Symposium. As a result of this procedure 78 active scientific participants from 22 countries followed the invitation, and 44 papers were presented in lecture and poster sessions. They are collected in this volume. At the Symposium an exhibition with experiments took place and the movie "An Introduction to the Analysis of Chaotic Dynamics" by E.J. Kreuzer et.al. was presented.

The scientific lectures were devoted to the following topics:

- Dynamic Structural Engineering Problems,
- Analysis of Nonlinear Dynamic Systems,
- Bifurcation Problems,
- Chaotic Dynamics and Control Problems,
- Miscellaneous Problems,
- Experimental and Theoretical Investigations,
- Chaotic Oscillations of Engineering Systems,
- Characterization of Nonlinear Dynamic Systems,
- Nonlinear Stochastic Systems.

Since many of the presentations are related to more than one of these topics, the papers in this volume are arranged in alphabetical order. The papers indicate the wide scope of engineering applications of nonlinear dynamics reaching from mathematics and physics to vibration of machines and structural dynamics including stochastic systems. The presentations and discussions during the Symposium will certainly stimulate further theoretical and applied investigations in the challenging field of

nonlinear dynamics. The publication of the proceedings may promote this development.

Generous financial and material support contributed to the success of the Symposium. The help of the following sponsors is gratefully acknowledged:

International Union of Theoretical and Applied Mechanics (IUTAM),
University of Stuttgart,
Robert Bosch GmbH, Stuttgart,
Daimler–Benz AG, Stuttgart,
M.A.N. Technologie AG, München,
City of Stuttgart.

The success of the Symposium would not have been possible without the excellent work of the Local Organizing Committee. Members of the Committee were:

R. Eppler, K. Kirchgässner, E. Kreuzer, W. Schiehlen (Chairman), D. Bestle, A. Eiber, M. Kleczka, R. Weber (Secretary).

In the editorial work for this volume the help of my colleague D. Bestle was especially valuable. In addition I would like to express my sincere thanks to all the members of the Institute B of Mechanics, they all contributed to the success of the Symposium. Furthermore, thanks are due to the Springer–Verlag for the efficient cooperation.

Stuttgart, October 1989

Werner Schiehlen

List of Participants

(Chairmen are identified by an asterisk)

Al–Athel, S.A., President of KACST, P.O. Box 60 86, Riyadh 11442, Saudia Arabia

* **Ariaratnam, S.T.**, Solid Mechanics Division, Faculty of Engineering, University of Waterloo, Waterloo, Ontario N2L 3G1, Canada

* **Arimoto, S.**, Department of Mathematical Eng. and Information Physics, Faculty of Engineering, University of Tokyo, Bunkyo–ku, Tokyo 113, Japan

Bajkowski, J., Sicherheitstechnische Regelungs– und Meßtechnik, Bergische Univ. –GH– Wuppertal, Gaußstraße 20, D–5600 Wuppertal 1, FRG

Beletzky, V.V., Keldysch–Institute of Appl. Mathem., USSR Academy of Sciences, Miusskaya pl. 4, Moscow 123047, USSR

Benedettini, F., Dipartimento di Ingegneria delle Strutture, Universita dell'Aquila, Monteluco di Roio, I–67040 l'Aquila, Italy

Bestle, D., Institut B für Mechanik, Universität Stuttgart, Pfaffenwaldring 9, D–7000 Stuttgart 80, FRG

Bournaski, E., Institute of Water Problems, Bulgarian Academy of Sciences, "Acad. G. Bontchev" Street Bl. 1, Sofia 1113, Bulgaria

Brauchli, H., Institut für Mechanik, ETH–Zentrum, CH–8092 Zürich, Switzerland

* **Brindley, J.**, Centre for Nonlinear Studies, University of Leeds, Leeds LS2 9JT, UK

Bucher, Ch., Institut für Mechanik, Universität Innsbruck, Technikerstraße 13, A–6020 Innsbruck, Austria

Campen van, D.H., Faculty of Mechanical Engineering, Eindhoven Univ. of Technology, Den Dolech 2, P.O. Box 513, NL–5600 MB Eindhoven, The Netherlands

Chen, Y.–S., Dept. of Mechanics, Tianjin University, Tianjin, China

* **Chernousko, F.L.**, Institute for Problems in Mech., USSR Academy of Sciences, pr. Vernadskogo 101, Moscow 117526, USSR

Cheshankov, B., ul. Rakovski No. 166 A, Sofia 1000, Bulgaria

* **Crandall, S.H.**, Dept. of Mech. Engineering., Rm. 3–360, Massachusetts Institute of Technology, Cambridge, MA 02139, USA

Cusumano, J.P., Dept. of Engineering Science and Mechanics, Hammond Bldg., Pennsylvania State University, University Park, PA 16802, USA

* **Dowell, E.H.**, Dean of Engineering, Duke University, 305 Teer Engineering Library Bldg., Durham, NC 27706, USA

Eick, I., Institut für Angewandte Physik, Technische Hochschule Darmstadt, Schloßgartenstraße 7, D–6100 Darmstadt, FRG

El Naschie, M.S., 51 Pitt Place, Church Street, Epsom, Surrey KT17 4PY, UK

Fey, R., Faculty of Mechanical Engineering, Eindhoven Univ. of Technology, Den Dolech 2, P.O. Box 513, NL–5600 MB Eindhoven, The Netherlands

Fritzen, C.–P., Lehrstuhl für Techn. Mechanik, Universität Kaiserslautern, Postfach 3049, D–6750 Kaiserslautern, FRG

Gabrielli, G., Large Turbogenerator Dept. KWDE3, Asea Brown Boveri Ltd, CH–5401 Baden, Switzerland

* **Guttalu, R.S.**, Dept. of Mechanical Engineering, Univ. of Southern California, Los Angeles, CA 90089–1453, USA

Habip, L.M., Siemens AG, U ED 24, Berliner Straße 295–303, D–6050 Offenbach 3, FRG

Higuchi, K., Dept. of Ind. Mech. Engineering, Faculty of Science and Engineering, Tokyo Denki University, Hatoyama, Hiki–Gun, Saitama 350–03, Japan

* **Hirai, K.**, Dept. of Systems Engineering, Kobe University, Rokko, Nada, Kobe 657, Japan

Hollingworth, N., Kluwer Academic Publishers b.v., Spuiboulevard 50, NL–3300 AA Dordrecht, The Netherlands

* **Hsu, C.S.**, Dept. of Mech. Engineering, University of California, Berkeley, CA 94720, USA

Ibrahim, R.A., Dept. of Mech. Engineering., Wayne State University, Detroit, MI 48202, USA

* **Iooss, G.**, Lab. de Mathematiques, Université de Nice, U.A. CNRS 168, Parc Valrose, F–06034 Nice Cedex, France

Isomäki, H.M., Main Building Y329, Otakaari, Institute of Mechanics, Helsinki Univ. of Technology, SF–02150 Espoo 15, Finland

Kleczka, M., Institut B für Mechanik, Universität Stuttgart, Pfaffenwaldring 9, D–7000 Stuttgart 80, FRG

* **Kounadis, A.N.**, Civil Eng. Department, National Tech. University of Athens, Patision 42, GR–10682 Athens, Greece

Kraker de, A., Faculty of Mechanical Engineering, Eindhoven Univ. of Technology, Den Dolech 2, P.O.Box 513, NL–5600 MB Eindhoven, The Netherlands

* **Kreuzer, E.J.**, Meerestechnik II – Strukturmechanik, TU Hamburg–Harburg, Eißendorfer Straße 42, D–2100 Hamburg 90, FRG

Kunert, A., Lehrstuhl B für Mechanik, TU München, Postfach 20 24 20, Arcisstraße 21, D–8000 München 2, FRG

Kurnik, W., Institute of Machine Design Fundamentals, Technical University of Warsaw, ul. Narbutta 84, PL–02–524 Warsaw, Poland

Lamarque, C.–H., Ecole Nationale des Travaux Publics de l'Etat, Rue Maurice Audin, F–69518 Vaulx en Velin Cedex, France

Lefeber, D., Dept. of Analytical Mechanics, Faculty of Applied Sciences, Vrije Universiteit Brussel, Pleinlaan 2, B–1050 Brussel , Belgium

Lin, Y.K., Center for Applied Stochastics, Research Florida Atlantic University, Boca Raton, FL 33434, USA

* **Moon, F.C.**, Sibley School of Mech. and Aerospace Engineering, 105 Upson Hall, Cornell University, Ithaca, NY 14853, USA

* **Müller, P.C.**, Sicherheitstechnische Regelungs– und Meßtechnik, Bergische Univ. –GH– Wuppertal, Gaußstraße 20, D–5600 Wuppertal 1, FRG

Narayanan, S., Machine Dynamics Laboratory, Dept. of Applied Mechanics, Indian Institute of Technology, Madras 600 036, India

* **Thompson, J.M.T.**, Dept. of Civil Engineering, University College London, Gower Street, London WC1E 6BT, UK

Tongue, B.H., Dept. of Mechanical Engineering, University of California, Berkeley, CA 94720, USA

* **Troger, H.**, Institut für Mechanik, TU Wien, Wiedner Hauptstraße 8–10/325, A–1040 Wien, Austria

Valkering, T.P., Center for Theoretical Physics, University of Twente, P.O. Box 217, NL–7500 AE Enschede, The Netherlands

Virgin, L.N., Department of Mechanical Engineering, Duke University, Durham, NC 27706, USA

* **Wedig, W.**, Institut für Techn. Mechanik, Universität Karlsruhe, Kaiserstraße 12, D–7500 Karlsruhe 1, FRG

Wesolowski, Z., Inst. of Fundamental Technological Research, Polish Academy of Sciences, ul. Swietokrzyska 21, PL–00–049 Warsaw, Poland

Wilmers, Ch., Meerestechnik II – Strukturmechanik, TU Hamburg–Harburg, Eißendorfer Straße 42, Postfach 90 14 03, D–2100 Hamburg 90, FRG

Wu, C.–W., 4–3, Lane 39, Roosevelt Rd. See. 6, Taipei, Taiwan

Xie, W.–C., Solid Mechanics Division, Faculty of Engineering, University of Waterloo, Waterloo, Ontario N2L 3G1, Canada

* **Ziegler, F.**, Institut für Allgem. Mechanik, TU Wien, Wiedner Hauptstraße 8–10/201, A–1040 Wien, Austria

Contents

Photograph: Annette Schiehlen

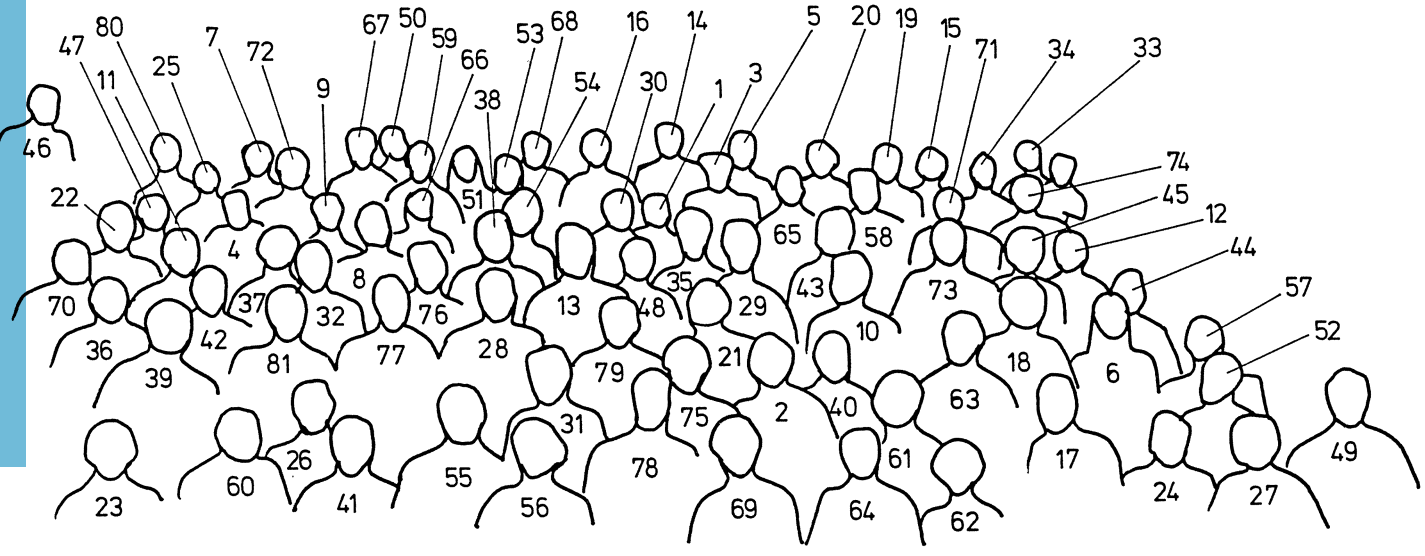

1. Ariaratnam
2. Bajkowski
3. Beletzky
4. Benedettini
5. Bestle
6. Boehm
7. Bournaski
8. Brauchli
9. Brindley
10. van Campen
11. Chen
12. Chernousko
13. Cheshankov
14. Crandall
15. Crandall, P.E.
16. Cusumano
17. Eiber
18. El Naschie
19. Eppler
20. Eppler, G.
21. Fritzen
22. Gabrielli
23. Gabrielli, B.
24. Guttalu
25. Higuchi
26. Hirai
27. Hsu
28. Ibrahim
29. Iooss
30. Isomäki
31. Kleczka
32. de Kraker
33. Kreuzer
34. Kreuzer, E.
35. Kunert
36. Kurnik
37. Lamarque
38. Lefeber
39. Müller
40. Narayanan
41. Nayfeh
42. Nocilla
43. Pfeiffer
44. Plaut
45. Popp
46. Purwins
47. Read
48. Rega
49. Reithmeier
50. Schiehlen
51. Schiehlen, Ch.
52. Schmidt
53. Seisl
54. Sethna
55. Shaw
56. Shaw, J.
57. Springer
58. Stein
59. Steindl
60. Stelter
61. Takahashi
62. Takahashi, H.
63. Thompson
64. Thompson, M.
65. Troger
66. Unmuth, I.
67. Valkering
68. Virgin
69. Weber
70. Wedig
71. Wedig, S.
72. Wilmers
73. Wu
74. Xie
75. Daberkow
76. Eismann
77. Kleczka, W.
78. Krause
79. Leister
80. Leukhardt
81. Schirm

Opening Address

W. Schiehlen, Chairman

Mr. Vice-Rector,
Mr. Ministerial Counsellor,
Highly Honoured Guests,
Dear Colleagues from so many countries.

On behalf of the International Union of Theoretical and Applied Mechanics I call this meeting to order, and in the name of the Local Organizing Committee I welcome you to the Symposium on Nonlinear Dynamics in Engineering Systems.

The logo of our Symposium is called the "Bird of Paradise". This colourful "Bird" is a typical example for the strange attractor of a nonlinear discrete system featuring chaotic behavior. You have to imagine that the computation of the "Bird" requires 5 millions of iterations. And the colours ranging from red over yellow and green to blue indicate a decreasing probability for the state of the system. Such highly sophisticated computer simulations are one face of Nonlinear Dynamics. The other faces are applied mathematics, theoretical mechanics and experimental physics. Many of the scientific results could only be discovered by the fertilizing cooperation between mathematicians and physicists. However, the mathematical theory is not within the scope of this Symposium, it is devoted to numerical methods for super computers and engineering applications.

There is a broad range of Nonlinear Dynamics problems in technical sciences. For example, the knots of a rope springing up during unfolding is nothing else than spatial chaos in an elastic continuum. The bifurcation and loss of stability of a nonlinear dynamical system may result, as another example, in the derailment of a railway vehicle. Grating beams or squeaking doors, respectively, cannot be analyzed without methods from Nonlinear Dynamics.

It is typical for such nonlinear dynamical problems that a failure of predictability of their motion may occur. In particular, Nonlinear Dynamics has very recently demonstrated that mechanical systems do not necessarily exhibit the predictability property well accepted in classical mechanics over three hundred years. The deterministic irregular motion, often called chaotic, and the stochastic motion of a dynamical system are closely related. Therefore, in the scope of our Symposium nonlinear random phenomena are also included.

What are the detailed topics of our Symposium? About 50 papers will be presented within two Poster-Discussion Sessions and twelve Lecture Sessions all of them guided by two Chairmen. The general topics are as follows:

- Dynamic structural engineering problems, including buckling and nonconservative phenomena,
- Analysis of nonlinear dynamic systems, especially by computer methods like cell mapping,

- Bifurcation Problems, featuring the global system behavior,
- Chaotic Dynamics and Control Problems with application to flexible robots,
- Experimental and Theoretical Investigations of resonance phenomena,
- Chaotic Oscillations of Engineering Systems, that means we are interested in the diagnosis or supression of chaos in engineering applications,
- Characterization of Nonlinear Dynamic Systems by fractals known from mathematics, and other criteria,
- Nonlinear Stochastic Systems, including simulation, stability, and application in offshore engineering.

After this survey on the scientific aspects of the Symposium let me speak on our sponsoring organization the International Union of Theoretical and Applied Mechanics, abbreviated as IUTAM. At the time being, IUTAM is the scientific umbrella organization of 38 national adhering organizations, one of which is the "Deutsches Komitee für Mechanik" representing the Federal Republic of Germany. The General Assembly of IUTAM, a body of nearly one hundred leading scientists from all over the world, approved this Symposium in 1986 in London. A Scientific Committee of highest international reputation was appointed, responsible for the scientific programme. It is my pleasure to report that all members of the Scientific Committee except one are present and that the Committee will continue its devoted service for the Symposium during this week.

In 1967, exactly twentytwo years ago, the first IUTAM Symposium was held in Stuttgart under the chairmanship of Professor Ekkehart Kröner. This first Symposium was devoted to the "Generalized Cosserat Continuum and the Continuum Theory of Dislocations with Applications". Twelve years later in 1979 the second IUTAM Symposium took place in Stuttgart. Professor Richard Eppler was chairman of the Symposium on "Laminar–Turbulent Transition". Thus, in a quarter of a century altogether three IUTAM Symposia were held at the University of Stuttgart in all the major fields which are Solid mechanics, Fluid mechanics and Dynamics.

But there are also other relations between the University of Stuttgart and IUTAM. From 1950 to 1963 Professor Richard Grammel of Stuttgart represented his country in IUTAM's General Assembly. Since 1984 I am serving myself as the Union's Secretary–General. And 1987 the annual Bureau meeting of IUTAM was held in Stuttgart including a visit of Kepler's birthplace in the nearby city of Weil der Stadt, one of the roots of mechanics as a science.

Last but not least I would like to thank all sponsors of this Symposium, namely, the University of Stuttgart and the State of Baden–Württemberg, the City of Stuttgart, and the industrial companies Robert Bosch, Stuttgart, Daimler Benz Corporation, Stuttgart, and M.A.N. Technology, Munich.

And very personally, I express my gratitude to all my co–workers of the Institute B of Mechanics for their devoted and engaged work. This work started more than one year ago and culminated last week. Especially, I would like to mention Professor Kreuzer who left the Institute to be a Professor at the Technical University Hamburg–Harburg. But even from this distance, Professor Kreuzer contributed much to the preparation

of the Symposium. If you have any problem, please feel free to contact anybody of the Institute's staff, indicated by yellow dots on the name tag.

So, I wish you that this Symposium may stimulate and satisfy your scientific interests and offer you many opportunities to personal contacts with scientists from more than 20 countries active in Nonlinear Applied Dynamics. I thank you.

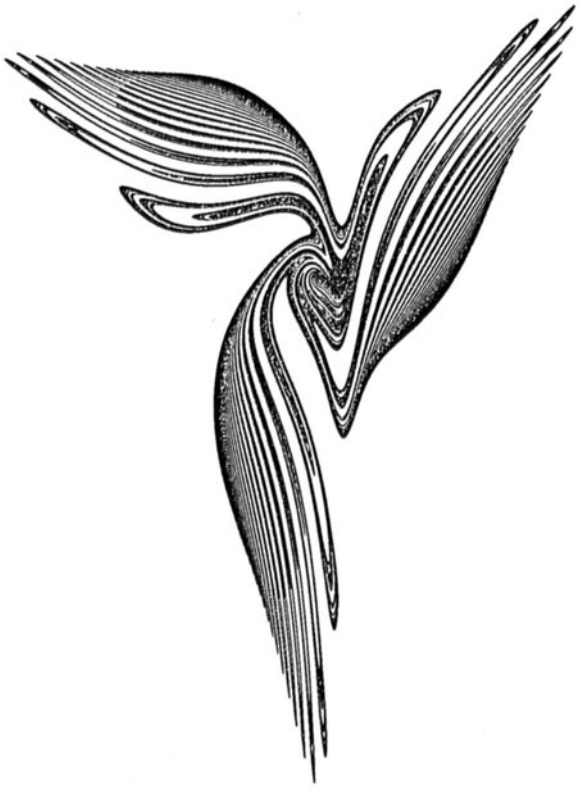

Logo of the Symposium

Lyapunov Exponents and Stochastic Bifurcations

S. T. Ariaratnam and **Wei Chau Xie**,
Solid Mechanics Division,
Faculty of Engineering, University of Waterloo,
Waterloo, Ontario, Canada, N2L 3G1.

Summary

The influence of stochastic perturbations on the bifurcational behaviour of dynamical systems commonly occurring in engineering mechanics is studied. Two types of bifurcation are discussed, namely pitchfork bifurcation and Hopf bifurcation. The results are applied to examples in the dynamic stability of elastic systems.

1. Introduction

The paper investigates the influence of stochastic perturbations on the bifurcational behaviour of dynamical systems that exhibit pitchfork and Hopf bifurcations. Most studies of nonlinear stochastic dynamical systems have dealt with the case when the systems are externally excited. However, in problems of bifurcation the excitation appears in the form of a coefficient or a parameter in the governing equations of motion. The stochastic stability of such a system is governed by the sign of the largest Lyapunov exponent of the corresponding linearized system. The Lyapunov exponents are related to the average exponential rate of growth or decay of the response of the system. When all the Lyapunov exponents are negative, the trivial solution is stable with probability 1 (w.p.1); if the largest Lyapunov exponent is positive, the trivial solution of the system loses its stability, implying that the vanishing of the largest Lyapunov exponent is an indication of a bifurcation or a change in the nature of the response.

In nonlinear systems it is of interest to study the steady-state solutions in the vicinity of bifurcation. When the parameter of the system fluctuates, the analogue of the steady-state solution is the stationary solution in the stochastic case. The following questions will be examined in this paper: (1) What does bifurcation mean in stochastic systems? (2) Does the bifurcation point shift and in which direction as a result of stochastic perturbations? (3) What is the form of the bifurcating solution?

Two examples of stochastic bifurcations commonly arising in problems in the dynamic stability of elastic systems will be illustrated in the following.

W. Schiehlen (Editor)
Nonlinear Dynamics in Engineering Systems
IUTAM Symposium Stuttgart/Germany 1989

2. Stochastic Pitchfork Bifurcation

The basic system considered is governed by a nonlinear differential equation of the form

$$\ddot{y} + 2\beta\dot{y} - \gamma' y + \alpha y^3 = 0, \quad \alpha, \beta > 0, \tag{2.1}$$

in which γ' is the dimensionless bifurcation parameter. As γ' changes from negative to positive values, the system undergoes a pitch-fork bifurcation from the stable trivial state $\mathbf{y}=\mathbf{0}$. When the parameter γ' is perturbed by a stochastic process, the equation governing the motion of the perturbed system will be of the form:

$$\ddot{y} + 2\beta\dot{y} - [\gamma' + \sigma\xi(t)]y + \alpha y^3 = 0, \tag{2.2}$$

where $\xi(t)$ is taken to be a 'unit' white Gaussian noise process. Examples of this equation are found in many applications in mechanics, particularly in problems of dynamical stability of elastic systems. In particular, the transverse vibrations of columns or flat plates under axial loading or end displacement are governed by equation (2.2).

2.1 Lyapunov Exponent

To examine the stochastic stability of the trivial solution, it is necessary to determine the variation of the largest Lyapunov exponent λ_y of the linearized system

$$\ddot{y} + 2\beta\dot{y} - [\gamma' + \sigma\xi(t)]y = 0. \tag{2.3}$$

Applying the transformation $y = \exp\{-\beta t\}x$, equation (2.3) becomes

$$\ddot{x} + [\gamma - \sigma\xi(t)]x = 0, \tag{2.4}$$

or, in the form of a pair of Itô equations,

$$dx_1 = x_2 dt, \quad dx_2 = -\gamma x_1 dt + \sigma x_1 dW, \tag{2.5}$$

where $\gamma = -\gamma' - \beta^2$, $W(t)$ is a 'unit' Wiener process. The Lyapunov exponents of systems (2.3) and (2.5) have the relationship $\lambda_y = -\beta + \lambda_x$. The Lyapunov exponent of system (2.5) is defined by

$$\lambda_x = \lim_{t\to\infty} \frac{1}{t} \log[\,|x_1(t)|^2 + |x_2(t)|^2]^{1/2}. \tag{2.6}$$

By setting $s_1 = x_1/\|\mathbf{x}\| = \cos\phi$, $s_2 = x_2/\|\mathbf{x}\| = \sin\phi$, $\|\mathbf{x}\| = (x_1^2 + x_2^2)^{1/2}$, and employing a well-known procedure due to Khas'minskii [1], the largest Lyapunov exponent is given by

$$\lambda_x = E[Q(s)] = \int_0^{2\pi} Q[s(\phi)]\, \mu(\phi) d\phi, \tag{2.7}$$

where $Q[s(\phi)] = (1-\gamma)\sin\phi\cos\phi + \frac{\sigma^2}{2}\cos^2\phi\cos 2\phi$. $\mu(\phi)$ is the density of the invariant

measure of the process $\phi(t)$ with respect to the uniform measure on the circle and is the solution of the Fokker-Planck equation associated with the $\phi(t)$—process. The largest Lyapunov exponent λ_x is found to be

$$\lambda_x = \frac{\int_{-\infty}^{+\infty}\left[\frac{(1-\gamma)u}{1+u^2}+\frac{\sigma^2}{2}\frac{1-u^2}{(1+u^2)^2}\right]\exp\left[-\frac{2}{3\sigma^2}(3\gamma u+u^3)\right]du \int_{-\infty}^{u}\exp\left[\frac{2}{3\sigma^2}(3\gamma v+v^3)\right]dv}{\int_{-\infty}^{+\infty}\exp\left[-\frac{2}{3\sigma^2}(3\gamma u+u^3)\right]du \int_{-\infty}^{u}\exp\left[\frac{2}{3\sigma^2}(3\gamma v+v^3)\right]dv} \tag{2.8}$$

Explicit evaluation of this integral does not seem feasible. Applying methods for asymptotic evaluation of integrals (Copson [2], Hsu [3]), it can be shown that, as $\sigma \to 0$,

$$\lambda_x = \frac{\sigma^2}{2(\sqrt{\gamma}+1)^2}, \quad \gamma>0; \qquad \lambda_x = \sqrt{-\gamma} + \frac{\sigma^2}{2}\frac{1+\gamma}{(1-\gamma)^2}, \quad \gamma<0. \tag{2.9}$$

When $\gamma=0$, equation (2.8) can be evaluated directly and the exact value of the largest Lyapunov exponent is $\lambda_x = 0.28931\sigma^{2/3}$, a result similar to that of Pinsky and Wihstutz [4].

Numerical values of λ_x were calculated from (2.8) as γ changes from negative to positive values and are shown in Figure 1. The asymptotic results were found to agree well with the numerical results.

It can be seen easily that in the vicinity of $\gamma=0$, the stochastic perturbation destabilizes the system; thus, the value of γ' at which the trivial solution $\mathbf{y}=\mathbf{0}$ loses its stability shifts to the left for undamped or slightly damped systems.

2.2 Bifurcating Solution

In order to study the bifurcating solution, setting the energy $E=\dot{y}^2/2+u(y)$, where $u(y)=\int_0^y(\gamma' z+\alpha z^3)dz = \gamma' y^2/2+\alpha y^4/4$, one obtains in place of (2.2) the two fluctuation equations:

$$\dot{y} = \{2[E-u(y)]\}^{1/2}, \quad \dot{E} = -4\beta[E-u(y)]-\sigma y\{2[E-u(y)]\}^{1/2}\xi(t). \tag{2.10}$$

Let β, σ^2 be $O(\epsilon)$. Then method of stochastic averaging (Khas'minskii [5]) may be applied to (2.10) and the averaged equation for E becomes

$$dE = m_E dt + \sigma_E dW, \tag{2.11}$$

where

$$m_E = \frac{1}{W(E)}\int_R\left\{-4\beta[E-u(y)]^{1/2} + \frac{\sigma^2}{2}\frac{y^2}{[E-u(y)]^{1/2}}\right\}dy,$$

$$\sigma_E = \left\{\frac{1}{W(E)}\int_R 2\sigma^2 y^2[E-u(y)]^{1/2}dy\right\}^{1/2}, \quad W(E) = \int_R \frac{dy}{[E-u(y)]^{1/2}}.$$

The region R of integration includes all values of y for which $E \geq u(y)$.

The stationary probability distribution $p(E)$ is governed by the associated Fokker-Planck equation and is found to be given by

$$p(E) = \frac{C}{\sigma_E^2} \exp\left\{2 \int_{E_1}^{E} \frac{M_E(z)}{\sigma_E^2(z)} dz\right\}, \tag{2.12}$$

where C is determined by the usual normalization condition.

Equation (2.12) was first evaluated numerically for different values of γ' to obtain the energy distribution. An interpolation algorithm was then applied to evaluate numerically the location of the centroid of the energy distribution that is given in the form of discrete points. The results for the mean energy are plotted in Figure 2, in analogy with the deterministic case. It may be noted that the stochastic bifurcation points for the nonlinear system (2.2), namely the points where the mean energy of the system becomes nonzero, are to the left of the points where the trivial solution loses stability w.p.1. This is due to the fact that the mean energy $\overline{E}$ contains the second and fourth moments of the response of the system (2.2), which are more unstable than the sample solution of the linearized system (Kozin and Sugimoto [6]).

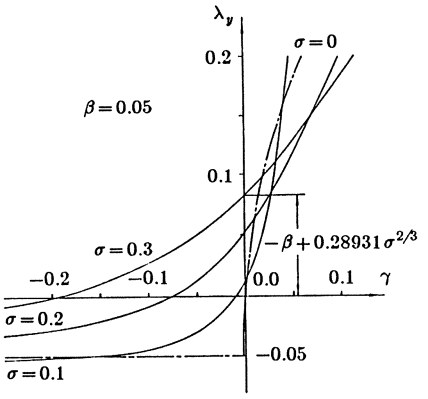

Fig. 1 Lyapunov exponent λ_y vs γ
$\ddot{y}+2\beta\dot{y}-[\gamma'+\sigma\xi(t)]y=0$

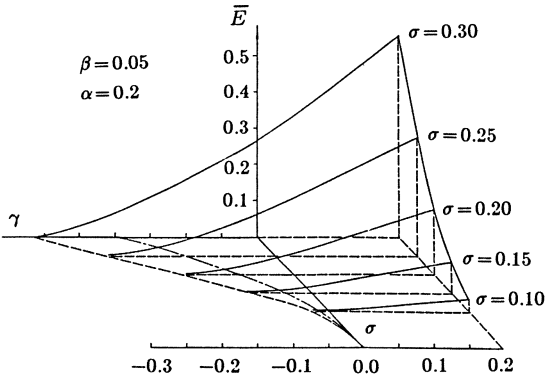

Fig. 2 Bifurcation diagram
- - - - - - - - Locus of points for which $\lambda_y=0$
———— Locus of points of stochastic bifurcation

3. Stochastic Hopf Bifurcation

A typical system exhibiting Hopf bifurcation may be described by the differential equation:

$$\ddot{x} + [\beta+\sigma\xi(t)]\dot{x} + x = f(x,\dot{x},\xi(t)), \tag{3.1}$$

where $\xi(t)$ is a 'unit' Gaussian white noise, $f(x,\dot{x},\xi(t))$ a nonlinear function, and β is the bifurcation parameter. For example, the vibration of transmission cables, suspension bridges and buildings under the turbulent wind loads is governed by equation (3.1) (Blevins [7]) with

$$f(x,\dot{x},\xi(t)) = \sum_{k=1}^{n} [A_{2k+1}+\alpha_{2k+1}\sigma\xi(t)]\,\dot{x}^{2k+1}.$$

3.1 Lyapunov Exponent

The linearized equation of motion is

$$\ddot{x} + [\beta+\sigma\xi(t)]\dot{x} + x = 0. \tag{3.2}$$

or, in the form of the Stratonovich stochastic differential equation,

$$d^*x_1 = x_2 dt, \quad d^*x_2 = -(x_1+\beta x_2)dt - \sigma x_2 dW, \tag{3.3}$$

where $d^*(\,)$ denotes the differential in the Stratonovich sense. The equivalent Itô equations are:

$$dx_1 = x_2 dt, \quad dx_2 = -[x_1-(\sigma^2/2-\beta)x_2]\,dt - \sigma x_2 dW. \tag{3.4}$$

For this system, following a procedure similar to that described in section 2, the largest Lyapunov exponent is found to be given by

$$\lambda = \frac{\int_{-\infty}^{0} \frac{P(u)}{f(u)} e^{-\nu h(u)}du \int_{-\infty}^{u} f(v)e^{\nu h(v)}dv + \int_{0}^{+\infty} \frac{P(u)}{f(u)} e^{-\nu h(u)}du \int_{0}^{u} f(v)e^{\nu h(v)}dv}{\int_{-\infty}^{0} \frac{1}{f(u)} e^{-\nu h(u)}du \int_{-\infty}^{u} f(v)e^{\nu h(v)}dv + \int_{0}^{+\infty} \frac{1}{f(u)} e^{-\nu h(u)}du \int_{0}^{u} f(v)e^{\nu h(v)}dv}, \tag{3.5}$$

where

$$\nu = \frac{2}{\sigma^2}, \qquad h(u) = u - \frac{1}{u}, \qquad f(u) = u^{\frac{2\beta-\sigma^2}{\sigma^2}}, \qquad P(u) = \frac{1}{1+u^2}\left(\frac{\sigma^2}{1+u^2}-\beta\right).$$

Asymptotic evaluation by the Laplace method gives

$$\lambda = -\beta/2 + \sigma^2/8, \qquad \text{as } \sigma \to 0. \tag{3.6}$$

It is obvious that the stochastic perturbation destabilizes the system.

3.2 Bifurcating Solutions

The nonlinear system considered is of the form:

$$\ddot{x} + [\beta+\sigma\xi(t)]\dot{x} + x = \sum_{k=1}^{n} [A_{2k+1}+\alpha_{2k+1}\sigma\xi(t)]\,\dot{x}^{2k+1}. \tag{3.7}$$

The transformation $x = a\sin\theta$, $\dot{x} = a\cos\theta$, $\theta = t+\phi$, results in

$$\dot{a} = a\cos^2\theta\Big[-\beta + \sum_{k=1}^{n} A_{2k+1}a^{2k}\cos^{2k}\theta + \Big(-1+\sum_{k=1}^{n}\alpha_{2k+1}a^{2k}\cos^{2k}\theta\Big)\,\sigma\xi(t)\Big],$$
$$\dot{\phi} = \cos\theta\sin\theta\Big[\,\beta - \sum_{k=1}^{n} A_{2k+1}a^{2k}\cos^{2k}\theta + \Big(1-\sum_{k=1}^{n}\alpha_{2k+1}a^{2k}\cos^{2k}\theta\Big)\,\sigma\xi(t)\Big]. \tag{3.8}$$

Let A_{2k+1}, α_{2k+1}, β, σ^2 be $O(\epsilon)$. Applying stochastic averaging leads to the Itô equations:

$$da = m_a\,dt + \Sigma_{aa}\,dW_1 + \Sigma_{a\phi}\,dW_2,$$
$$d\phi = m_\phi\,dt + \Sigma_{\phi a}\,dW_1 + \Sigma_{\phi\phi}\,dW_2, \tag{3.9}$$

It can be shown that the equation for a is decoupled from that for ϕ, and the first equation is equivalent to

$$da = m_a\,dt + \Sigma_a\,dW, \tag{3.10}$$

where

$$m_a = \hat{A}_1 a + \sum_{k=1}^{n} a^{2k+1}\big[\hat{A}_{2k+1} + B_1(k)\sigma^2 a^{2k} - B_2(k)\sigma^2\big],$$

$$\Sigma_a^2 = \frac{1}{8}\sigma^2 a^2 + \sum_{k=1}^{n}\sigma^2 a^{2k+2}\big[S_1(k)a^{2k} - S_2(k)\big]\,,$$

$$\hat{A}_{2k+1} = \frac{A_{2k+1}}{4^{k+1}}\binom{2k+2}{k+1}, \qquad \hat{A}_1 = \frac{3}{16}\sigma^2 - \frac{1}{2}\beta,$$

$$B_1(k) = \frac{\alpha_{2k+1}^2}{16^{k+1}}\Big\{(2k+1)\sum_{i=0}^{k}\binom{2k+2}{i}^2 + 2(k+1)\Big[\sum_{i=0}^{k}\Big[1+\binom{2k+1}{i}^2\Big] - 2\sum_{i=0}^{k-1}\binom{2k+1}{i+1}\Big]\Big\}\,,$$

$$B_2(k) = \frac{2\alpha_{2k+1}}{4^{k+2}}\Big[(k+1)\binom{2k+2}{k} + 2\binom{2k+1}{k}\Big]\,,$$

$$S_1(k) = \frac{\alpha_{2k+1}^2}{2^{4k+3}}\sum_{i=0}^{k}\binom{2k+2}{i}^2, \qquad S_2(k) = \frac{\alpha_{2k+1}}{4^{k+1}}\binom{2k+2}{k}, \qquad \binom{n}{k} = \frac{n!}{k!(n-k)!}.$$

Setting $\rho = \ln|a| = \ln\|\mathbf{x}\|$ and applying Itô's Lemma results in

$$d\rho = m_\rho\,dt + \frac{1}{a}\Sigma_a\,dW, \tag{3.11}$$

where

$$m_\rho = \Big(\hat{A}_1 - \frac{1}{16}\sigma^2\Big) + \sum_{k=1}^{n}\Big\{\Big[B_1(k) - \frac{S_1(k)}{2}\Big]\sigma^2 e^{4k\rho} + \Big[\hat{A}_{2k+1} - \sigma^2 B_2(k) - \frac{\sigma^2}{2}S_2(k)\Big]e^{2k\rho}\Big\}.$$

The Lyapunov exponent of the system is given by the coefficient of the dt term in the linearized form, i.e. $\lambda = -\beta/2 + \sigma^2/8$, which is the same as that obtained above.

The steady state probability distribution $p(a)$ satisfies the Fokker-Planck equation associated with (3.11) and is given by

$$p(a) = \frac{C}{\Sigma_a^2} \exp\left\{2 \int_{a_1}^{a} \frac{m_a(u)}{\Sigma_a^2(u)} du\right\} \tag{3.12}$$

The most probable amplitude $\hat{a}$ is obtained from the equation

$$\sum_{k=1}^{n} \{[B_1(k)-(2k+1)S_1(k)]\sigma^2 a^{4k} + \{\hat{A}_{2k+1} + [(k+1)S_2(k)-B_2(k)]\sigma^2\} a^{2k}\} + \frac{1}{2}\left(\frac{\sigma^2}{8}-\beta\right)=0.$$

When the effect of stochastic perturbation in only the linear term is considered, $\alpha_{2k+1}=0$ for $k=1,2,\cdots,n$. If the effect of stochastic perturbation in both linear and nonlinear terms is taken into account, α_{2k+1} is usually of the form $\alpha_{2k+1}=2k-1$ in the study of the wind induced vibration of transmission cables. For both cases the diagrams of stochastic bifurcation are plotted in Figures 3-4 for $n=2$, 3.

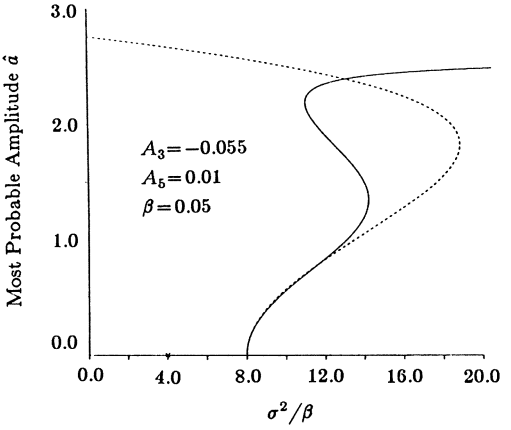

Fig. 3 Stochastic bifurcation diagram

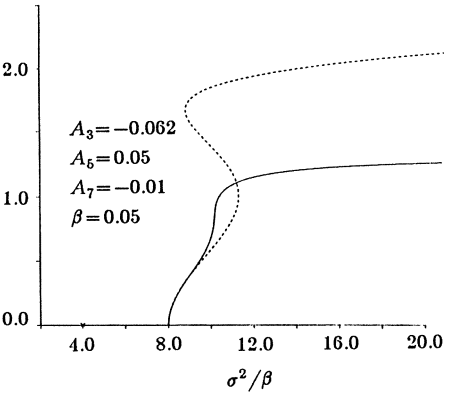

Fig. 4 Stochastic bifurcation diagram

- - - - - - - $\alpha_{2k+1}=0$
——— $\alpha_{2k+1}=2k-1$

From the above results, the following observations can be made:

(1) When $\sigma^2 \leq 4\beta$, $\lambda_{\max} \leq 0$, therefore $p(a)=\delta(a)$.

(2) When $4\beta<\sigma^2<8\beta$, $\lambda_{\max}>0$, the trivial solution is unstable w.p.1, $p(a)$ is a hyperbola-like function, and the most probable amplitude is 0;

(3) When $\sigma^2>8\beta$, the most probable amplitude $\hat{a}$ becomes nonzero and can be observed. From the physical point of view, the Hopf bifurcation of the parametrically perturbed stochastic system takes place at $\sigma^2=8\beta$;

(4) When $\sigma^2 > 8\beta$, for $n=3$ and some values of nonlinear coefficients, the $p(a)$ curve can have two peaks, i.e. $p(a)$ becomes a bimodal function and has two most significant most probable values;

(5) For $n=2$, $A_3<0$, $A_5>0$, the nonlinear system is unstable in probability near the bifurcation point when only the effect of stochastic perturbation in the linear term is considered. However, if the effect of stochastic perturbation in both linear and nonlinear terms is taken into account, the nonlinear system is stable. Therefore, the stochastic perturbation in nonlinear terms stabilizes the system, which is true for other values of n and nonlinear coefficients as well;

(6) For $n=2$ and when the coefficient of stochastic perturbation in nonlinear terms is considered, $p(a)$ can also have two significant most probable values. This is due to the fact that the parametric stochastic perturbation in the nonlinear terms introduces a correction term $0.5 f(a,\phi)\partial f(a,\phi)/\partial a$ into the system equation. This is a noise-induced phenomenon and cannot be observed in the deterministic case. This phenomenon indicates that the stochastic perturbation in the system, although small in magnitude, can change the behaviour of the system qualitatively. The result is of practical importance in stochastic modelling. In order to model certain properities of a system properly, the nonlinear terms of the system considered can be much simplified if the effect of stochastic perturbation is taken into account.

Acknowledgement

This research was supported by the National Sciences and Engineering Research Council of Canada through grant A-1815.

References

1. Khas'minskii, R.Z.: Necessary and sufficient conditions for the asymptotic stability of linear stochastic systems. *Theory of Probability and Its Applications.* **12** (1967) 144-147.
2. Copson, E.T.: *Asymptotic Expansions.* Cambridge University Press 1965.
3. Hsu, L.C.: A theorem on the asymptotic behaviour of a multiple integral. *Duke Mathematical Journal.* **15** (1948) 623-632.
4. Pinsky, M.A.; Wihstutz, V.: Lyapunov exponents of nilpotent Itô systems. *Stochastics.* **25** (1988) 43-57.
5. Khas'minskii, R.Z.: The averaging principle for stochastic differential equations. *Problemy Peredachi Informatsii.* **4** (1968) 86-87, (English translation).
6. Kozin, F.; Sugimoto, S.: Relations between sample and moment stability for linear stochastic differential equations. *Proceedings of the Conference on Stochastic Differential Equations and Applications.* Ed: J. David Mason. New York: Academic Press 1977.
7. Blevins, R.D.: *Flow-Induced Vibration.* New York:Van Nostrand Reinhold Company 1977.

Liapunov Stability Analysis for Control of Flexible Manipulators

S. Arimoto*), H.G.Lee**), and F.Miyazaki**)

*) Dept. of Mathematical Engineering and Instrumentation Physics, Fac. of Engineering, Univ. of Tokyo, Tokyo, 113 Japan

**) Dept. of Mechanical Engineering, Fac. of Engineering Science, Osaka University, Osaka, 560 Japan

Summary

A mathematical model of the dynamics of a multi-link flexible manipulator is derived by using Hamilton's principle. It is described by a bundle of nonlinear coupled partial differential equations with nonhomogeneous natural and geometric boundary conditions. Application of Galerkin's modal expansion method for this model yields a nonlinear lumped-parameter differential equation with finitely large or infinite dimension including centrifugal and Coriolis forces. Stability of PD and PDS(PD + Strain) feedback control schemes is discussed on the basis of Liapunov's method applied for the lumped - parameter model.

Modelling of Flexible multi-link Manipulator

Suppose that a manipulator is composed of p flexible links and p rotary joints and moves in three dimensional space without gravitational effect, for simplicity. Rigid-body motion and elastic behaviors are controlled simultaneously by only DC motors which are located at each joint. It is assumed that each joint is rigid and can be considered to be a concentrated mass as well as the end effector, and the root of each link is attached to the joint axis. The local coordinates for link i is defined as $x_i y_i z_i$ shown in Fig.1, that is, the origin of link i is set up at the center of joint i, the trangential line at the root of link i is in x_i direction, the rotational axis of joint i is z_i, and the axis orthogonal to $x_i z_i$ plane is y_i. It is also assumed that each link is a slender beam with symmetric cross section, its elastic deformation is small, and the longitudinal deformation can be negligible. These assumptions have been generally accepted in the case of small oscillation.

W. Schiehlen (Editor)
Nonlinear Dynamics in Engineering Systems
IUTAM Symposium Stuttgart/Germany 1989

After an elastic deformation, the position vector of a nominal point S on the center line of link i in terms of local coordinates $x_i y_i z_i$ can be expressed by using Denavit-Hartenberg's description

$$ {}^{i}r = [x_i, v_i(x_i t), w_i(x_i, t)]^T $$

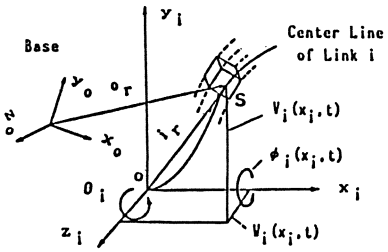

Fig.1 Coordinates system for flexible multi-link manipulator

where $v_i(x_i,t)$ and $w_i(x_i,t)$ are deflections in y_i and z_i directions at point x_i and time t respectively. Symbol "T" means transpose. Furthermore, the position of S in terms of the fixed coordinates $x_o y_o z_o$ shown in Fig. 1 can be expressed by using the transformation matrix ${}^{o}A_i$ defined by the following way:

$$ {}^{o}r = {}^{o}A_i \, {}^{i}r, \quad {}^{o}A_i = {}^{o}A_1 \, {}^{1}A_2 \cdots {}^{i-1}A_i, $$

$$ \begin{aligned} {}^{j-i}A_j = {} & \mathrm{Trans}[L_{j-1}, v_{j-1}(L_{j-1},t), w_{j-1}(L_{j-1},t)] \\ & \times \mathrm{Rot}[z, v'_{j-1}(L_{j-1},t)] \times \mathrm{Rot}[y, -w'_{j-1}(L_{j-1},t)] \\ & \times \mathrm{Rot}[x, \phi_{j-1}(L_{j-1},t)] \times \mathrm{Rot}[\alpha, \phi_j] \\ & \times \mathrm{Rot}[z, \theta_j], \quad \text{for } j = 1,2,\cdots, p, \end{aligned} \tag{1} $$

where θ_j, L_j, and $\phi_j(L_j,t)$ are relative rotational angle of joint j, the length of link j, and the torsional angle about axis x_j respectively. The prime symbol means differentiation with respct to x_j, and $\mathrm{Rot}[\alpha,\phi_j]$ is a transformation for the structual configuration of joint-link fittings, in which α is generally one of x_j, y_j, z_j, and ϕ_j is either 0 or 90 degree. It should be noted that, unlike a rigid manipulator, these transformations include the elastic deformations at the end of each link. In eq. (1), the order of the rotational transformations due to elastic deformation is changeable, because of small displacements.

The velocity of point S is given by

$$ {}^{o}\dot{r} = {}^{o}\dot{A}_i \, {}^{i}r + {}^{o}A_i \, {}^{i}\dot{r}, \tag{2} $$

and the kinetic energy of link i is described as

$$ K_i = \int_o^{L_i} \Gamma_i(x_i)\, dx_i, \quad \Gamma_i(x_i) = \frac{1}{2}\sigma(x_i)\, {}^{o}\dot{r}^T \, {}^{o}\dot{r} \tag{3} $$

where $\sigma(x_i)$ and Γ_i denote the distributed mass and the unit kinetic energy function respectively. The potential energy due to the elastic deformation of link i is given by

$$ V_i = \frac{1}{2}\int_o^{L_i} \{EI_z(x_i)(v''_i(x_i))^2 + EI_y(x_i)(w''_i(x_i))^2 + GJ(x_i)(\phi'_i(x_i))^2\} dx_i \tag{4} $$

where EI_z, EI_y, and GJ are bending stiffness of z_i, y_i direction, and torsional stiffness, respectively. Therefore, the total kinetic energy and the total potential energy are expressed as follows:

$$ K = \sum_{i=1}^{p} K_i, \qquad V = \sum_{i=1}^{p} V_i \tag{5} $$

On the other hand, virtual work for external torque τ_i is

$$ \delta W = \sum_{i=1}^{p} \tau_i \delta\theta_i \tag{6} $$

Hamilton's principle for energy equations described above and geometric boundary conditions determined by definition of local coordinates [1] are expressed by the forms

$$ \int_{t_1}^{t_2} \delta(K - V + W)\, dt = 0, \tag{7} $$

$$ v_i(0,t) = v'_i(0,t) = 0, \; w_i(0,t) = w'_i(0,t) = 0, \; \phi_i(0,t) = 0, \tag{8} $$

which yield the following variational equations

for $i = 1,2,\cdots,p$:

$$\int_0^{L_i} [Mv_i + E(I_z v''_i)'']\delta v_i dx_i = 0, \tag{9.1}$$

$$[Fv_i(L_i,t) - E(I_z v''_i(L_i,t))']\delta v_i(L_i,t) = 0, \tag{9.2}$$

$$[Fv'_i(L_i,t) + E(I_z v''_i(L_i,t))]\delta v'_i(L_i,t) = 0, \tag{9.3}$$

$$[F\theta_i - \tau_i]\,\delta\theta_i = 0, \tag{9.4}$$

$$\int_0^{L_i} [Mw_i + E(I_y w''_i)'']\delta w_i dx_i = 0, \tag{10.1}$$

$$[Fw_i(L_i,t) - E(I_y w''_i(L_i,t))']\delta w_i(L_i,t) = 0, \tag{10.2}$$

$$[Fw'_i(L_i,t) + E(I_y w''_i(L_i,t))]\,\delta w'_i(L_i,t) = 0, \tag{10.3}$$

$$\int_0^{L_i} [M\phi_i + G(J\phi'_i)']\delta\phi_i dx_i = 0, \tag{11.1}$$

$$[F\phi_i(L_i,t) - G(J\phi'_i(L_i,t))]\delta\phi_i(L_i,t) = 0, \tag{11.2}$$

where

$$Fx_i = \frac{d}{dt}\left[\frac{\partial K}{\partial \dot{x}_i}\right] - \frac{\partial K}{\partial x_i}\ , \tag{12}$$

$$Mx_i = \frac{d}{dt}\left[\frac{\partial \Gamma_i}{\partial \dot{x}_i}\right] - \frac{\partial \Gamma_i}{\partial x_i}\ . \tag{13}$$

Since the values of variations are arbitrary, each coefficient term in the above equations must vanish. Hence, three nonlinear partial differential equations (NPDE) and their natural boundary conditions (NBC) for each link are obtained. They are one NPDE (9.1) and three NBC's (9.2-4) for bending around z, one NPDE (10.1) and two NBC's (10.2,3) for bending around y, and one NPDE (11.1) and one NBC (11.2) for torsion around x.

Galerkin's Modal Expansion

Since these derived NPDE's are nonlinear and coupled each other and NBC's are nonhomogeneous, it is hard to obtain analytical solutions. Even if these equations are linearized, it is also hard to obtain the eigenvalues and eigenvectors analytically. Hence, we must apply Galerkin's modal expansion method by expressing the elastic deformations of each link by

$$v_i(x_i,t) = \sum_{j=1}^{N} \xi_{ij}(x_i) q_{ij}(t) \tag{14.1}$$

$$w_i(x_i,t) = \sum_{j=1}^{N} \xi_{iN+j}(x_i) q_{iN+j}(t) \tag{14.2}$$

$$\phi_i(x_i,t) = \sum_{j=1}^{N} \xi_{i2N+j}(x_i) q_{i2N+j}(t) \tag{14.3}$$

for $0 \leqq x_i \leqq L_i (i=1,2,\ldots p)$, where $\xi_{ij}(x_i)$ are admissible functions satisfying all the geometric boundary conditions and differentiability on $0 \leqq x_i \leqq L_i$, $q_{ij}(t)$ are unknown modal functions, and N is a number of order sufficiently large so that this approximation is in effect.

Since the eigenfunctions of a clamped-free beam obviously satisfy the GBC's of eq.(8),it is acceptable to choose them as admissible functions. Therefore, by using eq.(14) and orthogonalities of eigenfunctions of the clamped-free beam, all of GBC's, NPDE's and NBC's derived above become a bundle of ordinary differential equations, i.e., a lumpled parameter model. This can be described in the following way, if structural damping terms for the elastic modes q_{ij} are taken into account:

$$R\ddot{x} + \dot{R}\dot{x} - \left(\frac{\partial K}{\partial x}\right) + D^*\dot{x} + \Omega^* x = Bu \tag{15}$$

where $x = [x_r^T, x_e^T]^T$, $x_r = [\theta_1,\ldots,\theta_p]^T$, $x_e = [q_{11},\ldots,q_{1\,3N},q_{p1},\ldots,q_{p\,3N}]^T$, $R(x) = R^T(x) > 0$, $\Omega^* = \mathrm{diag}\,[0,\ldots,0,\Omega_{11}^2,\ldots,\Omega_{p\,3N}^2]$, $D^* = \mathrm{diag}[0,\ldots,0,d_{11},\ldots,d_{p\,3N}]$, $B = [I_p\ 0]^T$, and $u = [\tau_1,\ldots,\tau_p]^T$. Here, $K = \frac{1}{2}\dot{x}^T R(x)\dot{x}$ is the kinetic energy in the modal space form of eq.(5) and R(x) is the inertia matrix.

Ω_{ij}, $d_{ij} > 0$, and I_p are respectively eigenvalues for the considered clamped-free beam, coefficients of structural damping, and $p \times p$ unit matrix. Each matrix has an appropriate dimension corresponding to the state variable x.

PDS Control

The torque τ_i transmitted from the actuator (DC motor) to the root of link i can be described by

$$\tau_i = -J_{oi}\theta_i + \tau_{si} \tag{16}$$

where J_{oi} and τ_{si} are the inertia of each driving system and the generating torque of each actuator, in which the induced electromotive force and the friction force of driving system are included. The torque τ_i is balanced with the bending moment $M_i(0,t)$ around axis z_i at the root of link i, which implies

$$\tau_i = -M_i(0,t). \tag{17}$$

From the assumption of small elastic deformation, it follows that

$$-M_i(x,t)/EI_z = 1/\rho_{iz} = \varepsilon_i(x,t)/h_i \tag{18}$$

where ρ_{iz}, $\varepsilon_i(x,t)$, and h_i are a curvature due to bending, a strain on the link surface, and a distance in the direction of z_i from the center line of link i to the surface respectively. Therefore, if a strain gauge is attached to the root of link, the output can be described by

$$\varepsilon_i(0,t) = \gamma_i\tau_i. \tag{19}$$

We now consider the PDS control first introduced by one of the authors [2], which is composed of a conventional PD control and a feedback of strain detected at the root of the link. This is given by

$$\tau_{si} = -\alpha_i\varepsilon_i(0,t) + f_i, \quad i = 1,\ldots,p, \tag{20}$$

$$-f = -G_p(x_r - x_{rd}) - G_v\dot{x}_r. \tag{21}$$

The first term in the right hand side of eq.(20) represents the strain feedback and the second term does the PD control. x_{rd} is a desired position vector composed of rotational angles of joints.

Stability Analysis via Liapunov's Method

Theorem The closed-loop system with the PDS control described above is asymptotically stable, if

$$P > 0, \quad PG_p > 0, \quad PG_v > 0, \tag{22}$$

where

$$P = \mathrm{diag}[\beta_1, \ldots, \beta_p], \quad \beta_i = \frac{1}{1 + \alpha_i \gamma_i} \tag{23}$$

Proof It follows from eqs.(16),(19),(20), and (23) that

$$\tau_i = \beta_i [-J_{oi}\theta_i + f_i]. \tag{24}$$

Substitution of this into eq.(15) yields the closed-loop system

$$\bar{R}\ddot{x} + \dot{\bar{R}}\dot{x} - \left(\frac{\partial K}{\partial x}\right) + \bar{D}\dot{x} + \bar{\Omega}(x - x_d) = 0 \tag{25}$$

where $x_d = [x_{rd}^T, \ 0]^T$, $J_o = \mathrm{diag}[J_{o1}, \ldots, J_{op}] > 0$,

$\Omega = \mathrm{diag}[\Omega_{11}^2, \ldots, \Omega_{p3N}^2]$, $D = \mathrm{diag}[d_{11}, \ldots, d_{p3N}]$,

$\bar{D} = \begin{bmatrix} PG_v & 0 \\ 0 & D \end{bmatrix} > 0$, $\bar{\Omega} = \begin{bmatrix} PG_p & 0 \\ 0 & \Omega \end{bmatrix} > 0$, $\bar{R} = \begin{bmatrix} PJ_o & 0 \\ 0 & 0 \end{bmatrix} + R > 0$.

Now we introduce a candidate of Liapunov function[3]

$$L = \frac{1}{2}\{\dot{x}^T \bar{R}(x)\dot{x} + (x - x_d)^T \bar{\Omega}(x - x_d)\}. \tag{26}$$

After taking the derivative of L along the trajectories of eq. (25) and careful manipulation of resultant equations by refering to the relation (see [4])

$$\dot{x}^T \dot{\bar{R}}(x)\dot{x} = \dot{x}^T \frac{\partial}{\partial x}\{\dot{x}^T R(x)\dot{x}\},$$

we obtain

$$\dot{L} = -\dot{x}^T \bar{D}\dot{x} \leq 0 . \tag{27}$$

Then, it follows from LaSalle's theorem that the equilibrium point $[x = x_d, \ \dot{x} = 0]$ of eq.(25) is asymptotically stable.

It is evident from this proof that, since $\alpha_i = 0$ for all i implies $P = I_p$, the conventional PD control without use of the strain feedback is also asymptotically stable.

Remarks and Discussions

What kinds of effect in stabilization does strain feedback yield? To respond to this question, suppose that PD gains are taken to be large correspondingly to the strain feedback gains. That is, α_i are chosen to be large, diagonal components of P small, and those of G_p and G_v large so that PG_p and PG_v are fixed. Then PJ_o (a principal minor of $\bar{R}$) in the Liapunov function L of eq.(26) becomes small while $\bar{\Omega}$ and $\bar{D}$ in eq.(26) and eq.(27) respectively are fixed. This implies that a large remaining vibration (big $|\dot{x}_r|$ around $x_r = x_{rd}$) due to elastic vibrations contributes to mainly a certain decrease of the vibrational kinetic energy $(\dot{x}_e^T R\dot{x}_e)/2$ and the quadratic deviation $(x - x_d)^T\bar{\Omega}(x - x_d)/2$. In other words, strain feedback is effective in suppression of the elastic vibration and acceleration of the positioning stabilization. This is demonstrated by experimental results reported in our previous paper [5].

References

1. Lee,H.G.; Kanoh,H.; Kawamura,S.; Miyazaki,F.; Arimoto S.: Stability analysis of one-link flexible arm control by a linear feedback law. Proc. of IMACS/IFAC Int. Sym. DPS. Oct.(1987)

2. Kanoh,H.; Lee,H.G.; Vibration control of one-link flexible arm. Proc. of 24'th IEEE CDC. Dec. (1985)

3. Takegaki,M.; Arimoto.S.: A new feedback method for dynamic control of manipulators. Trans. ASME J. of DSMC.Vol.103 (1981) 119-125.

4. Arimoto,S.; Miyazaki, F.: Stability and robustness of PID feedback control for robot manipulators of sensory capability. in Robotics Research. First International Symposium. MIT Press (1984) 783-799.

5. Lee,H.G.; Arimoto, S.; Miyazaki, F.: Liapunov stability analysis for PDS control of flexible multi-link manipulators, Proc. of 27th IEEE CDC. Dec.(1988)

Nonlinear Effects in Dynamics of Controlled Two-legged Walking

V.V. BELETZKY

Keldysch Institute of Applied Mathematics
USSR Academy of Sciences
Miusskaya pl. 4, Moscow 123 047, USSR

Summary

Resonance of regular walking is evident: elements of a two–legged (or multi–legged) device oscillate in time with walking. In other words, oscillation frequencies of separate elements are commensurable with a basic frequency – the step frequency. Numerous studies of the two–legged walking process deal with describing mainly a regular periodic walking. However, in order to reveal specific nonlinear effects regular resonant walking should be analysed together with its nonresonant neighborhood. Some results of this analysis carried out by the author and his colleagues are discussed in this report.

Introduction

A nonlinear model of the periodic two–legged walking, which has in some sense the stability property, is constructed. The neighborhood of this stable periodic motion is considered within nonlinear formulations. In this neighborhood the walking is of a conditionally periodic or irregular chaotic nature. An integral characteristic of energy consumption for walking is introduced. It is shown that the energy functional has an extremum for the regular resonant walking. The extremum may be a minimum – then the periodic stable walking is more advantageous from the energy point of view in comparison with the irregular walking.

However, bifurcation of energy–advantageous methods of walking is possible when the system parameters are varied. The energy functional acquires a number of local maxima and minima. In this case, we may observe inconvenient and energy–unfavourable irregular gaits; convenient "comfortable" gaits but with a local energy maximum; and, finally, energy–advantageous , not necessarily convenient gaits with a local minimum.

W. Schiehlen (Editor)
Nonlinear Dynamics in Engineering Systems
IUTAM Symposium Stuttgart/Germany 1989

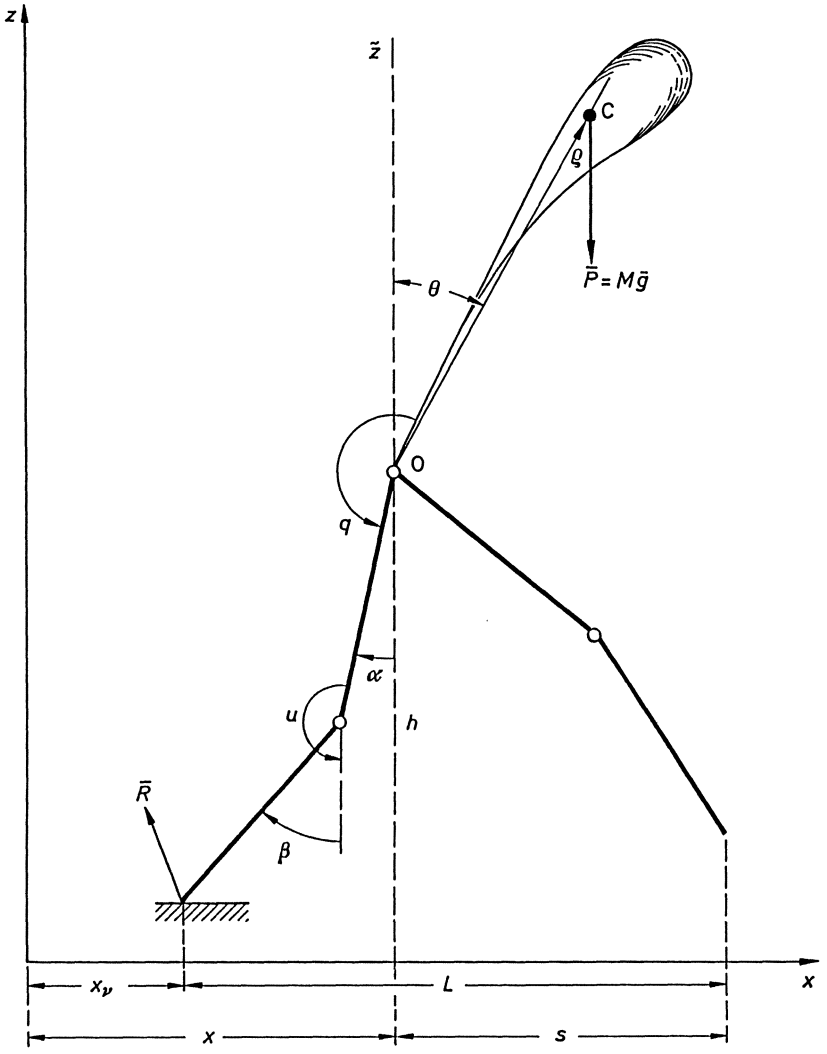

$\varrho = \overline{OC}; \quad \theta = \sphericalangle \text{ co } \tilde{z}$

Fig.1. Apparatus model: rigid body with two imponderable legs

Dynamical Model of Walking

The body oscillation equation at the given translational movement $x = x(t)$, $h = const.$ and given foot placing $x_v(t)$, see also Ref. [1], reads as

$$[1 + \mu_2 (\cos\theta - 1) + \mu_1 (\lambda \varphi(\tau) + \varkappa) \sin\theta] \theta'' + [\mu_1 (\lambda \varphi(\tau) + \varkappa) \cos\theta - \mu_2 \sin\theta] \theta'^2 - \sin\theta + [\mu_1 \cos\theta + \mu_2] \varkappa'' - (\lambda \varphi(\tau) + \varkappa) = 0$$

Here, the abbreviations are introduced as

$$\lambda \varphi(\tau) + \varkappa = (x - x_v)/\varrho;$$
$$\lambda = L/\varrho;$$
$$\varphi(\tau) = \tau/\tau_0 - [\tau/\tau_0] - a;$$
$$a = s/L = const.;$$
$$d\tau = \omega dt;$$
$$\tau_0 = \omega T;$$
$$\omega = \{ Mg\varrho / [J + M\varrho (\varrho + h)]\}^{1/2};$$
$$\mu_1 = M\varrho^2/[J + M\varrho (\varrho + h)];$$
$$\mu_2 = M\varrho h/[J + M\varrho (\varrho + h)].$$

Designations of symbols, see also Fig. 1:

$x, x_v, h, L, s, \varrho, \theta$	– geometrical quantities and variables;
M	– mass of the body;
J	– central moment of body inertia;
T	– step duration;
u, q	– controlling moments of forces, they are expressed by the finite formulas over the motion.

Conditions of Walking and Analysis

Two conditions of walking are considered.

I) Comfortable (straight–line uniform) motion of the suspension point, $\varkappa = 0$.

II) Stabilized motion: $\varkappa$ is chosen from the conditions of translational motion stability and body oscillations.

Construction of stabilized motion :

$\hat{\theta}(\tau)$ – periodic motion from condition I,

$\hat{\theta}(\tau) = \hat{\theta}(\tau + T)$,

$\vartheta = \theta - \hat{\theta}(\tau)$.

Linearized equations of the body oscillation and the back coupling equation read as

$$\vartheta'' + (\sigma \mathfrak{G}_0 - 1)\vartheta + (\sigma \mathfrak{G}_1 - 1)\varkappa = 0,$$

$$\varkappa'' - \mathfrak{G}_0 \vartheta - \mathfrak{G}_1 \varkappa = 0,$$

$$\sigma = \mu_1 + \mu_2,$$

$\mathfrak{G}_0, \mathfrak{G}_1$ – parameters of the back coupling.

Then, the stability conditions are found as

$$\sigma\mathfrak{G}_0 - \mathfrak{G}_1 - 1 > 0;$$
$$\mathfrak{G}_1 > \mathfrak{G}_0;$$
$$(\sigma\mathfrak{G}_0 - \mathfrak{G}_1 - 1)^2 - 4(\mathfrak{G}_1 - \mathfrak{G}_0) > 0.$$

The stable region is shaded in Fig. 2.

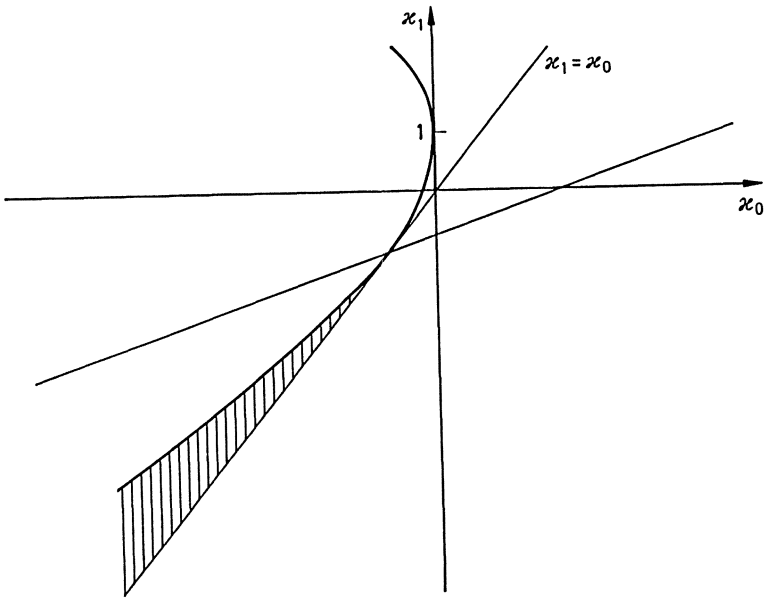

Fig. 2 Stability diagram

Investigation of condition I . The motion is natural unstable . Control creates only straight – line uniform (comfortable) motion of the legs' suspension point.

In this case the possible motions of the body are represented by point mappings in the phase plane θ, θ' . Mappings made at the beginning of each step.

The results for different parameters are shown in Fig. 3 to Fig. 6.

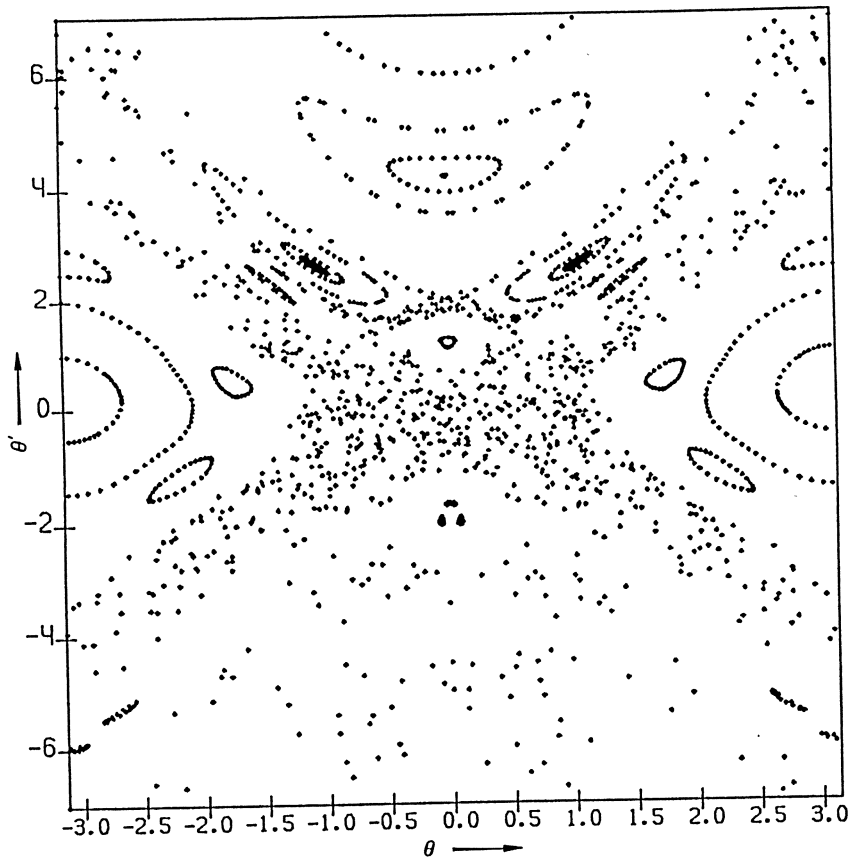

Fig. 3
Condition I: $\mu_1 = 0.1, \mu_2 = 0.3; \lambda = 1$. Small step. Low velocity. Stable motions with the body "head down" and the different periodic body rotations. There are many islands in the sea of chaos.

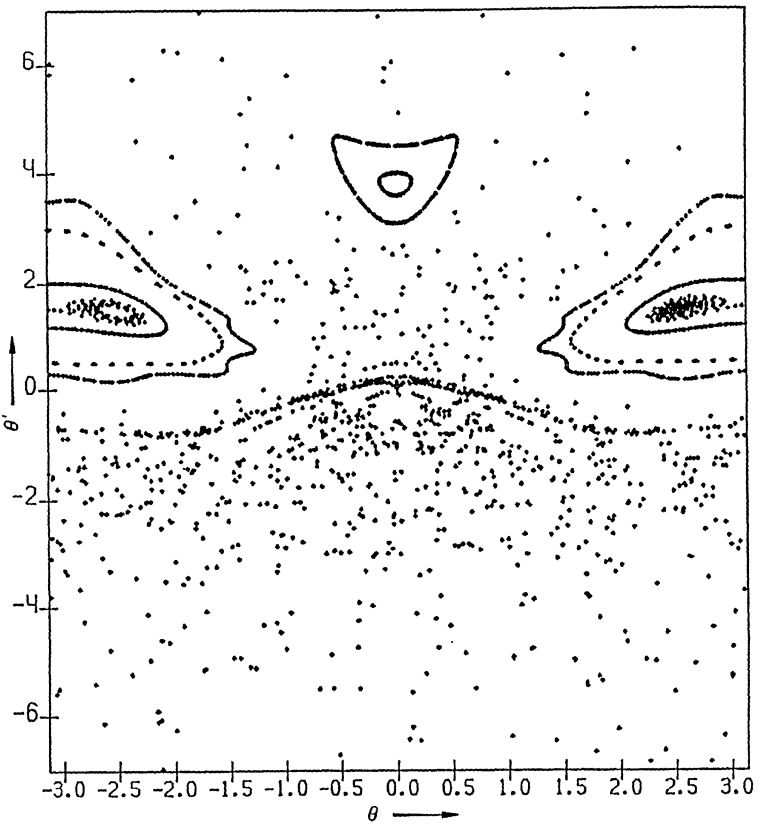

Fig. 4.

Condition I. $\lambda = 7{,}25$. Further increase of step size and velocity. The first bifurcation: the island with the stable oscillations is divided on two – "head forward" and "head back".

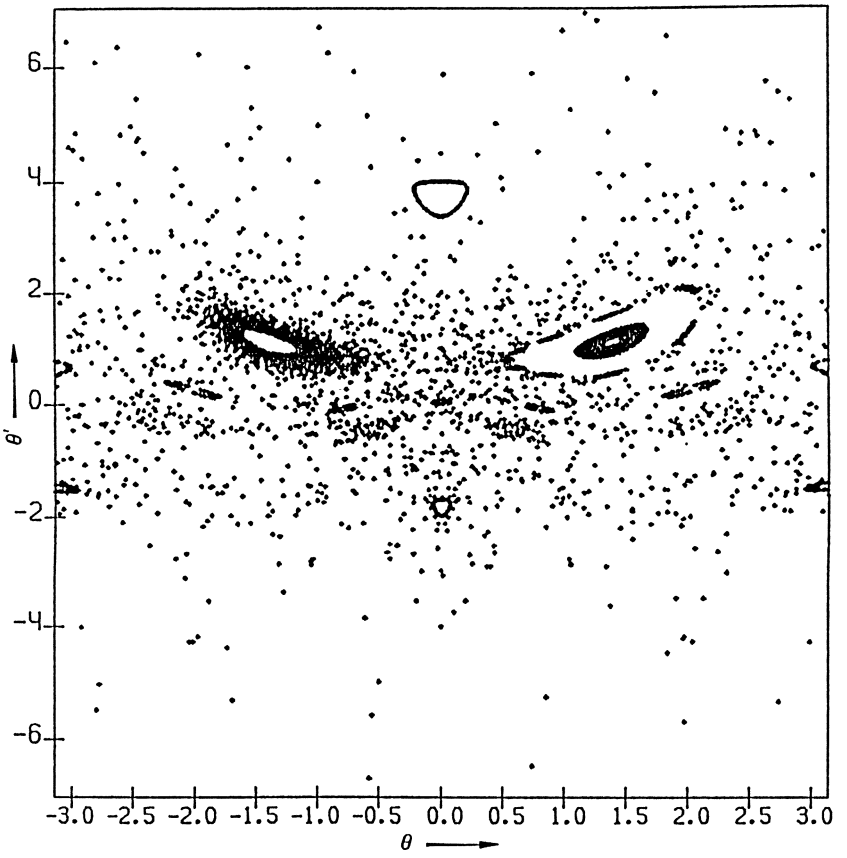

Fig. 5

Condition I. $\lambda = 9$. Left, in the centre appears an unstable solution; trajectories going away from it tend to join the loop in the right part. Right, in the centre an asymptotically stable solution occurs.

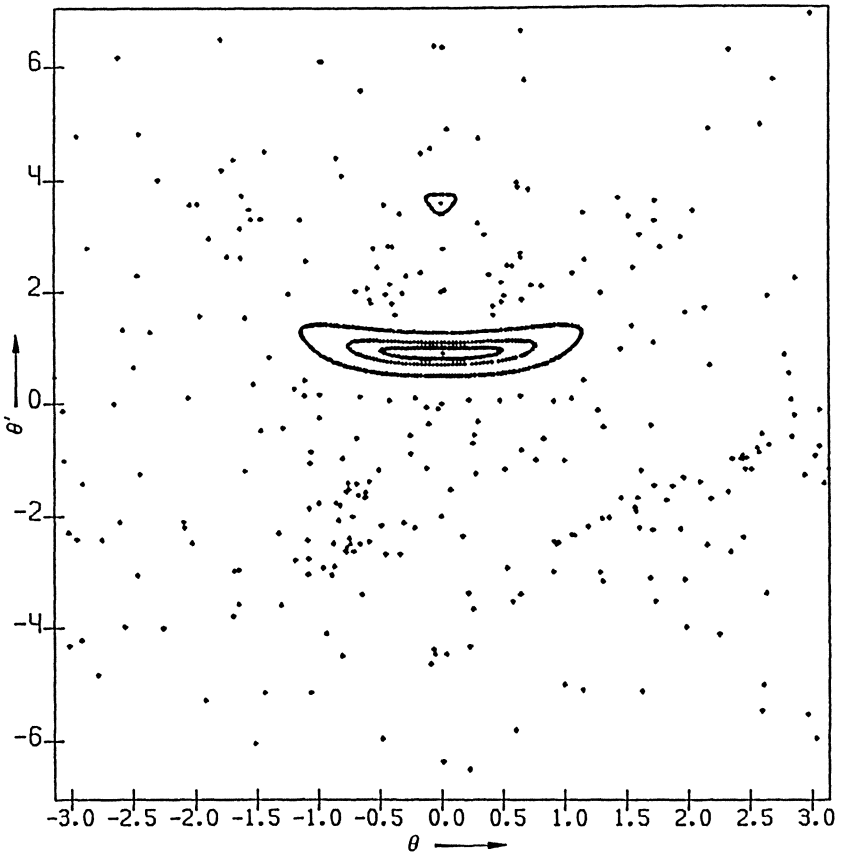

Fig. 6

Condition I. $\lambda = 11$. The next bifurcation. The stable oscillation "head up".

Condition II . The nonlinear equation of the body oscillations together with the equation of the back coupling are integrated for stable parameter conditions. The work which had been spent on walking and stabilization is calculated and presented in Fig. 7, where

$$W = \frac{1}{NL}\int_0^{NT} \left[\mid q(\dot{\theta} - \dot{\alpha}) \mid + \mid u(\dot{\alpha} - \dot{\beta}) \mid \right] dt ,$$

N – number of steps.

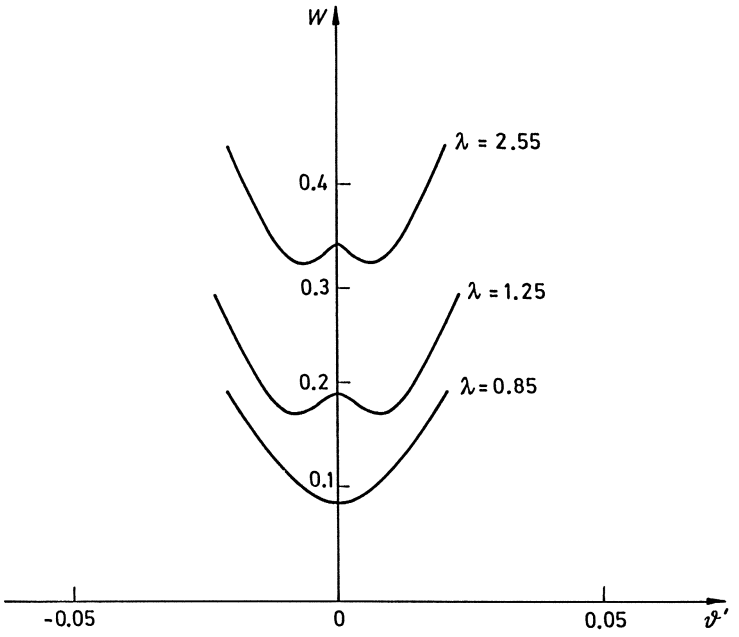

Fig. 7. Work depending on initial condition.

The work depends on the initial conditions of motion. The coordinate origin satisfies the periodic comfortable motion. A minimum of work is found for the periodic stable motion. There occurs a bifurcation of the periodic oscillation (with period doubling) at the parameter variation. Two period motions are shown in Fig. 8.

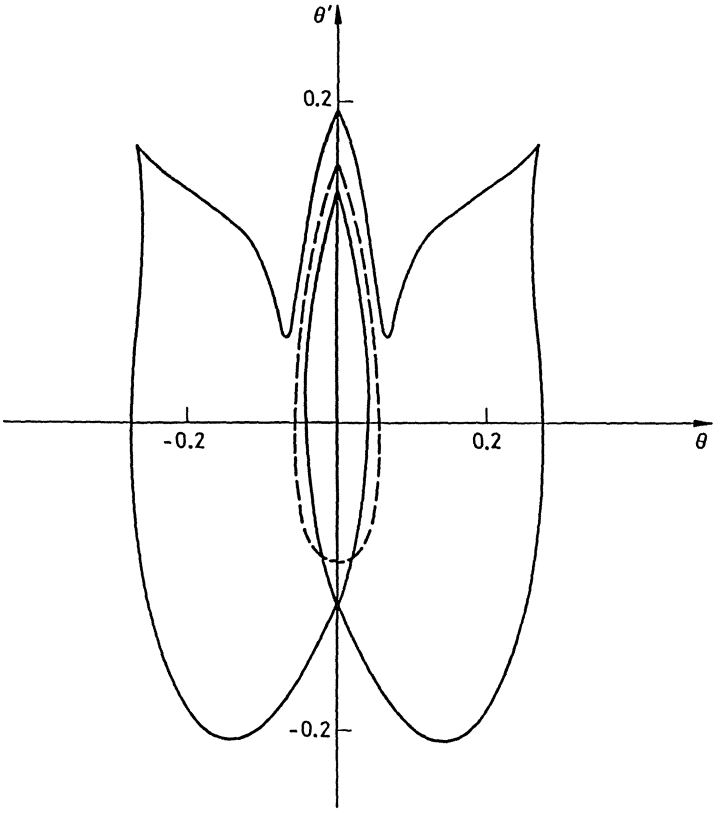

Fig. 8.
Condition II . Single and four periodic body oscillations.

Reference

[1] Beletzky, V.V.: Two-legged walking (in Russian). Moscow: Nauka 1984.

1/2 Subharmonic Resonance and Chaotic Motions in a Model of Elastic Cable

F. Benedettini and G. Rega

Dipartimento di Ingegneria delle Strutture, delle Acque e del Terreno
Università dell'Aquila, Monteluco Roio, 67040 L'Aquila, Italy

SUMMARY

The finite motions of a suspended elastic cable subjected to a planar harmonic excitation is studied through one ordinary equation with quadratic and cubic nonlinearities. The onset of chaotic motions in the neighbourhood of the 1/2 subharmonic resonance condition is analysed via numerical simulations.

INTRODUCTION

Non linear forced vibrations of a suspended elastic cable under primary or secondary resonance conditions have attracted some interest in recent years [1-3] because of both their theoretical interest associated with the occurrence of quadratic and cubic nonlinearities in the equations of motion and of their engineering relevance.

Since the "strange" behaviour of dynamical systems is often associated with the loss of stability of secondary responses [4], there is strong technical interest about the analysis and understanding of possible chaotic regimes for the cable. Referring to a one d.o.f. model of cable subjected to a planar harmonic forcing and starting from solutions obtained for the 1/2 subharmonic oscillations, a numerical investigation is made to obtain chaos charts and identify the mechanisms of transition from periodic to chaotic regimes.

EQUATION OF MOTION AND 1/2 SUBHARMONIC OSCILLATIONS

The moderately large oscillations of a parabolic elastic cable suspended between two fixed supports at the same level can be described

W. Schiehlen (Editor)
Nonlinear Dynamics in Engineering Systems
IUTAM Symposium Stuttgart/Germany 1989

by the unique partial equation in the vertical displacement v(x, t) [1]

$$\{Hv' + EA/l \cdot (y' + v') \int_0^l [y'v' + v'^2/2]\, dx\}' + p - \mu\dot{v} = m\ddot{v}, \quad (1)$$

where p(x, t) is a vertical distributed load and EA, H, m and μ are the axial rigidity, the initial tension, the mass and viscous damping coefficient per unit length respectively. Equation (1) is accurate for studying suspended cables used in overhead transmission lines. Using nondimensional quantities,representing the displacement through one linear eigenfunction and considering a monofrequent harmonic excitation with given spatial distribution, the application of the Galerkin method leads to one ordinary equation of motion

$$\ddot{q} + \mu^* q + q + c_2 q^2 + c_3 q^3 = p^* \cos \Omega t \quad (2)$$

which exhibits both quadratic and cubic nonlinearities. 2nd-order perturbation solutions obtained in the neighbourhood of the secondary resonance condition of order one half($\Omega \cong 2$) [3] give the frequency - response relationship for the 1/2 subharmonic plotted in Fig. 1b for an actually sagged (thin) and a nearly taut (thick) cable. Regions of non-existence (I), existence (II) and possible existence (III) of the stable subharmonic in the parameter space (Ω, p) of the excitation are plotted in Fig. 1a.

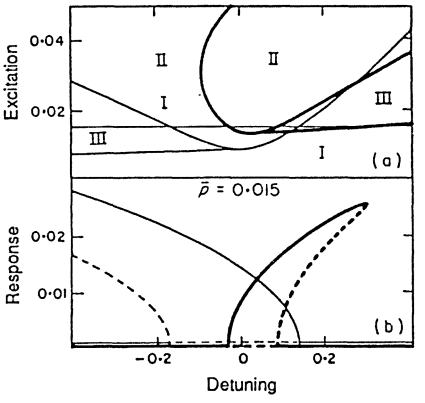

Fig. 1

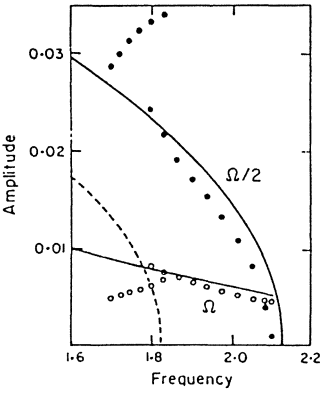

Fig. 2

For a sagged cable exhibiting a softening frequency-response curve, the approximate solution shows possible existence of a response with period 2 also at frequency values notably less than the nominal perfect tuning. Instead, some numerical integrations of equation (2) show that the response is actually of period 2 up to a certain frequency value ($\Omega \cong 1.7$) while it becomes of period 1 below it, since the 1/2 frequency-response curve turns to the right (Fig. 2) and the fundamental harmonic firmly prevails in the response right of the primary resonance condition. Thus the question arises of what kind of motion actually develops in the region between the 1/2 subharmonic and the primary resonance of the system.

NUMERICAL INVESTIGATION OF THE ONSET OF CHAOS

Extended numerical simulations have been made on equation (2) by considering values of the nonlinear coefficients ($c_2 = 35.952$, $c_3 = 534.53$) relevant to the sagged cable. The amplitude and frequency of the excitation are varied parametrically as well as the damping ratio, while the initial conditions are held fixed. Phase plane portraits, Poincarè maps, frequency power spectra, Lyapunov exponents, Lyapunov and correlation dimensions [5, 6] are used to identify chaotic responses. The numerical integration of the equation of motion has been made through a 4th-order Runge-Kutta method and checked through the Adams variable step method. Different total integration time lengths and time step increments have been considered to be reasonably sure that the response obtained is really a steady one and that chaos, whether occurring, actually pertains to the differential equation of motion and not to a difference approximation of it [7].

Attention is focused on the following practical aspects: (a) determination of significant regions of chaotic response of the system in the control parameters space of the dynamic problem; (b) analysis of the system's bifurcations from periodic to chaotic motions; (c) computational aspects in the use of the different measures of the dynamics for identifying chaotic responses.

Fig. 3, a chaos chart obtained with a time step increment equal to 1/200 and by considering 2000 forcing periods, shows the type of response

found in the neighbourhood of the 1/2 subharmonic resonance for different values of the forcing amplitude. Small dots denote periodic response while thick dots mean chaotic response. The boundary curve obtained numerically (thick) and separating the lower region of period 1 motions from that of period 2 motions shows good qualitative agreement with the 2nd-order perturbation boundary curves (thin). For a correct comparison one must remind that the numerical results refer to zero initial conditions while the two perturbation curves delimitates a region where the period 2 response can or cannot occur depending on the initial conditions (Fig. 1a).

A rather large region of chaotic motions is worthily noticed to occur at values of the excitation amplitude less above the threshold to be overcome for obtaining a period 2 response. Namely, for the cable, due to the high values of the nonlinear coefficients, chaos develops at values of the forcing amplitude notably lower than those in Ref. [4] and of practical interest. As the forcing amplitude increases, the two regions of period 1 and period 2 response extend to the right, consistent with the bending to the right of both the frequency-response curve of the fundamental oscillation obtained with a 4th-order perturbation solution [1] and with that of the subharmonic oscillation obtained numerically (Fig. 2).

In the close right neighbourhood of the chaotic region, a band of parameter values where regular motions with period other than 2 occur is found. To understand the mechanism of transition to chaos, a much thicker mesh spacing is considered for the frequency for a fixed value of the amplitude ($p = 0.04$). Fig. 4a shows the kind of steady state motion obtained according to Poincarè map and power spectrum: the periodicity of the output (period 1, period 2, etc.) is recorded as a function of the frequency. Fig. 4b shows the corresponding variations of the two Lyapunov exponents of the system. They were calculated by referring to a total time length of the trajectory equal to 500 forcing periods, which corresponds to well stabilized values of the exponents, and by performing the required orthonormalization at each time step of the motion integration. Notwithstanding they were obtained with a frequency mesh spacing larger and a number of forcing periods notably lower than those used for obtaining Fig. 4a, very good qualitative agreement with the indications given by

the measures of chaos used therein is observed. In substance, the spectrum of the Lyapunov exponents obtained by varying a control parameter proves to be a powerful tool for obtaining bifurcation diagrams [8]. Nevertheless, construction of these diagrams through Lyapunov exponents is more time consuming than through Poincarè map and power spectrum and these last dynamical measures allow to understand more effectively the mechanism of transition from periodic to chaotic motions.

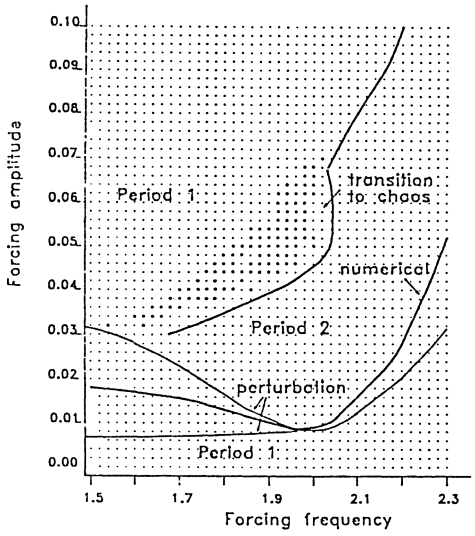

Fig. 3

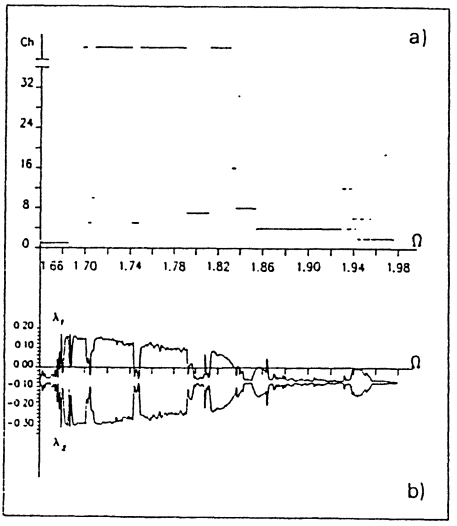

Fig. 4

By examining the results obtained with decreasing frequency in terms of just these measures,a main route to chaos through period doubling bifurcations (2, 4, 8, 16 - - - → chaos) is observed in Figs.5a-f. The values of the Lyapunov exponents and of the Lyapunov and correlation dimensions, $D_L = 1 - \lambda_1/\lambda_2$ and $D_c = \lim_{r \to 0} (\log C(r)/\log r)$ [6], qualify both these last two responses as chaotic, though their attractors in the Poincarè map differ notably. The transition to chaos is smooth, namely it occurs in a rather large range of frequency values. Once well-extablished (Fig. 6), the chaotic behaviour occurs in a quite large region.

Some more basic responses with period 6, 7 and 5 are observed prior to the extablishing of chaos and meddled with it (Fig. 4), which look like giving rise to further independent sequencies of period doubling

bifurcations (6-12, 7-14, 5-10-20). With the frequency spacing considered, these sequencies seem to be incomplete and the transitions to chaos, whether occurring, are observed to be jump phenomena.

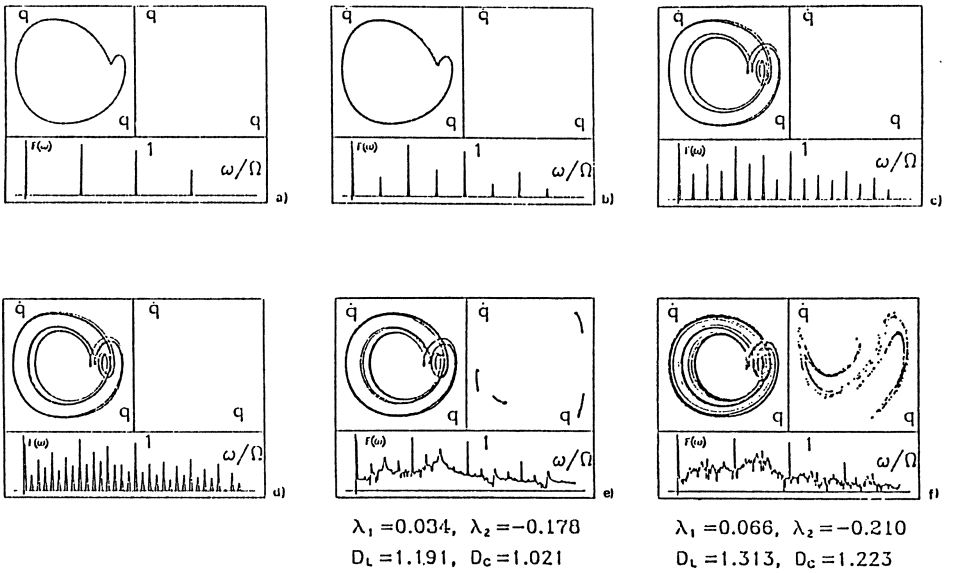

Fig. 5

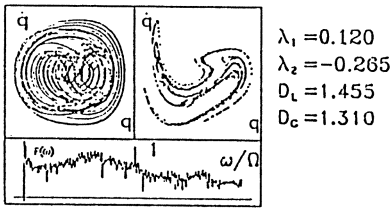

Fig. 6

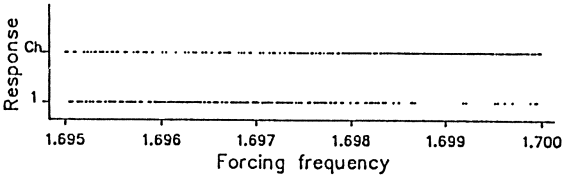

Fig. 7

As, by decreasing further the frequency, the left boundary of the chaos region is approached (Fig. 4), the transition to the stable period 1 motions occurs again via a sudden change (jump) bifurcation. Nevertheless, a more detailed investigation of what happens in the neighbourhood of this boundary (Fig. 7) shows that the transition develops in a finite width zone where the response continuously jumps from chaotic to period 1: as the frequency is decreased, the chaotic intervals become

smaller and smaller while the period 1 intervals extend progressively. This behaviour of the system is to be connected with the presumably fractal nature of the boundary of the chaos region, according to which different attractors of the motion coexist and the response becomes totally unpredictable in this range of frequency.

Some points are mentioned as far as the fractal properties of the strange attractor is concerned. A reliable calculation of its correlation dimension must pay attention to the minimum and maximum sizes of the box covering the attractor, which have to be correlated with the density of points in the map. From the computational point of view, calculating the fractal dimension through the D_c measure is more time consuming - though more reliable - than through the D_L measure, since D_c usually needs more than a thousand periods to remain unchanged while the λ_1 values do not vary any more after few hundreds of forcing periods. Here D_c was calculated by considering 2000 points in the 2D Poincarè map and about three points per box for the lower r value. It is given in Fig. 8 for three values of damping. As expected, D_c diminishes with increasing μ values, which give rise to thinner and thinner attractors in the map. Since the shape of the Poincarè map does not change with the phase of the forcing function, the fractal dimension of the chaotic attractor in the 3D phase space can be calculated simply as $d_c = 1 + D_c$ [6]: the value $d_c \cong 2.36$ is obtained.

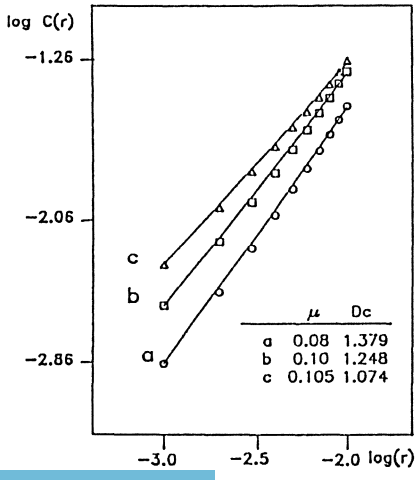

Fig. 8

CONCLUDING REMARKS

For a suspended cable subjected to a planar monofrequency excitation, chaotic responses can occur in the range of frequency between primary and 1/2 subharmonic resonance conditions. Chaos chart and bifurcation diagrams were built in the control parameter space of the system and the fractal properties of the strange attractors were quantified. Period doubling and sudden change bifurcations from periodic to chaotic motions were evidenced. The observed unpredictability of the system response has to be properly accounted for in technical applications.

ACKNOWLEDGMENTS - Research partially supported by M.P.I. 40% 1987 Grants.

REFERENCES

[1] Benedettini, F. and Rega, G., Nonlinear dynamics of an elastic cable under planar excitation, *Int. J. Non-Linear Mech.* **22**, 497-509(1987).

[2] Takahashi, K. and Konishi, Y., Non-linear vibrations of cables in three dimensions, Part II: Out-of-plane vibrations under in-plane sinusoidally time-varying load, *J. Sound Vibrat.* **118**, 85-97 (1987).

[3] Rega, G. and Benedettini, F., Planar nonlinear oscillations of elastic cables under subharmonic resonance conditions, *J. Sound Vibrat.* (to appear) (1989)

[4] Szemplinska-Stupnicka, W. and Bajkowski, J., The 1/2 subharmonic resonance and its transition to chaotic motion in a non-linear oscillator, *Int. J. Non-linear Mech.* **21**, 401-419 (1986).

[5] Thompson, J.M.T. and Stewart, H.B., *Nonlinear dynamics and chaos.* Wiley, Chichester (1986).

[6] Moon, F., *Chaotic vibrations.* Wiley, New York (1987)

[7] Tongue, B.H., Characteristics of numerical simulations of chaotic systems, ASME *J. Appl. Mech.***54**, 695-699 (1987).

[8] Kreuzer, E.J., On the numerical study of bifurcation problems, in *Bifurcations: Analysis, algorithms, applications* (Eds. T. Küpper, R.Seydel and H. Troger), 161-171, Birkhäuser, Basel (1987).

Nonlinear Dynamics of the Journal Bearing

J. BRINDLEY, M.D. SAVAGE AND C.M. TAYLOR

DEPARTMENTS OF APPLIED MATHEMATICAL STUDIES AND MECHANICAL ENGINEERING, CENTRE FOR NONLINEAR STUDIES AND INSTITUTE OF TRIBOLOGY, UNIVERSITY OF LEEDS, LS2 9JT, UK.

Summary

Our approach has been to develop an analytic description of the basic dynamics of the journal bearing, and of its potential instabilities, in a form simple enough to identify crucial physical mechanisms. This approach contrasts with, but is complementary to, the purely numerical analysis adopted by other authors. It permits the establishment of a "birds eye view" of behaviour in multi-dimensional parameter space at relatively small expense in time and effort, with identification of critical regions at which qualitative changes in behaviour are to be expected. Such regions may then be explored thoroughly by the use of more detailed and expensive numerical models.

1. Introduction

The journal bearing is widely used in mechanical systems as a support mechanism for rotating shafts, and reasonably stable behaviour under a wide range of operating conditions is a practical requirement in all cases. The complexity of many of the bearing shapes used precludes anything other than purely numerical modelling if detailed quantitive results are sought for particular bearings. Much qualitative information on the general effect of bearing design is, however, obtainable from simple mathematical models in which important physical controls may be represented in as simple a way as possible. Thus, for example, the effects of geometrical features of the bearing shape on the occurrence and extent of cavitation in the lubricant, which has been shown to affect stability very strongly, may be investigated systematically.

The dynamics is conveniently described in terms of the motion of the mass-centre of the journal, or rotor, which is determined by the interplay of the forces acting on it, comprising the external load and the stresses exerted by the fluid lubricant. It is usual to assume that the journal, almost invariably circular, rotates at a constant angular velocity, ω; this rotation drives the fluid motion of the lubricant which in turn determines the stress at the journal surface. The intrinsic nonlinearity of this process is clear; other nonlinearities arise through the action of the

W. Schiehlen (Editor)
Nonlinear Dynamics in Engineering Systems
IUTAM Symposium Stuttgart/Germany 1989

load, in general a varying vector quantity dependent on the position of the journal. The heartof the problem is the sensitivity of the net force exerted by the lubricant on the rotor to relatively minor differences in cavitation character and extent, or in geometry. In this paper we consider only the simplest geometry and the simplest acceptable cavitation condition in order to expose most clearly the qualitative character of the dynamic phenomena and their dependence on parameter values. A number of detailed investigations have been reported elsewhere [1-3].

2. Mathematical Formulation

Figure 1 displays a cross section of a rigid circular rotor of radius R-c, supporting a load W, contained within a rigid circular bush of radius R.

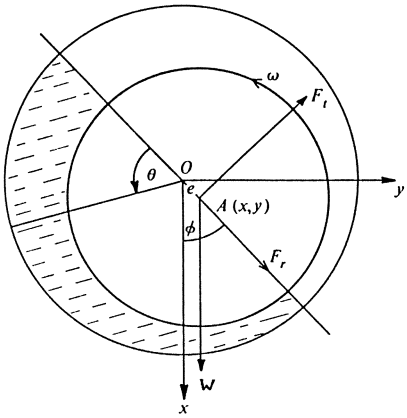

Fig. 1. A journal bearing in which the rotor centre, A, has displacement e from O, the centre of the bush. Lubricant shown occupying the π-film region.

Motion of the rotor centre is then described by the (non-dimensional) equations, [4]

$$\left.\begin{aligned} \ddot{\varepsilon} - \varepsilon\dot{\phi}^2 &= \frac{1}{\bar{\omega}^2}\left[\cos\phi + \frac{SF_r}{W}\right] \quad a \\ \varepsilon\ddot{\phi} + 2\dot{\varepsilon}\dot{\phi} &= -\frac{1}{\bar{\omega}^2}\left[\sin\phi - \frac{SF_t}{W}\right] \quad b \end{aligned}\right\} \qquad (2.1)$$

where ε is the eccentricity ratio e/c , φ is the attitude angle relative to the flow direction, F_r, F_t are the components in the directions along and perpendicular to OA of the total fluid stresses on the journal, and a dot denotes differentiation with respect to the non-dimensional time $\tau = \omega t$. (By assumming constant ω we of course effectively ignore any fluctuations in the moments about A of the fluid stresses). Additionally

we have introduced the non-dimensional parameters

$$S = LR^3\mu\omega/Wc^2 \quad , \quad \text{the Sommerfeld number} \qquad (2.2)$$

and $$\bar{\omega} = W\left[mc/W\right]^{1/2} \quad , \quad \text{a non-dimensional rotation speed} \qquad (2.3)$$

where L is a characteristic length along the rotor (z-direction), ie perpendicular to the (ε,φ) plane.

In order to calculate the hydrodynamic forces F_r, F_t, the pressure distribution $p(\theta,z)$ within the lubricant must be known. It may be obtained from the Reynolds equation, using the usual assumptions of lubrication theory, that the flow remain laminar and non-inertial (for which $\omega c^2/\nu << 1$ is sufficient).

This equation then takes the form,

$$\frac{\partial}{\partial\theta}\left\{(1+\varepsilon\cos\theta)^3\frac{\partial\bar{p}}{\partial\theta}\right\} + \left[\frac{R}{L}\right]^2\frac{\partial}{\partial z}\left\{(1+\varepsilon\cos\theta)^3\frac{\partial\bar{p}}{\partial z}\right\} = 6S\left\{-\varepsilon(1-2\dot{\phi})\sin\theta + 2\dot{\varepsilon}\cos\theta\right\} \qquad \ldots(2.4)$$

where the non-dimensional pressure, $\bar{p} = p/\mu\omega\left[\frac{R}{c}\right]^2$ and the forces F_r, F_t are given by

$$F_r = \int p\cos\theta\, dS \quad , \quad F_t = \int p\sin\theta\, dS \qquad (2.5)$$

taken over the surface of the rotor.

Further analytic progress with equations (2.4) requires the so called long- or short-bearing approximations, in which the second or first terms respectively on the left hand side are neglected. In either case, we need to specify boundary conditions on the pressure, and this is the crucial physical question in the modelling of the problem. The difficulty arises because of the possibility, for liquid lubricants, of cavitation in the diverging region of the fluid flow, downstream of the point of minimum gap. In this region, it is possible that the actual pressure in the fluid may fall below some "ambient value" at which a cavity may arise through vapourisation of the lubricant or gases dissolved in it, or much more usually, through "ventilation" - the introduction of air from other parts of the mechanical system.

Stability characteristics of the rotor are very sensitive to the extent of cavitation, and to the conditions on pressure assumed at the boundaries of any cavity [1]. The simplest model is the so called π-film, which assumes that the fluid film occupies the region of convergent flow ($0 < \theta < \pi$), and that the divergent region ($\pi <= \theta <= 2\pi$) is totally occupied by a cavity, within which pressure is presumed to be zero (ie atmospheric).

Clearly such a cavity moves with the angular position (φ) of the rotor and is usually called an oscillating π-film. We proceed with this model:

(1) Long-bearing approximation: set $p = 0$ at $\theta = 0$ and $\pi \leq \theta \leq 2\pi$ (2.6)

We find [5]

$$F_r = S\left\{12\pi\varepsilon^2(1 - 2\dot{\phi}) + 6[\pi^2(2 + \varepsilon^2) - 16](1 - \varepsilon^2)^{-1/2}\dot{\varepsilon}\right\}/\pi(2 + \varepsilon^2)(1 - \varepsilon^2) \quad ..(2.7)$$

$$F_t = S\left\{6\pi\varepsilon\ (1 - \varepsilon^2)^{1/2}(1 - 2\dot{\phi}) + 24\varepsilon\dot{\varepsilon}\right\}/(2 + \varepsilon^2)(1 - \varepsilon^2) \quad (2.8)$$

Where, for a given value of the Sommerfeld number, S, the position (ε_s, ϕ_s) of the static equilibrium is given by the solution of

$$S \equiv S(\varepsilon_s) = (2 + \varepsilon_s^2)\ (1 - \varepsilon_s^2)/6\varepsilon_s\left\{\pi^2(1 - \varepsilon_s^2) + 4\varepsilon_s^2\right\}^{1/2} \quad (2.9)$$

$$\tan\phi_s = \pi(1 - \varepsilon_s^2)^{1/2}/2\varepsilon_s \quad (2.10)$$

(2) Short bearing approximation: in this case, setting $p = 0$ at $z = 0$, L, we find that pressure is subambient in a range $\pi + \theta_1 < \theta < 2\pi + \theta_1$, where

$$\tan\theta_1 = 2\dot{\varepsilon}/\varepsilon(1 - 2\dot{\phi}) \quad (2.11)$$

Again, expressions for F_r and F_t are readily found, though they are more complicated than (2.7), (2.8), and we find, for static equilibrium

$$\left[\frac{L}{R}\right]^2 S = 4(1 - \varepsilon_s^2)^2/\varepsilon_s\left\{\pi^2(1 - \varepsilon_s^2) + 16\ \varepsilon_s^2\right\}^{1/2},\quad \tan\phi_s = \pi(1 + \varepsilon_s^2)^{1/2}/4\varepsilon_s \quad ..(2.12)$$

3 Linear Stability Analysis

A linear stability analysis of the equations (2.1, a,b), with the appropriate expressions for F_r, F_t reveals that the full film configuration is always unstable (as suspected from early numerical experiments [2]). The π-film model, on the other hand, is linearly stable for certain ranges of values of the imposed conditions (for both long and short bearings). Physically, these conditions are the values of ω and of W, but it is convenient to plot results in the $(\varepsilon_s, \bar{\omega})$ plane. For a given configuration, we assume that the geometry and lubricant properties are constant; we can then introduce a system parameter, σ, which is independent of ω and depends only on W, by writing $(\sigma = S/\bar{\omega} = LR^3\mu/(WMc)^{1/2}\ c^2)$ (3.1)

Then for fixed load W, σ is constant, and we can plot curves of constant σ on the $(\varepsilon_s, \bar{\omega})$ plane. Examples of these "operating curves" are shown on Figs 2 and 3, for, respectively, the linear stability results for long and short bearings. A constant load system traverses an operating curve as ω

is changed, and we are particularly concerned with nonlinear behaviour as the system crosses the linear stability curve.

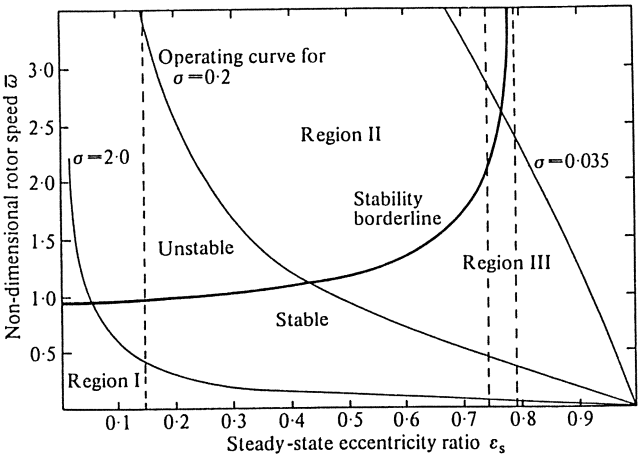

Fig. 2 Linear stability borderline for the long bearing approximation, together with three operating curves (σ = 2.0, 0.2, 0.035).

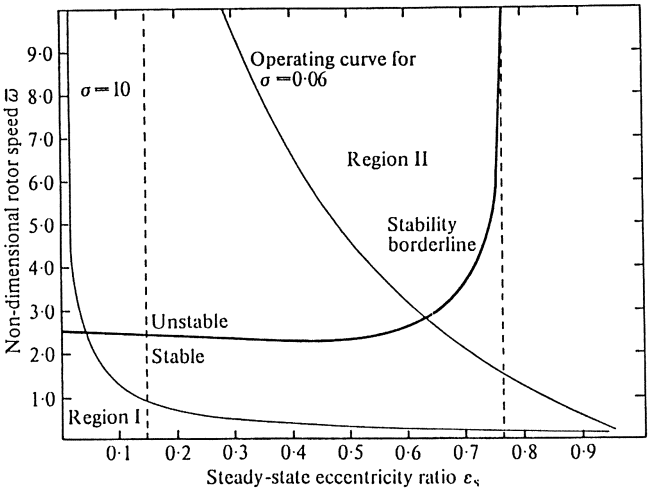

Fig. 3. Linear stability borderline for the short bearing approximation, with two operating curves (σ = 10.0, 0.06).

4 Nonlinear Analysis

Equations (2.1, a,b) are already highly nonlinear even when expressions (2.7), (2.8) are used for the fluid forces. In essence, the nonlinear problem takes the form

$$\left.\begin{aligned} \dot{x}_1 &= W\cos\phi + f_1(\mathbf{x},\lambda) + g_1 \quad , \quad \dot{x}_2 = W\sin\phi + f_2(\mathbf{x},\lambda) + g_2 \\ \dot{x}_3 &= x_1 \quad , \quad \dot{x}_4 = x_2 \quad ; \quad \mathbf{x} = (x_i) \end{aligned}\right\} \qquad (4.1)$$

where, for manipulative convenience we have used Cartesian coordinates (x_3, x_4) introduced functions f_i to represent the fluid forces acting on the rotor, and g_i to represent external forcing. $\underline{\lambda}$ is a vector of parameters having three important components, a Reynolds number, a radius ratio and an eccentricity parameter, and W constitutes a fourth parameter. It is clear that, in a mathematical sense, (4.1) is a fourth order nonlinear system with four independent parameters; its dynamic behaviour is potentially very rich even when the normal physical constraint of constant radius ratio is invoked to reduce the number of parameters to three. In this paper we have of course also assumed W to the constant, thus neglecting any feedback from the rest of the mechanical system, and effectivly reducing the number of independent parameters to two.

The full nonlinear problem is not, in general, responsive to analytical methods, and resort to numerics is necessary for detailed quantitative results. Much insight into the dynamics of the system, and of the crucial importance of certain physical effects, may however be gleaned from the analysis of the weakly nonlinear behaviour near the stability curve of linear theory. Additionally, information on large amplitude ocillations of the rotor may be obtained by various forms of "averaging".

Of several perturbation methods employed by ourselves and other authors, the most fruitful is a multiple time scale analysis of the behaviour of small displacements (x', y') away from the equilibrium position (x_s, y_s) obtained by linear theory. For a wide range of conditions, loss of stability occurs when a pair of complex conjugate eigenvalues crosses the imaginary axis at a finite speed, and the conditions for Hopf bifurcation are met. A standard multiple time scales analysis [3] then leads to the solutions

$$\left.\begin{aligned} x'(S,\tau) &= A_1(\tau)e^{i\Omega_0 S} + c.c \\ y'(S,\tau) &= \lambda A_1(\tau)e^{i\Omega_0 S} + c.c \end{aligned}\right\} \qquad (4.2)$$

where s, τ are fast and slow times, and c.c denotes a complex conjugate. The resulting amplitude equation, writing $A(\tau) = R(\tau)e^{i\theta(\tau)}$, takes the form

$$\frac{dR}{d\tau} = R\,(\alpha_1 + \alpha_3 R^2) \qquad (4.3)$$

and the phase equation is $\frac{d\theta}{d\tau} = \beta_1 + \beta_3 R^2$ (4.4)

where $\alpha_1, \alpha_3, \beta_1, \beta_3$ are real.

The signs of α_1 and α_3 as ω is perturbed above or below its value ω_s at static equilibrium indicate the occurrence of supercritical ($\alpha_1 > 0$, $\alpha_3 < 0$) or subcritical ($\alpha_1 < 0$, $\alpha_3 > 0$) Hopf bifurcation.

Results of the long bearing case are indicated on Fig. 2. Thus, in region I($0 < \varepsilon_s < 0.14$), and in region III ($0.75 \leq \varepsilon_s < 0.795$) we have $\alpha_3 > 0$ and therefore an ustable limit cycle exists for $\omega < \omega_s$. No periodic orbits exist for $\omega > \omega_s$. In region II ($0.15 < \varepsilon_s < 0.75$) we have $\alpha_3 < 0$, which implies that a stable periodic orbit bifurcates from $(\varepsilon_s, \omega_s)$ for $\omega > \omega_s$; for $\omega < \omega_s$ all solutions approach the equilibrium state.

Thus, if we vary ω at a fixed parameter value σ, eg $\sigma = 0.035$ or $\sigma = 2$, we encounter a subcritical Hopf bifurcation at the intersection with the stability curve. At value $\sigma = 0.2$, on the other hand, we encounter a supercritical Hopf bifurcation.

For the short bearing, the overall picture is similar (Fig. 3), except that, in this case, α_3 changes sign once only. Thus we have regions I and II in which bifurcation is subcritical and supercritical respectively, but there is no region of subcritical behaviour for large ε_s corresponding to region III in the long bearing case.

5 Discussion and Summary

The analytical predictions of the proceeding sections are borne out by full numerical solutions to the equations (2.1) supplemented by path following methods [5]. Typical bifurcation diagrams are shown in Fig. 4. Detailed numerical computations using a range of initial states confirm this general picture [2-4], and the existence of large amplitude periodic orbits has also been detected by the use of various averaging techniques, at some saving in effort over the direct computational approach.

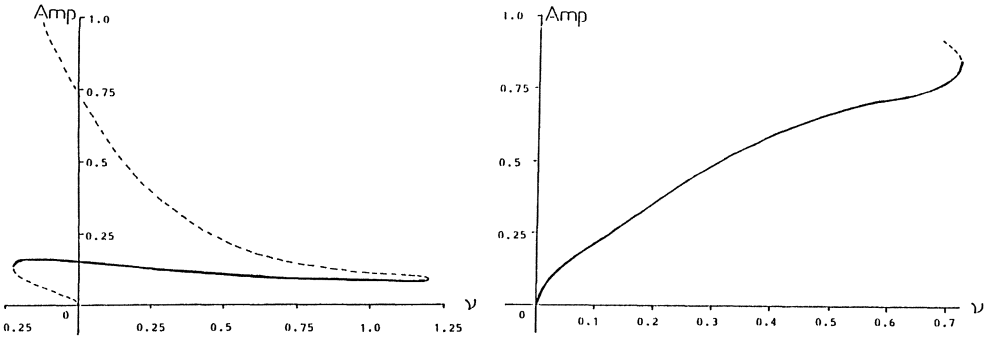

Fig. 4 Bifurcation diagrams for (a) $\sigma = 2.0$, (b) $\sigma = 0.2$ in long bearing approximation ; $\nu = \bar{\omega} - \bar{\omega}_c$. Stable solutions shown by solid lines, unstable solutions by dashed lines.

A second source of nonlinearity is fluid inertia in the lubricant. The inclusion of such effects in the equations of motion for the fluid introduces a region of stability at low rotation speeds which is totally absent when the fluid motion is modelled by the Reynolds equation (2.4). Again the response near to the linear stability boundary is one of supercritical or subcritical Hopf bifurcation according to the value ε_s. In summary we have described a basic model for studying the dynamics of a journal bearing. The existence of stable small amplitude limit cycles (whirl) orbits has been demonstrated for conditions near to those of neutural stability on linear theory, and path following methods have enabled us to construct bifurcation diagrams illustrating the existence of these orbits at amplitudes no longer small. In ongoing work we are exploring the use of multiple scales analysis in conjunction with a form of harmonic balance to identify and describe large amplitude orbits not necessarily connected with bifurcations from the linear stability curves.

Large areas of the field remain unexplored. Of particular importance is the proper description of cavitation. The effects on linear theory using different models has been well described; little comparative work with nonlinear models has yet been undertaken. Again the question of basins of attraction for the various stable solutions has not been addressed systematically, and finally may we end with a plea to experimentalists to enter this almost totally unexplored field. Without real experimental results, scientific assessment of the models we have developed is difficult and incomplete, relying as it does solely on comparison with numerical experiments.

References

1. Dowson, D, and C.M. Taylor. Ann. Rev. Fluid Mech. 11, 35, 1979.
2. Brindley, J., L. Elliott, and J.T. McKay. ASME J. Appl. Mech. 46, 767, 1979; 50, 72, 78, 1983; 53, 430, 1986.
3. Gardner, M. C. Myers and M.D. Savage. Q. J. Mech. Appl. Math. 38, 27, 1985.
4. Collins, D., M.D. Savage and C.M. Taylor. J. Fluid Mech. 168, 415, 1986.
5. Brindley, J., C. Kaas-Petersen and A. Spence. Physica D. 34, 456, 1989.

Extended Results of Subharmonic Resonance Bifurcation of Nonlinear Mathieu Equation and Some Experimental Results

Chen Yu shu Zhan Kaijun
Dept. of Mechanics
Tianjin University
Tianjin, China

W. F. Langford
Dept. of Math. & Stats
University of Cuelph
Cuelph, Ontario, Canada

Summary
The authors of [1] discussed the subharmonic resonance bifurcation of Nonlinear Mathieu equation and they obtained six bifurcation diagrams in (α, β)-plane. In this paper, we extended the results of [1] and pointed out that there exist as total as fourteen bifurcation diagrams which are not topological equivalence each other. Experimental results of mechanical model coinside with the results of paper [1].

It is useful in theory and practice to study the nonlinear Mathieu equation

$$u''+\delta[u'+h(u,u',\mu,\delta)]+(1+\mu)u+f(u,u',\mu) +(2\varepsilon\cos 2t)[u+g(u,u',\mu,\varepsilon)]=0 \qquad (0.1)$$

Applying Liapunov-Schmidt reduction in [1], we can obtain the bifurcation equation, where the tuning parameter μ is as a bifurcation parameter,

$$R=(\mu+A)^2+\delta^2(1+B)^2-\varepsilon^2[(1+C)^2+\delta^2 D^2]=0 \qquad (0.2)$$

where $A=\Sigma a_j r^{2j}$, $B=\Sigma b_j r^{2j}$, $C=\Sigma c_j r^{2j}$ and $D=\Sigma d_j r^{2j}$. The meanings and calculations of these symbols are referred to [1].
When $a_1 \neq 0$ and $\beta \neq 0$, we have a nonsingular and almost identity transformation to transform (0.2) to

$$(\mu+a_1 r^2)^2+\alpha+\beta r^2=0 \qquad (0.3)$$

where $\alpha=\delta^2-\varepsilon^2$, $\beta=2[b_1(0)\delta^2-c_1(0)\varepsilon^2]$: unfolding parameters.
There are six bifurcation diagrams with different topological structures in the plane of $(\alpha,\beta)\in O(R^2)$.

W. Schiehlen (Editor)
Nonlinear Dynamics in Engineering Systems
IUTAM Symposium Stuttgart/Germany 1989

However, only when α and β are both not zero, Eq.(0.3) is correct to be studied if we want to know some properties of subharmonic resonance. In equation (0.3), parameters α and β have double meanings, firstly they are as modal parameters and secondly, as universal unfolding parameters. But in practice, if (α, β) are very small, (0.3) cannot be used to study the bifurcation properties of (0.1) in a proper sense. Therefore, it is a new problem that what the bifurcation behaviors of (0.1) will be when (α, β) are both zero or nearly zero. In this paper, we find out a new bifurcation equation different from (0.3) and obtain an extended result that if $a_1 \neq 0$, there exist as many as fourteen bifurcation diagrams with different topological strueture.

1 Choise of Germ

When $\alpha=\beta=0$, (0.3) becomes

$$(\mu+a_1 r^2)^2=0 \tag{1.1}$$

The codimension of (1.1) is not zero and it cannot reflect the mechanics behaviors of (0.1) exactly. At first we calculate the codimension of germ (1.1).

Conclusion 1.1 Germ $(\mu+a_1 r^2)^2$ has infinite codimension.

Theorem 1.2 If an ideal $I \subset E_n$, where $n \geqslant 2$, is generated by only one germ p such that $p(0)=0$, then I has infinite codimension.

The proof of this theorem is referred to [2].

Let $u=r^2$ and $g=(\mu+a_1 u)^2 r$, then the restrict tangent space of g is

$$RT(g, Z_2)=\langle g, ug_u\rangle\{r\}=\langle(\mu+a_1 u)^2, 2a_1 u(\mu+a_1 u)\rangle\{r\}$$
$$\subset\langle\mu+a_1 u\rangle\{r\}=p\{r\}$$

We have $p(0)=0$ and the conclusion 1.1 is true from Theorem 1.2.

Conclusion 1.3 Germ $(\mu+A)^2$ has infinite conimension, where

$A=\Sigma a_j r^{2j}$.

Hence we have to add infinite unfolding parameters to germ $(\mu+a_1 r^2)^2$ to obtain a bifurcation equation with codimension zero if $\alpha=\beta=0$. We may see that it is impossible and unnecessary if we do so. We must search a new germ with finite codimension.

Rewrite (0.2) as the form of

$$R=(\mu+a_1 r^2+a_2 r^4+\cdots)^2+\delta^2(1+b_1 r^2+\cdots)^2 -\varepsilon^2[(1+c_1 r^2+\cdots)^2+\delta^2(d_1 r^2+d_2 r^4+\cdots)^2]=0 \qquad (1.2)$$

Since parameters a_j, b_j, c_j, d_j are all functions of μ, δ and ε, we may expand them in Taylor series of μ, δ and ε.

Now equaion (1.2) can be rewritten as

$$R=[\mu+a_1(0)u]^2+2[a_2(0)+a_1(0)a_{1\mu}(0)+b_{2\mu}(0)\delta^2 -c_{2\mu}(0)\varepsilon^2]\mu u^2+2[a_1(0)a_2(0)+b_1(0)b_2(0)\delta^2-c_1(0)c_2(0)\varepsilon^2 -d_1(0)d_2(0)\delta^2\varepsilon^2]u^3+2a_{1\mu}(0)u\mu^2+\ =0 \qquad (1.3)$$

Write $a_1(0)=a_1$ for convienience and a, b, c represent the coefficients of μu^2, u^3, $u\mu^2$.

We take it as the new germ:

$$g=(\mu+a_1 u)^2+a\mu u^2+bu^3+cu\mu^2 \qquad (1.4)$$

Theorem 1.4 Suppose there is a normal form

$$h^*=rh(u,\mu)=r[\phi u^3+\varepsilon u^2+2\delta u\mu+\varepsilon\mu^2]$$

where $\phi=sgn(g_{vvv})$, $\delta=sgn(g_{u\mu})$, $\varepsilon=sgn(g_{uu})$. Then $g^*=rg(u,\mu)\in E_{u,\mu}(Z_2)$ is Z_2-strongly equivalent to h^* if and only if at $(u,\mu)=(0,0)$

$$g=g_u=g_\mu=\det(d^2 g)=0, \quad g_{vvv}\neq 0 \qquad (1.5)$$

We have the formula of g_{vvv} in terms of darivatives of

g to u, μ:

$$g_{vvv}=v_1^3 g_{uuu}+3v_1^2 v_2 g_{uu\mu}+3v_1 v_2^2 g_{u\mu\mu}+v_2^3 g_{\mu\mu\mu}$$

Corallary 1.5 Suppose there is a germ $g^*=rg(u,\mu)$, where g is given by (1.4). Then g^* is Z_2-strongly equivalent to h^*, where

$$h^*=rh(u,\mu)=r[\phi u^3+\varepsilon u^2+2\delta u\mu+\varepsilon\mu^2] \qquad (1.6)$$

Proof. It is clear that, at $(u,\mu)=(0,0)$ we have $g=g_u=g_\mu=0$ and $g_{uu}=2a_1^2$, $g_{u\mu}=2a_1$, $g_{\mu\mu}=2$, eventually $\det(d^2g)=0$
Take $(v_1,v_2)=(1,-a_1)$ as eigenvector of zero eigenvalue of $\det(d^2g)=0$, then $g_{vvv}=6(b-aa_1+a_1^2c)\neq 0$
The conditions of Theorem 1.4 are all satisfied.
Since (1.4) is Z_2-strongly equivalent to h of (1.6), their bifurcation diagrams are topological eqvivalent. That is, the bifurcation behaviors of

$$g'=(\mu+\partial e\, u)^2+\phi u^3 \qquad (1.7)$$

are the same as that of (1.4). We only discuss the properties of (1.7) below.

2 Universal Unfolkings and Transition Variety

At first we state a theorem which tells us that the codimension of (1.7) is three.
Theorem 2.1 The unfolding terms of germ $g'=(\mu+\partial e\, u)^2+\phi u^3$ are $\{1, u, u\mu\}$ and the codimension is three.
Proof: We will prove it in terms of statements of [2].
Take $\partial e=+1$ for simplicity and we have

$$RT(g',Z_2)=\langle g', ug'_u\rangle \{r\}$$
$$=(M^4+R\{u^2+4u\mu+3\mu^2,\ 3\phi u^3+2u^2+2u\mu,$$
$$u^2\mu+u\mu^2,\ u\mu^2+\mu^3,\ u^3+u^2\mu\}]\{r\}$$

$$T(g',Z_2)=(RT(g',Z_2)+E_\mu\{g'_\mu\})\{r\}$$

$$=(M^4+R\{u^2+4u\mu+3\mu^2,\ 3\phi u^3+2u^2+2u\mu,\ u^2\mu+u\mu^2,$$
$$u\mu^2+\mu^3,\ u^3+u^2\mu,\ u+\mu,\ \mu^2+u\mu\})\{r\}$$

$$Itr\{T(g', Z_2)\}=M^4\{r\}$$

To find out the unfolding terms is to search a basis $\{p_1,\ldots,p_k\}$, such that,

$$\{Itr[T(g', Z_2)]\}^{\perp}=(V_{g'}+R\{p_1,\ldots, p_k\})\{r\} \qquad (2.1)$$

where k is the codimension. Now we have

$$V_{g'}=R\{u^2+4u\mu+3\mu^3,\ 3\phi u^3+2u^2+2u\mu,\ u^2\mu+\mu^2u,\ u\mu^2+\mu^3,$$
$$u^3+u^2\mu,\ u+\mu,\ \mu^2+u\mu\}$$

It is easy to see that if we choose $p_1=1$, $p_2=u$ and $p_3=u\mu$, Eq.(2.1) holds.
The universal unfolding of (1.7) is

$$R=\phi u^3+(\mu+\partial e u)^2+\alpha+\beta u+\nu u\mu=0 \qquad (2.2)$$

Now let us calculate the transition variety $\Sigma(Z_2)$ of (2.2). Geometrically, $\Sigma(Z_2)$ is a hypersurface which divides the space of unfolding parameters into several regions. Every two bifurcation diagrams are topological equivalence within any one region and are not equivalence in any two different regions. The bifurcation diagrams are not structural stable on $\Sigma(z_2)$.

$$\Sigma(Z_2)=B_1(Z_2)\cup B_0(Z_2)\cup H_1(Z_2)\cup H_0(Z_2)\cup D(Z_2) \qquad (2.3)$$

The sets of (2.2) are the following.

$$B_0(Z_2):\ \alpha=0;\ B_1(Z_2):\quad \alpha=-\nu u^2+2\phi u^3\quad \beta=2\nu u-3\phi u^2$$
$$H_0(Z_2):\ 16(1+\nu)^2\alpha+\beta^2=0;\quad H_1(Z_2)=D(Z_2)=\Phi \qquad (2.4)$$

where Φ represents zero set.

3 Bifurcation Diagrams and Their Properties

We may draw the hypersurface (2.4) in 3-dimensional space (α, β, ν). We take ν as auxillary parameters and draw these figures in (α, β)-plane. See Fig.3-1, where (a) is the transition variety for $\phi=1$ and (b) for $\phi=-1$. Fig.3-2 is the related bifurcation diagrams where $\partial e=-1$.

The analysis of mechanics behaviors of bifurcation diagrams:

1). Compared with [1], this paper has an extended result, that is, the subharmonic resonance bifurcation has fourteen types. The conclusion of [1] is a part of this paper. The numbers in brackets of Fig.3-2 are types of bifurcation diagrams in [1].

2). The parameter ϕ plays such a role that whether the response amplitude r is limited. r is unlimited for $\phi=-1$ and limeted for $\phi=+1$.

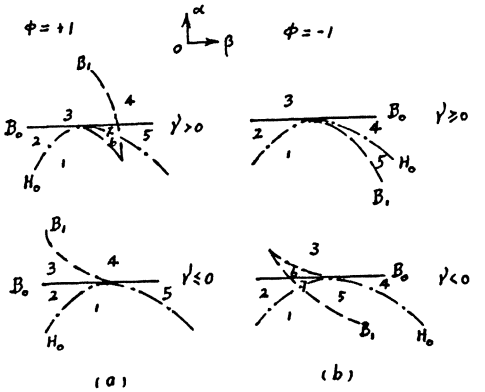

Fig.3-1

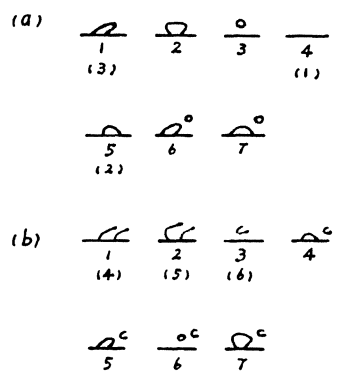

Fig.3-2

$$\phi=\mathrm{sgn}(g_{vvv})$$
$$=\mathrm{sgn}\{[b_1(0)b_2(0)-a_1(0)b_{2\mu}(0)]\delta^2-[c_1(0)c_2(0)-a_1(0)a_{2\mu}(0)]\varepsilon^2-d_1(0)d_2(0)\delta^2\varepsilon^2\} \qquad (3.1)$$

ϕ is mainly determined by first two terms of (3.1) when ε and δ are small parameters. Parameters $a_1(0)$, $b_1(0)$ and $c_1(0)$ have been given in [1] and the remainder parameters may be calculated by a similar proach. We should

note that $b_1(0)$, $b_2(0)$ and $b_{2\mu}(0)$ are determind mainly by nonlinear damping h and $c_1(0)$, $c_2(0)$ and $c_{2\mu}(0)$ by g. The mechanics backgrownd of $\phi=+1$ is that the system has greater damping and the damping restricts the increase of response amplitude. When $\phi=-1$ and the damping is smaller than parametric excitation. The response amplitude can increase infinitely. However, in fact, the nonlinear factors always change while the response amplitude increases and this change makes the amplitude limited.

3). Algebrially, there maybe exist three limit cycles when we discuss the solutions of (2.2). However we can prove that there are at most two limit cycles in fact.

4). In practice, the choise of germ can be considered as truncated terms (0.2). The truncated terms of this paper are much than that of [1]. It is first approximation in [1] and partically second approximation in this paper. Clearly they are different not only in quantity but also in quality.

4 Experimental research

Expermental equipment is a beam fixed supported at one end and simply supported at another end, which bears longitudinal excited force as shown in experimental frame Fig.4-1. The pizoelectric accelerometer is mounted on the center of the beam and measures transvere vibration of the beam. The excited frequency of the system is swept under the full control of the sweep generator. The amplitude of excited force is controlled by changing the excited current. Nonlinear damping of the system is produced by dry friction device, which is mounted in the simply supported end. When the beam is excited by the harmonic force, the nonlinear damping of system can be changed by adjusting the pressure to bear on the beam. Experimental results of mechanical model coinside with the results of paper [1], which are shown in the numbers in brackets of Fig.3-2. Two of the experimental results are shown in Fig.4-2 and Fig.4-3.

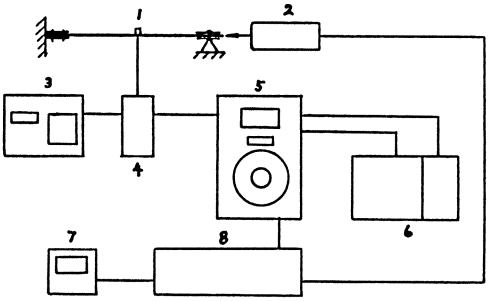

1-accelerometer 2-exciter
3-digital oscilloscope
4-charge amplifier
5-Heterodyne analyzer
6-x-y recorder
7-Amperemeter
8- Power amplifier
size of the beam; 190×24×1m.m

Fig.4-1 experimental frame

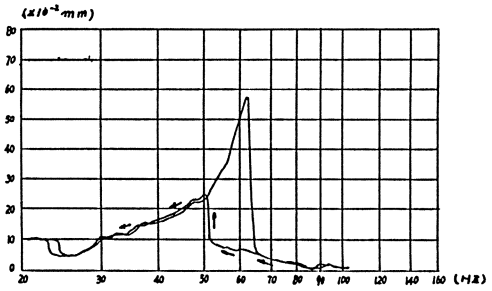

Fig.4-2 The bifurcation diagram corresponding to (3) of Fig.3-1 $\delta=0.06\sqrt{F}$, $\varepsilon=0.21P$

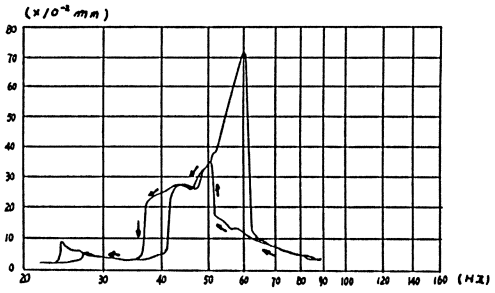

Fig.4-3 The bifurcation diagra, corresponding to (5) of Fig.3-2 $\delta=0.06\sqrt{F}$, $\varepsilon=0.182P$

References

[1] Chen Y. S., & Langfford W. F., Acta Mechanica Sinica, China, 4, 1988

[2] Golubitsky M., & Schaeffer D. G., Singularities and Groups in Bifurcation Theory, Vol.1, Springer-Verlag, 1985

Evolution of Rigid Body Motions due to Dissipative Torques

F.L. Chernousko
Institute for Problems in Mechanics
USSR Academy of Sciences
Moscow, USSR

Summary

Angular motions of a rigid body subjected to perturbation torques of different nature are considered by means of methods of small parameter: averaging and singular perturbations techniques. Evolution of perturbed Euler–Poinsot and Lagrange motions under the influence of small dissipative torques (both external and internal) is studied.

Introduction

We consider dynamics of a rigid body with arbitrary moments of inertia subjected to some external and/or internal torques which include small dissipative torques. It is well–known that equations of rigid body dynamics can be integrated in a closed form only in some special cases. Two of these cases – Euler–Poinsot and Lagrange motions – are taken as unperturbed (nominal) motions.

Different types of perturbation torques are considered: external resistence, torques due to internal degrees of freedom and internal friction, internal torques due to viscous fluid placed in the cavity inside the body etc.

In the case of external torques the method of averaging [1] is applied. The averaging procedure with respect to Euler–Poinsot and Lagrange motions is developed. In the case of internal perturbations the motion of the body is governed by a singularly perturbed system of differential equations. Here we apply singular perturbations technique [2] combined with averaging.

Nonlinear transient processes are studied which depend on the type of dissipative torques. The cases of external and internal dissipation differ drastically. For the first case the angular momentum tends to zero while in the second case it remains constant.

W. Schiehlen (Editor)
Nonlinear Dynamics in Engineering Systems
IUTAM Symposium Stuttgart/Germany 1989

The paper sums up briefly some results of research initiated by problems of satellite dynamics and carried out in the Institute for Problems in Mechanics, USSR Academy of Sciences, see [3 – 15].

Co-ordinate systems and equations of motion

Consider motion of a rigid body R about some fixed point (or its centre of mass) O. Introduce three Cartesian co-ordinate systems: inertial frame Ox_i ($i = 1,2,3$, Ox_3 *is vertical*); frame Oz_i associated with the principal axes of inertia of the body; and frame Oy_i whose axis Oy_3 lies along the vector $\overline{G}$ of the angular momentum of the body while axis Oy_2 lies in a horizontal plane. Equations of motion of the body can be presented in the form [3]

$$\dot{G} = L_3\,, \qquad \dot{\delta} = \frac{L_1}{G}\,, \qquad \dot{\lambda} = \frac{L_2}{G\sin\delta}$$

$$\dot{\theta} = G\,\sin\theta\,\sin\varphi\,\cos\varphi\,(A^{-1} - B^{-1}) + \frac{L_2\cos\psi - L_1\sin\psi}{G}$$

$$\dot{\varphi} = G\,\cos\theta\,(C^{-1} - A^{-1}\,\sin^2\varphi - B^{-1}\,\cos^2\varphi) + \frac{L_1\cos\psi + L_2\sin\psi}{G\,\sin\theta}$$

$$\dot{\psi} = G\,(A^{-1}\,\sin^2\varphi - B^{-1}\,\cos^2\varphi) - \frac{L_1\cos\psi + L_2\sin\psi}{G\,\tan\theta} - \frac{L_2}{G\tan\delta} \tag{1}$$

Here L_i are components of the torque $\overline{L}$ with respect to the axes Oy_i; angles λ and δ define the orientation of the vector $\overline{G}$ in the inertial space (δ is the angle between $\overline{G}$ and Ox_3 while λ is the angle between Ox_1 and the projection of $\overline{G}$ on the plane Ox_1x_2); $G = |\overline{G}|$; θ, φ, ψ are Euler angles (nutation, rotation and precession respectively); and A, B, C are principal moments of inertia with respect to the axes Oz_i.

The kinetic energy of the body is

$$T = \frac{G^2}{2}\left[(A^{-1}\,\sin^2\varphi + B^{-1}\,\cos^2\varphi)\,\sin^2\theta + C^{-1}\,\cos^2\theta\right] \tag{2}$$

Its time derivative is given by

$$\dot{T} = \frac{2T L_3}{G}$$
$$+ G \sin\theta \cos\theta \, (A^{-1} \sin^2\varphi + B^{-1} \cos^2\varphi - C^{-1}) \, (L_2 \cos\psi - L_1 \sin\psi)$$
$$+ \sin\varphi \cos\varphi \, (A^{-1} - B^{-1}) \, (L_1 \cos\psi + L_2 \sin\psi) \qquad (3)$$

In the absence of perturbations ($L_i = 0, \quad i = 1,2,3$) equations (1) describe Euler–Poinsot motion: G, δ, λ, T are constant.

Method of averaging

Let perturbations be comparatively small (in other words, rotation of the body is sufficiently rapid), i.e. $|L_i| T^{-1} \sim \varepsilon \ll 1$ where ε is a dimensionless small parameter. Then the torques can be presented as $L_i = \varepsilon \, L_i^0$ where $L_i^0 \sim 1$ are given functions of $G, \delta, \lambda, \theta, \varphi, \psi$. The motion of the body is perturbed Euler–Poinsot motion with "slow" variables G, δ, λ, T and "fast" variables θ, φ, ψ, see (1), (3). It is convenient to replace one of the fast variables (say, θ) by a slow variable T using (2). Following the method of averaging [1] we average equations (1), (3) with respect to fast Euler–Poinsot motion. This procedure was developed in [3] where angular motions of a satellite subjected to gravity torques were studied. As a result we derive a system of four equations for slow variables G, δ, λ, T. Intergrating it we obtain slow variables with an accuracy of $O(\varepsilon)$ for time interval of $O(\varepsilon^{-1})$. Note that in Euler–Poinsot motion with $A > B > C$ trajectories of the end of the vector $\overline{G}$ are closed curves which encircle either the axis Oz_1 or Oz_3. For motions around Oz_1 we introduce a new variable (instead of G or T)

$$k^2 = \frac{(B - C)(2TA - G^2)}{(A - B)(G^2 - 2TC)}, \qquad (2TB \le G^2 \le 2TA, \quad 0 \le k^2 \le 1) \qquad (4)$$

which is a modulus of elliptic functions arising in Euler–Poinsot case. For motions around Oz_3 we replace A by C and C by A in (4).

Euler–Poinsot motion perturbed by external dissipative and gravity torques

Let the torque consist of gravity and linear resistance terms

$$\overline{L} = m \, \overline{a} \times \overline{g} - I \, \overline{\omega} \qquad (5)$$

where m is the mass of the body R; $\bar{a}$ is a vector of its centre of mass with respect to the fixed point O; $\bar{g}$ is the gravity accelaration acting against Ox_3; and I is a symmetric non-negative definite tensor with constant components I_{ij} with respect to the axes Oz_i.

The averaged equations for the case (5) are

$$\dot{\lambda} = \frac{mg\, a_1}{2G^2\, K(k)} \left[\frac{A(G^2 - 2TC)}{A - C}\right]^{1/2}, \qquad \dot{\delta} = 0 \tag{6}$$

$$\frac{dk^2}{d\xi} = (1-\kappa)(1-k^2) - \left[(1-\kappa) + (1+\kappa)k^2\right]\frac{E(k)}{K(k)}$$
$$\kappa = \left(\frac{2I_{22}}{B} - \frac{I_{11}}{A} - \frac{I_{33}}{C}\right) N, \qquad \xi = \frac{t - t_*}{N}, \qquad N = \frac{AC}{I_{33}\, A - I_{11}\, C} \tag{7}$$

Equations (6), (7) correspond to the case (4). Here $K(k), E(k)$ are complete elliptic integrals of the first and second kind, a_1 is a projection of the vector $\bar{a}$ on the axis Oz_1, ξ is dimensionless time. The constant t_* can be chosen in such a way that $k^2 = 1$ at $\xi = 0$, $t = t_*$.

Equations (6), (7) as well as averaged equations for G and T were obtained and analyzed in [4]. It was proved that G and T decrease monotonically, and the estimates hold

$$G_0 \exp(-b_2\, t) \le G \le G_0 \exp(-b_1\, t)$$

where G_0, b_1, b_2 are positive constants. Similar estimates are true for T.

Equation (7) describing evolution of the motion with respect to the vector $\overline{G}$ was first obtained in [5] for a rigid body containing viscous fluid with high viscisity (small Reynolds number). Analysis and integration of (7) was performed in [4,5].

We shall sum up some conclusions from [4].

In the first approximation, perturbed motion of the body is made up of rapid Euler–Poinsot rotation about the vector $\overline{G}$ and slow evolution of the parameters of this motion. The magnitudes of the angular momentum G and kinetic energy T strictly (exponentially) decrease; their change depends only on the resistance of the medium. The motion of vector $\overline{G}$ in inertial space is described by equations (6) and involves a

constant deviation from the vertical: $\delta = const$. The rotational velocity of $\overline{G}$ about the vertical $\dot{\lambda}$ is variable. Evolution of the parameters of Euler–Poinsot motion described by equation (7) has the following properties.

If $|\kappa| \leq 3$ then all motions tend to rotation about the axis Oz_1 $(for\ N > 0)$ or Oz_3 $(for\ N < 0)$. If $|\kappa| > 3$ then there exists some quasi-stationary motion with $k = k_*$ defined by the equation

$$\kappa = \frac{k^2 - 1 + (1 + k^2)\, E(k)/K(k)}{(1 - k^2)\,[E(k)/K(k) - 1]}$$

If $\kappa N < 0$ then this motion is stable and all motions tend to it. If $\kappa N > 0$ then it is unstable and every motion tends to rotation about Oz_1 or Oz_3.

Other problems

Evolution of rigid body motions subjected to internal elastic and dissipative torques was considered in [6,7]. Some results on singular perturbations method [2] obtained in [8] are useful here. Concrete examples of rigid body motions when the body carries elastic and dissipative elements are given in [9,10].

The obtained results are extended in [11] to rigid bodies with non-rigid parts made up of continuous viscoelastic medium (Kelvin–Voight material). These results are compared with the case of a body having a cavity containing viscous fluid with small Reynolds number, see [5,12].

Perturbed Lagrange motions are studied in [13]. Perturbed motions of a rigid body that are close to regular precession are considered in [14].

Conclusion

Results summed up in this paper make it possible to analyze angular motions of artificial satellites and celestial bodies under the influende of small perturbation torques. Asymptotic approach permits to obtain some qualitative results and to describe evolution of rapid motion using simplified averaged equations. Thus it is possible to avoid numerical integration with small step needed in a direct approach. Results obtained in [3 – 15] made it possible to estimate influence of non-rigidity and dissipation

on satellite angular motions, to evaluate dynamic effects caused by the presence of flexible elements and liquid in tanks, to choose parameters of dampers etc. Note that we did not mention resonant phenomena that arise in averaging procedure when there are two or more slow variables. These phenomena need separate consideration.

References

1. Bogolyubov N.N.; Mitropolsky Yu.A.: Asymptotic methods in theory of nonlinear oscillations. Moskau: Nauka 1963.

2. Vasilyeva A.B.; Butuzov V.F.: Asymptotic expansions for solutions of singularly perturbed systems. Moscow: Nauka 1973.

3. Chernousko F.L.: Motion of a satellite relative to the centre of mass under the action of gravitational moments. Applied Mathematics and Mechanics (PMM) 27 (1963) 474–483.

4. Akulenko L.D.; Leshchenko D.D.; Chernousko F.L.: Fast motion of a heavy rigid body about a fixed point in a resistive medium. Mechanics of Solids (Izv. AN SSR, MTT) 17 (1982) 1–8.

5. Chernousko F.L.: Motion of rigid body with cavities filled with a viscous fluid at low Reynolds numbers. J. of Comput. Math. and Math. Physics (Zh. Vychisl. Matem. i Matem Fiz.) 5 (1965) 1049–1070.

6. Chernousko F.L.: On the motion of a solid body with elastic and dissipative elements. Applied Mathematics and Mechanics (PMM) 42 (1978) 32–41.

7. Chernousko F.L.; Shamayev A.S.: Asymptotic behavior of singular perturbations in the problem of dynamics of a rigid body with elastic and dissipative elements. Mechanics of Solids (Izv. AN SSR, MTT) 18 (1983) 31–41.

8. Chernousko F.L.; Shamayev A.S.: Evolutionary equations for slow variables in the theory of singularly perturbed systems. Doklady of USSR Academy of Sciences 227 (1984) 315–318.

9. Chernousko F.L.: On the motion of rigid body with moving internal masses. Mechanics of Solids (Izv. AN SSR, MTT) 8 (1973) 33–44.

10. Akulenko L.D.; Leshchenko D.D.: Some problems of motion of rigid body with a movable mass. Mechanics of Solids (Izv. AN SSR, MTT) 13 (1978) 29–34.

11. Chernousko F.L.: Motion of a viscoelastic solid relative to the centre of mass. Mechanics of Solids (Izv. AN SSR, MTT) 15 (1980) 17–21.

12. Chernousko F.L.: Motion of a rigid body with cavities containing viscous fluid. Moscow: Computing Centre of the USSR Academy of Sciences. (1968)

13. Akulenko L.D.; Leshchenko D.D.; Chernousko F.L.: Perturbed motions of a rigid body close to Lagrange case. Applied Mathematics and Mechanics (PMM) 43 (1979) 771–778.

14. Akulenko L.D.; Leshchenko D.D.; Chernousko F.L.: Perturbed motions of a rigid body that are close to regular precession. Mechanics of Solids (Izv. AN SSR, MTT) 21 (1986) 1–8.

15. Chernousko F.L.: Asymptotic methods in dynamics of systems with elastic and dissipative elements. Proc. 4th Intern. Conf. on Boundary and Interior Layers. Computational and Asymptotic Methods (BAIL IV). Dublin: Boole Press 1986.

Low Dimensional Behavior in Chaotic Nonplanar Motions of a Forced Elastic Rod: Experiment and Theory

J. P. Cusumano
Department of Engineering Science & Mechanics
The Pennsylvania State University
University Park, PA 16802

F. C. Moon
Department of Mechanical & Aerospace Engineering
Cornell University
Ithaca, NY 14853

Summary
The results of an experimental and theoretical investigation of the dynamics of a thin elastic rod are presented. Regular, planar motions of the rod are observed to become unstable in wedge-shaped regions of the forcing frequency- forcing amplitude parameter plane. Inside of these wedges, motions are nonplanar and generally chaotic. Fractal dimension calculations from experimental data indicate that the dynamics of the rod may be modelled by between two and six degrees of freedom. A family of asymmetric bending-torsion nonlinear modes are discovered experimentally, and their frequency-amplitude characteristic is obtained. A two degree-of-freedom system is derived by starting with a geometrically exact linearly elastic rod theory and projecting onto the first bending and torsional modes. Numerical simulations indicate that this two-mode model exhibits much of the behavior observed experimentally.

Introduction

In this paper, the results of an experimental and theoretical study of the dynamics of a thin, cantilevered elastic rod are presented. A more detailed discussion, along with a complete bibliography, can be found in Cusumano [1], as well as in a forthcoming paper by the authors.

The study of elastic rods is an old one. In fact, we will often refer to the elastic rod under consideration as "the elastica" in reference to the name given the static problem by Euler. While the study of the dynamics of the elastica has a long history, the majority of

W. Schiehlen (Editor)
Nonlinear Dynamics in Engineering Systems
IUTAM Symposium Stuttgart/Germany 1989

work done has dealt with small, linear vibrations. Space does not permit a complete review of the literature here, but a bibliography of works involving the nonlinear vibrations of beams can be found in the survey paper by Sathyamoorthy [2]. Of particular relevance to this study is the work of Crespo da Silva and Glynn [3,4], who used perturbation methods to show that planar motions of a fixed-free beam can lose stability. However, they neglected torsional inertia and assumed nearly equal bending rigidities, which is not the case here.

Experimental Observations

The elastica was clamped at the support end and oriented so that its undeformed neutral axis was vertical (see Fig. 1). The specimen studied was made of carbon steel, with overall dimensions of $28.8cm \times 1.27cm \times .21mm$. The support of the rod was harmonically displaced by means of an electro-mechanical shaker. The axis of displacement was aligned with the lateral axis of symmetry of the rod so that one would expect motions to remain in the x-y plane. Indeed, stable motions are observed in which the response of the rod is planar and regular (i.e. either periodic or quasiperiodic). However experiments showed that the planar motions become unstable in certain regions of the forcing frequency, forcing amplitude plane. The stability diagram of Fig. 2 shows a series of wedge-shaped regimes, each with its apex at a resonance of the system. In the diagram, the f_i, with $i = 2, 3, 4, 5$, are the second through the 5th in-plane bending natural frequencies, and f_τ is the first torsional natural frequency. Resonances occur at all in-plane natural frequencies. Combination resonances are present at frequencies equal to $f_2 + f_3$ and $f_\tau - f_1$. Another resonance at $f^* \cong 92$Hz is not readily identifiable as a combination resonance.

Inside of the regions of planar instability, motions were, in general, chaotic (the response was characterized by a broad-band, continuous power spectrum). Chaotic, nonplanar motions of the thin elastica exhibit dynamic two-well behavior: during excursions out of the x-y plane, the rod stays trapped away from the x-z plane. It should not be inferred that chaotic responses exist at all points inside of the nonplanar regions: in one instance, an asymmetric, period-two response was discovered.

A previously unobserved family of asymmetric bending-torsion nonlinear modes (periodic motions in the conservative system which do not pass through the equilibrium configura-

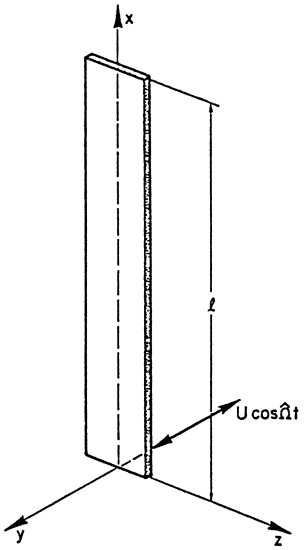

Figure 1: Geometry of the elastica system.

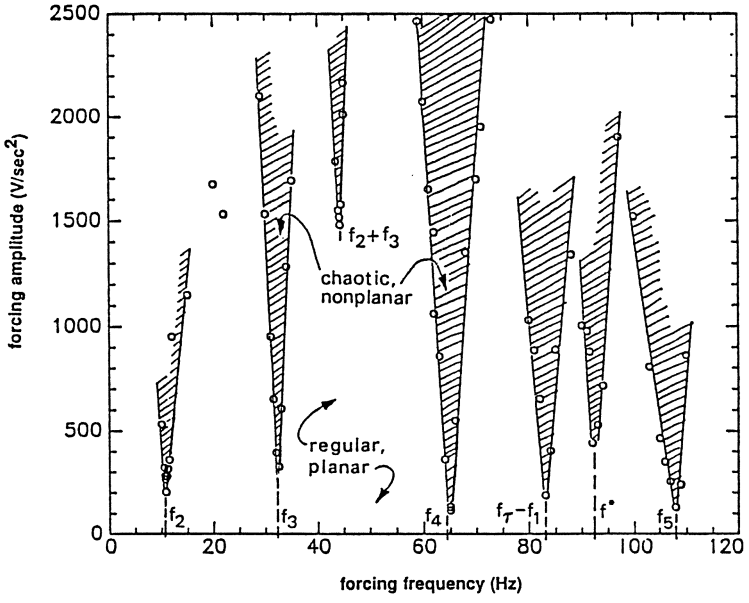

Figure 2: Stability boundaries for the elastica obtained by holding the forcing frequency fixed and increasing the forcing amplitude until planar motions lost stability.

tion of the rod) were found. These solutions pass back and forth through the x-y plane while the rod stays bent away from the x-z plane. The weak damping in the system allowed the frequency-amplitude characteristic for the nonlinear modes to be obtained by estimating the instantaneous frequency of a transient torsional strain signal and plotting the result against the estimated instantaneous torsional strain amplitude (see Fig. 3). The result shows that the frequency of vibration of the nonlinear modes is a decreasing function of their amplitudes. Spectral analysis results taken just after the loss of planar stability near all resonances are qualitatively similar in shape, and an "energy cascading" phenomenon is apparent: most of the power in chaotic tip displacement signals (obtained using an optical edge tracking system) lies well below the driving frequencies, lying instead in low frequency first bending and nonlinear bending-torsion modes.

Fractal Dimension Calculations

The fractal dimensions of attracting sets in different resonant wedges were estimated directly from experimentally-obtained time series using a numerical code based on the correlation dimension method of Grassberger and Proccacia [5]. A key element of the algorithm is the reconstruction of the actual phase-space trajectories from scalar data by means of the delay-embedding procedure. An introduction to fractal dimensions, and to other ideas from dynamical systems theory, along with an extensive bibliography, can be found in [6]. The fractal dimension for a given attractor is estimated by plotting the correlation dimension d_c versus the embedding dimension m used in the delay-embedding procedure (m can be thought of as a guess at the phase space dimension needed to model the observed dynamics). For a deterministic signal, d_c will level out at some critical value of m. For random noise, d_c will continue to grow: in the limit of an infinite number of data points $d_c(m) = m$ for random noise. The resulting dimension estimates for the thin elastica, with one exception, were below 5, which implies from dimension theory that it should be possible to model the dynamics of the rod with between two and six degrees of freedom (see Fig. 4).

Derivation and Analysis of a Two-mode Model

By starting with the classical three-dimensional rod theory due to Love [7] a geometrically exact theory for the experimental system can be developed. Physical scaling arguments

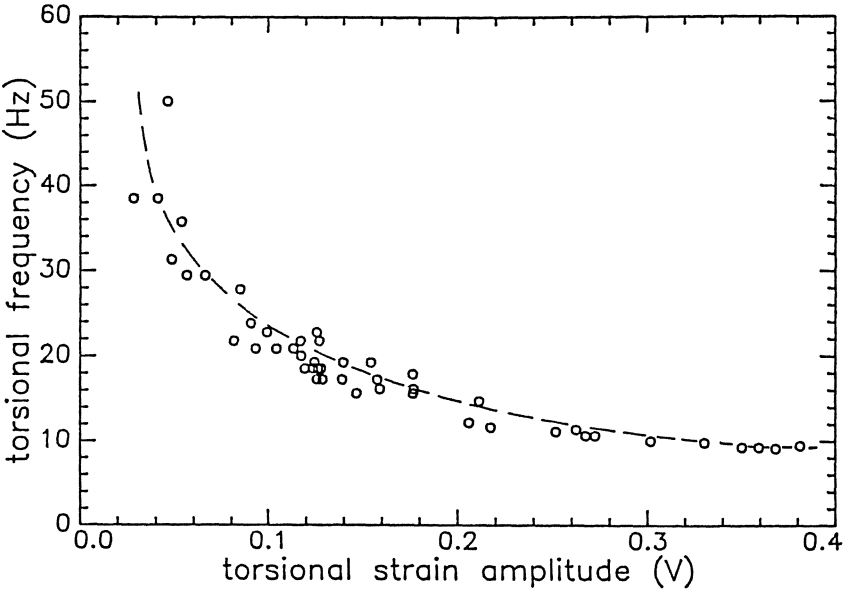

Figure 3: Experimental frequency-amplitude characterisitic for the family of nonlinear modes.

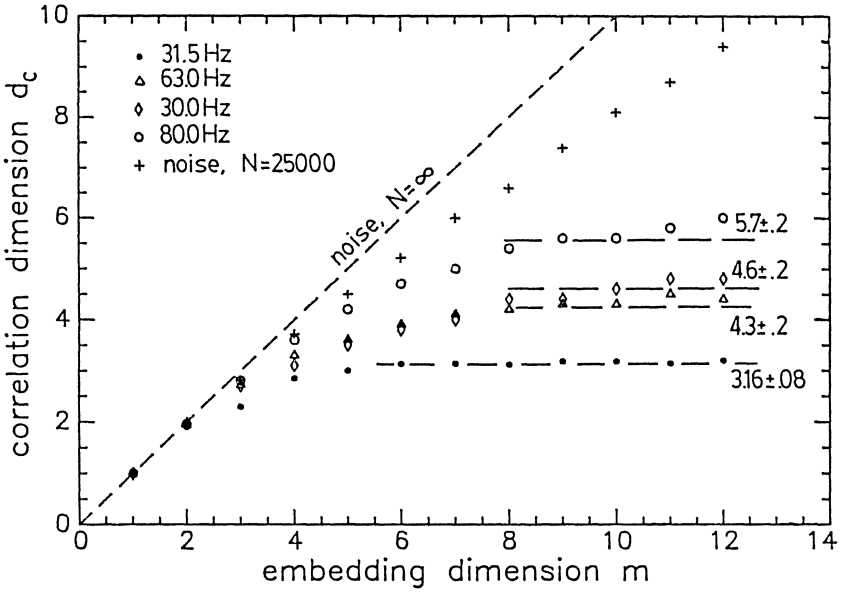

Figure 4: Summary of experimental fractal dimension results.

show that an additional curvature constraint is needed: the curvature component corresponding to bending in the stiff cross-sectional direction is zero. If in addition it is assumed that the torsion of the rod varies slowly along its length, it can be shown that a Lagrangian density in a generalized bending variable U and a generalized torsional variable ϕ is given to second order in U by:

$$\ell = \frac{1}{2}\dot{d}^2 + \dot{d}\dot{U}\cos\phi - \dot{d}U\sin\phi\dot{\phi} + \frac{1}{2}\dot{U}^2 + \frac{1}{2}(\mu + U^2)\dot{\phi}^2 - \frac{1}{1+\nu}(\phi')^2 + \frac{1}{2}(U'')^2 \qquad (1)$$

where $d \equiv D\cos\Omega t$, $\dot{(\,)} = \frac{\partial}{\partial t}$, and $()' = \frac{\partial}{\partial x}$. Then, application of Hamilton's principle leads to the set of partial differential equations:

$$\ddot{U} + U'''' - U\dot{\phi}^2 = D\Omega^2\cos(\Omega t)\cos\phi \qquad (2)$$

and

$$(\mu + U^2)\ddot{\phi} - \frac{2}{1+\nu}\phi'' + 2U\dot{U}\dot{\phi} = D\Omega^2 U\cos(\Omega t)\sin\phi, \qquad (3)$$

with boundary conditions $U(0,t) = U'(0,t) = U''(\bar{l},t) = U'''(\bar{l},t) = 0$ and $\phi(0,t) = \phi'(\bar{l},t) = 0$ (in the preceding, $\bar{l}$ is the dimensionless rod length). We remark that the unforced, linearized versions of equations (2) and (3) correspond to the Bernoulli-Euler beam equation, and the equation for torsional waves on a rod, respectively. Nonlinear coupling in the system comes from coriolis and centripetal acceleration terms, as well as a nonlinear inertia term in equation (3). Observe also that the condition $\phi = 0$, which corresponds to planar motions, defines an invariant manifold for the nonlinear system.

By means of the assumed-modes method, the above partial differential equations can be used to obtain a two-mode model system using the first bending and the first torsional mode of the system. The resulting model system can be put into the following form after the addition of linear modal damping terms:

$$\ddot{q}_1 + \Delta_1\dot{q}_1 + q_1 - \gamma q_1\dot{q}_2{}^2 = \alpha D\Omega^2\cos\Omega t + \beta q_2\dot{q}_2 D\Omega\sin\Omega t \qquad (4)$$

and

$$(\mu + \gamma q_1{}^2)\ddot{q}_2 + \mu\Delta_2\dot{q}_2 + \mu\omega^2 q_2 + 2\gamma q_1\dot{q}_1\dot{q}_2 = -\beta q_2\frac{d}{dt}(q_1 D\Omega\sin\Omega t), \qquad (5)$$

where q_1 and q_2 are, respectively, the bending and torsional modal amplitudes.

The dynamics of the two-mode model represented by equations (4) and (5) were studied numerically. A family of nonlinear modes analogous to those observed experimentally were found, and the computed frequency-amplitude characteristic of the family is qualitatively similar to that found for the rod (Fig. 5). A wedge of planar instability was found for the model inside of which the motions were chaotic and nonplanar (Fig. 6).

Conclusion

The behavior of a two-mode model captures much of the observed dynamics of the thin elastica studied experimentally. Thus, it appears that the precise mechanism of the planar instability observed in the thin elastica can be elucidated by studying a much simpler system. Future work will focus on the nature of modal coupling in the model system of partial differential equations (2) and (3), with the goal of understanding the energy cascading phenomenon observed in the experiments.

References

1. Cusumano, J.P.: Low-Dimensional Behavior in Chaotic Nonplanar Motions of a Forced Linearly Elastic Rod: Experiment and Theory. Ph. D. Thesis, Department of Theoretical and Applied Mechanics, Cornell University: 1989.

2. Sathyamoorthy, M: Nonlinear Analysis of Beams. Part I: Survey of Recent Advances. Shock and Vibration Digest, 14 (1982) 19-35.

3. Crespo da Silva, M.R.M. and Glynn, C.C.: Nonlinear Flexural Torsional Dynamics of Inextensional Beams. I: Equations of Motion. Journal of Structural Mechanics, 6 (1978) 437-448.

4. Crespo da Silva, M.R.M. and Glynn, C.C.: Nonlinear Flexural Torsional Dynamics of Inextensional Beams. II: Forced Motion. Journal of Structural Mechanics, 6 (1978) 449-461.

5. Grassberger, P. and Proccacia, I.: Characterization of Strange Attractors. Physical Review Letters, 50 (1983) 346-349.

6. Moon, F.C.: Chaotic Vibrations: An Introduction for Applied Scientists and Engineers. New York: Wiley 1987.

7. Love, A.E.H.: A Treatise on the Mathematical Theory of Elasticity, 4th edition. New York: Dover 1944.

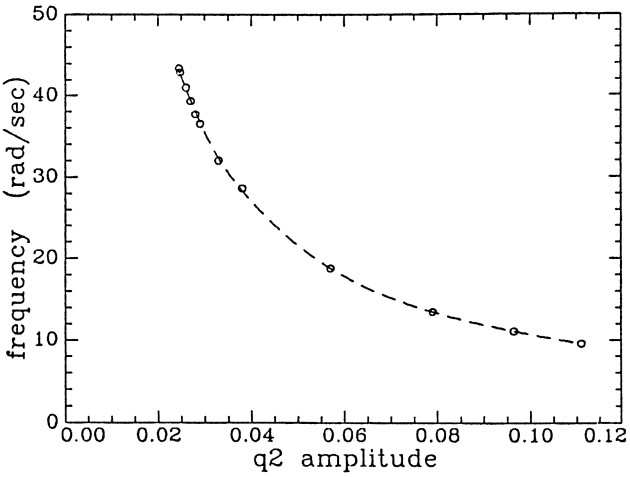

Figure 5: Frequency-amplitude characteristic for the nonlinear modes in the 2 mode model.

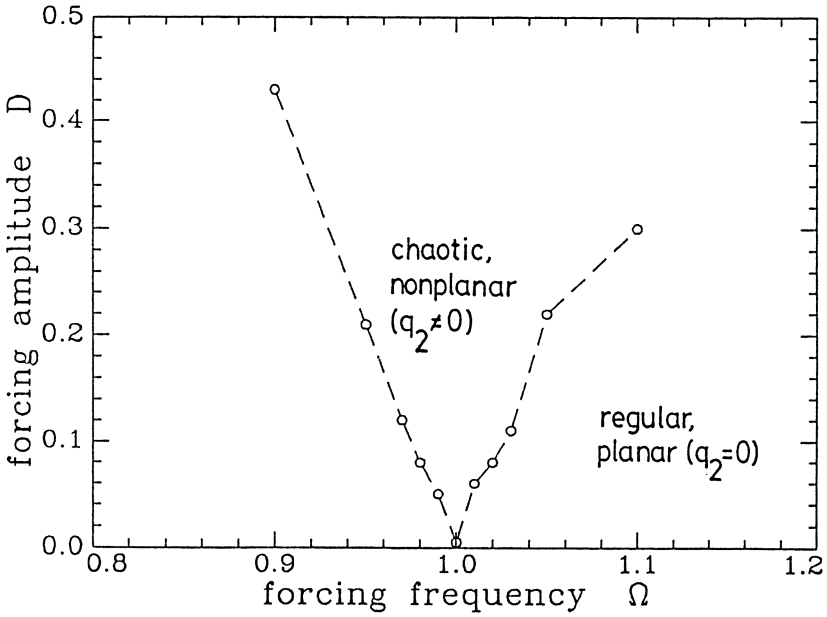

Figure 6: Stability diagram for the 2 mode model.

Localized Buckling as Statical Homoclinic Soliton and Spacial Complexity

M.S. EL NASCHIE , S. Al Athel
King Abdul Aziz City of Science and Technology
Riyadh, Kingdom of Saudi Arabia

A.C. Walker
Mechanical Engineering Department.
University of Surrey, Guildford, United Kingdom.

Summary
The work is aiming at establishing a connection between soliton, chaos and buckling of elastic structures. We discuss two evolutionary, completely integrable nonlinear differential equations with three types of localized solutions; loop soliton, cusp soliton and envelope soliton. After giving a mechanical interpretation to these equations, the first as the dynamical elastica and the second as that governing localized buckling waves in an elastic cylindrical shell, we use a blend of numerical, theoretical and experimental reasoning to show the homoclinicity of these solutions. This in turn may lead through deterministic spacial fluctuation to spacial asymptotic chaos in the sense of Roessler.

Introduction

At least in one incident, before E. Lorenz discovery, someone was looking for chaos and was disappointed to find inexplicable order [1]. Subsequent extension of the work of E. Fermi, et al hinted repeatedly at possible connections between the integrable soliton and the nonintegrable chaos [2, 3].

It is also some time ago when R. Thom [4] noted that "Time has been given a privileged role in the models of generalized catastrophes, but we can do the same for a space coordinates". This sounds today like a programmatic declaration of the "school" of statical chaos which was started in mechanics by the work of P. Holmes and J. Marsden [5], but may have had its roots earlier in unpublished discussions by F. Moon and P. Holmes on the role of the statical-dynamical analogies. Independently and a little later the connection between generalized bifurcation into turbulence on the one side and soliton and localized buckling of shells on the other side was conjunctured by the first author [3, 6-8]. Also independently and slightly later L. Virgin was experimenting already as postgraduate student with similar ideas and gave subsequently an elegant simplified version of the chaotic elastica of Holmes and Mielke [9,10]. Early ideas about localization and soliton may be found in an excellent book by Moon [11]. Spacial chaos in phase

W. Schiehlen (Editor)
Nonlinear Dynamics in Engineering Systems
IUTAM Symposium Stuttgart/Germany 1989

transition is discussed in a profound paper by G. Iooss [12].

In what follows we are investigating two evolutionary, completely integrable differential equations exhibiting three types of solitary wave solutions. The first which may be interpreted as a propagating Euler loop in an infinitely long elastic band was discovered by Ichikawa, et al [2] in connection with problems in plasma physics. The second is the cusp soliton, found by the same authors. The third is the more familiar envelope soliton [13] which may be interpreted as the travelling envelope of localized deformation waves in a buckled shell. In fact depending on the numbers and combinations of slow times and slow spaces involved in the analysis, different Schroedinger and Ginzburg-Landau types of envelope equations were found (see fig 5).

Finally it will be shown that by using a time-like coordinate, the homoclinicity of both loop and envelope soliton in the spacial domain may be established. It follows then that deterministic spacial fluctuation may lead to deterministic asymptotic chaos in the sense of O. Roessler [7, 14].

The dynamical elastica - loop and cusp soliton

Including the inertia terms in the elastica one finds

$$W_{tt} + (P/\rho A)W_{xx} + (\alpha/\rho\bar{A})[W_{xx}(1+W_x^2)^{-3/2}]_{xx} = 0 \qquad (1)$$

where W is the lateral deflection, x is the axial coordinate, P is the axial load, α is the bending stiffness, ρ is the density, $\bar{A}$ is the cross-sectional area of the elastica, $()_x = \frac{d()}{dx}$ and $()_t = \frac{d()}{dt}$. Nondimensionalizing one finds

$$Y_{tt} + \underline{Y_{xx}} + 2\varepsilon[Y_{xx}(1+Y_x^2)^{-3/2}]_{xx} = 0 \qquad (2)$$

where $\bar{x}=\sqrt{\bar{A}}x$, $\bar{t}=(\sqrt{\bar{A}}/\lambda)t$, $Y=\sqrt{\bar{A}}W$, $\lambda=\sqrt{P/\rho\bar{A}}$, $\varepsilon=(\alpha/2P\bar{A})<1$.

We have underlined the second term in eq.(2) to remember for later use that it was multiplied with $P/\rho\bar{A}$. Introducing the stretched coordinates $x_1 = \bar{x}+\bar{t}$, $t_1 = \varepsilon\bar{t}$,

noting that

$$()_{\bar{t}\bar{t}} = ()_{x_1x_1} + 2\varepsilon()_{x_1t_1} + \varepsilon^2()_{t_1t_1} \quad ; \quad ()_{\bar{x}\ldots} = ()_{x_1\ldots}$$

and retaining up to ε order only one finds

$$(Y'' + 2\varepsilon\dot{Y}' + \cdots) + (Y'') + 2\varepsilon[Y''(1+Y')^2)^{-3/2}] + \cdots = 0 \qquad (3)$$

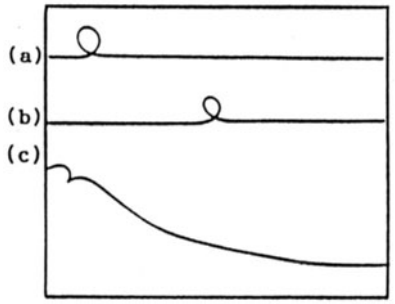

Fig 1

Photographs from an experiment with a very long flexible elastic band. (a) and (b) are travelling loop soliton. (c) seems to be a cusp soliton.

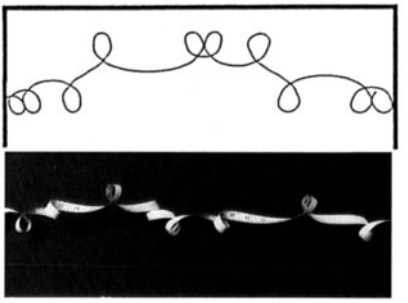

Fig 2

a) Result of numerical integration of the elastica
$\ddot{\phi} + 0.0272222 \sin\phi = 0.15 \sin\phi \sin s$
b) Random loops in a long elastic metal band with periodic torsional predeformation.

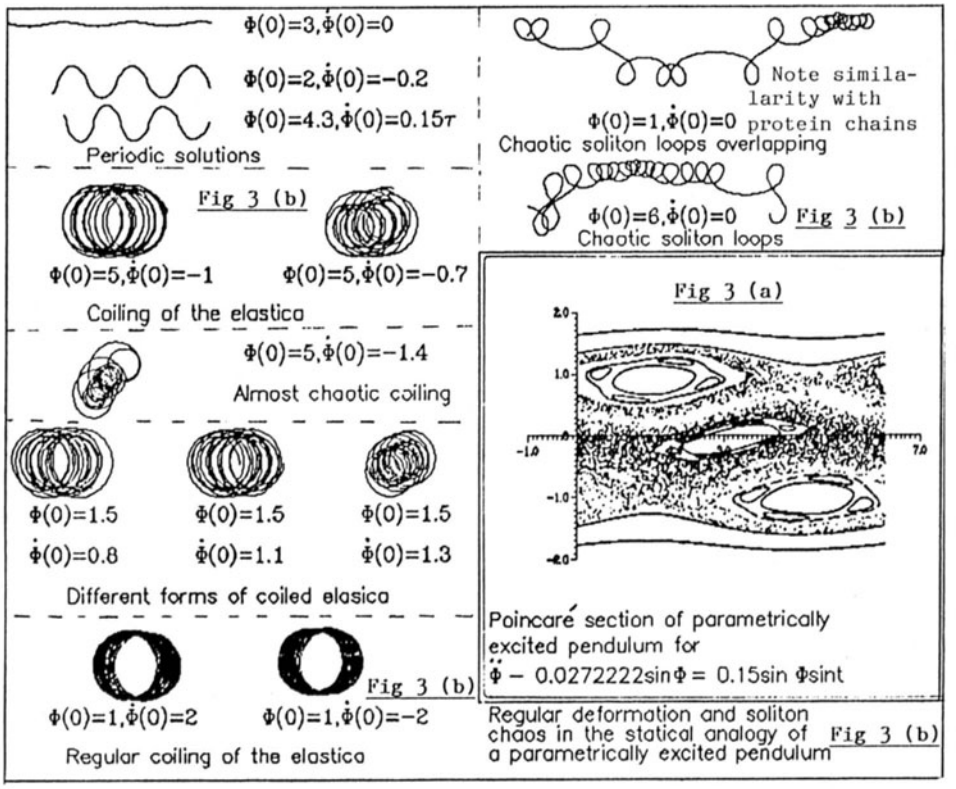

Fig 3 A dual spacial-temporal plot of a parametrically forced nonlinear ordinary differential equation.
(a) Poincaré maps for the parametrically excited pendulum.
(b) Spacial plot of the dual statical situation of (a).

Where $(\dot{})=d()/dx_1$ and $(\ddot{})=d()/dt_1$. Note now that the first term in the first bracket and the second bracket in eq.(3) would have cancelled each other if $P/\rho\overline{A}$ in eq.(1) would have been negative. This is of course only possible when P is a tensile force. In turn this is the case when a loop is formed. Consequently we may write for the looped elastica

$$\ddot{Y} + [\ddot{Y}\,(1+\dot{Y}^2)^{-3/2}]\dot{} = 0 \qquad (4)$$

Noting that $\dot{Y} = \phi$ where ϕ is the slope of the central line of the elastica and using the arch length s as a coordinate one finds

$$\ddot{\phi} + \cos\phi(\sec\phi\phi_{ss})_s = 0 \quad , \quad ()_s=d()/ds \qquad (5)$$

Using the inverse scattering method eq. (4) and (5) were shown by Ichikawa et al to possess travelling loop soliton and cusp soliton [2]. Equation (5) is investigated here numerically and also experimentally. Some photographs, extracted from a video film made by the first author, using a long, very flexible elastic rope are shown in fig (1). Another interesting aspect of eq.(5) in the stationary case is revealed when perturbing it in a hamiltonian way analogus to the parametrically excited pendulum

$$\ddot{\phi} - \lambda\sin\phi = a\sin\phi\sin s \qquad (6)$$

Fig 2 and 3 show the Poincaré plot and the spacial plot of this equation for the parametric value used in [16] namely, $\lambda = 0.0272222$ and $a=0.15$. The important point here is the spacial plot itself, which opens the eyes to new interpretation and countless analogies. In fig (3b) some interesting coiled forms as well as chaotic and periodic loop soliton are shown.

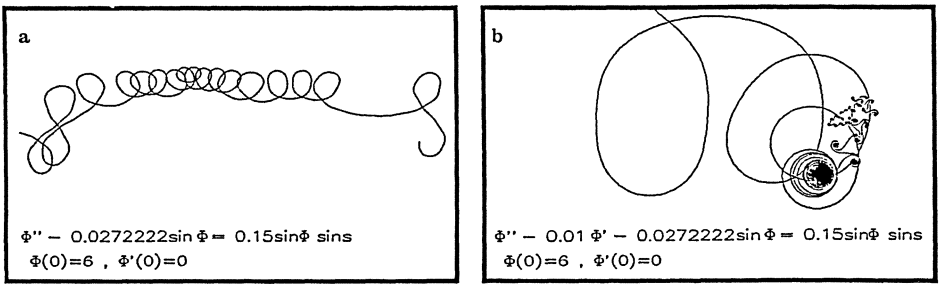

Fig 4 Influence of damping perturbation on the imperfect elastica.
(a) The conservative imperfect elastica.
(b) The nonconservative imperfect elastica.

Note further the resemblance of both to secondary polypeptide chains [17]. Finally in fig (4a, 4b) the effect of damping perturbation is studied for eq (6). Some parts of fig 4(b) are reminiscent of the spirals of the Mandelbrot set.

Buckling of shell-like structures - envelope soliton

Consider the following partial differential equation.

$$\alpha \overline{W}'''' + \sigma \overline{W}'' + C_1 W - C_2 W^2 - C_3 W^3 + \rho \ddot{W} = 0 \qquad (7)$$

Setting $\overline{\rho}=c_2=0$ in eq (7) one finds the equation of Amazigo et al [15]. In the case of $\sigma=c_2=0$ one find that used by A. Nayfeh et al [16]. Here, we draw attention to another interpretation. Setting $C_3=0$ this equation may be regarded as that of the axsymetrical dynamical buckling of an elastic cylindrical shell with logarithmic strain governing the circumferential deformation. Consequently we may regard W as the radial displacement, σ as the axial pressure, $C_1=E\delta/r^2$, $C_2=E\delta/r^3$, $\overline{\rho}$ is the inertia, r is the radius and δ is the thickness of the cylinder. $(')=d()/dx$, $(\dot{})=d()/dt$, and t is the time. Now we seek a perturbative reduction of this equation using a multiple scales method. The simplest solution is to introduce only one slow space using the loading increment $\varepsilon=\sqrt{\sigma^c-\sigma}$ as a parameter and allow the amplitude of deflection $A(x\ t)$ to modulate with the prior knowledge that the slope of the postcritical path is zero. Using $\overline{s}=\varepsilon x$ where $\overline{s}$ is a slow space and omitting details of the standard calculation one finds

$$2\sigma^c A^{**} - n_c^2 A + \gamma A|A|^2 = 0 \quad , \quad (^*)=d()/d\overline{s} \qquad (8)$$

where σ^c is the well known classical bifurcation pressure, n_c is the associated wave number and γ is a constant. Our fourth order partial differential equation has thus been reduced to an ordinary differential equation of the second order. In this drastic reduction the dynamics is lost and the solution is not different from that obtained from purely statical consideration for which $\gamma=\frac{38}{9r^4}$. Equation (8) may in fact be regarded as a stationary nonlinear Schroedinger equation due to obvious reasons. One could restore the time evolution of the problem by introducing several time and space scales. A deep insight into the nature of the prolem may be gained from comparing different categories of periodic and non-periodic solutions of the partial differential equations and the ordinary differential equation. Due to space limitations we proceed with the solution of the stationary case only. Scaling from

the complex to the real, the modulation equation of $A(\bar{s})$ becomes

$$2\sigma^c \overset{**}{A} - n_c^2 A + (19/18r^4) A^3 = 0 \qquad (9)$$

Setting for convenience $\alpha = c_1 = c_2 = r = 1$, noting that

$$\overset{**}{A} = d\overset{*}{A}/d\bar{s} = (d\overset{*}{A}/dA)A \qquad (10)$$

and inserting in eq. (7) one finds

$$\overset{*}{A}^2 = A^2/4 - (19/144)A^4 + k/4 \qquad (11)$$

where $k = 2\overset{*}{A}_o^2 - A_o^2/2 + (19/72)A_o^4$ represents the initial conditions of integration. Now a bounded localized solution implies that A and $\overset{*}{A}$ must vanish for $|\bar{s}| \to \infty$ and since eq (11) discribes for $A_o = \overset{*}{A}_o = 0$ a homoclinic separatrix loop, the phase space $A - \overset{*}{A}$ suggests that $A_\infty = \overset{*}{A}_\infty = 0$ may be regarded as initial values when running "time" $\bar{s}$ backwards and k may be set equal to zero. This leads then, after some elementary manipulations, to the soliton envelope solution

$$A = (6/\sqrt{19})\,\mathrm{sech}(19/12)\bar{s} \qquad (12)$$

In fact, the soliton of the Schroedinger nonlinear partial differential equation found using inverse scattering linearizing transformation (see fig 5) may be easily shown to differ by multiplication with a cosine from the previous solution, that is after appropriate scaling and freezing in time.

In conclusion we would like to demonstrate the predicted sensitivity to initial conditions. This is easily shown analytically since $\delta\overset{*}{A} / \delta k$ lends itself as a measure for this sensitivity. Thus $\partial\overset{*}{A} / \partial k = (1/4\sqrt{2})(1/\sqrt{H})$ shows that when

$$H = 2(A^2 - A_o^2) - (19/18)(A^4 - A_o^4) + 8\overset{*}{A}_o^2 = 0 \qquad (13)$$

then sensitivity becomes infinite. Clearly $\overset{*}{A}_o$ plays a crucial role in this condition. In our example it is easily shown that different approximation to $A_m = A\big|_{\bar{s}=o} = 12/2\sqrt{19} = 1.376494403$ as given by the maximum precision of an ordinary scientific calculator and keeping $\overset{*}{A}_o = 0$, result in a wide variation in the solution. In conclusion we may mention an interesting shell buckling problem (see fig 6a) where the final spacial buckling configuration is completely regular and elastically reversable, however the time evolution and order of appearance of these spacial pattern as we increase the axial pressure is completely random. Another interesting limited buckling problem relevant in oil drilling and may be also in theoretical biology (Ribbon Theory of DNA Double Helix) is shown in fig 6b.

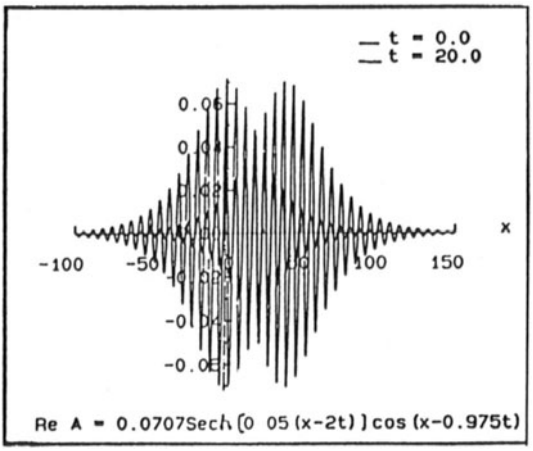

Fig 5
The time evolution of homoclinic soliton waves in the nonlinear Schroedinger equation. Depending on the number and combination of slow times and slow spaces different amplitude equations may be found. For one slow space x_1 and two slow times t_1, t_2 one finds for instance in our example that

$$A^{**} + A + A|A|^2 + iA_t = 0$$

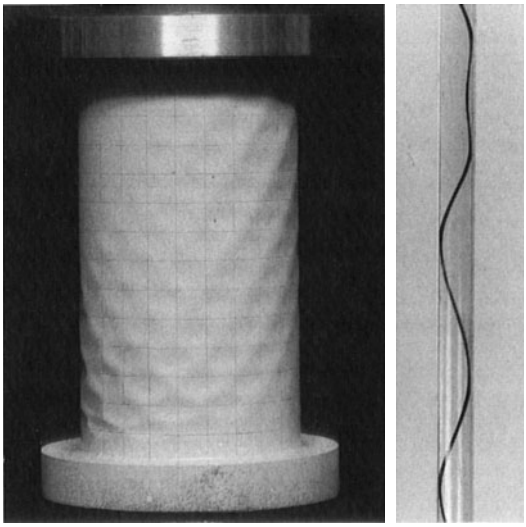

Fig 6
a) Buckling of an elastic cylindrical shell under axial pressure. The inward deflection is limited by another internal cylinder. The order of appearance of local buckles is completely random.

b) Buckling of a long metal band inside a long tube. As the axial force increases localized random waves start appearing abruptly. For certain wire forms spontaneous helical buckling forms appear which might be relevant in some problems connected to D.N.A. Double Helix as well as oil drilling engineering.

Conclusion

The dynamical elastica can sustain cusp and loop soliton. The loops are a new phenomenon in dynamics but their stationary contraparts are known since L. Euler. They were investigated experimentally by M. Born and referred to by R. Feynman in his lectures as fascinating forms. We found that the effect of damping and hamiltonian forcing can produce spacial forms of even more fascinating complexity. Axsymetrical buckling deformation of shells may take the form of envelope soliton and may be perturbed by shape imperfection into spacial chaos. The conclusions drawn here

admittedly from an extremely simplified model, are nevertheless of fundamental importance since we must recognize the existence of internal stochasticity due to the nonlinear deterministic dynamics of a structure besides the external stochasticity due to random imperfection.

References

1. Fermi, E.; Pasta, J.; Ulam, S.M.; Studies in nonlinear probblems. Los Alamos Tech. Rep. L.A. (1940).
2. Ichikawa, Y.H.; Yajima, N.; Recent developments of soliton research in plasma physics. In "Statistical physics and chaos in fusion plasmas". Editors C.W. Horton and L.E. Reichl, New York: Wiley (1984) 79-90.
3. El Naschie, M.S.; Chaos and generalized bifurcation in science and engineering. In "Current Advances in Mechanical Design and Production". Editors Y.H. Kabil and M.E. Said, Pergamon Press (1988) 389-399.
4. Thom, R.; Structural stability and morphogenesis (in particular page 104). London: Benjamin (1975).
5. Holmes, P.H.; Marsden, J.E.; Horseshoes and Arnold diffusion for Hamiltonian systems on Lie groups. Indiana University Mathematical Journal. 32, No 2, (1983) 273-309.
6. El Naschie, M.S.; Order,chaos and generalized bifurcation, K.S.U. Journal of Engineering science, (published by Wiley, London) Vol.14, No 2 (1988) 437-444.
7. El Naschie, M.S.; Al Athel, S.; On the connection between statical and dynamical chaos. Z. Naturforsch, 44a (1989) 645-650.
8. El Naschie, M.S.; Generalized bifurcation and shell buckling as spacial statical chaos. GAMM, Vienna April 5-7, 1988 and ZAMM 69, 5/6 (1989) T367-T377.
9. Mielke, A.; Holmes, P.J.; Spatially complex equilibria of buckled rods. Archive for rational Mechanics and Analysis, 101, 4, (1988) 319-348.
10. Thompson, J.M.T.; Virgin, L.N.; Spatial chaos and localisation phenomena in nonlinear elasticity, Physic letters A (1988) 491-496.
11. Moon, F.; Magneto Solid Mechanics. New York: Wiley (1984).
12. Iooss, G.; Mielke, A,; Demay, I.; Theory of steady Ginzburg-Landau equation in hydrodynamic stability problems, to appear in Eur. J. Mech. B. Fluids (1989).
13. Drazin,P.; Johnson,R.S.; Soliton, Cambridge, Cambridge University Press (1989).
14. Kahlert, C.; Roessler, O.E.; Chaos as a limit in a boundary value problem. Z. Naturforsch., 39a (1984) 1200-1203.
16. Amazigo, J.; Budiansky, B.; Carrier, G.; Asymptotic analysis of the buckling of imperfect columns on nonlinear elastic foundation, Int. J. Solids. Structure 6 (1970) 1341-1356.
17. Nayfeh, A.; Moak,D.; Nonlinear oscillations, New York: Wiley (1979).
18. Troger, H.; On point mapping for mechanical system possessing homoclinic and heteroclinic points, J. Appl. Mech. 46 (1979) 468.
19. Frauenfelder, H.; Biomolecules; In "Emerging syntheses in science", Editor D. Pines. New York: Eddison-Wesley (1988) 155-165.

Dynamic Plasticity: Structural Drift and Modal Projections

P. Fotiu, H. Irschik and F. Ziegler

Department of Civil Engineering
Technical University of Vienna, Austria A-1040/E201

Summary
A plastic source method is developed with structural applications as an alternative to the well-established incremental stiffness formulation of physically nonlinear problems. A combined model of rate-independent plasticity and damage is considered. Total solution is separated into two responses due to external loads and due to the material nonlinearities, which can be considered as defects in the structure. Modal decomposition is applied, where the quasistatic response due to external loads as well as defects is used in closed form whenever possible (e.g. for beam-like structures), which gives better accuracy compared to a series expansion of the total (quasistatic plus dynamic) solution. Defects act as sources of eigenstresses in the structure. Their intensity is determined in a time-stepping manner by means of the constitutive law. FFT is applied to responses in bending vibrations for inspection of changes in the frequency contents due to nonlinear material behaviour.

Introduction

There are two basic sources of nonlinearity in the dynamic behaviour of engineering structures : geometric and material nonlinearities. In the latter case it can be distinguished between elastic and inelastic behaviour. While for a nonlinear elastic material the equation of motion exists in a closed form for the whole time domain, the description of inelastic materials generally demands an incremental formulation, since material parameters change gradually according to prescribed evolution equations.

One of the most interesting phenomena in nonlinear elastic systems is chaotic motion (Moon [1]), which often results from bifurcations of the phase trajectory (see e.g. Guckenheimer, Holmes [2]). Various techniques can be used to visualize the characteristics of nonlinear (chaotic) vibrations, like phase portraits, Poincare maps, Fourier transforms or simply time histories of deflections. Although there are cases, where inelastic - plastic, say - deformations create bifurcation-like behaviour (Symonds, Yu [3], Poddar,Moon,Mukherjee [4]), even non-bifurcating motions of inelastic systems often show results, which in some aspects resemble those of chaotic motions. There exists a variety of analytical tools for investigation of bifurcation points and their characteristics in nonlinear elastic systems, [2]. No such methods can be used when inelastic behaviour occurs, since the state of the system is no longer uniquely determined by deflections alone. However, more insight into the structural behaviour can be achieved by considering inelastic effects (e.g. plastic deformation, material degra-

W. Schiehlen (Editor)
Nonlinear Dynamics in Engineering Systems
IUTAM Symposium Stuttgart/Germany 1989

dation, which are considered in the sequel) as defects, which act as an additional loading on the associated *linear elastic* structure. Of course, this type of loading depends on the prescribed external excitation. Because of linearity modal analysis can be used for solution, that is, the nonlinear response is projected into the eigenspace of the associated system. However, modal expansion is performed only on the purely dynamic part of solutions (due to inertia forces), whereas the quasistatic part is computed separately in closed form. This is favourable, because - depending on the type of loading - the quasistatic part may contain singularities or discontinuities, which are poorly modeled by series (Gibbs phenomenon). Eventually, the quasistatic response due to the additional (defect) loading represents a characteristic feature of elasto-plastic oscillators, namely the structural drift.

Bending Vibrations of Beams and Plates

A most general version of the plastic source method applicable to three-dimensional motions of a solid including large strains has been derived by Irschik and Ziegler [5]. Subsequent application of D`Alembert`s principle and the principle of virtual displacements render an integral equation for the displacement vector. In the case of bending vibrations the virtual deflection $\tilde{w}(\xi,x)$ is assumed as the statical Green`s function due to a transversal unit force F=1 at the point **x** in the midplane of the plate or at the axis of the beam. When considering the static equilibrium under the action of the unit force F=1 the virtual displacements are specified to be the actual dynamic deflection w at constant time t. Total strains ε_{ij} can be eliminated by inserting the constitutive relations and the linear elastic influence strains $\tilde{\varepsilon}_{ij}$ by means of Hooke`s law. The result within the limits of linearized geometric relations is

$$Fw(x,t) = \int_B \tilde{w}(\xi,x)\, p(\xi,t)\, dB_\xi + \int_V \tilde{\sigma}_{ij}(\xi,x)\, \varepsilon_{ij}^N(\xi,t)\, dV_\xi - \int_B \tilde{w}(\xi,x)\, \mu\dot{w}(\xi,t)\, dB_\xi \quad (1)$$

In case of a beam $dB_\xi = d\xi$, $dV_\xi = dA\, d\xi$ and μ is the mass per unit length, hence, integration is performed over the cross-section A. For a thin plate, $dB_\xi = d\xi d\eta$ is an element of the midplane, $dV_\xi = d\xi d\eta d\zeta$ and μ represents the mass per unit area. Integration of nonlinear strains over thickness h renders the nonlinear portion of curvature components κ^N (beam) and κ_{ij}^N (plate),

$$\kappa_{ij}^N = \frac{12}{h^3} \int_{-h/2}^{h/2} z\, \varepsilon_{ij}^N\, dz\,; \quad \kappa^N = \frac{1}{J} \int_A z\, \varepsilon^N\, dA\,, \quad J = \int_A z^2\, dA \qquad (2)$$

The integrals in Eq. (1) represent the deflection due to external load $p(x,t) = p(x)\, s(t)$, noncompatible strain components ε_{ij}^N and inertia loading, respectively. Hence, formally superposition applies and the deflection may be split into two linear portions w^e and w^*, where the former refers to external load, while the latter accounts for the inelastic strains ε_{ij}^N. To improve numerical accuracy a further sepa-

ration into the quasistatic solution and the dynamic part is emphasized, (see Boley and Barber [6] for the thermal shock problem)

$$w^e = w_S^e + w_D^e\,, \quad w^* = w_S^* + w_D^* \tag{3}$$

The quasistatic response w_S^* is a physical definition of the structural plastic drift. For a Kirchhoff plate and a Bernoulli-Euler beam follows, respectively

$$w_S^*(x,t) = \int_B \tilde{m}_{ij}(\xi,x)\ \kappa_{ij}^N(\xi,t)\ dB_\xi, \quad w_S^*(x,t) = \int_B \tilde{M}(\xi,x)\ \kappa^N(\xi,t)\ d\xi \tag{4}$$

In Eq. (4) $\tilde{m}, \tilde{M}$ are the static moment Green's functions, see e.g. [7]. The dynamic deflection is determined by the integral equation

$$w_D^{e,*}(x,t) + \int_B \tilde{w}(\xi,x)\ \mu\, \dot{w}_D^{e,*}(\xi,t)\ dB_\xi = -\int_B \tilde{w}(\xi,x)\ \mu\, \dot{w}_S^{e,*}(\xi,t)\ dB_\xi \tag{5}$$

Eq.(5) is solved by means of a modal decomposition of w_D

$$w_D^e(x,t) = \sum_n Y_n^e(t)\ \Phi_n(x)\ , \quad w_D^*(x,t) = \sum_n Y_n^*(t)\ \Phi_n(x) \tag{6}$$

Hence, the solution of the nonlinear problem is projected into the space of the orthogonal eigenfunctions $\Phi_n(x)$ of the associated linear elastic structure. Insertion of $Eq.(6)_1$ into Eq.(5) yields SDOF-oscillator equations for the generalized coordinates Y_n^e

$$\ddot{Y}_n^e + 2\zeta_n\omega_n\, \dot{Y}_n^e + \omega_n^2\, Y_n^e = -\frac{\Gamma_n^e}{m_n\, \omega_n^2}\, \ddot{s}(t) \tag{7}$$

where ω_n and ζ_n are the n-th eigenfrequency and light modal damping coefficient, respectively. Furthermore,

$$\Gamma_n^e = \int_B \Phi_n(\xi)\ p(\xi) dB_\xi\,, \quad m_n = \int_B \mu\, \Phi_n^2(\xi)\ dB_\xi \tag{8}$$

Care must be taken in determining initial conditions for Y_n^e. In case of homogeneous total initial conditions they read

$$Y_n^e(0) = -\frac{\Gamma_n^e}{m_n\,\omega_n^2}\,s(0), \qquad \dot{Y}_n^e(0) = -\frac{\Gamma_n^e}{m_n\,\omega_n^2}\,\dot{s}(0) \tag{9}$$

The response due to nonlinear material effects has to be evaluated in a stepwise manner, since their intensity is governed by the momentary state of the structure. This yields an implicit problem for determining the increments $\Delta\kappa^N$ within a time-step $\Delta t = t_i - t_{i-1}$. In contrast to $\kappa^N(\mathbf{x},t)$ the increment $\Delta\kappa^N(\mathbf{x},t)$ is separabel into a time- and space-dependent part $\Delta\kappa^N(\mathbf{x},t-t_{i-1}) = \Delta\kappa^N(\mathbf{x})\ f(t-t_{i-1})$, $t \le t_i$, where $f(t-t_{i-1})$ is a time shape function. Thus,the increments of the modal coordinates ΔY_n^* are given as the solution of SDOF–oscillator equations in the time interval Δt. In case of a beam , [8]

$$\Delta Y_n^* = \exp(-\zeta_n\omega_n\Delta t)\left(\frac{\dot{Y}_n^*(t_{i-1})+\zeta_n\omega_n Y_n^*(t_{i-1})}{\omega_n}\sin\omega_n\Delta t + Y_n^*(t_{i-1})\cos\omega_n\Delta t\right) -$$

$$- Y_n^*(t_{i-1}) - \int_B \mu\,\frac{L_n^*(\xi,\Delta t)}{m_n\,\omega_n}\,\Delta\kappa^N(\xi)\,d\xi \tag{10}$$

where $\sqrt{1-\zeta_n^2} \approx 1$ is assumed and

$$L_n^*(\xi,\Delta t) = \left(\int_B \tilde{M}(\xi,x)\,\Phi_n(x)\,dx\right)\left(\int_0^{\Delta t} \ddot{f}(\tau)\exp\left(-\zeta_n\omega_n(\Delta t-\tau)\right)\sin\omega_n(\Delta t-\tau)\,d\tau\right) \tag{11}$$

Assuming $f(\tau)$ as a linear ramp function, the second bracket in Eq.(11) has the value $(1/\Delta t)\exp(-\zeta_n\omega_n\Delta t)\sin\omega_n\Delta t$.

Constitutive Relations

The undamaged solid behaves according to an elasto-plastic kinematic hardening model

$$\sigma = \sigma_y + \eta = E(\varepsilon - \varepsilon^p), \quad \eta = \bar{E}\,\varepsilon^p \tag{12}$$

where σ_y is the yield stress and η marks the center of the yield surface in stress space. The yield-limit is given by

$$|\sigma-\eta| = \sigma_y \tag{13}$$

Damage is considered by Kachanov`s model, see Krajcinovic [9] for a review, by changing the nominal stress to an effective stress

$$\sigma \to \bar{\sigma} = \sigma/(1-D)\ , \quad \eta \to \bar{\eta}/(1-D) \tag{14}$$

With Eq.(14), Eqs.(12) take the incremental form

$$\Delta\sigma = \Delta\eta - \sigma_y \Delta D = E(\Delta\varepsilon - \Delta\varepsilon^N)\ ,\ \ \Delta\eta = \bar{E}\ (1-D)\ \Delta\varepsilon^p \tag{15}$$

with

$$\Delta\varepsilon^N = (1-D-\Delta D)\ \Delta\varepsilon^p + (D+\Delta D)\ \Delta\varepsilon + \Delta D\ (\varepsilon - \varepsilon^p) \tag{16}$$

The yield limit in the damaged material is given by

$$|\sigma-\eta| = (1-D)\ \sigma_y \tag{17}$$

The evolution equation for the damage parameter is taken in a form similar to that of Frantziskonis and Desai [10], but the argument containing the dissipated plastic energy W_D instead of the accumulated plastic strain

$$D = D_u\left[1 - \exp(-\alpha\ W_D^2)\right] \tag{18}$$

The increment of W_D is given by

$$\Delta W_D = \frac{\sigma_y}{1-D}\left(1 - \frac{E_1}{E}\right)|\Delta\varepsilon|\ ,\ \ E_1 = E\bar{E}/(E+\bar{E}) \tag{19}$$

Numerical Results

A clamped-clamped beam is considered, which is excited by an uniform load $p(x) = p_0$ sinusoidal in time with $s(t) = \sin \nu t$. The following parameters are used in the computations : $l/h = 20$, $E/\sigma_y = 2000$, $E_1/E = 0.1$, $p_0 l^3/EJ = 1.0$, $\nu/\omega_1 = 1.5$ and $\zeta_n = 0.02$ for all modes. The damage parameters are $D_u = 0.95$, $\alpha\sigma_y^2 = 50.0$. The influence of damage is rendered most impressively in a moment-curvature plot at the clamped edges, Fig.1. The different parts of deflections of the inelastic beam are shown in Fig.2. Note the periodic but sectionally constant shape of the structural drift w_S^*. This accounts for the additional peaks at multiples of ν in the Fourier spectrum, Fig.3. Phase diagrams of the projection of the total deflection on the fundamental mode are given in Fig.4 for the elasto-plastic beam without and with damage. While in the first case there exists an attracting point (see Fig.5.b), no such point appears in the damaging system (Fig.5.c). As can be seen in Fig.4.b, there appears an "intermediate attracting orbit" in the phase space. At first trajectories seem to be attracted by this "intermediate orbit", but after a certain amount of time move inward and tend to a new one. This attractor, too, does not seem to be the final one, because there is still plastic energy dissipating, producing additional damage in only slightly deteriorated regions of the beam. After a sufficient amount

of damage in those sections, trajectories again will leave this second "intermediate attractor". The associated linear elastic system obviously shows an attracting fixed point (Fig.5.a), but at a location different from that in the elastic-plastic case.

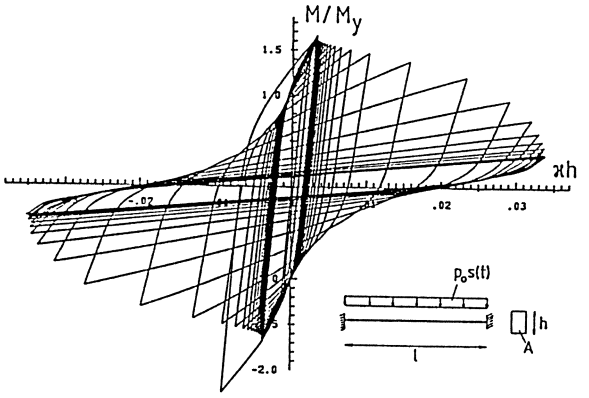

Fig. 1 : Moment-curvature relation at clamped edge in elastic-plastic damaging beam.
$M_y = \sigma_y Ah/6$.

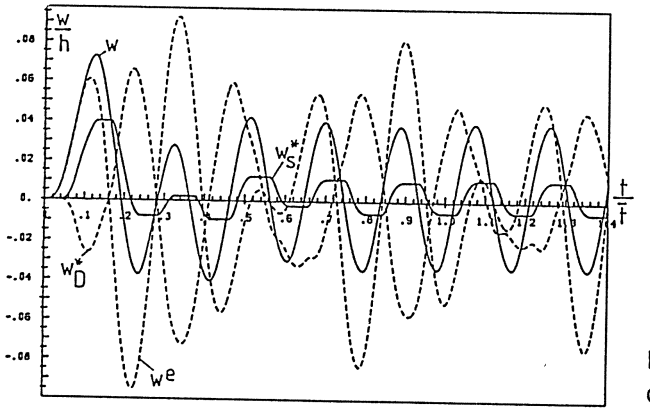

Fig. 2 : Different parts of midpoint deflections. $\bar{t} = l^2(\mu/EJ)^{1/2}$.

Conclusions

Due to the evolutionary character of plastic flow and damage vibrations of such systems cannot be handled by the same methods suitable for nonlinear elastic oscillations. More information about response characteristics is gained by a subdivision into responses of the associated linear elastic system due to external load and arising defects if the structural state crosses the elastic limit. The quasistatic part of the response due to defects represents the plastic drift, a characteristic feature of elasto-plastic oscillators, which makes it so difficult to model such kinds of vibrations by approximate global (non-incremental) methods (in case of random vibrations a possible way of including the drift process is described in [11]). Projections of the total response on the basic mode may serve

as approximate solutions comparable to a single term Ritz-Ansatz. Results show in some pictures chaos-like behaviour, although there are apparently no bifurcations.

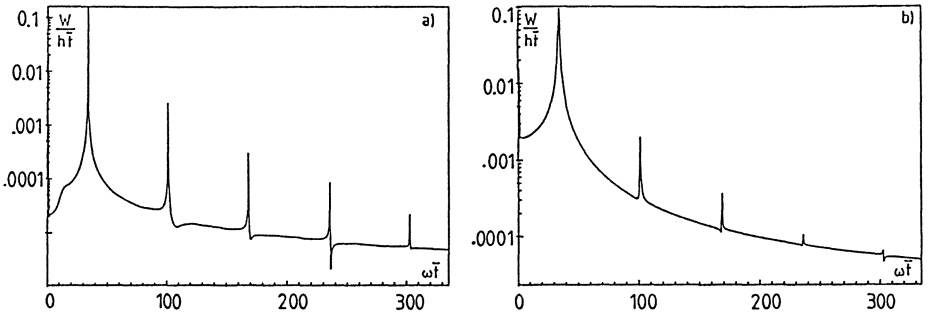

Fig. 3 : Absolute value of Fourier transform of midpoint deflection.
a) without damage, b) with damage .

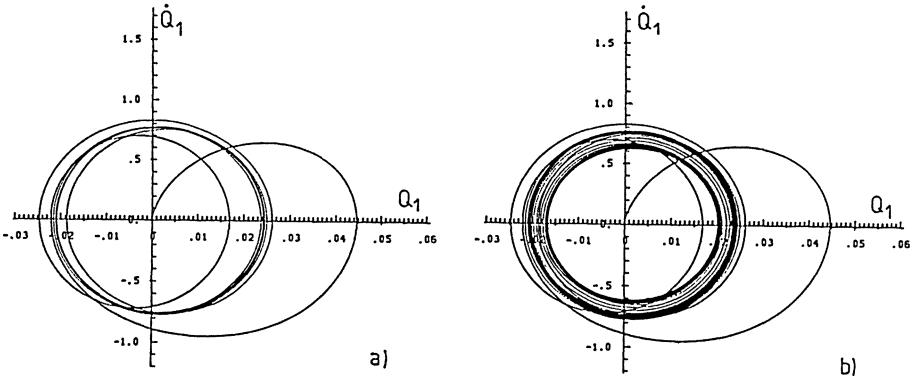

Fig. 4 : Phase diagram of first mode projection of midpoint total deflection.
a) without damage, b) with damage.

$$Q_1(t) = (1/h)\int_0^1 w(\bar{x},t)\,\Phi_1(\bar{x})\,d\bar{x}\ ,\quad \dot{Q}_1 = (\bar{t}/h)\int_0^1 \dot{w}(\bar{x},t)\,\Phi_1(\bar{x})\,d\bar{x}\ ,\quad \bar{x} = x/l$$

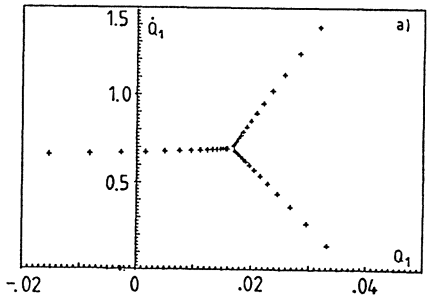

Fig. 5 : Poincaré maps of first mode projection of midpoint total deflection. a) elastic, b) elasto-plastic, c) elasto-plastic with damage. $\phi = 216°$.

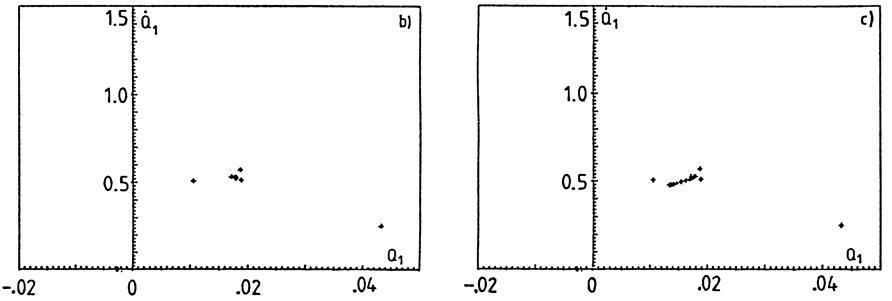

Acknowledgement
Support through the grant S30-03 of the Austrian National Science Foundation FWF is gratefully acknowledged. The authors are indebted to Professor Francis C. Moon for valuable hints with respect to plastic chaos.

References

1. Moon, F.C. : Chaotic Vibrations. New York : J. Wiley & Sons 1987.

2. Guckenheimer, J. ; Holmes, Ph. : Nonlinear Oscillations, Dynamical Systems, and Bifurcations of Vector Fields. New York : Springer 1983.

3. Symonds, P.S. ; Yu, T.X. : Counterintuitive behavior in a problem of elastic-plastic beam dynamics. J. Appl. Mech. 52 (1985) 517 – 522.

4. Poddar, B. ; Moon, F.C. ; Mukherjee, S. : Chaotic motion of an elastic-plastic beam. J. Appl. Mech. 55 (1988) 185 – 189.

5. Irschik, H. ; Ziegler, F. : Dynamics of linear elastic structures with selfstress : A unified treatment for linear and nonlinear problems. ZAMM 68 (1988) 199 – 205.

6. Boley, B.A. ; Barber, A.D. : Dynamic response of beams and plates to rapid heating. J. Appl. Mech. 24 (1957) 413 – 419.

7. Fotiu, P. ; Irschik, H. ; Ziegler, F. : Dynamic response of elasto-viscoplastic deteriorating beams and plates. Computational Mechanics ´88 , Atluri, S.N. ; Yagawa, G. (eds.), 40.i.1 – 40.i.5 . Atlanta : Proc. ICES 1988.

8. Fotiu, P. ; Irschik, H. ; Ziegler, F. : Forced vibrations of an elasto-plastic deteriorating beam. Acta Mech. 69 (1987) 193 – 203.

9. Krajcinovic, D. : Continuum damage mechanics. Appl. Mech. Update 1986, ASME, 397 – 406. New York 1986.

10. Frantziskonis, G. ; Desai, C.S. : Elastoplastic model with damage for strain-softening geomaterials. Acta Mech. 68 (1987) 151 – 170.

11. Irschik, H. ; Ziegler, F. : Nonstationary random vibrations of yielding frames. Nuc. Eng. Design 90 (1985) 357 – 364.

Nonlinear Vibrations of Carbon Brushes Sustained by Thermoelastic Effects of the Slipring

G. GABRIELLI

Large Turbogenerator Department
Asea Brown Boveri Ltd,
Baden, Switzerland

G. SCHWEITZER

Institute of Mechanics,
ETH Zürich, Switzerland

Summary

For the investigation of the brush vibrations a mechanical model with a rigid brush sliding on a predeformed slip ring surface is adopted. The rotation of the predeformed slip ring leads to brush vibrations causing a particular distribution of friction losses resulting then in a thermally induced deformation of the slip ring surface. At certain parameter configurations the thermal deformation reinforces the predeformation and the system becomes unstable. Due to a nonlinear contact geometry a strong sensitivity to small parameter variation exists. The model allows new explanations for measured phenomena.
In addition chaotic motion has also been observed in the mathematical model. This motion occurs at higher predeformation levels of the slip ring surface.

Introduction

Large generators usually have steel collector rings and brushgear for conducting the field current to the rotor. These sliding contacts can lead to brush vibrations which have always been of central importance [1].
For a generator running at 3000rpm the frequency spectrum of measured brush vibrations usually shows the highest amplitude between 1000 and 2500 Hz and only those frequencies which are a multiple of the rotational speed are present. Moreover, the vibrations are synchronized with the angular slip ring position and the pattern changes only slowly with time. The conclusion is therefore, that the slip ring surface has a decisive effect on the brush vibration phenomenon.

W. Schiehlen (Editor)
Nonlinear Dynamics in Engineering Systems
IUTAM Symposium Stuttgart/Germany 1989

In the past brush vibrations have been interpreted as a type of self-excited vibrations due to the decreasing coefficient of friction with increasing sliding velocity [2],[3]. However, as was shown in [4], the damping induced by the brush material is enough to stabilize this kind of self-excitation. Thus we see that other causes must be found.

Regenerative Brush Vibration

We make the assumption that the slip ring surface is not exactly round but, due to fabrication tolerance for example, has an initial existing sinusoidal deformation r_g (Fig. 1). As a result of the ring rotation, the surface has a velocity v and the brush would be excited in a steady-state vibration. It is further assumed, that as a result of the steady vibration, the friction force F_R between the ring and the brush is time varying as well. Therefore the friction losses will show a sinusoidal distribution q_R over the ring surface, too, producing a corresponding thermal surface displacement u in the radial direction.

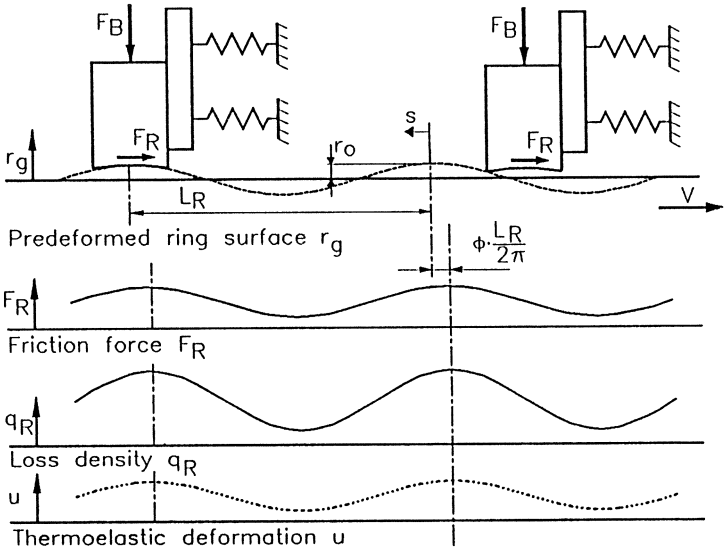

Fig.1. Mechanism of the regenerative brush chatter

Depending on the phase shift Φ between the initial ring deformation r_g and the thermal deformation u, the latter will be either increased or reduced. If in the region of deformation peaks, more energy is released than in the valleys, the deformation increases and a state of unstable growth exists.

This brush vibration, caused by the feedback trough thermal ring deformation, will be referred to as regenerative brush chatter. It strongly depends on the nonlinear constraints the sliding brush is subject to, and it is this mechanism that will be explained subsequently.

The Brush, Modelled as a Rigid Body

For the investigation of this hypothesis, the brush is modelled as a rigid body. Thus in the subsequent calculation of energy distribution on the slipring surface, the location of the contact between the brush and the ring is taken into account along with the magnitude of the friction force F_R.
A model is set up, similar to that used in [3]. The most important difference is the ring surface: in [3], the surface was assumed to be perfectly round, whereas we start with a surface having an initial sinusoidal deformation (Fig. 2), leading to a nonlinear contact geometry.
The sliding surface of the brush forms an arc of radius R_B about the instantaneous center of curvature at M_B. The center of curvature for the slip ring surface area at the contact A is at M_R. At contact A there is a normal force F_N in the radial direction and a friction force F_R in the tangential direction, in accordance with Coulomb's law.
The brush itself has two DOF, and it is also assumed that the brush is always in contact with the slip ring.
Clearence s_{sp} which normally exists between the brush holder and the brush is also taken into account.
The location of the contact is dependent in a very sensitive way on both the position of the brush and the angular position of the rotor. Due to this kinematic constraint, the mathematical model becomes strongly nonlinear.

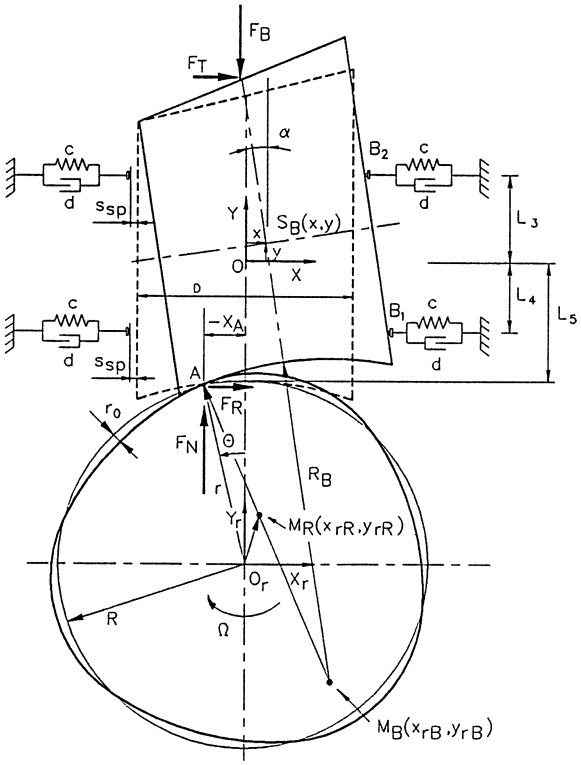

Fig.2. Model used for calculating the brush vibrations

We obtain the time-variable differential equation system of the form, derived in detail in [4]:

$$m \cdot \ddot{x} = f(x, \dot{x}, \alpha, \dot{\alpha}, t, \text{various parameters}) \qquad (1)$$

$$J \cdot \ddot{\alpha} = g(x, \dot{x}, \alpha, \dot{\alpha}, t, \text{various parameters}) \qquad (2)$$

Because of the nonlinearity and the time-dependence, these equations are handled by numerical simulation, thus yielding the magnitude and position of the friction force F_R between the brush and the slipring. The thermal displacement of the slip ring surface is calculated using the relations in [5]. The values used for the simulation are given in Table 1.

Brush thickness	D = 25mm	Brush force	F_B = 11N
Distance L_3	L_3= 20mm	Tangent. force	F_T = 5N
Distance L_4	L_4= 20mm	Coeff. of friction	μ = 0.16
Distance L_5	L_5= 25mm	Mass of brush	m =.05kg
Stiffness	c = 10^6N/m	Moment of inertia	J=$13\cdot10^{-6}$kgm^2
Damping $D_x=d/\sqrt{2c\cdot m}$	D_x= 0.01		

Table 1: Values used in the analysis

As the calculations have shown, the sensitivity factor

$$e = R/(R_B-R)$$

is crucial for the occurence of regenerative brush chatter.

In Fig.3 the sinusoidal portion u_1 of the thermal deformation of the slip ring surface is shown for two different sensitivity factors. For the greater sensitivity factor in Fig.3b the thermal deformation is higher at the top of the wave than between the tops. Consequently the initial slipring deformation r_g is amplified by the thermal deformation, and the brushes are excited into stronger vibration. The behaviour is thus unstable. The results from simulation compare very nicely to data and phenomena encountered in various experiments [4], and countermeasures for avoiding this built-up of vibrations are being derived.

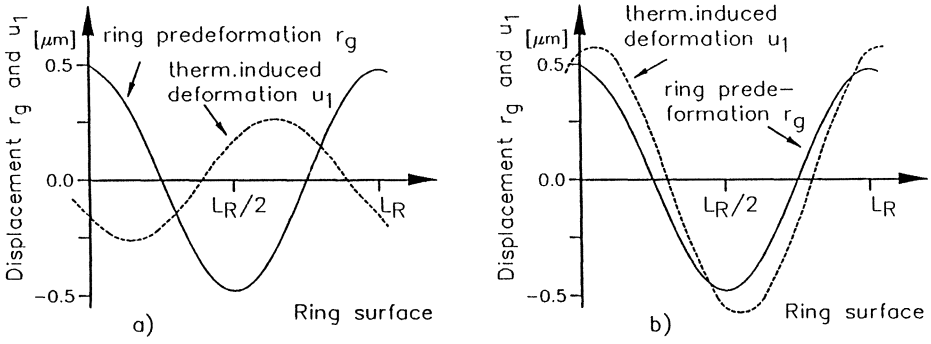

Fig.3. Comparison between stable behaviour (a) and unstable behaviour (b). Thermally induced displacement u_1 and, for comparison, the ring predeformation r_g at Θ=0; $r_o/R=1.05\cdot10^{-6}$; wave length: $L_R=2\cdot\pi\cdot R/32$.
a) e=38, stable behaviour; b) e=95, unstable behaviour

Chaotic Behaviour of Brush Vibration

The next step is to study how the brush vibrations behave when the thermal deformations develop further and excite the brushes more strongly. Fig.4 shows a number of phase curves for the inclination angle α of the brush, for various relative surface deformations r_o/R of the slip ring, where r_o is the small deviation from the ideal ring with radius R.

As can be seen, subharmonic vibrations occur at higher disturbance amplitudes. At disturbance amplitudes of

$$r_o/R > 2.3 \cdot 10^{-6},$$

periodicity could no longer be found, even though the simulation was continued for several hundred periods T_R. It must therefore be assumed that a condition of chaotic behaviour [6] is present.

Additional simulations have shown, that for the occurence of the chaotic vibration behaviour neither the tangential motion nor the clearence between the brushes and the holder are a determining factor.

Using (see Fig.4)

$$\omega = L_3\sqrt{2c/J}$$

and

$$D = d \cdot l_3/\sqrt{2c \cdot J}$$

the equation of motion (1) and (2) are reduced to the following non-linear equation:

$$\ddot{\alpha} + 2 \cdot D \cdot \omega \cdot \dot{\alpha} + \omega^2 \cdot \alpha + \mu \cdot L_5 \cdot m/J \cdot \ddot{y}(t,\alpha) + X_A(t,\alpha) \cdot m/J \cdot \ddot{y}(t,\alpha) + X_A(t,\alpha) \cdot F_B/J = 0. \qquad (3)$$

It should be noted that both the radial brush acceleration $\ddot{y}$ and the distance X_A depend in a complicated and sensitive way on time t and angle α [4].

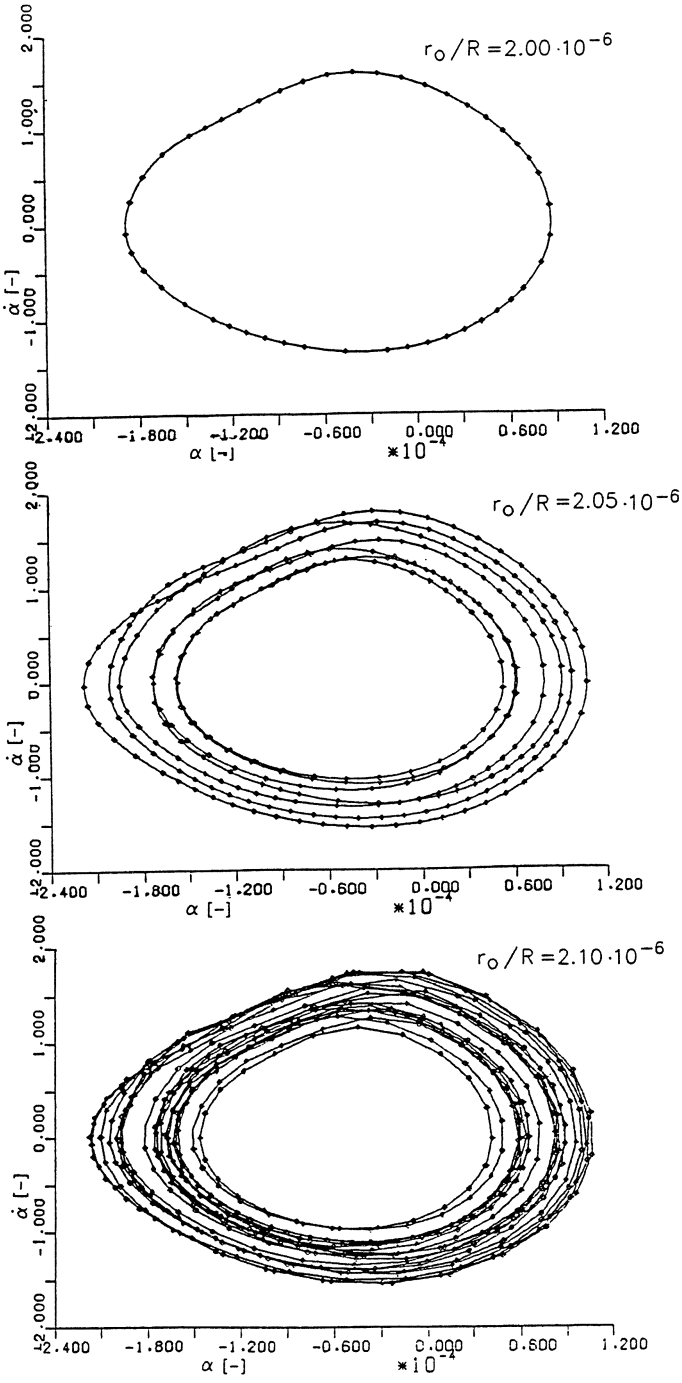

Fig.4. Inclination angle α in the phase plane for various specific ring surface deformations r_o/R; e=190; $L_R = 2 \cdot \pi \cdot R/32$.

From this equation it can be shown that it is the coefficient of friction μ between the brush and the slip ring, the dimensions of the brush, and the radial force F_B of the brush spring, which have a decisive effect on the occurence of chaotic vibration behaviour.

Conclusions

The calculations show that the system stability depends on a single pronounced sensitivity factor, and that is the ratio of the brush surface radius to the slipring radius. If the brush radius is close to the slip ring radius, the thermal deformation increases the existing deformation, and the system becames unstable. High brush vibrations occur in theory and in experiments which we have designated as regenerative brush chatter.

It has further been found in simulations that with large ring deformation, the brush vibration tends toward chaotic behaviour.

References

1. Shobert II, E.I.: Carbon-Brush Friction and Chatter. Power and Apparatus, AIEE, 30 (1957) 269-274.

2. Volkmann, W.: Kohlebürsten; Untersuchungsergebnisse, Erfahrungen, Empfehlungen. Schunk und Ebe GMBH, Brühlsche Universitätsdruckerei, Giessen, 1980.

3. Broniarek, C.A.; Taylor, O.S.: Mechanical Stability of Solid Brush Current Collection Systems. IEEE Trans. of Power Apparatus and Systems, PAS-99 (1980) 2413-2421.

4. Gabrielli, G.; Dynamisches Verhalten von Bürsten in Schleifringen von Turbogeneratoren - Eine neue Interpretation. Diss. ETH Zürich (to appear).

5. Dundurs, J.: Distorsion of a Body Caused by Free Thermal Expansion. Mech. Res. Comm., 1 (1974) 121-124.

6. Moon, C.F.: Chaotic Vibrations; An Introduction for Applied Scientists and Engineers. John Wiley and Sons, 1987.

Analysis of Dynamical Systems by Truncated Point Mappings and Cell Mapping

Ramesh S. Guttalu and Henryk Flashner

Department of Mechanical Engineering
University of Southern California, Los Angeles, CA 90089-1453, USA

Summary

Recent results obtained by the authors on the utility of truncated point mappings applicable to the analysis of multidimensional, multiparameter, periodic nonlinear systems are presented here. Based on multinomial truncation, an explicit analytical expression is determined for the point mapping in terms of the states and parameters of the system to any order of approximation. By combining this approach with analytical techniques, such as the perturbation method employed here, we obtain a powerful tool for finding periodic solutions and for analyzing their stability. A new approach for analyzing nonlinear systems which combines the techniques of truncated point mapping and cell mapping methods is also described here.

Introduction

The analysis of periodic differential equations presents a great mathematical challenge and has attracted a great deal of theoretical research. The importance of these periodic system stems from their many applications to various fields of science and engineering. An attractive way to analyze periodic systems is to formulate their discrete-time dynamics by defining a point mapping, i.e., a Poincaré map. The dynamics of the original system is then described in terms of difference equations rather than in terms of time varying differential equations. Point mapping techniques are widely employed today not only to study theoretical aspects of discrete time systems but also to provide a computational basis for understanding their global dynamics, see [1,2,4,7,10,12,14].

One of the main obstacles in applying the point mapping techniques to real problems is in obtaining the corresponding difference equations. Exact point mappings can only be determined in particular cases, such as those of impulsive excitation problems discussed in [10]. For general systems one is forced to accept an approximation to the point mapping. The aim of this paper is to introduce a numerical/analytical method based on the point mapping representation of dynamical systems which, when combined with other techniques such as perturbation analysis and cell mapping, forms a powerful tool for analyzing nonlinear systems. The method given by Flashner and Hsu [5] is modified to obtain approximate (truncated) point mappings by including variations in system parameters. This permits us to perform perturbation-like analysis. However, the analysis is carried out on discrete dynamical equations as opposed to conventional techniques that are usually applied to continuous-time dynamics of the system. Determination of periodic solutions using truncated point mappings reduces to solving multinomial equations which, when combined with perturbation techniques, provides a powerful analysis tool for establishing stability criteria for a large class of vibration problems. The proposed approach can handle multidimensional and multiparameter systems and higher order perturbations that are very difficult to compute by other methods can be readily obtained.

W. Schiehlen (Editor)
Nonlinear Dynamics in Engineering Systems
IUTAM Symposium Stuttgart/Germany 1989

It is known that the method of cell mapping (developed by Hsu [10]) introduces error in the time response of the system due to spatial discretization. A new application of the truncated point mappings to locate trajectories of the system inside the cells is provided in this paper. This approach provides a convenient way to increase the accuracy of time response and thus to reduce the error caused by discretization of the state space.

Point Mapping Analysis

Consider a dynamical system described by a set of N ordinary differential equations

$$\dot{\mathbf{x}}(t) = \mathbf{f}(t,\ \mathbf{x}(t),\ \mathbf{s}) \tag{1}$$

where $t \in \mathbf{R}^+$ denotes time, $\mathbf{x} \in \mathbf{R}^N$ is the state vector, $\mathbf{s} \in \mathbf{R}^L$ is a parameter vector, and $\mathbf{f} : \mathbf{R}^+ \times \mathbf{R}^N \times \mathbf{R}^L \to \mathbf{R}^N$ is analytic for every $\mathbf{x}$ for a given value of the parameter vector $\mathbf{s}$. Moreover, $\mathbf{f}$ is assumed to be periodic in t with period T. One can analyze this system by observing its state once at every period T. The dynamic relationship between the state of the system at $t = nT$ and the state at $t = (n+1)T$ results in a set of difference equations, also called a point mapping or the Poincaré map, which can be expressed as

$$\mathbf{x}(n+1) = \mathbf{G}(\mathbf{x}(n),\ \mathbf{s}), \quad n = 1, 2, \cdots \tag{2}$$

where $\mathbf{x}(n+1)$ and $\mathbf{x}(n)$ are the states of the system at $t = (n+1)T$ and $t = nT$, respectively. Note that because of the smoothness condition on $\mathbf{f}$, equation (1) satisfies Lipschitz conditions and $\mathbf{G}$ is one to one with $\mathbf{s}$ fixed. In order to analyze periodic solutions of (1), we use the notion of a $P-K$ solution. It is a periodic solution (equivalently a periodic solution of period KT of (1)) of the point mapping (2) for some $\mathbf{s} = \mathbf{s}^*$, and consists of K distinct points $\mathbf{x}^*(j)$, $j = 1, 2, \cdots, K$ such that

$$\mathbf{x}^*(m+1) = \mathbf{G}(\mathbf{x}^*(m),\ \mathbf{s}^*),\ m = 1, 2, \cdots, K-1 \tag{3}$$

$$\mathbf{x}^*(1) = \mathbf{G}^K(\mathbf{x}^*(1),\ \mathbf{s}^*) \tag{4}$$

Finding a $P-K$ solution of the corresponding point mapping is equivalent to finding a periodic solution of the original continuous time system. Having found a $P-K$ solution by solving the algebraic system of equations (4), its local stability properties are determined by the eigenvalues of the matrix $\mathbf{H}$ given by [10]

$$\mathbf{H} = \mathbf{H}^*(K)\,\mathbf{H}^*(K-1)\,\cdots\,\mathbf{H}^*(1), \quad \mathbf{H}^*(j) = \nabla_{\mathbf{x}}\mathbf{G}(\mathbf{x}^*(j), \mathbf{s}^*) \tag{5}$$

For two-dimensional point mappings, the asymptotic stability conditions can be expressed by

$$1 \pm \operatorname{tr}\mathbf{H} + \det\mathbf{H} > 0, \quad \det\mathbf{H} < 1 \tag{6}$$

To develop an algorithm for determining approximate point mappings of the system (1), we note that the function $\mathbf{f}(t, \mathbf{x}(t), \mathbf{s})$ is analytic and can be expressed by a Taylor series of the form $\mathbf{f}(t, \mathbf{x}, \mathbf{s}) = \mathbf{p}_k(t, \mathbf{x}, \mathbf{s})$ where $\mathbf{p}_k(t, \mathbf{x}, \mathbf{s})$ denotes a vector homogeneous polynomial of degree k in the state variables x_i, $i = 1, 2, \cdots, N$. Based on this, the numerical algorithm presented in [6,8] computes an approximation to the point mapping of (1) up to a polynomial of degree k by employing the Runge-Kutta method. The integration scheme used of the form

$$\mathbf{x}(t_p + h) = \mathbf{x}(t_p) + h\sum_{m=1}^{M} d_m \mathbf{k}_m(t,\ \mathbf{x}) \tag{7}$$

where M is the order of the Runge-Kutta method, h is the time step, and d_m are certain constants, see [9]. The vectors $\mathbf{k}_m$, $m = 1, 2, \cdots, M$, for equation (1) are given by

$$\mathbf{k}_m(t, \mathbf{x}) = \mathbf{f}(t_p + ha_m, \mathbf{x}(t_p) + c_m\mathbf{k}_{m-1}, \mathbf{s}) \tag{8}$$

The constants a_m and c_m are given by the particular Runge-Kutta method to be used with $a_1 = 0$ and $c_1 = 0$. The proposed numerical algorithm takes advantage of the fact that the operations of truncation and telescoping on multinomials can be interchanged, see [15]. Additionally, numerical integration can be broken up into a series of polynomial telescoping and truncation operations. Successive application of the Runge-Kutta scheme given by (7) to the initial state $\mathbf{x}(n)$ leads to the form $\mathbf{x}(n+1) = \mathbf{G}_k(\mathbf{x}(n), \mathbf{s})$, where $\mathbf{G}_k$ is a a truncated point mapping of degree k and $\mathbf{x}(n+1)$ is the state of the system at the end of one period of time.

The dependence of the coefficients of $\mathbf{G}_k$ on system's parameters can also be obtained using the proposed approach by assuming that the coefficients of $\mathbf{p}_k(t, \mathbf{x}, \mathbf{s})$ consist of powers of the components of the vector $\mathbf{s}$. The polynomial telescoping routine allows us to to keep track of the powers of the components of $\mathbf{x}$ and to perform an appropriate truncation with respect to $\mathbf{s}$. For details regarding the truncated point mapping algorithm, see [6,8].

Analysis of van der Pol's equation

To determine an approximate point mapping of the van der Pol's equation

$$\ddot{x} + x - \epsilon(1 - x^2)\dot{x} = 0,$$

we transform it by using the nondimensional time $\tau = \omega t$ to obtain

$$\frac{d^2x}{d\tau^2} + \frac{1}{\omega^2}x - \frac{\epsilon}{\omega}(1 - x^2)\frac{dx}{d\tau} = 0. \tag{9}$$

To obtain a truncated point mapping of $O(\epsilon)$, let $\omega = 1 + \epsilon\omega_1 + O(\epsilon^2)$. Then (9) may be expressed as

$$\frac{dx_1}{d\tau} = x_2, \quad \frac{dx_2}{d\tau} = -(1 - 2\epsilon\omega_1)x_1 + \epsilon x_2(1 - x_1^2) \tag{10}$$

Since the linearized equation corresponding to $\epsilon = 0$ of (9) has periodic solutions of period 2π, we integrate equation (34) from $\tau = 0$ to $\tau = 2\pi$ with step size $h = 2\pi/100$ and $M = 4$. The resulting point mapping $\mathbf{G}$ of $O(\epsilon)$ (see [8]) that includes all powers of x_1 and x_2 is

$$\begin{aligned} x_1(n+1) &= x_1(n) - 2\pi\epsilon\omega_1 x_2(n) + \frac{\pi\epsilon}{4}(4 - r^2(n))x_1(n) \\ x_2(n+1) &= x_2(n) + 2\pi\epsilon\omega_1 x_1(n) + \frac{\pi\epsilon}{4}(4 - r^2(n))x_2(n) \end{aligned} \tag{11}$$

where $r(n) = \sqrt{x_1^2(n) + x_2^2(n)}$. By letting $x_1 = r\cos\theta$, $x_2 = r\sin\theta$ with $r^2(n+1) = x_1^2(n+1) + x_2^2(n+1)$, then the map (11) becomes one-dimensional point mapping

$$r(n+1) \equiv G(r(n)) = \left\{1 + \frac{\epsilon\pi}{4}(4 - r^2(n))\right\} r(n) \tag{12}$$

which is independent of ω_1. By analyzing $P - 1$ solutions of the map (11), one obtains $\omega_1 = 0$ and $r^2(r^2 - 4) = 0$. While the solution $r = 0$ corresponds to the equilibrium at the origin, the solution $r = 2$ corresponds to the limit cycle. These $P - 1$ solutions and their stability coincide with those of the classical perturbation analysis.

In order to derive the point mapping of $\mathcal{O}(\epsilon^2)$, let $\omega = 1 + \epsilon^2\omega_2 + O(\epsilon^3)$. Then (9) becomes

$$\frac{dx_1}{d\tau} = x_2, \quad \frac{dx_2}{d\tau} = -(1 - 2\epsilon^2\omega_2)x_1 + \epsilon x_2(1 - x_1^2) \tag{13}$$

We integrate this from $\tau = 0$ to $\tau = 2\pi$ with $h = 2\pi/100$. The point mapping $\mathbf{G}$ of $\mathcal{O}(\epsilon^2)$ is

$$\begin{aligned} x_1(n+1) &= x_1(n) + \frac{\epsilon\pi}{4}A(r(n))x_1(n) - \frac{\epsilon^2\pi}{16}\left\{B(r(n)) + 2x_1^4 + 8x_2^2 + 32\omega^2\right\}x_2(n) \\ x_2(n+1) &= x_2(n) + \frac{\epsilon\pi}{4}A(r(n))x_2(n) + \frac{\epsilon^2\pi}{16}\left\{B(r(n)) + 2x_1^4 + 16x_2^2 + 32\omega^2\right\}x_1(n) \\ A(r) &= 4 - r^2 + 2\epsilon\pi\left(1 - r^2 + \frac{3}{16}r^4\right), \quad B(r) = 4 - 11r^2 + \frac{5}{8}r^4 \end{aligned}$$

and contains all the powers of x_1 and x_2. In polar coordinates, $P-1$ solutions (amplitude r) and ω_2 are determined from

$$\frac{3\epsilon\pi}{8}r^4 - (1 + 2\epsilon\pi - 2\epsilon\ \cos\theta\ \sin^3\theta)r^2 + 2(2+\epsilon\pi) = 0 \tag{14}$$

$$\omega_2 = -\frac{1}{32}\left\{4 - 3r^2 + \frac{5}{8}r^4 + 2r^2(r^2-4)\cos^4\theta\right\}, \quad 0 \le \theta \le 2\pi$$

As opposed to the classical perturbation result, ω_2 is dependent on the amplitude and phase, and $\omega_2 = -\frac{1}{16}$ for $r = 2$ only. For a detailed analysis of solutions of (14) and for high order truncated point mappings, see [8].

Analysis of Duffing's equation

We consider the Duffing's equation given by

$$\ddot{x} + \epsilon\mu\dot{x} + p^2x + \epsilon\beta x^3 = \epsilon F_0\ \cos\omega t + \epsilon G_0\ \sin\omega t \tag{15}$$

where the $\epsilon\mu$ is the damping coefficient, p the natural frequency, $\epsilon\beta$ the coefficient of the hard (or soft) spring, ω the forcing frequency, and ϵF_0 and ϵG_0 the forcing amplitudes. We present point mapping results of order ϵ to compare with the perturbation results. Let $\tau = \omega t$, $\omega = p + \epsilon\omega_1 + O(\epsilon^2)$, $x_1 = x$ and $x_2 = dx/d\tau$. Equation (15) containing terms up to $O(\epsilon)$ can be expressed as

$$\frac{dx_1}{d\tau} = x_2, \quad \frac{dx_2}{d\tau} = -\left(1 - \frac{2\epsilon\omega_1}{p}\right)x_1 - \frac{\epsilon\mu}{p}x_2 + \frac{\epsilon}{p^2}\left(-\beta x_1^3 + F_0\cos\tau + G_0\sin\tau\right) \tag{16}$$

We integrate (16) from $\tau = 0$ to $\tau = 2\pi$ with step size $h = 2\pi/100$ and $M = 4$. Define the amplitude $r(n) = \sqrt{x_1^2(n) + x_2^2(n)}$. The truncated point mapping $\mathbf{G}$ of $O(\epsilon)$:

$$x_1(n+1) = \left(1 - \frac{\pi\epsilon\mu}{p}\right)x_1(n) - A(r(n))x_2(n) - \frac{\pi\epsilon G_0}{p^2} \tag{17}$$

$$x_2(n+1) = \left(1 - \frac{\pi\epsilon\mu}{p}\right)x_2(n) + A(r(n))x_1(n) + \frac{\pi\epsilon F_0}{p^2}$$

$$A(r) = \frac{\pi}{p^2}\left[\omega^2 - p^2 - \frac{3\beta}{4}r^2\right]$$

where the substitution $2\epsilon\omega_1 p = \omega^2 - p^2$ has been made. Notice that the nonlinear terms in (17) are entirely due to β. Since $\mathbf{f}$ in (15) is odd in x_1 and x_2, the point map $\mathbf{G}$ above is also odd in x_1 and x_2. Moreover, the Hamiltonian structure is retained by $\mathbf{G}$ as $\epsilon \to 0$. The invariants of the Jacobian matrix $\mathbf{H}$ of $\mathbf{G}$ are given by

$$\text{tr}\ \mathbf{H} = 2\left(1 - \frac{\pi\epsilon\mu}{p}\right), \quad \det\mathbf{H} = \left(1 - \frac{\pi\epsilon\mu}{p}\right)^2 + \frac{\pi^2}{p^4}(\omega^2 - p^2)^2 - \frac{3\pi^2\epsilon\beta}{p^4}(\omega^2 - p^2)r^2 + \frac{27\pi^2\epsilon^2\beta^2}{16p^4}r^4$$

The frequency response of the system is determined by $P-1$ solutions of the map (17):

$$\epsilon\mu p x_1^* + \left\{\omega^2 - p^2 - \frac{3\beta}{4}r^{*2}\right\}x_2^* = -\epsilon G_0, \quad \epsilon\mu p x_2^* - \left\{\omega^2 - p^2 - \frac{3\beta}{4}r^{*2}\right\}x_1^* = -\epsilon F_0 \tag{18}$$

where $r^* = \sqrt{x_1^{*2} + x_2^{*2}}$. Defining the forcing amplitude to be $F^2 = F_0^2 + G_2^2$, it is easily deduced that $P-1$ solutions must satisfy the frequency-amplitude relationship

$$(\epsilon F)^2 = \left(\omega^2 - p^2 - \frac{3\epsilon\beta}{4}r^{*2}\right)^2 r^{*2} + (\epsilon\mu p)^2 r^{*2} \tag{19}$$

with period $2\pi/\omega = \frac{2\pi}{p}\left(1 - \frac{\epsilon\omega_1}{p}\right)$. The stability of $P-1$ solutions determined by (18) can be based on the geometric shape of the resonance curves (19). Let

$$R(\omega, r) = \left[\omega^2 - p^2 - \frac{3\epsilon\beta}{4}r^2\right]^2 r^2 + \epsilon^2\mu^2 p^2 r^2 - \epsilon^2 F^2$$

Then, the amplitude-frequency relationship (19) is expressed by $R(\omega, r^*) = 0$. Noting that the normal to the curve $R(\omega, r)$ along the $r-$direction is of $\mathcal{O}(\epsilon^2)$ and

$$\begin{aligned} 1 + \text{tr } \mathbf{H}(r^*) + \det \mathbf{H}(r^*) &= 4\left(1 - \frac{\pi\epsilon\mu}{p}\right) + \frac{\pi^2}{2p^4 r^*}\left[\frac{\partial R}{\partial r}\right]_{r=r^*} \\ 1 - \text{tr } \mathbf{H}(r^*) + \det \mathbf{H}(r^*) &= \frac{\pi^2}{2p^4 r^*}\left[\frac{\partial R}{\partial r}\right]_{r=r^*} \end{aligned}$$

the stability of $P-1$ solutions given by (18) is determined by the sign of the vertical component of the normal to the response curve $R(\omega, r^*)$. It follows from stability conditions that for $\epsilon\mu > 0$, the $P-1$ solutions of the map (17) are

$$\textit{asymptotically stable if } \left[\frac{\partial R}{\partial r}\right]_{r=r^*} > 0, \quad \textit{unstable if } \left[\frac{\partial R}{\partial r}\right]_{r=r^*} < 0 \tag{20}$$

Our results agree with those obtained by classical perturbation techniques.

Analysis of Parametrically Excited Duffing's equation

We consider a nonlinear form of Mathieu's equation given by

$$\ddot{x} + 2\lambda\mu\dot{x} + (\delta + 2\lambda\epsilon\cos 2t)x + \lambda\alpha x^3 = 0 \tag{21}$$

where λ is assumed to be a small parameter for the purpose obtaining a truncated point mapping. Let $\mu > 0$. To perform a primary resonance study, let $\delta = \delta_0 + \bar{\delta} = 1 + \lambda\sigma$ and rewrite (22) as

$$\dot{x}_1 = x_2, \quad \dot{x}_2 = -(1 + \lambda\sigma + 2\lambda\epsilon\cos 2t)x_1 - \lambda\alpha x_1^3 - 2\lambda\mu x_2 \tag{22}$$

The truncated point mapping $\mathbf{G}$ of $\mathcal{O}(\lambda)$, obtained by integrating (22) from $t = 0$ to $t = 2\pi$ with $h = 2\pi/500$, can be expressed as

$$\begin{aligned} x_1(n+1) &= (1 - 2\pi\lambda\mu)x_1 + \pi\lambda\left(\sigma - \epsilon + \frac{3\pi\alpha}{4}r^2\right)x_2 \\ x_2(n+1) &= (1 - 2\pi\lambda\mu)x_2 - \pi\lambda\left(\sigma + \epsilon + \frac{3\pi\alpha}{4}r^2\right)x_1 \end{aligned} \tag{23}$$

where $r^2 = x_1^2 + x_2^2$. The invariants of $\mathbf{H}$ can be shown to be

$$\text{tr } \mathbf{H} = 2(1 - 2\pi\lambda\mu) \tag{24}$$

$$\det \mathbf{H} = (1 - 2\pi\lambda\mu)^2 + \pi^2\lambda^2\left\{\sigma^2 - \epsilon^2 + \frac{27\alpha^2}{16}r^4 + \frac{3\alpha}{2}\left[2\sigma r^2 - \epsilon(x_1^2 - x_2^2)\right]\right\} \tag{25}$$

The $P-1$ solutions of (23) are obtained by solving the algebraic equations

$$-2\mu x_1^* + \left(\sigma - \epsilon + \frac{3\pi}{4}\alpha r^2\right)x_2^* = 0, \quad 2\mu x_2^* + \left(\sigma - \epsilon + \frac{3\pi}{4}\alpha r^2\right)x_2^* = 0 \tag{26}$$

There exists a trivial $P-1$ solution $\mathbf{x}^* = \mathbf{0}$ of (26) whose stability is determined by the sign of the expression

$$1 - \text{tr } \mathbf{H}(\mathbf{0}) + \det \mathbf{H}(\mathbf{0}) = \pi^2\lambda^2(\sigma^2 - \epsilon^2 + 4\mu^2)$$

Hence, $\mathbf{x}^* = \mathbf{0}$ is asymptotically stable if $\epsilon^2 < \sigma^2 + 4\mu^2$ and is unstable if $\epsilon^2 > \sigma^2 + 4\mu^2$.

The non-trivial $P-1$ solutions of (26) lead to the frequency response

$$\left(\sigma + \frac{3\alpha}{4} r^{*2}\right)^2 = \epsilon^2 - 4\mu^2 \tag{27}$$

which exist when $\epsilon^2 \geq 4\mu^2$. The stability of these solutions can be analyzed in a manner similar to the case of Duffing's equation. Define the resonance curve $R(\sigma, r)$ as

$$R(\sigma, r) = \left(\sigma + \frac{3\alpha}{4} r^2\right)^2 - \epsilon^2 + 4\mu^2 \tag{28}$$

and note that $\frac{\partial R}{\partial r} = 3\alpha r \left(\sigma + \frac{3\alpha}{4} r^2\right)$. With some algebraic manipulations, it can be shown that

$$\det \mathbf{H}(r^*) = 1 - 4\pi\lambda\mu + r^* \left[\frac{\partial R}{\partial r}\right]_{r=r^*} \tag{29}$$

As before, the stability of the $P-1$ solutions given by (27) can be inferred from

$$\begin{aligned} \det \mathbf{H}(r^*) &= 1 - 4\pi\lambda\mu + \mathcal{O}(\lambda^2) \\ 1 + \operatorname{tr} \mathbf{H}(r^*) + \det \mathbf{H}(r^*) &= 4(1 - \pi\lambda\mu) + \mathcal{O}(\lambda^2) \\ 1 - \operatorname{tr} \mathbf{H}(r^*) + \det \mathbf{H}(r^*) &= r^* \left[\frac{\partial R}{\partial r}\right]_{r=r^*} \end{aligned}$$

Once a $P-1$ solution is calculated from (27), then its stability can be established by the sign of the vertical component of the normal to the solution curve $R(\sigma, r^*)$. We note that there are only two positive solutions of (27), r_1^* and r_2^* with $r_1^* > r_2^*$. The $P-1$ solution having the larger amplitude is asymptotically stable while the one having the smaller amplitude is unstable. When these two steady state responses coincide, higher order terms are needed to ascertain their stability. These results agree with those obtained by perturbation analysis, see [3,13].

Application to Cell Mapping Method

When the cell mapping method (see Hsu [10]) is used to determine the time response of nonlinear dynamical systems, an error is introduced due to spatial discretization. Moreover, the error is accumulated as time grows. This inaccuracy may lead to erroneous results or may force one to use extremely small cell sizes imposing computational restrictions, especially when treating high order systems. Recently, Tongue [16] and Tongue and Gu [17] have used linear interpolation technique and its refinements to improve on the accuracy of the simple cell mapping method. Here, we use the truncated point mapping approach to approximately locate trajectories inside the cells. This approximation can be carried out up to any order of multinomial approximation and can be developed for systems of arbitrary dimension. In addition, the analytical expression obtained for the truncated point mapping permits us to study the stability properties of the cell-to-cell mapping, which is quite important in the analysis of periodic solutions and chaotic behavior.

Let $\phi^*(t) \in \mathbf{R}^N$ be a trajectory of the dynamical system (1) and $\xi(t) \in \mathbf{R}^N$ be its perturbation such that $\xi(t) = \mathbf{x}(t) - \phi^*(t)$. Assuming that f is analytic, the perturbed trajectory satisfies $\dot{\xi}(t) = \mathbf{p}_m(\xi, t) + \mathbf{h}(\xi, t)$, where $\mathbf{p}_m$ is a multinomial of degree m in ξ and $\mathbf{h}$ is the remainder which is a higher order multinomial. In some neighborhood of $\phi^*(t)$ for which $\|\xi\| < \rho$, the truncated system

$$\dot{\xi}(t) = \mathbf{p}_m(\xi, t) \tag{30}$$

provides a good approximation to the dynamics of the perturbed system. Moreover, the stability of the system trajectory $\phi^*(t)$ can be determined from the system (30) by using Lyapunov's indirect method and its extension, see [11,18].

Assume that the system (1) is integrated from $t = kT$ to $t = (k+1)T$, for some integer k, thus determining a solution $\phi^*(t)$ for $t \in [kT, (k+1)T]$. Also, assume that the coefficients of the mth order approximation to the point mapping obtained by using (30) is in the form

$$\xi(k+1) = \mathbf{G}_m(\xi(k)) \tag{31}$$

where $\mathbf{G}_m$ is a multinomial of order m. Then, since $\xi(k+1) = \mathbf{x}((k+1)T) - \phi^*((k+1)T)$ and $\xi(k) = \mathbf{x}(kT) - \phi^*(kT)$, $\|\xi(kT)\| < \rho$ defines a region about the location $\phi^*(t)$ and equation (31) approximates the map of any point in this region. If we choose the norm $\|\cdot\|$ to be the infinity norm, that is $\|\xi\| = \max_i \|\xi_i\|$, with an appropriate scaling, then $\|\xi\| < \rho$ defines a rectangular region. This rectangular region is considered by Hsu [10] as a definition of a cell occupying a region of state space. Therefore, the map given by equation in (31) defines a map of the entire cell. When $m = 1$, the approximation is linear and one can express the map in (31) as

$$\xi(k+1) = \mathbf{H}\xi(k) \tag{32}$$

where $\mathbf{H}$ is an $N \times N$ matrix. The system (32) is linear and implies that straight lines map into straight lines and the mapping of the boundaries of a cell is defined by straight lines. Note that (32) defines the map of any point within the cell.

To compute a trajectory of the nonlinear system (1) using the modified cell mapping approach, let $\phi_i^*(0)$ represent coordinates of the center point of a cell i. Let cell j be the image of the cell i (mapping of cell i). and $\phi_i^*(T)$ represent the map of $\phi_i^*(0)$. Let $\xi^{(i)}$ represents the perturbation of the trajectory with respect to the center of the cell i. Suppose that the region of state space under consideration contains a total of N_c cells. For each cell $i = 1, 2, \cdots, N_c$ in the cell state space, compute the quantity $\phi_i^*(T)$ and the coefficients of the truncated point mapping $\mathbf{G}_m^{(i)}(\xi)$. For a linear approximation, this result is provided by $N \times N$ matrices $\mathbf{H}^{(i)}$.

The steps needed for trajectory computing algorithm can be summarized as follows:

I. Set $k = 0$, $i = 0$, $\xi^{(i)}(0) = \mathbf{x}(0) - \phi_i^*(0)$.

II. Compute $\xi^{(i)}(k+1)$ using equation (30), and the mapping of the trajectory point $\mathbf{x}((k+1)T) = \phi_i^*(T) + \xi^{(i)}(k+1)$.

III: Compute the perturbation about the center point of the mapped cell j given by

$$\xi^{(j)}(k) = \phi_i^*(T) - \phi_j^*(0) - \xi^{(i)}(k+1).$$

IV. Set $k = k+1$, $i = j$ and repeat steps II and III above until all the cells are examined.

With the above algorithm, the following information regarding the dynamics of the system can be obtained: *(i)* periodic solutions (or $P-K$ solutions) can be determined when $\|\mathbf{x}(k) - \mathbf{x}(k+K)\| < \epsilon$, where $\epsilon > 0$ is a preset tolerance and K corresponds to the periodicity of the solution, and *(ii)* the stability of periodic solutions which can be determined analytically by computing the eigenvalues of the matrix $\mathbf{H} = \prod_{i=1}^{K} \mathbf{H}^{(i)}$.

The truncated point mapping technique can be used to advantage for developing an efficient tool for the cell mapping analysis of nonlinear systems. The approach is general in the sense that it is applicable to an arbitrary number of degrees of freedom and the computational procedure does not change for different orders of approximation. This is an advantage over the interpolated cell mapping introduced in [17]. Further research on this topic is currently underway.

Acknowledgments: The research reported here was partially supported by the USC Faculty Research and Innovation Fund and a grant from the National Science Foundation.

References

1. Bernussou, J.: *Point Mapping Stability.* Oxford: Pergamon 1977.
2. Bogoliubov, N.N; Mitropolsky, Y.A.: *Asymptotic Methods in the Theory of Nonlinear Oscillations.* New York: Gordon and Breach 1961.
3. Boston, J.R.: Response of a nonlinear form of the Mathieu equation, *J. Acous. Soc. Amer.* **49** (1970) 299-305.
4. Cesari, L.: *Asymptotic Behavior and Stability Problems in Ordinary Differential Equations* New York: Academic Press 1971.
5. Flashner, H.; Hsu, C.S.: A study of nonlinear periodic systems via the point mapping method, *Int. J. Num. Meth. Engr.* **19** (1983) 185-215.
6. Flashner, H.; Guttalu, R.S.; Analysis of nonlinear nonautonomous systems by truncated point mappings. *Int. J. Non-Linear Mech.* (1989) (in press).
7. Guckenheimer, J.; Holmes, P.J.: *Nonlinear Oscillations, Dynamical Systems, and Bifurcation of Vector Fields.* New York: Springer-Verlag 1983.
8. Guttalu, R.S.; Flashner, H.: Periodic solutions of non-linear autonomous systems by approximate point mappings, *J.Sound Vibrat.* **129** (1989) 291-311.
9. Henrici, P.: *Discrete Variable Methods in Ordinary Differential Equations.* New York: John Wiley and Sons 1962.
10. Hsu, C.S.; *Cell-to-Cell Mapping.* New York: Springer-Verlag 1987.
11. Malkin, I.G.: *Theory of Stability of Motion.* US Atomic Energy Commission, Technical Information Service 1952.
12. Moon, F.C.: *Chaotic Vibrations.* New York: John Wiley and Sons 1987.
13. Nayfeh, A.H.; Mook, D.T.: *Nonlinear Oscillations.* New York: John Wiley and Sons 1979.
14. Poincaré, H.: *Les Methodes Nouvelles de la Mechanique Celeste.* Paris: Gautiers-Villars 1891.
15. Poston, T.; Stewart, I.: *Catastrophy Theory and its Applications.* London: Pitman Publishing 1978.
16. Tongue, B.H.; On obtaining global nonlinear system characteristics through interpolated cell mapping, *Physica* **28D** (1987) 401-408.
17. Tongue, B.H.; Gu, K: Interpolated cell mapping of dynamical systems, *ASME J. Appl. Mech.* **55** (1988) 461-466.
18. Vidyasagar, M.: *Nonlinear Systems Analysis.* Englewood Cliffs: Prentice-Hall 1978.

Effect of Constant Transverse Force on Chaotic Oscillations of Sinusoidally Excited Buckled Beam

K. Higuchi* and E. H. Dowell

Department of Mechanical Engineering and Materials Science
Duke University, Durham, NC 27706, U.S.A.
* Current address: Tokyo Denki University, Hatoyama, Saitama 350-03, JAPAN

Summary
The chaotic oscillation of a buckled beam under sinusoidally varying and static constant transverse external forces is investigated. A harmonic balance method and a direct numerical integration are applied to a Duffings equation model of the buckled beam. For a small transverse constant force, there exist three static equilibrium points, and the near contact between the two orbits of a stable and an unstable limit cycle in the phase plane can predict the onset of chaos. For a large transverse constant force, there exists only one static equilibrium point, but there may exist three different dynamic response amplitudes due to nonlinear resonance phenomena. The near contact between two vibration regions of a stable and an unstable limit cycle can predict the onset of chaos.

Introduction

A one mode model of the oscillation of a buckled beam under sinusoidally varying plus constant external force can be written as a particular form of Duffings equation with a negative linear stiffness and a positive cubic stiffness [1]

$$\ddot{A} + \gamma \dot{A} - \frac{1}{2} A (1 - A^2) = F_s + F_o \sin \omega t \qquad (1)$$

where γ is a damping coefficient, F_s a transverse static force, F_o a sinusoidal force amplitude, ω an excitation frequency and t time. It is known that this equation with $F_s = 0$ has a solution with chaotic oscillations under certain conditions of γ, F_o, and ω [2][3].

In the case of $F_s = 0$, three static equilibrium positions can be obtained by neglecting the terms involving time in equation (1), and two of the static equilibrium positions are stable and the third is unstable with respect to infinitesimal disturbances. A stable or unstable steady state limit cycle around each

W. Schiehlen (Editor)
Nonlinear Dynamics in Engineering Systems
IUTAM Symposium Stuttgart/Germany 1989

static equilibrium position can be considered for a small force amplitude F_o, and the magnitudes of the limit cycles grow with F_o. This is a case of a symmetric two-well-potential, and the orbits of the two stable limit cycles nearly contact the orbit of the unstable limit cycle on the phase plane (A, $\dot{A}$) at a certain value of the force amplitude F_o. This value of F_o provides a very good approximation to the lowest onset boundary of sustained chaos [3].

It is of interest to investigate the role and effect of the transverse static force, F_s, on the onset of chaos by observing the near contact of orbits on the phase plane.

Analysis and discussion

1. Small F_s For a small F_s (>0), three static equilibrium positions, A_s, can be obtained from equation (1) by neglecting the terms involving time, as follows,

$$-\frac{1}{2}A_s\left(1-A_s^2\right)=F_s. \qquad (2)$$

Two of the three static equilibrium positions are stable and the third is unstable (Figs.1(a) and (b)).

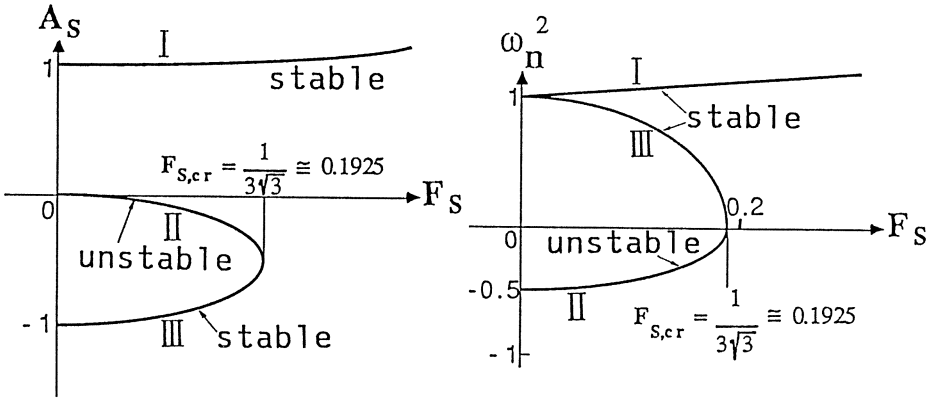

(a) A_s vs F_s (b) ω_n^2 vs F_s

Fig.1. Static equilibrium position A_s for static transverse force F_s and natural frequency ω_n of a small oscillation around the equilibrium position.

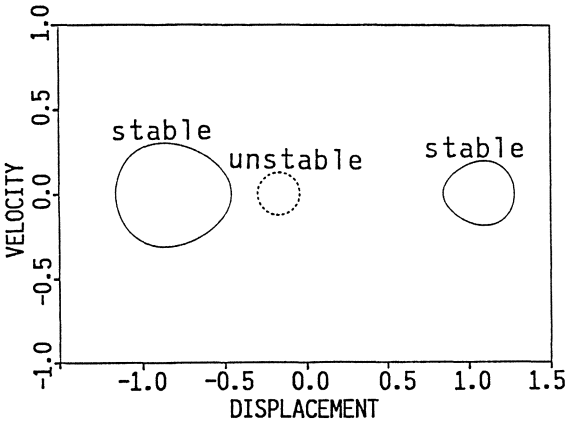

(a) Stable and unstable limit cycles.
The excitation frequency is the natural frequency of a small oscillation around the stable equilibrium point in the negative displacement region of the phase plane; $\omega = \omega_n = 0.858$.

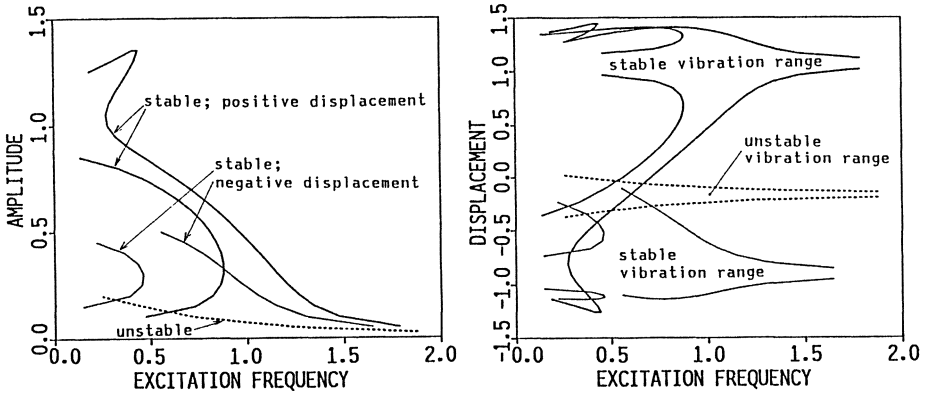

(b) Amplitude

(c) Vibration bounds

Fig.2. Resonance for a small F_s ; $F_s = 0.08$, $F_o = 0.10$.

The onset of chaos may be explained in a similar manner to the case of $F_s = 0$ for the case of a small F_s (>0), although the phase plane portrait for non-zero F_s does not have a mirror image with respect to displacement, because the two-well-potential is not symmetric (Fig.1(a)). Two stable steady-state limit cycles and one unstable limit cycle around each static equilibrium position can be considered on the phase plane, as shown in Fig.2(a). In this paper, the magnitude of the damping

coefficient, γ , is 0.168 [3]. The orbits of the stable limit cycles are obtained directly through numerical integration of the governing equation (1). Resonance curves shown in Figs.2(b) and (c) are calculated by the harmonic balance method which contains one fundamental harmonic term and one constant term, viz.

$$A\ (t) = \overline{A_o} \sin(\omega t + \phi) + C \qquad (3)$$

where $C = \pm 1$ (only) when $\overline{A_o} = 0$.

One cannot predict the onset of chaos from the amplitude-excitation relation such as Fig.2(b), because each center of vibrations C varies with amplitude $\overline{A_o}$ of response. The phase plane portrait of steady-state limit cycles has a mirror image with respect to velocity (Fig.2(a)), so a displacement-excitation frequency relation such as Fig.2(c) is useful to determine the near intersection between the stable and unstable limit cycle orbits. Figure 2(a) can be considered to be a cutting plane of Fig.2(c) at a certain cutting-plane line of excitation frequency, $\omega = \omega_n$.

The magnitude of the limit cycles grow with force amplitude, and so the regions of possible displacement of response become wider in Fig.2(c). And at the same time, the frequency at the intersection point increases with force amplitude. Therefore, if the force amplitude is larger than the force level of the resonance curve shown here and the excitation frequency is fixed to the frequency of the intersection point, or if the excitation frequency is smaller than the frequency of the intersection point and the force amplitude is fixed as shown here, the orbit of response on the phase plane (A , $\dot{A}$) is chaotic and wanders around two stable equilibrium points and one unstable equilibrium point. Numerical studies showed a good agreement with the onset boundary of chaos determined by the intersection of two regions, one of which is the region where a stable limit cycle exists and the other of which is the region where an unstable limit cycle is present.

This is the basic idea of a necessary condition for the lowest onset of chaos for a small F_s . The limit cycles approach

each other monotonically with increasing force amplitude on the phase plane, but not linearly in actual cases, because the system often undergoes a series of period doubling bifurcations.

2. Large F_s The two static equilibrium points, A_s, approach each other with increasing F_s, as shown in Figs.1, and merge at a critical value, $F_{s,cr} = 1/3\sqrt{3}$ ($\cong 0.1925$), which is obtained from static equation (2). Beyond the critical value, only one static equilibrium position, which is positive and stable, remains. An asymmetric two-well-potential changes to an asymmetric one-well-potential at the critical value $F_{s,cr}$. This may be thought to imply that there is no chaos for a large transverse static force beyond this point. This is true, however, only if one predicts the onset of chaos by applying the criterion stated above that the existence of two stable and one unstable static equilibrium position is a necessary condition of chaos. Actually, however, chaos due to a different mechanism of onset occurs in the case for $F_s \geqq F_{s,cr}$.

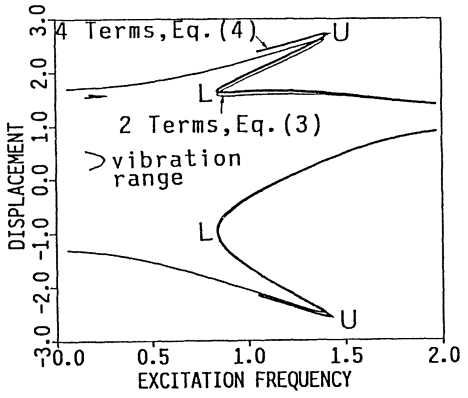

(a) Vibration bounds. U and L denote upper and lower perpendicular points, respectively.

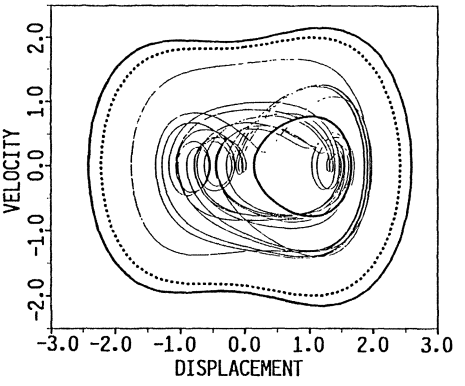

(b) Phase plane trajectory; $\omega = \omega_n = 1.268$. Solid broad line: stable limit cycle; broken broad line: unstable limit cycle; thin line: chaotic trajectory.

Fig.3. Resonance for a large F_s ; $F_s = 0.24$, $F_o = 0.60$.

The governing equation (1) is essentially nonlinear regardless of the magnitude of transverse static force F_s. This may imply that the resonance curve is bent, allowing the system to have nonlinear jumping phenomena, if the force amplitude F_o is large enough. The displacement-excitation relation in Fig.3(a), where $F_s > F_{s,cr}$, shows that multi-value amplitudes are possible for a certain range of excitation frequency. Two of the magnitudes of the resonance are stable and the third is unstable. They grow with force amplitude, and the frequency of an upper perpendicular point on the resonance curve also increases. Therefore, three different orbits with different amplitudes and different centers exist for a frequency just below that of the upper perpendicular point or for a force amplitude just above the value shown here. Chaos may occur under this condition.

The orbits calculated from the harmonic balance method using

$$A(t) = \overline{A_{o1}}\sin(\omega t + \phi) + \overline{A_{o2}}\cos(2\omega t + \phi) + \underline{A_{o3}}\sin(3\omega t + \phi) + C \qquad (4)$$

are also shown together in Fig.3(a), where the three harmonic terms included are chosen from the observation of the phase plane portrait of the limit cycle. There is no significant change of resonance curves between the two and four term harmonic balance methods.

Chaotic motion is actually observed. A study using a direct numerical integration of the governing equation (1) gives the onset boundary of chaos. For example, for $F_s = 0.24$ and the excitation frequency set to ω_n, which is the natural frequency of small oscillation around the static equilibrium position for the given F_s, an onset boundary of force amplitude $F_{o,cr}$ was found to be 0.46.

A chaotic trajectory and three orbits of limit cycles are shown in Fig.3(b), corresponding to the case of Fig.3(a). The trajectory is obtained by the direct numerical integration, and the limit cycles are obtained by the harmonic balance of equation (4).

The upper perpendicular point represents an onset boundary of chaos, $F_{o,cr}$, because, for a fixed excitation frequency with increasing force amplitude, the upper perpendicular point comes first as a trigger of multiple amplitude. Period doubling was observed just before the critical value for the onset of multiple amplitude, when F_o is increased.

The frequency range where multiple amplitude appears is a necessary condition for chaos. Three centers of vibration appear in this case dynamically, while by contrast three equilibrium points appear statically for a small F_s ($< F_{s,cr}$). In the case that F_o is large enough, chaos of this dynamic type is possible even for a small F_s.

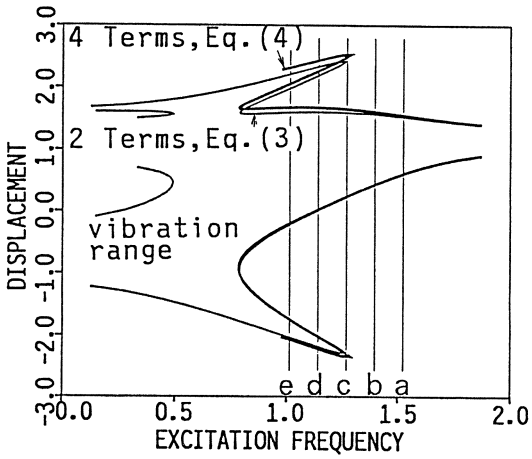

Fig.4. Vibration bounds of resonance; $F_s = 0.24$, $F_o = 0.50$. Force amplitude $F_o = 0.50$ is just above the onset boundary of chaos for $\omega = \omega_n = 1.268$.

a : $\omega = 1.2\omega_n$, stable limit cycle of one-period motion,
b : $\omega = 1.1\omega_n$, stable limit cycle of two-period motion,
c : $\omega = \omega_n$, chaotic orbit,
d : $\omega = 0.9\omega_n$, chaotic orbit,
e : $\omega = 0.8\omega_n$, stable limit cycle of one-period motion.

The presence of multiple amplitudes is not a sufficient condition of chaos. Chaos occurs at an excitation frequency just below the upper perpendicular point, but a stable limit cycle appears again at a much lower excitation frequency in the multiple amplitude range. For example, an orbit for excitation

frequency $\omega = 0.8\omega_n$ in Fig.4 is a stable limit cycle. It is interesting to note that period doubling was observed at the excitation frequency just above the upper perpendicular point, for example, $\omega = 1.1\omega_n$.

Concluding remarks

(1) For a small F_s ($< F_{s,cr}$), the near contact between a stable limit cycle and an unstable limit cycle on the phase plane closely predicts the onset of chaos. The chaotic motion wanders on the phase plane around two stable and one unstable static equilibrium points.

(2) For a large F_s ($\geq F_{s,cr}$), another approach to the onset of chaos is possible. Multiple amplitude nonlinear resonance is a necessary condition for chaos of this type. An upper perpendicular point of the resonance curve stands for the onset of chaos with increasing force amplitude, because it is the onset of two stable and one unstable amplitudes dynamically. A near contact between a stable limit cycle orbit and an unstable one on the phase plane closely predicts the onset of chaos. The chaotic motion wanders on a phase plane around the three centers of the three vibrations, two of which are stable and the third is unstable.

(3) The chaos of the above-mentioned type (2) is possible even for a small F_s , if the force amplitude F_o is large enough.

(4) The presence of multiple amplitudes per se is not a sufficient condition of chaos.

ACKNOWLEDGEMENT: This work was supported in part by the Army Research Office, Contract DAAL03-87K0023. Dr. Gary Anderson is the program director.

References

1. Moon, F.: Experiments on Chaotic Motions of a Forced Nonlinear Oscillator: Strange Attractors. J.Appl.Mech., 47, (1980), 638-644.
2. Guckenheimer, J.; Holmes, J.: Nonlinear Oscillations, Dynamic Systems and Bifurcations of Vector Fields. Springer-Verlag, 1983.
3. Dowell, E. H.; Pezeshki, C.: On Necessary and Sufficient Conditions for Chaos to Occur in Duffing's Equation: An Heuristic Approach. J.Sound Vib., 121(2), (1988), 195-200.
4. Von Dooren, R.: On the Transition From Regular To Chaotic Behavior in the Duffing Oscillator. J.Sound Vib., 123(2), (1988), 327-339.

Coexistence of Periodic Points and Chaos in a Nonlinear Discrete-Time System

K.HIRAI

Department of Systems Engineering,
Faculty of Engineering,
Kobe University, Kobe, Japan

Summary

The coexistence phenomenon of periodic points and chaos in a first and second order discrete-time nonlinear control system is discussed. The coexistence phenomenon discussed here is such that the coexisting different kinds of periodic points or chaotic attractors do appear catastrophically in the bifurcation diagram. Several modes of such coexistence phenomenon are shown. It is shown that the system behavior depends not only upon the initial values but also upon the parameter values.

1. Introduction

One of the most interesting topics in nonlinear system research is chaos. Since the discovery of chaotic behavior, there are many investigations on chaos such as the occurrence condition, system structure, and many related problems [1],[2].

The problem of the coexistence phenomenon of periodic points and chaos is also an interesting topic. In nonlinear system, it is well known that different kinds of periodic points or chaotic attractors coexist if the initial values are changed. The coexistence phenomenon discussed in this paper is such that the coexisting periodic points or chaotic attractors do appear catastrophically in the bifurcation diagram. It is interesting that to which attractors the system behavior is attracted depends not only upon the initial values but also upon the parameter values.

Such coexistence phenomenon has hitherto been observed, e.g.,in the bifurcation diagram of an impulse-shocked mechanical system [3] or a Josephson circuit [4]. In this paper, the coexistence phenomenon in a discrete-time nonlinear control system will be studied.

W. Schiehlen (Editor)
Nonlinear Dynamics in Engineering Systems
IUTAM Symposium Stuttgart/Germany 1989

2. Coexistence phenomenon in the first order system

2.1. System description

Consider a simple nonlinear feedback control system, whose dynamical behavior is governed by

$$x(n+1)=F(x(n))=ax(n)-f(x(n))+r, \quad (1)$$

where $x \in R^1$, f(x) is a saturation element as shown in Fig.1 and is represented by

$$f(x)=h\tanh 2x, \quad (2)$$

and r is a constant input.

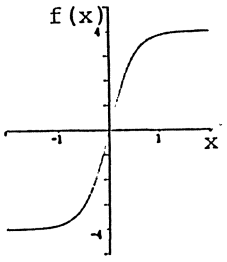

Fig.1 Nonlinear function

In the following, we write

$F^n(x)=F(F^{n-1}(x))$, $n=1,2,\ldots$,

and $F^0(x)=x$.

By substituting (2) into (1), a one-dimensional map of F(x(n)) is obtained as shown in Fig.2. It is to be noted that this map is different from the map of logistic equation, that is, there exist two peaks in the minimum invariant interval. In the following it will be shown that the mapping curve as shown in Fig.2 plays an important roll for the coexistence phenomenon.

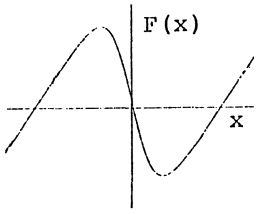

Fig.2 Graph of F(x) of (1)

2.2. Coexistence of periodic points

Two types of the coexistence phenomenon will be shown. One is the coexistence of different types of periodic points and the other is that of chaotic attractors. In this section the coexistence phenomenon of periodic points is shown.

Let h=4, r=0.18. The bifurcation diagram of (1) for x(0)=0.8 is obtained by computer simulation as shown in Fig.3. If the initial value is changed, several modes of the coexistence phenomenon can be observed. In Fig.4 (a) it is shown that 3 periodic points occur catastrophically if x(0)=-0.74 and a=1.47. By checking the curve of $F^3(x)$ at this point, it can be made clear that 3 periodic points occur by the saddle-node bifurcation. Although 2 periodic

points are still stable, the states are attracted to stable 3 periodic points. It is observed that 3 periodic points finally become chaos after the successive period doubling bifurcation, and, after that, the state of the system returns back to the original 2 periodic points. Similarly 5 and 7 periodic points also occur by the saddle-node bifurcation if the initial value and/or parameter value are changed as shown in Fig.4 (b)-(c). In these bifurcation diagrams, the initial value is changed in each computation step, that is, it is chosen as the state value of one computation step before, so that the coexisting states in the bifurcation diagram can be made clear. Comparing these simulation results with Fig.3, it is interesting that the bifurcation diagram depends upon the initial values.

From these simulation results the following question arises: what are the necessary conditions for such coexistence phenomenon to occur ? It can be considered as follows:

1) Firstly it will be considered that at least two peaks must exist in the minimum invariant interval, so that the iterative map is complicated. Moreover, a map of (1) must be unsymmetric with respect to the origin , so that periodic points of odd number occur. It has already been shown that such coexistence phenomenon does not occur if there is only one peak in the minimum invariant interval [1].

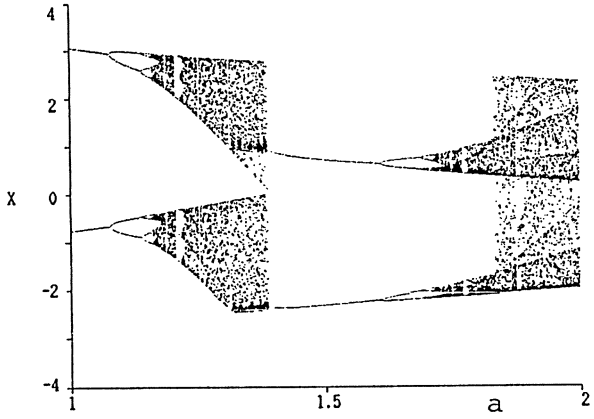

Fig.3 Bifurcation diagram of (1) for x(0)=0.8

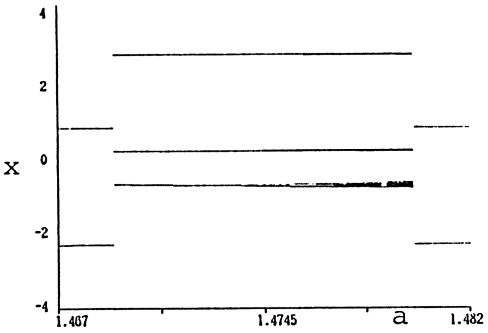

(a) 3 periodic points to chaos

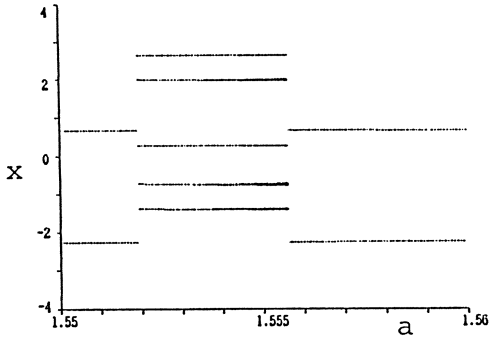

(b) 5 periodic points to chaos

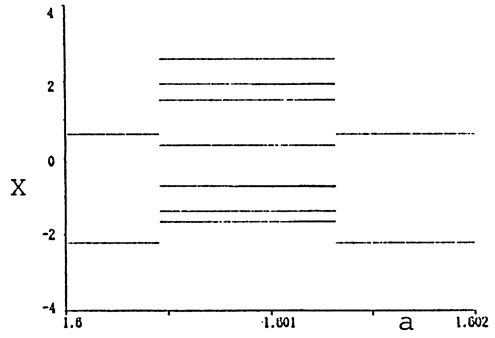

(c) 7 periodic points to chaos

Fig.4 Several modes of the coexistence phenomenon

2) The second condition is that the neighborhood of the peak in a map of F(x(n)) must be differentiable. If k periodic points occur by the saddle-node bifurcation, it must be satisfied for this periodic points to be stable that $|dF^k(x(n))/dx(n)| < 1$ at points of contact with 45° slope line. This condition might be satisfied for a certain value of k and a , if a map of F(x(n)) is differentiable. If f(x) in (1) is piecewise linear function, a map of F(x(n)) will become pointed at these points of contact, and the above slope condition will not be satisfied. In fact the coexistence phenomenon of periodic points can not be observed in computer simulation in case of a piecewise linear saturation element.

It is to be noted that, although the coexistence phenomenon of periodic points will not occur, the coexistence phenomenon of chaos is possible to occur in case of a piecewise linear function.

2.3 Coexistence of chaos

It can be considered that if the map of F(x) is symmetric and has two pointed peaks, the chaotic attractors will coexist. It will be checked by computer simulation.

Now, consider the nonlinear system (1) where f(x) is a piecewise linear saturation element (slope h', break point ±D). Let h'=8, D=0.5, and r=0. The bifurcation diagram for x(0)=0.5 and -0.5 are shown in Fig.5 (a) and (b) respectively. It will be clear that there exist two different chaotic attractors.

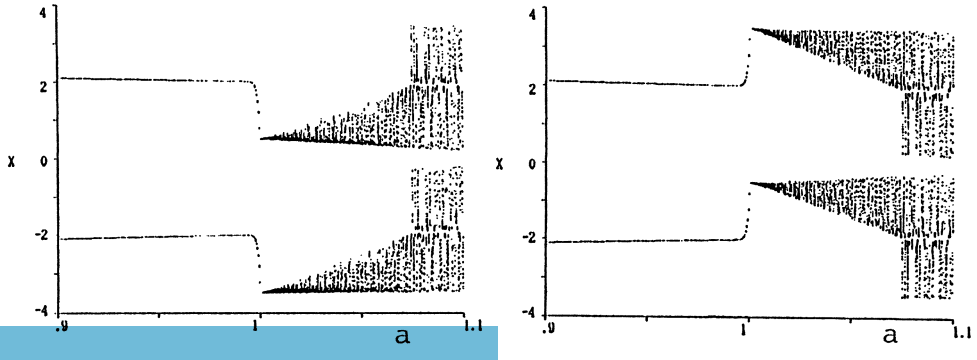

Fig.5 Coexistence of chaotic attractors

The coexistence of chaotic attractors can also be observed in a first order pulse width modulated (PWM) control system as shown in Fig.6. The continuous-time error signal is converted to the pulse train by a sampling period T. The width of each pulse is not constant, but it depends upon the amplitude of the input signal as shown in Fig.7.

Let r=0. Then the system behavior is governed by

$$x(n+1)=F(x(n)), \tag{4}$$

where

$$F(x)=\begin{cases} gx+(g-1)/p & x<-1 \\ gx+g(1-g^{x})/p & -1\leq x\leq 0 \\ gx-g(1-g^{-x})/p & 0<x\leq 1 \\ gx-(g-1)/p & x>1, \end{cases} \tag{5}$$

g=exp(pT), and p is a parameter of the linear element.

For want of space the detailed results of analysis are omitted here [5] and the simulation results are only shown.

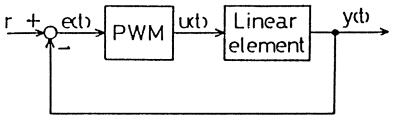

Fig.6 PWM control system

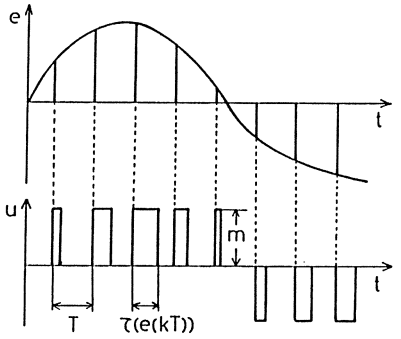

Fig.7 Illustration of e(t) and u(t)

The map of F(x) in this system for r=0 is shown in Fig.8, which has also two peaks in the minimum invariant interval. Figure 9 shows a bifurcation diagram of this system. It is to be noted that there exist 4 chaotic attractors and to which attractors the system behavior is attracted depends not only the initial values but also upon the sampling period.

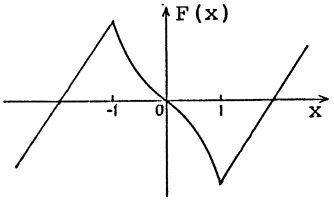

Fig.8 Graph of F(x) of (5)

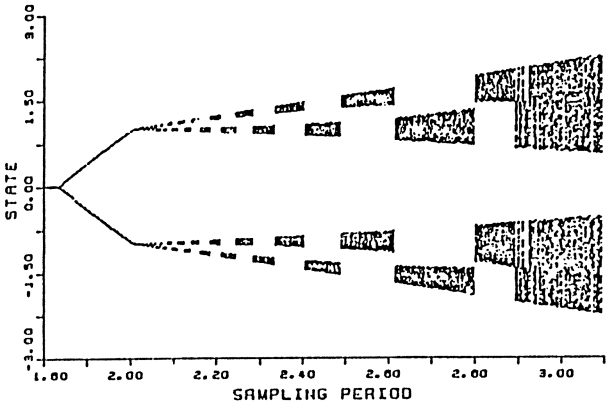

Fig.9 Coexistence of chaotic attractors in PWM system
(p=0.1, m=1, x(0)=0.01)

3. Coexistence phenomenon in the 2nd order system

In the foregoing sections the coexistence phenomenon of periodic points and chaos in the first order system are discussed. In order to show the similar phenomenon in a second order system, a nonlinear sampled-data control system with the first order holder as shown in Fig.10 is considered.

The system equation is represented by

$$\begin{aligned} \dot{x}(t) &= ax(t)+bu(t), \\ y(t) &= cx(t), \qquad (6) \\ u(t) &= H(r-f(y(t))), \end{aligned}$$

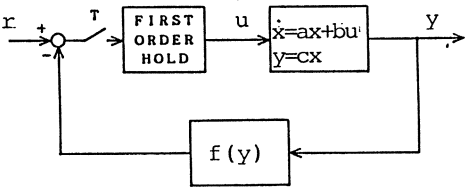

Fig.10 Sampled-data control system

where $x,y,u \in R^1$,
and $H(\cdot)$ is the output of the first order holder and is represented by

$$H(h(t))=h(nT)+[h(nT)-h((n-1)T)](t-nT)/T \qquad (7)$$
$$nT \leq t \leq (n+1)T$$

Now, demote $h(nT)=h(n)$, and let $r=0$, $c=1$, $f(y)=y^3$. Then (6) becomes

$$x(n+1)=F(x(n)), \qquad (8)$$

where $x(n)=(x_1(n), x_2(n))'$, $F(x)=(x_2, \#)'$, (':transpose)

$$\#=[-1/a-(1-\exp(aT))/a^2T]bx_1{}^3(n)+\exp(aT)x_2(n)$$
$$+[(1-\exp(aT))/a^2T+(2-\exp(aT))/a]bx_2{}^3(n).$$

Now, let $a=3$, $b=1$, and the bifurcation of a fixed point is investigated by computer simulation as shown in Fig.11. If the initial values are changed, several modes of the coexistence phenomenon similar as Fig.4 are obtained as shown in Fig.12. Figure 12 (a) is an enlargement of a part of Fig.11, (b) and (c) show the occurrence of 6 and 8 periodic points by the saddle-node bifurcation respectively. In order to make clear the coexisting states, the initial values are changed in each computing step. The more complex coexistence phenomenon can be seen in this system [6], while the occurrence mechanism of the coexistence phenomenon in the second order system has not been made clear.

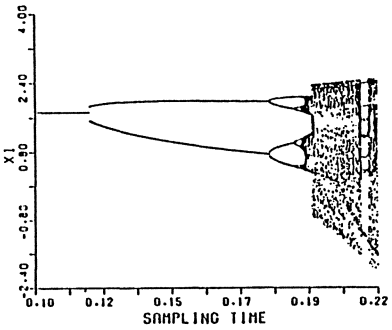

Fig.11 Bifurcation diagram of (8)

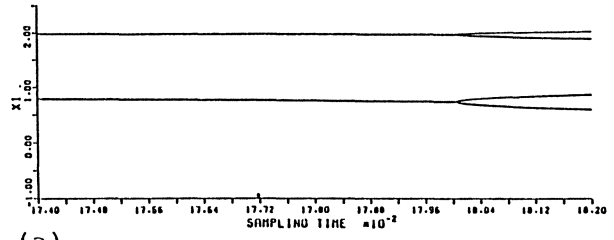

(a)

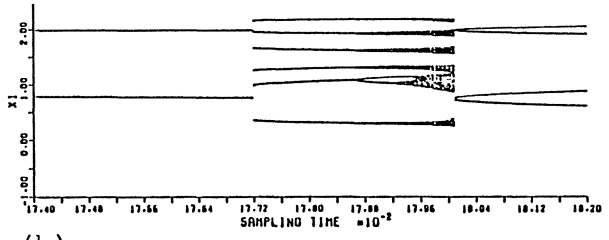

(b)

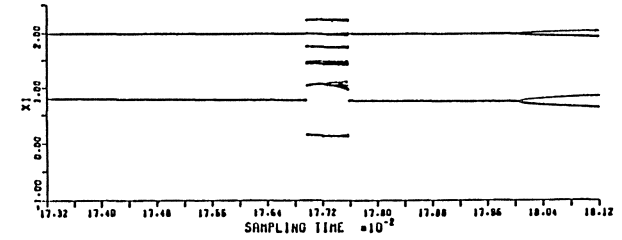

(c)

Fig.12 Several modes of Coexistence phenomenon in (8)

4. Conclusion

In this paper the coexistence phenomenon of periodic points and chaotic attractors in a discrete-time nonlinear control system is investigated. The coexistence phenomenon treated here is such that the coexisting periodic points or chaos do appear catastrophically in the bifurcation diagram. The bifurcation diagram of a simple first order discrete-time control system with saturation, a first order PWM control system, and a nonlinear sampled-data control system with the first order holder, are investigated and the several modes of the coexistence phenomenon are observed.

Acknowledgment

The author wishes to express his thanks to Dr.T.Ushio and Messrs.O.Kondo and T.Adachi for their valuable discussions and assistance.

References:

[1] Guckenheimer,J. and Holmes,P.: Nonlinear Oscillations, Dynamical Systems, and Bifurcations of Vector Fields, Springer Verlag, 1983.

[2] Moon, F.C.: Chaotic Vibrations, John-Wiley & Sons, 1987.

[3] Hsu,C.S.: Cell to Cell Mapping, Springer Verlag, 1987.

[4] Hocket,K. and Holmes,P.: Nonlinear Oscillations, Iterated Maps,Symbolic Dynamics, and Knotted Orbits, Proc. IEEE, 75,(1987), 1071-1080.

[5] Ushio,T. and Hirai,K.: Chaotic Behavior in Pulse-Width Modulated Feedback Systems, Trans.SCICE, 21, (1985), 539-545 (in Japanese).

[6] K.Hirai and O.Kondo: Coexistence of Chaos and Periodic Points in a Nonlinear Sampled-data Control System, Nonlinear Problems in Dynamical Systems, ed. M.Hiller and H.Sorg, Univ. of Stuttgart,(1987), 6.1-6.6.

Experimental and Analytical Investigation of Nonlinear Coupled Oscillators under Random Excitation

R. A. Ibrahim, Y. J. Yoon and M. Evans

Wayne State University,
Department of Mechanical Engineering
Detroit, Michigan 48202, U. S. A.

Summary

The nonlinear interaction of a two degree-of-freedom oscillator subjected to a wide band random excitation is investigated analytically and experimentally. The analytical investigation employs the Fokker-Planck equation together with a non-Gaussian closure scheme. The solution predicts response statistics in terms of system parameters and excitation spectral density level. In the experimental study, tests are conducted for long time intervals which are enough to reveal all possible dynamic characteristics of the system. The measured signals are processed to estimate response statistics such as mean squares, spectral densities, and probability density functions. The results show a qualitative agreement between predicted and measured response statistics. Both approaches give common features such as the autoparametric vibration absorbing effect, and nonstationarity in the coupled oscillator statistics. The measured probability density functions show a slight deviation from Gaussian curves.

Analytical Approach

Figure 1 shows a schematic diagram of the model which consists of the main system of mass M and stiffness K_1 provided by four leaf springs each of length L. The main mass carries a cantilever beam of length ℓ_c, and stiffness K_2. The cantilever beam carries a mass m whose location can be adjusted to provide the desired value of the natural frequency of the secondary system. In deriving the equations of motion, the axial displacement in the elastic elements will be considered in the estimation of the system kinetic energy. Applying Lagrange's equation for the two generalized coordinates x and y, the equations of motion in nondimensional form are:

$$X'' + 2\zeta_1 X' + X + \varepsilon^2(XX'^2 + X^2X'') - \varepsilon(L/\ell_c)R(Y'^2 + YY'') = W''(\tau) \qquad (1a)$$

$$Y'' + 2\zeta_2 rY' + r^2Y - \varepsilon(L/\ell_c)\{W''(\tau) + X''\}Y + \varepsilon^2(L/\ell_c)^2(Y'^2 + YY'')Y = 0 \qquad (1b)$$

where

$$X = x/X_o,\ Y = y/X_o,\ r = \omega_2/\omega_1,\ \omega_1^2 = \frac{K_1}{(M+m)},\ \omega_2^2 = \frac{K_2}{m},\ R = m/(M+m),$$

$$\tau = \omega_1 t,\ \mu = 1 - R,\ \varepsilon = 6X_o/5L,\ \zeta_1 = \frac{C_1}{2(M+m)\omega_1},\ \zeta_2 = \frac{C_2}{2m\omega_2}, \qquad (2)$$

$$X_o = \sqrt{\pi S_o/\{2\zeta_1\omega_1^3\}},\qquad W''(\tau) = U''(\tau/\omega_1)/X_o\omega_1^2$$

a prime denotes differentiation with respect to the dimensionless time τ, and X_o is a reference length which is taken as the root mean square displacement of the system in the absence of nonlinear coupling.

W. Schiehlen (Editor)
Nonlinear Dynamics in Engineering Systems
IUTAM Symposium Stuttgart/Germany 1989

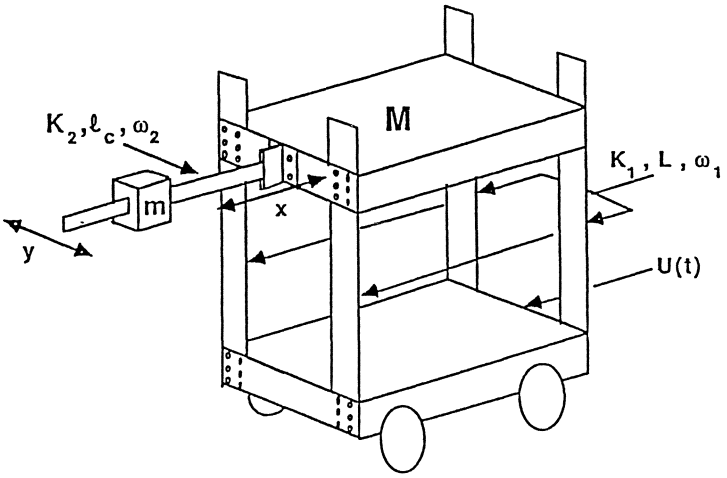

Figure 1 Schematic diagram of the model

It is seen that the ground acceleration W``(τ) appears in equation (1a) as a non-homogeneous term while it acts as a parametric term in equation (1b) of the cantilever beam. The motion of the main mass also appears as a parametric excitation to the cantilever beam and since X`` is an implicit function of time, the nonlinear term X``Y in equation (1b) is referred to as an *autoparametric* coupling term. Another important feature in this particular model is that the linear portion of equations(1a,b) represents uncoupled linear oscillators. In other words, the generalized and principal coordinates are the same.

The ground motion acceleration is assumed to be a zero mean, stationary Gaussian process with a smooth spectral density S_o, up to some frequency limit ω_o, where $\omega_o >> \omega_1$. Its autocorrelation function is

$$R_u(\tau') = E[U''(\tau)U''(\tau+\tau')] = 2S_o\omega_o\{\frac{\sin\omega_o\tau'}{\omega_o\tau'}\}$$

It follows that the autocorrelation function of W``(τ) is

$$R_w(\tau') = E[W''(\tau)W''(\tau+\tau')] = \frac{2S_o\omega_o}{X_o^2\omega_1^4}\{\frac{(\sin\Omega\tau')}{\Omega\tau'}\}$$

$$= \frac{2\pi S_o \sin\Omega\tau'}{\omega_1^3 X_o^2 \quad \pi\tau'} = 2D\delta(\tau')$$

where $D = \pi S_o/\omega_1^3 X_o^2$ and $\delta(\,)$ is the Dirac delta function.

Equations (1) cannot be written in the Markov vector form due to the presence of coupled nonlinear acceleration terms. However, these terms can be removed by successive elimination. In this case, one can write equations (1) in the form of the Ito stochastic differentials:

$$dX_i'(\tau) = \{f_i(X,\tau) + \frac{1}{2}\sum_k^4\sum_j^4 G_{kj}(X,\tau)\frac{\partial G_{ij}(X,\tau)}{\partial X_k}\}d\tau + \sum_j^4 G_{ij}(X,\tau)dB_j(\tau) \qquad (3)$$

through the coordinate transformation $\{X_1,X_2,X_3,X_4\} = \{X,Y,X`,Y`\}$.

In equation (3) the function $f(X,\tau)$ is a vector whose elements f_i are linear and nonlinear functions of the state coordinates X, $G(X,\tau)$ is a 4x4 matrix whose elements are also linear and nonlinear, and the random process $W`(\tau)$ is replaced by the time derivative of the Brownian motion process $B_j(\tau)$, i. e. $W`(\tau) = \sigma dB(\tau)/d\tau$, where $\sigma^2 = 2D$.

The evolution of the joint probability density of the response coordinates $p(X,\tau)$ can be described by the Fokker-Planck equation. In view of the system nonlinearity, it is not possible to solve the system Fokker-Planck equation for the response probability density even for the stationary case. Instead, one may derive a general first order differential equation for the response dynamic moments by using the Fokker-Planck equation approach or the Ito stochastic calculus [1]. The resulting equation is found to constitute an infinite set of coupled moment equations which may be closed via one of the appropriate closure scheme. In reference [2] a Gaussian closure scheme was used and a set of fourteen differential equations in the first and second order moments were solved numerically. In this paper, a first order non-Gaussian closure is used by generating moment equations up to fourth order and replacing fifth and sixth order moments in terms of lower order moments. This is done by setting the corresponding fifth and sixth order cumulants to zero. This procedure results in 69 first order coupled differential equations which are solved numerically by using the DIVPRK (solution of an Initial Value Problem using Runge-Kutta-Verner fifth-order and sixth-order method, double precision) subroutine and by using DIVPAG (solution of an Initial Value Problem using an Adam-Moulton or Gear method, double precision) subroutine of the IMSL package (International Mathematical and Statistical Library). The two methods give the same steady state solution when the two modes are fully coupled. However, at the threshold of the autoparametric interaction region (where the cantilever beam is about to oscillate) the DIVPRK subroutine experiences numerical instability while the Gear method yields numerical stability.

The results shown in figure 2 show that the non-Gaussian closure solution exhibits less nonstationarity than the Gaussian solution and the two modes are interacting in the form of energy exchange. In addition, the non-Gaussian response of the main mass fluctuates within the boundaries of the Gaussian solution, while for the cantilever beam, it is slightly higher than the Gaussian solution. The degree of nonstationarity depends on the damping ratios and the nonlinear coupling parameter ε. It is also found that the system achieves a complete stationary response for relatively higher damping ratios depending on the value of the nonlinear coupling parameter, ε.

Figure 3 shows the variation of the mean square responses versus the internal detuning parameter r. In the neighborhood of r = 0.5 the energy is transferred from the main mass to the cantilever beam which acts as a nonlinear vibration absorber. The dependence of the mean square responses on the excitation spectral density level is shown in fig. 4. This figure indicates that the solution remains stationary up to an excitation level ($D/2\zeta_1 >$ 0.6) above which the solution becomes nonstationary as indicted by the two branches. Currently, the authors are in the process of establishing a three dimensional diagram showing the dependence of the different response regimes on the damping ratios, excitation spectral density, and internal detuning parameter.

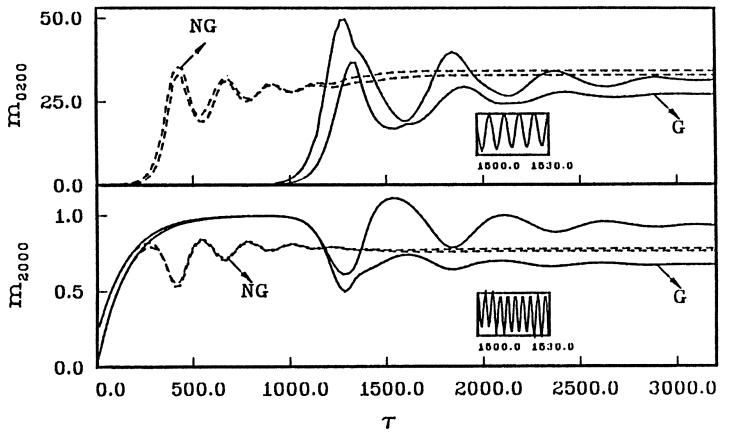

Fig. 2 Time history of mean square responses (G=Gaussian, NG=Non-Gaussian)
$D/2\zeta_1$=1.0, r=0.5, ε=0.02, ζ_1=0.00324, ζ_2=0.00301

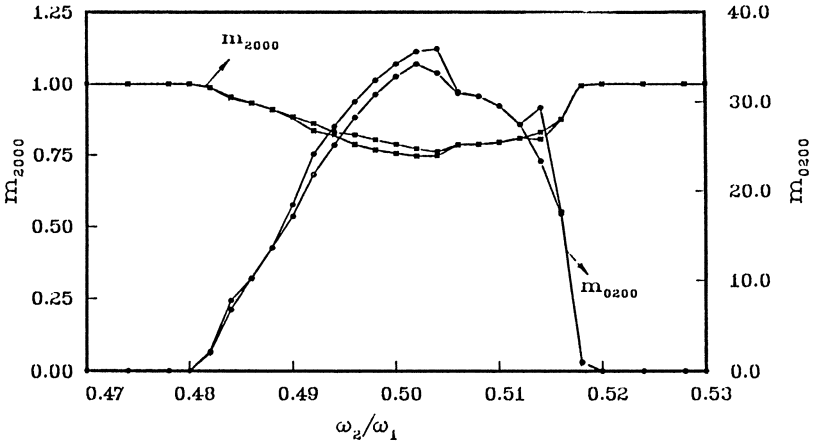

Figure 3 Mean square response versus internal detuning ratio
ζ_1= 0.00324, ζ_2 = 0.00301, ε = 0.02, and $D/2\zeta_1$ = 1.0

Experimental Investigation

The experimental model emulates the analytical model shown in figure 1. A complete description of the model, arrangement of test equipment, test procedure, and data processing is given in reference [2]. The early results reported in reference [2] were found to include interaction with the shaker. In this paper, the instrumentation includes the use of a Scientific Atlanta SD1715 sine/random control system. This control unit is mainly used to generate a feedback signal to the shaker such that the shaker output signal maintains a constant spectral density level. Each experimental test is allowed to run for 45 minutes. This period is found to be sufficient for

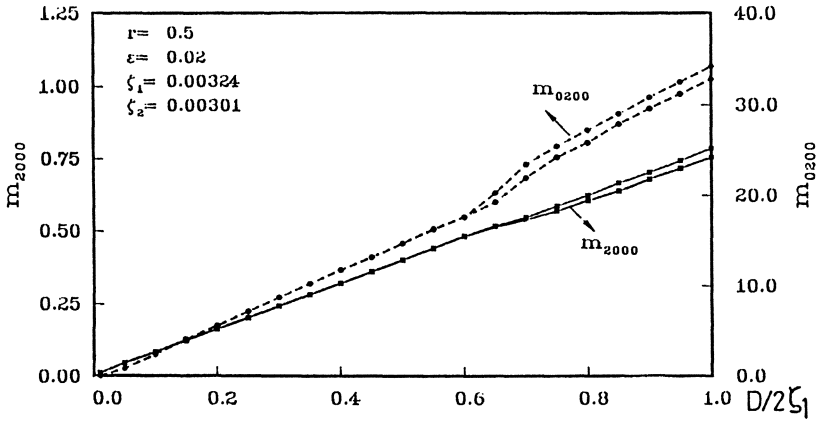

Figure 4 Mean square response versus excitation spectral density level

the system to display all possible dynamic characteristics and to establish the system response stationarity. The response signals are processed to estimate the dependence of the mean square response on the excitation spectral density and to plot the probability density functions.

The time history mean squares of the shaker, main mass, and cantilever beam are plotted in fig. 5. These are used to establish whether or the not the signal is stationary in the wide sense. It is seen that both the shaker and main mass signals are considered stationary after 540 seconds and 1080 seconds, respectively. The cantilever beam, on the other hand, exhibits small fluctuations indicating that the signal is nonstationary. The power spectral densities of the three signals are shown in fig. 6. It is seen that the observed dip in the power spectral density of the shaker signal, at the main mass natural frequency, reported in reference [2] has significantly been reduced in this plot since the vibration control is used. The shaker signal has almost flat spectral density while both the main mass and cantilever beam have narrow band spectral densities whose center frequencies correspond to the natural frequencies of the two modes.

The dependence of the mean square responses upon the internal detuning ratio r is shown in figure 7. The plotted values are normalized by dividing the actual mean square of the two modes by the unimodal mean square response of the main mass (measured when the tip mass is directly attached to the main mass such that no interaction can take place). Each couple of points (one for the main mass, shown by the full circle, and one for the cantilever beam, shown by a triangle) are obtained for one internal detuning setting. When the test is repeated for the same internal detuning one obtains two different points as shown. For each test the shaker power spectral density is estimated and it is found that the two tests which are believed to be identical are actually conducted under different excitation power spectral densities. This is the main reason for the observed scattering of the mean square response versus r. Figure 8 shows the mean square responses versus the excitation power spectral density for r = 0.5. This figure establishes the threshold value at which the cantilever beam starts to oscillate. It is found that when the motion of the beam is fully developed the slope of the main mass mean square

response with respect to the excitation spectral density level is reduced indicating a transfer of energy to the cantilever beam. However, the well known saturation phenomenon [3] reported in the deterministic theory of nonlinear vibration of systems with quadratic nonlinearity is not observed since the excitation is random and contains a wide range of excitation frequencies. Figure 7 provides qualitative agreement with the predicted results shown in figure 4 in that the cantilever beam acts as a nonlinear vibration absorber.

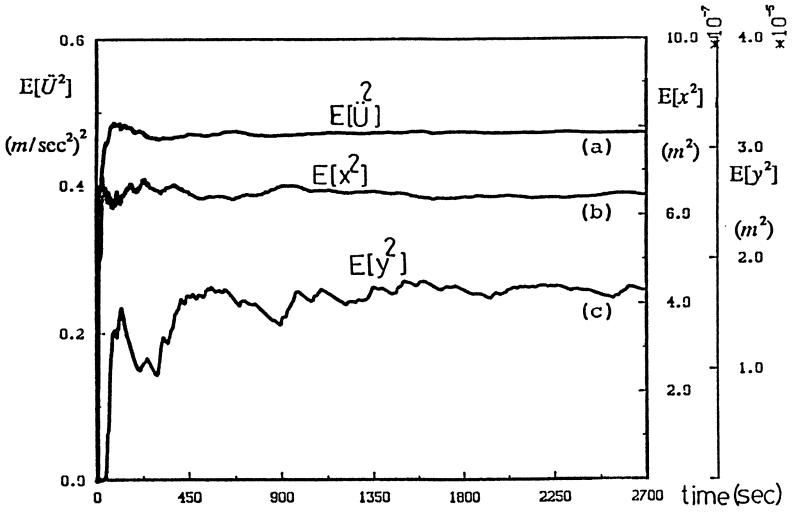

Figure 5 Time history records of mean squares of the (a) shaker, (b) main mass, and (c) cantilever beam

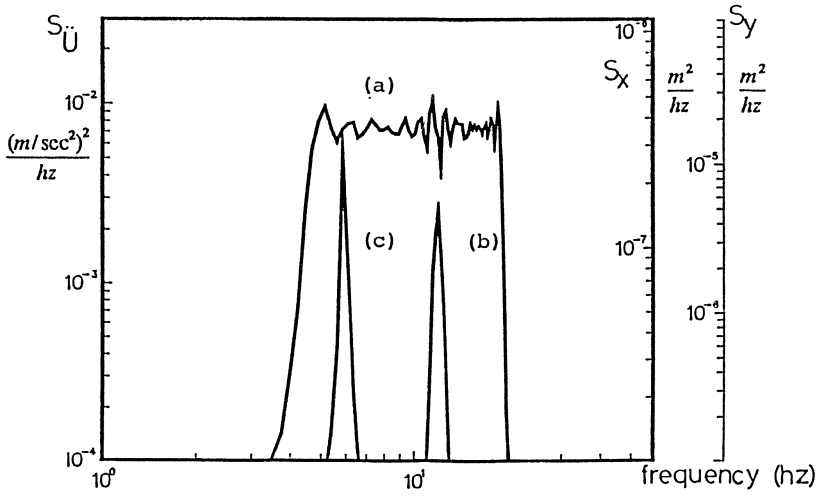

Figure 6 Power spectral density functions of the (a) shaker, (b) main mass, and (c) cantilever beam

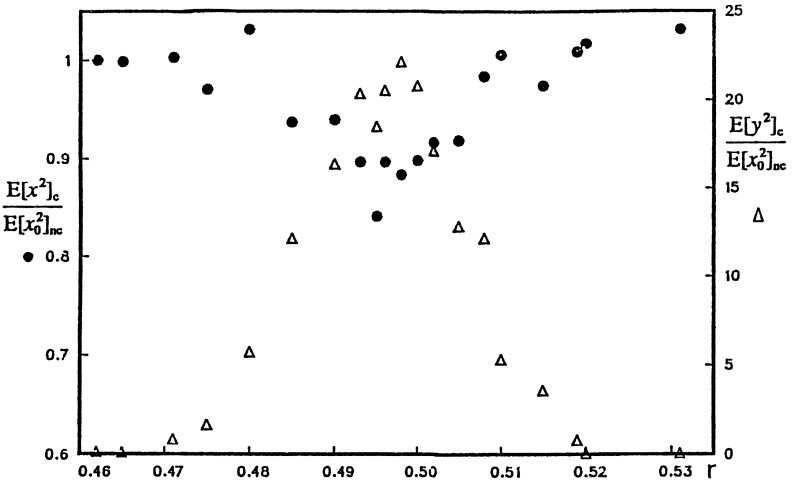

Figure 7 Dependence of mean square responses on the internal detuning ratio

The probability density functions as estimated from the three signals are plotted by the histograms shown in figure 9. The degree of deviation of the response processes from normality can be inferred by plotting the corresponding Gaussian curves which are determined from the mean and variance of each process. It is seen that the main mass response is nearly Gaussian while the cantilever beam response has significant deviation from normality. The degree of deviation from normality depends on the excitation spectral density and internal detuning parameter.

Conclusions

The random response of a nonlinear coupled oscillator is examined analytically and experimentally. A non-Gaussian closure scheme is used to predict response statistics and the results are compared with those measured experimentally. The analytical and experimental results are in good qualitative agreement. Both results exhibit common features such as autoparametric vibration absorbing effect and nonstationarity in the response statistics. The experimental probability density functions of the system response show slight deviation from normality. Within the context of the present system, the Gaussian closure scheme may be regarded as sufficient to predict the response of systems with nonlinear inertia coupling.

References

1. Ibrahim, R. A., *Parametric Random Vibration*, John Wiley & Sons, New York, 1985.
2. Ibrahim, R. A., Evans, M. and Yoon, Y. J., "Experimental Investigation of Random Excitation of Nonlinear Systems with Autoparametric Coupling," Proc. of the Symposium on Stochastic Structural Dynamics, University of Illinois at Urbana-Champaign, October 30-November 1, 1988.
3. Nayfeh, A. H. and Mook, D. T., *Nonlinear Oscillations*, Wiley-Interscience, New York, 1979.

Acknowledgment

This research is supported by a grant from the National Science Foundation under research grant no. 87-96342 and by an additional grant from the Institute for Manufacturing Research.

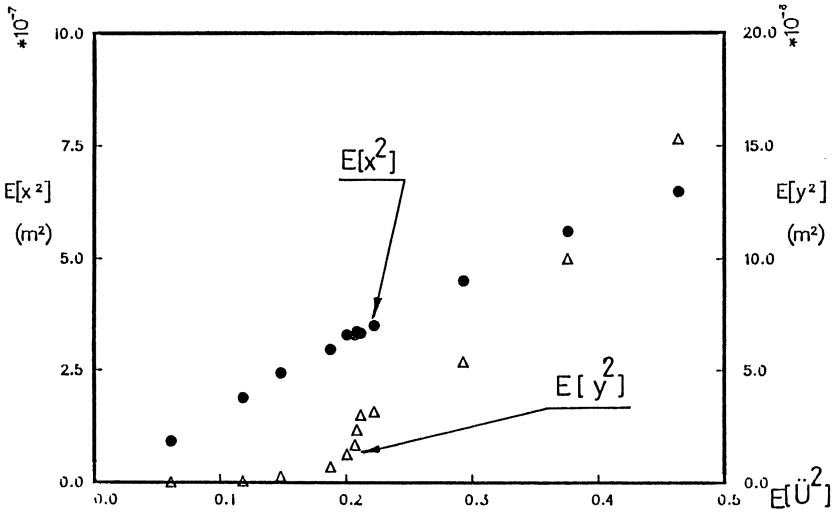

Figure 8 Dependence of mean square responses on the excitation mean square level

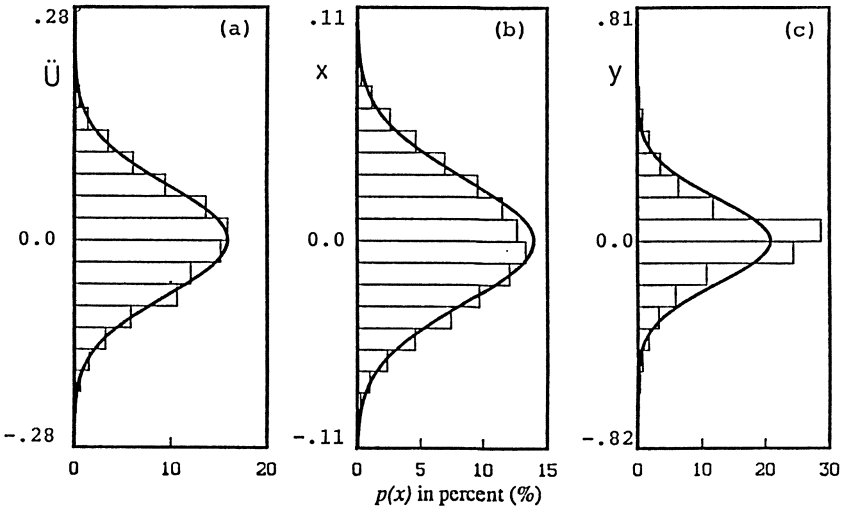

Figure 9 Probability density functions for the (a) shaker, (b) main mass, and (c) cantilever beam

Fractal Properties of the Bouncing-Ball Dynamics

HEIKKI M. ISOMÄKI

Main Building
Helsinki University of Technology
SF-02150 Espoo 15, Finland

Summary

We study the mechanical bouncing-ball system, which is a modification of the classical Fermi-Ulam problem. We calculate the basin structure and find that the basin boundaries are fractal curves. The observed multidimensionality is discussed in terms of the Smale-horseshoe dynamics generating the chaotic basic set.

The mechanical bouncing ball system is a modification of the classical Fermi-Ulam problem [1,2]. In this modified set-up the ball is made to fly and impact dissipatively on a sinusoidally vibrating surface. A nice feature of the modified dynamics is that they are well feasible via mechanical experiments, which makes quite accurate tests possible [3,4]. The theoretical analysis is often based on the 2-dimensional dissipative standard map of Zaslavsky and Rachko (ZR) [2,3,5], which is the high-bounce approximation of the real dynamics. However, recently also the full equations of motion are adapted in the investigations [3,4,6]. The purpose of this paper is to inquire into the rich Fermi-Ulam dynamics by computing the basin structure using the full equations of motion. The basin is the catchment set asymptoting the attractor with time. The computation of basins [7] also facilitates the analysis of the appearance of the so called self-reanimating chaos [4] and the noise effects. Quite generally, the future evolution of a system starting from an initial condition depends significantly on the structures of the basins and their boundaries.

In the equations of motion time and length are given in units $1/\omega$ and $g/2\omega^2$, respectively, where ω is the angular frequency of

W. Schiehlen (Editor)
Nonlinear Dynamics in Engineering Systems
IUTAM Symposium Stuttgart/Germany 1989

the sinusoidally vibrating surface and g the acceleration of gravity. t_i is the time of the i'th surface-ball impact, T_i is the flight time, h is the surface's height, $h_i = h(t_i)$, v_i is the ball's velocity after the i'th impact, H is the amplitude of the surface's vibration and κ is the coefficient of restitution. Using the above definitions and Newton's 2nd law of motion and law of impact [8] the full equations of motion are found

$$v_{i+1} = \kappa(2T_i - v_i) + (1+\kappa)\dot{h}_{i+1} \tag{1a}$$

$$-T_i^2 + v_i T_i + h_i = h_{i+1} \tag{1b}$$

$$t_{i+1} = t_i + T_i \tag{1c}$$

$$h_i = H \cos t_i \tag{1d}$$

The attractor is represented as (i,p) by giving the number of impacts i within the attractor period p. Note that p is given here in the units $2\pi/\omega$. Hence, e.g., the ZR attractors (see below) are of the form $(2^n, 2^n\alpha)$, where n = 0,1,2,... denotes the bifurcation level (α = 1,2,...). Two types of exotic mute modes exist: if the ball sticks permanently to the surface the attractor is $(\infty,0)$ (fully mute mode [4]) and if temporarily (chirping mode [4]) the attractor is (∞,n) (attractors at least up to n = 11 have been found [7]).

When eqs. 1 are compared with ZR mapping [2] they are found to be the same provided that $T_i = v_i = \alpha 2\pi$ (α = 1,2,...). Under these conditions the only exactly physical attractors appearing in ZR mapping are those of the form $(1,\alpha)$ (ZR attractors) located at

$$t_i = 2\pi - \arcsin\left(2\pi\alpha(1-\kappa)/H/(1+\kappa)\right) \tag{2}$$

The other solutions at $t_i' = 3\pi - t_i$ are unstable (see, e.g., fig. 1 in ref. [5]). In this paper we utilize the full equations of motion (eqs. 1).

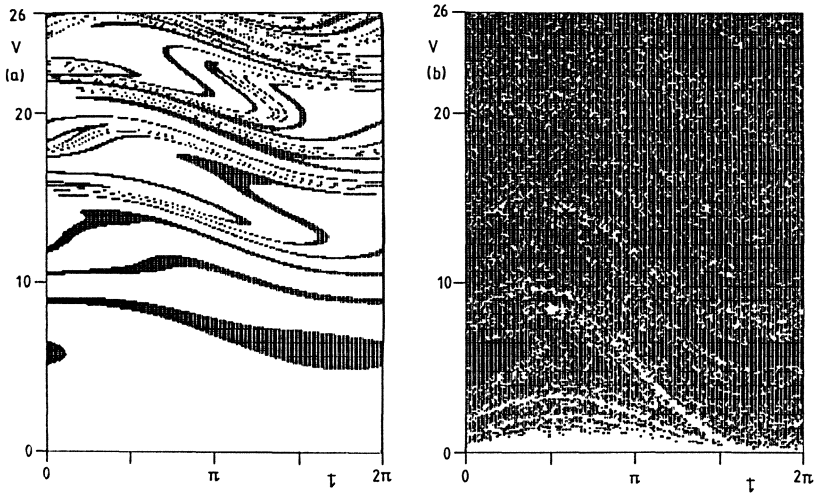

Fig. 1. (t,v) basins. (a) H = 0.6, the white denotes the (∞,0) basin and the grey denotes the ZR (1,1) basin. (b) H = 2.3, the white denotes the (∞,1) basin and the grey denotes the union of the ZR (2,2), (2,4), (1,3) and (1,4) basins.

The dynamics are studied for $\kappa = 0.86$, which is a typical value for steel sphere experiments [4]. We present in figs. 1-4 a few representative (t,v) basins (with blow-ups) at different H's. The starting moment $t = t_i$ on the surface and the relative starting velocity $v = v_i - \dot{h}_i$ with respect to the surface are chosen as the most natural initial conditions. Hence t and t+2π are equivalent. In all basin plots the grid in (t,v) plane is 200x260. White regions denote the basins of the attractors of the mute type (∞,0) or (∞,1) (in fig. 1b only) and the grey ones the union of the basins of ZR attractors (or their bifurcated attractors in fig. 1b). The black regions represent the basins of exotic attractors, such as (2,1) in figs. 2-4. The first ZR orbit (1,1) becomes stable at H ≈ 0.473 (see eq. 2) and bifurcates to (2,2) at H ≈ 2.065. The basins near these H's are presented in fig. 1. In fig. 1a the lone ZR attractor (1,1) is stable whereas the grey basin in fig. 1b is a union of (2,2), (2,4), (1,3) and (1,4) basins of attraction. The basins of permanent (∞,0) and temporary (∞,1) mute modes in figs. 1a and 1b,

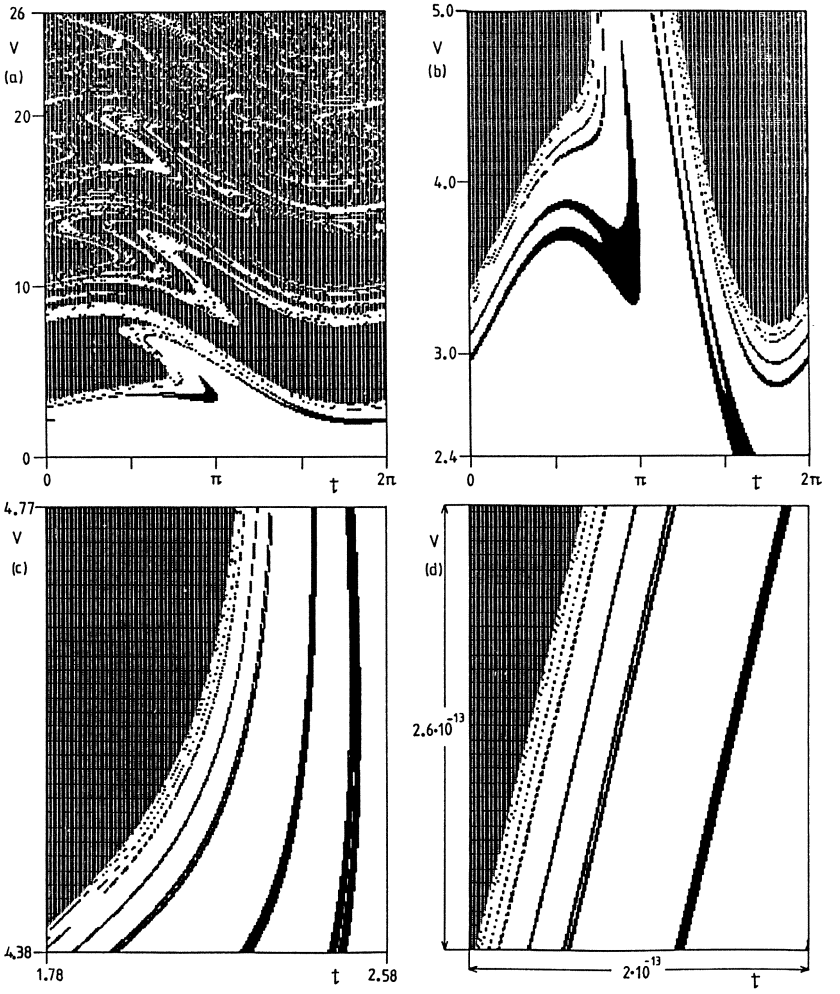

Fig. 2. (t,v) basins at H = 1.4. The white, grey and black denote the $(\infty,0)$ basin, the union of the ZR (1,1) and (1,2) basins and the (2,1) basin, respectively. The magnified lower part of (a) is in (b), the magnified grey corner to the left of (b) is in (c) and the highly magnified grey-white boundary at the top of (c) is in (d).

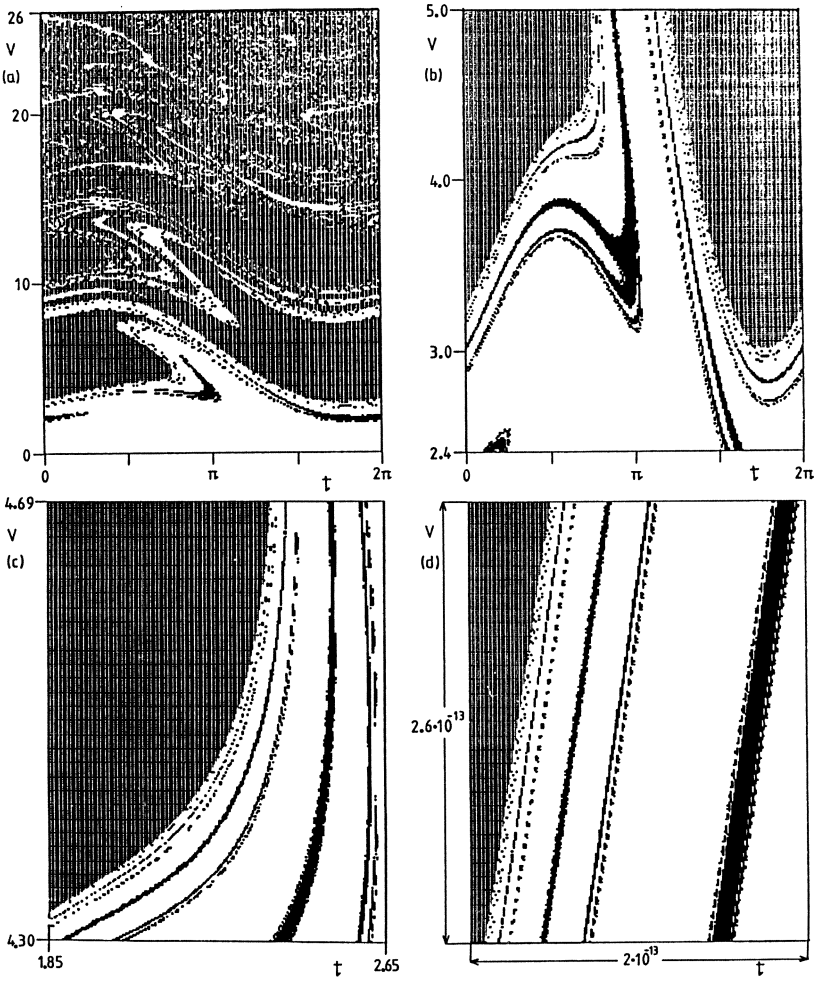

Fig. 3. (t,v) basins at H = 1.5. The white, grey and black denote the (∞,0) basin, the union of the ZR (1,1), (1,2) and (1,3) basins and the (2,1) basin, respectively. The magnified lower part of (a) is in (b), the magnified grey corner to the left of (b) is in (c) and the highly magnified grey-white boundary at the top of (c) is in (d).

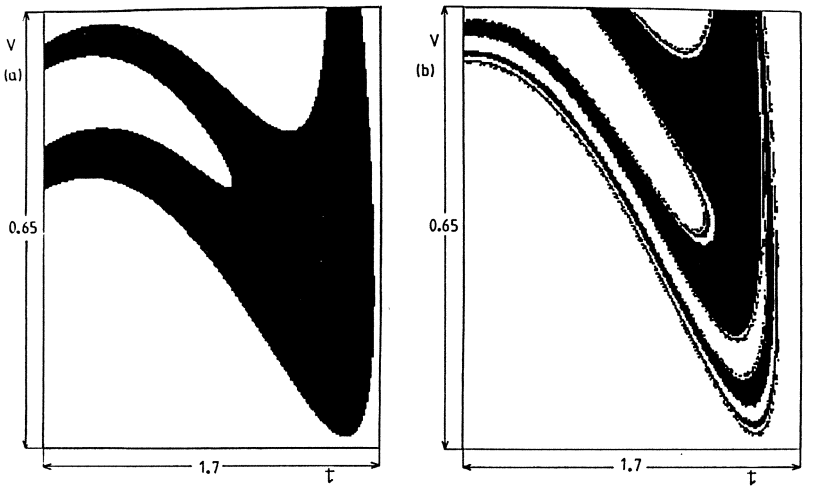

Fig. 4. Magnified (t,v) basins at (a) H = 1.4, (b) H = 1.5. The white and black denote the (∞,0) basin and the (2,1) basin, respectively. (a) and (b) are blow-ups of the black structures in the center of figs. 2b and 3b, respectively.

respectively, decrease continuously when H is further increased. The change of stability (∞,0)→(∞,1) occurs at H = 2.0.

The basins of attractors (∞,0), ZR and (2,1) are presented at H = 1.4 and 1.5 in figs. 2-4. In order to find out the structure of the basins and the quality of the basin boundary several magnifications are presented in figs. 2 and 3: the magnified lower part of (a) is in (b), the magnified grey corner to the left of (b) is in (c) and the highly magnified grey-white boundary at the top of (c) is in (d). The basins are intertwined in a complicated way. It is evident that the black (2,1) basin is sandwiched between the white (∞,0) basin and does not touch the grey ZR basin. No fractal basin boundaries are present for H = 1.4 in fig. 2. However, at H = 1.5 the black-white boundary becomes fractal (fig. 3). This difference is even more clearly seen in figs. 4a and 4b in which the black structures in the center of figs. 2b and 3b, respectively, are magnified: the smooth and fractal boundaries, respectively,

are evident. At H = 1.5 the fractal black-white boundary exists simultaneously with the smooth grey-white boundary (fig. 3). This behaviour is attributed to the possibilities for multiple homoclinic and heteroclinic bifurcations [9,10] that occur independently at different parameter values and create a Smale-horseshoe-type chaotic basic set [10,11] corresponding to a fractal basin boundary.

References

1. E. Fermi, Phys.Rev. 75, 1169-1174 (1949); S.M. Ulam, in: Proc. Fourth Berkeley Symposium on Mathematical Statistics and Probability, California 1960, University of California Press, 315-320; G.M. Zaslavsky and B.V. Chirikov, Usp. Fiz. Nauk. 105, 3-39 (1971); An interesting generalization of the standard map is found in A.A. Chernikov, T. Tél, G. Vattay and G.M. Zaslavsky, Chaos in the Relativistic Generalization of the Standard Map, 1-19, preprint.

2. G.M. Zaslavsky and Kh.-R. Ya. Rachko, Zh. Eksp. Teor. Fiz. 76, 2052-2064 (1979).

3. K. Wiesenfeld and N.B. Tuffilaro, Physica D26, 321-335 (1987).

4. P. Pierański and J. Małecki, Phys. Rev. A34, 582-590 (1986); Z.J. Kowalik, M. Franaszek and P. Pierański, Phys. Rev. A37, 4016-4022 (1988).

5. P.J. Holmes, J. of Sound and Vibration 84, 173-189 (1982).

6. S. Celaschi and R.L. Zimmerman, Phys. Lett. A120, 447-451 (1987).

7. H.M. Isomäki and M. Franaszek, in preparation.

8. E.A. Fox, Mechanics, Harper and Row, London 1967.

9. G.X. Li and F.C. Moon, Multiple Homoclinic Bifurcation Criteria for Chaos for a Two-degree-of-freedom Nonlinear Oscillator, Cornell University, New York 1987, 1-14.

10. P.M. Battelino, C. Grebogi, E. Ott, J.A. Yorke and E.D. Yorke, Physica D32, 296-305 (1988); See also J. Peinke, J. Parisi, B. Röhricht, O.E. Rössler and W. Metzler, Z. Naturforschung 43a, 287-288 (1988).

11. C. Grebogi, H.E. Nusse, E. Ott and J.A. Yorke, in: Lecture Notes in Mathematics 1342, ed. J.C. Alexander, Springer, Berlin 1988, 220-250; H.E. Nusse and J.A. Yorke, Physica D36, 137-156 (1989).

Analysis of Nonlinear Structural Vibrations by Normal Transform Theory

L. JEZEQUEL

Ecole Centrale de Lyon
- 69131 Ecully Cedex

C-H. LAMARQUE

Ecole Nationale des Travaux Publics
de l'Etat - 69518 Vaulx en Velin Cedex

Summary

The normal form theory is applied to free and forced nonlinear oscillators in order to find again some classical results obtained from others classical theories (averaging method ,multiple scales ,...), and to obtain results about SNM, NNM, forced response of damped nonlinear mechanical systems and to build an extension of modal synthesis in the nonlinear case .

Introduction

The idea of normal transform is due to H. Poincaré [1] ; many authors brought it further successfully (Birkhoff [2], Arnold [3], Moser [4],...). It deals with finding a change in variables which transforms a system of analytical nonlinear ODE into a simpler one, sometimes a linear one. In references [5] and [6],Brjuno studies existence and stability of normal forms in the case of analytical forms of ODE.

The order one normalization correspond to the diagonalisation of the lineary part, or the use of his Jordan form, if possible. The analysis of eigenvalues of the lineary part permits a first study of the behavior of the system : we have critical or non critical eigenvalues (Hsu [7], [8]). In order to analyze free vibrations of Hamiltonian systems, our method leads to the notion of non-linear modes. It permits an easy analysis of orbital stability : therefore normal transform was introduced, in agreement with Center Manifold Theorem[9]. So we can find again the results of bifurcation given by Month and Rand [10] in the case of a system possessing Similar Normal Modes. We find again from the normal form of the starting Hamiltonian system, a first integral:it is independant of the integral of energy H = h: so we can build a Poincaré Map, and obtain NNM, and analyze their stability like in Month [11]. In the case of forced vibrations, we use an augmented system : so we show small parameters of bifurcation. We solve the problem of normalization of the non-linear system in the frame of Hopf bifurcation.In the case of several forced degrees of freedom system, we can bind the forced response to the non-linear modes obtained for free vibrations.In her works [12], W Szemplinska-Stupnicka emphasizes the interest of such a thing. She shows the difficulty of taking into account several non-linear

W. Schiehlen (Editor)
Nonlinear Dynamics in Engineering Systems
IUTAM Symposium Stuttgart/Germany 1989

modes in the forced response. Our method permits to analyse the coupling level between non-linear modes, and permits a generalization of the modal superposition technique in the case of cubic non linearities. Though the method is a general one to describe the behaviour of dynamical systems with analytical non linearities, we use simple examples in order to display the main ideas, and to compare with classical results. By studying systems with cubic non linearities we can get the frame to enlarge modal synthesis methods.

In a first part, we present the normal transform method. Then we study free vibrations of single and two dof, and compare with classical methods. Last, we apply the method to forced vibrations. We introduce detuning. We study two dof system with close frequencies in order to show coupling between non-linear modes.

Normal Form Theory

Let be a mechanical non-linear system (even not conservative)

$$\frac{dX}{dt} = AX + F_2(X) + \ldots\ldots\ldots + F_M(X) \qquad (1)$$

with, $X \in \mathbb{R}^n$, F_k^j vectors gathering non linearities with components f_{jk} polynomials of degree $K = 2,\ldots, N$ with $j = 1,\ldots,$ in $X = (x_1, \ldots, x_n)$; $0 (X^{N+1})$ gathers the terms of order $\geq N + 1$ with appropriate change in variables, we transform non linearities from degree 2 up to an arbitrary degree $K \leq N$. The obtained system will be the normal form of order N of (1). Let us introduce $P_2,\ldots, P_k, \ldots$ the spaces of polynomials of degree 2, ..., k, ..., in n variables then we build the space $\mathbb{P}_k = P_k e_1 \oplus \ldots \oplus P_k e_n$ where $(e_1, \ldots, e_n)$ is the usual basis of $\mathbb{R}^n$.In order to normalize, we use a recurrence on the order of normalization. First, with a lineary change in variables, we write A in the form D + N, where D is a diagonal matrix, and N a nilpotent one (If possible A becomes a diagonal or a Jordan form matrix). Let be J the obtained matrix. Let be the normal system of order $K < N$ written with the variable X_k of the step K :

$$\frac{dX_k}{dt} = JX_k + Q_2(X_k) + \ldots + Q_k(X_k) + F_{k+1,k}(X_k) + \ldots + F_{N,k}(X_k) + O(X_k^{N+1}) \qquad (2)$$

where $JX_k + Q_2(X_k) + \ldots + Q_k(X_k)$ is the normal form of order K of (1), and $F_{k+1,k},\ldots,F_{N,k}$ are nonlinear of order $\geq k$ in the variable X_k. Let be :

$$X_k = X_{k+1} + D_{k+1}(X_{k+1}) \,,\, X_{k+1} \in \mathbb{R}^n \,,\, D_{k+1} \in \mathbb{P}_{k+1} \qquad (3)$$

After some calculation and right settlement of orders, we obtain :

$$\frac{dX_{k+1}}{dt} = \partial D_{k+1}(X_{k+1}) JX_{k+1} - JD_{k+1}(X_{k+1}) \qquad (4)$$

$$= JX_{k+1} + Q_2(X_{k+1}) + \ldots + Q_k(X_{k+1}) + F_{k+1,k+1}(X_{k+1}) + \ldots + F_{N,k+1}(X_{k+1}) + O(X_k^{N+1}) \qquad (5)$$

with $F_{k+1,k+1}(X_{k+1}) = F_{k,k+1}(X_{k+1})$,and $F_{j,k+1}(X_{k+1})$ $j>k+1$ new non linearities of degree $K+2,\ldots, N$; $Q_2 \ldots, Qk$ do not vary. $\partial D_{k+1}(X_{k+1})$ is the Jacobian matrix of D_{k+1}.In the space $\mathbb{P}_{k+1}$ we obtain the basic equation :

$$\partial D_{k+1}(X_{k+1}) JX_{k+1} - JD_{k+1}(X_{k+1}) = F_{k,k+1}(X_{k+1}) \qquad (6)$$

which can be written as a lineary system in the basis $b_1{}^{k+1}e_1,\ldots,b_{\dim(P_{k+1})}{}^{k+1}e_1,\ldots,$

$b_1^{k+1}e_n,...,b_{\dim(P_{k+1})}^{k+1}e_n$ of $\mathbb{P}_{k+1}$, with $b_1^{k+1},..., b_{\dim(P_{k+1})}^{k+1}$ ordered basis of P_{k+1}. The kernel of the lineary system gives resonant non linearities of order k+1 of (1). Solving the lineary system on a complement of the kernel gives the normal transform D_{k+1} ; it is determined except for an element of the kernel ; we take it equal to zero.

Free vibrations

a)*One degree of freedom system* :We take as simple example,the undamped Duffing oscillator :

$$\frac{d^2x}{dt^2} + \omega_1^2 \; x = c\,x^3 \qquad (7)$$

We diagonalize and normalize unto order 5 and obtain a backbone curve identical to the one obtained from a classical analysis (averaging method) :

$$\theta = -\omega_1 + \frac{3c}{8\omega_1} x_0^2 + \frac{15c^2}{256\,\omega_1^3} x_0^4 \qquad (8)$$

It is the same as in [11] [12] for small x_0.We obtain the solution x of equation (5) of order 5 with its first, third and fifth harmonic:

$$x=(x_0+\frac{3c}{16\omega_1^2}x_0^3+\frac{15c^2}{512\omega_1^4}x_0^5)\cos(\theta t)-(\frac{c}{32\omega_1^2}x_0^3+\frac{5c^2}{32\omega_1^4}x_0^5)\cos(3\theta t) + \frac{c^2}{1024\omega_1^4}x_0^5\cos(5\theta t) \qquad (9)$$

A comparison with results obtained by perturbation method or multiple scales gives a difference only from order 5 [12],[13] .

b)*Systems with n degrees of freedom* : let be the following system without damping :

$$\frac{d^2x_j}{dt^2} + \omega_j^2 \; x_j = F_2^j(X)+.....+F_M^j(X)\ ,\ j=1\ ,...,n \qquad (10)$$

with $F_k^j(X)$ homogeneous polynomials in $X = (x_1,\ldots,x_n)$ of degree 2, ..., M. Starting from the normal form of equation (8) :

$$\frac{dU}{dt}=DU+Q_2(U)+...+Q_K(U)\ \ ,U=(u_1,...,u_{2n}) \qquad (11)$$

with D diagonal matrix of $-i\omega j$, $i\omega j$, we look for periodic solutions of equation (10).

i)*Case without internal resonance* : the ω_j are incommensurable on the whole. A decoupling appears between equations (13) take two by two (we have n couples of conjugate equations) u_{2j-1}, u_{2j}, j=1,..., n, when we switch off the 2n-2 other components 2n-2 equations are obviously verified. The two last equations :

$$\frac{du_{2j-1}}{dt}=-i\omega_j u_{2j-1}+Q_2^{2j-1}(0,..,0,u_{2j-1},u_{2j},0,..,0)+..+Q_K^{2j-1}(0,..,0,u_{2j-1},u_{2j},0,..,0)$$
$$\frac{du_{2j}}{dt} =i\omega_j u_{2j}+Q_2^{2j}(0,..,0,u_{2j-1},u_{2j},0,..,0)+..+Q_K^{2j}(0,..,0,u_{2j-1},u_{2j},0,..,0) \qquad (12)$$

give the j th mode where Q_r^l, k=2 to K, l=1 to 2n, are the components of the Q_k :

$$x_l=u_{2l-1}+u_{2l}+T_K^{2l-1}(0,..,0,u_{2j-1},u_{2j},0,..,0)+T_K^{2l}(0,..,0,u_{2j-1},u_{2j},0,..,0),l=1 \text{ to } n \qquad (13)$$

$$u_{2j-1}=u^0_j \exp(i\theta_{jj}t)\ ,\ u_{2j} =u^0_j \exp(-i\theta_{jj}t),\ u^0_j\ ,h_{jj} \text{ reals},\ u_{2k-1}=u_{2k}=0 \text{ if } k\neq j \qquad (14)$$

$T_k^m(V)$ are the normal transform (the sum of the transform of degree 2,..., K dissociated to

the m^{th} component). The fixation to zero of 2n-2 components in equation (13) correspond to the building of a kind of Poincaré Map in V-coordinates. A fixed point correspond to a periodic solution of equation (11) which is a non-linear mode because of its building.

ii) *Case with internal resonance :* here, we can find in the couple of equations (2j-1, 2j) of the equation (12) some non-linear resonant terms without u_{2j-1}, u_{2j}.The same thing may appear in the others equations. Then if we lock the 2n-2 coordinates of V except u_{2j-1}, u_{2j} at zero, we can not verify some of the equations where all the terms are zero except some resonant terms like $u_{2j-1}^{k}\, u_{2j}^{K-k}$ .We cannot decouple as we do in i). We must write equation (14) for all the coordinates and solve algebraic system of equations to define non-linear modes.

iii) *Example* : n=2, let us consider the non-linear system with cubic non linearities :

$$\begin{aligned} &\frac{d^2x}{dt^2} + \omega_1^2\, x = -k\,x^3 - (x-y)^3 \\ &\frac{d^2y}{dt^2} + \omega_2^2\, y = -k\,y^3 - (y-x)^3 \end{aligned} \qquad (15)$$

For ω_1/ω_2 irrationnal, we obtain the first non-linear mode :

$$x = u_1+u_2+ \frac{k+1}{8\omega_1^2}u_1^3 - \frac{3(k+1)}{4\omega_1^2}u_1^2u_2 - \frac{3(k+1)}{4\omega_1^2}u_1u_2^2 + \frac{k+1}{8\omega_1^2}u_2^3$$

$$y = \frac{1}{\omega_2^2-9\omega_1^2}u_1^3 + \frac{3}{\omega_2^2-\omega_1^2}u_1^2u_2 + \frac{3}{\omega_2^2-\omega_1^2}u_1u_2^2 + \frac{1}{\omega_2^2-9\omega_1^2}u_2^3 \qquad (16)$$

$$u_1=u_1^0\exp\left(-i\left(\omega_1+\frac{3(k+1)}{2\omega_1}u_1^0u_2^0\right)t\right),\ u_2=u_2^0\exp\left(i\left(\omega_1+\frac{3(k+1)}{2\omega_1}u_1^0u_2^0\right)t\right),\ u_1^0, u_2^0 \text{ reals} \qquad (17)$$

We consider the case $\omega_1=\omega_2=1$.We have the normalized system without conjugate equations:

$$\begin{aligned} \frac{du_1}{dt} &= -iu_1 - \frac{i}{2}\left(3(k+1)u_1^2u_2 + 6u_1u_3u_4 - 6u_1u_2u_3 - 3u_1^2u_4 + 3u_3^2u_2 - 3u_3^2u_4\right) \\ \frac{du_3}{dt} &= iu_3 - \frac{i}{2}\left(3(k+1)u_3^2u_4 + 6u_1u_2u_3 - 6u_1u_3u_4 + 3u_1^2u_4 - 3u_3^2u_2 - 3u_1^2u_2\right) \end{aligned} \qquad (18)$$

let be $u_3 = Cu_1$, $u_4 = Cu_2$ in equation (18) : we find again the SNMof [9] : C verifies

$$C^4 + (k-2)\,C^3 - (k-2)\,C - 1 = 0\,. \qquad (19)$$

In such an example, we find a first integral independant from H=h, where H is the Hamiltonian of equation (15), by integrating the PDE :

$$\frac{du_1}{dt} = -\frac{1}{i\omega_1}\frac{\partial W}{\partial u_2},\ \frac{du_2}{dt} = \frac{1}{i\omega_1}\frac{\partial W}{\partial u_1},\ \frac{du_3}{dt} = -\frac{1}{i\omega_1}\frac{\partial W}{\partial u_4},\ \frac{du_4}{dt} = \frac{1}{i\omega_1}\frac{\partial W}{\partial u_3} \qquad (20)$$

Let be $W=W_{(2)} + W_{(4)}$ with $W_{(2)}$ and $W_{(4)}$ homogeneous polynomial of degree 2 and 4. Some calculations lead to $W_{(4)}$ =constant. It is a first integral. With H=h, $W_{(4)}$ = constant, we could build a Poincaré map and analyze the stability of nonlinear normal modes .

Forced vibrations of one dof system : we consider the following simple example :

$$\frac{d^2x}{dt^2} + a\frac{dx}{dt} + \omega_1^2\, x = cx^3 + f\cos(\omega t) \qquad (21)$$

We use a detuning parameter round eigenvalue -iω , and we normalize in order to obtain the exact solution of equation (23) in the linear case ; we introduce some parameters :

$$\alpha=\lambda_1+i\omega;\lambda_1=0.5(-a-ir_1);\lambda_2=0.5(-a+ir_1);r_1^2=4\omega_1^2-a^2;g=\frac{1}{8\omega\omega_1}\frac{1}{1+\frac{\alpha}{2i\omega}};A=\frac{ci}{2\omega};B=\frac{i}{4\omega_1} \quad (22)$$

with $i^2=-1$, α and $\bar{\alpha}$ conjugate ; if we suppose after normalization that near primary resonance uo is of order 1 and f of order 2 (With the method of multiple scales we should have decided it at the beginning) we obtain a frequency-amplitude equation of order 3 :

$$u_0+\frac{Bf}{\alpha}+\frac{3A}{\alpha}u_0u_0^2-\frac{6gA}{\alpha}fu_0u_0-\frac{3A}{\alpha}\eta u_0^2f+o(5)=0 \quad (23)$$

and with the normal transform, we obtain the first harmonic of the displacement :

$$x=u_1+u_2+gf_1+\eta f_2-\frac{3Ai}{2\omega}(u_1+u_2)u_1u_2 \text{ with } u_1=u_0\exp(-i\omega t),u_2=\bar{u}_0\exp(i\omega t) \quad (24)$$

The validity of our method is bound to the convergence of the formal series in the change of variables (Brjuno [5],[6]).We work in the neighbourhood of zero : we never exceed $|2u_0|<0.8$. We could analyze the stability by the normal form of equation (21). So we obtain the classical skeleton curve .

Forced vibrations of a two dof oscillator

For example , we consider the following example without damping coupling :

$$\begin{aligned}&\frac{d^2x}{dt^2}+a_1\frac{dx}{dt}+\omega_1^2x=-ax^3-b(x-y)^3+F_1\cos(\omega t)\\&\frac{d^2y}{dt^2}+a_2\frac{dy}{dt}+\omega_2^2y=-ay^3-b(y-x)^3+F_2\cos(\omega t)\end{aligned} \quad (25)$$

i)First we introduce a detuning round -iω and a detuning round -iω2 :we suppose ω near ω_1 and ω far from ω_2.We introduce some parameters which permit us to normalize equation (25):

$$\lambda_1=\frac{-a_1-ir_1}{2};\lambda_2=\frac{-a_1+ir_1}{2};(r_1)^2=4\omega_1^2-a_1^2;\lambda_3=\frac{-a_2-ir_2}{2};\lambda_4=\frac{-a_2+ir_2}{2};(r_2)^2=4\omega_2^2-a_2^2;$$

$$\alpha_1=\lambda_1+i\omega,\alpha_2=\lambda_3+i\omega_2,(F_2/F_1)=r;f_1=F_1\exp(-i\omega t);f_2=rF_1\exp(i\omega t);f=F_1; \quad (26)$$

$$g=\frac{1}{4\omega r_1}\frac{1}{1+\frac{\alpha_1}{2i\omega}};S=\frac{r\omega_2}{r_2(\omega_2^2-\omega^2)}$$

These parameters bring out an exact solution of equations (25) in the linear case;they lead to the following expression of the displacements x and y of the first nonlinear mode:

$$\begin{aligned}x&=(u_1+u_2+gf_1+\eta f_2-\frac{3(a+b)}{4\omega_1}(u_1+u_2)u_1u_2)+\frac{(a+b)}{8\omega_1\omega}(u_1^3+u_2^3)\\y&=(S(f_1+f_2)+\frac{3b}{2\omega_2(\omega_2^2-\omega^2)}(u_1+u_2)u_1u_2)+\frac{b}{2\omega_2(\omega_2^2-9\omega^2)}(u_1^3+u_2^3)\end{aligned} \quad (27)$$

where $u_1=u_0\exp(-i\omega t),u_2=\bar{u}_1$ and u_3,u_4 have been neglected: $u_3=h_0\exp(-i\omega_2 t)$,$u_4=\bar{u}_3$ and u0, h_0 verify the two following frequency-amplitude equations of formal order 3:

$$\alpha_1 u_0 + \frac{if}{2r_1} + \frac{i}{2\omega_1}(-3(a+b)u_0^2\bar{u}_0 - 3(a\eta - b(S-\eta))u_0^2 f - 6(ag - b(S-g)u_0\bar{u}_0 f$$

$$-6(ag\eta + b(S-g)(S-\eta))u_0 f^2 - 3(ag^2\eta + b(S-g)^2)\bar{u}_0 f^2 - 3(ag^2\eta + b(S-g)^2(S-\eta))f^3) = 0 \quad (28)$$

$$(\omega_2 - \omega)h_0 - ia_2 h_0 = \text{terms with } |u_0|^2 h_0, u_0 h_0 f, \bar{u}_0 h_0 f, |h_0|^2 h_0, h_0 f^2 \quad (29)$$

So with some reasonable hypothesis near resonance (u0 of order 1,f of order >1),with ω close to ω_1 and far from ω_2 , a general solution h0 of equation (29) is of order 4 at least . So we can decouple equation (25) in normal coordinates and write $u_3=u_4=0$ to obtain the first mode.

ii)*We suppose ω near ω_1 and ω_2* : we introduce *a double detuning* round iω with expressions similar to those of i) .In order to build a modal synthesis with nonlinear modes ,we introduce :

$$g_1 = \frac{1}{4\omega r_1}\,\frac{1}{1 + \frac{\alpha_1}{2i\omega}}, \quad g_2 = \frac{1}{4\omega r_2}\,\frac{1}{1 + \frac{\alpha_2}{2i\omega}} \quad (30)$$

$$U_0 = u_0 + g_1 F_1, V_0 = v_0 + g_2 F_2 , x_0 = 2U_0 \quad (31)$$

We obtain 2 equations where we neglect the terms of order ≥ 5 like $U_0 V_0^2$; so they are uncoupled :

$$F_1 = 2\delta l_1 U_0 + 3(a+b)|U_0|^2 U_0 (1+2\omega) + 3(a+b)\frac{2a_1}{r_1}|U_0|^2 U_0 - 3b(1+2\omega)(U_0^2 + 2|U_0|^2)g_2 F_2$$

$$F_2 = 2\delta l_2 V_0 + 3(a+b)|V_0|^2 V_0 (1+2\omega) + 3(a+b)\frac{2a_2}{r_2}|V_0|^2 V_0 - 3b(1+2\omega)(V_0^2 + 2|V_0|^2)g_1 F_1 \quad (32)$$

with $\delta l_1 = (\omega_1^2 - \omega^2 - ia_1\omega)$; $\delta l_2 = (\omega_2^2 - \omega^2 - ia_2\omega)$;we get back the complete displacement x for example :

$$x = x_0 - \frac{3(a+b)}{16\omega r_1}|x_0|^2 x_0 + 3b\left(\eta_2 - \frac{\omega i}{4r_1 2\omega}\right)x_0^2 F_2 + \frac{3b}{4 r_1 \omega}\left(g_2 - \frac{2b\,\omega i}{(\omega_2-\omega)(\omega_2-3\omega)2\alpha_2 r_2}\right)|x_0|^2 F_2 \quad (33)$$

With equations 31,32,33 and similar equations , we write :

$$\begin{pmatrix} x \\ y \end{pmatrix} = \frac{T_1\,{}^t T_1'}{m_1 \delta l_1} \begin{pmatrix} F_1 \\ F_2 \end{pmatrix} + \frac{T_2\,{}^t T_2'}{m_2 \delta l_2} \begin{pmatrix} F_1 \\ F_2 \end{pmatrix} \quad (34)$$

where m1 , δ11 are equal to :

$$m_1 = 1 + \frac{3(a+b)}{4} X_0^2 \left(\frac{\omega_1 - \omega}{2\omega_1} + \frac{ia_1}{r_1}\right) \quad (35)$$

$$\delta l_1 = \omega_1^2 - \omega^2 - ia_1\omega + \frac{3(a+b)}{4}|X_0|^2 \quad \text{with } X_0 = 2U_0 \quad (36)$$

and similar terms for m2 Dl2 and :

$${}^t T_1 = \begin{pmatrix} 1 - \frac{3(a+b)}{8\omega_1^2} X_0^2 , & \frac{3b}{4(\omega_2^2 - \omega_1^2)}|X_0|^2 \end{pmatrix}, \quad {}^t T_2 = \begin{pmatrix} 1 - \frac{3(a+b)}{8\omega_2^2} Y_0^2 , & \frac{3a}{4(\omega_1^2 - \omega_2^2)}|Y_0|^2 \end{pmatrix}$$

$$(37)$$

$${}^t T_1' = \begin{pmatrix} 1 - \frac{3(a+b)}{8\omega_1^2} X_0^2 , & \frac{9b}{4\omega_2(\omega_2+\omega)} X_0^2 \end{pmatrix}, {}^t T_2' = \begin{pmatrix} 1 - \frac{3(a+b)}{8\omega_2^2} Y_0^2 , & \frac{9ba}{4\omega_1(\omega_1+\omega)} Y_0^2 \end{pmatrix}$$

Keeping with these results W. Szemplinska-Stupnicka [12] writes forced near-resonance responses is close to the corresponding nonlinear mode .But she can not describe the part of the other modes.From equation 33 , we can justify the superposition of nonlinear modes up to fourth order in the case of cubic nonlinearities .We note that reciprocity is not verified : $T1'$ is different from T1.The gap grows when the resonance frequencies of linear modes are close. We show the comparison between numerical results and our synthesized response in figure 1.

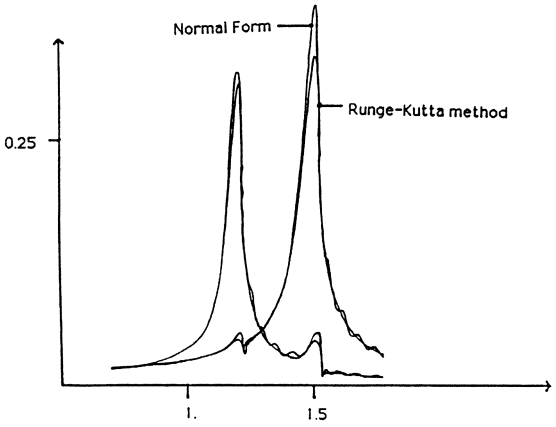

Fig. 1

Amplitude of x and y versus ω by synthesized normal form response , and Runge Kutta method

References:

1.Poincare,H., Les Méthodes Nouvelles de la Mécanique Céleste,Gauthier-Villars,Paris,1889.

2.Birkhoff,G.D., Dynamical Systems,AMS. Collection Publications,vol.9,reprinted 1966 .

3.Arnold,V.I., Mathematical Methods of Classical Mechanics , Springer , New-York Heidelberg Berlin,1978.

4.Moser,J.,Stable and Random Motion in Dynamical Systems,Hermann Weyl Lectures, Princeton, New-Jersey, 1973.

5.Brjuno,A.D.,Analytical forms of Differential Equations I , Transactions of the Moscow Mathematical Society, 25 , pp.132-198 , 1971 .

6. Brjuno,A.D.,Analytical forms of Differential Equations II , Transactions of the Moscow Mathematical Society, 26 , pp.199-299 , 1972 .

7.Hsu,L.,Analysis of Critical and Post-critical Behaviour of Nonlinear Dynamical Systems by the Normal form Method.Part I : Normalisation Formulae , J. of Sound and Vibration , 89(2),pp. 169-181,1983.

8.Hsu, L.,Analysis of Critical and Post-critical Behaviour of Nonlinear Dynamical Systems by the Normal form Method.Part II : Divergence and Flutter , J. of Sound and Vibration , 89(2),pp. 183-194,1983.

9.Marsden,J.E.,McCracken,M., The Hopf Bifurcation and its Applications, Springer, Applied Mathematical Sciences vol.19,New-York Heidelberg Berlin,1976.

10.Month,L.A.,Rand,R.H.,An Application of The Poincaré Map to the Stability of Nonlinear Normal Modes , Journal of Applied Mechanics ,vol.47,sept.,pp.645-654,1980 .

11.Month,L.A.,Rand,R.H.,The Stability of Bifurcating Periodic Solutions in a Two Degree Of Freedom Nonlinear System,Journal of Applied Mechanics,pp.782-783,1977.

12.Szemplinska-Stupnicka,W.,Nonlinear Normal Modes and the Generalized Ritz Method in the Problems of Vibrations of Nonlinear Elastic Continuous Systems ,Int. J. of Nonlinear Mechanics ,vol. 18, 2 , pp. 149-165, 1983 .

13.Hamdan,M.N.,Burton,T.D.,Analysis of Forced Nonlinear Undamped Oscillators by a Time Transformation Method, J. of Sound and Vibration , 110 , 2 , pp. 223-232 , 1986 .

14.Howland, J. of Computational Physics ,67,19-27, 1986.

Crises in Mechanical Systems

M. Kleczka*, E. Kreuzer**, and C. Wilmers**

* Institut B für Mechanik, Universität Stuttgart, Stuttgart, FRG
** Arbeitsbereich Meerestechnik II, TU Hamburg-Harburg, Hamburg, FRG

Summary

In mechanical systems nonlinear effects due to stick slip and backlash are often observed. If such systems are harmonically driven, then besides well known bifurcation phenomena also sudden changes of the chaotic dynamics occur. These types of qualitative change of system's behavior, the so-called crises, result from a collision between an unstable periodic orbit and a chaotic attractor. Different crises phenomena are discussed and it is demonstrated how the occurrence of crises can be determined numerically.

1 Introduction

Technical dynamical systems contain in general quite a number of nonlinearities. Besides the real nonlinear character of springs and dampers, also stick slip effects and backlash between mechanical parts are important. A detailed knowledge of the dynamics due to the aforementioned nonlinearities could help the engineers to avoid instabilities of an evolving dynamical system in which parameters are varying slowly with time.

As a representative example we study the dynamics of a simple one degree of freedom oscillator with backlash, which includes all relevant parameters, i.e. stiffness, clearance, damping, and forcing. Under variation of these parameters different kinds of qualitative dynamic behaviour is observed. The qualitative change in the behaviour of the system, i.e. bifurcation, is generally related to the occurrence of a critical case.

Besides well known bifurcation phenomena we focus our attention to sudden unexpected changes of the chaotic dynamics. Ueda [1] was the first to describe by Duffing's equation the explosion of chaotic attractors, Grebogi et. al. [2] analyzed these phenomena and introduced the term crises. They showed that a crisis results from a collision between an unstable periodic orbit and a chaotic attractor. We distinguish two types of crises phenomena, the interior crisis and the boundary crisis. The sudden blow up but finite enlargement of a chaotic attractor is called interior crisis, while the boundary crisis causes the chaotic attractor and its basin of attraction to disappear. The latter happens if the unstable solution is part of the boundary of the basin of attraction. The crises

W. Schiehlen (Editor)
Nonlinear Dynamics in Engineering Systems
IUTAM Symposium Stuttgart/Germany 1989

phenomena are also called catastrophic or discontinuous bifurcations, e.g. Thompson and Stewart [3].

2 Model Description

The system under investigation is an oscillator with piecewise linear characteristic and harmonic forcing, Figure 1.

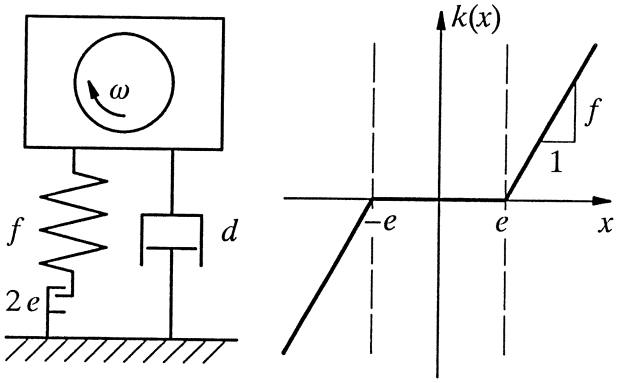

Figure 1: Model of the system and characteristic of the nonlinearity

Its normalized governing differential equation is

$$\ddot{x} + 2d\dot{x} + k(x) = a\cos\omega t \quad , \tag{1}$$

with

$$k(x) = \begin{cases} f(x-e), & x > e, \\ 0, & |\,x\,| \leq e, \\ f(x+e), & x < -e. \end{cases} \tag{2}$$

The parameters of the system are:

damping coefficient	$d =$	0.15,
clearance	$e =$	1.0,
stiffness ratio	$f =$	3.0 – 17.0,
amplitude of excitation	$a =$	10.0,
frequency of excitation	$\omega =$	1.0.

This simple model of a system with backlash shows the whole scenario of nonlinear behaviour like periodic, solutions of multiple period, and chaotic solutions, various types

of bifurcations and coexistence of even qualitative different solutions. All results presented are computed numerically by means of a piecewise analytical integration scheme, for more detail see [4].

Instead of looking at trajectories in the time domain, we use the so-called Poincaré map

$$\boldsymbol{y}_{n+1} = \boldsymbol{g}(\boldsymbol{y}_n), \tag{3}$$

where $\boldsymbol{y}_i = (x, \dot{x})^T$ is the state of the system at $t = 2\pi\omega i$. Hence, a solution with period n of the continuous system (1), called $P-n$ solution, corresponds to a set of n fixpoints $\bar{\boldsymbol{y}}_i$ with periodicity n of the discrete system (3),

$$\bar{\boldsymbol{y}}_{m+1} = \boldsymbol{g}^m(\bar{\boldsymbol{y}}_1), m = 1, \ldots, n-1, \tag{4}$$

and

$$\bar{\boldsymbol{y}}_i = \boldsymbol{g}^n(\bar{\boldsymbol{y}}_i), i = 1, \ldots, n. \tag{5}$$

In general, the nonlinear map (3) cannot be given in an analytical form, it has to be calculated numerically.

A thorough investigation of bifurcation problems requires not only the knowledge of stable solutions and their basins of attraction, but the location of unstable fixpoints as well.

An efficient method for the determination of attractors, both regular and chaotic, and their basins of attraction is the cell mapping approach, developed by Hsu [5], see also [6]. This method is based upon a discretization of the state space into a large collection of small cells. The cells are obtained from a normally rectangular grid. All grid points are mapped according to (3). From this set of data the long-time behaviour for each cell is calculated, yielding a good approximation for the original system, as long as the grid is not to coarse. An important feature of this approach is that it is tailored for todays vector processors or tomorrows parallel computers, since it is straightforward to vectorize or parallelize.

For the calculation of fixpoints, equation (5) is written in another form,

$$\boldsymbol{g}^n(\bar{\boldsymbol{y}}_i) - \bar{\boldsymbol{y}}_i = 0, i = 1, \ldots, n. \tag{6}$$

Hsu and Zhu [7] presented a method to locate zeros of a nonlinear function in a discretized state space, which is used to compute the periodic solutions $\bar{\boldsymbol{y}}$, regardless their stability. This method has a close relation to the cell mapping approach, and it is possible to use the aforementioned map of a grid as well.

With these numerical tools the analysis of the nonlinear system (1) was taken out.

3 Bifurcations and Crises

A useful method to demonstrate the influence of parameters on the steady-state behaviour of nonlinear systems is the calculation of bifurcation diagrams, from which the parameter values for different regular or chaotic solutions can be determined easily. A well known phenomenon thereby is the occurence of windows with periodic solutions within a chaotic range.

In Figure 2 a small portion from the bifurcation diagram of system (1) is shown. Included in this diagram is a $P-3$ solution together with its unstable parts that emerge from a saddle-node or tangent bifurcation at $f \approx 8.22$.

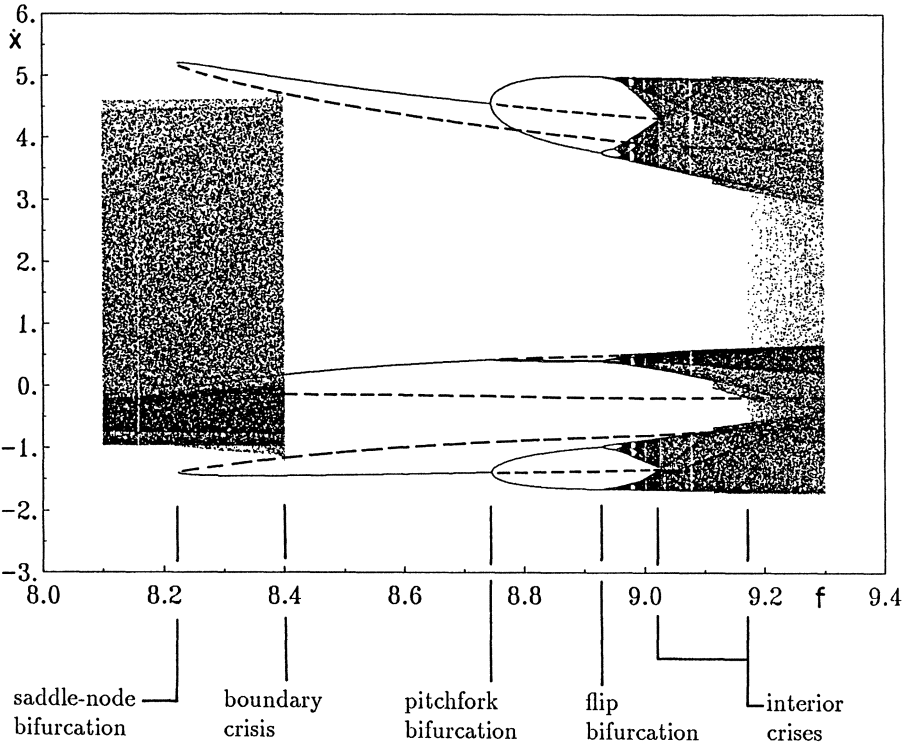

Figure 2: Bifurcation diagram with coexisting solutions. The dashed curves denote the unstable $P-3$ solution created at the saddle-node bifurcation.

3.1 Boundary Crisis

The sudden death of the chaotic attractor at $f \approx 8.4$ is caused by a boundary crisis. From the saddle-node bifurcation at $f \approx 8.22$ originates a stable as well as an unstable P–3 solution. This unstable solution is of saddle type, its stable manifold is the boundary of the domain of attraction of the chaotic attractor.

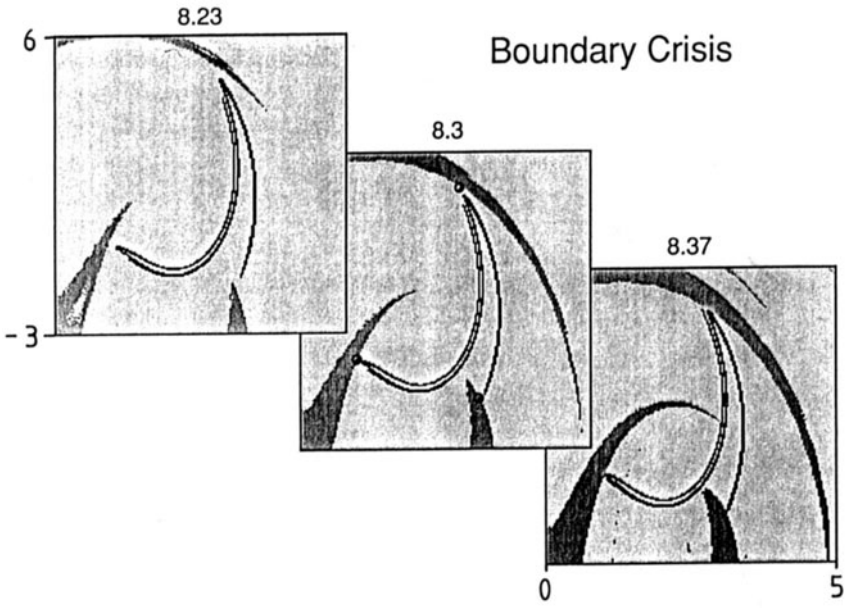

Figure 3: Coexisting periodic and chaotic solutions with their basins of attraction; the symbol • denotes $P-3$ saddle-points.

In Figure 3 the basins of attraction of the chaotic and the regular solutions are plotted for different values of f. The pictures show that

1. the chaotic attractor approaches the $P-3$ saddle points,
2. the domain of attraction of the periodic solution grows toward the strange attractor in form of *needles*,

and the boundary crisis is triggered when the stable manifold of the saddle touches the unstable manifold. This causes the basin of attraction of the chaotic solution to disappear and the attractor itself ceases to exist after a short period of time, called *chaotic transient*. Solely the $P-3$ solution survives.

3.2 Interior Crisis I

Following the periodic solution in Figure 2, we observe a pitchfork bifurcation at $f = 8.74$. Further increase of f causes a sequence of flip bifurcations and finally a chaotic attractor is formed, consisting of three pieces. A sudden but finite enlargement of these three parts is observed at $f = 9.03$. In Figure 4 the bifurcation diagrams of the two coexisting stable $P-3$ solutions, emerging from the pitchfork bifurcation, are plotted together.

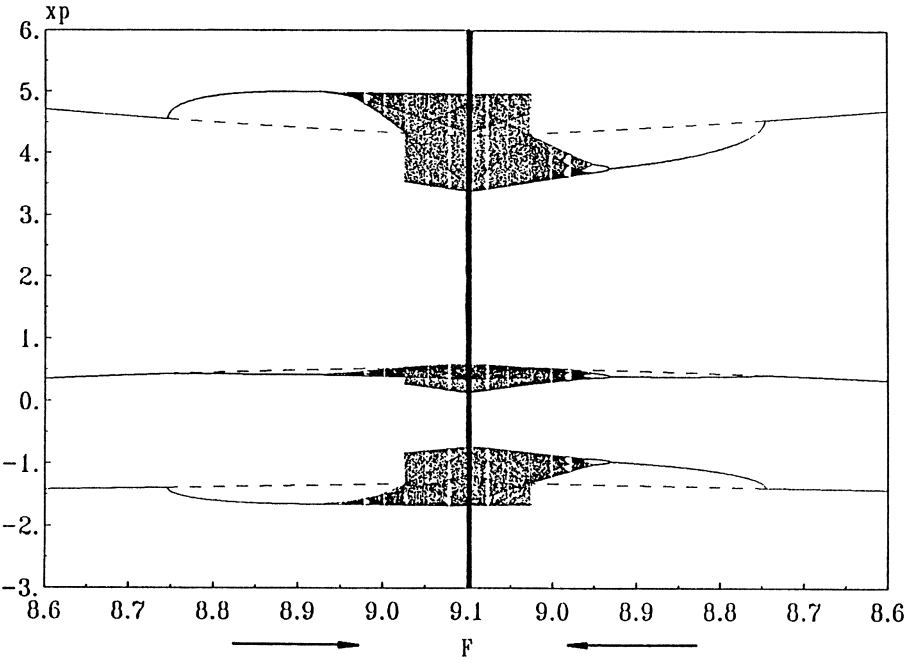

Figure 4: Bifurcation diagram of the coexisting solutions. $P-3$ saddle-points:- - - -

Again, the $P-3$ solutions of saddle type are the connecting link. Together with the creation of the new coexisting solutions, the former stable solution becomes unstable at the pitchfork bifurcation. The coexistence disappeares when this unstable solution touches the chaotic attractors. Or from another point of view: the interior crisis occurs when the two chaotic attractors touch each other and merge into one three-piece attractor.

An important aspect in understanding crises is, that the unstable solution evolving together with the coexistence destroys this coexistence later on.

3.3 Interior Crisis II

Further development in Figure 2 reveales a sudden change of the solution for a value $f = 9.17$. The three-piece chaotic attractor blows up to a large chaotic attractor. Figure 5 shows the formerly empty regions between the three parts getting filled and a fully developed irregular behavior after this interior crisis.

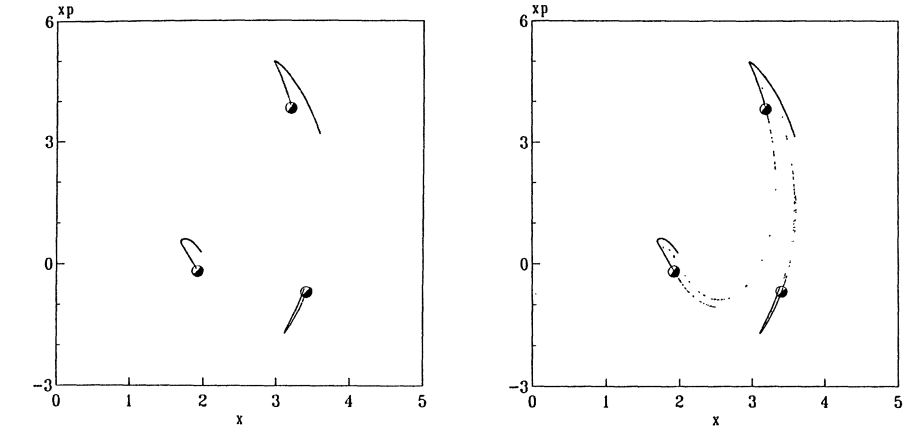

$f = 9.15$ $f = 9.19$

Figure 5: Poincaré map before and after the interior crisis II, $P-3$ saddle-points: ◕

As before, the interior crisis is caused by the collision of the $P-3$ chaotic attractor with the unstable $P-3$ solution. The unstable $P-3$ solution which caused already the boundary crisis is also the source of this crisis.

The qualitative behaviour of the system before the boundary crisis and after the interior crisis II is the same. That is, when a new solution is created, the cause for a later destruction of this solution is generated too.

4 Conclusions

We demonstrated the use of numerical tools based on the Poincaré map to achieve a detailed insight into nonlinear dynamics. The calculation of coexisting stable solutions und their domains of attraction was done with the cell mapping approach.

Furthermore, it was necessary to compute unstable periodic solutions in order to understand and predict the occurence of crises. A numerical algorithm, based on finding zeros in a discrete state space, was used to compute fixpoints with arbitrary stability and multiple period. All calculations were carried out for the example of a harmonically driven oscillator with backlash using an analytical integration scheme.

In addition to well known bifurcations of regular solutions, sudden changes of the chaotic behaviour, called crises, are often observed. The main key for understanding these crises are unstable periodic solutions. Two different types can be destinguished, boundary and interior crises.

The contact of a chaotic attractor with an unstable periodic solution that is part of the basin boundary, is called boundary crisis and destroys the chaotic attractor together with its domain of attraction. Interior crises are sudden but finite blow-ups of a chaotic attractor. These are caused by the collision of the attractor with an unstable solution that does not lie on the boundary of the domain of attraction.

The relation between the various bifurcations should be emphasized, since following universal scenario was observed. A new, coexisting solution evolves from a bifurcation together with an unstable one. Later on, this unstable branch destroys the new solution by a crisis and reestablishes a behaviour qualitatively equivalent to the original one before the bifurcation.

This scenario is one explanation for the occurrence of windows of periodic solutions within the chaotic range in bifurcation diagrams.

References

[1] Y. Ueda. Explosion of strange attractors exhibited by duffing's equation. *Annals of the New York Academy of Sciences*, 357 (1980) 422 – 434.

[2] C. Grebogi, E. Ott, and J. Yorke. Crises, sudden changes in chaotic attractors, and transient chaos. *Physica D*, 7 (1983) 181 – 200.

[3] J.M.T. Thompson and H.B. Stewart. *Nonlinear Dynamics and Chaos.* Chichester: John Wiley & Sons 1986.

[4] C. Wilmers. *Verzweigungsphänomene in mechanischen Oszillatoren.* Diplomarbeit DIPL-24. Stuttgart: Universität Stuttgart, Institut B für Mechanik 1988.

[5] C.S. Hsu. *Cell-to-Cell Mapping.* New York /...: Springer 1987.

[6] E. J. Kreuzer. *Numerische Untersuchung nichtlinearer dynamischer Systeme.* Berlin /...: Springer 1987.

[7] C.S. Hsu and W.H. Zhu. A simplicial mapping method for locating the zeros of a function. *Quarterly of Applied Mathematics* (1984) 41 – 59.

New Instability Aspects for Nonlinear Nonconservative Systems with Precritical Deformation

A.N.KOUNADIS

National Technical
University of Athens,Athens

Summary

The large displacement and time response of a two-degree-of freedom,dissipative, nonlinear cantilever-model under a partial follower load is discussed by using a complete nonlinear dynamic analysis. Considering the stability of motion in the large, in the sense of Lagrange,the mechanism of dynamic instability is thoroughly reexamined for perfect or imperfect systems. New findings for the stability of critical states contradict existing results based on linearized analyses. Critical states of divergence or of nonexistence of adjacent equilibrium may be stable or unstable depending on the amount of material nonlinearity.The nonlinear static buckling loads coincide with the corresponding dynamic ones when there is no precritical deformation; otherwise the latter loads are always less than the former.It was also found that systems statically stable may be proven unstable when a nonlinear dynamic analysis is employed. Clobal bifurcations have revealed that this autonomous system even when damping is excluded may exhibit phenomena looking like chaos.

Introduction

The loss of stability of nonconservative systems under follower forces may happen either by flutter or by divergence depending on the values of the parameter involved[1-7].The critical divergence load can be determined by using either a static or a dynamic analysis. Necessary and sufficient conditions for the existence of regions of divergence instability have been also established[7]. However,the above findings and studies refer to linear nonconservative systems losing their stability without precritical deformation.Recently,it was shown[8] that the inclusion of material nonlinearity in a nonconservative imperfect system may extend the region of divergence instability.A thorough study for the postbuckling response of nonlinear nonconservative systems with or without precritical deformation has been presented by Plaut[9].

The reliability of the aforementioned nonlinear stability analyses has not as yet been confirmed with the aid of an exact nonlinear dynamic analysis.

W. Schiehlen (Editor)
Nonlinear Dynamics in Engineering Systems
IUTAM Symposium Stuttgart/Germany 1989

Hence,the validity of existing findings based on linearized or approximate dynamic analyses[10,11] is questionable.Recently some interesting nonlinear dynamic analyses by Huseyin and his associates[12,13] are based on local solutions such as higher perturbation schemes and averaging techniques.
In this investigation,considering the stability of motion in the large in the sense of Lagrange,the dynamic instability is defined as the long-term state for which an unbounded(divergent)motion is initiated (leading to overflow). Then the corresponding dynamic buckling load is defined as the smallest load for which an unbounded motion occurs. The results presented herein are based on global solutions of the original nonlinear equations of motion including also linear viscous damping. Such global solutions allow us to explore also strange attractor (or chaotic) phenomena.[14,15,16]

Statement of the problem

Consider the two-degree-of freedom,partially fixed,cantilever model shown in Fig.1, composed of two weightless rigid bars of equal length ℓ interconnected to each other by a rotational spring.The model carries two concentrated masses $m_1=2m$ and $m_2=m$ at B and C,respectively.The deformed configuration is specified by the angles ϑ_1 and ϑ_2 between the vertical and each of the bar axis, while the unrestrained configuration is identified by the initial angle imperfections $\vartheta_1=\varepsilon_1$ and $\vartheta_2=\varepsilon_2$.

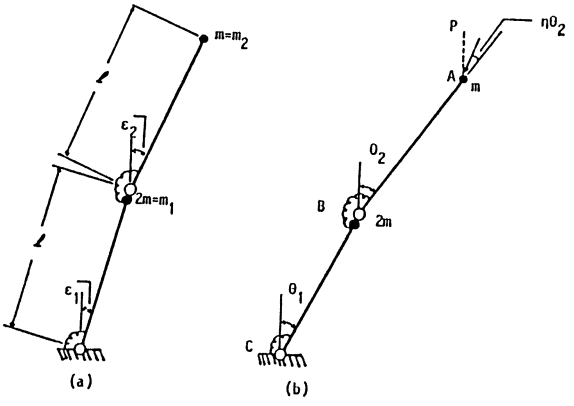

Fig.1.Unstressed(a)and stressed(b)state of a two-mass cantilever-model

The system is subjected to a partial follower tip load P acting at an angle $\eta\vartheta_2$ with respect to the upper bar,where η is the nonconservativeness loading parameter. The restoring moments developed at B and C are given by

$$\frac{M_B}{k} = \vartheta_2-\varepsilon_2+\vartheta_1-\varepsilon_1+\delta_2(\vartheta_2-\varepsilon_2-\vartheta_1+\varepsilon_1)^2+\gamma(\vartheta_2-\varepsilon_2-\vartheta_1+\varepsilon_1)^3$$

$$\frac{M_c}{k} = \vartheta_1-\varepsilon_1+\delta_1(\vartheta_1-\varepsilon_1)^2+\gamma(\vartheta_1-\varepsilon_1)^3 \qquad (1)$$

where k is the linear dimensionless spring component, whereas δ_i (i=1,2) and γ are the nonlinear dimensionless spring components. In addition to geometric and material nonlinearities a precise modeling should also include damping. The effect of linear viscous damping can be included by adding to the moments M_B and M_c the terms $c_2(\dot{\vartheta}_2-\dot{\vartheta}_1)$ and $c_1\dot{\vartheta}_1$, respectively.
Lagrange's equations of motion for the above nonconservative autonomous dissipative system are[16]

$$\frac{d}{dt}\left(\frac{\partial K}{\partial \dot{\vartheta}_i}\right) - \frac{\partial K}{\partial \vartheta_i} + \frac{\partial V}{\partial \vartheta_i} - \frac{\partial F}{\partial \dot{\vartheta}_i} - Q_i = 0 \quad (i=1,2) \qquad (2)$$

where

$$K = \frac{1}{2} m_1 \ell \dot{\vartheta}_1^2 + \frac{1}{2} m_2 \ell^2 \left[\dot{\vartheta}_1^2+\dot{\vartheta}_2^2+2\dot{\vartheta}_1\dot{\vartheta}_2\cos(\vartheta_1-\vartheta_2)\right]$$

$$V = \frac{U}{k} = \frac{1}{2}(\vartheta_1-\varepsilon_1)^2 + \frac{1}{3}\delta_1(\vartheta_1-\varepsilon_1)^3 + \frac{1}{4}\gamma(\vartheta_1-\varepsilon_1)^4 + \frac{1}{2}(\vartheta_2-\varepsilon_2-\vartheta_1+\varepsilon_1)^4 + \frac{1}{3}\delta_2(\vartheta_2-\varepsilon_2-\vartheta_1-\varepsilon_1)^2 + \frac{1}{4}\gamma(\vartheta_2-\varepsilon_2-\vartheta_1+\varepsilon_1)^4$$

$$F = \frac{1}{2}c_1\dot{\vartheta}_1^2 + \frac{1}{2}c_2(\dot{\vartheta}_1-\dot{\vartheta}_2)^2$$

$$Q_1 = p\sin\left[\vartheta_1+(n-1)\vartheta_2\right], \quad Q_2 = p\sin n\vartheta_2 \text{ with } p=P\ell/k \qquad (3)$$

After introducing the dimensionless quantities

$$\Theta(\tau)=\vartheta(t), \quad \tau=t(k/m_2\ell^2)^{1/2}, \quad m=m_1/m_2, \quad c_i^*=c_i(km_2\ell^2)^{-1/2} \quad (i=1,2)$$

equation (3) become

$$(1+m)\ddot{\Theta}_1+\ddot{\Theta}_2\cos(\Theta_1-\Theta_2)+\dot{\Theta}_2^2\sin(\Theta_1-\Theta_2)+(c_1^*+c_2^*)\dot{\Theta}_1-c_2^*\dot{\Theta}_2+2(\Theta_1-\varepsilon_1) - -(\Theta_2-\varepsilon_2)+\delta_1(\Theta_1-\varepsilon_1)^2+\gamma(\Theta_1-\varepsilon_1)^3-\delta_2(\Theta_1-\varepsilon_1-\Theta_2+\varepsilon_2)^2+\gamma(\Theta_1-\varepsilon_1-\Theta_2+\varepsilon_2)^3-p\sin\left[\Theta_1+(n-1)\Theta_2\right]=0$$

$$\ddot{\Theta}_2+\ddot{\Theta}_1\cos(\Theta_1-\Theta_2)-\dot{\Theta}_1^2\sin(\Theta_1-\Theta_2)+c_2^*\dot{\Theta}_2-c_2^*\dot{\Theta}_1-(\Theta_1-\varepsilon_1)+(\Theta_2-\varepsilon_2)+\delta_2(\Theta_1-\varepsilon_1-\Theta_2+\varepsilon_2)^2-\gamma(\Theta_1-\varepsilon_1-\Theta_2+\varepsilon_2)^3-p\sin n\Theta_2=0 \qquad (4)$$

Setting $\dot{\Theta}_1=\dot{\Theta}_2=\ddot{\Theta}_1=\ddot{\Theta}_2=0$ into eqs(4) we obtain the nonlinear equilibrium eqs given by Plaut [9] (1976). If $\delta_1=\delta_2=\gamma=0$ the system is made of linearly elastic material (Hookean model); that is its stiffness is linear. In this case eqs (4) after linearization and setting $m=2, \eta=1-a$ coincide with those presented by Herrmann and Bungay[2]. Such a linearization consists of adopting the following approximations

$$\cos(\Theta_1-\Theta_2)\cong 1,\quad \sin\left[\Theta_1+(n-1)\Theta_2\right]\cong \Theta_1+(\eta-1)\Theta_2,\quad \sin\eta\Theta_2\cong\eta\Theta_2$$

$$\dot{\Theta}_1^2\sin(\Theta_1-\Theta_2)\cong 0,\quad \dot{\Theta}_2^2\sin(\Theta_1-\Theta_2)\cong 0 \qquad (5)$$

As will be shown subsequently these terms and particularly the last two ones govern the mechanism of the long-term behavior of the system; although the latter look like damping terms one can show with the aid of the Lie derivative that they do not lead to contraction (as an attractor does).

Perfect system ($\varepsilon_1=\varepsilon_2=0$)

The divergence buckling load p^c in case of no precritical deformation (static bifurcational system) can be determined by using a classical linearized either static or dynamic analysis. Such a load, being independent of the values of m, γ, δ_1 and δ_2, is given by

$$p^c=\frac{1}{2}\left(3\mp\sqrt{9-\frac{4}{\eta}}\right)\qquad (\eta\geq 4/9, \eta<0) \qquad (6)$$

If $\gamma=0$ but δ_1 and δ_2 are not both zero (quadratic model) the loss of static stability occurs through an asymmetric branching point, while if $\delta_1=\delta_2=0$ but $\gamma\neq 0$ (cubic model) the system is associated with a symmetric branching point, whose stability depends on the value of γ. Indeed, for the last case after a cumbersome manipulation (since the partial differentiation is not commutative) the following stability condition is obtained

$$\gamma f_1+f_2>0$$

with

$$f_1=6p^c+18(1-p^c)\left[\frac{1}{1-\eta p^c}-\frac{1}{(1-\eta p^c)^2}+\frac{1}{3(1-\eta p^c)^3}\right]$$

$$f_2=p^c\left[1+\frac{3(\eta-1)}{1-\eta p^c}+\frac{3(\eta-1)^2}{(1-\eta p^c)^2}+\frac{(\eta-1)^3+\eta^3(2-p^c)}{(1-\eta p^c)^3}\right] \qquad (7)$$

where if $\eta=0.50$ we must have $p^c\neq 2$ since otherwise both f_1 and f_2 are undefined.

For a Hookean material ($\gamma=\delta_1=\delta_2=0$) it follows $f_2>0$ regardless of the values of p^c and η; that is all divergence critical states are stable for the entire range of variation of η except the small interval $0.451<\eta<0.50$ correspon-

ding to the 2nd buckling load $p^c=0.5(3+\sqrt{9-4/\eta})$.These results can be verified with the aid of a nonlinear dynamic analysis.Indeed, for any initial angular velocities $\dot{\Theta}_i\neq 0$ (i=1,2) the trivial critical states ($\Theta_1=\Theta_2=0$) are stable since the resulting motion for $p=p^c$ is of bounded amplitude as $t\to\infty$ .Such a finding contradicts existing results presented first by Herrmann and Bungay[2] and widely accepted later on by many other researchers[3].This is basically due to the neglect of the last two terms in relation (5).

From Fig.2 one can see the variation of the divergence buckling load p^c(or

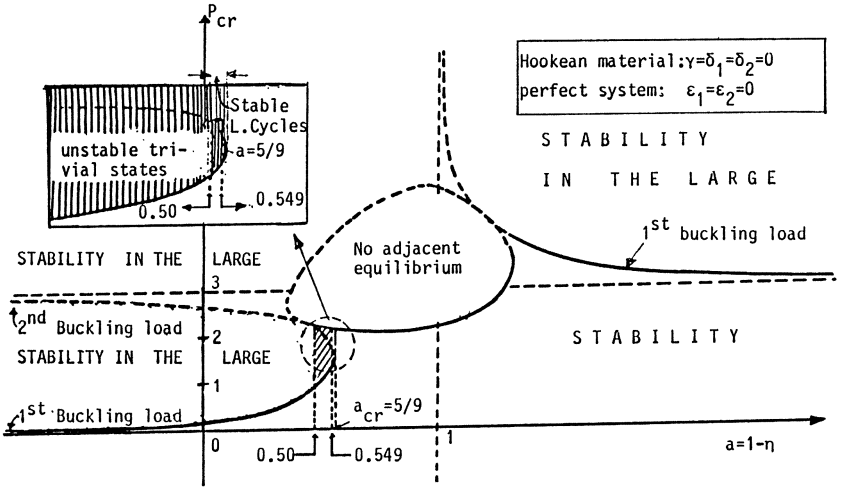

Fig.2.Stable divergence critical states in the plot p_{cr} vs a

p_{cr})versus the nonconservativeness parameter a=1-n for a Hookean perfect system.Note that if a<0.50 the trivial state ($\Theta_1=\Theta_2=0$) is unstable for $p>p^c$.For loads suffiently higher than the critical load we may have chaotic transients.When a<0.50 the model exhibits two stable postbuckling paths(one corresponding to the 1st branching point and another corresponding to the 2nd branching point).This is clearly shown in Fig.3 which illustrates the postbuckling paths for six characteristic cases of a.For 0.50 <a<5/9 there is only one postbuckling path connecting the two branching points. For 0.50<a<0.549 the model displays a limit point (above both branching points). When η=0.50 and $p^c=2$ the nondissipative model exhibits a chaotic regime (with large displacements) which is not due to a strange attractor since there is no contraction of phase-space volumes. For a=5/9 we have an isolated stable equilibrium point. For sufficiently negative γ depending on the value of η(=1-a) all the above divergence critical states become unstable[16].

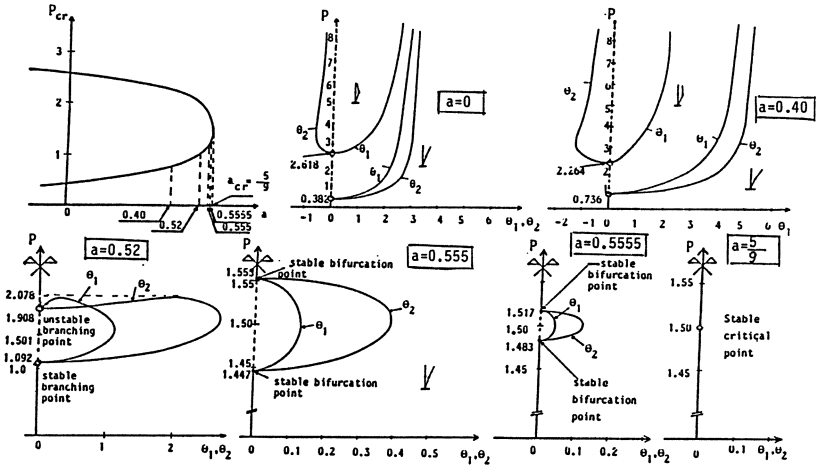

Fig.3.Postbuckling paths for six characteristic values of a

For loads p slightly higher than p^c when damping is included the motion converges towards the stable equilibrium point of the postbuckling path corresponding to the lower branching point. When there is only one postbuckling path (i.e for a>0.50) regardless of the value of a we have at p=1.50 a dynamic Hopf bifurcation; the equilibrium point attractor valid for p<1.50 is transformed into a stable limit cycle attractor for p≧1.50.This is illustrated in Fig.4 . Following the definition for the dynamic instability load such a critical load can be established for bifurcational systems by using a nonlinear either static or dynamic analysis.

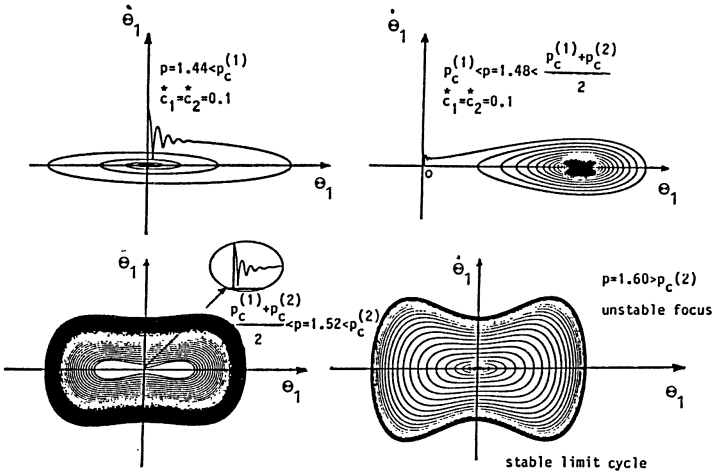

Fig.4.Phase planes of a system with a=0.555,$\gamma=\delta_1=\delta_2=0$ and $\varepsilon_1=\varepsilon_2=0$

According to linearized analyses[2,3] the critical states corresponding to the load

$$p^c = \frac{7+\eta \pm \sqrt{8+14\eta-40\eta^2}}{2(1+\eta^2)} \qquad -0.305 \leq \eta < 4/9 \qquad (8)$$

are found to be unstable associated with a divergent motion (flutter instability).However,application of a nonlinear dynamic analysis shows that all critical states in the region of nonexistence of adjacent equilibrium are stable(associated with bounded motion).Such a finding which contradicts existing results[2,3] is also due to the neglect of the last two terms in relation (5). This author has also shown[16] than there is no any destabilizing phenomenon due to slight damping if the foregoing terms are taken into account. The above findings hold for a Hookean material ($\gamma=\delta_1=\delta_2=0$).However, for γ sufficiently negative depending on the value of η the critical states in the region of nonexistence of adjacent equilibrium may become unstable (associated with a divergent motion).Clearly, the last case is associated with an unstable Hopf bifurcation,if damping is included.

Imperfect system

For systems with precritical deformation one can distinguish two characteristic cases: The 1st case refers to limit point systems and the 2nd one refers to limit point systems which under certain values of the control parameter become stable(exhibiting a continuously rising equilibrium path).The most im-

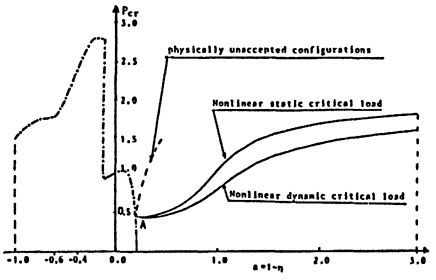

Fig.5.Dynamic critical load P_{cr} vs a

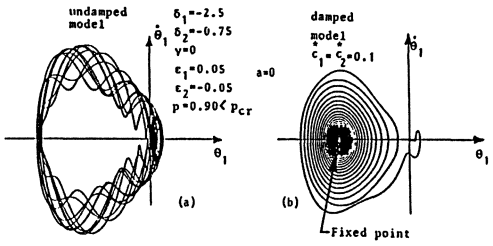

Fig.6.Chaotic and damped motion

portant finding regarding limit point systems is the following:It can be shown with the aid of nonlinear dynamic analysis that these systems become unstable(associated with a divergent motion) at (dynamic)loads always less than the corresponding limit point loads.Hence, the latter are higher than the co-

rresponding dynamic buckling loads.Such a result is still valid if we eliminate the effect of the mass (which may be appreciable for the dynamic buckling load).In Fig.5 one can see the difference between these loads versus the nonconservativeness parameter a.Note that for values of a to the left of the point A the system exhibits chaotic transients (Fig.6a,b).
Regarding the 2^{nd} case referring to stable systems,the nonlinear dynamic analysis revealed(under certain values of the control parameter) three phenomena;a)loss of dynamic stability,b)strong SIC and c) a jump in the dynamic critical load.For instance a system with $a=0,\gamma=0,\delta_1=-2.5,\delta_2=-0.75,p=0.75,\varepsilon_1=0.05$ and $\varepsilon_2<-0.0315$(where ε_2 is the control parameter) experiences a like chaos (random) motion. If damping is included the dynamic buckling load is associated with a saddle point on the unstable postbuckling path.However, one should note that the determination of the dynamic buckling load is practically meaningless when there is SIC.
Finally,for the imperfect model under discussion the inclusion of material nonlinearity does not increase the region of divergence instability.One should also notice that global solutions revealed that the magnitudes of critical displacements were not consistent with the approximations in relation(5). Hence,the true nature of instability can be explored only by discussing large time solutions associated with the original nonlinear equations of motion.

References

1.Ziegler,H(1953),"Linear Elastic Stability"ZAMP,4,168-185.
2.Herrmann,G.and Bungay,R.W(1964),"On the Stability of Elastic Systems Subjected to Nonconservative Forces",J.Appl.Mech.Trans.ASME 86,435-440.
3.Leipholz,E.H.(1975),"Aspects of the Dynamic Stability of Structures" J.Engng.Mech.DIV.EM2,101,109-124.
4.Kounadis,A.N.(1977),"Stability of Elastically Restrained Timoshenko Cantilevers with Attached Masses Subjected to a Follower Force" J.Appl.Mech.44, 731-736.
5.Kounadis ,A.N.(1980),"On the Static Stability Analysis of Elastically Restrained Structures Under Follower Forces" AIAA J.,18,473-476.
6.Kounadis,A.N.(1981),"Divergence and Flutter Instability of Elastically Restrained Structures Under Follower Forces" Int.J.Engng.Sci.19,553-562.
7.Kounadis,A.N.(1983),"The Existence of Regions of Divergence Instability for Nonconservative Systems Under Follower Forces" Int.J.Solids and Structures 9(8),725-733.
8.Kounadis,A.N.and Mahrenholtz,O.(1988),"Divergence Instability Conditions

in the Optimum Design of Nonlinear Elastic Systems Under Follower Loads" Proc.IUTAM Symp.On shape Optimization,Melbourne.

9. Plaut,R.H.(1976),"Postbuckling Analysis of Nonconservative Elastic Systems" J.Struct.Mech.4,395-416.
10. Roorda,J.,and Nemat-Nasser,S.(1967),"An Energy Method for Stability Analysis of Nonlinear Nonconservative Systems"AIAA J.5(7),1262-1268.
11. Burgess, I.N.and Levinson,M.(1972),"The Post-Flutter Oscillations of Discrete Symmetric Structural Systems with Circulatory Loading "Int.J.Mech.Sci. 14,471-488.
12. Huseyin,K.and Atadan A.S.(1983),"On the Analysis of Hopf bifurcations" Int. J.Engng. Sci.21(3),247-262.
13. Huseyin,K.(1986),"Multiple-parameter Stability Theory and Its Aplications" Oxford University Press.
14. Holmes,P.J.and Moon F.C.,(1983),"Strange Attractors and Chaos in Nonlinear Mechanics" J.Appl.Mech.,50,1021-1032.
15. Thompson ,J.M.T.and Stewart H.B.(1986)",Nonlinear Dynamics and Chaos"John Wiley and Sons,New York.
16. Kounadis,A.N.(1989),"On the Validity of the Paradox of Destabilizing Effect of Damping in Nonconservative Systems" 2nd Nat.Congress on Mechanics,Athens,June 29-July 1.

The Exact Almost Sure Stability for a Specific Class of Non-Linear Ito Differential Equations

Frank Kozin and Z.Y. Zhang
Polytechnic University Farmingdale, NY

Summary

The classic stability studies for linear Ito differential equations were developed by Khas'minskii in the 1960's. The main concept is to norm the solution and study the properties of the normed vector on the surface of the unit sphere. In the 1970's many ordinary second order dynamical systems were generated to their exact stability regions by Kozin and his students. The recent methods due to Wedig are the most efficient ways to determine the stability regions and Lyapunov exponents for the Ito one degree of freedom equations. There has not been in the past an exact study for non-linear Ito equations. In this paper we shall show that there is a class of homogeneous non-linear oscillators that can be transformed on the unit sphere and the exact stability regions can be determined. Two simple examples will be presented.

I. Introduction

The classical transformation methods for the linear Ito equations can be found in reference [1]. Consider the system

$$dx_i(t) = \sum_{j=1}^{l} b_i^j x_j(t)\,dt + \sum_{r=1}^{n}\sum_{j=1}^{l} \sigma^j_{ir} x_j(t)\,dB_r(t), \qquad i=1,\ldots,l \tag{1.1}$$

where

$$\vec{x} = \begin{pmatrix} x_1 \\ \vdots \\ x_l \end{pmatrix}, \quad b = (b_i^j), \quad \vec{B} = \begin{pmatrix} B_1 \\ \vdots \\ B_n \end{pmatrix}.$$

$\vec{B}$ is a vector of independent Wiener components with $E\{B_r(t)\}=0$, $E\{[B_r(t)-B_r(s)]^2\}=t-s$.

The classical generator for the system (1.1) can be written as

$$Lu = (b\vec{x},\ \text{grad}\ u) + \frac{1}{2}\sum_{i,j=1}^{l} a_{ij}(\vec{x})\,\frac{\partial^2 u}{\partial x_i \partial x_j} \tag{1.2}$$

where

$$a_{ij}(\vec{x}) = \sum_{k,s=0}^{l}\sum_{r=1}^{n} \sigma^k_{ir}\sigma^s_{jr} x_k x_s.$$

W. Schiehlen (Editor)
Nonlinear Dynamics in Engineering Systems
IUTAM Symposium Stuttgart/Germany 1989

The classic method for linear systems is that one may make the change into the unit vector $\vec{\lambda} = \frac{\vec{x}}{\|\vec{x}\|}$ and study the magnitude of the solution in the logarithm form $\rho = \log \|\vec{x}\|$. Thus the stability properties of the solution can be determined. The following form can be obtained

$$d\rho(t) = Q(\lambda)dt + \sum_{r=1}^{n} (\sigma(r)\vec{\lambda}(t), \vec{\lambda}(t))dB_r(t), \tag{1.3}$$

and

$$Q(\lambda) = (b\vec{\lambda}, \vec{\lambda}) + \frac{1}{2}\sum_{i=1}^{l} a_{ii}(\vec{\lambda}) - \sum_{i,j=1}^{l} a_{ij}(\vec{\lambda})\lambda_i\lambda_j.$$

In the limit, we obtain

$$\lim_{t\uparrow\infty} \frac{1}{t} [\log \|\vec{x}(t)\| - \log \|\vec{x}_0(t)\|] = \lim_{t\uparrow\infty} \frac{1}{t} \int_0^t Q(\vec{\lambda}(s))ds. \tag{1.4}$$

On the unit sphere (or circle), the $\vec{\lambda}$ is an ergodic process, and thus the stability of the solution process is determined by the value of the average $E\{Q(\vec{\lambda})\}$. Indeed if the average is positive the system is unstable and if the average is negative the system is stable. Thus, the stability curve is obtained by the expression $E\{Q(\vec{\lambda})\}=0$. One of the early papers to present the stability regions for a large class of stochastic mechanical oscillators is [2].

The interesting fact is that we can do this same analysis for an unusual class of non-linear oscillators as we shall see in the next section.

II. Stability Study for a Certain Class of Non-Linear Ito Differential Equations

We are interested in the non-linear equations of the form

$$d\vec{x}(t) = \vec{f}(\vec{x}(t))dt + G(\vec{x}(t))d\vec{B}(t) \tag{2.1}$$

where $\vec{x}$, $\vec{f}$ are l-dimensional vectors, G is an $l \times n$ matrix and $\vec{B}$ is the n-vector of Brownian motions.

The two general properties of (2.1) are

$$\begin{cases} \text{(a).} \quad \lim_{\|\vec{x}\|\downarrow 0} \vec{f}(\vec{x}) = \vec{0}, \quad \lim_{\|\vec{x}\|\downarrow 0} G(\vec{x}) = (0) \\ \text{(b).} \quad (G(\vec{x})G^T(\vec{x})\vec{\alpha}, \vec{\alpha}) \geq m\|\vec{x}\|^2\|\vec{\alpha}\|^2 \end{cases} \tag{2.2}$$

for arbitrary vector $\vec{\alpha}$, $m>0$.

We now assume the simple homogeneous property

$$k\vec{f}(\vec{x}) = \vec{f}(k\vec{x}), \; kG(\vec{x}) = G(k\vec{x}). \tag{2.3}$$

The interesting surprise is that (2.3) allows us to determine the same functions as (1.3), (1.4) for the linear system. The exact function $Q(\lambda)$ can be written as

$$Q(\vec{\lambda}) = \vec{\lambda}^T\vec{f}(\vec{\lambda}) + \frac{1}{2}\sum_{i=1}^{l}(G(\vec{\lambda})G^T(\vec{\lambda}))_{ii}\left[\sum_{j=1}^{l}(\lambda_j^2-\lambda_i^2)\right] - \sum_{\substack{i\neq j \\ i,j=1}}^{l}(G(\vec{\lambda})G^T(\vec{\lambda}))_{ij}\lambda_i\lambda_j. \tag{2.4}$$

The exact stability region is determined simply by $E\{Q(\vec{\lambda})\}=0$. What is interesting is that one can now look at various homogeneous oscillators that could possess unusual non-linear functions of $(x,\dot{x})$. Furthermore, the numerical procedure $\int_0^{2\pi} Q(\theta)p(\theta)d\theta = E\{Q(\theta)\}$ on the unit circle is obtained by Wedig's method for computing $p(\theta)$, [3]. We will now show two examples.

III. Examples

Consider the oscillator, which is homogeneous,

$$dx_1 = x_2dt, \qquad dx_2 = -(x_1+2\xi x_2)dt - \sigma\sqrt{x_1^2+x_2^2}\,dB(t) \tag{3.1}$$

Since $\vec{\lambda} = \begin{pmatrix}\cos\theta \\ \sin\theta\end{pmatrix}$ on the unit circle we find that the θ-equation becomes

$$d\theta = -[1+(2\xi+\sigma^2)\sin\theta\cos\theta]dt - \sigma\cos\theta\,dB(t). \tag{3.2}$$

The generator of L of the θ-process becomes

$$L = -[1+(2\xi+\sigma^2)\sin\theta\cos\theta]\frac{d}{d\theta} + \frac{1}{2}\sigma^2\cos^2\theta\frac{d^2}{d\theta^2},$$

$$\left(= \Phi(\theta)\frac{d}{d\theta} + \frac{1}{2}\Psi^2(\theta)\frac{d^2}{du^2}\right). \tag{3.3}$$

On the unit circle, the singular points that are left shunts [2] occur only at $\theta=\pm\pi/2$. It is easy to show that the $Q(\theta)$ function as from (2.4) is

$$Q(\theta) = -\frac{\sigma^2}{2} - (2\xi+\sigma^2)\sin^2\theta. \tag{3.4}$$

To determine the stability region of the form $\int_0^{2\pi} Q(\theta)\,p(\theta)\,d\theta = 2\int_0^{\pi} Q(\theta)\,p(\theta)\,d\theta$, the method of [3] is used to write the Fokker-Planck equation

$$\frac{1}{2}\frac{d^2}{d\theta^2}[\psi^2(\theta)p(\theta)] - \frac{d}{d\theta}[\Phi(\theta)p(\theta)] = 0$$

into the first order equation

$$\frac{1}{2}\psi^2(\theta)\frac{dp(\theta)}{d\theta} + \left(\psi(\theta)\frac{d\psi(\theta)}{d\theta} - \Phi(\theta)\right)p(\theta) = C, \tag{3.5}$$

where C is the integral constant.

The sequential fraction to obtain the discrete values of p_n, which is a backward difference form, [3], can be written as

$$p_{n+1} = \frac{2\Delta\theta\,p_1 + \psi_n^2 p_n}{\psi_n^2 + 2\Delta\theta(\psi_n\psi_n' - \Phi_n)}, \quad n = 1,2,3,\ldots,N \tag{3.6}$$

where $\Delta\theta$ is a small increment in the unit circle angle θ, and ψ_n' is the value of the derivative of ψ at the nth θ-value. Figure 1 shows us the exact almost sure stability region, $J<0$, in terms of the horizontal damping ξ, and the vertical variance σ^2.

Let us now consider another unusual non-linear oscillator, which is homogeneous,

$$dx_1 = x_2dt, \qquad dx_2 = -(2\xi x_2+x_1)dt + \sigma x_1^{4/5}\sqrt[5]{x_1-x_2}\,dB(t). \tag{3.7}$$

The transformation onto the unit circle yields the θ-equation,

$$d\theta = [-1-2\xi\cos\theta\sin\theta - \sigma^2\cos^{13/5}\theta\sin\theta(\cos\theta-\sin\theta)^{2/5}]dt + \sigma\cos^{9/5}\theta(\cos\theta-\sin\theta)^{1/5}dB(t). \quad (3.8)$$

The generator L for the θ-process is given as

$$L = [-1-2\xi\cos\theta\sin\theta-\sigma^2\cos^{13/5}\theta\sin\theta(\cos\theta-\sin\theta)^{2/5}]\frac{d}{d\theta} + \frac{1}{2}\sigma^2\cos^{18/5}\theta(\cos\theta-\sin\theta)^{2/5}\frac{d^2}{d\theta^2}. \quad (3.9)$$

Recall, $L=\Phi(\theta)\frac{d}{d\theta}+\frac{1}{2}\psi^2(\theta)\frac{d^2}{d\theta^2}$ For this nonlinear oscillator, we find the singularity, $\psi^2(\theta)=0$, occurs at $\theta_{1,2}=\pm\frac{\pi}{2}$, and $\theta_{3,4}=\frac{\pi}{4},\frac{5\pi}{4}$ The points $\theta_{1,2}$ are the usual left shunts and $\theta_{3,4}$ are regular shunts and regular boundaries.

We evaluate the stability region, as above for

$$J = E\{Q(\theta)\} = \int_0^{2\pi} Q(\theta)p(\theta)d\theta$$

where

$$Q(\theta) = [-2\xi\sin^2\theta + \frac{\sigma^2}{2}\cos^{8/5}\theta(\cos\theta+\sin\theta)(\cos\theta-\sin\theta)^{7/5}]. \quad (3.10)$$

Upon solving the p_n as in (3.6) above, we find the exact stability region for $J<0$. Figure 2, shows the stability region, again as the relation between the damping quantity ξ, and the variance σ^2.

IV. Conclusion

We find this interesting accurate method for homogeneous non-linear oscillators, can allow us to determine these stability regions. A very large class of oscillators can be studied, for interesting applications.

Bibliography

[1] Khas'minskii, R.Z., Necessary and Sufficient Conditions for Asymptotic Stability of Linear Stochastic Systems, Theor. Prob. and Appls. 12 (1967) 144-147.

[2] Mitchell, R.R., Kozin, F., Sample Stability of Second Order Linear Differential Equations with Wide Band Noise Coefficients, SIAM Jour. Appl. Math, 27(1974), 571-605.

[3] Wedig, W., Pitchfork and Hopf Bifurcations in Stochastic Systems - Effective Stochastic Analysis (Eds. P. Kree, W. Wedig) published by Springer-Verlag.

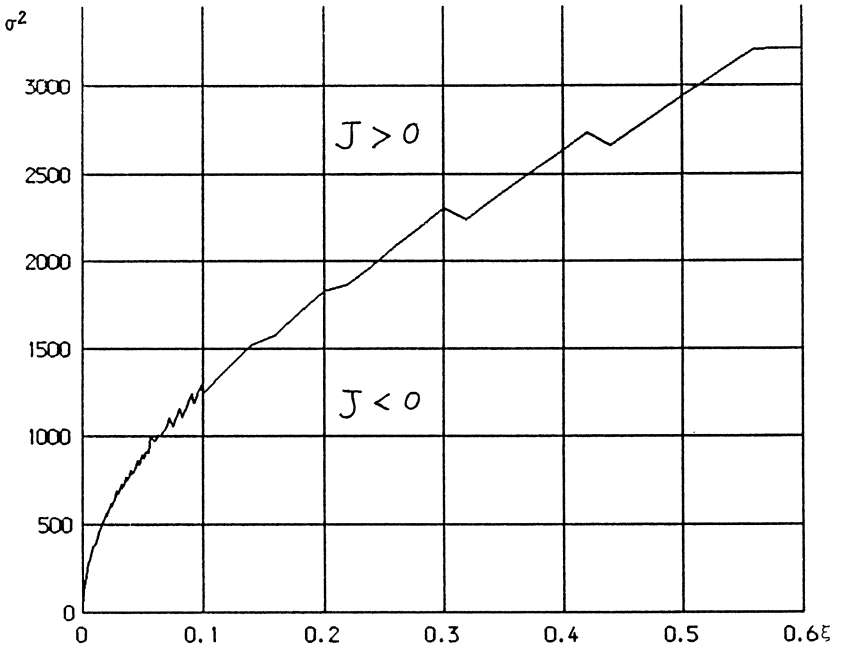

Fig. 1 - Stability region for first example.

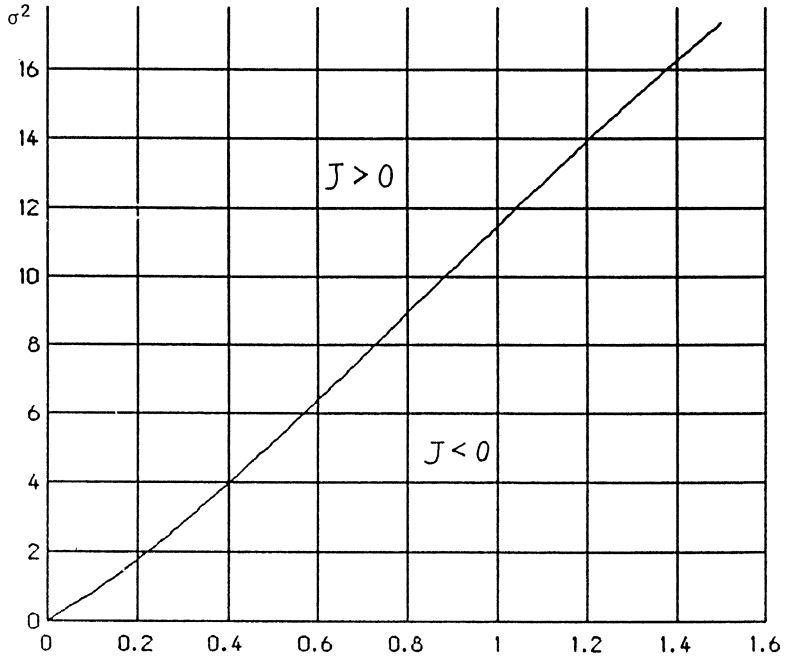

Fig. 2 - Stability region for second example.

Some Aspects of the Analysis of Systems with Local Nonlinearities

A. de Kraker, R.H.B. Fey, D.H. van Campen
Eindhoven University of Technology, Fac. of Mechanical Engineering,
Eindhoven, The Netherlands
C.J. Langeveld
TNO-Institute for Mechanical Constructions, Delft, The Netherlands

Summary
In this paper the influence of a reduction technique on the dynamic behaviour of mechanical systems consisting of linear components and local physical nonlinearities is examined. Reduction takes place by applying a component mode synthesis method which uses free interface eigenmodes and residual flexibility modes. A numerical method for determining the steady state behaviour of nonlinear dynamic systems is presented and combined with this reduction technique.

1. Introduction

In engineering practice many mechanical systems consisting of complex components with linear elastic behaviour and local physical nonlinearities can be found. Examples are a pipeline supported by stiffening springs and the exhaust of a road vehicle in which dry friction hinges are found.
Accurate information about displacements, stresses etc. asks for (finite element) models with a large number of degrees of freedom (dof) resulting in excessive computing times, necessary for the numerical integration of the nonlinear differential equations.
In this paper a component mode synthesis (CMS) method for the reduction of linear components is presented. The use of this reduction strategy in case local nonlinearities are present is evaluated by studying time response calculations of a nonlinear system with different levels of reduction. A numerical method developed by Crooijmans (1987) based on time-discretization and an arc-continuation method will be combined with the reduction technique for the determination of periodic solutions of complex nonlinear systems.

2. CMS: reduction of linear components

The Ritz method, used to reduce the component equations, approximates the coördinate-space of a component by a linear combination of a limited number of so-called component modes. By selecting the proper component modes an accurate reduced model can be created. It would be convenient if the well-known frequency criterium for the complete system-model evaluation could also be applied to the component reduction. Preceding research (Langeveld, 1986) shows that

W. Schiehlen (Editor)
Nonlinear Dynamics in Engineering Systems
IUTAM Symposium Stuttgart/Germany 1989

this is possible with a CMS method based on low frequency free interface eigenmodes and residual flexibility modes. Using component eigenmodes up to a certain cut-off frequency f_c will result in accurate eigenmodes of the complete system also up to f_c. Moreover the reduced system model will produce exactly the same solution as the original system model under quasi-static loads, provided that these loads act on dof for which residual flexibility modes have been defined. An ASKA process control program has been developed for this CMS method. The discretized equations of motion of a component are given by:

$$\underline{M}_x \ddot{\underline{x}} + \underline{B}_x \dot{\underline{x}} + \underline{K}_x \underline{x} = \underline{f}_x \qquad (2.1)$$

Column $\underline{x}$ (n*1) will be partitioned into internal dof $\underline{x}_I$ (n_I*1), which are not loaded and boundary dof $\underline{x}_B$ (n_B*1), which are loaded by interface loads $\underline{f}_{xif}$ and/or external loads $\underline{f}_{xex}$:

$$\underline{x}^T = [\underline{x}_I^T \; ; \; \underline{x}_B^T] \; ; \qquad \underline{f}_x^T = [\underline{0}^T \; ; \; \underline{f}_{xif}^T + \underline{f}_{xex}^T] \qquad (2.2)$$

Assuming proportional damping gives free interface eigenmodes from:

$$(-\omega_i^2 \underline{M}_x + \underline{K}_x) \underline{\varphi}_i = \underline{0} \qquad (i = 1, \ldots, n) \qquad (2.3)$$

The eigenfrequencies and -modes in the range of interest 0 - f_c Hz, which are kept in the component model, are stored in diagonal matrix $\underline{\Omega}_{KK}$ (n_K*n_K) respectively matrix $\underline{\Phi}_K$ (n*n_K). The deleted eigenfrequencies and -modes fill the matrices $\underline{\Omega}_{DD}$(n_D*n_D) and $\underline{\Phi}_D$ (n*n_D).
To get a reduced system model, with unaffected static load behaviour, so called residual flexibility (rf) modes are defined for each of the boundary dof of the component. The rf modes appear to be important for accurate eigenmodes ($<f_c$) of the reduced system model and also for the frequency response functions near anti-resonances. For a statically determinate component the matrix with flexibility modes $\underline{G}_A$ (n*n_B) is given by:

$$\underline{G}_A = \underline{K}_x^{-1} \begin{bmatrix} \underline{0} \\ \underline{I}_{BB} \end{bmatrix} = \underline{\Phi} \, \underline{\Omega}^{-2} \, \underline{\Phi}^T \begin{bmatrix} \underline{0} \\ \underline{I}_{BB} \end{bmatrix} = \underline{\Phi} \, \underline{\Omega}^{-2} \, \underline{\Phi}_B^T \qquad (2.4)$$

The matrix with rf modes $\underline{G}_B$ (n*n_B) follows from $\underline{G}_A$ by deleting the contribution of the kept eigenmodes $\underline{\Phi}_K$:

$$\underset{\sim}{G}_B = \underset{\sim}{G}_A - \underset{\sim}{\Phi}_K \, \underset{\sim}{\Omega}_{KK}^{-2} \, \underset{\sim}{\Phi}_{KB}^T = \underset{\sim}{\Phi}_D \, \underset{\sim}{\Omega}_{DD}^{-2} \, \underset{\sim}{\Phi}_{DB}^T \tag{2.5}$$

The Ritz reduction matrix $\underset{\sim}{T}_1$ $(n^*(n_K + n_B))$ which is used now reads:

$$\underset{\sim}{x} = \underset{\sim}{T}_1 \, \underset{\sim}{p}_1 \quad \text{or} \quad \begin{bmatrix} \underset{\sim}{x}_I \\ \underset{\sim}{x}_B \end{bmatrix} = \begin{bmatrix} \underset{\sim}{\Phi}_{KI} & \underset{\sim}{G}_{BI} \\ \underset{\sim}{\Phi}_{KB} & \underset{\sim}{G}_{BB} \end{bmatrix} \begin{bmatrix} \underset{\sim}{p}_K \\ \underset{\sim}{p}_B \end{bmatrix} \tag{2.6}$$

To permit simple coupling of the reduced component equations we write:

$$\underset{\sim}{p}_1 = \underset{\sim}{T}_2 \, \underset{\sim}{p} \quad \text{or} \quad \begin{bmatrix} \underset{\sim}{p}_K \\ \underset{\sim}{p}_B \end{bmatrix} = \begin{bmatrix} \underline{I} & \underline{0} \\ -\underset{\sim}{G}_{BB}^{-1} \, \underset{\sim}{\Phi}_{KB} & \underset{\sim}{G}_{BB}^{-1} \end{bmatrix} \begin{bmatrix} \underset{\sim}{p}_K \\ \underset{\sim}{x}_B \end{bmatrix} \tag{2.7}$$

Combining (2.6) and (2.7) gives:

$$\underset{\sim}{x} = \underset{\sim}{T} \, \underset{\sim}{p} \; ; \; \underset{\sim}{T}(n^*(n_K+n_B)) = \underset{\sim}{T}_1 \underset{\sim}{T}_2 \; ; \; n_K + n_B \text{ generally} << n \tag{2.8}$$

Using this transformation matrix $\underset{\sim}{T}$, the component equations become:

$$\underset{\sim}{M}_p \, \ddot{\underset{\sim}{p}} + \underset{\sim}{B}_p \, \dot{\underset{\sim}{p}} + \underset{\sim}{K}_p \, \underset{\sim}{p} = \underset{\sim}{f}_p ; \quad \underset{\sim}{M}_p = \underset{\sim}{T}^T \underset{\sim}{M}_x \underset{\sim}{T}, \; \underset{\sim}{B}_p = \underset{\sim}{T}^T \underset{\sim}{B}_x \underset{\sim}{T}, \; \underset{\sim}{K}_p = \underset{\sim}{T}^T \underset{\sim}{K}_x \underset{\sim}{T}, \; \underset{\sim}{f}_p = \underset{\sim}{T}^T \underset{\sim}{f}_x \tag{2.9}$$

When all components have been reduced we can assemble the (reduced) system model by demanding compatibility of interface dof and equilibrium of interface loads. We define $\underset{\sim}{q}$ (n_q*1) as the column with independent dof of the reduced system model (modal dof $\underset{\sim}{p}_k^{(i)}$ (i = 1, ..., N) belonging to the N linear components and $\underset{\sim}{x}_T$, containing all boundary dof of the system):

$$\underset{\sim}{q}^T = [\underset{\sim}{p}_K^{(1)\,T}, \; \ldots, \; \underset{\sim}{p}_K^{(N)\,T}, \; \underset{\sim}{x}_T^T] \tag{2.10}$$

The equations of motion of the reduced system model finally are given by:

$$\underset{\sim}{M}_q \, \ddot{\underset{\sim}{q}} + \underset{\sim}{B}_q \, \dot{\underset{\sim}{q}} + \underset{\sim}{K}_q \, \underset{\sim}{q} = \underset{\sim}{f}_q \tag{2.11}$$

3. Addition of local nonlinearities and numerical integration

Local nonlinearities are added to (2.11) by means of internal loads $\underset{\sim}{f}_{nl}$ (n_q*1). Local nonlinearities are assumed to act only on boundary dof $\underset{\sim}{x}_T$:

$$\underset{\sim}{M}_q \, \ddot{\underset{\sim}{q}}(t) + \underset{\sim}{B}_q \, \dot{\underset{\sim}{q}}(t) + \underset{\sim}{K}_q \, \underset{\sim}{q}(t) + \underset{\sim}{f}_{nl}(\ddot{\underset{\sim}{x}}_T, \; \dot{\underset{\sim}{x}}_T, \; \underset{\sim}{x}_T, \; t) = \underset{\sim}{f}_q(t) \tag{3.1}$$

If the response of this reduced model (for example calculated by numerical integration) is sensitive for increasing the number of kept modes in the components we should be sceptical of the value of this model. If additional modes have negligible influence on the frequency spectra of $f_{\sim q} - f_{\sim nl}$ and if all dominant frequencies of the spectra are present in the linear component models, the model reduction is successful.

Example 3.1: (all quantities in SI units) Consider the 1D system shown in fig. 3.1. A continuous linear bar (mass density ρ = 5, cross section A = 0.1, modulus of elasticity E = 15, length ℓ = 3) is clamped at its right end and coupled with a sdof system of the Duffing type at its left end.

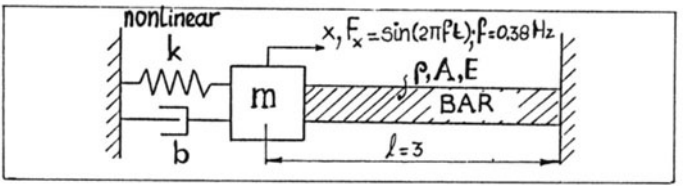

Fig. 3.1 Simple nonlinear system.

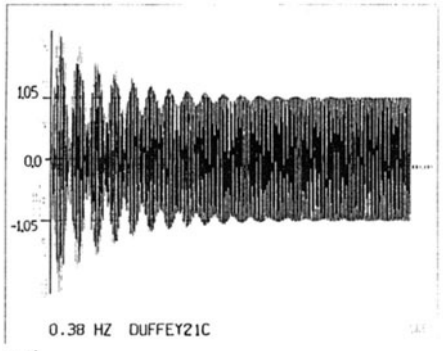

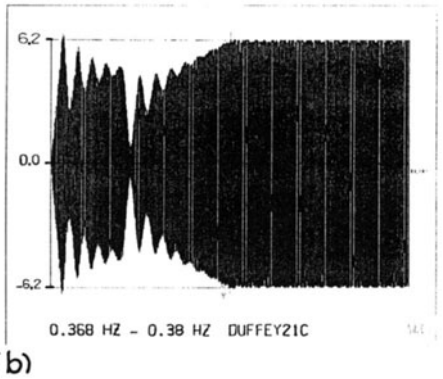

Fig. 3.2 Nonlinear time responses.

The homogeneous differential equation of the Duffing system is given by $0.5\,\ddot{x} + 0.02\,\dot{x} + 0.5\,x + 0.04\,x^3 = 0$. The bar is modelled with 50 elements. Three models were created and evaluated: 4C, 6C and 21C (undamped linear system reduced to 1 rf and respectively 3,5 and 20 kept eigenmodes). Numerical integration showed 2 steady-states at 0.38 Hz as given in fig. 3.2a (zero initial conditions, 21C) and fig. 3.2b (frequency sweep 0.368 Hz→0.38 Hz). With an FFT-algorithm frequency spectra for the 3 models were calculated for displacement x and load F_x-F_{nl} in the steady-state range of fig. 3.2b, see fig. 3.3a-3.3.f.

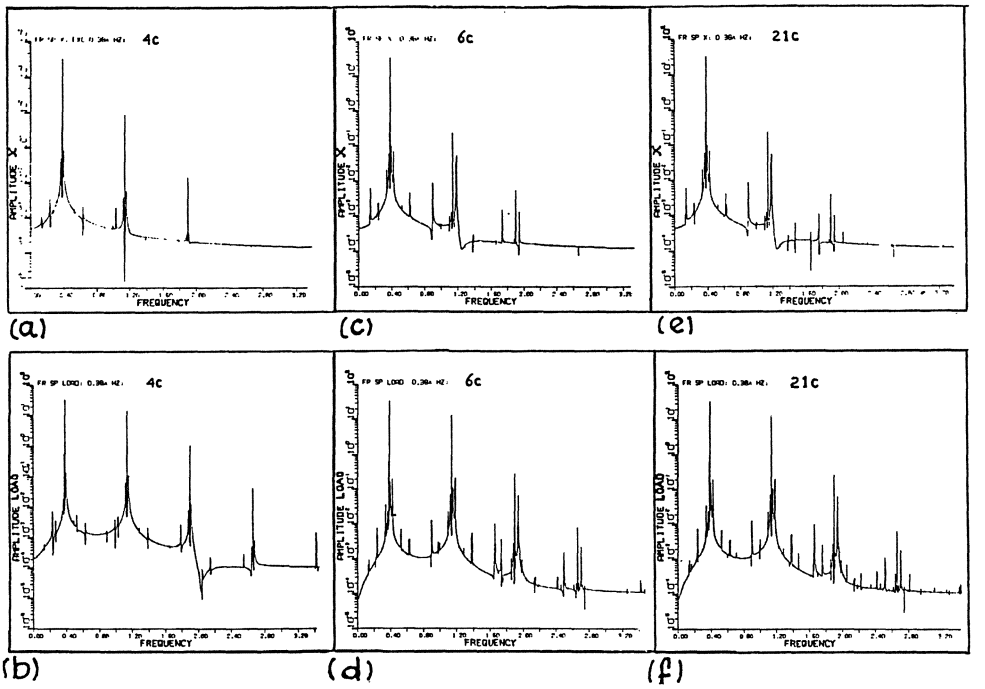

Fig. 3.3 Frequency-spectra for steady state responses.

Small differences were found between corresponding spectra calculated with model 4C and 21C. No significant differences were found between those calculated with 6C and 21C. The maximum displacement errors were -0.24(4C-21C) and 3.0E-3(6C-21C). The CPU times needed for the integration were 1024[s](4C); 1522[s](6C) and 11983[s](21C). So 6C provides an accurate solution and saves a lot of CPU-time.

4. Periodic solutions of nonlinear dynamic systems combined with reduction of linear components

The software program LIMSET (Crooijmans, 1987) has been developed for determining static, periodic and quasi-periodic equilibria of nonlinear dynamic systems. Stable equilibria as well as unstable equilibria can be computed. Equations (3.1) are transformed into a set of ($m*n_q$) nonlinear algebraic equations using time-discretization of the periodic solution (for details, see Crooijmans). This results in:

$$\underset{\sim}{H}(\underset{\sim}{z}, \underset{\sim}{r}) = \underset{\sim}{0} \qquad (4.1)$$

where $\underset{\sim}{z}$ contains the discretized values of the resulting dof $\underset{\sim}{q}$ at the times $0, \Delta t, 2\Delta t, \ldots, (m-1)\Delta t$ and $\underset{\sim}{r}$ contains selected design variable(s), (stiffness values, prescribed frequencies, etc.). Equation (4.1) can be solved by using a Newton-Raphson process or by using an arc-continuation method (Fried, 1984) which makes it possible to investigate how changes in a design variable will influence the periodic equilibrium.

By coupling the ASKA program with LIMSET it became possible to obtain approximations of periodic equilibria of complex dynamic systems with local nonlinearities. For illustration we will now investigate the steady state behaviour of the system presented in *example* 3.1.

Example 4.1: The discrete mass of the system was loaded by the periodic external load $F_x = \sin(2\pi ft)$. By choosing f as the design variable to be varied, we are able to calculate frequency respons functions (frf). Two models were evaluated: 4c from example 3.1 and 4a which is identical with the exception that in the calculation of the rf- and the (3) eigenmodes the whole Duffing system was ignored.

Table 4.1 gives the four lowest eigenfrequencies of the unreduced system model, model 4a and 4c for the linear, undamped case.

	unreduced	4a	4c
1	0.1504	0.1504	0.1504
2	0.3589	0.3589	0.3589
3	0.6187	0.6199	0.6187
4	0.8957	0.9648	1.0210

Table 4.1 Eigenfrequencies (Hz) of linear, undamped models.

The frf of 4a and 4c are shown in fig. 4.1a and fig. 4.1b. In the calculations 40 discretisation points were used. Each analysis costed approximately 9000 s. CPU time on an APOLLO workstation. The two figures look very similar with exception of the behaviour near 0.2 Hz.

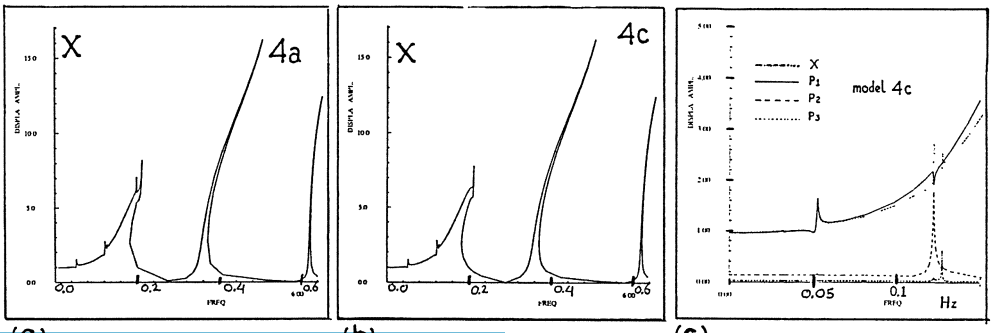

Fig. 4.1. Frequency respons functions for models 4a and 4c.

The first three small peaks can be identified as superharmonic resonances. They occur at 1/3 f_1, 1/3 f_2 and 1/5 f_3. In fig. 4.1c the frf of x is split into the contribution of the 3 modal coordinates p_1, p_2 and p_3. Clearly can be seen that p_1 is responsible for the peak at 1/3 f_1, p_2 for the peak at 1/3 f_2 and p_3 for the peak at 1/5 f_3.

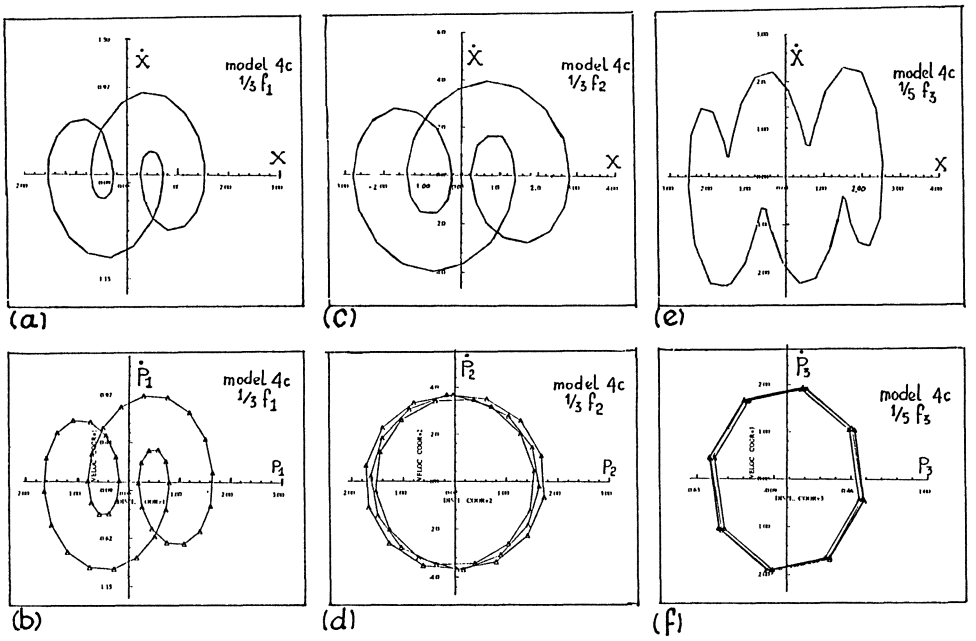

Fig. 4.2 Phase portraits of some periodic solutions and -contributions.

Figures 4.2 show the periodic solutions of x resp. the modal dof responsible for the superharmonic resonance mapped in phase space at 1/3 f_1, 1/3 f_2 and 1/5 f_3. We verified the superharmonic resonance at 1/3 f_2 by numerical integration of model 21c (see example 3.1). The result shown in fig. 4.2c covers completely fig. 4.3.

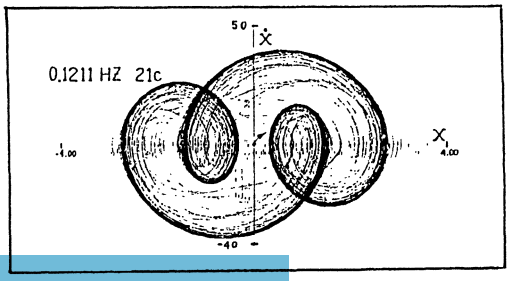

Fig. 4.3 Phase portrait of model 21c by numerical integration.

Near 0.2 Hz we see in fig. 4.1a two peaks whereas in fig. 4.1b only one peak is found. This is caused by the fact that the superharmonic solution at 1/5 f_4 occurs at a lower frequency with 4a than with 4c. An annoying fact is that this superharmonic solution will not occur in reality because f_4 is an artificial eigenfrequency due to the rf mode. On the other hand the rf mode showed to have a strong positive influence near the anti-resonances.

Finally we look at the periodic solutions of x at 0.38 Hz. At this frequency LIMSET found three periodic solutions of which two are stable (amplitudes 1.049 and 6.248) and one is unstable (amplitude 5.176). The two stable periodic solutions were also found by numerical integration in example 3.1, the unstable one could only be found by the LIMSET program.

5. Review and conclusions

1) A CMS method based on free interface eigenmodes and residual flexibility modes is presented. With this method a frequency criterium can be applied at component level to reduce linear components.
2) A strategy has been proposed for sensible reduction of systems, consisting of linear components and local nonlinearities. It has been applied successfully to a system with a local nonlinearity of the Duffing type. The amount of CPU time that could be saved in a time integration analysis by reducing the linear component was considerable.
3) A numerical method for the calculation of periodic solutions of nonlinear dynamic systems is combined with the reduction technique for linear components. Results for systems with a local nonlinearity of the Duffing type showed a very good agreement with numerical integration solutions.
4) Artificial eigenfrequencies above the cut-off frequency f_c caused super harmonic resonances below f_c which will not occur in the original system model. Therefore it should be advised to truncate the system eigenfrequencies above f_c after coupling of reduced linear components. Consequently responses near anti-resonances can become less accurate.

References:

* Crooijmans, M.T.M.; On the computation of stationary deterministic behaviour of non-linear dynamic systems with applications to rotor-bearing structures, Thesis, Eindhoven University of Technology, The Netherlands, 1987.
* Fried, I.; Orthogonal trajectory accession to the nonlinear equilibrium curve, Computer methods in applied mechanics and engineering 47, 1984, pp. 283-297.
* Langeveld, C.J.; Een koppelingsmethode voor mechanische componenten, TNO-rapport 5025002-86-1, TNO-IWECO, Delft, The Netherlands, 1986 (in Dutch).

Stochastic Model for Rattling in Gear-Boxes

A. Kunert, F. Pfeiffer

Institut B für Mechanik, TU München,
Arcisstr. 21, D–8000 München 2

Summary

Considering dynamics of drive trains, rattling in gear boxes is examined. After a time-continuous description by a patching method and the derivation of discrete mappings for arbitrary systems with backlashes, in a third step influence of noise excitation which is present in any technical system is studied. The probability density is obtained by numerical solution of the Fokker-Planck-Equation and results are discussed in comparison to velocity distributions calculated by discrete mappings without noise excitation.

Introduction

In the last few years rattling in gearboxes has become interesting to engineers because of developments in car technology. Combustion engines have become less noisy, gearbox casings have been reduced in weight and as a consequence rattling of gearwheels may be heard. So rattling has become a problem of comfort.

Gearbox Model

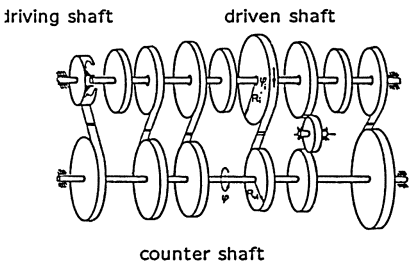

Fig. 1: Gearbox Model

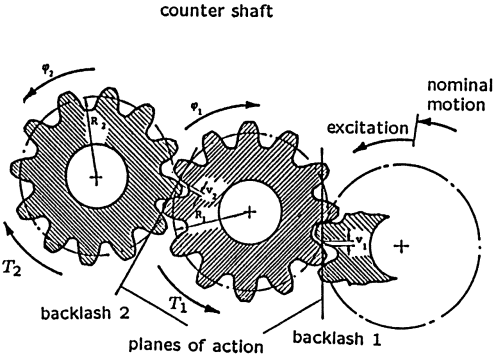

Fig. 2: Meshing gearwheels

At first, the main features of a gearbox and the cause of rattling is discussed briefly. In figure (1) a diagrammatic view of a gearbox is shown. On the left hand side the driving shaft is displayed. It rotates with a nominal frequency and a superimposed fluctuation due to variations of the engine's rotational speed. In the following this fluctuation will be considered only because it excites rattling vibrations. The countershaft and gearwheels fixed on it are driven by the driving shaft and transmit power to the driven shaft via loaded gears. The remaining gearwheels which are not fixed on the driven shaft are excited by the motion of the countershaft as it is shown in figure (2). Meshing gearwheels move freely within the

W. Schiehlen (Editor)
Nonlinear Dynamics in Engineering Systems
IUTAM Symposium Stuttgart/Germany 1989

backlash until an impact takes place at the end of a backlash and rotational speed is changed suddenly. Rattling will be most significant if the gearbox is not under load because every pair of gearwheels contributes to rattling noise. Similarly, in the case when the driven shaft is connected directly to the driving shaft noise will be very significant. In the usual case of power transmission the gearbox is under load. Power transmitting gearwheels stay in contact because of the load and only gearwheels which are not concerned with power transmission may rattle. So later we will concentrate on the motion of a meshing pair of gearwheels.

General numerical concept

Subsequently, basic ideas for the numerical solution of rattling will be pointed out. This procedure works for arbitrary systems with multiple backlashes and is discussed in more detail by [PFEIFFER 1984].

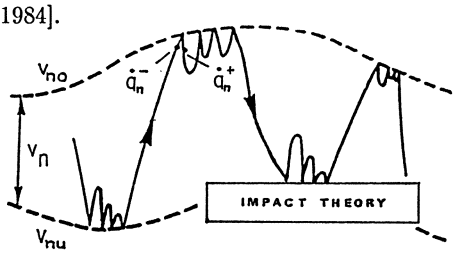

Fig. 3: Free flight and contact phase

The equations of motion for an gearbox with n backlashes are given by equation (1), where $\mathbf{q} \in \mathbb{R}^n$ is the vector of coordinates in configuration space.

$$\mathbf{M}(\mathbf{q})\ddot{\mathbf{q}} - \mathbf{Q}(\mathbf{q}, \dot{\mathbf{q}}, t) = \mathbf{0} \tag{1}$$

Motion takes place in a restricted area, where boundaries for space variables are equivalent to switch planes. At these switch planes constraints of motion have to be evaluated. These constraints are given by the impact equations (2).

$$\dot{\mathbf{q}}^+ = \mathbf{U}_n \dot{\mathbf{q}}^- + \mathbf{b}_n \dot{e}_n \tag{2}$$

$$\mathbf{M}\ddot{\mathbf{q}} + \mathbf{D}\dot{\mathbf{q}} + \mathbf{T} = \mathbf{0} \tag{3}$$

The velocities just after an impact in the n-th backlash $\dot{\mathbf{q}}^+$ are given by a transformation of the velocities just before an impact $\dot{\mathbf{q}}^-$ according to the matrix $\mathbf{U}_n$ and the excitation velocity $\dot{e}$ at the time of impact. The Matrix $\mathbf{U}_n$ and the vector $\mathbf{b}_n$ depend on the stage where an impact takes place. The velocities after an impact are initial values for the following free flight phase, where motion is described by forces of inertia (given by matrix $\mathbf{M}$), damping (matrix $\mathbf{D}$) and the matrix $\mathbf{T}$ which contains the drag torques (3). During integration of free flight equations (3) it has to be checked, which switch plane is reached first. For an impact in the determined stage appropriate impact equations (2) are used to calculate initial values for the next free flight. So free flight and impacts are alternating in this time-continuous description. In a second step, a time discrete procedure is choosen instead of a time continuous one. The switch planes are taken as Poincaré sections and so only states just before an impact are considered. This leads to a recursive mapping which describes motion from k-th impact to $(k+1)$-th impact.

The mapping is given by an implicit formula (4) because determining the time of the next impact requires calculation of relative distances in all n stages.

$$G(\mathbf{x}_{k+1}, \mathbf{x}_k) = 0 \ , \qquad \mathbf{x} = (\mathbf{q}, \dot{\mathbf{q}}, t) \tag{4}$$

The advantage of time-discrete mappings over a time-continuous description is given by an analytical integration of equations of motion within the backlashes. Using mapping equations (4) a lot of computational time is saved because algebraic equations are used instead of ordinary differential equations.

Single stage rattling

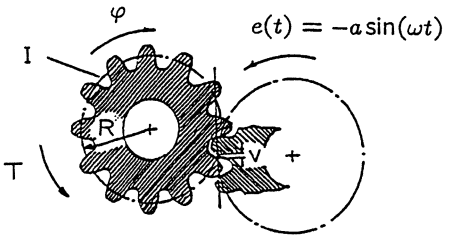

Fig. 4: Meshing pair of gearwheels

As an example, mapping equations for an unloaded pair of meshing gearwheels are given. The displacement of the gearwheel at the right is given by excitation $e(t)$ which is assumed to be harmonic with frequency ω and amplitude a. In the plane of action the backlash is given by its magnitude v. The damping force and drag torque are taken into account by parameters d and T. R represents the radius of the reference circle of the driven gearwheel with moment of inertia I. Mapping equations for velocity before the k-th impact Ψ_k, time of impact Φ_k and space coordinate χ_k are derived with parameters given in equations (5-6).

$$\Psi_k = \frac{\dot{\varphi}_k}{\omega c}; \qquad \vartheta = \frac{T}{d\omega c}; \qquad \varrho = \frac{d}{I\omega}; \qquad \chi_k = \pm\frac{v}{2a}; \qquad c = \frac{a}{R}; \tag{5}$$

$$\Psi_k^+ = -\varepsilon\Psi_k - (1+\varepsilon)\cos\Phi_k; \qquad \phi = \omega t\,. \tag{6}$$

Ψ_k^+ is the velocity just after an impact, which is given by impact equation (6) in dependence of the coefficient of restitution ε. Integration from impact to impact then yields:

$$\Psi_{k+1} = (\vartheta + \Psi_k^+)\exp(-\varrho\Delta\Phi_k) - \vartheta \tag{7}$$

$$\Phi_{k+1} = \Phi_k + \Delta\Phi_k; \qquad (\mathrm{mod}\ 2\pi) \tag{8}$$

$$\chi_{k+1} = \chi_k - \sin\Phi_{k+1} + \sin\Phi_k - \frac{1}{\varrho}(\vartheta + \Psi_k^+)(1 - \exp(-\varrho\Delta\Phi_k)) + \vartheta\Delta\Phi_k \tag{9}$$

The mapping equations (7-8) describe motion in a Poincaré section. The switch planes are equivalent to the Poincaré sections which are given by both boundaries of the backlash χ_k, so time and velocity are the remaining variables in the case of single stage rattling. The timestep $\Delta\Phi_k$ between two impacts is given implictly by equation (9).

Poincaré section and probability density

Fig. (5) shows a typical strange attractor for single stage rattling. In this figure all impacts at both sides of the clearance are plotted. The velocities are transformed to relative ones, so negative velocities indicate an impact at the left side of backlash and vice versa for positive velocities. For chaotic motion very irregular motion is found with a high rate of divergence of nearby trajectories described by positive Ljapunov exponents. The motion is spread around on the attractor, so one has some inherent diffusion in the case of chaotic motion as opposed to periodic solutions. For chaotic motion there is not much sense in looking at highly irregular trajectories over time, so in figure (6) timedependent velocity distributions are plotted against the Poincaré section. This provides a better survey of the appearing velocities. Due to the coarse grid, distributions look smoother than they are in reality. Examination of rattling noise which is caused mainly by high relative velocities before an impact requires looking at the attractor in more detail. In figures (6a),(6b) the distributions against the Poincaré section of figure (5) are shown. Figure (6a) shows the distribution for successive impacts at the same side of clearance. Higher velocities are due to successive impacts at different sides of backlash (Fig.6b). Especially for great drag torques the impacts take place mostly at one side of the backlash which leads to reduced rattling noise.

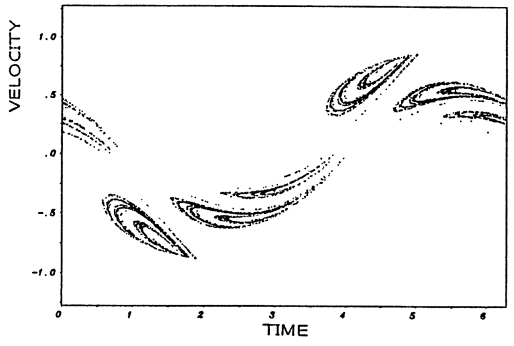

Fig.5: Strange attractor

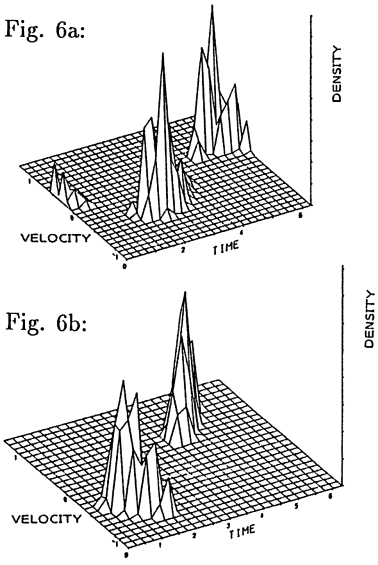

Fig. 6: Timedependent velocity distributions

Stochastic model

In the model used above (Fig. 4) technical imperfections are not considered. Imperfections in tooth geometry, oil splashing and noise excitation destroy the fractal structure of the strange attractor as has been observed in experiments [KARAGIANNIS 1989]. So the influence of additive random noise is examined. If external noise is added to the equations of motion the solution for the dynamical response is given by a probability density . There are several ways

calculate the evolution of probability density, but different problems arise. Using Markov ıains the problem is given by determining transition probabilities. Iterative calculation the invariant measure fails in general for nonsmooth distributions because of lack of ınvergence. Approximation techniques can be applied using the special structure of the apping equations (7,8), as in [KARAGIANNIS 1989], where an assumed distribution for ıe times of impact is used to calculate statistical moments for the velocities.

ı this paper the Fokker-Planck-Equation is used to describe stochastic behaviour. This par-al differential equation provides probability density in dependence of state space variables ıd time for any dynamical system under additional white noise excitation.

ıfluence of additive random noise

ı principle, the influence of additive random noise is described by [CRUTCHFIELD et al. 982] for the logistic map. Additional random noise does not change the global structure f the attractor. Small periodic windows vanish after the onset of chaos because any finite xternal noise leads to a scaling of amplitudes and so all subharmonics above a certain order re eventually suppressed. Subharmonic solutions of high order become unobservable because hey have merged into the chaos provided by external noise. Theoretically and practically it ′ould be of great importance to obtain the probability density of the unperturbed strange ttractor by a limiting process for vanishing noise intensity, providing the limit exists.

?okker-Planck-Equation for single stage rattling

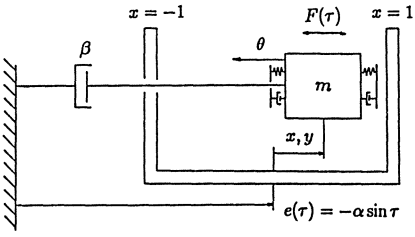

Fig. 7a: Equivalent model

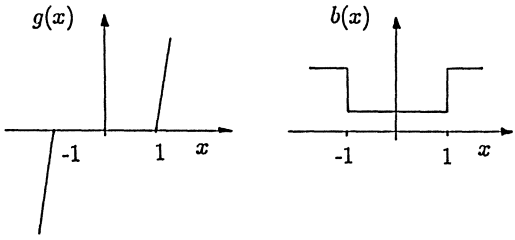

Fig. 7b: Restoring force $g(x)$, damping ratio $b(x)$

An equivalent model for single-stage rattling is shown in figure (7). Dimensionless relative coordinates x, y are used and the boundaries of backlash are given by $x = \pm 1$. Excitation by displacement is given by the dimensionless harmonic function $e(\tau)$ where τ represents dimensionless time and α contains the ratio of excitation amplitude to magnitude of backlash. The damping ratio during a free flight phase is given by β. θ is the generalized drag force. The random force is described by $F(\tau)$ which is δ-correlated for white noise excitation. The dynamical system for single-stage rattling is then described by state space equations (11) using the given parameters.

$$x = 2(R\varphi - e(t))/v; \quad \alpha = 2a/v; \quad \beta = d/(I\omega); \quad \theta = 2RT/(Iv\omega^2) \tag{10}$$

$$\begin{aligned} \dot{x} &= y \\ \dot{y} &= -b(x)y - g(x) - \theta - \alpha(\sin\tau - \beta\cos\tau) + F(\tau) \end{aligned} \tag{11}$$

Contact is modeled by a linear spring and a damper. The restoring force is given by the function $g(x)$. Damping within backlash ($|x| < 1$) equals β, for contact phase b depends on the coefficient of restitution ε. The evolution of probability density $\varrho(x, y, \tau)$ is described by the Fokker-Planck-Equation which is a partial differential equation of parabolic typ.

$$\frac{\partial \varrho}{\partial \tau} = -\frac{\partial}{\partial x}(y\varrho) - \frac{\partial}{\partial y}((-b(x)y - g(x) - \theta - \alpha \sin\tau + \alpha\beta\cos\tau)\varrho) + \frac{1}{2} S_y \frac{\partial^2 \varrho}{\partial y^2} \tag{12}$$

The change of probability density over time is given by so called drift and diffusive terms. The drift terms contain the right hand sides of the dynamical system and the density itself. The diffusive term is due to white noise excitation with noise intensity S_y. The given equation (12) is a conservative equation for probability flux.

Numerical solution of Fokker-Planck-Equation

Several solution techniques for the Fokker-Planck-Equation are discussed in [RISKEN 1984]. Using finite differencing methods, ADIP (alternating direction implicit procedure) is an appropriate procedure ([MITCHELL 1969]). The continuous density $\varrho(x, y, \tau)$ is approximated by discrete values $d(x_j, y_l, \tau_n)$ at spacial grid points x_j, y_l and at discrete timesteps τ_n. For evolution in time each timestep is devided into two substeps. At each substep the differential operator in one space direction is evaluated implicitly according to a Crank Nicholson scheme. L_x , L_y are discrete difference operators in x and y direction derived by Taylor expansion of equation (12) up to an accuracy of second order.

$$d_{j,l}^{n+1/2} = d_{j,l}^{n} + \frac{1}{2}\Delta\tau\,(L_x\, d_{j,l}^{n+1/2} + L_y\, d_{j,l}^{n}) \tag{13}$$

$$d_{j,l}^{n+1} = d_{j,l}^{n+1/2} + \frac{1}{2}\Delta\tau\,(L_x\, d_{j,l}^{n+1/2} + L_y\, d_{j,l}^{n+1}) \tag{14}$$

Boundary conditions for probability density are given by a vanishing density at state space boundaries.

A separation of free flight and contact phase according to the mapping equations is also tried for high restoring forces during contact. The Fokker-Planck-Equation is solved within the backlash according to the procedure given above. Impacts are described by boundary conditions for probability density at $x = \pm 1$. There are still some open questions regarding concurrent diffusive and advective transport during contact phase.

For smooth functions $g(x), b(x)$ the Galerkin method is applied with Hermite functions as an orthogonal set of shape functions for the probability density in state space. Investigating a wide range of system parameters, shape functions have to be fitted for more accurate results. Up to now results for small noise intensities are not yet satisfactory.

Results

Results for the Fokker-Planck-Equation using ADI procedure are given below and are compared to results obtained by discrete mapping without noise excitation. In figure (8) deterministic motion is displayed in the phase plane described by relative space x and relative

locity y. Trajectories move within backlash ($-1 < x < 1$) and reaching boundaries at $= \pm 1$, velocities are changed according to impact equations. Small velocities lead to ccessive impacts at the same side of backlash while higher velocities change the side of .cklash for the next impact. Chaotic trajectories fill out areas of attraction completely, probability density against phase plane (Fig.9) and distribution for velocities before an ıpact at $x = -1$ (Fig. 10) is considered.

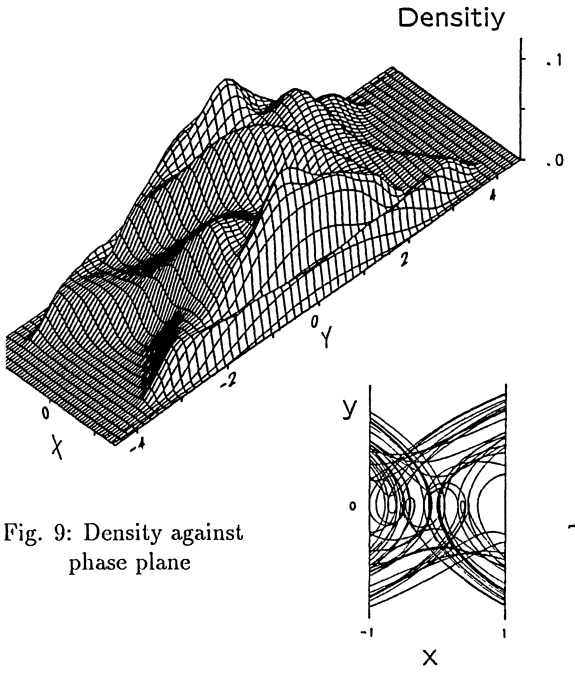

Fig. 9: Density against phase plane

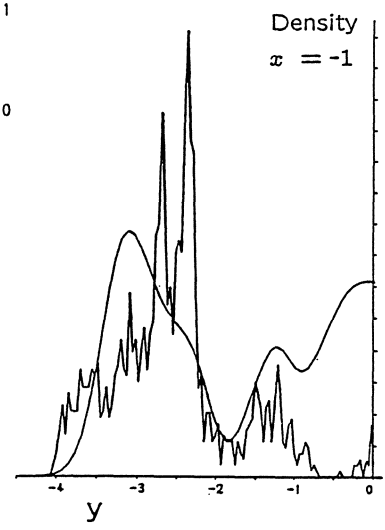

Fig. 10: Density section

Fig. 8: Phase portrait

'he density shown in figure (9) is calculated with smoothed transitions in $g(x)$ and $b(x)$. t gives the integral value of $\varrho(x, y, \tau)$ over one period of the excitation function $e(\tau)$. For ıigh velocities the areas of attraction are in good agreement with results given in the phase ›ortrait (Fig 8). For a detailed discussion it is necessary to look at a section of the density or instance at $x = -1$, shown in figure (10). The smooth probability density is obtained by ıumerical solution of the Fokker-Planck-Equation while the nonsmooth density results from . velocity distribution calculated by a mapping without any noise. Due to noise excitation .nd its diffusive effect, the nonsmooth fractal structure of the strange attractor is destroyed. t is noticed that noise leads to an increased density for small velocities in comparison to he system without noise. This can be interpreted physically. Due to the presence of noise here are trajectories with reduced velocities compared to the unperturbed deterministic case vhich lead to repeated impacts at the same side of backlash. So the probability of finding rajectories at the wall is increased for small velocities. In [LICHTENBERG/LIEBERMAN .983] a similar result is obtained for the Fermi attractor which describes the motion of a ›ouncing ball between a fixed and a moved wall using a modeled diffusive term.

Further work

As noise is present in all technical systems a next step consists of including noise excitation to the mapping equations. The modeling of the diffusive term has to be done carefully. Numerical problems arising for small noise intensities and stiff springs describing contact forces will be handled. Different shape functions for the Galerkin method will be examined because the use of Galerkin method reduces the partial differential Fokker-Planck-Equation to a set of ordinary differential equations. The problem of multistage rattling under noise excitation is still unsolved and requires different solution techniques.

Acknowledgement

This work is supported by a grant from the Volkswagen-Stiftung under project I/62 888.

References

[CRUTCHFIELD et al. 1982]
Crutchfield, J:P., Farmer, J.D., Hubermann, B.A.: Fluctuations and Simple Chaotic Dynamics, Phys. Rep. **92**,45 (1982)

[KARAGIANNIS 1989]
Karagiannis, K.: Analyse stoßbehafteter Schwingungssysteme mit Anwendung auf Rasselschwingungen beim Zahnradgetriebe. Doctor thesis at Lehrstuhl B für Mechanik, TU München (1989)

[LICHTENBERG/LIEBERMAN 1983]
Lichtenberg, A.J.; Lieberman, M.A.: Regular and Stochastic Motion. Springer-Verlag, Berlin-Heidelberg-New York-Tokyo (1983)

[MITCHELL 1969]
Mitchell, A.R.: Computational Methods in Partial Differential Equations. John Wiley & Sons, London-New York-Sidney-Toronto (1969)

[PFEIFFER 1984]
Pfeiffer, F.: Mechanische Systeme mit unstetigen Übergängen. Ingenieur Archiv, Bd. 54, Nr. 3, 232-240 (1984)

[PFEIFFER 1988 a]
Pfeiffer, F.: Seltsame Attraktoren in Zahnradgetrieben. Ingenieur Archiv, Bd. 58, 113-125 (1988)

[PFEIFFER 1988 b]
Pfeiffer, F.: Theorie des Getrieberasselns. VDI-Berichte Nr. 697, 45-65 (1988)

[RISKEN 1984]
H. Risken: The Fokker-Planck Equation. Springer Verlag, Berlin- Heidelberg-New York-Tokio (1984)

Hopf Bifurcation in the Dynamics of a Rotor/Bearing System

W. KURNIK

Institute of Machine Design Fundamentals
Warsaw University of Technology
Warsaw

Summary

An approximate nonlinear analysis of self-excited near critical vibrations of a rigid transversally loaded rotor supported in journal bearings is presented in this paper using the theory of bifurcations due to Iooss and Joseph. Analytic expressions for amplitudes, frequency and phase displacements for both radial and circumferential components of the rotor in-plane vibration are derived and the role of system parameters is explained. The second order approximation periodic solution is constructed and its orbital stability is discussed.

Introduction

Rotors supported in journal bearings being essential parts of such machinery as generators, turbines, compressors etc. show interesting dynamical features connected with complicated nonlinear hydrodynamical forces of an oil film action. The dynamics of rotor/bearing systems has been studied for more than 60 years from the early paper by Newkirk and Taylor [1] through more advanced research done by Hori [2] and Tondl [3] to the recent results reported by Hori [4] and Muszyńska [5]. A comprehensive experimental as well as theoretical study of transverse vibrations of an unloaded flexible rotor/bearing system was presented in [5]. However, there are structures in which rotors work under significant transverse loads. Their near-critical behaviour and self-excited vibration still remain a problem of question. It is also a problem of big practical importance. On the one hand, sometimes rotors have to operate under conditions close to criticality and a vibration of small amplitude is acceptable provided that it can be controlled. On the other hand, it is important to be able to detect and exclude subcri-

W. Schiehlen (Editor)
Nonlinear Dynamics in Engineering Systems
IUTAM Symposium Stuttgart/Germany 1989

tical self- excited vibrations which, being unstable, are more dangerous to the system than usually considered supercritical ones.

In the prasent paper a nonlinear local analysis of self-excited vibrations of a rigid transversally loaded rotor supported in journal bearings is done using the Hopf bifurcation theory developed by Hassard [6], Iooss, Joseph [7] and others. The self-excited vibrations in a physical system which occur at criticality and develop in a neighbourhood of it correspond to the Hopf bifurcation in the differential equations of motion. Applying the theory of bifurcation due to Iooss, a periodic solution (vibration) of the second approximation is constructed in a parametric form of a series. Moreover, some interesting qualitative features of near-critical vibrations are reported. The most important property is that both sub- and supercritical vibrations are possible and the type of self-excitation depends on all structural parameters of the system. In the subcritical region, for insrance, usually treated as safe, an unstable limit cycle may exist and a sufficiently big accidental initial condition can lead to large vibrations with all their bad consequences.

Formulae derived in the paper can be used to determine permissible sets of points in a multidimensional space of system parameters (feasible domains). This is of big importance in CAD and diagnostics of rotating machinery.

Equations of motion

The considered system is a rigid rotor of mass m supported in

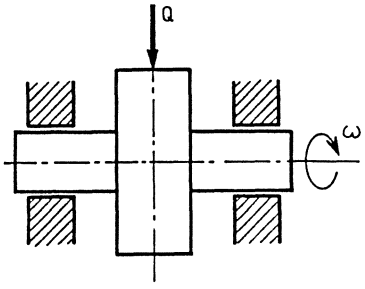

Fig.1 Vibrating system

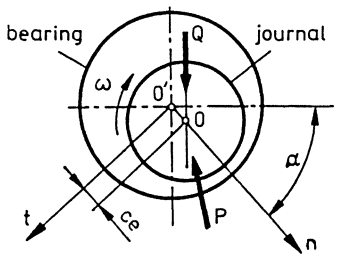

Fig.2 Coordinate system

journal bearings and statically loaded by a transverse force Q of constant direction (Fig.1). The system is symmetric and assumed to have two degrees of freedom. Applying a plane journal bearing model based on superposition of hydrodynamical forces corresponding to the wedge and squeeze effects treated separately, we obtain the following equations of motion in the polar coordinate system shown in Fig.2.

$$\left.\begin{aligned} mc\left(\ddot{e} - e\dot{\alpha}^2\right) &= P_n + Q\sin\alpha \\ mc\left(e\ddot{\alpha} + 2\dot{e}\dot{\alpha}\right) &= P_t + Q\cos\alpha \end{aligned}\right\} \qquad (1)$$

where $P_t = \Pi Ce\left(\omega-2\dot{\alpha}\right)U^{-0.5}V^{-1}$, $U = 1-e^2$, $V = 2+e^2$, $C = 6\mu RL/m\delta^3$

$$P_n = -2C\left[e^2\left|\omega-2\dot{\alpha}\right|U^{-1}V^{-1} + e\dot{e}U^{-1} + 2eU^{-1.5}\operatorname{arc\,tg}\left(\left(1+e\right)U^{-0.5}\right)\right]$$

and the notations are as follows

μ - oil viscosity, L - bearing total length, R - journal radius, c - bearing clearance, δ = c/R - clearance ratio, m - rotor mass, ω - angular speed of rotation, Q - static load.

Equations of motion (1) contain seven parameters: rotational speed ω which plays the role of the bifurcation parameter and six other parameters $p = [\mu,R,L,\delta,m,Q]$, that are also important to the bifurcation problem.

Putting $\dot{e} = \dot{\alpha} = 0$ and $\ddot{e} = \ddot{\alpha} = 0$ in (1) we can determine the set of equilibrium points

$$\operatorname{tg}\alpha_o = -2e_o\Pi^{-1}\left(1-e_o^2\right)^{-0.5} \qquad (2)$$

Particular equilibrium coordinates can be calculated as functions of parameters $e_o = e_o(\omega,p)$ and $\alpha_o = \alpha_o(\omega,p)$.

Introducing new variables: $u_1 = e-e_o$, $u_2 = \dot{e}$, $u_3 = \alpha-\alpha_o$ and $u_4 = \dot{\alpha}$, we obtain the following matrix equation of motion

$$\dot{u} = f(\omega,u,p) \qquad (3)$$

where $u = \left[u_1,u_2,u_3,u_4\right]^T$ and the right hand side function f is determined upon equations (1).

Stability of equilibrium

we shall determine the region of stability for the trivial solution of (3) using the Hurwitz criterion to the linearized

equation of motion $u = A(\omega,p)u$. The condition of stability can be expressed in terms of the relative eccentricity and so called dynamic bearing parameter $\psi = \mu L m^{-1}\omega^{-1}\delta^{-3}$

$$b_1 b_2 b_3 - b_0 b_3^2 - b_1^3 \geq 0 \qquad (4)$$

where $b_i = b_i(e_0,\psi)$ are coefficients of the corresponding characteristic equation (i=0,1,2,3). Inequality (4) can be solved with respect to ψ and written in the form $\psi \geq h(e_0)$, where $h(e_0)$ is a monotonically decreasing function shown in Fig.3.

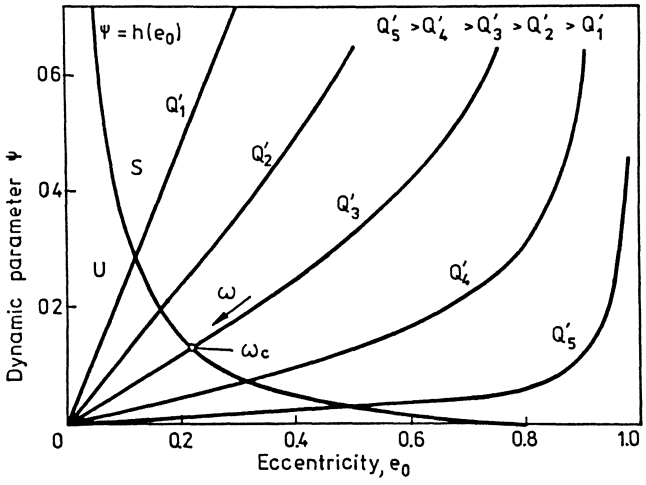

Fig.3. Journal equilibrium stabilityand instability regions S - stable, U - unstable. Effect of dimensionless load on critical journal eccentricity.

Introducing another parameter, so called dimensionless load $Q' = Qm\delta^5/(6\mu^2L^2R)$, we can show a family of curves (Fig.3) being sets of operating points for various values of the dimensionless load Q' and varying speed of rotation. The family equation can be written as follows

$$\psi = Q'^{-1}e_0U^{-1}V^{-1}(4e_0^2+\Pi^2U)^{0.5} \qquad (5)$$

At points of intersection of curves (5) and the stability limit $h(e_0)$ there exists always a pair of imaginary eigen-values and this is one of the necessary conditions for the Hopf bifurca-

tion. The dominat role is played by the first eigen-value $r_1(\omega,Q') = \xi(\omega,Q')+i\eta(\omega,Q')$ which becomes imaginary at criticallity i.e. $r_1(\omega_c,Q') = i\Omega_o(Q')$. It was numerically examined that the complex plane trajectory of the first eigen-value r_1 intersected the imaginary axis for every Q' and this implies inequality $\xi_\omega(\omega_c,Q') > 0$ which expresses the second condition for the Hopf bifurcation.

Bifurcating solution

In this section we shall construct the bifurcating periodic solution in a parametric form of a series due to Iooss [7].

$$\left.\begin{aligned} u(s,\varepsilon) &= (n!)^{-1}\varepsilon^n u^{(n)}(s), s=\Omega(\varepsilon)t \\ \Omega(\varepsilon) &= (n!)^{-1}\varepsilon^n\Omega_n \\ \omega(\varepsilon) &= (n!)^{-1}\varepsilon^n\omega_n \end{aligned}\right\} \qquad (8)$$

where Ω is the frequency of bifurcating solution, ε is a parameter interpreted as a distance between periodic and trivial solutions, $u^{(n)}(s)$ are 2Π-periodic vector functions and ω_n,Ω_n are constans to be determined. The unknown functions are described by the following linear recurrent equations

$$I_o u^{(n)} = g_n(s); \quad g_1(s) \equiv 0 \qquad (7)$$

where $I_o(\cdot) = -\Omega_o\frac{d(\cdot)}{ds} + A(\omega,Q')(\cdot)$,

$g_n(s) = n\Omega_{n-1}\frac{du^{(1)}}{ds} - n\omega_{n-1}f_{u\omega}(\omega_c,0|u^{(1)}) - R_{n-1}$,

$f_{u\omega}$ is a multilinear operator [7] and R_{n-1} contains terms of order lower than n. Solving the first and the second equations of (7) under the solvability condition (Fredholm alternative), we can show that the second order approximation periodic solution of equation (3) can be expressed as follows

$$u(s,\varepsilon) = 2\varepsilon Re\left\{qe^{is}\right\} + 0.5\varepsilon^2 K + \varepsilon^2 Re\left\{Le^{i2s}\right\} \qquad (8)$$

where

$s = \Omega t, \quad \Omega = \Omega_o + 0.5\varepsilon^2\Omega_2, \quad \omega = \omega_c + 0.5\varepsilon^2\omega_2,$

$$\omega_2 = -\mathrm{Re}\{D\}/3\xi_\omega(\omega_c), \quad \Omega_2 = 3\omega_2\eta_\omega(\omega_c) + \frac{1}{3}\,\mathrm{Im}\{D\},$$

$$D = \frac{3}{2}\langle f_{uu}(\omega_c,0|q|K),\, q^*\rangle + \frac{3}{2}\langle f_{uu}(\omega_c,0|\bar{q}|L),\, q^*\rangle +$$

$$+ 3\langle f_{uuu}(\omega_c,0|q|q|q),\, q^*\rangle,$$

$$K = -2\left\{A(\omega_c,Q')\right\}^{-1} f_{uu}(\omega_c,0|q|\bar{q}),$$

$$L = -\left\{A(\omega_c,Q')-2i\Omega_0 I\right\}^{-1} f_{uu}(\omega_c,0|q|q),$$ I is a unit matrix, q,q^* are orthonormal eigen-vectors of the linearized system matrix $A(\omega_c,Q')$ corresponding to the first eigen-value and $\langle a,b\rangle = a_i\bar{b}_i$ is the scalar product in the four dimensional Euclidean complex space.

On the factorization theorem [7] the Floquet exponent determining the orbital stability of the bifurcating solution can be expressed as follows

$$\sigma(\varepsilon) = -\xi_\omega(\omega_c,Q')\omega_2\varepsilon^2 + O(\varepsilon^4) \qquad (9)$$

Since $\xi_\omega(\omega_c,Q') > 0$, the limit cycle is stable if $\omega_2 > 0$.

Exemplary results

In the numerical calculations the effect of nondimensional load Q' has been examined. It represents all the system parameters except the speed of rotation. For every Q' the follwing quantities were calculated: ω_c - critical rotation speed, e_{oc},ψ_c - critical eccentricity and dynamic parameter, $\xi_\omega(\omega_c),\eta_\omega(\omega_c)$ - ω--derivative of the first eigen-value at criticality, Ω_0 - initial flutter frequency, ω_2,Ω_2 - first coefficients in $\omega(\varepsilon)$ and $\Omega(\varepsilon)$ series, K - vector of the constant component, L - second harmonic vector, q,q*-orthonormal eigen-vectors at criticality. One of the most important results can be seen in Fig.4. The system exhibits two dimensionless load domains. For small Q' ($Q' < Q'_I$) we deal with a subcritical bifurcation in which an unstable vibration exists for $\omega < \omega_c$. For $Q' > Q'_I$ the Hopf bifurcation is supercritical and the corresponding limit cycle is orbitally stable. Two limit cycles projected on the plane of displacements-stable and unstable are shown in Fig.5.

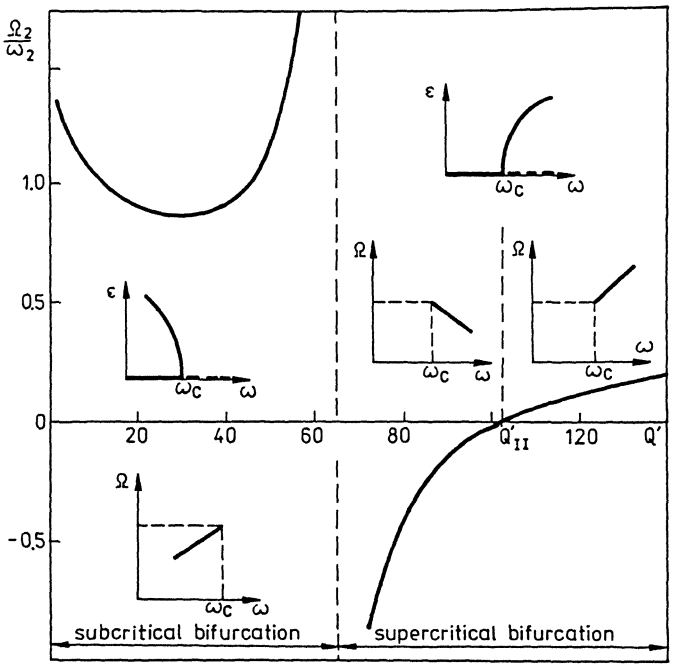

Fig.4 Regions of sub- and supercritical Hopf bifurcation

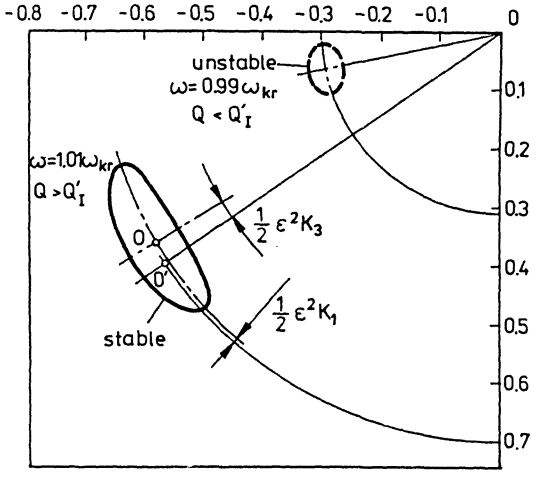

Fig.5 Exemplary limit cycles - stable and unstable

Conclusions

The theory of bifurcations is a powerful mathematical tool for the dynamical analysis of self-excited vibrations of rotors. It is also applicable in other systems exhibiting self-excitation (aeroflutter, vibrations of cutting tools etc.) In the considered rotor/bearing system the self-excited vibrations may occur in a large of static loads. There is no characteristic critical eccentricity as shown in some papers. The application of the bifurcation theory allowed to discover that the system can exhibit not only supercritical vibrations as usually reported but also subcritical ones and this corresponds to more dangerous loss stability. The type of bifurcation and its stability depends on all the system parameters and this depedance has been determined above. Formulae derived in this paper can be applied in CAD (dynamics-induced regional constraiints of parameters) as well as in diagnostics of rotating machinery (role of parameters in vibration).

References

1. Newkirk, B.L.; Taylor, H.D.: Shaft Whipping Due to Oil Action in Journal Bearings. Gen. Electr. Rev. 28 (1925) 559-568
2. Hori, Y.: A Theory of Oil Whip. Transactions of the ASME Journal of Applied Mechanics 26 (1959) 189-198.
3. Tondl, A.: Some Problems of Rotor Dynamics. London: Chapman and Hall 1965.
4. Hori, Y.; Malik, M.: An Approximate Nonlinear Transient Analysis of Journal Bearing in Unstable Region of Line- arized System. International Conf. on Rotordynamics Tokyo 1986.
5. Muszyńska, A.: Whril and Whip-Rotor/Bearing Stability Problems. Journal of Sound and Vibration 110 (1986) 443-462.
6. Hassard, B.D.; Kazarinoff, N.D.; Wan, Y.H.: Theory and Applications of Hopf Bifurcation. New York: Cambridge University Press 1981.
7. Iooss, G.; Joseph, D.D.: Elementary Stability and Bifurcation Theory. New York: Springer Verlag 1980.
8. Kurnik, W.: Bifurcating Self-Excitet Vibrations of a Horizontally Rotating Viscoelastic Shaft. Ingenieur-Archiv 57 ...(1987) 467-476.

Random Vibration of Hysteretic Systems

Y. K. LIN and G. Q. CAI

Center for Applied Stochastics Research
Florida Atlantic University
Boca Raton, FL 33431 USA

Summary

An approximation procedure is used to compute probability densities for the response variables of a hysteretic system under Gaussian white noise excitations. The excitations can be both additive and multiplicative. Accuracy of the procedure is substantiated by comparison with simulation results.

Governing Equations

We consider a single-degree-of-freedom system governed by

$$X'' + 2\zeta X' + [\alpha - \kappa - \eta(\tau)]X + (1 - \alpha)Z = \xi(\tau); \qquad 0 \leq \kappa < \alpha \leq 1 \tag{1}$$

where each prime denotes one differentiation with respect to a non-dimensional time τ, where ζ, α, and κ are constants, where $\eta(\tau)$ and $\xi(\tau)$ are Gaussian white noises, and where Z is a hysteretic restoring force. Various mathematical models for Z have been proposed. We shall use in our numerical examples the bilinear model, described by

$$Z' = \begin{cases} 0, & Z \ \mathrm{sgn} X' = 1 \\ X', & |Z| < 1 \end{cases} \tag{2}$$

and the Bouc-Wen model [1,2], described by

$$Z' = -\gamma |X'| Z |Z|^{n-1} - \beta X' |Z|^{n} + AX' \tag{3}$$

Physically, equation (1) may represent a simplified version of a beam-column subjected to a static axial load κ, a dynamic axial load $\eta(\tau)$ and a dynamic transverse load $\xi(\tau)$, all of which are suitably normalized and nondimensionalized. Our

W. Schiehlen (Editor)
Nonlinear Dynamics in Engineering Systems
IUTAM Symposium Stuttgart/Germany 1989

objective is to determine the probability densities of X and X', or other response variables related to X and X'.

Dissipation Energy Balancing

Exact probabilistic solution for equation (1) is not obtainable at the present time. An approximation scheme, developed recently for nonlinear but generally non-hysteretic systems [3] will now be adapted to treat hysteretic systems. In this scheme, the original system is substituted by another system which is solvable exactly. The exact solution of the substituting system is then taken as an approximate solution of the substituted system. The criterion for substitution is called "dissipation energy balancing" namely, the average dissipated energy remains the same for the two systems.

Consider

$$X'' + h(X,X') = f_i(X,X')W_i(\tau) \tag{4}$$

where $W_i(\tau)$ are Gaussian white noises, and

$$E[W_i(\tau)W_j(\tau + u)] = 2\pi K_{ij}\delta(\tau) \tag{5}$$

It can be shown that if

$$h(X,X') = \pi X' K_{ij} f_i f_j \phi'(\lambda) - \pi K_{ij} f_i \frac{\partial}{\partial X'} f_j + g(X) \tag{6}$$

then the response of the stochastic system (4) has an exact stationary probability density

$$p_s(X,X') = C \exp[-\phi(\lambda)] = \rho(\lambda) \tag{7}$$

where

$$\lambda = \frac{1}{2}(X')^2 + \int_o^X g(u)du = \frac{1}{2}(X')^2 + G(X) \tag{8}$$

in which case system (4) is said to belong to the class of generalized stationary potential [4]. Function g(X) in equation (6) represents the conservative spring force or "effective"

conservative spring force which does not dissipate energy. If (6) is not satisfied, then a substituting system with an exact solution (7) can be constructed by keeping the same g(X) function and the same terms on the right hand side of (4). An expression for $\phi'(\lambda)$ for such a system can be found by requiring

$$E\{X'h(X,X')\} = E\{X'[\pi X'K_{ij}f_if_j\phi'(\lambda) - \pi K_{ij}f_i\frac{\partial}{\partial X'}f_j]\} \quad (9)$$

where $E\{\ \}$ denotes the ensemble averaging, which can be carried out using $p_S(X,X')$ given in (7). Equation (9) implies that the average dissipated energy for the substituting system is the same as that of the original system (4).

It follows from (9),

$$\phi'(\lambda)=\frac{\int_{a_1(\lambda)}^{a_2(\lambda)}\{[h+\pi K_{ij}f_i\frac{\partial f_j}{\partial X'}]_{X'=b(\lambda,X)}-[h+\pi K_{ij}f_i\frac{\partial f_j}{\partial X'}]_{X'=-b(\lambda,X)}\}dX}{\pi\int_{a_1(\lambda)}^{a_2(\lambda)}\{[X'K_{ij}f_if_j]_{X'=b(\lambda,X)}-[X'K_{ij}f_if_j]_{X'=-b(\lambda,X)}\}dX} \quad (10)$$

where $a_1(\lambda)$ and $a_2(\lambda)$ are the two roots of the equation $G(a)=\lambda$, and $b(\lambda,X)=\sqrt{2\lambda-G(X)}$. Equation (11) is, in fact a stronger sufficient condition, requiring that dissipation energy balancing be satisfied for every energy level λ.

Application to Hysteretic Systems

For hysteretic systems, the h function in (10) is given by

$$h = 2\zeta X' + (\alpha-\kappa)X + (1-\alpha)Z \quad (11)$$

where the hysteretic component Z is described, e.g. by (2) or (3). For use in (10), Z must be expressed in terms of X and X'. Integration of (2) or (3) yields

$$Z = \begin{cases} g_1(X,\delta) & X' \geq 0 \\ g_2(X,\delta) & X' \leq 0 \end{cases} \quad (12)$$

where δ is an integration constant. If the excitation were deterministic and cyclic, g_1 would represent one half of the

hysteresis loop for increasing X, and g_2 would represent the other half for decreasing X, and each value of the integration constant δ would correspond to a given size of the hysteresis loop. Clearly, such a loop size would be determined uniquely by the level of the total energy λ. Thus, we can also write, instead of (12),

$$Z = \begin{cases} \tilde{g}_1(X,\lambda) & X' \geq 0 \\ \tilde{g}_2(X,\lambda) & X' \leq 0 \end{cases} \tag{13}$$

A larger λ is associated with a larger loop and a longer period. Under random excitations, λ becomes a random process. By allowing λ to be randomly varying with time, the system response is no longer cyclic. Equations (11) and (13) can now be substituted into (10). The integrations can be carried out either in closed forms or numerically.

In the special case where the constitutive law of the hysteretic system is symmetric, (11) can be simplified to

$$\phi'(\lambda) = \frac{2\zeta \int_{-a(\lambda)}^{a(\lambda)} \sqrt{2\lambda-2G(X)}\, dX + \frac{1}{2} A_r(\lambda)}{\pi \int_{-a(\lambda)}^{a(\lambda)} (K_{\xi\xi} + K_{\eta\eta}X^2)\sqrt{2\lambda-2G(X)}\, dX} \tag{14}$$

where $K_{\xi\xi}$ and $K_{\eta\eta}$ are spectral densities of $\xi(\tau)$ and $\eta(\tau)$ respectively, and $A_r(\lambda)$ is the area of the hysteresis loop representing the dissipated energy per cycle at an energy level λ, and where use is made of the fact that $a_2(\lambda) = -a_1(\lambda)$. The potential energy G(X) for a hysteretic system should be interpreted as the recoverable energy at a given X. For a bi-linear system [5]

$$G(X) = \begin{cases} \frac{1}{2}(1-\kappa)X^2 & a \leq 1 \\ \frac{1}{2}(\alpha-\kappa)X^2 + \frac{1}{2}(1-\alpha)(X+a-1)^2 & a \geq 1,\ -a \leq X \leq -a+2 \\ \frac{1}{2}(\alpha-\kappa)X^2 + \frac{1}{2}(1-\alpha) & a \geq 1,\ -a+2 \leq X \leq a \end{cases} \tag{15}$$

$$A_r = \begin{cases} 0 & a \leq 1 \\ 4(1-\alpha)(a-1) & a \geq 1 \end{cases} \tag{16}$$

For a smooth hysteresis given by (3) with n = A = 1 and $\beta = \gamma$,

$$G(X) = \begin{cases} \frac{1}{2}(\alpha-\kappa)X^2 + \frac{1}{2}(1-\alpha)(X+x_0)^2 & -a \leq X \leq -x_0 \\ \frac{1}{2}(\alpha-\kappa)X^2 + \frac{1}{8\gamma^2}(1-\alpha)[1-e^{-2\gamma(X+x_0)}]^2 & -x_0 \leq X \leq a \end{cases} \tag{17}$$

$$A_r = (1-\alpha)\left[\frac{2x_0}{\gamma} - (a-x_0)^2\right] \tag{18}$$

where x_0 is uniquely determined for a given amplitude a by solving $Z(\pm x_0) = 0$. See [6] for the case $\beta \neq \gamma$.

The probability densities for the energy level λ and the amplitude a, respectively, can be found readily from (7) and (14). Specifically,

$$p_S(\lambda) = 2\rho(\lambda) \int_{-a(\lambda)}^{a(\lambda)} \frac{dX}{\sqrt{2\lambda - 2G(X)}} \tag{19}$$

and

$$p_S(a) = 2 \mid g(a) \mid \rho[\lambda(a)] \int_{-a}^{a} \frac{dX}{\sqrt{2\lambda(a) - 2G(X)}} \tag{20}$$

As indicated, λ must be expressed in terms of the amplitude a in (20). It is of interest to note that for bilinear systems, g(a) and consequently $p_S(a)$ are discontinuous.

Numerical Examples

Computed stationary probability densities of the response amplitude are shown in Fig. 1 for the Bouc-Wen model with α = 0.1, representing a strongly hysteretic system. Two nondimensional quantities $D_\eta = \sqrt{2K_{\eta\eta}}$ and $D_\xi\sqrt{2K_{\xi\xi}}$ are introduced to represent the strengths of multiplicative and additive excitations. The presence of a multiplicative excitation

shifts the peak toward right, thus decreasing the distribution for lower amplitudes and increasing the distribution for higher amplitudes. However, these effects are significant only when the additive excitation is sufficiently strong. The general shape of the probability density depends primarily on the relative contribution of the hysteresis components and to a lesser degree on the additive excitation intensity. For the present case of strong hysteresis (α=0.1), the response amplitude is close to being Rayleigh distributed only if the additive excitation is either very weak (D_ξ=0.1) or very strong (D_ξ=5). In the intermediate range (D_ξ=0.5 and D_ξ=1) the amplitude distribution is far from Rayleigh, and in some cases it can have two peaks.

To assess the accuracy of the present approach, sample functions were digitally simulated for the wide-band excitation processes $\eta(\tau)$ and $\xi(\tau)$, and equations of motion were numerically integrated to obtain the corresponding sample functions of the response [5]. The root-mean-square (RMS) values computed from these response sample functions were then compared with those obtained from the theoretical probability densities. Excellent agreements were found between the theoretical and simulated results, as shown in Fig. 2 for the case of bi-linear systems. Also shown in Fig. 2 in dotted lines are the results obtained from the equivalent linearization procedure [7].

In the case of moderate hysteresis (α=0.5) the linearization results are in good agreement with those from simulation and from dissipation energy balancing, but in the case of nearly elasto-plastic systems (α=0.1) they deviate far from the simulation results in the range of intermediate additive excitations. Yet, it is in this range that hysteresis in the restoring force plays a dominate role. The large discrepancy is attributable to the assumptions in the linearization method that the response is of a narrow band, and that the response amplitude is approximately Rayleigh distributed.

Acknowledgement

The research reported herein has been supported by Contract No. NCEER 88-2007 under the auspices of the National Center for Earthquake Engineering Research under NSF Grant ECE-86-07591.

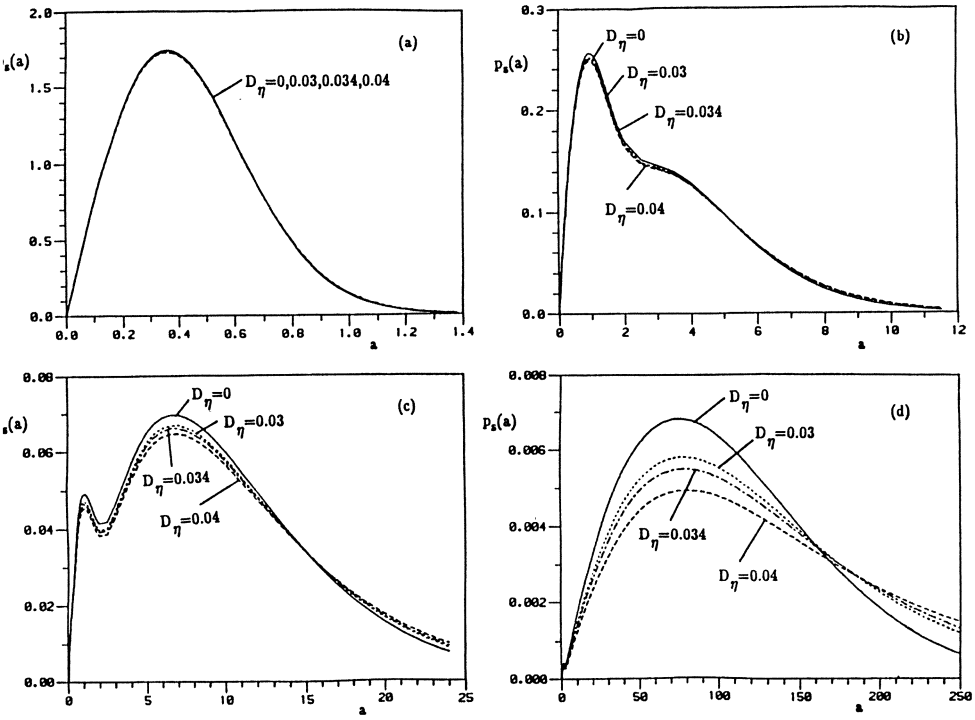

FIGURE 1 Stationary Probability Density of the Response Amplitude of a Smooth Hysteretic System with ζ = 0.025, κ = 0.04, γ = β = 0.5 and α = 0.1;
(a) Horizontal Excitation Spectral Level D_ξ = 0.1;
(b) Horizontal Excitation Spectral Level D_ξ = 0.5;
(c) Horizontal Excitation Spectral Level D_ξ = 1;
(d) Horizontal Excitation Spectral Level D_ξ = 5.

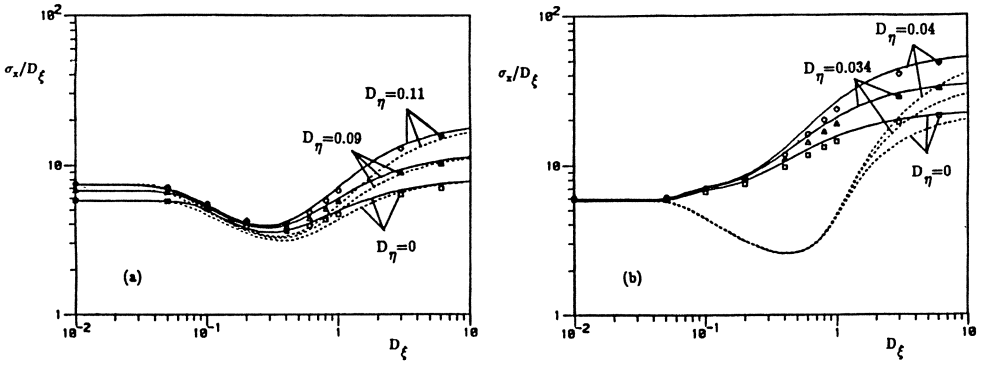

FIGURE 2 RMS Response of a Bi-Linear Hysteretic System with ζ = 0.025, κ = 0.04; (a) Moderate Hysteresis α = 0.5; (b) Strong Hysteresis α = 0.1. ——— Dissipation energy balancing, ----- Linearization; o Δ □ Simulations.

References

1. Bouc, B.: Forced vibration of mechanical system with hysteresis. Abstract, Proceedings of 4th Conference on Nonlinear Oscillation, Prague, Czechoslovakia, 1967.

2. Wen, Y. K.: Method for random vibration of hysteretic systems. Journal of Engineering Mechanics Division, 102, EM2 (1976) 249-263.

3. Cai, G. Q.; Lin, Y. K.: A new approximate solution technique for randomly excited nonlinear oscillators. Int. J. Non-Linear Mechanics. 23, No.5/6 (1988) 409-420.

4. Lin, Y. K.; Cai, G. Q.: Exact stationary-response solution for second order nonlinear systems under parametric and external white noise excitations - part II. J. Appl. Mechanics. 55 (1988) 702-705.

5. Cai, G.Q.; Lin, Y. K.: Hysteretic columns under random excitations. NCEER-89-003, National Center for Earthquake Engineering Reearch, State University of New York at Buffalo 1989.

6. Cai, G. Q.; Lin, Y. K.: A new solution technique for randomly excited hysteretic structures. NCEER-88-0012, National Center for Earthquake Engineering Research, State University of New York at Buffalo, 1988.

7. Iwan, W. D.; Lutes, L. D.: Response of the bilinear hysteretic system to stationary random excitation. J. Acoustic Society of America. 43 (1968) 542-552.

Spacial and Temporal Chaos in Elastic Continua

Francis C. Moon
Mechanical and Aerospace Engineering
Cornell University, Ithaca, New York, USA

Summary

Preliminary experiments on the interaction of nonlinear impact oscillators and linear elastic continua such as strings and elastic plates provide evidence for spacial complexity in the elastic medium akin to spacial chaos. These models may also be paradigms for understanding deterministic sources of machine noise.

Until recently most studies of chaos in elastic systems have assumed the existence of a low order attractor. These systems have generally been modelled as a projection onto one or two of the linear spacial modal functions. Thus these models have exhibited temporal chaotic dynamics with spacial coherence. In this report we explore the possibility of spacial dynamics in elastic continua such as strings and elastic plates. These studies have been mainly experimental. We hope these data on spacial complexity in solid mechanics will inspire theoreticians to explore the possibility of a kind of "spacial turbulence" in solid mechanics. In a recent paper, Thompson and Virgin (1988) have discussed the idea of spacial chaos in the static elastica. Similar work has appeared in reports by Meilke and Holmes (1988) at Cornell University. Computer studies of spacial complexity and temporal chaos in a chain of coupled oscillators have recently appeared by Crutchfield and Kaneko (1987) and Umberger, et al. (1989). However, experimental evidence of spacial chaos seems to be lacking at present.

Spacial Chaos in Structural Mechanics

A Simple Paradigm - Semi-Infinite Wave Guide

Consider a nonlinear oscillator consisting of a mass M_o connected to a nonlinear spring which is harmonically excited

W. Schiehlen (Editor)
Nonlinear Dynamics in Engineering Systems
IUTAM Symposium Stuttgart/Germany 1989

as shown in Figure 1. For many nonlinear springs, such as a cubic spring, or a two-well potential or a bilinear or trilinear spring, temporally chaotic motions W(t) can be found with positive Lyapunov exponent for given values of the forcing amplitude and frequency and initial conditions (see e.g., Moon 1987). Imagine now a semi-infinite wave guide connected to the mass in some benign way so that the vibration of the string has negligible effect on the chaotic motion of the mass.

If the motion of the string u(x,t) is assumed to satisfy the classical wave equation with speed c_o, then the string will admit right and left running wave solutions of the form

$$u(x,t) = f(x-c_o t) + g(x+c_o t)$$

If the wave guide is semi-infinite or is terminated in a characteristic impedance, then we can invoke a radiation condition and set $g(x+c_o t) = 0$. Thus, if the transducer between the string and mass is $u(o,t) = A\ W(t)$, then the motion of the string is given by

$$u(x,t) = A\ W(t-x/c_o)$$

Thus a chaotic motion in time $[W(t);\ t_o \le t \le t]$ is stored spacially in $[u(x,t);\ 0 \le x \le c_o(t-t_o)]$

This suggests that a Lyapunov exponent in space can be approximated by a calculation in the phase space with coordinates $(u, \frac{\partial u}{\partial x}, x)$ for a given time $t >> t_o$.

If the string is pinned at x = L, then right running waves will be reflected as left running waves with negative amplitude. Thus, if the chaotic information is stored in a finite string, the phase space may be imagined as folded an infinite number of times. Conceptually, we could still calculate a Lyapunov function in space, but one would have to keep track of the thousands of reflections. Practically, however, one only has the sum of all these left and right waves, so it becomes

difficult to define a Lyapunov function for spacial chaos, but the idea appears to be analogous to that of temporal chaos.

If the wave guide is dispersive, i.e., the wave speed depends on the frequency, the chaotic temporal history W(t) will be distorted in space, but one still expects a "chaotic" spacial pattern in the space $(u, \frac{\partial u}{\partial x}, x)$.

Thus, in problems in which a nonlinear descrete system is coupled to a linear hyperbolic system, one should expect to find spacial as well as temporal chaos. Since small disturbances in solids travel with finite speeds, one should expect to see spacial chaos in strings, beams, plates and shells when they interact with discrete nonlinear oscillators. One would expect to see spacial complexity in such systems when the excitation period is smaller than the wave transit time for the finite wave system.

Chaos in the String or Elastic Cable

The simplest elastic continuum is the string. In experiments at Cornell (Moon and O'Reilly, 1989) we have looked at nonlinear boundary conditions as well as large deformations in the forced vibrations. In one set of experiments we looked at the effect of displacement limiting stops on the vibration as the amplitude is increased as shown in Figure 2.

The experiments were carried out near the natural linear frequencies with sinusoidal excitation. When the string began to hit the stops, the classical modal spacial pattern was destroyed, as shown by the disappearance of the node. The dynamics had the appearance of traveling waves rather than standing waves and the modal pattern or zero displacement points disappeared. We have attempted to look at the cross corrrelation function between different points along the string using two optical measuring cameras. Also, quasi-periodic vibrations are often a precursor to the chaotic motions. The region of chaotic dynamics is shown in Figure 3.

Chaotic Vibrations in Elastic Plates - Paper Chaos

As mentioned above there has been discussion on the existence of spacial chaos in the classical elastica. One can also look into whether complex spacial patterns can be observed in a two-dimensional elastica. By this we mean a very thin plate which can undergo very large deformations. In this work we have performed some preliminary experiments on paper and steel plates and have observed broadband vibration output with a sinusoidal excitation. This problem may have application to xerographic and computer printing technology in which paper must be moved and deformed simultaneously.

In this experiment a sheet of paper was supported on one edge and allowed to statically deform under gravity in the shape of an elastica as shown in Figure 4. When attempts were made to find natural frequencies of the paper plate with an electromagnetic shaker, no clear resonances were found, due perhaps to the large fluid (air) damping. At sufficiently large amplitudes, however, broadband chaotic motions could be observed with wave-like motions moving from the shaker edge to the free edge. This work is still in progress.

Chaotic Interaction of an Impact Oscillator and a Thin Circular Plate

In another study conducted at the Technische Hochschule Darmstadt (Moon and Brochart, 1989), the interaction of a periodically excited bouncing mass impacting a circular aluminum plate 0.5 meter in diameter was examined as shown in Figure 5. When the mass was excited into chaotic motions such that it hit the plate, accelerometers were used to measure the cross correlation between vibrations at the plate center and those at various radii from the plate edge. The correlation time was found to decrease as one moved away from the plate center indicating a loss of coherence between points at different motions in the plate (Figure 6).

These experiments suggest that machine noise generated by the relative motion of machine parts such as gears, bearings, etc., may be subject to analysis based on deterministic models for chaos.

References

1. Crutchfield, J.P.; Kaneko, K.: "Phenomenology of Spacial-Temporal Chaos," *Directions in Chaos*, Vol. 1, Hao Bai-lin (ed.) World Scientific Publishers 1987, 272-353.

2. Meilke, A.; Holmes, P.J.: Archive for Rational Mech. & Anal., No. 4, (1988).

3. Moon, F.C.: *Chaotic Vibrations*. New York: J. Wiley & Sons, 1987.

4. Moon, F.C.; O'Reilly, O.: "Chaotic dynamics and spacial complexity in a string with nonlinear boundary conditions." Cornell University Report, Mechanical and Aerospace Engineering, August 1989.

5. Moon, F.C.; Brochart, T.: "Chaotic Sources of Noise in Machine Acoustics." Technical Report of the Technische Hochschule Darmstadt, 18, August 1989.

6. Thompson, J.M.T.; Virgin, L.M.: "Spatial Chaos and Localization Phenomena in Nonlinear Elasticity," Physics Letters A **126**, (1988).

7. Umberger, D.K.; Grebogi, C.; Ott, E.; Afeyan, B.: "Spatiotemporal dynamics in a dispersively coupled chain of nonlinear oscillators," Physical Review A **39** (1939) 4835-4842.

Acknowledgements

The author acknowledges the contributions of O. O'Reilly and W. Holmes of Cornell University, as well as T. Brochart of Technische Hochschule Darmstadt. The author wishes to thank Professor F. Kollmann for the use of his laboratory at Technische Hochschule Darmstadt, F.R.G. as well as support from the Humboldt Foundation of F.R.G., and IBM Corporation.

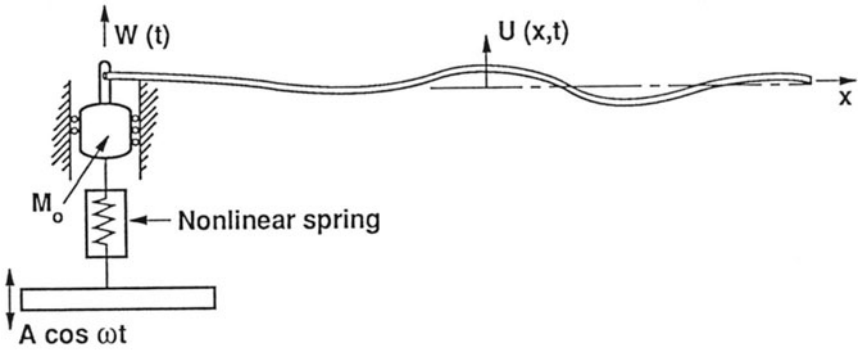

Figure 1. Sketch of Nonlinear oscillator and linear wave system.

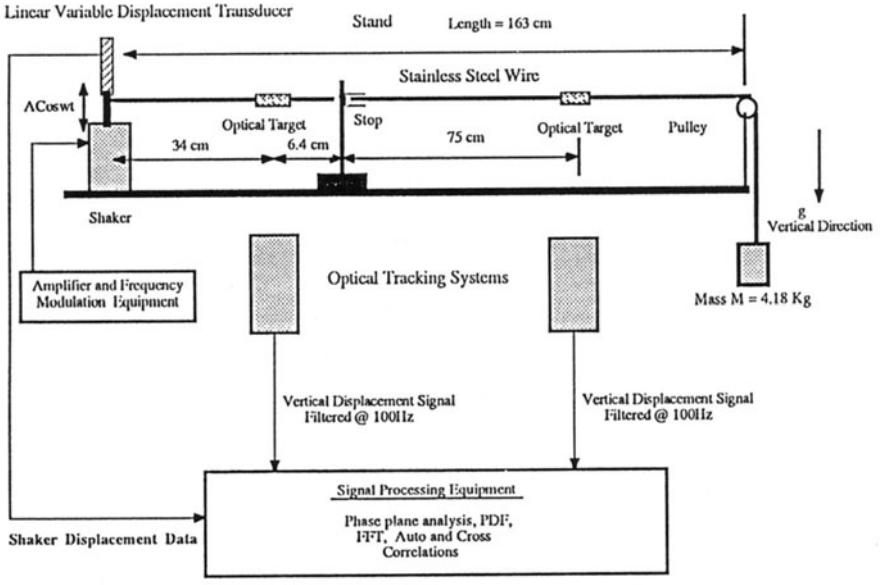

Figure 2. Diagram showing apparatus for studying chaotic vibrations of a string with motion limiting stops.

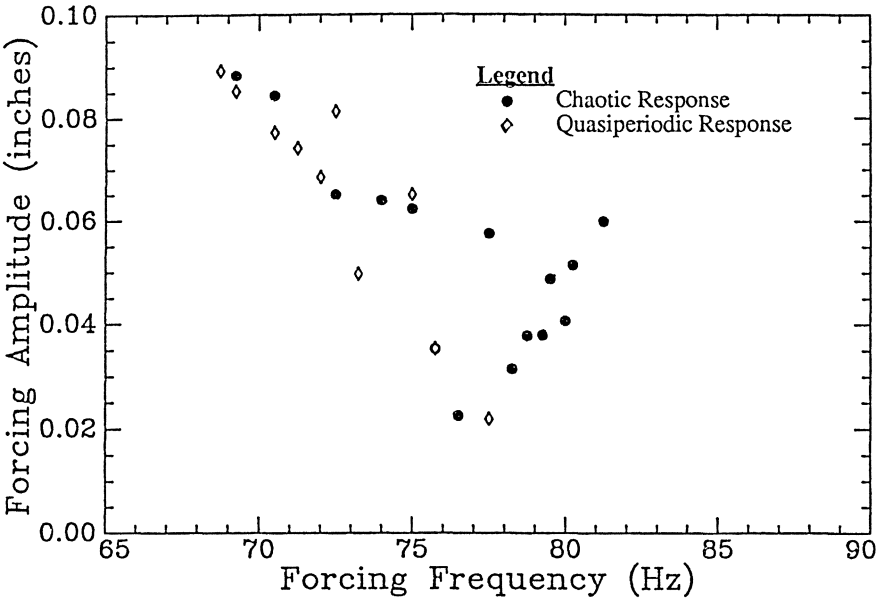

Figure 3. Diagram showing regions of chaotic and quasi-periodic motions for the vibrating string with motion constraints. Data taken near the second natural frequency of the string.

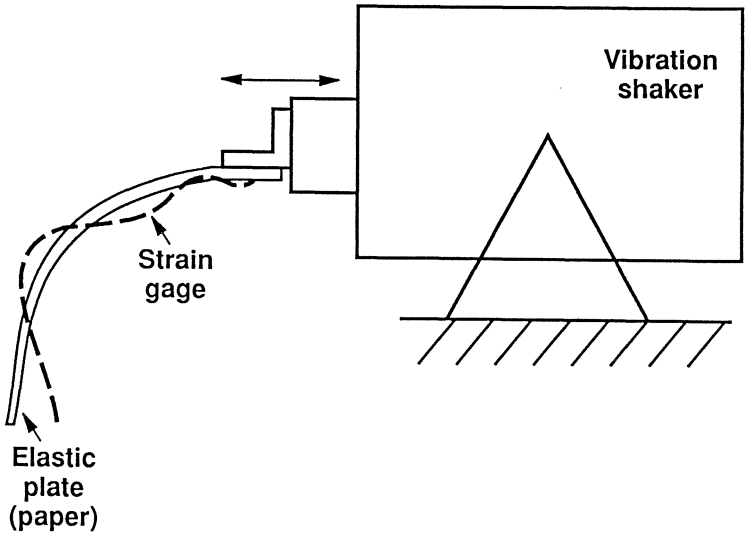

Figure 4. Sketch of apparatus to study chaotic dynamics in a paper plate bent in the shape of the elastica.

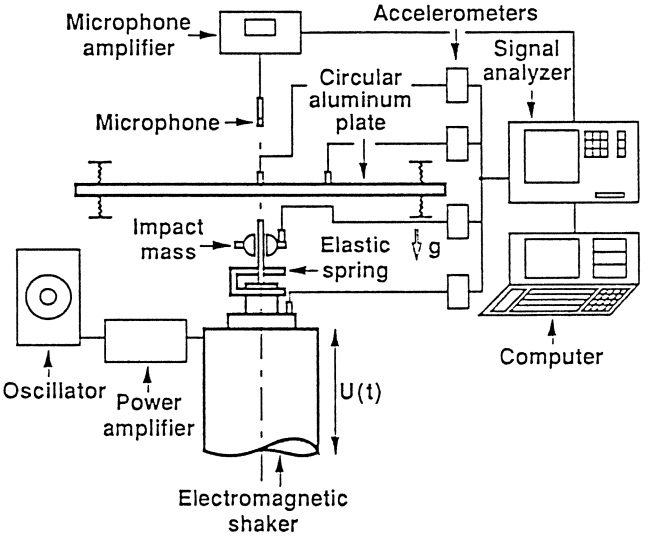

Figure 5. Diagram showing apparatus to study the chaotic interaction of an impact oscillator and a circular aluminum plate.

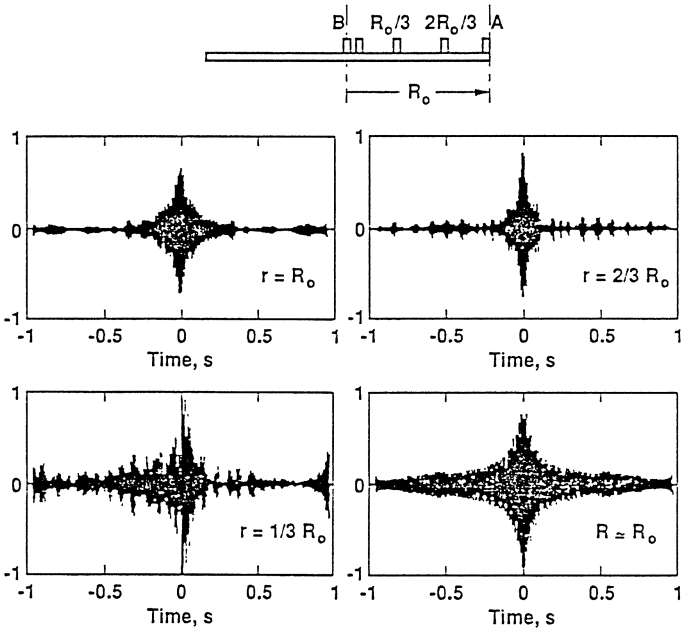

Figure 6. Cross correlation functions for chaotic motions in a circular plate between motions at the center B, and motions at points A along radius.

Indirect Measurement of Nonlinear Effects by State Observers

P. C. MÜLLER

Safety Control Engineering
University of Wuppertal
D-5600 Wuppertal 1, FRG

Summary

Vibration and control systems are often influenced by troublesome nonlinear effects such as Coulomb friction, backlash, or hysteresis. In this contribution an indirect measuring technique of the actual values of those nonlinearities is presented. Based on a fictitious model of the time behaviour of the nonlinearities a state observer of an extended dynamical system is designed resulting in estimates of the nonlinear effects. In the paper the theory of this approach, an illustrative example, and a practical application in the position control of robots are considered. The proposed method is a successful tool to register indirectly the nonlinear effects of vibration and control systems.

Introduction and Problem Statement

Vibration and control systems are often influenced by troublesome nonlinear effects such as Coulomb friction, backlash, or hysteresis. For the analysis and design of those systems certain informations on the nonlinear characteristics are required. Sometimes preceding off-line measurements are available, but often direct measurements of the nonlinearities are not possible. Particularly, the change of the nonlinear characteristics under changes of operating conditions usually cannot be measured directly.

In this contribution an indirect measuring technique of actual values of nonlinear effects is presented. Based on a fictitious model of the time behaviour of the nonlinearities a state observer of an extended dynamical system is designed resulting in estimates of the actual nonlinearities. Due to the theory of estimating unknown disturbances of a control system simple measurements of displacements or velocities of the vibration system are used to reconstruct additional time signals

W. Schiehlen (Editor)
Nonlinear Dynamics in Engineering Systems
IUTAM Symposium Stuttgart/Germany 1989

by a state observer to obtain estimates of the nonlinear effects. According to the above-mentioned fictitious model of the nonlinearities the state observer is based on the linear part of the vibration system and the linear fictitious model. In spite of this linear model, generally good estimates of the nonlinearities are obtained.

To be more precise the problem is defined in mathematical terms. Applying state space notation, the vibration or control system under consideration is described by

$$\dot{x}(t) = A\,x(t) + N\,n\,(x(t)) + b(t) \quad , \tag{1}$$

$$y(t) = C\,x(t) \quad . \tag{2}$$

Here x denotes the n-dimensional state vector (consisting of displacement and velocity variables in case of a mechanical vibration system), n(x) characterizes the f-dimensional vector of nonlinear functions, A is the n x n-matrix characterizing the linear dynamic behaviour, the n x f-matrix N can be interpreted as an input matrix of the nonlinearities into the dynamic system, and b(t) denotes the n-dimensional vector of control inputs and/or excitation functions. Additionally, y represents the m-dimensional vector of (linear) measurements of the system characterized by an m x n-matrix C. To avoid redundant formulations it is assumed

$$\text{rank } N = f, \quad \text{rank } C = m \quad . \tag{3}$$

Now, the problem of indirect measurements of the nonlinear effects can be stated as follows. Assuming that the system parameters as well as the input and output time signals are known,

$$(A, N, C) \quad , \quad (b(t), y(t)) \quad \text{are known} \quad , \tag{4}$$

then it is the object of the procedure presented here to reconstruct the unknown nonlinearities n(x(t)) by certain estimates applying state observers:

$$n(x(t) \quad \approx \quad \hat{n}(\hat{x}(t)) \quad . \tag{5}$$

The paper is organized as follows. The general theory will be presented in section 2. In section 3 a simple example illustrates the procedure. Section 4 is related to a practical application of the proposed method to the compensation of Coulomb

friction in the position control of industrial robots. Finally, the concluding section 5 will give some hints at further research work.

General Theory

According to the theory of disturbance rejection control, cf. the surveys by Müller and Lückel [1,2], the time signals of the nonlinearities are interpreted as "external disturbances" which can be characterized by a suitable fictitious model:

$$n(x(t)) \approx H\, v(t) \quad , \tag{6}$$

$$\dot{v}(t) = F\, v(t) \quad . \tag{7}$$

The approximation (6,7) may be regarded as a model of the interactions of the nonlinearities acting from "outside" to the linear subsystem. It may be also considered as an approximate aggregation of the signals of the linear subsystem deformed by the nonlinearities. Therefore, usually the model (6,7) will be chosen as a reduced order model of these deformed signals. In practical applications the engineer will know, how the dominant time behaviour of the dynamical system (1) will be. Then the model matrices (F, H) are chosen with respect to this technical background of the problem.

The estimation of the time behaviour of the nonlinearities is based on their substitution by the model (6,7):

$$\begin{bmatrix} \dot{x}(t) \\ \dot{v}(t) \end{bmatrix} = \begin{bmatrix} A & NH \\ 0 & F \end{bmatrix} \begin{bmatrix} x(t) \\ v(t) \end{bmatrix} + \begin{bmatrix} b(t) \\ 0 \end{bmatrix} , \tag{8}$$

$$y(t) = \begin{bmatrix} C & 0 \end{bmatrix} \begin{bmatrix} x(t) \\ v(t) \end{bmatrix} . \tag{9}$$

For this fictitious system the estimation of the states x and the "disturbances" v has to be considered. This will be performed by a state observer which is a commonly used tool in control theory, cf. [3,4]. The observer essentially consists of a simulated model with a correction feedback of the estimation error between real and simulated measurements. If for simplicity an identity observer is used, the observer is gouverned by the equation

$$\begin{bmatrix} \dot{\hat{x}} \\ \dot{\hat{v}} \end{bmatrix} = \begin{bmatrix} A & NH \\ 0 & F \end{bmatrix} \begin{bmatrix} \hat{x} \\ \hat{v} \end{bmatrix} + \begin{bmatrix} b \\ 0 \end{bmatrix} + \begin{bmatrix} L_x \\ L_v \end{bmatrix} (y - \hat{y}) \quad , \tag{10}$$

$$= \underbrace{\begin{bmatrix} A-L_xC & NH \\ -L_vC & F \end{bmatrix}}_{A_e} \begin{bmatrix} \hat{x} \\ \hat{v} \end{bmatrix} + \begin{bmatrix} b \\ 0 \end{bmatrix} + \begin{bmatrix} L_x \\ L_v \end{bmatrix} y \quad . \tag{11}$$

The asymptotic stability of the observer can be guaranteed by a suitable design of the gain matrices L_x, L_v if the system (8,9) is completely observable, cf. [3,4]. The observability of the extended system (8,9) depends on the choice of the fictitious model (6,7). To avoid any sensitivity of the observability with respect to the chosen model (6,7) the condition

$$\text{rank} \begin{bmatrix} \lambda I - A & N \\ C & 0 \end{bmatrix} = n + f \tag{12}$$

has to be satisfied for all complex numbers λ, cf. [1,2] (I denotes the identity matrix). This requires $m \geq f$, i. e. the number of nonlinearities must not be larger than the numbers of measurements.

Using the asymptotically stable observer (10,11) the reconstruction of the time signals of the nonlinearities is given by

$$\hat{n}(\hat{x}(t)) = H\hat{v}(t) \quad . \tag{13}$$

If one is interested in the characteristics of the nonlinearities then additional informations are required about the structural dependences of n on x. If this à priori information is available the reconstruction of the nonlinear characteristics is determined by

$$\hat{n}(\hat{x}) = H\hat{v}\,\big|_{\text{related to } \hat{x}} \quad . \tag{14}$$

Even though the observer (10,11) is asymptotically stable the estimates (13,14) may not converge to the true values of the real nonlinearities. To guarantee convergence additional sufficient conditions have to be established. For this, the differential equations of the estimation errors are considered. Introducing the estimation errors

$$e_x(t) = \hat{x}(t) - x(t) \quad , \tag{15}$$

$$e_v(t) = \hat{v}(t) - v(t) \quad , \tag{16}$$

$$e_n(t) = H\, v(t) - n(x(t)) \tag{17}$$

and the abbreviations

$$e(t) = \begin{bmatrix} e_x(t) \\ e_v(t) \end{bmatrix} \quad , \quad N_e = \begin{bmatrix} N \\ 0 \end{bmatrix} \tag{18}$$

the estimation error equation

$$\dot{e}(t) = A_e\, e(t) + N_e\, e_n(t) \tag{19}$$

is derived. If the asymptotic stability of (19) can be assured then the reconstructed signals (13,14) will converge to the true nonlinearities. These design requirements will be sufficiently satisfied by two steps. Firstly, the observer (10,11) has to be asymptotically stable, as mentioned above. This is a common design problem in the theory of state observers; a lot of procedures is available such as pole assignment or filter theory. The author recommends the design of optimal observers according to the requirement

$$\int_0^\infty E\{ e^T(t)\, e(t) \}\, dt \rightarrow \text{minimum} \tag{20}$$

where it is assumed that the initial conditions x_0, v_0 are normally distributed with zero mean and a certain covariance matrix (for details cf. [5,6]).

Secondly, the influence of the error $e_n(t)$ must not cancel out asymptotic stability of (19). For this, the inequality of Bellman and Gronwall or Lyapunov's direct method can be applied to estimate a bound for the accuracy of the model (6,7), cf. [7]. If the error $e_n(t)$ satisfies

$$\| e_n(t) \| \leq k \| e(t) \| \tag{21}$$

for a sufficiently small constant k, then the error system (19) is asymptotically stable. The constant k can be estimated. If

$$\| \exp(A_e t) \| \leq c\, e^{-ht} \quad , \quad \| N_e \| \leq n_e \tag{22}$$

then

$$k < \frac{h}{c n_e} \tag{23}$$

is obtained by the Bellman-Gronwall inequality. Another bound can be derived by using the Lyapunov function $V(x_e) = x_e^T P_e x_e$ where P_e and Q_e are positive definite matrices satisfying the Lyapunov matrix equation

$$A_e^T P_e + P_e A_e = -Q_e \quad . \tag{24}$$

The derivative of $V(x_e)$ for the differential equation (19) still remains negative definite as long as

$$k < \frac{q}{2 s} \tag{25}$$

where q is the smallest eigenvalue of Q_e and s is the largest singular value of $P_e N_e$. Therefore, if the fictitious model (6, 7) is suitably chosen, and if the system (8, 9) is completely observable, then the observer (10, 11) leads to good estimates (13, 14) of the nonlinear effects.

Illustrative Example

The example consists of a simple 1-dof vibration system including Coulomb friction:

$$\ddot{z}(t) + f(\dot{z}(t)) + z(t) = a \cos \omega t \tag{26}$$

where

$$f(\dot{z}) = \begin{cases} \operatorname{sgn} \dot{z} \ , & \dot{z} \neq 0 \ , \\ \operatorname{sgn} f_s \ , & \dot{z} = 0 \ , \quad |f_s| > 1 \ , \\ f_s \ , & \dot{z} = 0 \ , \quad |f_s| < 1 \end{cases} \tag{27}$$

with the reaction force f_S in case of stick friction. The measurement is assumed to be

$$y(t) = z(t) \quad . \tag{28}$$

In this case, all steps of the method can be evaluated analytically. The condition (12) of robust observability is satisfied.

According to the proposed method the choice of the fictitious model (6, 7) has to be effected. Because of (27) the time signal of the nonlinearity can be considered as piecewise constant leading to

$$f(z) \approx v \quad , \quad \dot{v} = 0 \quad , \quad \text{i. e.} \quad H_1 = 1 \quad , \quad F_1 = 0 \quad . \tag{29}$$

But in the case of stick friction the reaction force will also include a harmonical signal with frequency ω. Therefore, another fictitious model makes sense, too:

$$f(z) = v_1 + v_2 \quad , \quad \dot{v}_1 = 0 \quad , \quad \ddot{v}_2 + \omega^2 v_2 = 0 \quad ,$$

$$\text{i. e. } H_2 = [1 \;\; 1 \;\; 0] \quad , \quad F_2 = \begin{bmatrix} 0 & 0 & 0 \\ 0 & 0 & 1 \\ 0 & -\omega^2 & 0 \end{bmatrix} \quad . \tag{30}$$

Using the first fictitious model the observer (11) is easily written as

$$\begin{bmatrix} \dot{\hat{z}} \\ \dot{\hat{z}} \\ \dot{\hat{v}} \end{bmatrix} = \begin{bmatrix} -l_1 & 1 & 0 \\ -1-l_2 & 0 & -1 \\ -l_3 & 0 & 0 \end{bmatrix} \begin{bmatrix} \hat{z} \\ \hat{z} \\ \hat{v} \end{bmatrix} + \begin{bmatrix} 0 \\ a\cos\omega t \\ 0 \end{bmatrix} + \begin{bmatrix} l_1 \\ l_2 \\ l_3 \end{bmatrix} y \tag{31}$$

with the observer gains l_1, l_2, l_3. The characteristic polynomial of the system matrix A_e of (31) reads

$$p(\lambda) = \det(\lambda I - A_e) = \lambda^3 + l_1 \lambda^2 + (1+l_2)\lambda - l_3 \tag{32}$$

such that the procedure of pole assignment can be easily applied to design the observer.

The reconstruction of the characteristic (27) by an estimated signal is performed according

$$f(\dot{z}) \approx \hat{x}_3(\hat{x}_2) = \hat{v}(\hat{z}) \,. \tag{33}$$

In the following figures typical results are shown for different values of the observer gains. Always an amplitude of a = 1.5 and frequencies $\omega_1 = 0.3$ or $\omega_2 = 1.25$ of the excitation are assumed. Fig. 1 shows the reconstruction of the characteristic of the nonlinearity (27) by an observer (31) with small observer gains. Obviously the observer is designed too slow such that an essential phase shifting of the estimates appears. If the observer gains are increased leading to a much faster observer the reconstruction matches the characteristic (27) very well as shown in Fig. 2. The influence of the excitation frequency ω is also demonstrated. The observer design must be related to this excitation signal too, although the error dynamics (19) are independent on it.

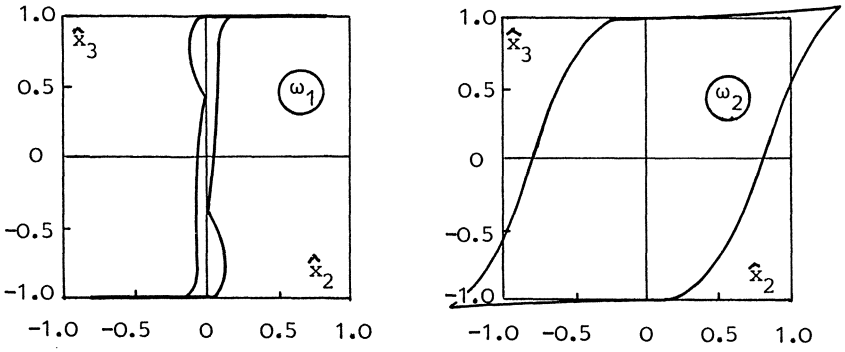

Fig. 1. Characteristic of nonlinearity (27) reconstructed by (33) with observer gains l_1=24.6, l_2=101, l_3=- 200 using model (29)

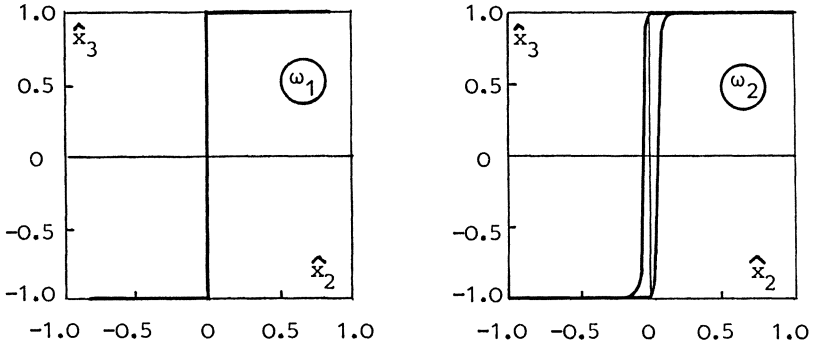

Fig.2. Characteristic of nonlinearity (27) reconstructed by (33) with observer gains l_1=280, l_2=17599, l_3=-320000 using model (29)

In Fig. 3 a result is shown in the case of the second fictitious model (30) requiring an observer with 5 gains. While the reconstruction is very convincing in the case of the frequency ω_1, in the case of the frequency ω_2 a large overshooting for very small velocities is observed. To overcome these undesired peaks the observer has to be designed aperiodically.

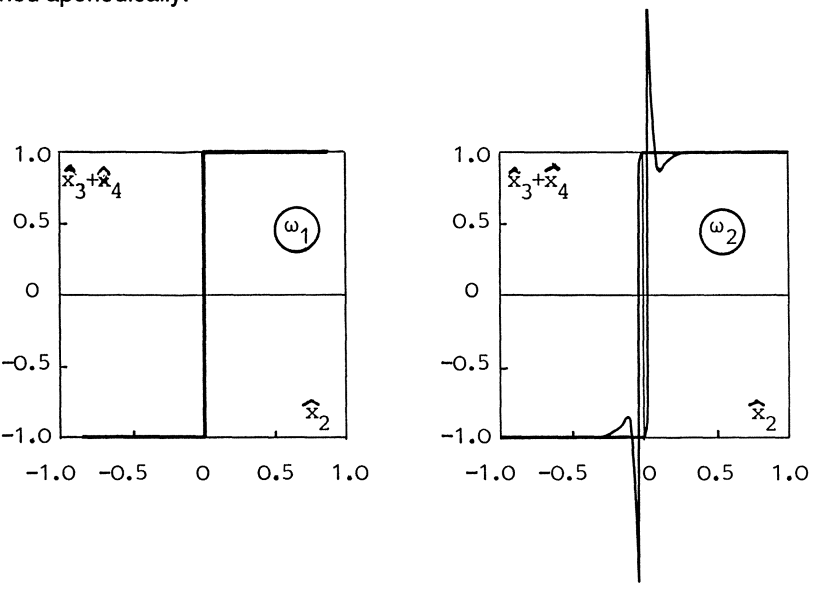

Fig. 3. Characteristic of nonlinearity (27) reconstructed by (33) with observer gains l_1=360, l_2=41599, l_3=-1/ω^2 512 · 10^6, l_4=-2175800 + 1/ω^2 512 · 10^6, l_5=-53719400 using model (30)

This simple example illustrates very well the applicability of the proposed method to reconstruct nonlinear effects. But the quality of the indirect measurement depend strongly on the choice of the fictitious model as well as on the design of the observer.

Application

The proposed method of indirect measurement of nonlinear effects was successfully applied to design a highly accurate position control of an elastic industrial robot which is effected by nonlinear Coulomb friction within the electric drives. Conventional control algorithms yield steady-state inaccuracy, untimely stops of the motion or limit cycles depending on the type of controller. Therefore, a linear feedback control system was designed by Ackermann und Müller [8 - 10] applying

disturbance rejection control technique. By this design method the effects of Coulomb friction are compensated. Coulomb friction depends on velocity, actuating force and normal pressure. Additionally there are two different regions of operation: there are sliding and sticking modes dependent on the ratio of friction due to normal pressure and actuating force. Although the nonlinear characteristic of the multi-valued function of friction is very complicated, the simple model (29) of piecewise constant functions was used to model approximately the time signals of the Coulomb friction. The reconstruction of these signals was realized by a reduced-order functional observer instead of an identity observer (10, 11) to keep the amount of calculation and hardware realization low. Therefore, direct measurements of Coulomb friction are not necessary and the load depending friction is also reconstructed automatically. Due to the fast dynamic behaviour of the observer the friction could be estimated very fast. These estimates could be used to counteract the Coulomb friction, i.e. to compensate the effects of Coulomb friction, using the theory of rejection control. This rejection control algorithm was tested under real conditions at an experimental robot with three rotational degrees of freedom showing the efficiency of the proposed method of indirect measurement and of the designed control. Untimely stops (due to sticking) or limit cycles are completely avoided. The new position control of the elastic industrial robot is faster and more accurate than conventional control and the robot dynamics are considerably improved. The details of all theoretical and experimental investigations are found in the report of Ackermann [10].

Conclusion

In this contribution it was proved that the theory of state observers permits to reconstruct nonlinear characteristics in vibration and control systems. The proposed method is a successful tool to measure indirectly unknown nonlinear effects. An essential advantage of this method is its adaptation to changes of the nonlinearities during operation. E.g. the dependence of friction on load and temperature is automatically included in the reconstructed signals. Although the convergence properties have been shown, the successful application of the proposed procedure depend essentially on the suitable choice of a fictitious model (6, 7) of the time behaviour of the nonlinearities and on a good design of the state observer (10, 11). Here are still open research problems to improve the proposed method. If the procedure converges then good estimates (13) of the time signals of the nonlinearities are obtained. To get additionally good estimates (14) of the nonlinear characteristics, actually the à priori information of the dependence of the

nonlinearities on the state variables is required. It would be valuable to generalize the proposed method to reconstruct the nonlinear functions without this knowledge on the structural dependence.

References

1. Müller P.C.; Lückel, J.: Zur Theorie der Störgrößenaufschaltung in linearen Mehrgrößenregelungssystemen. Regelungstechnik 25 (1977) 54-59.

2. Müller P.C.; Lückel, J.: Optimal multivariable feedback system design with disturbance rejection. J. Problems of Control and Information Theory 6 (1977) 211-227.

3. Luenberger, D.G.: An introduction to observers. IEEE Transact. Automatic Control AC-16 (1971) 596-602.

4. Ackermann J.: Einführung in die Theorie der Beobachter. Regelungstechnik 24 (1976) 217-226.

5. Müller, P.C.; Truckenbrodt, A.: Entwurf eines optimalen Beobachters. Regelungstechnik 25 (1977) 381-387.

6. Müller, P.C.: Design of optimal state-observers and its application to maglev vehicle suspension control. Proc. 4the Int. IFAC Symposium on Mulitvariable Technological Systems, Fredericton/Canada, 4-8 July 1977, Paper No. 25 (revised version).

7. Cesari, L.: Asymptotic behavior and stability problems in ordinary differential equations, 2nd ed. Berlin, Heidelberg, New York: Springer-Verlag 1963.

8. Ackermann, J.; Müller, P.C.: Dynamical behaviour of nonlinear multibody systems due to Coulomb friction and backlash. Preprints IFAC/IFIP/IMACS Int. Symp. Theory of Robots. Wien, Austria, 3-5 Dec. 1986, Austrian Center for Productivity and Efficiency, Wien 1986, 289-294.

9. Müller. P.C.: Compensation of Coulomb friction in the position control of industrial robots. In: Hiller, M; Sorg, H. (eds.): Proc. 3rd German-Japanese Seminar on Nonlinear Problems in Dynamical Systems - Theory and Applications; University of Stuttgart 1987, 13.0-13.11.

10. Ackermann, J.: Positionsregelung reibungsbehafteter elastischer Industrieroboter. VDI-Fortschr.-Ber. Reihe 8, Nr. 180, Düsseldorf 1989.

Chaotic Motion in Nonlinear System with Coulomb Damping

S.Narayanan and K.Jayaraman*
Department of Applied Mechanics
Indian Institute of Technology,Madras,600 036,India

Summary

Chaotic motion of a harmonically excited nonlinear system with Coulomb damping is investigated in a range of excitation frequencies.Phase plane diagrams,Poincare'maps,time histories and power spectral densities are obtained and Lyapunov exponents are computed.Period doubling route to chaos is observed in certain frequency ranges which is explained using harmonic balance analysis.The stability of the strange attractors with respect to initial conditions is investigated by interpolated cell mapping technique.

Introduction

In recent years, the study of chaos in nonlinear dynamical systems has emerged as a very active area of research in physics, mathematics and engineering. Chaos may be described as a bounded,aperiodic random like motion exhibited by deterministic nonlinear systems characterized by its sensitivity to initial conditions. Classical studies of nonlinear oscillators mainly concern with the stability and domains of attraction of steady state solutions corresponding to equilibrium points,periodic and quasiperiodic motions, which when stable are associated respectively with point, limit cycle and torus attractors having simple geometric structures. Chaos, on the other hand represents a strikingly different type of steady state behaviour associated with strange attractor having no such simple geometric structure. Not all nonlinear systems exhibit chaos, nor does chaos occur for all combinations of system parameters and initial conditions for a given nonlinear system. Indeed, no general conditions have been clearly established as yet to apriori identify chaos for a given set of parameters and initial conditions.Mostly, chaotic motion is identified by numerical simulation of system responses and inspection of phase plane plots, which are of complicated pattern, Poincare' maps which show strange attractors and time histories which are aperiodic. Chaos is also characterized by positive Lyapunov exponents, continuous power spectra and fractal dimensions.

Most of the work in the area of chaos in mechanical systems is on the Duffing's oscillator with linear viscous damping.The dissipation mechanism in a large class of problems is of the dry friction type. Awrejcewicz[1]

* Presently at Department of Aeronautical Engineering, MIT, Madras 44

W. Schiehlen (Editor)
Nonlinear Dynamics in Engineering Systems
IUTAM Symposium Stuttgart/Germany 1989

has briefly reported chaotic motion in a nonlinear system with Coulomb damping.The present paper presents a detailed analysis of chaos in a harmonically excited nonlinear oscillator with cubic stiffness and damping terms as well as Coulomb damping.Chaos is observed in a range of exciting frequencies.The phase plane plots and the Poincare' maps which show strange attractors are varied in appearance in the different frequency ranges.In certain frequency ranges the route to chaos is through period doubling. A harmonic balance analysis is carried out on the lines of Szemplinska Stupnika[2] to determine regions of subharmonic motion and relate the same to the period doubling sequence.Lyapunov exponents and power spectra are computed. An interpolated cell mapping technique[3] is used to investigate the stability of strange attractors with respect to initial conditions.

Equation of Motion

Figure 1 shows a single degree of freedom mass m with displcement x sliding relatively with respect to the belt moving with velocity v. The mass is assumed to be supported by a spring with linear stiffness k_1 and cubic stiffness k_2 and a damper with cubic damping coefficient c_2 and a negative linear damping coefficient c_1. Dry friction is also present between the mass and the belt with friction coefficient μ. The mass is subjected to harmonic excitation of amplitude P_0 and frequency ω. The equation of motion of the mass is given by

$$m\ddot{x}+c_2(\dot{x}-v)^3-c_1(\dot{x}-v)+k_1x+k_2x^3+mg\mu\ \mathrm{sgn}(\dot{x}-v)=P_0\cos\omega t \qquad (1)$$

where g is the acceleration due to gravity.

Equation (1) can be expressed as

$$\dot{x}_1= x_2 \qquad (2)$$

$$\dot{x}_2= -g\{\mu\ \mathrm{sgn}(x_2-v)-\alpha(x_2-v)+\beta(x_2-v)^3\}-\gamma_1x_1-\gamma_2x_1^3+F_0\cos\omega t \qquad (3)$$

with $\alpha = c_1/(mg)$, $\beta = c_2/(mg)$, $\gamma_1 = k_1/m$, $\gamma_2 = k_2/m$, $F_0 = P_0/m$, and $x_1 = x$.

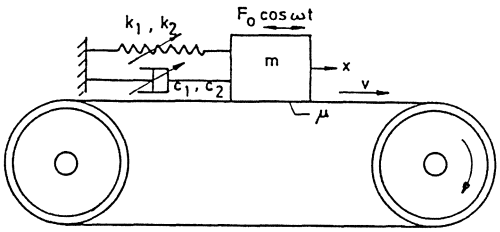

Fig.1 Nonlinear Oscillator on a moving belt

Phase Plane Plots and Poincare' Maps

For the parameters values α = 0.05 sec/m, β = 0.02 sec/m^3, γ_1 =0, γ_2 = 1000 (m sec)$^{-2}$, μ = 0.6, v = 1 m/sec (2) and (3) are numerically integrated in the frequency range $2 \leq \omega \leq 32$ by a fourth order Runge-Kutta method with a time step of $\Delta t = T/200$ with $T = 2\pi/\omega$. Whenever the velocity of the mass is in the range of $0.97 < x_2 < 1.03$ a finer time interval of Δt, is used to account for the directional change in the Coulomb force. The time steps were chosen such that further decrease in the steps did not significantly change the integrated values of displacement and velocity.

The phase plane plots and Poincare' maps which are stroboscopic projection of the phase points corresponding to the forcing period T are obtained for different values of ω and plotted. Figure 2 shows the phase plane diagram and Poincare'map for ω = 2 which are typical of chaotic motion,obtained by integration upto 1000 periods with initial conditions x_1 = 0.001 and x_2 = 0.0. The phase plane corresponds to the final 20 periods of integration and the Poincare' map contains 800 points leaving the initial 200 points. The phase plane is of complicated pattern and the Poincare' map shows strange attractor behaviour. The equations of motion are also integrated with other initial conditions and in each case the phase plane diagrams and Poincare' maps had the same appearance. The phase plane diagram resembles that for a chaotic stable Duffing's oscillator. For increasing values of the exciting frequency ω, the system exhibits chaotic behaviour mainly in three frequency ranges even though the system motion is observed to change from periodic to chaotic motion in other frequency ranges with very narrow frequency windows.

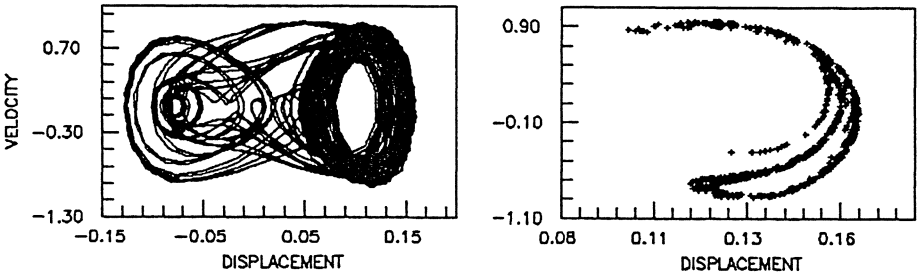

Fig. 2. Phase plane plot and Poincare' map for ω = 2

In the frequency range $15 \leq \omega \leq 16.3$, $23.3 \leq \omega \leq 23.65$ and $24.5 \leq \omega \leq 27.0$ the motion is chaotic. Typical phase plane diagrams and Poincare' maps in these frequency ranges for ω = 15, ω = 26 are shown in Figures 3 and 4

respectively. In all these cases the route to chaos is through a period doubling sequence as the frequency is decreased from a higher value. For example, for ω = 16.35 a period 2 motion, for ω = 16.25 a period 4 motion were obtained. Similarly in the frequency range $23.3 \leq \omega \leq 23.65$, for ω = 24 a period 4 motion and ω = 23.7 a period 8 motion and in the frequency range $24.5 \leq \omega \leq 27$ for ω = 30 a period 2 motion and for ω = 27.4 a period 4 motion were obtained. In these frequency ranges the effect of Coulomb damping is evident from the flattening of the phase plane trajectories corresponding to the relative velocity between the mass and the belt becoming zero.

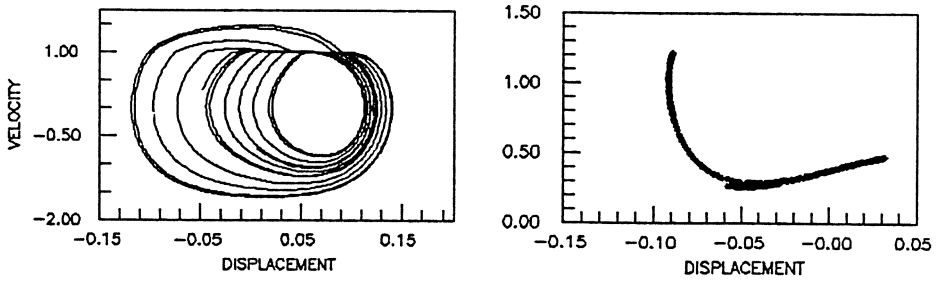

Fig. 3. Phase Plane and Poincare' map for ω = 15

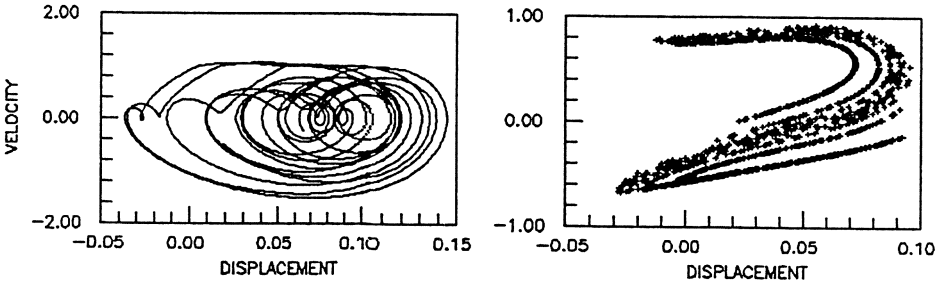

Fig.4. Phase Plane and Poincare' map for ω = 26

Harmonic and Subharmonic Solutions and Their Stability

The period doubling route to chaos can be explained by performing a harmonic and subharmonic analysis using the harmonic balance method and analysing the stability of the solutions. Assuming a solution of the form

$$x_0(t) = a + b \cos(\omega t + \varphi) \qquad (4)$$

and substituting in (1) and equating coefficients of constant, cos ωt and sin ωt terms in either side the following nonlinear algebraic equations for the amplitudes a and b and the phase angle φ are obtained.

$$\{-b\omega^2+3\gamma_2 a^2 b+\frac{3}{4}\gamma_2 b^3\}^2+\{g\alpha\omega b-3g\beta v^2 b\omega-\frac{3}{4}g\beta(b\omega)^3\}^2-F_0^2=0 \tag{5}$$

$$\{g\alpha v-g\beta v^3-\frac{3}{2}g\beta v(b\omega)^2+\gamma_2 a^3+\frac{3}{2}\gamma_2 ab^2\}^2\pm g\mu=0 \tag{6}$$

$$\tan\varphi=\frac{g\alpha b\,\omega-3gv^2 b-3g\beta ab^3\omega^3}{-b\omega^2+3\gamma_2 a^2 b+\frac{3}{4}\gamma_2 b^3} \tag{7}$$

Equations (5) and (6) are solved by using a two dimensional Newton-Raphson algorithm the results of which are shown in Figure 5. The two curves shown which are close to each other correspond to $\pm g\mu$ in (6). The dotted portions of the curves represent the unstable branch of the solution. The points of vertical tangency are $\omega = 14.5$ and $\omega = 18.8$ for $+g\mu$ and $\omega = 14.8$ and $\omega = 19$ for $-g\mu$ which are again very close.

As the period doubling occurred corresponding to the non resonant branch of the harmonic amplitude curve ,the stability of the harmonic motion can be examined with respect to build up of $\frac{1}{2}$ sub harmonic motion in these frequency ranges. Assuming a perturbed solution in the form

$$\tilde{x}_0(t)=x_0(t)+\delta x(t) \tag{8}$$

and substituting in (1) the following variational equation is obtained for the perturbed motion $\delta x(t)$.

$$\delta\ddot{x}+g[-\alpha\,\delta\dot{x}+\beta\{3(\dot{x}_0-v)\,\delta\dot{x}+3(\dot{x}_0-v)\delta\dot{x}^2+\delta\dot{x}^3\}+\mu\{\mathrm{sgn}(\dot{x}_0+\delta\dot{x}-v)-\mathrm{sgn}(\dot{x}_0-v)\}]+\gamma_2\{3x_0^2\,\delta x+3x_0\delta x^2+\delta x^3\}=0 \tag{9}$$

The stability of the perturbed solution can be examined considering the linearized form of (9)

$$\delta\ddot{x}+\delta\dot{x}\{-g\alpha+3g\beta(\dot{x}_0-v)^2\}+3\gamma_2 x_0^2\,\delta x=0 \tag{10}$$

and using Floquet's theory.Assume a solution of the form for (10)

$$\delta x(t)=e^{\nu t}\,b_{1/2}\cos(\omega t/2+\theta) \tag{11}$$

which is unstable for ν real and positive. Substituting (11)in (10) with $\nu = 0$ and using the harmonic balance method with respect to the $\frac{1}{2}$ subharmonic we obtain the condition for bifurcation from period 1 to period 2 motion

$$[\frac{\omega}{2}\{-g\alpha+3g\beta(v^2+\frac{1}{2}(b\omega)^2\}]^2+[3\gamma_2(a^2+\frac{1}{2}b^2)-\frac{\omega^2}{4}]^2-[3\gamma_2 ab-\frac{3}{2}g\beta vb\omega^2]^2=0 \tag{12}$$

The values of a and b obtained from (6) and (7) are substituted in (12) yielding the bifurcation points respectively as $\omega = 15.037$ and 31.69 and

ω = 15.608 and 30.527 for $\pm g\mu$ in (6) which are marked as points A and B for + $g\mu$ and A' and B' for - $g\mu$ in Figure 5. Between the bifurcation points the harmonic solution is unstable with respect to subharmonics and hence the period 2 solutions begin to appear in these frequency ranges. Likewise the period 2 solutions may bifurcate into period 4 solution when they become locally unstable with respect to period 4 solution.Thus the period doubling can be explained in terms of successive bifurcations.

Assuming a solution for the $\frac{1}{2}$ subharmonic of the form

$$x_0(t) = a_1 + b_1 \cos \omega t + d_1 \cos(\omega t/2 + \varphi_1) \qquad (13)$$

and substituting in (1) and applying the harmonic balance method one can obtain a set of equations after comparing the harmonic and subharmonic terms on either side ,which when solved gives the amplitudes a_1, b_1, d_1 and φ_1. The amplitude d_1 is plotted in Figure 6 separately for $+g\mu$ and $-g\mu$.

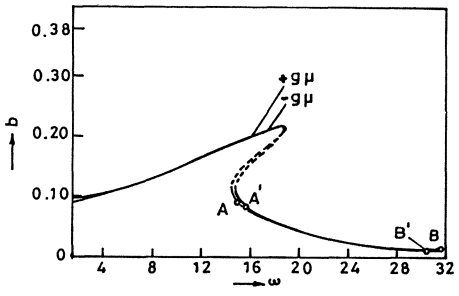

Fig.5. Harmonic Response

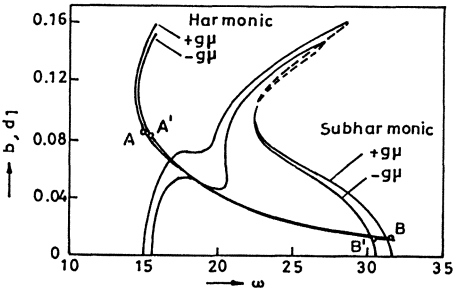

Fig.6.Subharmonic Response

It can be noted that the frequencies relating to the beginning and end of the subharmonics correspond to the stability limits obtained previously.

Power Spectral Density and Lyapunov Exponents

As chaos is characterized by aperiodic and random like motion the power spectral density is continuous. Typical time history and power spectral density for ω = 26 is shown in Figure 7.

Lyapunov exponent is a measure of average exponential divergence or convergence of nearby trajectories and an indicator of bifurcations in nonlinear dynamical systems. Negative Lyapunov exponents signal periodic motion whilst at least one positive Lyapunov exponent indicates chaos.The

nonlinear system can be represented by a set of vector differential equations

$$\dot{\bar{x}} = \bar{f}(\bar{x}(t),\bar{\mu}) \tag{14}$$

The vector field $\bar{f}$ in(14) generates a flow $\phi_t(\bar{x})$ on a manifold M which is a solution of(14).Considering the manifold M of two neighbouring trajectories starting from $\bar{x}_0$ and $\bar{x}_0+\Delta\bar{x}_0$, the tangent vector $\bar{w} \in T_{\bar{x}}M$,where $T_{\bar{x}}M$ is the tangent space to M at $\bar{x}$ is described by the linearized system of equations

$$\dot{\bar{w}} = [\nabla\bar{f}(\bar{x},t)]\bar{w} \tag{15}$$

where $\nabla\bar{f}(\bar{x},t)= \partial\bar{f}(\bar{x})/\partial\bar{x}|_{\bar{x} = \bar{x}(t)}$ is the Jacobian matrix. The one dimensional Lyapunov exponent is defined as

$$\lambda(\bar{x}_0,\bar{w}_0) = \lim_{t\to\infty} \left[\frac{1}{t} \frac{\| \bar{w}(t) \|}{\| \bar{w}_0 \|} \right] \tag{16}$$

The Lyapunov exponents are computed using a Gram-Schimdt orthonormalization procedure as given by Wolf et.al[4] and they are λ_1= 1.97, λ_2= -1.74, λ_3=0 for ω = 26. The convergence of the positive Lyapunov exponent is shown in Figure 8 as a function of time.

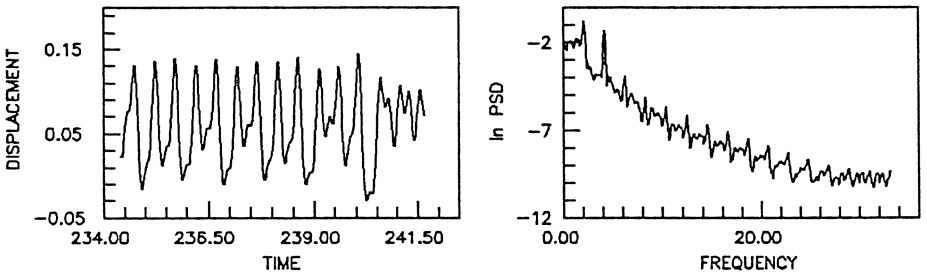

Fig.7. Time History and Power Spectral Density for ω = 26

Interpolated cell mapping

Different initial conditions can lead to multiple sets of steady state behaviour in nonlinear systems. Determination of the different solutions for all initial conditions in a region of the phase space by numerical integration is extremely time consuming. Tongue and Gu[3] have proposed an interpolated cell mapping(ICM) technique in which the phase plane is discretized into a large number of cells. The equations are integrated for a small time (one forcing period) with the state of each cell centre as initial conditions. The terminal point after integration upto one period for each cell centre is recorded and located with respect to the centres of four adjacent cells surrounding it. The final position corresponding to a

large number of periods is determined by an iterative scheme of interpolation between the final locations of the trajectories at the end of one period emanating from these four corners. This method is both time saving and reasonably accurate.

The Poincare' maps are obtained using the ICM technique for ω = 2,15 and 26 with the phase plane divided into 100×100 cells. For all the cells in the three cases we obtained the corresponding strange attractor. The Poincare' map for ω = 26 is shown in Figure 8 which is as good as obtained by numerical integration(Fig.4).

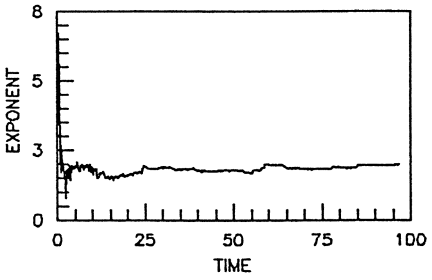

Fig.8. Lyapunov Exponent(ω = 26)

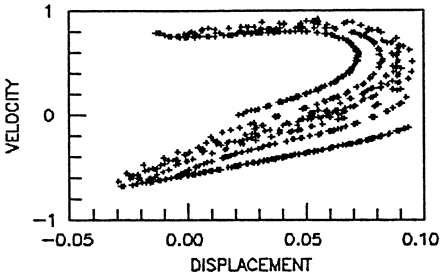

Fig.9.Poincare' map by ICM(ω = 26)

Conclusion

Chaotic motion of a harmonically excited nonlinear oscillator with Coulomb damping is investigated by numerical integration. A period doubling route to chaos is identified in different ranges of excitation frequency. From a subharmonic motion and stability analysis it can be concluded that period doubling is due to a build up of higher subharmonics of even order. Chaotic motion is also confirmed by computation of Lyapunov exponents and power spectrum. The strange attractors are shown to be stable with respect to initial conditions by the interpolated cell mapping technique.

References

1. Awrejcewicz,J.,Chaos in Simple Mechanical System with Friction.J.Sound and Vibration, 109 (1986) 178-180.

2. Szemplinska-Stupnicka,W.,Secondary Resonances and Approximate Models of Route to Chaotic Motion in Nonlinear Oscillators. J.Sound and Vibration 113(1987) 155-172.

3. Tongue,B.H. and Gu,K., Interpolated Cell mapping of Dynamical Systems ASME J. App. Mech. 55(1988) 461-466

4. Wolf,A., Swift,J.B., Swinney,H.L.and Vastano,J.A.,Determining Lyapunov Exponents from Time Series Physica 16D(1985) 285-317

A Theoretical and Experimental Investigation of the Influence of Modal Interactions on the Nonlinear Response of Structures

A. H. Nayfeh and B. Balachandran

Engineering Science and Mechanics Department
Virginia Polytechnic Institute and State University
Blacksburg, Virginia

Abstract

The influence of two-to-one internal or autoparametric resonances on the nonlinear response of metallic and composite structures subjected to a harmonic excitation has been investigated theoretically and experimentally. The experimental observations are in good agreement with the theoretical predictions. When the excitation frequency is near the natural frequency of the second flexural mode, the autoparametric resonance gives rise to the saturation phenomenon and two-period quasi-periodic and chaotically modulated motions.

Introduction

We conducted experiments with a metallic structure which consisted of two light-weight steel beams and two concentrated masses, as shown in Figure 1. Although the model has an infinite number of modes of vibration, the lower two modes are well separated from the other modes so that at low excitation frequencies, the structure can be regarded as a two-degree-of-freedom system. The first two modes of the structure are flexural modes and they are shown in Figure 1. Denoting the undamped

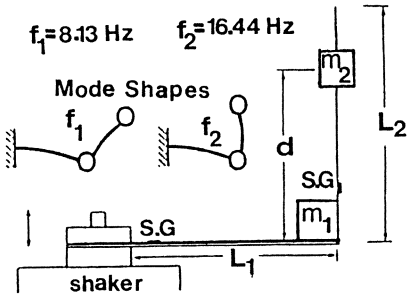

Figure 1. Metallic structure and accompanying flexural mode shapes. Beam 1: 1.68 mm x 12.83 mm x 154.51 mm, ρ_1 = 0.162 g/mm, m_1 = 31.1 g; Beam 2: 0.56 mm x 12.80 mm x 152.40 mm, ρ_2 = 0.0498 g/mm, m_2 = 40.0 g; d = 84.18 mm.

W. Schiehlen (Editor)
Nonlinear Dynamics in Engineering Systems
IUTAM Symposium Stuttgart/Germany 1989

modes of vibration as $\phi_1(\vec{r})$ and $\phi_2(\vec{r})$, we express the displacement $w(\vec{r}, t)$ at any location $\vec{r}$ and time t as

$$w(\vec{r}, t) = u_1(t)\,\phi_1(\vec{r}) + u_2(t)\,\phi_2(\vec{r}) \tag{1}$$

where u_1 and u_2 are the generalized coordinates of the motion. Substituting equation (1) into the governing partial differential equations and the boundary conditions and

$$\ddot{u}_1 + \omega_1^2 u_1 + 2\mu_1\dot{u}_1 + \delta_1\dot{u}_1^2 + \delta_2\dot{u}_1\dot{u}_2 + \delta_3\dot{u}_2^2 + \delta_4 u_1\ddot{u}_1 + \delta_5 u_2\ddot{u}_1$$
$$+ \delta_6 u_1\ddot{u}_2 + \delta_7 u_2\ddot{u}_2 + (h_{11}u_1 + h_{12}u_2)\cos(\Omega t) = F\cos(\Omega t) \tag{2}$$

$$\ddot{u}_2 + \omega_2^2 u_2 + 2\mu_2\dot{u}_2 + \alpha_1\dot{u}_1^2 + \alpha_2\dot{u}_1\dot{u}_2 + \alpha_3\dot{u}_2^2 + \alpha_4 u_1\ddot{u}_1 + \alpha_5 u_2\ddot{u}_1$$
$$+ \alpha_6 u_1\ddot{u}_2 + \alpha_7 u_2\ddot{u}_2 + (h_{21}u_1 + h_{22}u_2)\cos(\Omega t) = G\cos(\Omega t) \tag{3}$$

where the highest order of terms retained is quadratic. Here, the ω_i are the circular natural frequencies, the μ_i are the modal damping coefficients, F, G, h_{ij}, and Ω are parameters which depend on the excitation, and δ, and α_i are constants that depend on the values of the concentrated masses and the dimensions and properties of the beams. Equations (2) and (3) have inertial quadratic nonlinearities and harmonic excitation terms. They have the same form as the equations governing a variety of other physical systems, such as ships, shells, arches, and surface waves in a closed basin [1]. Hence, these equations can be used to predict the qualitative behavior of many physical systems.

In the current article, we consider the resonant excitations $\Omega \simeq \omega_i$ in the presence of a two-to-one internal resonance $\omega_2 \simeq 2\omega_1$. However, the length of the article permits us to treat only the case $\Omega \simeq \omega_2$ in some detail. Sethna [2], Nayfeh, Mook, and Marshall [3], Yamamoto, Yasuda, and Nagasaka [4], Hatwal, Mallik, and Ghosh [5] and Haddow, Barr, and Mook [6] and a few others [1] studied special forms of the current problem. Nayfeh et al. [3] found a saturation phenomenon, which was experimentally verified by Haddow et al. [6]. Yamamoto et al. [4] observed modulated motions in their analog-computer simulations, while Hatwal et al. [5] reported experimental observations of chaotic responses at moderately high excitation levels. The case $\Omega \simeq \omega_1$ has been considered by Miles [7] and several others [1]. Miles [7] showed theoretically that quasi-periodic and chaotic motions are possible for some excitation parameter values. In this case, Nayfeh and Zavodney [8] experimentally observed modulated motions.

Analysis

We describe the internal and external resonances by the relations $\omega_2 = 2\omega_1 + \sigma_1$ and $\Omega = \omega_2 + \sigma_2$, where σ_1 and σ_2 are small detuning parameters. For weakly nonlinear vibrations, using the method of multiple scales, one finds that to the first approximation the structure's response is [9]

$$u_1 = a_1 \cos(\frac{1}{2}\Omega t - \frac{1}{2}\gamma_1 - \frac{1}{2}\gamma_2) + \ldots , \quad u_2 = a_2 \cos(\Omega t - \gamma_2) + \ldots \tag{4}$$

where the amplitudes a_n and phases β_n are governed by

$$\dot{a}_1 = -\mu_1 a_1 - \Lambda_1 a_1 a_2 \sin\gamma_1 \tag{5}$$

$$\dot{a}_2 = -\mu_2 a_2 + \Lambda_2 a_1^2 \sin\gamma_1 + f\sin\gamma_2 \tag{6}$$

$$a_1\dot{\beta}_1 = -\Lambda_1 a_1 a_2 \cos\gamma_1 \tag{7}$$

$$a_2\dot{\beta}_2 = \Lambda_2 a_1^2 \cos\gamma_1 - f\cos\gamma_2 \tag{8}$$

$$\gamma_1 = \sigma_1 t + \beta_2 - 2\beta_1 \quad \text{and} \quad \gamma_2 = \sigma_2 t - \beta_2 \tag{9}$$

Here,

$$4\omega_1\Lambda_1 = \delta_2\omega_1\omega_2 - \delta_5\omega_1^2 - \delta_6\omega_2^2 , \quad 4\omega_2\Lambda_2 = -(\alpha_1 + \alpha_4)\omega_1^2 , \quad f = G/2\omega_2 \tag{10}$$

Periodic solutions of equations (2) and (3) correspond to the fixed points of equations (5)-(9). They are obtained by setting $\dot{a}_1 = \dot{a}_2 = \dot{\gamma}_1 = \dot{\gamma}_2 = 0$. Similar equations describing the evolution of the amplitudes and phases can also be obtained for the case of primary resonance of the first mode [9]. Equations (5)-(9) are used to determine the stability of the fixed points.

The theoretically predicted amplitude-response curves exhibit the saturation phenomenon [9]. As a control parameter, such as the excitation amplitude or frequency, is varied, a fixed point loses its stability in one of two ways. First, a real eigenvalues moves into the right-half of the complex plane along the real axis, resulting in a jump. Second, a pair of complex eigenvalues crosses the imaginary axis transversely and with a nonzero speed into the right-half plane. The value of the parameter corresponding to this crossing is called a Hopf bifurcation value. Figure 2 shows theoretically determined curves in the $\hat{\sigma}_1 - \hat{\sigma}_2$ plane corresponding to Hopf bifurcation for $\hat{\mu}_n = \mu_n/\sqrt{\Lambda_1 f}$ = 0.02, 0.04, and 0.06. As the parameters $\hat{\sigma}_n = \sigma_n/\sqrt{\Lambda_1 f}$ are varied to

cross the bifurcation curves, the nonlinear periodic solution loses stability and modulated motions occur in the region enclosed by the bifurcation curves. Inside this region, periodically modulated and chaotically modulated motions occur. There is also a period-doubling sequence leading from the quasi-periodic motions to the chaotic motions [10].

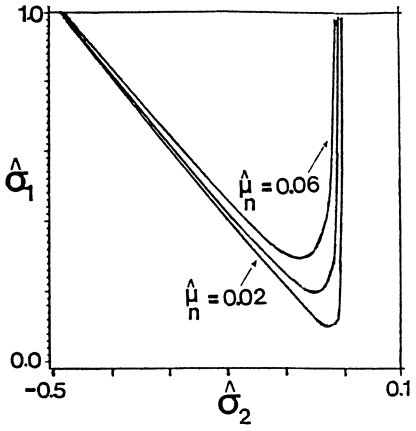

Figure 2. Bifurcation curves across which the real part of a complex conjugate pair of eigenvalues changes sign (it is positive inside the curves) for $\hat{\mu}_n$ = 0.02, 0.04, and 0.06.

Experiments

The experimental set up and procedure is as described in [11]. The first two linear resonant frequencies of the metallic structure shown in Figure 1 are 8.13 Hz and 16.44 Hz. The responses were analyzed by using Fourier spectra, Poincaré maps, time-dependent modal decompositions, and dimension calculations [11]. Figure 3 shows experimentally observed amplitude-response curves. The symbols a_1^* and a_2^* correspond to the amplitudes of the first and second flexural modes, respectively. The point where periodic motion ceased to exist is labeled Hopf bifurcation and the observations made during forward and reverse sweeps are marked by circles and triangles, respectively in Figures 3 and 5. As we increased the excitation amplitude from zero, a_2^* increased linearly while a_1^* remained trivial, in accordance with linear theory. As we increased the excitation amplitude above a threshold (about 7.8 mili g's), a_2^* remained constant while a_1^* increased nonlinearly; that is, the second mode saturated and the extra input energy spilled over into the lower mode. As we increased the excitation amplitude beyond a second threshold, the saturated response lost its stability and we observed amplitude- and phase-modulated motions. The experimentally observed frequency-response curves are in good agreement with the

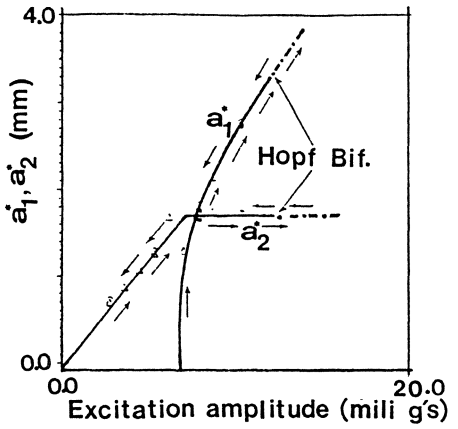

Figure 3. Experimentally obtained amplitude-response curves for the metallic structure when the excitation frequency is held constant at 16.38 Hz: _____ periodic, _._._. modulated

theoretical predictions [11]. Figure 4 shows the response spectrum for different excitation frequencies f in a region where modulated motions were observed. Figures 4a to 4c correspond to periodically modulated responses. As we go from Fig. 4a to Fig. 4c, subharmonics of the modulation frequency appear in the spectrum. In fact, the modulation period doubles as we go from Fig. 4a to Fig. 4b. Figures 4d and 4e correspond to a chaotically modulated response for which the pointwise dimension was determined to be 2.748. The chaotically modulated response was observed at an excitation level of about 33.00 mili g's (r.m.s value). Poincaré maps and results of time-dependent modal decomposition analysis were found to be consistent with the observed frequency spectra.

In an experimental study of the response of the structure during primary resonant excitations of the first mode [12], we found two-period quasi-periodic and chaotically modulated motions. However, unlike the previous case we did not find any doubling in the modulation period in the transition from quasi-periodic to chaotically modulated motions. In both cases, the chaotically modulated responses were observed at very small excitation levels. Also, the excitation levels needed to produce chaotic motions during primary resonance of the lower mode (about 150.00 mili g's r.m.s) were found to be higher than those required during excitation of the second mode.

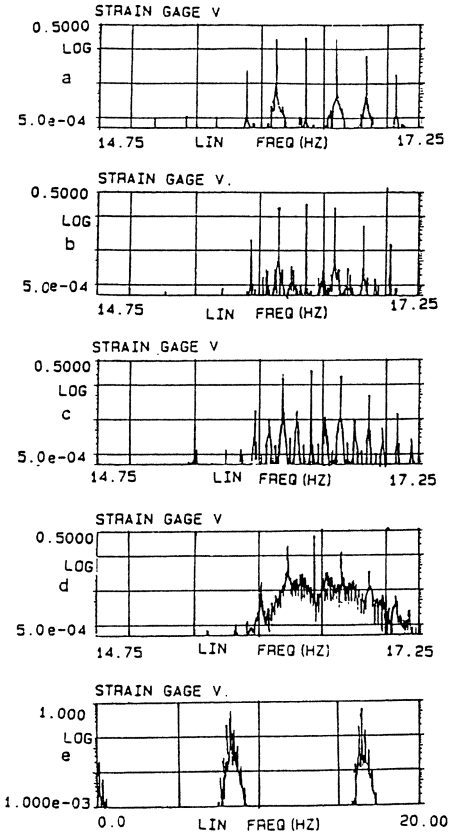

Figure 4. Spectra of the response on a log scale: a) f = 16.36 Hz, b) f = 16.37 Hz, c) f = 16.41 Hz, d) f = 16.44 Hz, and e) f = 16.44 Hz. We note the subharmonics of the modulation frequency appearing in the spectrum as we go from a) to b) to c) and broadening around the carrier frequencies in d) and e).

Recently, we conducted experiments with a structure made of two light-weight glass/epoxy composite beams and two concentrated aluminum masses (a model similar to that shown in Figure 1). The first three modes of oscillation of the structure are well separated from the other modes and their linear resonant frequencies are 5.84, 8.67, and 17.64 Hz. The first and third frequencies correspond to the first and second flexural modes while the second frequency corresponds to the first torsional mode. In this case, there is a two-to-one internal resonance between the second flexural and first torsional modes and a three-to-one internal resonance between the two flexural modes. The modal interaction due to the two-to-one internal resonance gives rise to the saturation phenomenon, periodically modulated motions, and chaotically modulated motions. Also, the modulation period doubles in the transition from

periodically to chaotically modulated motions. The chaotic motions in this case were observed at an excitation level of 40.00 mili g's (r.m.s value). Figure 5 shows the amplitude-response curves for the composite structure. Here, the symbols a_2^* and a_t^* correspond to the amplitudes of the second flexural and first torsional modes, respectively. The composite structure exhibits the saturation phenomenon and its breakdown to modulated motions like the metallic structure. However, the responses in this case are nonplanar due to the presence of the torsional mode. The experimental study of modal interactions in the composite structure is discussed in detail in [13].

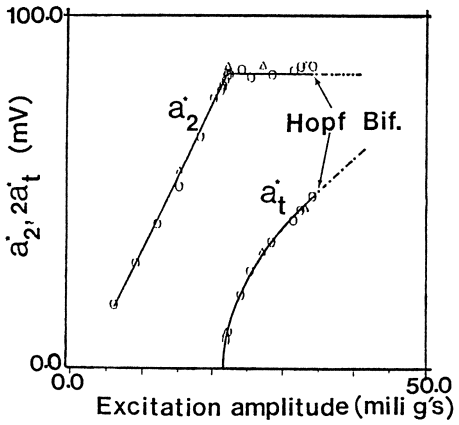

Figure 5. Experimentally obtained amplitude-response curves for the composite structure when the excitation frequency is held constant at 17.53 Hz: _____ periodic, _.-._. modulated

Acknowledgement

This work was supported by the Air Force Office of Scientific Research under Grant No. AFOSR-86-0090 and the National Science Foundation under Grant No. MSM-8521748.

References

1. Nayfeh, A. H.; Balachandran, B.: Modal Interactions in dynamical and structural systems. Appl. Mech. Rev. (in press).

2. Sethna, P. R.: Vibrations of dynamical systems with quadratic nonlinearities. J. Appl. Mech. 32 (1965) 576-582.

3. Nayfeh, A. H.; Mook, D. T.; Marshall, L. R.: Nonlinear coupling of pitch and roll modes in ship motions. J. Hydronautics 7 (1973) 145-152.

4. Yamamoto, T.; Yasuda, k.; Nagasaka, I.: On the internal resonance in a nonlinear two-degree-of-freedom system (forced vibrations near the high resonance point when the natural frequencies are in the ratio 1:2). Bull. Jap. Soc. Mech. Engg. 20 (1977) 1093-1101.

5. Hatwal, H.; Mallik, A. K.; Ghosh, A.: Forced nonlinear oscillations of an autoparametric system - Part 2: Chaotic responses. J. Appl. Mech. 50 (1983) 663-668.

6. Haddow, A. G.; Barr, A. D. S.; Mook, D. T.: Theoretical and experimental study of modal interaction in a two-degree-of-freedom structure. J. Sound and Vib. 97 (1984) 451-473.

7. Miles, J. W.: Resonantly forced motion of two quadratically coupled oscillators. Physica D. 13 (1984) 247-260.

8. Nayfeh, A. H.; Zavodney, L. D.: Experimental observation of amplitude- and phase-modulated responses of two internally coupled oscillators to a harmonic excitation. J. Appl. Mech. 55 (1988) 706-711.

9. Nayfeh, A. H.: Application of the method of multiple scales to nonlinearly coupled oscillators, In Lasers, Molecules and Methods, Hirschfelder, J. O.; Wyatt, R. E.; Coalson, R. D. (eds.), New York : Wiley 1989.

10. Nayfeh, A. H.; Raouf, R. A.: Nonlinear forced response of infinitely long circular cylindrical shells. J. Appl. Mech. 54 (1987) 571-577.

11. Nayfeh, A. H.; Balachandran, B.; Colbert, M. A.; Nayfeh, M. A.: An experimental investigation of complicated responses of a two-degree-of-freedom structure. J. Appl. Mech. (in press).

12. Nayfeh, A. H.; Balachandran, B.: Experimental investigation of resonantly forced oscillations of a two-degree-of-freedom structure. Int. J. Non. Mech. (in press)

13. Balachandran, B; Nayfeh, A. H.: Nonlinear oscillations of a harmonically excited composite structure, submitted to Journal of Composite Structures.

Nonlinear Oscillations of Structures Induced by Dry Friction

K. Popp and P. Stelter

Institute of Mechanics
University of Hannover

1. Introduction

Self-sustained oscillations due to dry friction often occur in engineering systems, cf. *Magnus* [1]. One example, the phenomenon of machine tool chattering which deteriorates the production quality and increases the tool wear is – at least partly – caused by friction forces with a decreasing characteristic. Another phenomenon is the curving noise of tram wheels, induced by nonlinear slip forces, which annoys passengers and city dwellers. Recent investigations of oscillations induced by dry friction show that beside the well-known limit cycle behaviour, chaotic motions are also possible, depending on the system parameters.

The aim of this paper is to investigate regular and chaotic motions of simple multi-body and continuous mechanical systems under self-excitation due to dry friction, in order to show the parameter dependencies and routes to chaos. Emphasis is laid on experiments which allow a comparison with numerical results. Here, the noise in the measurements can create problems.

Dry friction appears in two different phenomena in nature: i) As a resistance against the beginning of a motion from equilibrium (stick mode). ii) As a resistance against an existing motion (slip mode). The friction resistance is a constraining force in the stick mode and an applied force during the slip mode. In an oscillatory motion both phenomena show up, resulting in a stick-slip mode. Since the friction characteristic consists of two different parts with a non-smooth transition, one has to deal with a system of *variable* structure where the resulting motion shows a nonsmooth behaviour. Other examples of this type are systems with play, stops, impacts, hysteresis or delay. It is well-known that variable structure systems can exhibit chaotic behaviour. Engineering problems where chaos was found numerically and/or experimentally have been investigated by *Moon, Shaw* [2] (vibrating beam with an amplitude constraining stop), *Hendriks* [3] (impact print hammers in a matrix printer), *Szczygielski* [4] (rotor touching a boundary), *Kaas-Petersen, True* [5] (lateral motion of a railway bogie), *Pfeiffer* [6] (rattling gear drives), *Païdousis et.al.* [7] (constrained pipe conveying fluid). Unfortunately, this type of system cannot be analyzed by methods which require certain smoothness assumptions on the nonlinear functions involved. For instance, the common methods for calculating Lyapunov exponents do not work. Here, new ways have to be paved.

There exists a rich literature on chaos in self-excited systems with smooth nonlinearities, cf. *Thompson, Stewart* [8], *Abraham, Shaw* [9], *Kunick, Steeb* [10]. However, in case of self-excitation due to dry friction only a few hints for chaotical behaviour can be found in [11], *Fingberg* [12], *Grabec* [13]. The present paper intends to show more.

2. System description

In the systems under consideration, self excitation is induced by the friction force of a running belt, acting on the structure. Four models are investigated, two discrete and two continuous, as shown in Fig. 1.

W. Schiehlen (Editor)
Nonlinear Dynamics in Engineering Systems
IUTAM Symposium Stuttgart/Germany 1989

The two discrete systems are investigated numerically only. They serve as simple model problems to show different phenomena, parameter dependencies and routes to chaos. The two continuous systems are investigated experimentally as well as numerically. The aim of the experiments performed are: i) to get evidence of chaotical behaviour, ii) to develop analysis techniques applicable in presence of noise, and iii) to gain data for comparisons with numerical results. Important questions which should be answered by means of experiments are: How to develop simple models for continuous systems which allow us to describe chaos? How to separate measuring noise from deterministic chaos?

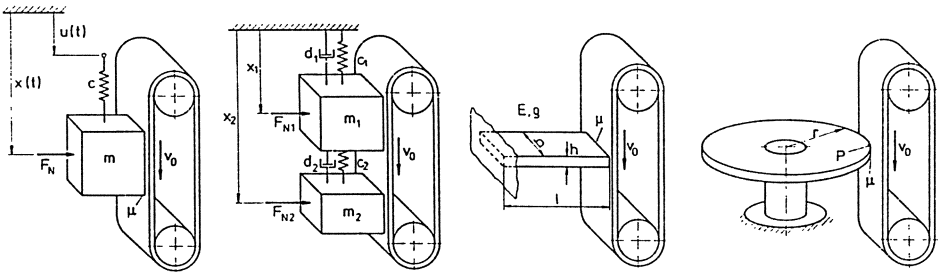

Fig. 1: Discrete and continuous models of systems which show friction induced selfsustained oscillations a) A single-degree-of-freedom oscillator with external harmonic excitation, b) a two-degree-of-freedom spring-mass-damper-system, c) a cantilever beam as a one-dimensional continuous system, d) a thin centrally fixed plate as a two-dimensional continuous system.

Self-excitation due to dry friction is only possible if the friction force has a decreasing characteristic, cf. [1]. Thus, for numerical simulations the following model for the friction force F_R has been used, see also Fig. 2:

$$v_r \neq 0: \qquad F_R = -\mu(v_r)\, F_N \operatorname{sgn}(v_r), \qquad \text{applied force,} \qquad (1)$$

$$v_r = 0: \qquad |F_R| \leq \mu(0)\, F_N, \qquad \text{constraining force,} \qquad (2)$$

$$\mu(v_r) = \frac{\mu_0 - \mu_1}{1 + \lambda|v_r|} + \mu_1 + \alpha v_r^2, \qquad (3)$$

$$\mu_0 = 0.4,\ \mu_1 = 0.1,\ \alpha = 0.01\ s^2/m^2,\ \lambda = 1.42\ s/m,$$

where v_r denotes relative velocity, F_N normal force, and $\mu(v_r)$ the velocity dependent friction coefficient.

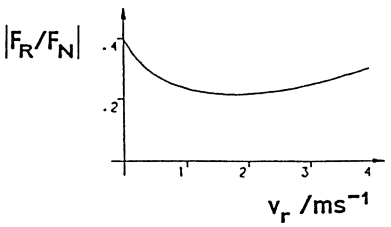

Fig. 2: Friction force with decreasing characteristic

The equations of motion for model a) read in nondimensional state space notation:

$$\begin{aligned} x_1' &= x_2, \\ x_2' &= -x_1 + \left[F_R(-v_0) - F_R(v_r)\right]/c + u_0\cos(x_3), \\ x_3' &= \eta, \end{aligned} \tag{4}$$

$$(*)' = d(*)/d\tau,\ \tau = \omega_0 t,\ \omega_0 = \sqrt{c/m},\ \eta = \Omega/\omega_0,\ v_r = \omega_0 x_2 - v_0,\ x_s = \mu(v_0)F_N/c, \tag{5}$$

where m means mass, c spring stiffness, v_0 belt velocity, u_0 excitation amplitude and Ω excitation frequency. The parameter values (initial conditions) are, if not specified otherwise: $v_0 = 1.0$ m/s, $F_N/c = 10.0$ m, $u_0 = 0.5$ m, $\omega_0 = 1.0$ rad/s, $\eta = 2.1$, ($x_1(0) = 0$, $x_2(0) = 1.0$ m/s)

Similarily, for model b) we have:

$$\begin{aligned} x_1' &= x_2, \\ x_2' &= \frac{1}{\gamma}\left\{-(1+\kappa)x_1 - 2D(1+\delta)x_2 + x_3 + 2D x_4 + \left[F_R(-v_0) - F_R(v_{r1})\right]/c_2\right\}, \\ x_3' &= x_4, \\ x_4' &= x_1 + 2D\, x_2 - x_3 - 2D\, x_4 + \left[F_R(-v_0) - F_R(v_{r2})\right]/c_2, \end{aligned} \tag{6}$$

$$(*)' = d(*)/d\tau,\ \tau = \omega_2 t,\ \omega_2 = \sqrt{c_2/m_2}\ ,\ \gamma = m_1/m_2,\ \kappa = c_1/c_2,\ \delta = d_1/d_2, \tag{7}$$
$$D = d_2/(2\sqrt{c_2 m_2}),\ v_{r2} = \omega_2 x_2 - v_0,\ v_{r2} = \omega_2 x_4 - v_0.$$

The meaning of the parameters can be seen from Fig 1 b). The parameter values (initial conditions) are, if not specified otherwise: $v_0 = 1.0$ m/s, $F_{N1}/c_2 = F_{N2}/c_2 = 20.0$ m, $\omega_2 = 1.0$ rad/s, ($x_1(0) = x_3(0) = 0$, $x_2(0) = x_4(0) = 1.0$ m/s).

3. Numerical results for discrete models

The simulation results for models a) and b) have been visualized by means of time histories, phase-plane plots, Poincaré-maps and frequency spectra, while bifurcation diagrams show the parameter dependencies. Because of lack of space only some results will be shown here.

The results for model a) are given in Fig. 3, and 4. Fig. 3 shows the bifurcation diagram depending on the frequency ratio η together with some phase-plane plots. Chaos occurs in certain frequency bands which are separated by bands with p-periodic solutions of order p=1 to at least p=6. The bifurcation diagram depending on the normal force F_N looks similar. Fig. 4 shows the chaotic solution for $\eta = 2.1625$ in the three-dimensional state space as well as two Poincaré sections ($x_3 = \pi/4$ and $x_3 = 5\pi/4$) which exhibit a Cantor set like structure. Obviously, the stick mode captures the periodic motions as well as the chaotic ones. Thus, all phase-plane plots are bounded by a line $x' = v_0 = \text{const}$. Further investigations show that the transition into chaos in the frequency range $0.9 \leq \eta \leq 0.96$ is similar to the intermittency route described by *Pomeau, Manneville* [14].

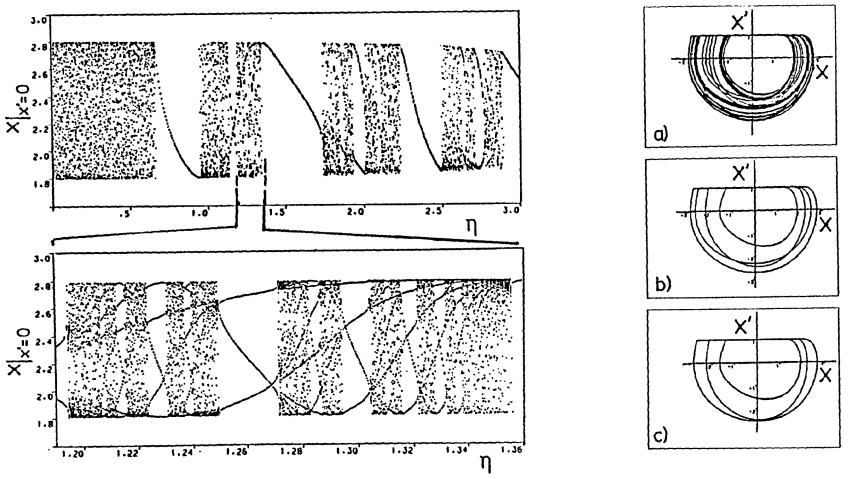

Fig. 3: Bifurcation diagram for model a) depending on the frequency ratio η with enlargement and phase-plane plots for a) η = 1.22, b) η = 1.26 and c) η = 1.30

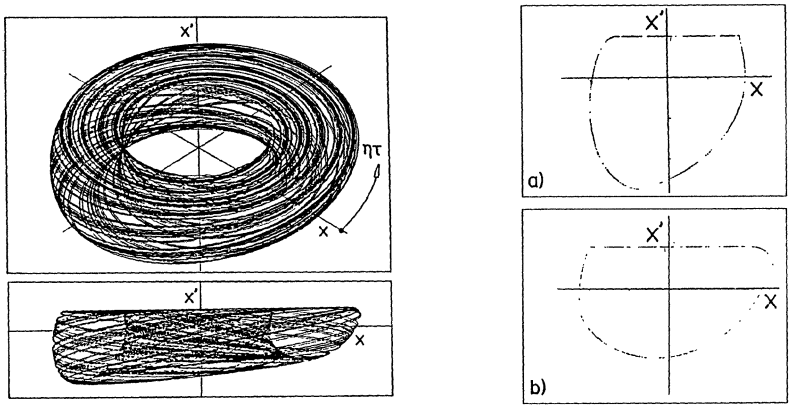

Fig. 4: Chaotic motion in the three-dimensional phase space with Poincaré sections, a) ηT = π/4 and b) ηT = 5π/4

The results for model b) are presented in Fig. 5, 6 and Fig. 7. Fig. 5 shows the bifurcation diagram for both masses depending on the damping ratio D ($\kappa = 2.0$, $\gamma = 2.5$, $\delta = 1.0$). The transition to chaos occurs for $0.07 \geq D \geq 0.04$.

The corresponding phase-plane plots and frequency spectra for mass 1 reveal, see Fig. 6, that with decreasing damping the number p of p-periodic solutions increase in the manner p = 1, 2, 4. However for D = 0.05 this sequence seems to be interrupted and a p = 9 solution appears. In contrast to model a), chaos is approached similar to the well-known period-doubling route. For high damping, D > 0.07, only p = 1 solutions occur. Beyond critical damping, D = 1, only mass 2 performs stick-slip vibrations, while mass 1 remains in a pure slip mode, cf. Fig. 7.

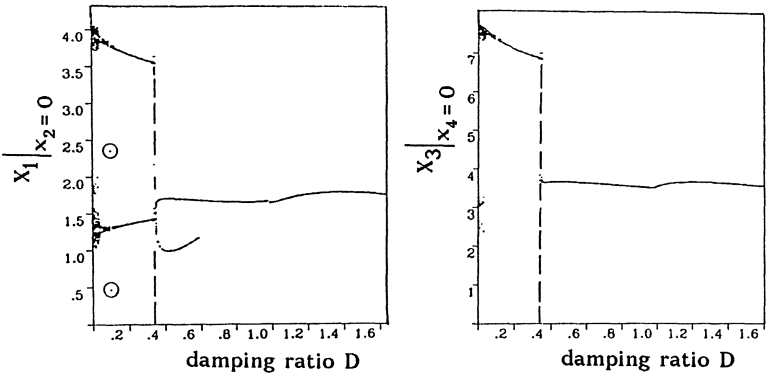

Fig. 5: Bifurcation diagrams for model b) depending on the damping ratio D.

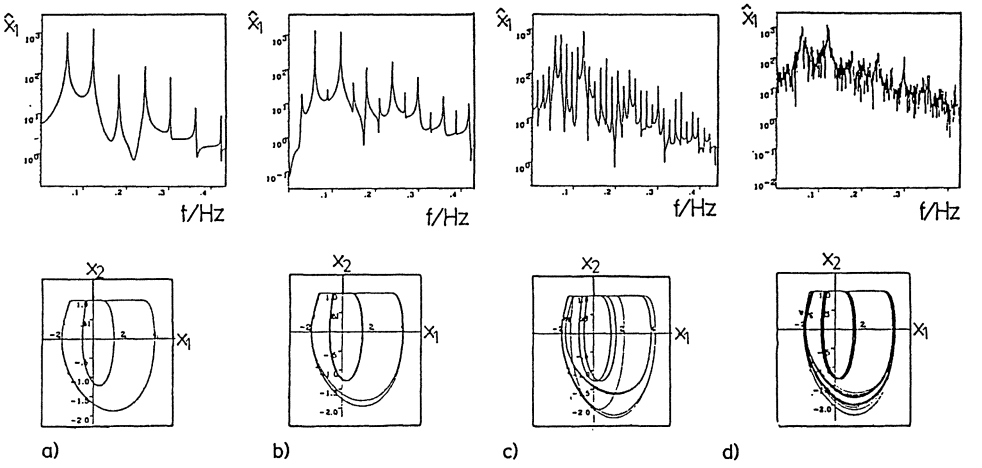

Fig. 6: Route to chaos for decreasing damping ratio D, a) D = 0.060, b) D = 0.053, c) D = 0.050 and d) D = 0.040

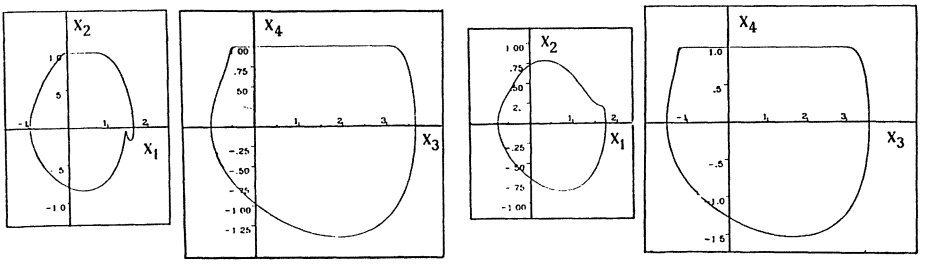

D = 0.8 D = 1.2

Fig. 7: Suppression of the stick mode of mass 1 with increasing damping

4. Experimental results for continuous models

In case of the cantilever beam c), and for the thin, centrally fixed plate d), measured signals are the deflection z(t) near band contact. The signals have been processed in order to gain frequency spectra, a pseudo state space, Lyapunov exponents and the correlation integral. According to *Packard et.al.* [15], from a single time series of a state variable z(t) a pseudo state space,

$$\mathbf{z}^T = \left[z(t_0)\ z(t_0+T) \ldots z(t_0+(m-1)T) \right], \tag{8}$$

can be reconstructed, where m denotes the embedding dimension and T the separation time. Then, applying the procedure given by *Sano, Sawada* [16], the spectrum of Lyapunov exponents can be computed and following *Grassberger, Procaccia* [17] the correlation integral $C(r) \sim r^{\nu}$ can be found. Here, r denotes the radius of a hypersphere in the pseudo state space and ν the correlation exponent, which depends on the embedding dimension m. For sufficiently large values of m and decreasing radius r the correlation exponent tends to the correlation dimension D_C for a regular or chaotic attractor, while for a pure random noise signal $C(r) \sim r^m$ holds. For a noise signal on top of a deterministic signal, the plot log C(r) versus log r has two regions. If the noise level is greater than r, then the slope will increase with m, $C(r) \sim r^m$, and if the noise level is less than r, the slope will be constant, $C(r) \sim r^{Dc}$. Therefore, it is possible to distinguish between chaotic and stochastic behaviour of measured signals. On the other hand, the correlation dimension D_C gives a hint to the state space dimension required to model a system which exhibits chaotic behaviour. Fig. 8 shows the reconstructed time series and the corresponding autocorrelation function for model c) (cantilever beam).

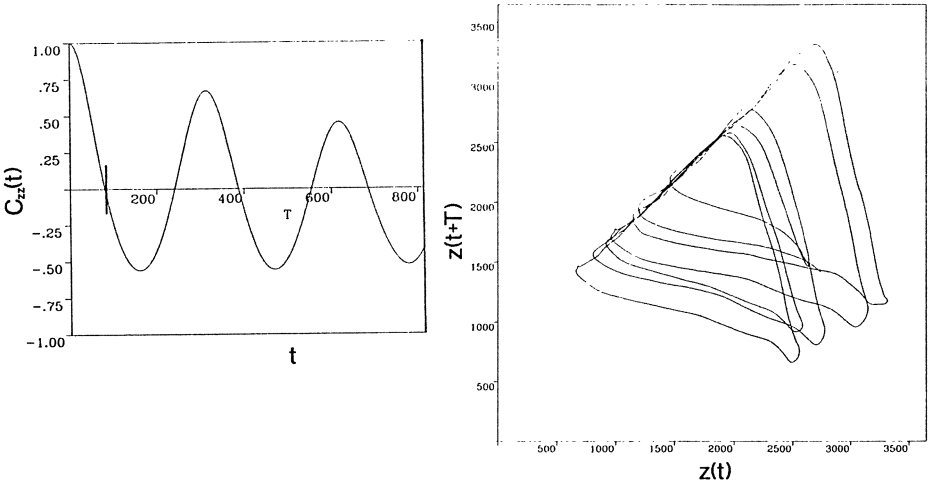

Fig. 8: Autocorrelation function and reconstructed time series

The correlation integral C(r) as a function of the radius r of the hypersphere is shown in Fig. 9 The results are summarized in Table 1.

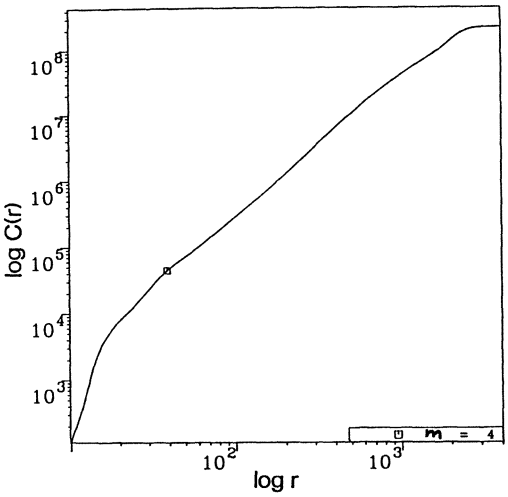

Fig. 9: Correlation-integral C(r) versus radius r for a measured time series with m = 4, T = 80, n=15000, v_0=0.043 m/s, F_N= 9.0 N

Lyapunov exponents: (m=3)	$\lambda_1^1 \approx 11$, $\lambda_2^1 \approx 0.00$, $\lambda_3^1 \approx -3$
Correlation dimension: (m=4)	$D_C = 2.046$

Table 1: Lyapunov exponents and correlation dimension for model c)

Furthermore the friction characteristic has been measured using a special test set up. The friction characteristic in relation of the normal force can be seen in Fig. 10. A curve fit with friction model (3) resulted in the parameters $\mu_0 = 0.7$, $\mu_1 = 0.35$, $\lambda = 0.25$, $\alpha = 0.00$.

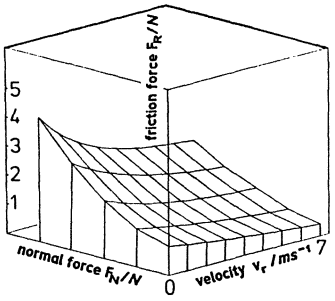

Fig. 10: Measured friction characteristic

5. Concluding remarks

Friction induced self-sustained oscillations exhibit a variety of phenomena. Chaotic motions have been found numerically and experimentally. Simulations based on two discrete models resulted in p-periodic solutions of nearly any period up to p = 9 as well as in chaotic motions. In the case of a single-degree-of-freedom oscillator with external harmonic excitation the routes to chaos are similar to intermittency. All motions showed stick and slip modes. In the case of a two-degree-of-freedom spring-mass- damper-system the routes to chaos have been found similar to period-doubling. Here, for certain parameters one mass showed stick-slip motion while the other remained in a pure slip mode. Experiments performed with a cantilever beam and a thin centrally fixed plate, where in either case friction forces were applied by means of a running belt acting on the structure, friction forces with decreasing characteristic have been measured. A pseudo state space was reconstructed from time series and Lyapunov exponents as well as correlation dimension have been computed from measured signals. They proved that the measured irregular motions are in fact chaotic.

Acknowledgement

This research was financed by the Volkswagen foundation under contract Nr. I/63177. The authors acknowledge grateful this support.

6. References

[1] Magnus, K.: Schwingungen. Teubner, Stuttgart 1961.
[2] Moon, F.C.; Shaw, S.W.: Chaotic vibrations of a beam with non-linear boundary conditions. Int. J. Non-Linear Mechanics 18 (1983), pp. 465-477.
[3] Hendriks, F.: Bounce and chaotic motion in impact print hammers. IBM Journal of Research and Development 27 (1983).
[4] Szczygielki, W.M.: Dynamisches Verhalten eines schnell drehenden Rotors bei Anstreifvorgängen. Diss. ETH Zürich, Nr. 8094 (1986).
[5] Kaas-Petersen, Chr.; True, H.: Periodic biperiodic and chaotic dynamical behavior of railway vehicles. Proc. 9th IAVSD-Symp., Linkoping 1985, pp. 208–221.
[6] Pfeiffer, F.: Seltsame Attraktoren in Zahnradgetrieben. Ing.-Arch. 58 (1988), pp. 113-125.
[7] Païdoussis, M.P.; Li, G.X.; Moon, F.C.: Chaotic oscillations of the autonoumous system of a constrained pipe conveying fluid. J. Fluid and Structures.
[8] Thompson, J.M.T.; Stewart, H.B.: Nonlinear Dynamics and Chaos – Geometrical Methods for Engineers and Scientists. John Wiley & Sons, Chichester, New York, Brisbane, Toronto, Singapore, 1986.
[9] Abraham, R.H.; Shaw, C.D.: Dynamics – the geometry of behaviour. Part 2, 3, 4. Aerial Press, Santa Cruz, 1983–1988.
[10] Kunick, A.; Steeb, W.-H.: Chaos in dynamischen Systemen. BI, Mannheim, Wien, Zürich, 1986.
[11] Popp, K.; Schneider, E.; Irretier, H.: Noise generation in railway wheels due to rail-wheel contact forces. Proc. 9th IAVSD Symp., Linkoping 1985, pp. 448-466.
[12] Fingberg, U.: A wheel-rail-squealing-noise model. Proc. Polish-German Workshop on Dynamical Problems in Mechanical Systems. Madralin, Poland 1989.
[13] Grabec, I.: Explanation of random vibrations in cutting on grounds of deterministic chaos. Robotics & Computer-Integrated Manufacturing (1988), pp. 129–134.
[14] Pomeau, Y.; Manneville, P.: Intermittent transition to turbulence in dissipative dynamical systems. Comm. Math. Physics 74 (1980), pp. 189–197.
[15] Packard, N.H.; Crutchfield, J.P.; Farmer, J.D.; Shaw, R.S.: Geometry of time series. Phys. Rev. Lett. 45 (1980), pp. 712–716.
[16] Sano, M.; Sawada, Y.: Measurement of the Lyapunov Spectrum from a Chaotic Time Series. Physica 16D (1985), pp. 285–317.
[17] Grassberger, P.; Procaccia, I.: Measuring the strangeness of strange attractors. Physica 9D (1983), pp. 189–208.

Characterisation of Chaotic Regimes and Transitions in a Thermally-Driven, Rotating Stratified Fluid

P. L. Read, M. J. Bell, D. W. Johnson & R. M. Small*

Meteorological Office, London Road, Bracknell, Berkshire, UK.

Summary

The transitions from regular, steady or periodic baroclinic waves to aperiodic, chaotic flow in a thermally-driven, rotating fluid annulus are discussed. Two distinct transitions are found, depending mainly on the value of the thermal Rossby number Θ. *At moderate* Θ *a transition to chaos occurs via a doubly-periodic 'amplitude vacillation' which develops a very low frequency irregular modulation. The transition towards classical 'geostrophic turbulence' at low* Θ *occurs at a well-defined point in parameter space, apparently via an intermittent 'structural vacillation'. Emphasis is placed on the characterisation of the transitions and chaotic states from phase portraits constructed using singular value decomposition methods.*

1. Introduction

Prediction and assessment of intrinsic predictability have long been of primary interest in meteorology. The vast complexity of atmospheric behaviour has suggested that the finite predictability of the weather and climate may be due principally to the excitation of *many* degrees of freedom (DOF). Most recent studies of atmospheric predictability have therefore employed the most complex numerical simulations of atmospheric circulation [1], but with, as yet, rather inconclusive results as to the atmosphere's *intrinsic* predictability. With the development of the theory of chaos in low-order dynamical systems during the past 20 years [2], however, it has become apparent that complex, aperiodic behaviour with finite predictability can be exhibited in systems with as few as 3 DOF. Such a result challenges the pessimistic assertion that atmospheric motion *necessarily* requires immense complexity in order to model its behaviour. The dynamics of weather and climate, however, is almost certainly still too complex to be characterised unambiguously by existing methods; even if its dynamical behaviour does lie on a low– dimensional attractor, its dimension is probably too large to be characterised from existing datasets [3].

In studying possible low-order processes which may contribute to the finite predictability of the atmosphere, however, the use of laboratory experiments with dynamical similarities to atmo-

* Present address: Hooke Institute for Atmospheric Research, Clarendon Laboratory, Oxford University, UK.

W. Schiehlen (Editor)
Nonlinear Dynamics in Engineering Systems
IUTAM Symposium Stuttgart/Germany 1989

spheric circulation can be a valuable source of physical insight, as well as providing a 'test-bed' for the development of analysis techniques which may eventually be applied to meteorological data. Thermal convection in a rotating, cylindrical fluid annulus, differentially heated in the *horizontal*, has been studied for many years [4] as one such laboratory analogue of the large-scale circulation of a planetary atmosphere. As with a generic atmosphere on a spherical planet, the annulus in its typical form possesses circular symmetry about the rotation axis in its boundary conditions, and exhibits a rich variety of flow regimes depending upon the external conditions (e.g. temperature contrast ΔT and rotation rate Ω). These regimes range from steady axisymmetric flow (analogous to tropical Hadley flow, at low Ω), through regular steady or periodic *baroclinic waves* (at moderate Ω) to highly irregular aperiodic 'geostrophic turbulence' (at high Ω). As in the mid-latitude atmosphere, waves develop as the result of a potential energy-releasing (*baroclinic* [4]) instability of the azimuthally-symmetric component of the flow driven by differential heating.

In the following sections, results are presented from analyses of high precision time series of measurements of temperature and total heat transport in a rotating annulus, concentrating upon regions of parameter space close to observed transitions to spatio-temporal chaos. Section 2 outlines the experimental details, and the analysis methods are described in Section 3, concentrating especially on the use of singular value decomposition (SVD) techniques to construct and characterise phase portraits from the measured data. Some results on transitions to chaotic flows in the rotating annulus are presented in Section 4.

2. Apparatus and data acquisition

The working fluid was contained in a cylindrical annulus with thermally conducting sidewalls at r = 2.0 cm and r = 8.5 cm, and rigid, insulating boundaries in contact with the fluid at z = 0 and z = 14.0 cm. The apparatus was rotated about its axis of symmetry and differentially heated in the horizontal at the sidewalls (the outer cylinder being the warmer). The annulus was designed for the precision measurement of fluid and boundary temperatures and of total heat transport, and was essentially the same as described by Hignett et al. [5]. The working fluid consisted of a 25% solution by volume of glycerol in water, with a Prandtl number of 26.4. Temperatures at the boundaries and in the fluid were measured using copper–constantan thermocouples (sensitivity $\sim 40\mu$V per K). In the fluid, 32 thermocouples were equally spaced in azimuth at mid-height and mid-radius, enabling the azimuthal wavenumber spectrum to be obtained readily by fast Fourier Transform techniques. The total heat transport through the inner side boundary was measured using the method described by Hignett [5], from the coolant

(water) flow rate and the difference in temperature between the inlet and outlet. Total heat transport on timescales as small as $\sim$ 20s could be measured to an absolute precision of $\sim \pm 2\%$, though much smaller relative changes ($\sim$ parts in 10^3) could be detected.

A variety of different procedures were used to take in and analyse the data. Short time series of measurements at all thermocouples in the fluid and boundaries, and of the total heat transport, were recorded and used to identify the dominant flow type and to measure the wave drift rates and (where appropriate) vacillation frequencies (e.g. see [5]). At selected points, much longer, high precision time series of temperature at one of the ring thermocouples and the total heat transport, averaged over 1-2s, were recorded for up to 250 drift periods (requiring up to 20 hrs of measurements) for subsequent analysis. Mainly for practical reasons, the long time series were taken at constant $\Delta T = 10K$ and variable Ω, corresponding to a constant Grashof number ($= \Theta\mathcal{T}$, where Θ is the thermal Rossby number and $\mathcal{T}$ the Taylor number [4]) of $\sim 6.19 \times 10^5$.

3. Phase portrait analyses

The long time series were required primarily for the reconstruction of 'phase portraits' by the method of time-delay embedding (e.g. [2]). In the latter, a scalar time series T(t) is represented as a trajectory in a K-dimensional embedding space by denoting the state of the flow at time t by the vector $[T(t),T(t+\tau),T(t+2\tau)....T(t+(K-1)\tau)]$. In the present work, phase portrait reconstruction was further refined by the use of singular value decomposition (SVD - [6]) to reproject the trajectory onto a statistically optimal orthogonal basis. The latter comprises the eigenvectors of the covariance matrix computed using a sliding 'window' of n points (where $n \gg$ maximum required embedding dimension) which is stepped along the time series. As discussed in [6], this method removes some of the arbitrary choices to be made in time-delay reconstruction (e.g. of delay time τ). Use of a truncated set of the derived eigenvectors, ordered according to their eigenvalues, also introduces a useful element of filtering and averaging which can remove some of the unwanted non-deterministic components of the signal and enhance the signal-to-noise ratio of the deterministic component. An example of the application of this method to data from the rotating annulus [7] from a quasi-periodic flow on a very narrow 2-torus is illustrated in Fig. 1.

The penalty which must be paid for these advantages is a need to sample the signal somewhat more frequently than would be strictly necessary for the simple form of delay embedding. For the present work, time series were typically sampled at 1-2 s intervals, placing 200 or more samples per wave drift period (though rather fewer per typical vacillation period, which ranged

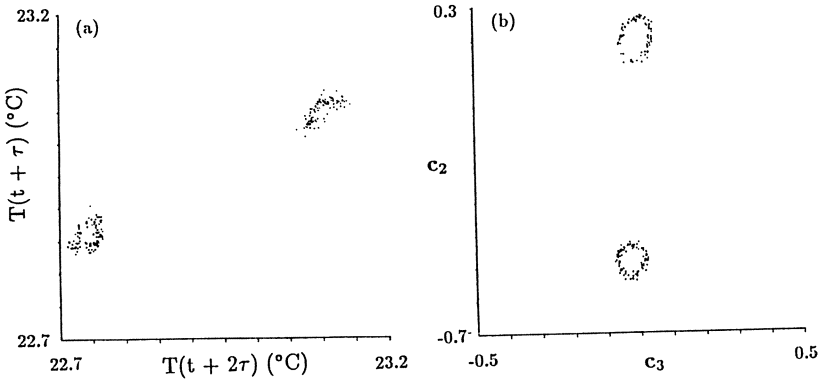

Figure 1. Poincaré sections from a weakly quasi-periodic annulus wave [7], reconstructed (a) using delay-embedding with τ=10s at T(t)=23.0°C and (b) using SVD with a 25-point window in the (c_2,c_3) *plane at* c_1=0.

typically from 50s - 300s). A window length τ_w of between 75s and 100s proved most suitable, given the relatively long wave drift periods. This value of τ_w is somewhat longer than would be suggested from the discussion of [6] (Eq 3.20) though, even for τ_w = 100s, is still less than most typical fundamental vacillation frequencies.

In characterising the behaviour of non-linear systems, it is often desirable to detect the onset of chaotic behaviour, and to obtain estimates of the degree of complexity of the flow. A variety of methods have appeared in the literature in recent years (e.g. [2]). The most common method is to estimate the correlation dimension [2] of the reconstructed attractor. This method is now known, however, generally to require very large and densely sampled datasets. Smith [8], for example, concludes that the number of statistically independent points N_{min} required to estimate the correlation dimension to within ±5% of its true value exceeds 42^M, where M is the greatest integer less than the dimension of the underlying attractor. With the present datasets ($N < 5 \times 10^4$), this would preclude the reliable estimate of dimensions significantly exceeding about 2. The SVD method itself provides an estimate of the dimensionality of a dataset from the number of eigenvalues in the singular value spectrum lying significantly above the 'noise floor' (cf [6]). This measure is not a robust estimate of the dimensionality, however, but depends on factors such as the local curvature of the underlying manifold which, in turn, may depend upon the choice of sampling and window timescales τ_s and τ_w. Accordingly, we follow the approach recommended by Smith [8] in using methods based on the analysis of *localised regions* of the reconstructed attractor. In the following analyses, we make use of the pointwise dimension D_p

[9] derived from the SVD phase portraits down to length scales limited only by the sampling and instrumental noise. For a given flow, the dimension quoted is an average over several (typically 20) randomly-selected points across the reconstructed attractor.

Static invariants, such as the various dimension estimates discussed above, provide an indication of the overall intrinsic complexity of the behaviour of a dynamical system, but are not a particularly sensitive means of directly detecting the onset of chaos. Sensitive dependence on initial conditions is the critical property of chaotic behaviour, suggesting that an estimate of the largest non-negative Lyapunov exponent λ_1 would be the most suitable means of detecting the onset of chaos. In the present work, we use the algorithm suggested by Wolf et al. [10], which directly measures the divergence of initially nearby segments of trajectories on the reconstructed attractor. Estimates of λ_1 were derived from attractors reconstructed using the simplest delay method as well as via SVD, with similar results being obtained. Consequently, results derived from the SVD trajectories were used to obtain the results given below. As with the dimension calculations, the robustness of the results obtained was verified by repeating the calculations using a range of embedding dimensions, delay/window times and evolution timescales.

4. Results

Fig. 2 shows estimates of both D_p (a) and λ_1 (b) for all the flows studied in the Gr = 6.19 x 10^5 section as a function of Taylor number $\mathcal{T}$. Solid squares in Fig. 2 denote estimates derived from the temperature time series, and open symbols denote results for heat transport. Steady wave and regular amplitude vacillation flows (drifting waves periodically modulated in amplitude [4]) consistently exhibit D_p slightly exceeding 1.0 and 2.0 respectively, consistent with their respective appearance in phase portraits [7] as limit cycles and 2-tori. Pointwise dimensions for the amplitude vacillation cases were also calculated from the corresponding heat transport time series, and consistently resulted in $D_p \sim 1$ i.e. 1 less than that of the corresponding temperature dataset because of the absence of the component due to the wave drift (cf [11]). The largest Lyapunov exponent associated with these flows is consistently indistinguishable from zero, with an upper limit for λ_1 of around 4 x 10^{-4} bits s^{-1} (implying an intrinsic error-doubling time of > 2500s.

Sharp boundaries between quasi-periodic and apparently chaotic behaviour are found at Taylor numbers of 4.8 x 10^6 and 1.0 x 10^7 (and also probably at 3.8 x 10^6). The boundaries at $\mathcal{T}$ = 3.8 x 10^6 and 4.8 x 10^6 correspond to sudden transitions at which the modulation index of regular amplitude vacillation develops an irregular variation (termed 'modulated amplitude vacillation'-

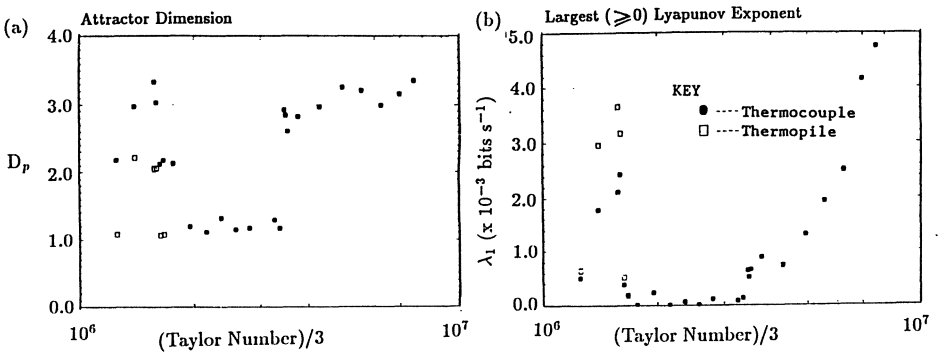

Figure 2. Measurements of (a) D_p and (b) λ_1 for baroclinic annulus waves [7] as a function of $\mathcal{T}$ at Gr=6.2 x 10^5, from SVD-reconstructed attractors.

MAV, [7]) on a timescale ~ 1500-2500s. Spatial measurements show the azimuthal wavenumber m=3 component growing and decaying, and apparently competing with m=2 in the MAV regime [7]. On crossing the boundary into the MAV regime, D_p jumps to a value around 3.2 and λ_1 becomes significantly positive at ~ 2.0 x 10^{-3} bits s^{-1}, with little variation in these quantities across the MAV regime. The heat transport datasets also indicate a sharp transition to chaotic behaviour at this point, with D_p jumping to around 2 and λ_1 consistent with the temperature data (around 3 x 10^{-3} bits s^{-1}). Phase portraits from the MAV regime cases are shown in Fig. 3. The basic toroidal structure in the temperature phase portrait is qualitatively similar to that of pure amplitude vacillation, but the Poincaré section reveals that the 'walls' of the torus have a finite thickness significantly greater than can be accounted for by instrumental effects. Little systematic structure is apparent within the wall thickness itself, though the Poincaré section does contain some strand-like features in both branches. In the heat transport phase portrait, the wave drift component is absent, and the trajectories appear to lie on a nearly disk-like structure of small though finite thickness (cf Hart [11]). The thickness of the disk-like structure is comparable with or somewhat greater than that due to instrumental drift.

At the transition to structural vacillation (SV - in which regular waves undergo modulations of their structure but not primarily in the amplitude of the dominant wavenumber [4]) at $\mathcal{T}$ = 1.0 x 10^7, λ_1 becomes significantly positive (Fig. 2) but initially quite small, then increases rapidly with $\mathcal{T}$. D_p in this regime, however, remains close to 3, though with some evidence for a gradual increase in D_p with increasing $\mathcal{T}$. The temperature phase portraits in this region (see [7]) show evidence of the underlying limit cycle associated with drifting regular waves, but otherwise little discernible structure. The transition into SV occurs within a very narrow region of parameter space, apparently going from steady, regular, drifting waves into fully-developed chaotic SV via a change in $\mathcal{T}$ of only 0.5%. The transition appears to entail an intermediate state

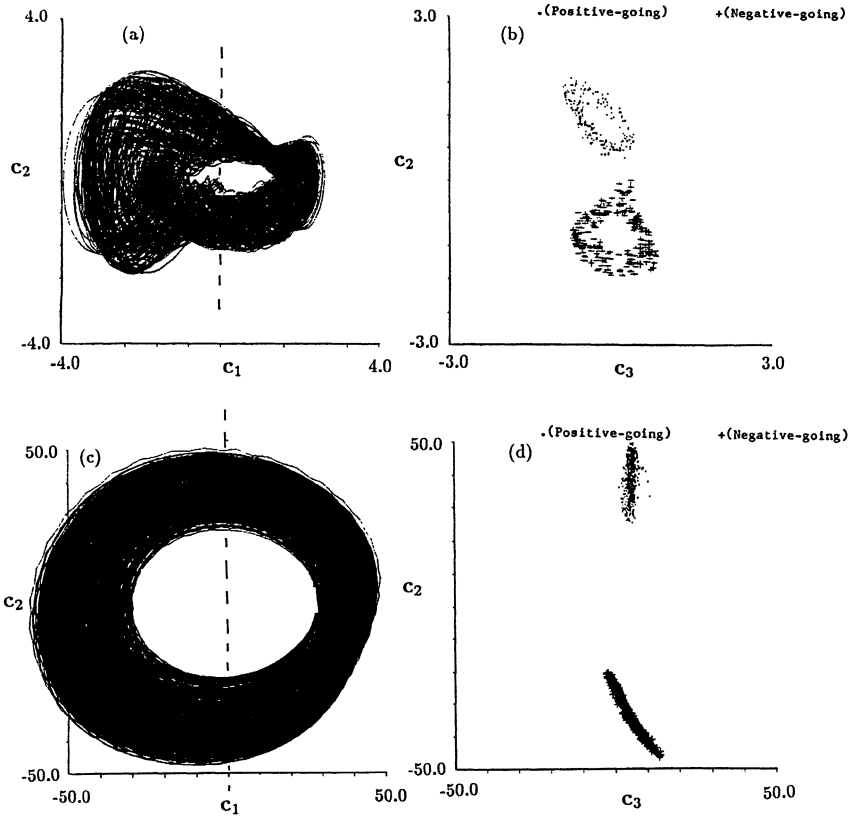

Figure 3. SVD phase portraits in the MAV regime derived from single-point temperature measurements [(a) & (b)] and total heat transfer [(c) & (d)] using a (25,2) window (τ_w=85s). Poincaré sections [(b) & (d)] are at c_1=0.

which comprises intermittent bursts of vacillation (as apparent in the heat transport time series, see Fig. 4), though it was not possible to explore any possible scaling behaviour associated with this transition because of inadequate resolution in the control of the experimental conditions. This observation of a sudden transition to the chaotic SV regime is in contrast to previous work [12], and has not been observed in the two-layer system [11]. Neither transition described herein has been adequately reproduced to date in any low-order non-linear model.

References

[1] Shukla, J. (1985). *Adv. in Geophys.*, **28B**, 87–122.

[2] Eckmann, J.-P. & Ruelle, D. (1985). *Rev. Mod. Phys.*, **57**, 617–656.

[3] Grassberger, P. (1986). *Nature*, **323**, 609–612.

[4] Hide, R. & Mason, P. J. (1975). *Adv. in Phys.*, **24**, 47–100.

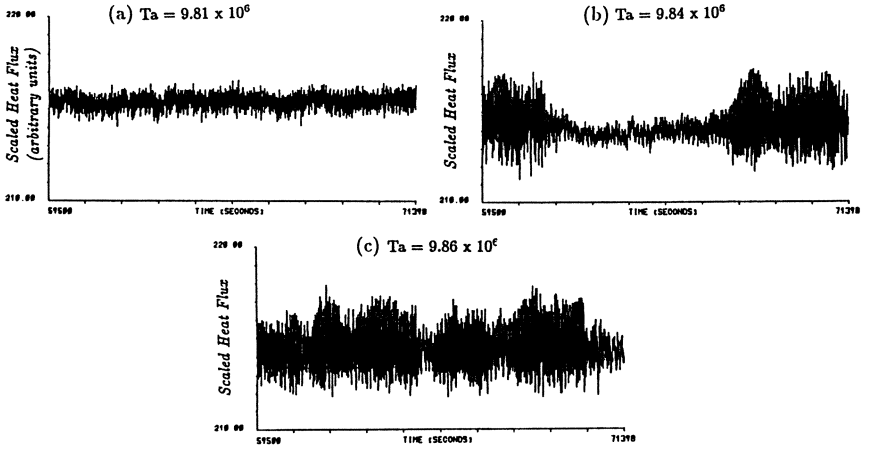

Figure 4. Extracts from heat transfer time series near the steady wave/SV transition at Gr=6.2 x 10^5 and (a) $\mathcal{T}$ =9.81 x 10^6, (b) $\mathcal{T}$ =9.84 x 10^6 and (c) $\mathcal{T}$ =9.86 x 10^6.

[5] Hignett, P., White, A. A., Carter, R. D., Jackson, W. D. N. & Small, R. M. (1985). *Quart. J. R. Met. Soc.*, **111**, 131–154.

[6] Broomhead, D. S. & King, G. P. (1986) *Physica,* **20D**, 217–236.

[7] Read, P. L., Bell, M. J., Johnson, D. W. & Small, R. M. (1989). *Geophys. Astrophys. Fluid Dyn.*, to be submitted.

[8] Smith, L. (1988). *Phys. Lett.*, **133**, 283–288.

[9] Farmer, J. D., Ott, E. & Yorke, J. A. (1983). *Physica,* **7D**, 153–180.

[10] Wolf, A., Swift, J. B., Swinney, H. L. & Vastano, J. A. (1985). *Physica,* **16D**, 285–317.

[11] Hart, J. E. (1985). *Tellus,* **37A**, 286–296.

[12] Buzyna, G., Pfeffer, R. L. & Kung, R. (1984). *J. Fluid Mech.*, **145**, 377–403.

Periodic Solutions of Nonlinear Dynamical Systems with Discontinuities

– Numerical Construction, Stability, Bifurcation –

E. Reithmeier

Institut B für Mechanik, TU München,
Arcisstr. 21, D–8000 München 2

Summary

For large areas of the parameter space of a nonlinear dynamical system with discontinuities the behavior is – such as in differentiable systems – characterized by limit cycles. Among other things, this can be put down to the fact that in each asymptotic stable area of the state space exactly one limit cycle must exist. In this paper a technique for computing a limit cycle will be presented. Furthermore it will be shown, how stability- and bifurcation-analysis can be applied to periodic solutions with discontinuities. The methods are demonstrated on the mechanical model of non-loaded gear wheels of a transmission.

1 Introduction

For technical problems it may in many cases be necessary to use mechanical models whose mathematical description has discontinuities with respect to the state space variables. Important examples are mechanical systems with impacts and play or stick-slip systems with dry-friction. Systems with impact and play are mainly investigated by authors as [SHAW, HOLMES 1983], [PFEIFFER 1984], [SHAW 1985], [HEIMANN, BAJAJ, SHERMAN 1988], [PFEIFFER 1988 a, b] and [KARAGIANNIS 1989]. Stick-slip systems are dealt with especially by [LÖTSTEDT 1981], [SCHIELEN 1983], [JEAN, PRATT 1985], [SHAW 1986], [MOREAU 1987] and [HAJEK 1989]. These papers concentrate mainly on mathematical modelling, computation and simulation. Some authors as HEIMAN et. al or SHAW also discuss stability and bifurcation problems of periodical solutions with discontinuities. The behavior of nonlinear vibrating systems is mostly characterized by limit cycles, which are asymptotically stable. The consequence is that – in spite of small perturbations – limit cycles determine the dynamical behavior. The size of the asymptotic stable areas depends on the systemparameters $\mathbf{p} \in P$, which – for technical reasons – belong to a set $P \subset \mathbb{R}^m$. Hence, it is important to investigate the stability- and bifurcation-behavior depending on $\mathbf{p} \in P$. For this purpose the first step is to compute the periodic solutions. In the second step it will be shown, how stability- and bifurcation-investigations can be applied to limit cycles. To demonstrate these steps, an example will be given.

2 Theory

2.1 Numerical computation of limit cycles with discontinuities

With some modifications all results about the existence, stability and bifurcation of periodic solutions of a nonlinear differentiable dynamical system $\dot{\mathbf{x}} = \mathbf{f}(\mathbf{x}, \mathbf{p})$ can be transferred to systems with discontinuities with respect to the variables $\mathbf{x}$ of the state space.

W. Schiehlen (Editor)
Nonlinear Dynamics in Engineering Systems
IUTAM Symposium Stuttgart/Germany 1989

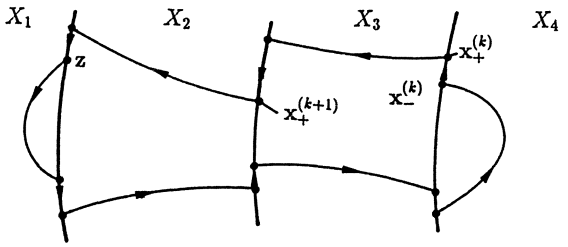

Fig.1: Partition of state space TM with trajectory

The most essential modification is the partition of the state space $TM\,(\cong \mathbb{R}^n)$ into those open subsets $X_i \subset TM$, on which the vectorfield $\mathbf{f} : TM \to TM$ is C^k – continous. On each set X_i the mechanical system is described by a field $\mathbf{f}_i$, that is

$$\mathbf{f}(\mathbf{x},\mathbf{p}) = \begin{cases} \mathbf{f}_1(\mathbf{x},\mathbf{p}) & \forall\ \mathbf{x} \in X_1 \\ \vdots & \\ \mathbf{f}_N(\mathbf{x},\mathbf{p}) & \forall\ \mathbf{x} \in X_N \end{cases} \tag{2.1}$$

If there are structural differences between the vectorfields $\mathbf{f}_i$, then the system is called "structural–variant". Otherwise it is called "structural–invariant". Stick-slip systems, for instance, are structural variant, systems with impact and play are structural–invariant. The border $\partial\overline{X_i}$ of the set X_i constitutes the "set of discontinuities" or "switch-plane" of codimension 1 (c.f. Fig.1). In this case the separation of the state space is as follows:

$$TM = \overline{\bigcup_{i=1}^{N} X_i}\ . \tag{2.2}$$

Without restrictions, it is possible to describe the switch-plane as the set of solutions of a nonlinear algebraic equation:

$$g_i(\mathbf{x}) = 0\ ;\quad g_i : TM \to \mathbb{R} \tag{2.3}$$

The switch-planes are POINCARÉ-sections for the trajectories. Therefore it is useful to describe the motion recursively. For the uniqueness of a trajectory Φ_ξ $(\Phi_\xi(0) = \boldsymbol{\xi})$ in the state space (c.f. Fig.1) a law

$$\sigma_i : g_i^{-1}(0) \to g_i^{-1}(0)\ ,\quad \mathbf{x}_-^{(k)} \mapsto \mathbf{x}_+^{(k)} \tag{2.4}$$

is necessary. σ_i maps a point $\mathbf{x}_-^{(k)}$ immediately before the discontinuity to a point $\mathbf{x}_+^{(k)}$ immediately after the discontinuity. To compute a limit cycle means to determine a series of m points

$$\mathbf{z} := \mathbf{x}_+^{(0)}, \mathbf{x}_+^{(1)}, \ldots, \mathbf{x}_+^{(m-1)} \tag{2.5}$$

which have to lie on the switch-plane.

Furthermore the following equation must hold

$$\mathbf{x}_+^{(m)} = \mathbf{x}_+^{(0)} + n\,T\,\mathbf{e}_{2f+1}\ . \tag{2.6}$$

It is presumed that the state-space coordinate x_{2f+1} represents the time, if the dynamical system (equation (2.1)) is nonautonomous. $\mathbf{f}$ is the number of degrees of freedom. In this case, the vectorfield f has to be $T-$periodically with respect to x_{2f+1}, that is

$$\mathbf{f}(x_1, \ldots, x_{2f+1} + T, \mathbf{p}) = \mathbf{f}(x_1, \ldots, x_{2f+1}, \mathbf{p})\ . \tag{2.7}$$

$n \in \mathbb{N}$ indicates the number of periods of the excitation of the system. $\mathbf{e}_{2f+1}$ is the unit-vector in "$2f+1$ direction" of $\mathbb{R}^{2f+1}$. In the following, a limit cycle (according to equation (2.6)) will be called a $(m:n)$-cycle. To compute a $(m:n)$-cycle it is useful to presume that the cycle-length m and the number of excitation-periods n are known. Moreover the series $(i_1,\ldots,i_m)$ of indices of the sets X_i, which are passed by the trajecory, should be given. Let us assume that the recursion $\Psi_{i_k} : g_{i_k}^{-1}(0) \to g_{i_k}^{-1}(0)$ maps the state $\mathbf{x}_+^{(k)}$ to the state $\mathbf{x}_+^{(k+1)}$, then the equation

$$\mathbf{R}(\zeta) := \begin{bmatrix} \Psi_{i_1}(\mathbf{z}) - \mathbf{x}_+^{(1)} \\ \vdots \\ \Psi_{i_{m-1}}\left(\mathbf{x}_+^{(m-2)}\right) - \mathbf{x}_+^{(m-1)} \\ \Psi_{i_m}\left(\mathbf{x}_+^{(m-1)}\right) - \mathbf{z} - n \cdot T\,\mathbf{e}_{2f+1} \end{bmatrix} = \mathbf{0} \tag{2.8}$$

is valid for the cycle $\zeta := \left(\mathbf{x}_+^{(0)},\ldots,\mathbf{x}_+^{(m-1)}\right)$.

If the state $\mathbf{x}_+^{(k)}$ is determined, then the state $\mathbf{x}_+^{(k+1)}$ can be computed from the boundary-value-problem (BVP) according to equation (2.9).

$$\begin{aligned} \begin{bmatrix} \mathbf{x} \\ t^{(k+1)} \end{bmatrix}' &= \begin{bmatrix} t^{(k+1)}\mathbf{f}_{i_k}(\mathbf{x},\mathbf{p}) \\ 0 \end{bmatrix} \\ \mathbf{r}(\mathbf{x}(0),\mathbf{x}(1)) &= \begin{bmatrix} \mathbf{x}(0) - \mathbf{x}_+^{(k)} \\ g_{i_k}(\mathbf{x}(1)) \end{bmatrix} = \mathbf{0}\,. \\ \mathbf{x}_-^{(k+1)} &:= \mathbf{x}(1) \\ \Psi_{i_k}\left(\mathbf{x}_+^{(k)}\right) &:= \sigma_{i_k}\left(\mathbf{x}_-^{(k+1)}\right) \end{aligned} \tag{2.9}$$

The BVP can be solved by the program system BOUNDSOL (c.f. [BULIRSCH, STOER, DEUFLHARD 1977]). The numerical computation of the $(m:n)$-cycle ζ requires the Jacobian of the function $\mathbf{R}$. It turns out that the Jacobian

$$D\mathbf{R}(\zeta) = \begin{bmatrix} \mathbf{G}_{i_1} & \mathbf{E} & & \\ & \ddots & \ddots & \\ & & \ddots & \mathbf{E} \\ -\mathbf{E} & & & \mathbf{G}_{i_m} \end{bmatrix}, \qquad \mathbf{G}_{i_k} := D\Psi_{i_k}\left(\mathbf{x}_+^{(k-1)}\right) \tag{2.10}$$

is the same matrix as used by the multiple-shooting-method. Using the unit matrices $\mathbf{E}$ on the superdiagonal of $D\mathbf{R}(\zeta)$ as PIVOT-elements, it is possible to make a LR-decomposition with $(m-1)$ block GAUSS steps.

2.2 Numerical stability- and bifurcation-analysis of a $(m : n)$-cycle

Let $\mathbf{z}$ be an arbitrary point on one of the switch-planes, then the recursion

$$\mathbf{x}_+^{(0)} := \mathbf{z} \quad , \qquad \mathbf{x}_+^{(k)} := \Psi_{i_k}\left(\mathbf{x}_+^{(k-1)}\right) \quad ; \quad (k = 1, 2, \ldots) \tag{2.11}$$

constitutes a unique series of break-through-points, induced by the trajectory $\Phi_{\mathbf{z}}$. This recursion may also be written as

$$\Gamma_{\mathbf{z}} : \mathbb{N} \to S \quad , \quad k \mapsto \mathbf{x}_+^{(k)} = (\Psi_{i_k} \circ \ldots \circ \Psi_{i_1})(\mathbf{z}) \qquad \text{with} \qquad S := \bigcup_{i \in \mathbb{N}} g_i^{-1}(0) \ . \tag{2.12}$$

$\Gamma_{\mathbf{z}}$ is called "asymptotic–stable" iff:

(a) $\Gamma_{\mathbf{z}}$ is restricted in $\mathbb{R}^n$.

(b) There is a $\varepsilon(\mathbf{z}) > \mathbf{0}$, so that for every neighbor-series $\Gamma_{\mathbf{z}'}$ with $\| \mathbf{z} - \mathbf{z}' \| < \varepsilon(\mathbf{z})$
$\lim\limits_{k \to \infty} \| \Gamma_{\mathbf{z}}(k) - \Gamma_{\mathbf{z}'}(k) \| = 0$ is valid.

The simply connected components $Z^+ := \{\mathbf{z}' \in S \ | \Gamma_{\mathbf{z}'}$ is asymptotic–stable $\}$ are called "stability domains". From this definition an interesting theorem results:

Theorem: In every stability domain $Z^+ \subset S$ exists one and only one periodic solution $\Gamma_{\mathbf{z}}$, which is – of course – asymptotical–stable.

In other words: It exists a $(m\ ,\ n) \in \mathbb{N}^2$ and a $\mathbf{z} \in Z^+$ so that $\Gamma_{\mathbf{z}}$ is a $(m : n)$-cycle. For a proof see [REITHMEIER 1989]. The determination of a $(m : n)$-cycle according to chapter (2.1) doesn't depend on whether it is stable or not stable. The eigenvalues of the monodromymatrix indicate whether a $(m : n)$-cycle is stable or not. To compute this matrix it is assumed that $\mathbf{z}_0 \in S$ is – for an appropriate $(m\ ,\ n) \in \mathbb{N}^2$ – a fixpoint of the mapping

$$\mathbf{F} : \mathbf{z} \mapsto \Gamma_{\mathbf{z}}(m) - nT\mathbf{e}_{2f+1} \ . \tag{2.13}$$

After some algebraic manipulations one gets the monodromymatrix $D\mathbf{F}(\mathbf{z}_0)$ at $\mathbf{z}_0$ by means of the formula

$$D\mathbf{F}(\mathbf{z}_0) = \prod_{k=m}^{1} \mathbf{G}_{i_k} \ . \tag{2.14}$$

The matrices $\mathbf{G}_{i_k}$ are the Jacobians of the multiple-shooting-matrix (equations (2.12) and (2.13)), which has already been computed. Therefore no additional computation is necessary to build $D\mathbf{F}(\mathbf{z}_0)$. The stability of the limit cycle depends essentially on the choice of the parameters $\mathbf{p}$. Furthermore the influence of the parameters on the bifurcation-analysis is important, too. The reason for this is the direct connection between the stability and the bifurcation of the $(m : n)$-cycle. That is to say, the point $\mathbf{z}$ is a unique solution of

$$\mathbf{r}(\mathbf{z}) := \mathbf{F}^l(\mathbf{z}) - \mathbf{z} = \mathbf{0} \ , \tag{2.15}$$

with $\mathbf{F}^l := \mathbf{F} \circ \ldots \circ \mathbf{F}$ (l-times) iff

$$det(D\mathbf{r}(\mathbf{z})) \neq 0 \tag{2.16}$$

(implicit function theorem!). l is an arbitrary integer. It's evident that

$$D\mathbf{r}(\mathbf{z}) = (D\mathbf{F}(\mathbf{z}))^l - \mathbf{E} \tag{2.17}$$

is true, if $\mathbf{z}$ is a fixpoint of F. Hence

$$\lambda(D\mathbf{F}(\mathbf{z})) = e^{2\pi i \frac{k}{l}} \quad , \quad (k, l \in \mathbb{Z}) \tag{2.18}$$

is necessary for the bifurcation of a $(m : n)$-cycle. $\lambda(D\mathbf{F}(\mathbf{z}))$ is one of the eigenvalues of the monodromymatrix $D\mathbf{F}(\mathbf{z})$. The numbers $e^{2\pi i \frac{k}{l}}$ lie densely on the unit circle in $\mathbb{C}$. Therefore it is necessary that none of the eigenvalues of the monodromymatrix passes – by variation of $\mathbf{p}$ – the unit circle (c.f. Fig.2).

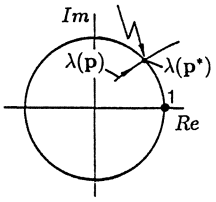

Fig.2: Necessary condition for bifurcation of a $(m : n)$-cycle

According to LIAPUNOV, a limit cycle $\Gamma_{\mathbf{z}}$ is asymptotical–stable, iff all eigenvalues of the monodromymatrix lie inside the unit circle. That means, the loss of stability of a $(m : n)$-cycle is a necessary condition for its bifurcation. Therefore a metamorphosis of the solutions of the dynamical system is possible only if the system loses its stability.

3 Example

The vibrations of mechanical models of non-loaded gear wheels of a transmission are – with increasing amplitudes or frequencies of the driving shaft – characterized by a series of bifurcations of periodic solutions.

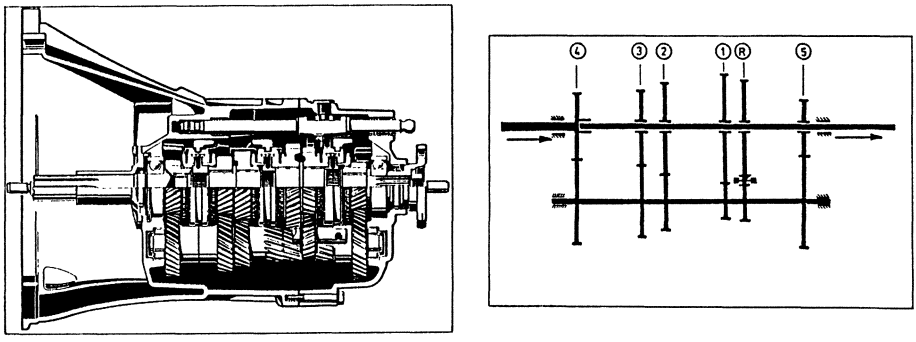

Fig.3: Manual-transmission with its mechanical model

To demonstrate this bifurcation behavior, a simple non-loaded gear wheel model with one degree of freedom (DOF) will be considered. [PFEIFFER 1988a] investigated a rattling model of a gear wheel pair, which is equivalent to the model shown in Fig.4.

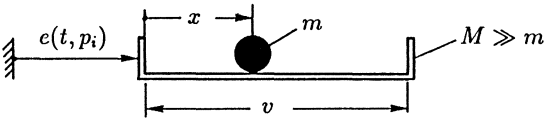

Fig.4: Mechanical model of a non-loaded gear wheel pair

A masspoint m is moving in a pan (mass $M \gg m$) of the length v. The mass is damped proportionally to its velocity (damping coefficient δ). The pan will be excited according to the function $e(t, p_i)$. This function e corresponds to the excitement caused by the motor. Using the relative-coordinate x, the equation of motion reads after transformation to an autonomous ODE of first order ($x_1 := x, x_2 := \dot{x}, x_3 := t$)

$$\begin{aligned} \dot{x}_1 &= x_2 \\ \dot{x}_2 &= -\ddot{e}(x_3, \mathbf{p}_i) - \left(\frac{\delta}{m}\right) x_2 \\ \underbrace{\dot{x}_3}_{\dot{\mathbf{x}}} &= \underbrace{1}_{\mathbf{f}(\mathbf{x},\mathbf{p})} \end{aligned} \tag{3.1}$$

The state space $TM = [0, v] \times \mathbb{R}^2$ is restricted with respect to the relative coordinate x_1. If the mass m reaches the right or left border, an impact will take place. The time at this impact marks the discontinuity. It is assumed that for every discontinuity the same law

$$\sigma\left(\mathbf{x}_-^{(k)}\right) := diag\{1, -\varepsilon, 1\} \cdot \mathbf{x}_-^{(k)} \tag{3.2}$$

is true. ε is the impact-number. The index i_k, indicating the set X_{i_k} may be ignored, because the law σ applies to the whole area of the switch-plane. For $e(t, p_i) := A \sin \omega t$ the vector of the systemparameters is represented by:

$$\mathbf{p} = (d, A, \omega, \varepsilon) \; ; \quad d := \left(\frac{\delta}{m}\right) \; . \tag{3.3}$$

Fig.5 shows a computed (2:1)-cycle with period $T = 2\pi/\omega$. For investigating the stability of this cycle, the monodromymatrix is needed.

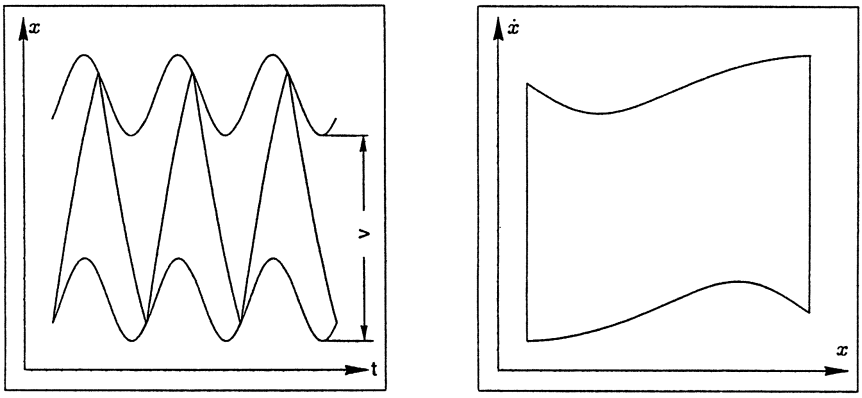

Fig.5: (2:1)-cycle projected into the (x_3, x_1)-plane and into the (x_1, x_2)-phase-space.

After some algebraic manipulations one gets – independent of the excitation e – for the determinant of the monodromymatrix:

$$det(D\mathbf{F}(\mathbf{z}_0) = \varepsilon^{2m}\, e^{-2d(n \cdot T)} \; . \tag{3.4}$$

On the other hand

$$det(D\mathbf{F}(\mathbf{z}_0)) = \lambda_1 \cdot \lambda_2 \tag{3.5}$$

is always true. This equation leads – together with positive damping ($d > 0$) and $\varepsilon \leq 1$ – to

$$\lambda_1 \cdot \lambda_2 < 1 \; , \tag{3.6}$$

or – in case of complex conjugate eigenvalues – to $|\lambda_1| < 1$. That means that the eigenvalues can leave the unit circle only on the real axis. As Fig.6a shows, the (2:1)-cycle will be deformed, if the amplitude of the excitation e decreases. Fig.6b shows the corresponding course of the eigenvalues λ_1 and λ_2.

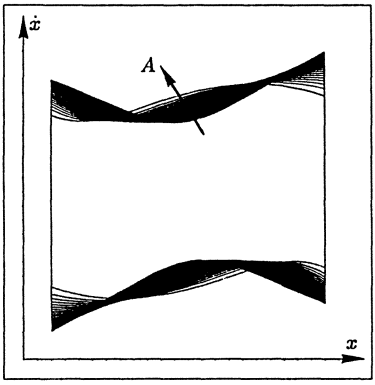

Fig.6a: (2:1)-cycle obtained by variation of A

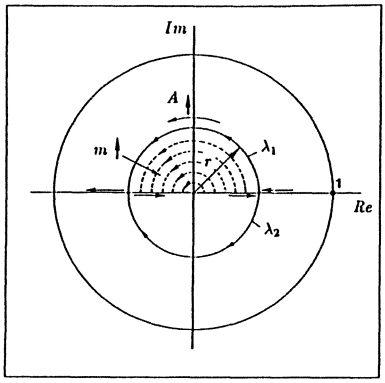

Fig.6b: Course of the eigenvalues of $D\mathbf{F}(\mathbf{z}_0)$ obtained by variation of A

One of the eigenvalues leaves the unit circle on the negative real axis, that is, a perioddoubling to a (4:1)-cycle will take place.

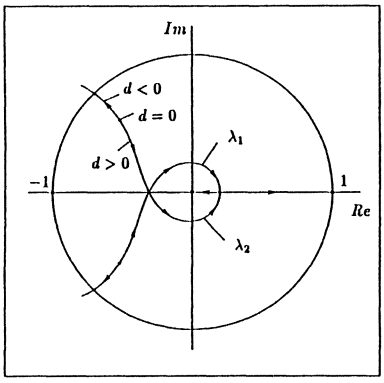

Fig.7: Course of the eigenvalues λ_1, λ_2 obtained by variation of d

In contrast to the perioddoubling, a pitch fork-bifurcation will take place, if one varies the damping parameter d (c.f. Fig.7).

4 Discussion

For large areas of the parameter-space the behavior of nonlinear dynamical systems with discontinuities is reduced to stable limit cycles. Therefore an efficient way to investigate a nonlinear dynamical system is to compute the $(m : n)$-cycles and determine their behavior stability- and bifurcation. Furthermore the way to irregularity or chaos can be studied – independently of the individual problem – in detail. The necessary algorithms are usually composed by standard algorithms – such as multiple-shooting-method or modified NEWTON algorithms – of the numerical analysis. The methods have been demonstrated by systems with impact and play. An application

to other systems – such as stick-slip-systems with dry friction [REITHMEIER 1989] – can be made without any difficulty in an analogous way.

5 References

[HAJEK 1989]
Hajek, M.: Numerische Behandlung mechanischer Systeme mit Trockenreibung. ZAMM Z. angew. Math. Mech. 69, 5, T297-T299 (1989)

[HEIMANN, BAJAJ, SHERMAN 1988]
Heimann, M.S.; Bajaj, A.K.; Sherman, P.J.: Periodic Motions and Bifurcations in Dynamics of an Inclined Impact Pair. Journal of Sound and Vibration 124(1), 55-78 (1988)

[JEAN, PRATT 1985]
Jean, M., Pratt, E.: A System of Rigid Bodies with Dry Friction. Int. J. Engng. Sci., 23, 497-513 (1985)

[KARAGIANNIS 1989]
Karagiannis, K.: Analyse stoßbehafteter Schwingungssysteme mit Anwendung auf Rasselschwingungen beim Zahnradgetriebe. Dissertation am Lehrstuhl B für Mechanik, TU München (1989)

[LÖTSTEDT 1981]
Lötstedt, P.: Coulomb Friction in Two-Dimensional Rigid Body Systems. ZAMM, 61, pp.605-615 (1981)

[MOREAU 1987]
Moreau, J.J.: Unilateral Contact and Dry Friction in Finite Freedom Dynamics (Preliminary Version). Lecture Notes, CISM-Course on: Non-smooth Mechanics and Applications (1987)

[PFEIFFER 1984]
Pfeiffer, F.: Mechanische Systeme mit unstetigen Übergängen. Ingenieur Archiv, Bd. 54, Nr. 3, 232-240 (1984)

[PFEIFFER 1988 a]
Pfeiffer, F.: Seltsame Attraktoren in Zahnradgetrieben. Ingenieur Archiv, Bd. 58, 113-125 (1988)

[PFEIFFER 1988 b]
Pfeiffer, F.: Theorie des Getrieberasselns. VDI-Berichte Nr. 697, 45-65 (1988)

[REITHMEIER 1989]
Reithmeier, E.: Periodische Lösungen nichtlinearer Schwingungssysteme – Numerische Berechnung, Stabilität, Bifurkation. Dissertation am Lehrstuhl B für Mechanik, TU München (1989)

[SCHIEHLEN 1983]
Schiehlen, W.: Reibungsbehaftete Bindungen in Mehrkörpersystemen. Ing. Arch., 53, 265-273 (1983)

[SHAW 1986]
Shaw, S.W.: On the Dynamic Response of a System with Dry Friction. J. Sound Vib., 108 (2), 305-325 (1986)

Integrated System for Numerical Analysis of Nonlinear Dynamics

P. ROSENDORF, J. ORSÁG, I. SCHREIBER and M. MAREK

Department of Chemical Engineering
Prague Institute of Chemical Technology
166 28 Prague 6
Suchbátarova 5
Czechoslovakia

Summary

An expert system CONEX for the analysis of nonlinear dynamical systems is described in the paper. It enables an automatic generation of continuation programs, interactive computations, graphical representation and interpretation of results. As an application this system is used for the study of periodic regimes of a driven impact oscillator.

Introduction

In recent years a large number of numerical methods for analysis of the dependence of solutions of nonlinear models of dynamical systems on parameters has been developed. Path following (continuation) techniques appear to be most effective for the global description of (both steady state and dynamic) behaviour of such systems. Curves of stationary or periodic solutions, bifurcation points and limit (fold) points in dependence on parameters can be constructed, as it was described in several recent papers and textbooks [1-7]. Also specialized textbooks devoted to the use of continuation techniques in the nonlinear problems of mechanics of deformable solid bodies are beginning to appear [8]. Original software is being developed but often it can be used only at the place of its origin and by highly specialized research workers. The reason is that productive application of such a software often requires profound knowledge both of specialized numerical techniques and of the theory of nonlinear dynamical systems. In this paper we briefly describe results of gradual development of an expert system for the analysis of nonlinear dynamical systems - CONEX (CONtinuation EXpert system). The CONEX is based on a unification of numerical algorithms with the means

W. Schiehlen (Editor)
Nonlinear Dynamics in Engineering Systems
IUTAM Symposium Stuttgart/Germany 1989

and approaches of logical programming and it can be used in the several ways :

1) in the simplest form as a source of numerical subroutines for construction of dependences on parameters by continuation methods (the user can modify the generated program either independently or in the CONEX environment),
2) as a tool for program generation, interactive computations and presentation of results in the form of graphs or tables,
3) in its full form where computed parametric dependences are analyzed, inferences from obtained information are stored in the Problem Database and further course of computations is suggested by the CONEX.

Here we briefly describe the structure of the CONEX and an example of its application.

Structure of CONEX

The CONEX has been developed as an open modular system. It enables an interactive use of routines for continuation and bifurcation analysis of model equations, construction of solution branches and their analysis. The CONEX provides users with: 1) an automatic generation of subroutines in FORTRAN 77 for model-dependent part of the problem (computation of right-hand sides, Jacobi matrix, etc.) by means of symbolic manipulations, 2) interactive data input controlled by menus, 3) formation and continuous updating of a database of the studied problem, suggestions on further steps of analysis, 4) interactive analysis of the obtained results stored in the database including various ways of graphical representation of results.

The CONEX can automatically prepare the actual continuation program in a runable form, control its execution and incorporate results into the database. It works with a library of numerical subroutines. Minimal hardware requirement is IBM PC/XT compatible computer with a hard disc and 640 kB of RAM. Numerical computations can be executed on a mainframe computer. All parts of CONEX have been designed so as to permit easy modification for other applications.

The CONEX consists of several parts (cf. Fig. 1). The control program which is built from a number of specialized parts is res-

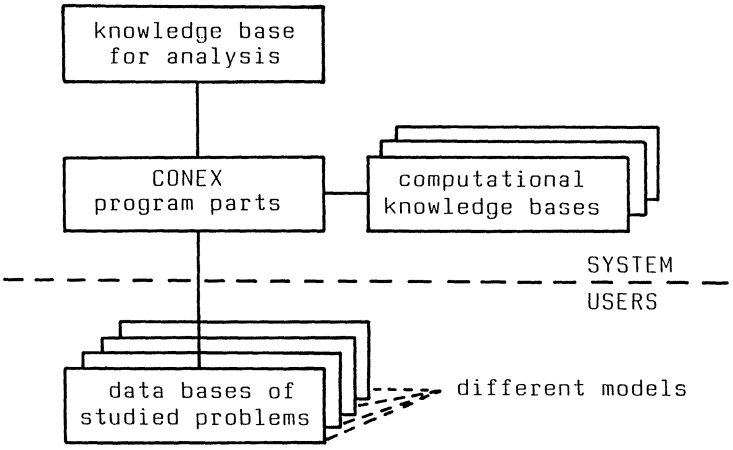

Fig. 1. Overall structure of the CONEX.

ponsible for the dispatching of processes, formation of a user interface and an error handling. The dispatcher is the only permanently resident part of the CONEX. It calls all other modules and programs and allocates memory and other resources for them. The dispatcher calls modules sequentially on the basis of a special description file which can be either generated by the CONEX automatically or can be created by the user in any editor. The user interface provides comfortable input of all the user defined data. Because of a large variety of the possible types of the data (menu choices, numbers, equations etc.), this part of the CONEX consists of a number of modules. The module MAINM builds the description file for the dispatcher on the basis of a number of user choices from available menus. It also handles creating and/or setting of the model. From the user point of view a model is a problem expressed as a set of equations and written down in a symbolic form (in notation similar to mathematical rules) as an input into the program. The names of variables are defined by the user. Symbolic terms can be introduced and there is no restriction on their nesting.

The input of the data for numerical programs is provided by the DATED module. This module works on the basis of the description of the structure of the input data for the particular continuation program.

Several types of outputs are available in the CONEX in the course of actual computations. Standard output files are mandatory. The user can choose either from a graphical or a text (numerical) representation of results on the console.

The computational knowledge base consists 1) of libraries necessary to build proper continuation program (e.g. the library of continuation routines, library of graphics support routines, etc.) and of a set of system routines (e.g. compiler, linker, editor, etc.) and 2) of the knowledge base containing information on the use of the above routines and libraries. The continuation library currently includes software for construction of stationary and periodic solutions, limit points, Hopf bifurcation and period-doubling bifurcation points of both autonomous and periodically perturbed systems of ordinary differential and difference equations.

The problem database is formed both in the course of the communication between the CONEX and the user, and in the course of computations (automatically). It consists of three parts: the first one is formed by the output data sets, the second one contains names of the ouput data sets, description of their structure and information on the studied problem resulting from an automatic analysis of data sets and/or heuristics. The third part contains knowledge derived from computational experience, together with additional information derived from the structure of the model equations and from the analysis of the output data sets.

The problem analysis knowledge base consists of two parts. The first one contains algorithms and subroutines for an analysis of the output data, location of specific points on solution curves, e.g. limit points, branching points, etc. The second part contains general rules of inference from the obtained databases.

An Example

As an example, we take a periodically driven damped impact oscillator and find its periodic solutions by numerical continuation.

The system is described by the equations [9,10]

$$\ddot{x} + 2\alpha\dot{x} + x = A\cos(2\pi t/T) \quad , \quad x > \delta \tag{1}$$

and

$$\dot{x}(t_i+) = -r\dot{x}(t_i-) \quad , \quad x = \delta \ , \tag{2}$$

where x is relative displacement of an impacting body and α, δ, r, A and T are parameters. We will be interested in changes of p/q-periodic orbits as the forcing period T is varied. Here q is the period of the stroboscopic Poincaré map associated with Eqs (1), (2) and p is the number of impacts occuring within the period of the orbit.

We can use either stroboscopic mapping representation (i.e. the map relating two points separated by the time distance of the size T) or impact mapping representation (i.e. the map relating two points separated by apriori unknown time of flight between two sucessive impacts). The system (1), (2) can be rewritten as follows :

a) set of autonomous differential equations applied from one impact to the next one,

$$\begin{aligned} \dot{x} &= y \quad , \\ \dot{y} &= -2\alpha y - x + A\cos(2\pi t/T) \quad , \\ \dot{t} &= 1 \end{aligned} \tag{3}$$

which is valid for $x > \delta$ and

b) the impact mapping at time t_i ,

$$\begin{aligned} x(t_i+) &= x(t_i-) \quad , \\ y(t_i+) &= -ry(t_i-) \quad , \end{aligned} \tag{4}$$

which is applied at points located in the impact manifold $M = \{(x, y, t) \ ; \ x = \delta\}$.

The flow of Eqs (3) induces a map which upon composition with a map defined by (4) gives the impact mapping. This implies that the impact representation is easy to obtain. However, a new impact on a periodic orbit of (3), (4) may emerge via tangency of the orbit of (3) with the impact manifold M as a parameter is varied. Similarly, an old impact can be missed with varying parameter. These events manifest themselves as discontinuities in the impact mapping representation but the stroboscopic representation is continuous and piecewise differentiable. Thus the parametrized periodic orbits of Eqs (3), (4) form a piecewise smooth manifold. The points, at which the dependence of a p/q- periodic orbit on a parameter is not smooth, a tangency to M occurs and the number of impacts changes by one, i.e., either $(p-1)/q$- or $(p+1)/q$- orbit continues to exist.

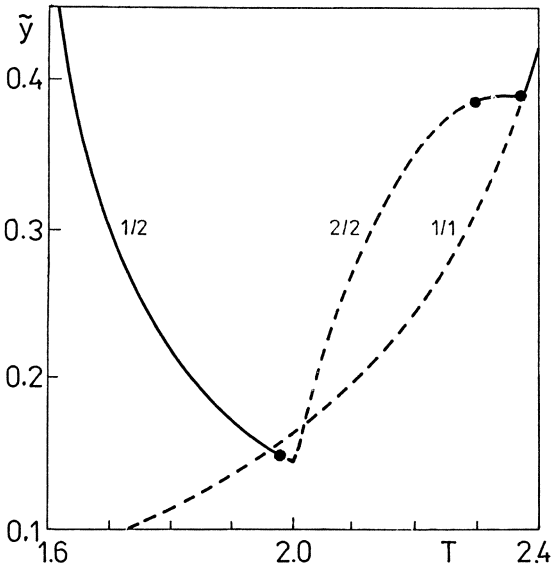

Fig. 2. Plot of $\tilde{y} = \sum_{i=1}^{p} y(T_i)/q$ vs T for one- and two-periodic orbits. Branch of period two orbits changes its impact/period ratio at the point of non-smoothness. Full lines - stable orbits, dashed lines - unstable orbits, circles - period doubling points; $\alpha = 0.2$, $A = 1$, $\delta = 0$, $r = 1$.

The continuation routine implemented in CONEX makes use of the impact mapping representation and indicates whether a new impact emerges or an old impact is likely to become extinct. Then the user is provided with an estimate of a starting point behind the point of non-smoothness. The simplest example of such a computation is shown in Fig. 2. Here the branch of 1/2-periodic orbits changes non-smoothly to the branch of 2/2-periodic orbits which in turn terminates at the branch of 1/1-periodic orbits via period-doubling bifurcation.

References

1. Kubíček, M.; Marek, M. : Computational Methods in Bifurcation Theory and Dissipative Structures. Berlin : Springer Verlag 1983.

2. Holodniok, M.; Klíč, A.; Kubíček, M.; Marek, M. : Methods of Analysis of Nonlinear Dynamical Models. Prague : Academia 1986 (in Czech).

3. Rheinboldt, W.C. : Numerical Analysis of Parametrized Nonlinear Equations. New York : J. Wiley 1986.

4. Doedel, E.J.; Kernevez, J.P. : AUTO : Software for Continuation and Bifurcation Problems in Ordinary Differential Equations. California Institute of Technology : Applied Mathematic Technical Report 1986.

5. Küpper, T.; Seydel, R.; Troger, H. : Bifurcation: Analysis, Algorithms, Applications. Basel : Birkhäuser Verlag 1987.

6. Seydel, R. : From Equilibrium to Chaos. New York : Elsevier Science Publ. 1988.

7. Marek, M.; Schreiber, I. : Chaotic Behaviour of Deterministic Dissipative Systems. Cambridge: Cambridge University Press, Prague : Academia Press 1989.

8. Grigorjuk, E.I.; Shalashilin, V.I. : Problems of Nonlinear Deformation. Moscow : Nauka Publ. House 1988 (in Russian).

9. Shaw, S.; Holmes, P. : A periodically forced piecewise linear oscillator. J. Sound and Vibration 90 (1983) 129.

10. Isomäki, H.M.; von Boehm, J.; Räty, R.: Devil´s attractors and chaos of a driven impact oscillator. Phys. Lett. 107A (1985) 343.

Self-Similar Basin Boundary in a Continuous System

O.E. ROSSLER[1], J.L. HUDSON[2], M. KLEIN[1] and C. MIRA[3]

[1]Institute for Physical and Theoretical Chemistry, U. of Tubingen, 7400 Tubingen, F.R.G.

[2]Department of Chemical Engineering, University of Virginia, Charlottesville, VA 22901, U.S.A.

[3]Systèmes Nonlinéaires et Applications, INSA Toulouse, F-31077 Toulouse CEDEX, France

Summary

A four-variable ordinary differential equation with hyperchaos is investigated further numerically. A self-similar Sierpinski-type fractal is found in a plane of initial conditions if the prospective fate of each point (whether it escapes through the one or the other escape hole in the exploded hyperchaotic attractor) is used for a coloring criterion. A basin boundary of the same qualitative shape therefore exists in either this equation or a closely related one. All hyperchaotic systems are eligible for an analogous investigation - both numerically and, if possible, experimentally.

Introduction

Modern "nonlinear science," the theory and application of dynamical systems theory, is presently divided up into two major subfields characterizable by the two labels "chaos" and "fractals." Both these terms are frequently used interchangeably (in book titles, for example) even though the mathematical relationship is far from clear. On the one hand, it is correct that all chaotic limit sets arising in differentiable dynamical systems necessarily are fractal objects because transversal cuts through their cross sections reveal a Cantor set structure[1]. On the other hand it is also correct that virtually all of the more spectacular fractal structures found in complex-analytic maps[2] have so far resisted reproduction in generic continuous systems, that is, in the main class of dynamical systems that are of applicational interest.

In the following, a prototype 4-variable ODE with hyperchaos[3,4] will be reconsidered because it reveals a "Sierpinski-type" self-similarity in a 2-D set of initial conditions.

The Equation

The following four-variable system[3] is considered:

W. Schiehlen (Editor)
Nonlinear Dynamics in Engineering Systems
IUTAM Symposium Stuttgart/Germany 1989

$$
\begin{aligned}
\dot{x} &= w\ (-y - c) &&+ (1 - w)\ (z + c) \\
\dot{y} &= w\ (x + a - 1) &&+ (1 - w)\ y\ (z + c)/(x + b - 1) \\
\dot{z} &= w\ z\ (-y - c)/(x - b) &&+ (1 - w)\ (-x + a) \\
\varepsilon\,\dot{w} &= w\ (1 - w)(w - 1 + x) &&- \delta(w - 0.5)\ .
\end{aligned}
\tag{1}
$$

In the singular-perturbation limit ($\varepsilon \to 0$), and if also simultaneously $\delta \to 0$ so that the slow manifold of w becomes literally letter-Z shaped, one finds that the trajectories of this 4-dimensional system possess two 2-dimensional projections (in the x,y and the x,z plane) that cover those of the corresponding projections of two simpler, 3-dimensional systems. The first of these ordinary-chaos generating, 3-variable systems is

$$
\begin{aligned}
\dot{x} &= w\ (-y - c) &&+ (1 - w)\ (x + b - 1) \\
\dot{y} &= w\ (x + a - 1) &&+ (1 - w)\ y \\
\varepsilon\,\dot{w} &= w\ (1 - w)(w - 1 + x) &&- \delta(w - 0.5)\ ;
\end{aligned}
\tag{2}
$$

the second is

$$
\begin{aligned}
\dot{x} &= w\ (x - b) &&+ (1 - w)\ (z + c) \\
\dot{z} &= w\ z &&+ (1 - w)\ (-x + a) \\
\varepsilon\,\dot{w} &= w\ (1 - w)(w - 1 + x) &&- \delta(w - 0.5)\ .
\end{aligned}
\tag{3}
$$

It is not hard to see that Eq.(3) transforms into Eq.(2) under a change of variables, namely, the substitution $y = z$, $x(\text{Eq.2}) = 1 - x(\text{Eq.3})$ and $w(\text{Eq.2}) = 1 - w(\text{Eq.3})$.

The limiting version to Eq.(2) - with a nonexplicit right-hand function in the third line - was indicated by Mira[5] as a particularly transparent illustration of chaos generation by means of the reinjection principle[6]. One easily sees from Eq.(2) that in the singular-perturbation limit, where (if also δ is allowed to approach zero) w is always equal to either 1 or 0, the two-dimensional motion generated by the first two variables always consists of trajectories that are either concentric circles ($\dot{x} = -y - c$, $\dot{y} = x + a - 1$) corresponding to a harmonic oscillator (with center $x = 1 - a$, $y = -c$), or straight lines ($\dot{x} = x + b - 1$, $\dot{y} = y$) emanating from a star-shaped unstable node (at $x = 1 - b$, $y = 0$).

Because of this maximal simplicity of all submotions in the singular limit, it is possible to write down explicitly the corresponding Poincaré cross section. Thus, one obtains for Eq.(2) the following noninvertible 1-D map[5], at $x=0$, $w=1$:

$$y_{n+1} = -c + \sqrt{2a - 1 + \left(\frac{b}{b-1}\, y_n + c\right)^2} \quad . \tag{4a}$$

Similarly, one obtains for the limiting cross section of Eq.(3), at $x=0$, $w=1$:

$$z_{n+1} = \frac{b}{b-1}\left(-c + \sqrt{2a - 1 + (z_n + c)^2}\right) . \tag{4b}$$

Both equations are identical, except for a linear factor ($z = \frac{b}{b-1}\, y$) that is due to the fact in generating the second cross section, not the symmetrically corresponding location ($x=1$) was chosen. The two equations were written down explicitly here because the combined equation, Eq.(4), at the same time represents the noninvertible 2-D map that applies to Eq.(1) as its own limiting cross section, at $x=0$, $w=1$. Therefore the two "smoothened letter-V" shaped hyperbolas of Eq.(4) - obtained with $a = 0.51$ and both b,c larger than unity - combine to give an "ironed-flat" folded-handkerchief map, just as two logistic maps do. For numerical simulations of both Eq.(1) and Eq.(4), see[4].

To promote a better intuitive understanding of how Eq.(1) actually works, Figure 1 shows in graphical form the two major "pure" projections that determine the system's behavior.

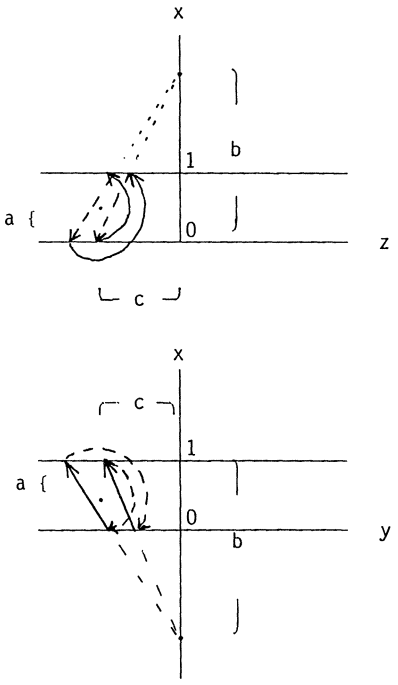

Figure 1 Principal two-dimensional projections for the limiting flow of Eq.(1). Note that these two projections are compatible because they are mutually rotated 90 degrees about the x-axis. The trajectories seen are either circle segments or straight-line segments. The continuously drawn segments lie on the $w = 0$ floor of the letter-Z shaped slow manifold of the fourth variable while the dashed segments lie on the $w = 1$ floor. The instantaneous up and down transitions occur whenever an arrowhead reaches the precipice at $x = 1$ or $x = 0$, respectively.

Double Explosion

The system of Eq.(1) is capable of exhibiting two "independent" types of chaos, simultaneously. The decisive parameter is b. If b is much larger than unity, there is no chaos - only a limit cycle that consists of a straight-line segment and a curved arc joined together, in either partial system. As b is decreased, the two letter-V shaped maps, Eqs.(4a) and (4b), acquire a steeper and steeper slope each. (The slope becomes numerically equal to 2 as b reaches 2 from above.) In the process, a chaotic attractor develops through period-doubling in each subsystem.

We are interested in what happens if b is decreased somewhat further still. There exists a threshold shortly below two that is directly analogous to the well-known critical value $b = 4$ in the logistic map, $x_{n+1} = bx_n(1 - x_n)$, beyond which the attractor disappears (explodes). In Figure 1, this transition manifests itself in a characteristic fashion: The dense recurrent region then touches the x-axis, from the left. As a consequence, eventually the arrowhead

of a circle segment comes to lie to the right of the x-axis. Once this has happened, there is no return. A spiral of approximately constant diameter but exponentially growing steepness leads toward infinity, on the right.

The full equation - that is, Eq.(1) with both ε and δ small positive but nonzero - still possesses an analogous threshold in b, although this threshold ceases to be exactly equal in the two subsystems. At some value of b not far below two, once more either chaotic subflow is punctured by an "escape hole" of its own.

The described principle of "double puncturing" (double explosion) has a non-trivial consequence. It enables one to classify initial conditions according to whether they are going to explode along the one, or along the other, escape route. While it takes a long time to check this by hand, the computer is a convenient tool when looking at the facts is at stake. Figure 2 gives an illustration of what can be found numerically.

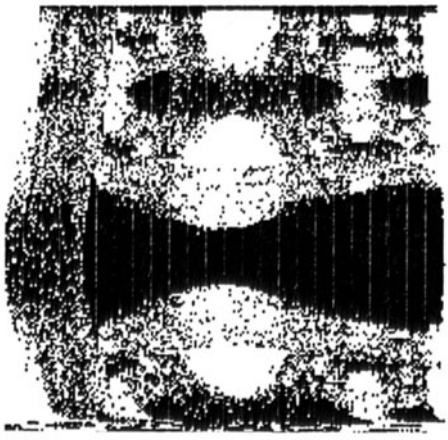

Figure 2 A scan of initial conditions in the y,z plane, while x and w are initially at 0 and 0.01, respectively. Numerical simulation of Eq.(1) using a standard Runge-Kutta-Merson integration routine with variable step size implemented on a 19-digit desk-top computer. Parameters: $a = 0.5$, $b = 1.55$, $c = 1.3$, $\varepsilon = \delta = 0.005$, maximum step error 10^{-4}. Axes: - 1 to 0.1 for y (abscissa), and - 2.28 to 0.1 for z (ordinate). Criteria used for coloring: Black, when $y(t) > 0.2$ while $w(t) > 0.8$ and $x(t) < 0.2$. White, when $z(t) > 0.2$ while $w(t) < 0.2$ and $x(t) > 0.8$; or else step size $< 10^{-15}$ (< 0.5 % of points). Note: Taking $w(0) = 0.95$ gives virtually identical results.

Discussion

A new type of qualitative behavior in an ODE has been described. Initial conditions can behave differently in space in such a way that a Sierpinski-type[2] self-similar fractal is formed in a plane in 4 dimensions.

From the mathematical point of view, our result can be understood as an implication of global analysis. If in an ordinary Smale[1] "horseshoe" map (like Hénon's map[7]), the recurrent region is invaded by more than a single basin, the two saddles that have encroached on the former chaotic attractor divide the latter's domain up in a very complicated manner. This was demonstrated in[8] following earlier work on the underlying noninvertible case by Gumowski and Mira[9]. These authors also coined a new term for the arising complexity, "frontière floue" (fuzzy boindary). Every point of the Smale basic set[1], the set of surviving periodic (and therefore returning) points that forms a product of two Cantor sets, is adjacent to either basin. So is the point's 1-D stable manifold. The union of all these repelling 1-D manifolds forms the actual 1-D boundary. The visible outcome, locally, is a set of Cantor lines separating two "thick" Cantor sets (Cantor stripes) of initial conditions.

The present case is analogous but involves one more dimension. A "hyperhorseshoe" (folded towel) can likewise be looked at under a condition where the formerly present attractor has been invaded by two external basins. Every point of the generalized basic set (which now is a product of three Cantor sets) then is adjacent to either basin. So is, again, the point's 1-D stable manifold. The latter, however, now in addition spans a whole 2-D "stable sheet." The union of all these repelling sheets forms the actual 2-D boundary. However, similarly as with an unstable node in a 2-variable continuous dynamical system - where it is the arbitrary location of a neighboring saddle that selects which one from the infinitude of unstable trajectories that emerge from the node becomes the new boundary passing through that node - , so in the present case an infinitude of alternative sheets is available to each point as far as the connection with an external orthogonal saddle is concerned. Every member of the - when looked at from the top, along the direction of the stable manifolds - 2-dimensional Cantor set of points of the basic set is subject to this imperative to connect. Since the shapes of the lateral sheets of the two invading fixed points have to be accommodated primarily, and since every local patch gets eventually blown up to the full size of the map, it is plausible that the externally imposed shape selection will be repeated on all scales in a self-affine manner. In the prototypic case - two uncoupled exploded logistic maps

(or Eq.4, respectively) - , one obtains an Alexandrov-cross like fractal within the Sierpinskian class - the "iterated Swiss Flag"[10]. This structure, which already exists in the noninvertible limit, "survives" the transition toward an adjacent 3-D invertible equation (hyper Hénon map)[11]. Interestingly, even the nonexploded hyperchaotic attractor already contains all of those self-affine fractals embedded in its own symbolic dynamics[10], so that they can be recovered from a time series[12].

The present result thus appears to "confirm" that continuous differentiable systems are faithful to their own maps (cross sections). However, there is a grain of salt - the present example is not quite finished. The initial conditions were not classified according to the final attractors reached, which is what classically defines a basin boundary, but only according to a finite criterion (one or the other escape hole reached). It might therefore happen that the final attractors "re-unite" some or even all of the features found. To find out, the equation will need to be modified - most simply by the addition to b of small higher-order terms in y and z. The reason has to with Eq.(1)'s becoming non-Lipschitz as $x(t)$ approaches b from below or $1-b$ from above; for then one of the two denominators on the right-hand side becomes zero. This "late" complication plays no role in the above simulation. Nevertheless the fact remains that the picture of Figure 2 applies rigorously only to an "analogue" to Eq.(1) that is close to it in parameter space but has yet to be written down explicitly. The palm for presenting the first "totally clear-cut" example in the present class therefore remains to be won. Next, use should be made of a much simpler hyperchaos-generating equation like that of[13] which is globally Lipschitz. Eq.(1) had only been chosen because it offers analytical guidance as to what combination of parameters to select for a double explosion to occur, and where to then place the initial plane.

Perhaps, the above example is already strong enough, however, to effectively narrow the "gulf" that still sets apart complex-analytic from real-life systems (cf. Introduction). Recently, another 4-variable continuous system has been found which, too, generates a new type of fractal behavior - a "nonsmooth" (nowhere differentiable) boundary[14]. Chaotic forcing of a single-variable system that possesses an unstable equilibrium suffices. Only one direction of folding - and no "puncturing" - is involved. The two examples nevertheless complement each other it appears. Taken together they show that the two most surprising features of noninvertible (both complex-analytic[2] and real[15]) dynamical systems, "self-similarity" and "nonsmoothness" of a boundary, can be retrieved in generic differentiable continuous systems - separately.

What remains open is whether or not the combination can be expected to be found in the realistic class, too. A brute-force numerical analysis of Eq.(1) in further parameter regions (with a,b,c split into a pair each) might be all that is required to answer this question. Alternatively, a second look at data already in the literature might suffice. There exists an interesting example of a periodic orbit on a boundary, in a 4-variable continuous system (two coupled van-der-Pol oscillators), that possesses two positive Lyapunov characteristic exponents[16]. This property is also a characteristic of periodic orbits lying on the present boundary, as well as of those of[14]. Battelino's orbit, which was discovered using the numerically demanding "straddle orbit method"[16], may thus deserve to be reinvestigated - for example, by means of the simple Mandelbrot[2] scanning method employed above. To judge from the (dots) picture already available (Figure 8b of[16]), all three possibilities mentioned - the Sierpinskian, the Weierstrassian, and the combined Julian type of behavior - might possess a positive chance of being retrieved. Thirdly, search for a new principle may turn out to be indispensable. After the principle of the doubly punctured folded towel, and that of the once folded-over towel that is nonpunctured but bilaterally expanding, what might come next? A once-folded towel that, while bilaterally expanding on the outsides, is centrally contracting is one possible candidate. Its two "parallel" nonsmooth boundaries can be brought to "fusion." The surviving boundary born thereby might be "web-like" in addition to its being nonsmooth. Chaotic forcing of a single-variable system governed by an "inverted" (rather than ordinary) letter-W type potential offers itself under a condition of moderate back-coupling. An alternative possibility will be a return to Smale's[1] axiom-A principle under a condition of stability inversion. A 4-variable axiom-A ODE for which this can be accomplished is available[17]. A close similarity to the complex-logistic map (which too harbors a repelling solenoid) can thereby be forced perhaps.

To conclude, Mandelbrot's scanning method proves useful in continuous systems as well. After chaotically forced systems[14], now hyperchaotic systems follow suit. Four-variable systems are a new frontier. Mechanical engineering "takes off" from two-degree-of-freedom dissipative (that is, generic 4-variable) systems[18]. Well-stirred chemical reaction systems, too, exhibit signs of intrinsically 4-variable behavior[19]. Indeed, the "natural analogue computers" of the real world may turn out to be candidates for the present type of investigation themselves[14]. For nothing lends itself more readily to inspection than self-similarity.

We thank Werner Schiehlen, Hans Troger, Francis Moon, Igor Gumowski and M.S. El Naschie for discussions. Work supported in part by the N.S.F.

References

1. S. Smale (1967). Bull. Amer. Math. Soc. 73, 747.
2. B. Mandelbrot, The Fractal Geometry of Nature. Freeman, San Francisco 1983.
3. O.E. Rössler and C. Mira (1981), Higher-order chaos in a constrained differential equation with an explicit cross section, extended abstract in: Tagungsbericht 40/1981, pp. 9-10. Mathematisches Forschungsinstitut Oberwolfach, 7620 Oberwolfach-Walke, West Germany.
4. O.E. Rössler (1983). Z. Naturforsch. 38 a, 788.
5. C. Mira (1978), Complex dynamics generated by a third-order differential equation (in French), in: Proc. "Equadiff 78" (R. Conti, G. Sestini and G. Villari, Eds.), pp. 25-36. Florence, Italy.
6. O.E. Rössler (1976). Z. Naturforsch. 31 a, 259.
7. M. Hénon (1976). Commun. Math. Phys. 50, 69.
8. C. Mira (1979). C. R. Acad. Sc. Paris 288 A, 591.
9. I. Gumowski and C. Mira (1975). C. R. Acad. Sc. Paris 280 A, 905.
10. O.E. Rössler, C. Kahlert, J. Parisi, J. Peinke and B. Röhricht (1986). Z. Naturforsch. 41 a, 819.
11. O.E. Rössler, J. Hudson, M. Klein and R. Wais (1988), Self-similar basin boundary in an invertible system (folded-towel map), in: Dynamic Patterns in Complex Systems (J.A.S. Kelso, A.J. Mandell and M.F. Shlesinger, Eds.), pp. 209-218. World Scientific, Singapore.
12. O.E. Rössler and J.L. Hudson (1989), Self-similarity in hyperchaotic data, in: Chaotic Dynamics in Brain Function (E. Basar, Ed.), pp. 113-121. Springer-Verlag, Berlin.
13. O.E. Rössler (1979). Phys. Lett. 71 A, 155.
14. O.E. Rössler, J.L. Hudson and M. Klein (1989). J. Phys. Chem. 93, 2858.
15. O.E. Rössler and C. Kahlert (1987). Z. Naturforsch. 42 a, 324.
16. P.M. Battelino, C. Grebogi, E. Ott, J.A. Yorke and E.D. Yorke (1988). Physica 32 D, 296.
17. O.E. Rössler (1985), Example of an axiom-A ODE, in: Chaos, Fractals and Dynamics (P. Fischer and W.R. Smith, Eds.), pp. 105-114. M. Dekker, New York.
18. F. Moon, Personal communication 1989.
19. G. Baier, K. Wegmann and J.L. Hudson (1989). Phys. Lett. A (submitted).

Global Nonlinear Oscillations and Onset of Chaos

G. SCHMIDT

Institute of Mechanics
Academy of Sciences of the G.D.R., Berlin

Recent results by Mrs. Szemplińska-Stupnicka and others /5,6, 7,3/ have shown that an indication of the onset of chaotic vibrations can be got by higher analytical approximation of the vibrational solution or its stability. In what follows, nonlinear vibrations under 1) general anharmonic parametric and combined forced excitation and 2) asymmetric forced excitation and the onset of chaotic behaviour are discussed by higher analytical approximation and numerical evaluation. The numerical and computeralgebraic evaluations were carried out by R. Dum with the Cyber of the University Innsbruck.

1. General Anharmonic Parametric and Forced Excitation

We first investigate the stationary vibrations modelled by a differential equation which can be written in the transformed dimensionless shape

$$\nu^2 x'' + \sigma x + 2\sum_{n=1,2,3,\dots} (p_n \cos 2nt + q_n \sin 2nt)x + 4rx^3 + dx' = \sum_{n=1,3,5,\dots} (f_n \cos nt + g_n \sin nt) \tag{1}$$

where ν is the frequency and $\sigma = \pm 1$ or 0 represents the linear, $r \gtrless 0$ a nonlinear restoring force, d a linear damping, p_n, q_n, and f_n, g_n a general periodic parametric and forced excitation respectively. Especially the last ones (inertial excitation) and d are often functions of ν .

We seek for the periodic solutions of (1) by help of an ansatz

$$x = a\cos t + \alpha \sin t + b\cos 3t + \beta \sin 3t + c\cos 5t + \gamma \sin 5t \tag{2}$$

in which even harmonics can be omitted because no constant and

W. Schiehlen (Editor)
Nonlinear Dynamics in Engineering Systems
IUTAM Symposium Stuttgart/Germany 1989

no even nonlinearities occur in (1) as the integral equation method /4/ and the following analysis show.

Introducing (2) into (1) and comparing the coefficients of $\begin{matrix}\cos\\ \sin\end{matrix}$ nt (n=1,2,3) yields the six coupled nonlinear equations

$$\begin{aligned}&(\delta-\nu^2+3\gamma A^2+6\gamma B^2+6\gamma C^2)\begin{pmatrix}a\\ \alpha\end{pmatrix}+p_1\begin{pmatrix}a\\ -\alpha\end{pmatrix}+q_1\begin{pmatrix}\alpha\\ a\end{pmatrix}+d\begin{pmatrix}\alpha\\ -a\end{pmatrix}\\&+(3\gamma a^2+3\gamma\alpha^2+p_1)\begin{pmatrix}b\\ \beta\end{pmatrix}+(6\gamma a\alpha+q_1)\begin{pmatrix}\beta\\ -b\end{pmatrix}+p_2\begin{pmatrix}b\\ -\beta\end{pmatrix}+q_2\begin{pmatrix}\beta\\ b\end{pmatrix}+(6\gamma ab-6\gamma\alpha\beta+p_2)\begin{pmatrix}c\\ \gamma\end{pmatrix}\\&+(6\gamma a\beta+6\gamma\alpha b+q_2)\begin{pmatrix}\gamma\\ -c\end{pmatrix}+(3\gamma b^2-3\gamma\beta^2+p_3)\begin{pmatrix}c\\ -\gamma\end{pmatrix}+(6\gamma b\beta+q_3)\begin{pmatrix}\gamma\\ c\end{pmatrix}=\begin{pmatrix}f_1\\ g_1\end{pmatrix},\end{aligned}\tag{3}$$

$$\begin{aligned}&(\delta-9\nu^2+6\gamma A^2+3\gamma B^2+6\gamma C^2)\begin{pmatrix}b\\ \beta\end{pmatrix}+p_3\begin{pmatrix}b\\ -\beta\end{pmatrix}+q_3\begin{pmatrix}\beta\\ b\end{pmatrix}+3d\begin{pmatrix}\beta\\ -b\end{pmatrix}+p_1\begin{pmatrix}a\\ \alpha\end{pmatrix}+q_1\begin{pmatrix}-\alpha\\ a\end{pmatrix}\\&+p_2\begin{pmatrix}a\\ -\alpha\end{pmatrix}+q_2\begin{pmatrix}\alpha\\ a\end{pmatrix}+\gamma\begin{pmatrix}(a^2-3\alpha^2)a\\ (3a^2-\alpha^2)\alpha\end{pmatrix}+(3\gamma a^2-3\gamma\alpha^2+6\gamma ab+6\gamma\alpha\beta+p_4)\begin{pmatrix}c\\ \gamma\end{pmatrix}\\&+(6\gamma a\alpha+6\gamma a\beta-6\gamma\alpha b+q_1)\begin{pmatrix}\gamma\\ -c\end{pmatrix}+p_4\begin{pmatrix}c\\ -\gamma\end{pmatrix}+q_4\begin{pmatrix}\gamma\\ c\end{pmatrix}=\begin{pmatrix}f_3\\ g_3\end{pmatrix}\end{aligned}\tag{4}$$

and

$$\begin{aligned}&(\delta-25\nu^2+6\gamma A^2+6\gamma B^2+3\gamma C^2)\begin{pmatrix}c\\ \gamma\end{pmatrix}+p_5\begin{pmatrix}c\\ -\gamma\end{pmatrix}+q_5\begin{pmatrix}\gamma\\ c\end{pmatrix}+5d\begin{pmatrix}\gamma\\ -c\end{pmatrix}\\&+p_2\begin{pmatrix}a\\ \alpha\end{pmatrix}+q_2\begin{pmatrix}-\alpha\\ a\end{pmatrix}+(3\gamma b^2-3\gamma\beta^2+p_3)\begin{pmatrix}a\\ -\alpha\end{pmatrix}+(6\gamma b\beta+q_3)\begin{pmatrix}\alpha\\ a\end{pmatrix}\\&+(3\gamma a^2-3\gamma\alpha^2+p_1)\begin{pmatrix}b\\ \beta\end{pmatrix}-(6\gamma a\alpha+q_1)\begin{pmatrix}\beta\\ -b\end{pmatrix}+p_4\begin{pmatrix}b\\ -\beta\end{pmatrix}+q_4\begin{pmatrix}\beta\\ b\end{pmatrix}=\begin{pmatrix}f_5\\ g_5\end{pmatrix}\end{aligned}\tag{5}$$

where

$$A=\sqrt{a^2+\alpha^2},\qquad B=\sqrt{b^2+\beta^2},\qquad C=\sqrt{c^2+\gamma^2}$$

are the partial amplitudes of the first three harmonics of the solution.

The usual "infinitesimal" nonlinear iteration with $b=\beta=c=\gamma=0$ transforms (3) into the amplitude formula

$$\begin{aligned}&[(\delta-\nu^2+3\gamma A^2)^2-p_1^2-q_1^2+d^2]^2A^2=[(\delta-\nu^2+3\gamma A^2-p_1)^2+(q_1-d)^2]f_1^2\\&+[(\delta-\nu^2+3\gamma A^2+p_1)^2+(q_1+d)^2]g_1-4[(\delta-\nu^2+3\gamma A^2)q_1-p_1d]f_1g_1\end{aligned}\tag{6}$$

for the amplitude of the main harmonic only which shows the influence only of the harmonic parts (p_1, q_1, f_1, g_1) of parametric and forced excitation and includes as special cases the well-known formulae for pure parametric excitation and for Duffing-type forced oscillators.

Taking for a "global" iteration also b,β,c,γ into consideration, we get, for simplicity in case of $p_2=q_2=0$, by a first step from (4)

$$\begin{pmatrix} b_1 \\ \beta_1 \end{pmatrix} = ip_1\begin{pmatrix} a \\ \alpha \end{pmatrix} + iq_1\begin{pmatrix} -\alpha \\ a \end{pmatrix} + ir\begin{pmatrix} (a^2-3\alpha^2)a \\ (3a^2-\alpha^2)\alpha \end{pmatrix} - i\begin{pmatrix} f_3 \\ g_3 \end{pmatrix} \tag{7}$$

and from (5)

$$\begin{pmatrix} c_1 \\ \gamma_1 \end{pmatrix} = jp_3\begin{pmatrix} a \\ -\alpha \end{pmatrix} + jq_3\begin{pmatrix} \alpha \\ a \end{pmatrix} - j\begin{pmatrix} f_5 \\ g_5 \end{pmatrix} \tag{8}$$

where for abbreviation the frequency functions

$$i = \frac{1}{9\nu^2 - \sigma}, \qquad j = \frac{1}{25\nu^2 - \sigma}$$

are introduced. By (7) the third harmonic of forced excitation (f_3, g_3), by (8) the fifth harmonic (f_5, g_5) and the third harmonic of parametric excitation (p_3, q_3) are brought into play. Insertion of (7), (8) into (3) leads to the pair of equations

$$d\begin{pmatrix} \alpha \\ -a \end{pmatrix} + p_1\begin{pmatrix} a \\ -\alpha \end{pmatrix} + F\begin{pmatrix} a \\ \alpha \end{pmatrix} + G\begin{pmatrix} \alpha \\ a \end{pmatrix} - 4irq_1\begin{pmatrix} \alpha^3 \\ a^3 \end{pmatrix} + 4irp_1\begin{pmatrix} a^3 \\ -\alpha^3 \end{pmatrix} = \begin{pmatrix} f \\ g \end{pmatrix}$$

where for abbreviation

$$F = \sigma - \nu^2 + 3rA^2 + i(p_1^2 + q_1^2) + j(p_3^2 + q_3^2) + 3ir^2A^4$$

$$G = q_1 + 6irq_1A^2,$$

$$f = f_1 + ip_1f_3 + iq_1g_3 + jp_3f_5 + jq_3g_5 + 3ir(a^2-\alpha^2)f_3 + 6ira\alpha g_3,$$

$$g = g_1 + ip_1g_3 - iq_1f_3 - jp_3g_5 + jq_3f_5 + 3ir(a^2-\alpha^2)g_3 - 6ira\alpha f_3$$

is written. Due to the terms of global iteration containing i,j, these equations are nonlinear in a,α, nevertheless in important special cases they admit analytical solutions in form of amplitude formulae.

In case of pure parametric excitation, $f_n = g_n = 0$, the amplitude formula of second approximation

$$(1+2irA^2)^2[\sigma - \nu^2 + 3rA^2 + i(p_1^2+q_1^2) + j(p_3^2+q_3^2) + 3ir^2A^4]^2$$
$$= (1+2irA^2)^2(1+4irA^2)^2(p_1^2+q_1^2) - (1+4irA^2)^2d^2$$

can be found, generalizing by i,j the infinitesimal first approximation. In the same way a third approximation can be evaluated which cannot be given here.

Similar formulae can be derived for an additional forced excitation. All these formulae reveal the influence of anharmonic components of parametric and forced excitation.

Numerical evaluations have been done in two different ways, by numerically solving i) the approximate amplitude equations found and ii) the six coupled nonlinear equations (3), (4), (5)

for the Fourier coefficients of the solution via Powell method. The necessary starting values for the Powell method could be found from the approximate analytical formulae.

The numerical results showed a "fanning", that is a sensitive dependence of the solution on the stage of analytical or numerical approximation, or even a breaking off of the resonance curves, for pure harmonic parametric excitation (for which a comparison is possible) just in the frequency domain where the Melnikov criterion led to the onset of chaos /1/.

2. Asymmetric Forced Excitation

The differential equation

$$\nu^2 x'' + \sigma x + 4\nu x^3 + dx' = g + f\cos st \tag{9}$$

where s is an integer and the constant g considers an asymmetry, covers also an additional quadratic nonlinearity as in Josephson junctions; the form (9) is obtained by a suitable shift of the coordinate.

The ansatz for the solution shall now comprise also the s-th subharmonic solutions (s=3,2,1):

$$x = h + a\cos t + \alpha\sin t + b\cos 2t + \beta\sin 2t + c\cos 3t + \gamma\sin 3t.$$

Insertion into (9) and comparison of coefficients leads now to the seven coupled nonlinear equations

$$\sigma h + 4\nu h^3 + 3\nu(a^2-\alpha^2)b + 6\nu a\alpha\beta + 6\nu h(A^2+B^2+C^2) = g, \tag{10}$$

$$\frac{1}{i_1}\begin{pmatrix} a \\ \alpha \end{pmatrix} = (12\nu h^2 + 3\nu A^2 + 6\nu B^2 + 6\nu C^2)\begin{pmatrix} a \\ \alpha \end{pmatrix} + d\begin{pmatrix} \alpha \\ -a \end{pmatrix} + 12\nu hb\begin{pmatrix} a \\ -\alpha \end{pmatrix} + 12\nu h\beta\begin{pmatrix} \alpha \\ a \end{pmatrix} + 12\nu hc\begin{pmatrix} b \\ -\beta \end{pmatrix} + 12\nu h\gamma\begin{pmatrix} \beta \\ b \end{pmatrix} + 3\nu(a^2-\alpha^2)\begin{pmatrix} c \\ \gamma \end{pmatrix} + 6\nu a\alpha\begin{pmatrix} \gamma \\ -c \end{pmatrix} + 3\nu(b^2-\beta^2)\begin{pmatrix} c \\ -\gamma \end{pmatrix} + 6\nu b\beta\begin{pmatrix} \gamma \\ c \end{pmatrix} - d_s^{-1}\begin{pmatrix} f \\ 0 \end{pmatrix}, \tag{11}$$

$$\frac{1}{i_2}\begin{pmatrix} b \\ \beta \end{pmatrix} = 6\nu h\begin{pmatrix} a^2-\alpha^2 \\ 2a\alpha \end{pmatrix} + (12\nu h^2 + 6\nu A^2 + 3\nu B^2 + 6\nu C^2)\begin{pmatrix} b \\ \beta \end{pmatrix} + 2d\begin{pmatrix} \beta \\ -b \end{pmatrix} + 12\nu hc\begin{pmatrix} a \\ -\alpha \end{pmatrix} + 12\nu h\gamma\begin{pmatrix} \alpha \\ a \end{pmatrix} - d_s^{-2}\begin{pmatrix} f \\ 0 \end{pmatrix}$$

and

$$\frac{1}{i_3}\begin{pmatrix} c \\ \gamma \end{pmatrix} = \nu\begin{pmatrix} (a^2-3\alpha^2)a \\ (3a^2-\alpha^2)\alpha \end{pmatrix} + 12\nu hb\begin{pmatrix} a \\ \alpha \end{pmatrix} - 12\nu h\beta\begin{pmatrix} \alpha \\ a \end{pmatrix} + 3\nu(b^2-\beta^2)\begin{pmatrix} a \\ -\alpha \end{pmatrix} + 6\nu b\beta\begin{pmatrix} \alpha \\ a \end{pmatrix} + (12\nu h^2 + 6\nu A^2 + 6\nu B^2 + 3\nu C^2)\begin{pmatrix} c \\ \gamma \end{pmatrix} + 3d\begin{pmatrix} \gamma \\ -c \end{pmatrix} - d_s^{-3}\begin{pmatrix} f \\ 0 \end{pmatrix} \tag{12}$$

with the frequency functions

$$\frac{1}{i_n} = n^2\nu - \sigma \qquad (n = 1, 2, 3).$$

We will confine ourselves here on the third subharmonic solutions (s=3), for which the equations (12) contain the forced excitation f and are thus, besides (10), the most important ones . They are linear in c, γ ; solving for these quantities, squaring and adding gives

$$(I^2 + 9d^2)C^2 = R^2 + S^2 \tag{13}$$

where for abbreviation

$$I = \frac{1}{i_3} - 12r\eta^2 - 6rA^2 - 6rB^2 - 3rC^2$$

and

$$\begin{pmatrix} R \\ S \end{pmatrix} = \begin{pmatrix} f \\ 0 \end{pmatrix} - r\begin{pmatrix} (a^2 - 3\alpha^2)a \\ (3a^2 - \alpha^2)\alpha \end{pmatrix} - 12r\eta b\begin{pmatrix} a \\ \alpha \end{pmatrix} + 12r\eta\beta\begin{pmatrix} \alpha \\ -a \end{pmatrix} + 3r(\beta^2 - b^2)\begin{pmatrix} a \\ -\alpha \end{pmatrix} - 6rb\beta\begin{pmatrix} \alpha \\ a \end{pmatrix}.$$

If we set, in first approximation, a=α=b=β=0, the two equations (13) and (10) determine C^2 and h, for instance by inserting C^2 from (10) into (13), solving for h and evaluating C^2 from (10).

We can find a second approximation if we also take a,α into consideration. Then the equations (11) read

$$3r(a^2 - \alpha^2)\begin{pmatrix} c \\ \gamma \end{pmatrix} + 6ra\alpha\begin{pmatrix} \gamma \\ -c \end{pmatrix} = J\begin{pmatrix} a \\ \alpha \end{pmatrix} - d\begin{pmatrix} \alpha \\ -a \end{pmatrix} \tag{14}$$

where for abbreviation

$$J = \frac{1}{i_1} - 12r\eta^2 - 3rA^2 - 6rC^2.$$

Multiplication of (14) by $\begin{pmatrix} a^2 - \alpha^2 \\ -2a\alpha \end{pmatrix}$ and $\begin{pmatrix} 2a\alpha \\ a^2 - \alpha^2 \end{pmatrix}$ respectively leads to

$$3rA^4\begin{pmatrix} c \\ \gamma \end{pmatrix} = J\begin{pmatrix} (a^2 - 3\alpha^2)a \\ (3a^2 - \alpha^2)\alpha \end{pmatrix} + d\begin{pmatrix} (\alpha^2 - 3a^2)\alpha \\ (a^2 - 3\alpha^2)a \end{pmatrix},$$

squaring and adding yields, besides of A=0, the quadratic equation

$$J^2 - 9r^2A^2C^2 + d^2 = 0$$

for C^2 in dependence of A^2 and h^2 which represents an ellipse in the coordinates A^2 and C^2.

These are some simple examples for analytical approximations

which can reveal, together with numerical evaluations, the behaviour of subharmonic vibrations for the asymmetric oscillator at hand.

References

1. Koch, B.P; Leven, R.W.: Subharmonic and homoclinic bifurcations in a parametrically forced pendulum. Physica 16D (1985) 1-13.

2. Moon, F.C.: Chaotic vibrations. J. Wiley & Sons, New York 1987.

3. Schmidt, G.; Dum, R.: Van der Pol - Duffing oscillators and trigonometric iteration. Z. angew. Math. Mech. 69 (1989) 267-274.

4. Schmidt, G.; Tondl, A.: Non-linear vibrations. Akademie-Verlag, Berlin and Cambridge Univ. Press, Cambridge 1986.

5. Szemplińska-Stupnicka, W.; Bajkowski, J.: The 1/2 subharmonic resonance and its transition to chaotic motion in a non-linear oscillator. Int. J. Non-Linear Mechanics 21 (1986) 401-419.

6. Szemplińska-Stupnicka, W.: Secondary resonances and approximate models of routes to chaotic motion in non-linear oscillators. J. Sound Vibr. 113 (1987) 155-172.

7. Szemplińska-Stupnicka, W.: Bifurcation of harmonic solution leading to chaotic motion in the softening type Duffing's oscillator. Int. J. Non-Linear Mechanics 23 (1988) 257-278.

8. Zavodney, L.D.; Nayfeh, A.H.; Sanchez, N.E.: The response of a single-degree-of-freedom system with quadratic and cubic nonlinearities to a principal parametric resonance. J. Sound Vibr. 129 (1989) 417-442.

On Symmetry Breaking Bifurcations: Local and Global Phenomena

by P. R. Sethna
Z. C. Feng and X. Yang
Department of Aerospace Engineering and Mechanics
University of Minnesota
Minneapolis, MN 55455

Abstract This study is concerned with local and global bifurcation analysis of a system of equations with symmetry that occurs frequently in the study of surface waves in containers and vibrations of plates.

1. Introduction

In this work we give a study of dynamical systems that have two linear modes with frequencies that are nearly equal, when excited strongly so that nonlinear effects have to be taken into account. The occurrence of two nearly equal frequencies and other symmetries in the equations is often, but not always, due to physical symmetry in the system under investigation.

Specifically, we discuss certain types of equations with symmetries that occur in the study of surface waves in containers with a fluid, vibrations of beams and plates, etc. See, for instance, Feng and Sethna (1989), Yang and Sethna (?), Nayfeh and Pei (1989), Miles and Henderson (1989) and Umeki and Kambe (1989).

We give here results based on local as well as global bifurcation analysis with physical interpretations in the context of surface wave motions in nearly square containers subjected to vertical sinusoidal excitation as discussed in Feng and Sethna (1989) and vibration of nearly square simply supported elastic plates with in-plane boundary displacement as given in Yang and Sethna (?).

2. The Nature of the System

We work with "amplitude equations" of the form

$$\dot{Z}_1 = -dZ_1+i\,[-(\sigma-\beta)Z_1+F_1Z_1^* + \pi_1Z_1^2Z_1^*+ \pi_2 Z_1Z_2Z_2^* + \pi_3Z_1^*Z_2^2]$$

$$\dot{Z}_2 = -dZ_2+i\,[-(\sigma+\beta)Z_2+F_2Z_2^* + \pi_1Z_2^2Z_2^*+ \pi_2 Z_1Z_2Z_1^* + \pi_3Z_2^*Z_1^2] \qquad (2.1)$$

W. Schiehlen (Editor)
Nonlinear Dynamics in Engineering Systems
IUTAM Symposium Stuttgart/Germany 1989

where Z_1 and Z_2 are complex variables and a * indicates complex conjugates. All other quantities are real and $d>0$ and β can be taken positive without loss of generality. The constant d represents damping. The constants σ and β represent the deviation of the excitation frequency from the natural frequencies and the difference in the natural frequencies, respectively. The F_1 and F_2 represent amplitude of the parametric excitations in each mode. The π_j, j=1, 2, 3, the coefficients of the nonlinear terms, determine the nature of the system under investigation. They are, for instance, –2.349, 0.1803, and –3.647 in the case of (0, 1) and (1, 0) model motions of surface waves in the appropriate dimensionless variables and they are B, 2D and D, with B and D positive constants, in the case of nearly square plates, with B and D varying according to the mode numbers.

The system (2.1) has $Z_2 \oplus Z_2$ symmetry, i.e. it has the invariance $(Z_1, Z_2) \leftrightarrow (-Z_1, Z_2) \leftrightarrow (Z_1, -Z_2)$ when β is not zero and an additional $(Z_1, Z_2) \leftrightarrow (Z_2, Z_1)$ symmetry, i.e. D_4 symmetry, when $\beta=0$. If in addition $\pi_1-\pi_2-\pi_3=0$ it has O(2) symmetry generating the equivariance $(Z_1, Z_2) \leftrightarrow (\cos\theta Z_1+\sin\theta Z_2, -\sin\theta Z_1+\cos\theta Z_2)$ $0<\theta\leq 2\pi$. The transformation $V=Z_1+iZ_2$, $W=Z_1^*+iZ_2^*$ (Steindl and Troger, [1987]) makes this more clear.

We now give below a brief summary of a local and global analysis of bifurcation phenomena which is based on Yang and Sethna (?) and Feng and Sethna (1989), (??).

3. Local Analysis

The fixed points of (2.1) represent wave motions and the stability of the fixed point determines the stability of the waves. Periodic solutions of (2.1) represent almost periodic, amplitude modulated waves and what is true of fixed points regarding stability is also true of periodic solutions.

A local bifurcation analysis in (σ, β) space has been completed in the case of surface waves in the case of symmetric excitation $F_1=F_2$ and is given in Feng and Sethna (1989). In the case of waves in plates the same is done both for the symmetric and antisymmetric excitation $F_1=-F_2$ and the results are given in Yang and Sethna (?). Both co-dimension one and two local bifurcations are shown to occur. All co-dimension one bifurcations occur in the case of water waves while all but Hopf bifurcations are shown to occur in the case of plates.

We note that fixed points $Z_1=0$, $Z_2\neq 0$ and $Z_1\neq 0$, $Z_2=0$ are both possible. From this it can be concluded that motion is possible in either mode. These are called one mode motions. Fixed points with both $Z_1\neq 0$ and $Z_2\neq 0$ are also possible. These represent mixed mode motions. These motions can be standing waves when Z_1 and Z_2 have the same phase angle. When Z_1 and Z_2 do not have the same phase angle, we have traveling waves of different kinds. One mode motions and mixed motions of both kinds occur in the two studies mentioned above. In the case of water waves, amplitude modulated waves arising from Hopf bifurcations are also shown to occur.

The physical meaning of the excitation is clear. In the case of plates, all four edges move in and out in phase in the symmetric case. In the antisymmetric case, since the excitation is at twice the frequency, the edge displacement has a phase so that the edges move in and out in a sequence in either clockwise or anticlockwise directions. In the case of water waves, the physics is similar except for the fact that the container edges move vertically.

In Figs. 1 and 2 are given bifurcation diagrams for a square plate (with $\beta=0$, i.e. D_4 symmetry) in the case of symmetric and antisymmetric excitations, respectively. It is to be noted that the dominant motions in the symmetric and antisymmetric cases are respectively standing and rotating waves when the detuning is small. The rotating wave, however, is stable for all reasonable values of detuning of the external excitation, while the standing wave gets unstable at a critical value of detuning.

In Fig. 3 we give a bifurcation diagram for the case of water waves and experimental data, both as given in Feng and Sethna (1989).

4. Global Analyses

We follow here a procedure similar to Holmes (1984) and Wiggins (1988) and rely on some mathematical results of Robinson (1988) to get conditions on the system parameters for which Smale horseshoes and chaotic dynamics are expected to occur.

Let $d=0$ and $F_1=\varepsilon f_1$ and $F_2=\varepsilon f_2$ when ε is small in (2.1). We thus study the case when energy dissipation is zero and when the excitation is small.

Let

$$Z_1 = (2I_1)^{1/2}\sin\theta_1 + i(2I_1)^{1/2}\cos\theta_1 ,$$

$$Z_2 = (2I_2)^{1/2}\sin\theta_2 + i(2I_2)^{1/2}\cos\theta_2 \tag{4.1}$$

in (2.1) and introduce a second canonical change of variables by using the generating function

$$F = (\theta_1 - \theta_2)p_1 + \theta_2 p_2$$

then if

$$p_1 = \frac{P_1}{|\pi_3|} \quad , \quad p_2 = \frac{P_2}{|\pi_3|} , \; f_1=F_1 , \; f_2= -F_2 \operatorname{sgn} \pi_3$$

$$\alpha = \frac{-\pi_1 + \pi_2}{|\pi_3|} \tag{4.2}$$

$$q_1 = (1+\operatorname{sgn} \pi_3)\frac{\pi}{4} + Q_1, \; q_2 = (1+\operatorname{sgn} \pi_3)\frac{\pi}{4} + Q_2 .$$

and if

$$H_\varepsilon = H_2 + \varepsilon\tilde{H}$$

where

$$H_2 = -2\beta P_1 - 2P_1(P_2-P_1)(\alpha-\cos 2Q_1) + (\sigma+\beta)P_2 - \delta P_2^2 \tag{4.3a}$$

$$\tilde{H} = f_1 P_1 \cos(2Q_1+2Q_2) + f_2(P_2-P_1)\cos 2Q_2 . \tag{4.3b}$$

then the equations become

$$\begin{aligned}
\dot{P}_1 &= -\frac{\partial H_\varepsilon}{\partial Q_1} = 4P_1(P_2-P_1)\sin 2Q_1 + \varepsilon[2f_1P_1\sin(2Q_1+2Q_2)] \\
\dot{Q}_1 &= \frac{\partial H_\varepsilon}{\partial P_1} = -2\beta + 2(2P_1-P_2)(\alpha-\cos 2Q_1) + \\
&\quad \varepsilon[f_1\cos(2Q_1+2Q_2) - f_2\cos 2Q_2] \\
\dot{P}_2 &= -\frac{\partial H_\varepsilon}{\partial Q_2} = \varepsilon[2f_1P_1\sin(2Q_1+2Q_2) + 2f_2(P_2-P_1)\sin 2Q_2] \\
\dot{Q}_2 &= \frac{\partial H_\varepsilon}{\partial P_2} = \sigma + \beta - 2P_1(\alpha-\cos 2Q_1) + \varepsilon f_2\cos 2Q_2
\end{aligned} \tag{4.4}$$

Analysis of the unperturbed system

When $\varepsilon=0$ we have the unperturbed system

$$\begin{aligned}
\dot{P}_1 &= 4P_1(P_2-P_1)\sin 2Q_1 , \\
\dot{Q}_1 &= -2\beta + 2(2P_1-P_2)(\alpha-\cos 2Q_1) , \\
\dot{P}_2 &= 0 , \\
\dot{Q}_2 &= \sigma + \beta - 2P_1(\alpha-\cos 2Q_1) .
\end{aligned} \tag{4.5}$$

We note that (4.5) depends on the parameters σ, β and α and $P_2=P_{20}$ a constant. A detailed analysis of (4.5) in Feng and Sethna (??) for all values of the parameters shows that there are six qualitatively different kinds of flows depending on six open sets in the $\left(\alpha, \frac{\beta}{P_{20}}\right)$ plane. Of these six flows, four contain heteroclinic cycles of three distinct kinds. When these cycles break under perturbation, Smale horseshoes are shown to occur. Thus there are three distinct types of geometric structures.

Our analytical procedures require the explicit computations of the orbits of the heteroclinic cycles in $(P_1\ Q_1)$ space and furthermore the explicit solutions, as functions of t, of

the entire vector $(P_1(t), Q_1(t), P_2=P_{20}, Q_2(t))$. The computations are difficult and of considerable complexity.

The Melnikov Function

Our global results depend on the computation of the Melnikov function on the heteroclinic orbits. Specifically we compute

$$M = \lim_{j\to\infty} \int_{-T_j^u}^{T_j^s} \frac{\partial \tilde{H}}{\partial Q_2}\, dt \tag{4.6}$$

where the integrand is computed on the heteroclinic cycles and T_j^s and $T_j^u \to \infty$ as $j\to\infty$ in an appropriate manner. The detailed calculations in all cases lead to an expression for M with the following structure.

$$M = \sin 2Q_{20}\ m(P_{20}, \sigma, \beta, \alpha, f_1 \text{ and } f_2)$$

Q_{20} is a parameter. It can be shown that m remains bounded and in general away from zero with the result that M has simple zeroes as a function of Q_{20} and this gives us the result regarding the occurrence of Smale horseshoes.

In Fig. 4 we give the geometry of the coordinate system for the unpertubed system and in Fig. 5 the coordinate system for the Poincaré section for Q_2 a constant. The results of the theory have been checked against numerical computations for specific parameter values in the six open sets in the parameter space mentioned above. Three dimensional Poincaré sections of the flow indicate only almost periodic behavior in those cases when the unperturbed system does not have heteroclinic cycles and show distinctly chaotic behavior in three dimensional Poincaré sections when the unperturbed problem has heteroclinic cycles.

We remark that although these results are proved for Hamiltonian systems, since the Smale horseshoes are structurally stable they will persist, though somewhat modified in structure, in damped systems; the damping, however, in all probability, will have to be very small in most cases.

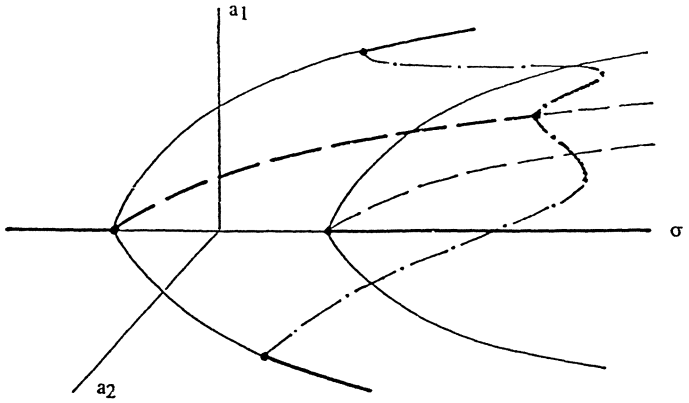

Figure 1. Bifurcation diagram of square plate with symmetric excitation. (——— pure one-mode, — — — — standing waves, —·—·— rotational waves.)

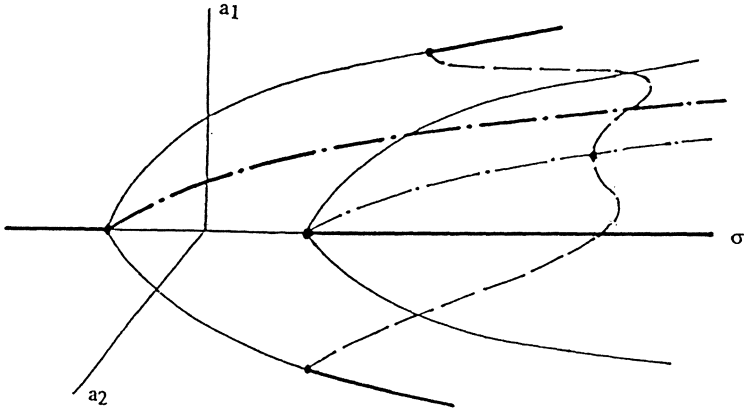

Figure 2. Bifurcation diagram of square plate with antisymmetric excitation. (——— pure one-mode, — — — — standing waves, —·—·— rotational waves.)

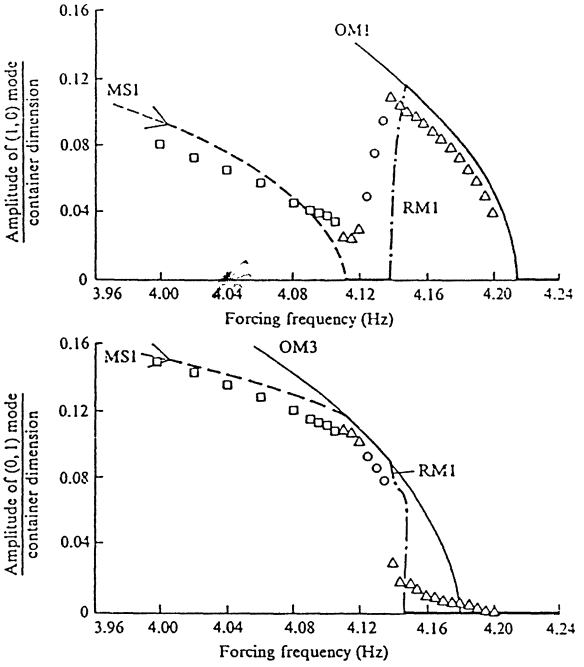

Figure 3. Experimental verification of bifurcation diagram. The notation for experimental data is: □, standing wave; O, rotational wave; Δ, pure one-mode.

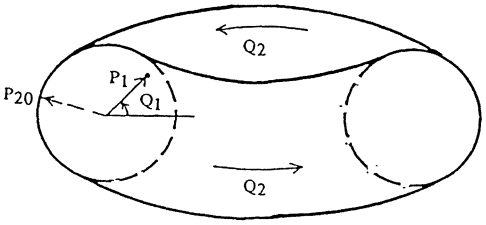

Figure 4. Coordinates for unperturbed system.

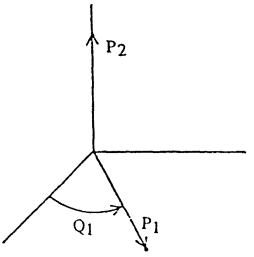

Figure 5. Coordinates for Poincare section, Q_2=constant.

Global Bifurcations

References

Feng, Z.C.; Sethna, P.R. Global bifurcation and chaos in nonautonomous systems with $Z_2 \oplus Z_2$ symmetry. In preparation.

Feng, Z.C.; Sethna, P.R. Symmetry breaking bifurcations in resonant surface waves. *J. Fluid Mech.* Vol. **199** (1989), 495–518.

Holmes, P. Chaotic motions in a weakly nonlinear model for surface waves. *J. Fluid Mech.* Vol. **162** (1986), 365–388.

Miles, J.W.; Henderson, D. Parametrically forced surface waves. Preprint.

Nayfeh, A.H.; Pai, P.F. Non-linear non-planar parametric responses of an inextensional beam. *Int. J. Nonlinear Mech.* Vol. **24** (1989), 139–158.

Robinson, C. Horseshoes for autonomous Hamiltonian systems using the Melnikov integral. *Ergod. Th. & Dynam. Sys.* Vol. **8** (1988), 395–409.

Steindl, A.; Troger, H. Bifurcations of the equilibrium of a spherical double pendulum at a multiple eigenvalue. *International Series of Numerical Math.* Vol. **79** (1987), 277–287.

Umeki, M.; Kambe, T. Nonlinear dynamics and chaos in parametrically excited surface waves. *J. Phys. Soc. Japan* Vol. **58** (1989), 140–154.

Wiggins, S. *Global bifurcations and chaos—analytical methods.* New York: Springer-Verlag 1988.

Yang, X.L.; Sethna, P.R. Bifurcation phenomena in the vibrations of nearly square plates with parametric excitations. In preparation.

The Supression of Chaos in Periodically Forced Oscillators

Steven W. Shaw
Department of Mechanical Engineering
Michigan State University
East Lansing, MI 48824 U.S.A.

Summary

A method for suppressing chaos in a class of periodically forced oscillators is presented. The method involves the manipulation of higher harmonics in the periodic excitation such that the homoclinic tangles which lie at the heart of the chaos are destroyed. The procedure is demonstrated via a particular example: an inverted pendulum with amplitude constraints subjected to periodic base excitation. The general theory is developed using a Melnikov type method (see [1-3]) and is supported by some experimental evidence.

Introduction

Virtually every example of chaos observed in forced oscillators (as well as in autonomous systems and discrete maps) is a manifestation of the Smale horseshoe or one of its generalizations [3]. This is true independent of the "route to chaos", e.g. period doubling, quasiperiodic breakdown, intermittantcy, etc. These horseshoes are not strange attractors, but are chaotic saddle type invariant sets and are thus not realiazable steady states in practice. In order to prove that sustained chaos, that is, a *strange attractor*, exists more is needed; specifically it must be shown that the horseshoes lie in an attracting set which contains no stable motions of finite period. Such a result is not available for even the simplest nonlinear forced oscillators. Regardless, the existence of horseshoes provides the recognized features of chaos including sensitive dependence on initial conditions and nonperiodic solutions, and their presence is required before chaos, either transient or sustained, is observed.

The unifying theme in these types of chaos is that of *homoclinic* behavior - that is recurrent behavior near a saddle point, which contain horseshoes in a wide range of circumstances [3]. There does exist one class of problems for which one can prove (usually in an asymptotic sense) parameter conditions for the existence of horseshoes in specific systems; this is the method of Melnikov [1,2] and its generalizations [3]. It provides a boundary in parameter space which separates domains for which the system does and does not have horseshoes near a specific saddle type invariant set. On the "no horseshoe" side of the boundary there can be no chaos associated with the invariant set in question, while on the other side the system will exhibit at least transient chaos, and possibly steady state

W. Schiehlen (Editor)
Nonlinear Dynamics in Engineering Systems
IUTAM Symposium Stuttgart/Germany 1989

chaos. Moon et al. [4] used this fact, along with extensive computer simulations and experiments, to label homoclinics as a "precursor to chaos." Also, the Melnikov criteria provides the conditions for the fractal basin boundaries which separate initial conditions in phase space leading to different long term behavior (see [5]). In this paper a Melnikov type method will be used as a guide for designing inputs which are optimal (in a sense to be defined) in the elimination of chaos.

Homoclinic orbits are solutions which are forward and backward asymptotic (in time) to a saddle-type fixed point (or a more general invariant set [3]). They occur at the intersection of the of the sets which are forward and backward asymptotic to the saddle point, i.e. the stable and unstable manifolds, respectively. Melnikov's method measures the separation between these manifolds and can thus predict when such an intersection occurs. The connection between transverse intersections, horseshoes, and chaos, and the fact that the separation can be measured without solving the equation directly, provides the method with its predictive capability. Introductions to the method can be found in [2] and [4] and extensions and generalizations in [3].

The present treatment will consider a specific forced oscillator for which the separation for a general periodic input can be measured exactly using an extension of the ideas demonstrated in [6]. The method of determining those inputs which are optimally suited for extinguishing chaos (subject to certain constraints which make the problem non-trivial) is then presented along with one piece of experimental evidence in support of the analysis.

The System Under Investigation

The physical device is depicted in Figure 1; it is the same as that considered in [6,7], except that the base excitation is taken to be a general periodic function of time. After rescaling, the equation of motion governing the pendulum angle measured from the vertical, including impacts with the constraints, is

$$\ddot{x} + 2\delta\dot{x} - x = \sum_{j=1}^{\infty} \gamma_j \sin(j\omega t + \psi_j) \qquad |x|<1 \qquad (1a)$$

$$\dot{x} \to -r\dot{x} \qquad |x|=1 \qquad (1b)$$

where $x = \theta/\theta_{max}$ ($\theta_{max} < 10°$ for linearization), δ is the free flight damping ratio, ω is the dimensionless driving frequency, r is the coeffi-

cient of restitution for the impacts (which are assumed to be instantaneous), and γ_j and ψ_j are the excitation amplitude and phase for the jth harmonic, respectively. Details are provided in [6,7]. This system is qualitatively similar to the widely studied Duffing oscillator with negative linear stiffness [1-3]; when unforced it has an unstable central position (x=0) with stable rest positions on either side (x=±1). The phase portrait for the δ=0, γ_j=0 system is shown in Figure 2, with $y = \dot{x}$; the impacts are taken to be instantaneous changes in velocity at $x = \pm 1$ according to equation (1b). Note that there exist two homoclinic motions for the origin when r = 1 (elastic rebounds). For $\gamma_j \neq 0$ the unstable equilibrium becomes a saddle type periodic motion which does not involve impacts, under the condition that the peak value of the particular solution of (1a) not exceed unity. This saddle type motion has stable and unstable manifolds, W^s and W^u, respectively.

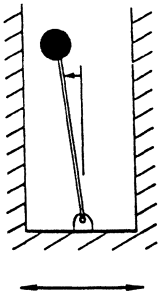

Figure 1

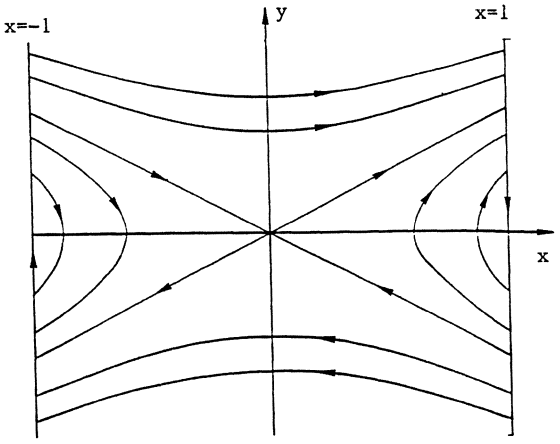

Figure 2

Now suppose that this constrained pendulum is subjected to a purely harmonic input, say $\gamma_1 \sin(\omega t)$ with ψ_1=0 and γ_j=0 for all $j \geq 2$, and has transverse homoclinic solutions, i.e. W^s and W^u intersect transversely. Can (γ_j, ψ_j) for $j \geq 2$ be chosen so as to separate the manifolds? The answer

is yes, under certain conditions. In order to demonstrate the circumstances under which this is possible, and to demonstrate the method of choosing optimal values for (γ_j, ψ_j), $j \geq 2$, the separation between W^u and W^s must be computed. The separation is computed in the Poincare Section $\sum = \{(x,y,t): x=1, y>0\}$ as follows: The homogeneous and particular solutions of (1a) are written in the form

$$x = x_h + x_p = c_1 e^{s_1(t-t_o)} + c_2 e^{s_2(t-t_o)} + \sum_{j=1}^{\infty} (\gamma_j/\Gamma_j) \sin(j\omega t + \psi_j + \phi_j) \qquad (2)$$

$$s_1 = -\delta + \sqrt{1+\delta^2}\ ;\ s_2 = -\delta - \sqrt{1+\delta^2}\ ;$$

$$\tan(\phi_j) = -2\delta j\omega/(1+(j\omega)^2),\ \frac{3\pi}{2} \leq \phi_j \leq 2\pi;$$

$$\Gamma_j = [(1+(j\omega)^2 + (2\delta j\omega)^2]^{1/2}\ .$$

Those solutions which start in $\sum \cap W^u$ must approach x_p as $t \to -\infty$ and must therefore have $c_2 = 0$ (since $s_2 < 0$ and $e^{s_2 t} \to \infty$ as $t \to -\infty$). Employing initial conditions in $\sum$, $(x,y,t) = (1, y^u, t_o)$, along with $c_2 = 0$, yields the curve for $y^u(t_o)$, i.e. $\sum \cap W^u$:

$$y^u(t_o) = s_1(1 - x_p(t_o)) + \dot{x}_p(t_o)\ .$$

To determine $\sum \cap W^s$ the impact rule must be included in the analysis. Points in W^s must be asymptotic to x_p as $t \to \infty$, therefore c_1 must be zero. Using this and the inverse of the impact rule yields the curve $\sum \cap W^s$:

$$y^s(t_o) = -[s_2(1-x_p(t_o)) + \dot{x}_p(t_o)]/r.$$

The separation is then given by

$$d(t_o) = y^u(t_o) - y^s(t_o)$$

$$= [(s_1 r + s_2)(1 - x_p(t_o)) + (1+r)\dot{x}_p(t_o)]/r.$$

Standard trigonometric manipulations then provide the separation as a function of the phase t_o in the following form

$$d(t_o) = \frac{D_o}{2} + \sum_{j=1}^{\infty} D_j \sin(j\omega t_o + \psi_j + \phi_j + \nu_j) \qquad (3)$$

$$D_o = 2(rs_1+s_2)/r \ (< 0); \ D_j = \gamma_j \Lambda_j / r\Gamma_j;$$

$$\tan(\nu_j) = (1+r)j\omega/(s_1 r + s_2), \ \pi/2 \le \nu_j \le \pi;$$

$$\Lambda_j = [(1+r)^2 (j\omega)^2 + (s_1 r + s_2)^2]^{1/2}$$

It is important to note how the amplitudes of the input and separation harmonics are related, in particular the ratio $\gamma_j/D_j = r\gamma_j/\Lambda_j$. In order for the separation series to converge, the D_j's must decrease by at least j^{-1} as $j \to \infty$. Since $r\gamma_j/\Lambda_j$ grows like $rj\omega/(1+r)$ for large j, this implies that the γ_j's are asymptotically a constant (at best) as $j \to \infty$. This leads to a divergent and unrealistic input. A practical solution is to design the optimal input for one additional harmonic input. The separation for a purely harmonic input is composed of a negative constant, $D_o/2$, and a purely harmonic term of amplitude D_1, frequency ω, and relative phase $\phi_1 + \nu_1$. It has tangent zeroes when $|D_o/2| = D_1$ and transverse zeroes for $|D_o/2| < D_1$; this yields the criteria for chaos obtained in [6]:

$$\gamma_1 \ge \gamma_{1cr} = -(s_1 + rs_2)\Gamma_1/\Lambda_1 \qquad (>0).$$

The chaos which occurs when the above condition is satisfied involves motions in which the pendulum undergoes irregular sequences of impacts at the left and right. If a symmetric pair of stable periodic motions exist, one each impacting on only a single side, then the domains of attraction for those two steady states will have a fractal boundary for $\gamma_1 > \gamma_{1cr}$ [5].

The Optimal Solution for One Additional Harmonic

If it is possible to eliminate the zeroes of the separation, then the chaos can be destroyed. The optimal input is the one which reduces as much as possible the amplitude of the oscillating part of the separation $d(t_o)$. For the present case the goal is to determine

$$(j,\gamma_j,\psi_j)^* = \min_{\substack{j,\gamma_j,\psi_j \\ j\neq 1}} \max_{t_o\in[0,2\pi/\omega)} [D_1 \sin(\omega t_o + \phi_1 + \nu_1) + D_j \sin(j\omega t_o + \psi_j + \phi_j + \nu_j)].$$

That $j^* = 3$ is obvious; the third harmonic can reduce the peak better than any other harmonic (the even harmonics are useless here). Also, the optimal choice will have the first and third harmonics in phase, hence $\psi_3^* = j(\phi_1+\nu_1) - (\phi_3+\nu_3)$. The problem is then essentially reduced to determining

$$\alpha^* = \min_{\alpha} \max_{t_o\in[0,2\pi)} [\sin(t_o) + \alpha \sin(3t_o)] \quad . \tag{4}$$

Standard operations yield $\alpha^* = 1/6$ with the peak reduced by a factor of $\sqrt{3}/2$. Following back through the calculations leads to

$$\gamma_3^* = \gamma_1 \Lambda_1 \Gamma_3 / 6\ \Lambda_3 \Gamma_1 .$$

Summarizing to this point, the optimal input is given by

$$\gamma_1 \sin(\omega t) + \gamma_3^* \sin(3\omega t + \psi_3^*)$$

and it results in a separation of

$$D_o/2 + D_1 [\sin(\omega t_o + \phi_1 + \nu_1) + (1/6) \sin(3(\omega t_o + \phi_1 + \nu_1))].$$

The corresponding criteria for chaos is now

$$\gamma_1 \geq \frac{2}{\sqrt{3}} \gamma_{1cr},$$

that is, about a 15% increase in the original harmonic force amplitude can be achieved before introducing chaos.

The addition of the single optimal input harmonic is guaranteed to separate the manifolds for $\gamma_{1cr} < \gamma_1 < 2/\sqrt{3}\ \gamma_{1cr}$. In addition, it may well be that it is practically useful for eliminating steady state chaos even without untangling the manifolds. Figure 3 shows the inputs and the response of an experimental apparatus (described in detail in [7]; it has $\delta \cong 0.03$ and $r \cong 0.95$) for $\gamma_1 \cong 1.24$ and $\omega \cong 8.0$. The optimal additional harmonic input (which cannot untangle the manifolds here since γ_1 is significantly greater than $\gamma_{1cr} \cong 0.5$) for this case is a third harmonic with approximately one half the amplitude of the first, $\gamma_3^* \cong \gamma_1/2$, and approximately in phase, $\psi_3^* \cong 0$. Addition of this input results in the

response shown, simple periodic boundary on one side. Both the chaotic and periodic steady states shown in Figure 3 are robust, and the only ones found at those parameter values for several initial conditions (for their respective inputs).

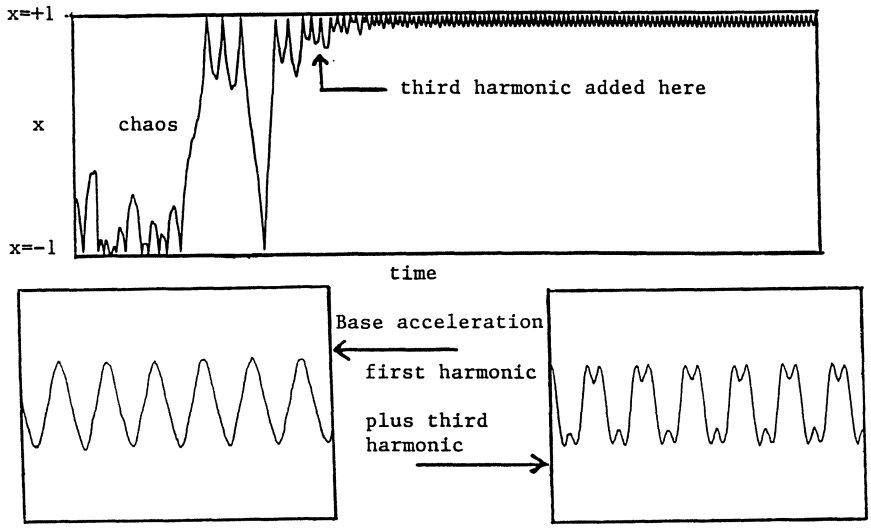

Figure 3

Conclusions

The example above demonstrates the general method and provides some evidence that it works. More thorough studies of both experimental and numerical nature should be carried out. Also, it may be that the addition of the third harmonic leads to problems, possibly in the form of nonlinear resonances; this must be considered on a case by case basis. Finally, it should be noted that the 15% increase in the critical value of γ_1 is a general result for cases in which the separation is given by a constant plus a pure harmonic and one additional harmonic is added; all such situations will lead to finding α^* as in condition (4).

Acknowledgement

The author is grateful to Prof. Alan Haddow of Michigan State University for the experimental results given above.

References

1. Melnikov, V.K.: "On the stability of the center for time periodic perturbations," Trans. Moscow Math. Soc. 12 1-57, 1963.

2. Guckenheimer, J.; Holmes, P.: Nonlinear Oscillations, Dynamical Systems, and Bifurcations of Vector Fields. 2nd printing, Springer Verlag, New York, Berlin, Heidelberg, Tokyo, 1986.

3. Wiggins, S.: Global Bifurcations and Chaos-Analytical Methods, Springer Verlag, New York, Berlin, Heidelberg, Tokyo, 1988.

4. Moon, F.C.; Cusumano, J.; Holmes, P.J.: "Evidence for homoclinic orbits as a precursor to chaos in a magnetic pendulum," Physica 24D 383-390 1987.

5. Moon, F.C.: Chaotic Vibrations, Wiley-Interscience, New York, 1987.

6. Shaw, S.W.; Rand, R.H.: "The transition to chaos in a simple mechanical system," Int. J. of Nonlinear Mech. 24 41-56 1988.

7. Moore, D.B.; Shaw, S.W.: "The experimental response of an impacting pendulum system," Int. J. of Nonlinear Mech., to appear.

Dynamics of Dot-Matrix Printers

H.Springer
Institute of Mechanics, University of Hannover, FRG

M.Ullrich
Mannesmann Tally GmbH, Elchingen, FRG

SUMMARY

This paper deals with electromagnetic and stored energy needle printer systems. Mechanical models and differential equations of motion are developed in order to simulate printing characteristics of both systems by numerical integration. For example, needle displacements, velocities, and accelerations, peak values of the printing forces and the period of contact between the needle and the ribbon can be calculated. Different modes of failure, as instability of the synchronous needle motion, or a break-down of the printing force with increasing printing frequency, are investigated for various design parameters of the system. All calculations can be carried out on a personal computer, and very good agreement is obtained between computed and measured results.

1. INTRODUCTION

The printing operation of a single needle must be stable up to a frequency range of about 2000 Hz, and synchronous with the applied current of the electromagnetic circuit. No feedback control is applied between the needle displacement and the driving current, and particular attention has to be paid to the stability of the synchronous printing mode. Further, the peak values of the printing forces must stay within a narrow band width of magnitudes independent of whether the needle performs a single shot or is operated in a periodic mode (permanent fire). Beside that, the needle impact forces have to be rather insensitiv with respect to changes of the paper properties, number of paper sheets, needle stroke, and manufacturing tolerances. In [1], digital simulation models have been introduced to predict characteristics of the electromagnetic and the stored energy printer systems, see Fig.1 and Fig.2 , respectively. In the electromagnetic system the armature 1 is pressed against a damper mass 3 by a helical spring 4 in a static equilibrium position. When the driving current in coil 5 is turned on, a magnetic flux is generated in the ferromagnetic circuit and an attractive magnetic force, acting within airgap 7, accelerates the armature 1 towards

W. Schiehlen (Editor)
Nonlinear Dynamics in Engineering Systems
IUTAM Symposium Stuttgart/Germany 1989

the paper-ribbon-platen system and generates a dot. When the current is turned off, the needle rebounds and moves towards the damper system 3 which dissipates the kinetic energy of the armature and stabilizes the needle motion. By turning on the current again, the process is repeated. Fig. 2 shows a schematic diagram of the stored-energy printer system. In the stationary state the armature lever 1 (carrying the needle 2) is attracted by a permanent magnet 8 and pressed against the ferromagnetic pole 6 and the damper ring 3. In this static equilibrium position the leaf spring 4 is prestressed, storing potential energy. By turning on the current in coil 5, a magnetic flux is generated, acting in the opposite direction of the permanent field. Thus, the armature lever is released from the pole, the needle is accelerated towards the paper-ribbon-platen system, and a dot is produced. By turning off the current, the permanent magnet attracts the armature lever back to the pole and the damper ring. Because of internal damping within the lever material and the damper ring the remaining kinetic energy of the lever is dissipated and stabilizes the system. By turning on the current, the process is repeated. In both printer systems the needle motion must synchronously follow the frequency of the applied current. For an acceptable printing process the transient period from zero (static) initial conditions to periodic synchronous response of the needle must be extremely short.

2. SYSTEM MODELING AND EQUATIONS OF MOTION

In general, a printer is composed of four subsystems: the oscillating armature, carrying the needle, the damper system, the paper-ribbon-platen system (PR-PL), and the electromagnetic excitation system. Each of these components must be modeled carefully according to measured properties.

Modeling of the electromagnetic components and the PR-PL-system.

The time response of the applied current is approximated in the analysis by trapezoidal functions as shown in Fig.3. The geometric structure of the ferromagnetic circuit is rather complicated for both printer systems. Therefore, a numerical calculation of the time response of the magnetic flux density within the primary airgaps 7 (see Fig.1 and 2) is extremely laborious and is not applied in this simulation model. Experiments have been carried out to measure the attractive magnetic forces FM(g,t) in the primary airgaps in terms of the coil current i(t) and the airgap length g. An empirical equation of the form

$$FM(g,t) = FM_o[n - i(t)/i_o]^2/[1 + g/g_o]^{\alpha} \qquad (1)$$

has been introduced to match the experimental results by the parameters FM_o, i_o, g_o, and the exponent α. For the electromagnetic system n = 0, and for the stored energy system n = 1. Since the airgap length g is not constant and varies with the armature displacement, the exciting magnetic force FM depends on both the applied current and the needle displacement.

The PR-PL-system of the printer, see Figures 4 and 5, is modeled as a visco-elastic surface with either piecewise linear or nonlinear spring characteristics. Inertia effects of the ribbon and the paper are neglected. For different numbers of paper sheets the stiffness and damping parameters of the PR-PL-system have been obtained from experiments. Note that the contact (printing) force FN between the needle and the ribbon surface is of compressive type only, i.e. even for a linear visco-elastic PR-PL-system the dynamic equations of motion for the needle are highly nonlinear.

Modeling of the electromagnetic system.

Fig.4, for example, shows a two degrees of freedom mechanical model where x_A and x_D represent the displacements of armature and damper mass, respectively. The contact forces FDA between the armature and the damper mass are introduced as one-sided compressive and visco-elastic. From Fig.4 the equations of motion can be written in the simple form

$$m_A \ddot{x}_A = -FDA + FS + FM + FG + FN \qquad (2)$$

$$m_D \ddot{x}_D = FDA + FDH \qquad (3)$$

where FS is the linear restoring spring force , $FG = -|FG|\,\mathrm{sgn}(\dot{x}_A)$ is a dry friction force exerted by the needle guide bearing, FDH is a linear visco-elastic force between the housing and the damper mass, and FN is the needle printing force as mentioned above. Equ.(2) and (3) are highly nonlinear and no analytical solution is available. Therefore, a digital simulation language is applied to obtain numerical results, see [2].

Modeling of the stored energy system.

Fig.5 shows a schematic diagram of the mechanical model. Magnetic pole contact forces $FP(x_M,\dot{x}_M)$ and damper forces $FD(x_D,\dot{x}_D)$ are introduced as one-sided compressive and visco-elastic. The crooked needle is represented by a massless spring of effective stiffness k_N, attached to the free end of the armature lever. The lever is modeled by finite elements, and a modal model, including 3 to 4 major bending modes up to a frequency range of about 25 kHz, is used for the simulation analysis. Beside the needle peak displace-

ment x_N the deflections x_M, x_D, x_A are introduced as master coordinates by the vector $\underline{w} = [x_M, x_D, x_A]^T$, see Fig.5. The modal equations of motion for the armature lever have the diagonal form

$$\ddot{\underline{y}} + 2\,\underline{D}\,\dot{\underline{y}} + \underline{\Omega}^2\,\underline{y} = \underline{\Phi}^T\,\underline{H}^T\,\underline{F} \tag{4}$$

with $$\underline{F}(\underline{w},\dot{\underline{w}}) = [FP + FM,\ FD,\ FN + FG]^T \tag{5}$$

$$\underline{w} = \underline{H}\,\underline{\Phi}\,\underline{y} \tag{6}$$

In Equ.(4), $\underline{y}$ represents the modal coordinates, $\underline{D}$ is the internal damping matrix of the lever, $\underline{\Phi}$ is the reduced modal matrix obtained from a FE-analysis, and $\underline{H}$ is an incidence matrix. The above equations are highly nonlinear, and a numerical solution is obtained by digital simulation, [2].

3. NUMERICAL SIMULATION AND RESULTS

Electromagnetic printer system.

Fig.6 shows typical time response characteristics of a stable synchronous printing mode at 2000 Hz. The nominal printer parameters are indicated in the figure caption. Starting from zero initial conditions at z=0, the required synchronous limit cycle of the needle motion is immediately approached after the first impact, i.e. there is practically no modulation of phase and magnitude of the printing force within a transient period. The solution is stable within practical tolerances of the needle stroke, the printing frequency and the paper stiffness values. The maximum printing force in this example is about 13 N, the damper impact force reaches 18.5 N; this corresponds to maximum accelerations of the needle of about -8000 g and 11000 g, respectively. The printing contact time is about 60 μs, the impact momentum is 0.4 mNs. High impact forces between the armature head and the damper system may gradually lead to extensive wear-out or plastic deformation which finally increase the initial airgap length g(0), see Fig.4, and thus decrease the magnetic driving forces. This effect may destabilize the synchronous printing mode. Fig.7(a) shows a phase plane projection of the needle motion for increased values of the airgap and the nominal needle stroke at a frequency of 2500 Hz. A long transient period of the needle motion over about 35 current cycles can be observed which finally approaches a periodic subharmonic attractor of second order, see Fig.7(b). The system seems to be very close to a steady chaotic motion since extremely small changes of the initial conditions lead to dramatic changes in the needle motion. Note that the electromagnetic printer system may roughly be considered as a double sided impact oscillator, and therefore, the appearance

of a chaotic regime is a characteristic feature; for example, see [3]. For practical operation of a needle printer, a long transient period or chaotic motions are totally unacceptable even if a coexisting synchronous solution is possible. Also, subharmonics of order n >1 cannot be used for regular printer operation.

Stored energy printer system.

This printer system is much less sensitiv with respect to chaotic needle motions. In Fig.8(a) a stable synchronous time response of the needle motion is shown for an exciting current frequency of 1500 Hz. Practically no transient period can be observed. The peak value of the printing force is about 8 N in this example. The needle contact period is about 100 μs and the impact momentum is 0.4 mNs which is the same value as obtained for the electromagnetic system. However, the stored energy printer produces the dot in a "softer" way than the electromagnetic system. It is worth to note that for increasing frequency the transient period increases and the printing force magnitude finally breaks down to unacceptable low values, see Fig.8(b). Here, the synchronous component is still predominant but is slightly modulated by a third order subharmonic. In general, the mode of failure for the stored energy system is less critical than for the electromagnetic system. Fig.9 shows the peak forces in terms of the printing frequency. There is a very good agreement between measured and numerical results. The force break-down frequency limit can be predicted also very accurately.

4. CONCLUSION

Optimal simulation models have been developed for two different types of electromechanical needle printer systems. A minimum number of degrees of freedom has been introduced in order to minimize the numerical effort and run the models on a personal computer. Reliable predictions of printer characteristics can be carried out by numerical simulation and a substantial percentage of printer developing costs can be saved.

REFERENCES

1. Springer,H.; Ullrich,M.: Simulationsmodelle für Nadeldruckersysteme. Proceed. Simulationstechnik, Aachen, Springer Verlag, 1988.

2. Advanced Continuous Simulation Language (ACSL),Reference Manual, 4th Edition. Mitchel and Gauthier Associates, Concorde Mass., 1986.

3. Thompson,J.M.T.; Stewart,H.B.: Nonlinear Dynamics and Chaos, John Wiley & Sons, New York, 1986.

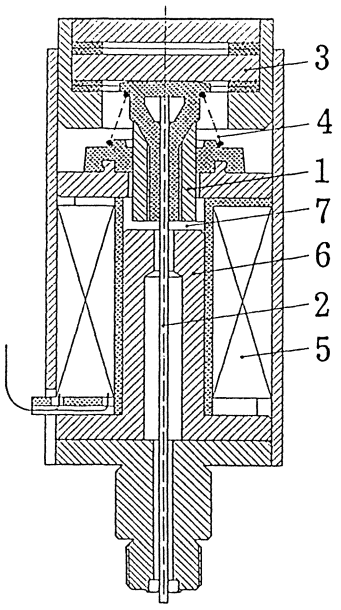

Fig.1. Diagram of the elecromagnetic printer system.

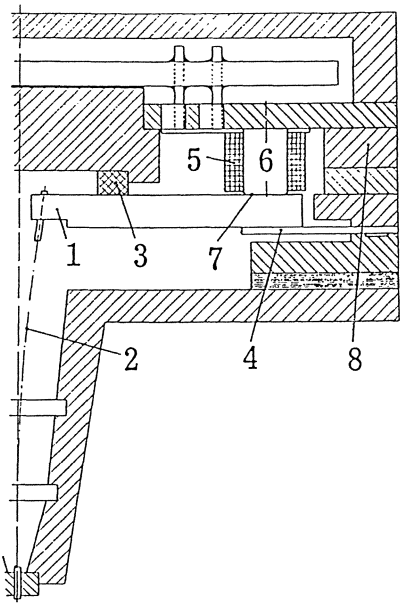

Fig.2. Diagram of the stored-energy printer system.

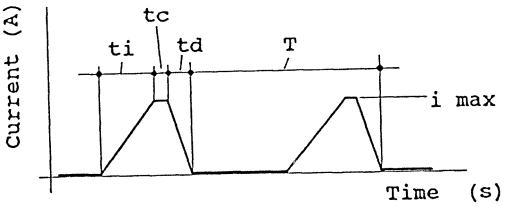

T...Printing Period

tc..Constant-Period

ti..Increasing-Period

td..Decreasing-Period

i max.. Maximum Current

Fig.3. Time response of the applied current.

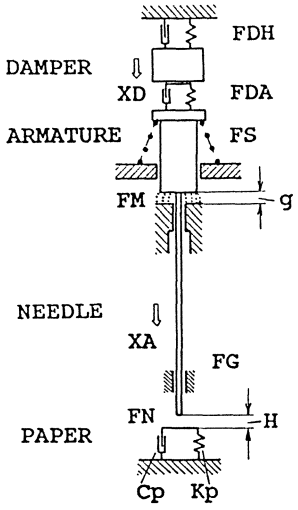

Fig.4. Mechanical model of the electromagnetic system.

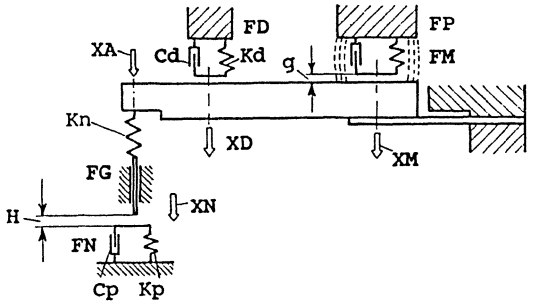

Fig.5. Mechanical model of the stored energy system.

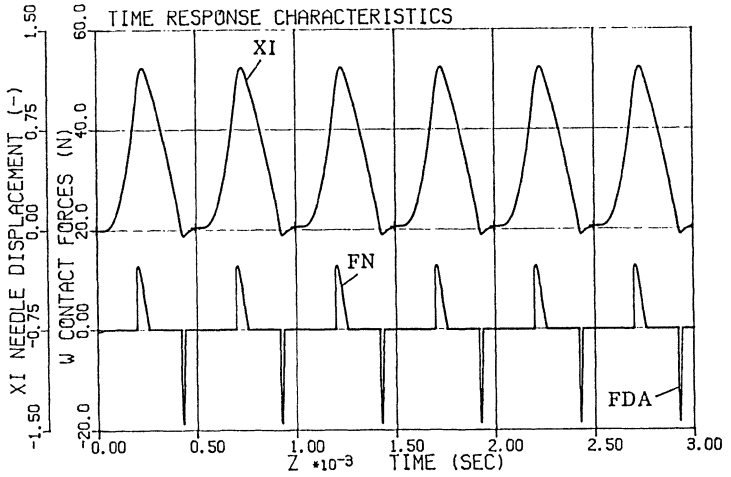

Fig.6. Electromagnetic printer system: Synchronous time response. XI=XA/H(0) = dim.less needle displacement, FN = printing force, FDA = damper contact force, frequency f=2 kHz, needle stroke H(0)=150 μm, airgap length g(0)=350 μm, 5 paper sheets.

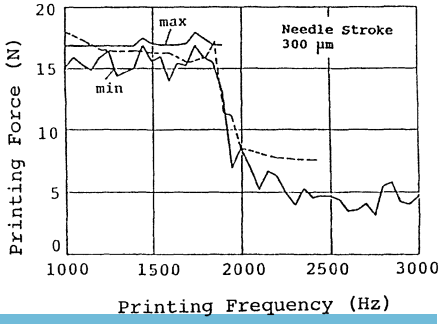

Fig.9. Stored energy printer system: Printing forces in terms of printing frequency.
—— numerical simulation
---- measurements (4 needles)

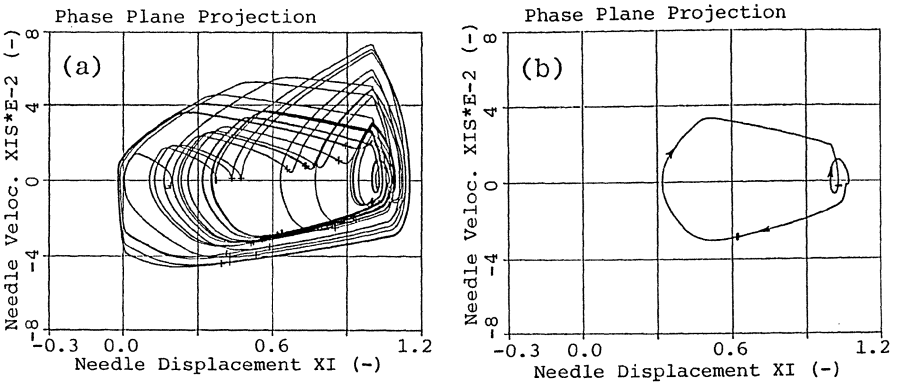

Fig.7. Electromagnetic printer system:
(a)...transient response to (b)...subharmonic attractor of second order
H(0)=275 μm g(0)=400 μm f=2.5 kHz 5 paper sheets
"+"...Poincaré points

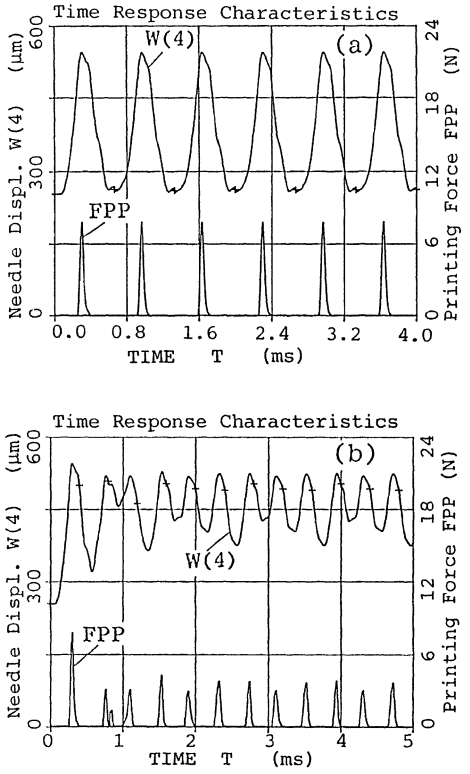

Fig.8. Stored energy system:
(a)...synchronous response f=1.5 kHz
(b)...transient to periodic response f=2.5 kHz
H(0)=200 μm, 1 paper sheet

The Approximate Criteria for Chaos in Multi-well Potential Vibrating Systems

W.SZEMPLINSKA-STUPNICKA

Institute of Fundamental
Technological Research PAS
Warsaw, Poland

Summary

Application of perturbation methods to the study of transition to/from chaotic motion and determination of the system parameter critical values are discussed. The qT-periodic motion is definied by low order approximate solution obtained by perturbation methods. Higher order instabilities are examined by considering the variational Hill's type equation. The instabilities which bring a build-up of 2qT harmonic components, or even order harmonics in symmetric systems, are determined in the first or second approximation, and are identified as the approximate criteria for chaos.

Observations and assumptions

Recent studies of chaotic phenomena in nonlinear oscillators used extensively qualitative and computational methods. Engineering applications, however, demand also closed form formulae, that might give an approximate estimation of the system parameter critical values, i.e. the values for which chaotic motion can be expected.

In this paper we consider nonlinear oscillators governed by:

$$\ddot{x} + f(x, \dot{x}, \nu t) = 0,$$
$$f(x, \dot{x}, \nu t) = h\dot{x} + \alpha_1 x + \alpha_2 x^2 + \alpha_3 x^3 + P\cos\nu t + xP\cos\nu t + \ldots, \tag{1}$$

and two scenarios for transition to/from chaos [1 - 5]:

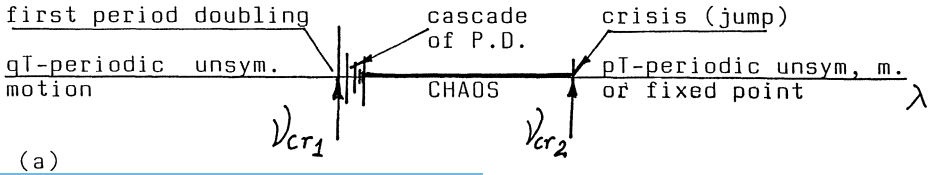

(a)

W. Schiehlen (Editor)
Nonlinear Dynamics in Engineering Systems
IUTAM Symposium Stuttgart/Germany 1989

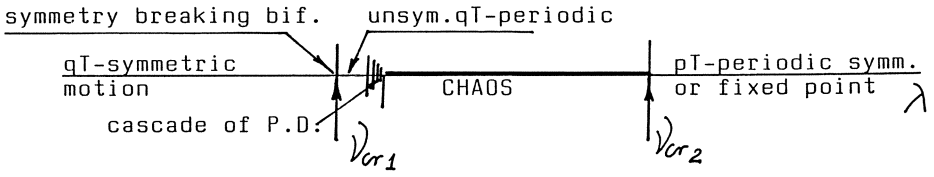

(b)

We assume that the value of bifurcation parameter ν, where chaos occurs, is close to the first period doubling in scenario (a), and is close to the symmetry braking bifurcation in (b). Moreover we approximate the periodic motion which undergoes the first bifurcation by a few term Fourier series:

$$x_0(t) = x_0(t+qT) = \sum_{n=0,1,2\ldots} A_n \cos\left(\frac{n\nu}{q}t + \varphi_n\right); \qquad (2)$$

The approximate criterion for chaos is now reduced to determination of two critical values ν_{cr1} and ν_{cr2}, which in turn, are identified with instability limits in the variational Hill's type equation. The value ν_{cr1} is associated with the higher order instability of $x_0(t)$, the instability which brings a build-up of 2qT harmonic components in the unsymmetric system, ν_{PD}, or the even order harmonic components in the symmetric solution, ν_{SB}. The crisis type critical value ν_{cr2} is identified with the first order instability of $x_0(t)$, the instability which coincides with the point of vertical tangent on the resonance curve.

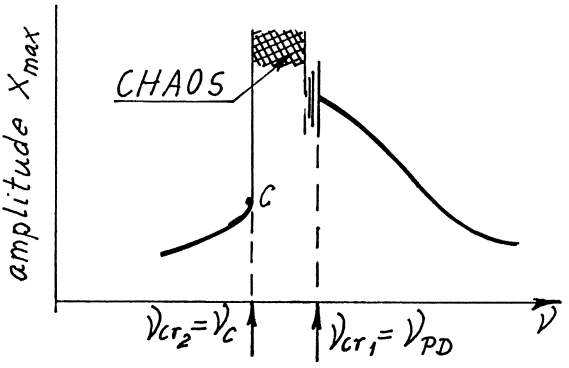

Fig. 1. Resonance curve and scenario (a) of the transition to or from chaos in the unsymmetric system, $f(x,\dot{x}) \neq -f(-x,-\dot{x})$

Period doubling and symmetry breaking instabilities in the variational Hill´s type equation

We consider the qT-periodic solution (2) obtained by perturbation methods and the associated variational equation:

$$\delta\ddot{x} + h\delta\dot{x} + \delta x\left[\lambda_0 + \Omega_1(t) + \Omega_2(t)\right] = 0, \tag{3}$$

where

$$\Omega_1(t) + \Omega_2(t) = \frac{\partial f}{\partial x}\Big|_{x_0}(t) = \frac{\partial f}{\partial x}\Big|_{x_0}(t+T_1);$$
$$\Omega_1(t) = \Omega_1(t+qT) \quad ; \quad \Omega_2(t) = \Omega_2\left(t+\frac{qT}{2}\right) \tag{4}$$

From the Floquet theory we know that the following two types of unstable regions exist:

$$\delta x(t) = e^{\varepsilon t}\phi(t), \quad \varepsilon\text{- real and positive} \tag{5a}$$

or, (5b)

$$\phi_I(t) = \phi_I(t+T_1), \tag{5c}$$
$$\phi_{II}(t) = \phi_{II}(t+2T_1);$$

(a) Period doubling instability can occur only if $\Omega_1(t) \neq 0$, that is if $T_1 = qT$. The condition is satisfied if the system is unsymmetric, $f(x, \dot{x}) \neq -f(-x, -\dot{x})$, or, if $x_0(t)$ is unsymmetric ($A_n \neq 0$ n = 0, 2,.. in eq. 2). To examine the instability we rewrite eq.(3) into:

$$\delta\ddot{x} + h\delta\dot{x} + \delta x\left[\lambda_0 + \sum_{p=1,2,3\ldots}\lambda_p \cos\left(\frac{p\nu t}{q} + \phi_p\right)\right] = 0 \tag{7}$$

and assume $\phi_{II}(t)$ in the form of truncated Fourier series:

$$\phi_{II}(t) = \sum_{n=1,3,5\ldots}^{R}\left(b_{n1}\cos\frac{n\nu t}{2q} + b_{n2}\sin\frac{n\nu t}{2q}\right); \tag{8}$$

Next we insert eq. (8) into eq. (7) and equate to zero coefficients of the harmonic components, which are assumed in the solution (8). Thus we arrive at 2n simultaneous homogeneous algebraic equations for $b_{11}, b_{12}, \ldots, b_{n2}$. Characteristic determinant of the

equations gives us the desired relationship between driving frequency ν and the amplitudes $A_0, A_1, \ldots$, to be satisfied at the stability limit:

$$\Delta_1 = F_1 (\nu_{PD}, A_1, \ldots) = 0 \; ; \tag{9}$$

This also leads us to a relationship between ν and the excitation amplitude P :

$$F_2 (\nu_{PD}, P) = 0 \; ; \tag{10}$$

Within the unstable region the 2qT harmonic components begin to grow over time and nonlinearities induce 2qT periodic stable solution:

$$x_0 (t)_{qT} \rightarrow \bar{x}_0 (t)_{2qT} \; ; \tag{11}$$

(b) Symmetry breaking instability.

Now we consider symmetric system, $f(x, \dot{x}) = - f(-x, -\dot{x})$, and symmetric solution $x_0(t) = - x_0(t + \frac{qT}{2})$. Consequently $\Omega_1 (t) = 0$, $T_1 = \frac{1}{2} qT$.

The symmetry breaking instability is now definied by eq. (5b) and results in a build-up of even order harmonics:

$$\delta x(t) = e^{\varepsilon t} \underline{\Phi}_I (t) = e^{\varepsilon t} \sum_{n=0,2,4\ldots} b_n \cos\left(\frac{n \nu t}{q} + \varphi_n\right); \tag{12}$$

By applying the harmonic balance method we again obtain a closed form formulae to be satisfied at the stability limit:

$$F_1 (\nu_{sB}, A_1, \ldots) = 0 \; ; \quad F_2 (\nu_{sB}, P) = 0 \; ; \tag{13}$$

Within the unstable region the even order harmonics begin to grow over time and consequently the symmetric solution bifurcates into an unsymmetric solution:

$$x_0^{s} (t)_{qT} \rightarrow x_0^{us} (t)_{qT} \; ; \tag{14}$$

Approximate criteria for chaos in a model of a buckled beam

We consider the classic now two-well potential system, a mathematical model of a single-mode motion of a buckled beam under transverse harmonic excitation 1, 2 :

$$\ddot{x} + h\dot{x} + 0.5(x^2 - 1)x = P\cos \nu t \; ; \tag{15}$$

The system has three positions of equilibrium: $x_1^{(o)} = 0$ - unstable, $x_2^{(o)} = +1$ and $x_3^{(o)} = -1$ - stable fixed points, and can exhibit periodic motion around one stable rest point (Small Orbit), periodic motion which encircles all three rest points (Large Orbit), or chaotic motion.
Small Orbit is governed by equation of motion in the form

$$\ddot{z} + z + h\dot{z} \mp \frac{3}{2} z^2 + \frac{1}{2} z^3 = P\cos \nu t \quad , \quad z = x \mp 1 \; ; \tag{16}$$

The main chaotic region occurs in the neighbourhood of the principal resonance, that is close to $\nu = 1$, and follows scenario (a) of transition to/from chaos (see also Fig. 1). Here Large Orbit does not interfere and coexists with Small Orbit, or with chaotic motion. Therefore, the approximate criterion for chaos in the region was derived by considering eq.(16) [2]. First the second approximate T-periodic solution was derived by a perturbation scheme as:

$$z_0(t) = a_1 \cos(\nu t + \varphi_1) - \frac{3}{4} a_1^2 + \frac{1}{4} a_1^2 \cos(2\nu t + 2\varphi_1) \; ;$$

$$a_1 = \frac{P}{\sqrt{[\omega^2(a_1) - \nu^2]^2 + h^2 \nu^2}} \qquad \omega^2(a_1) = 1 - \frac{3}{2} a_1^2 \; ; \tag{17}$$

Then the period doubling instability limit was determined by assuming two frequency solution in the Fourier series (8) and the relationship (9) at $h = 0$ was reduced to the second polynominal in ν^2 :

$$\nu_{PD}^4 + 2B\nu_{PD}^2 + C = 0 \quad ; \quad B \equiv B(a_1) \; ; \; C \equiv C(a_1) \; ; \tag{18}$$

The crisis type transition to/from chaos, ν_c , was determined by considering the point on the resonance curve $a_1(\nu)$, which has vertical tangent i.e. $\frac{d\nu}{da_1} = 0$, with the results:

$$\nu_{c\,h=0} = 1 - \frac{3}{2} a_1^{\,2} \cong 1 - 2.163\, P^{2/3} \;; \qquad (19)$$

The theoretical and computer simulation results presented in Fig. 2a show surprisingly good coincidance:

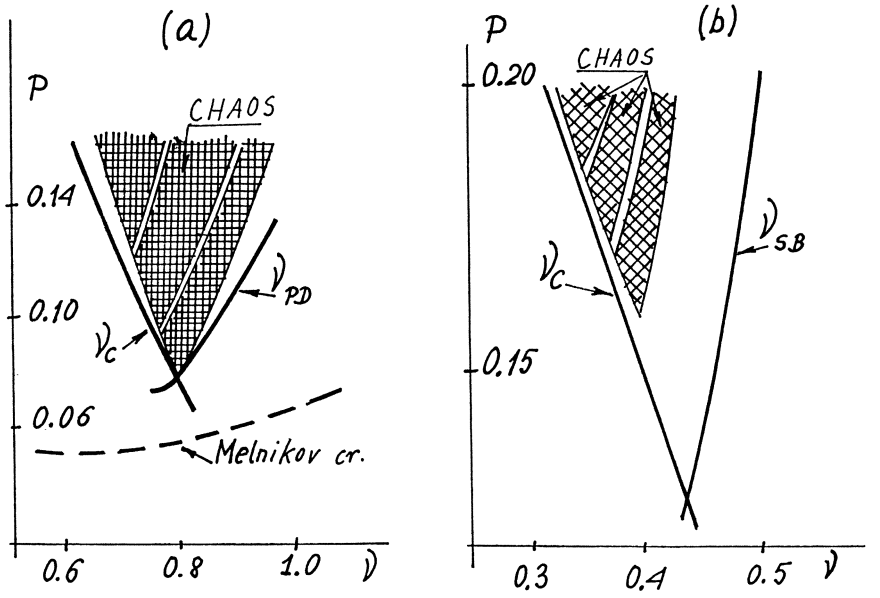

Fig. 2. Theoretical criteria for chaos and true chaotic regions

In this paper we focus on the second chaotic region which occurs near the second order ultraharmonic resonance of the Small Orbit motion, that is close to $\nu = 0.5$. Scenario of transition to/from chaos observed in the region is more complex and involves an interaction of the Small and Large Orbits [3]. From Fig. 3 we learn that Small Orbit loses stability first and bifurcates into symmetric T-periodic Large Orbit. Next, on further decrease of ν, symmetric Large Orbit bifurcates into unsymmetric periodic solution, which ends with a cascade of period doublings and chaotic region. Chaos ends sharply at ν_{cr_2}, where the stable nonresonant branch of the Small Orbit appears. No hysteresis phenonenon was observed, when the experiment was carried out at increasing frequency parameter ν. Here we construct the approximate criterion for chaos by considering symmetry breaking instability of Large Orbit and crisis type instability of S.O.

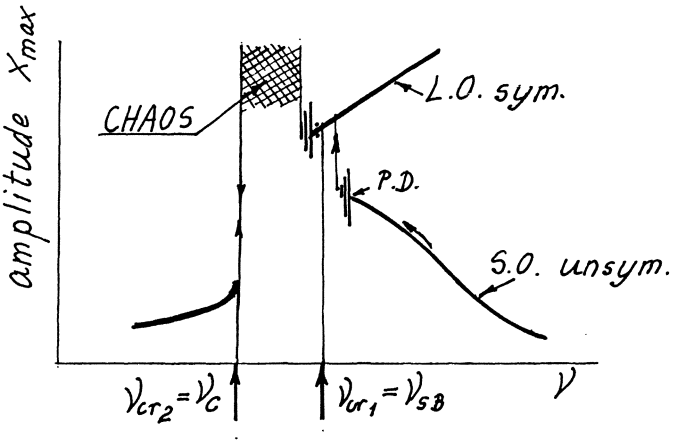

Fig. 3. Scenario of transition to/from chaos in the ultraharmonic resonance region.

We begin with the T-periodic symmetric solution for L.O. by transforming eq. (15) into the form:

$$\ddot{x} + \omega^2(A_1)x + \mu(\bar{h}\dot{x} + \bar{\alpha}_1 x + \bar{\alpha}_3 x^3 - \omega^2(A_1)x - P\cos\nu t) = 0 ; \quad (20)$$

where $\mu\bar{h} = h$; $\mu\bar{\alpha}_1 = -\frac{1}{2}$; $\mu\bar{\alpha}_3 = \frac{1}{2}$; $\omega^2(A_1) = -\frac{1}{2} + \frac{3}{8}A_1^2 > 0$;

and assume: $\omega^2(A_1) - \nu^2 = 0(\mu)$; $\nu \approx 0.5$;

Now the perturbation technique allows us to obtain the refined first approximate solution as

$$x_0(t) = A_1\cos(\nu t + \varphi) + A_3\cos(3\nu t + 3\varphi) ; \quad A_3 = \frac{A_1^3}{16}$$
$$A_1 = \frac{P}{\sqrt{[\omega^2(A_1) - \nu^2]^2 + h^2\nu^2}} ; \quad (21)$$

Next we examine the symmetry breaking instability by considering eq. (7) and the first approximate solution in the series (12):

$$\delta x(t)\Big|_{\varepsilon=0} = b_0 + b_{21}\cos 2\nu t + b_{22}\sin 2\nu t ; \quad (22)$$

This reduces eq. (13) into: $\nu_{SB}^4 + 2B\nu_{SB}^2 + C = 0$; (23)

To find the crisis type instability limit ν_c, we have to consider Small Orbit T-periodic solution in the region $\nu \cong 0.5$; Following the classic theory of secondary resonances we put:

$$z = C\cos\nu t + z_1 \; ; \qquad C = \frac{P}{1-\nu^2} \; ; \tag{24}$$

and apply a perturbation technique to eq. (16) to find the new variable z_1, with the result:

$$z_{10}(t) = a_0(a) + a_2\cos(2\nu t + \varphi_2) + a_3(a_2)\cos(3\nu t + \varphi_2) + a_4(a_2)\cos(4\nu t + 2\varphi_2) \tag{25}$$

and

$$F_2(a_2, \nu)_{P=const} = 0 \; ; \tag{26}$$

Finally the desired point of the vertical tangent on the resonance curve is defined by the relation:

$$\frac{\partial F_2}{\partial a_2} = 0 \tag{27}$$

The theoretical criterion for chaos ν_{SB} and ν_c given by eqs.(21, 23) and (26, 27) are shown in Fig. 2b along with true chaotic regions obtained by computer simulations [3,5]. It is worth noticing that the classic Melnikov criterion gives $P_{cr} \cong 0.05$, which is below the area of Fig. 2b.

References

1. Moon F.C.: Chaotic vibrations, New York, John Wiley and Sons, 1987.
2. Szemplińska-Stupnicka W.: The Refined Approximate Criterion for Chaos in a Two-State Mechanical Oscillator, Ing. Archiv 58, 1988, 354-366.
3. Rudowski J.: Transition from symmetric periodic oscillations to chaos in a nonlinear oscillator, Reports of I.F.T.R. 22/1988 (in polish).
4. Szemplińska-Stupnicka W.: Plaut R.H.; Hsieh J.C.: Period Doubling and Chaos in Unsymmetric Structures under Parametric Excitation, J,Appl.Mech. (to appear).
5. Szemplińska-Stupnicka W.: Transition to Chaos in the Two-Well Potential System in the ultraharmonic resonance frequency region. Journal of Sound and Vibration (to appear).

Loss of Engineering Integrity due to the Erosion of Absolute and Transient Basin Boundaries

J.M.T. THOMPSON

Dept of Civil Engineering, University College London,
Gower Street, London, WC1E 6BT, United Kingdom

SUMMARY
This paper explores the engineering relevance of the homoclinic tangling, and associated fractal basins, that are a feature of damped oscillators driven out of a potential well by periodic excitation. For optimal escape under forcing at just below the linear natural frequency, the homoclinic tangency is shown to precipitate a sharp erosion of the safe phase-space basin. This offers a new safety criterion, based on transient motions, that might be extremely valuable in ship capsize. Fractal boundaries in control space arise when an ambient system is suddenly subjected to a pulse of excitation, and their relevance to earthquake studies is briefly discussed.

INTRODUCTION

Much theoretical interest has focused on fractal basin boundaries in phase space, created at homoclinic tangencies, and we explore here the engineering relevance of a dramatic erosion of the safe basin triggered by such a tangency. Associated fractal boundaries in control space are also examined. The results derive from recent computer studies of an archetypal single-well Duffing oscillator.

THE DRIVEN OSCILLATOR AND ITS STEADY STATES

We consider in this paper the escape from a cubic potential well under sinusoidal forcing, an archetypal problem with a clearly defined *failure* associated with escape to infinity over the potential barrier. The specific equation is

$$\ddot{x} + \beta\dot{x} + x - x^2 = F\sin(\omega t)$$

and we write $\dot{x}=y$, $\phi=\omega t \ (mod\ 2\pi)$. We hold $\beta=0.1$ throughout, leaving the two controls, F and ω. The detailed response of this oscillator is given in [1].

Due to the nonlinear softening character of the restoring force, the *optimal escape* from the well, at *minimum* F, occurs close to $\omega=0.85$, and for this reason we shall concentrate on this frequency. This ω is in fact just above the optimal frequency, and the sequence of stable steady states that would be encountered as F is slowly increased from zero is: (a) a growing harmonic oscillation at the period of the forcing $(n=1)$, originating from the stable equilibrium state at $F=x=y=0$; (b) a large amplitude $n=1$ oscillation generated by a jump to resonance, associated with the usual

W. Schiehlen (Editor)
Nonlinear Dynamics in Engineering Systems
IUTAM Symposium Stuttgart/Germany 1989

nonlinear hysteresis of a softening Duffing oscillator; (c) subharmonics of order $n=2, 4, 8, 16,...\infty$ in a period-doubling Feigenbaum cascade leading to; (d) a chaotic attractor on a Möbius strip, which experiences a final blue sky instability at a boundary crisis when it collides with a directly unstable $n=6$ subharmonic solution at $F^E=0.109$. After this crisis there are no available stable states in the well, and all trajectories tend to the *attractor at infinity*. Relative F values can be seen in Fig 4.

SMOOTH AND FRACTAL PHASE-SPACE BASINS

From an engineering point of view, the basins of attraction, in the space of the starting conditions $x(t_0)$, $y(t_0)$, are likely to be just as important as the steady state attractors. We have therefore explored the metamorphoses of these basins [2,3], and a typical sequence under increasing F is shown in Fig 1: these correspond to the driving phase $\phi=180°$ so that $t_0=\pi/\omega$. Here $\omega=0.85$ and $-0.8<x<1.2$, $-0.9<y<0.8$.

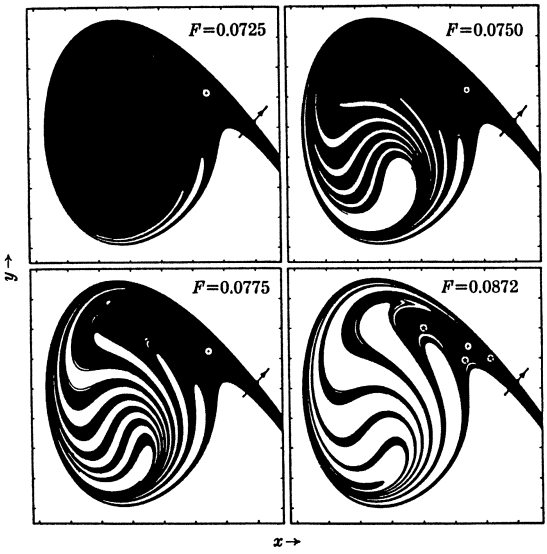

Fig 1. Development of the fractal phase-space boundary

Each diagram is based on the computed stable manifold or *inset* of the hill-top saddle cycle (emerging from the unstable equilibrium at $F=0$, $x=1$), whose outgoing eigenvector can be seen on the right of each picture. The inset was located by automated procedures developed at University College by Alexander [4]: in these, time is run backwards on the computer from a constantly refined ladder of starts along the incoming eigenvector of the saddle cycle.

The black regions represent starting points that are captured by steady states within the well. These attractors, identified in the diagrams by their Poincaré mapping points, are here an *n=1* oscillation in the first three diagrams, and either an *n=1* or a competing *n=3* in the last diagram. The white regions represent starting points that escape over the hill-top and tend to the attractor at infinity.

Over the *F* interval represented by these diagrams, we see a sharp reduction in the basin, triggered by a homoclinic tangency at *F=0.0633* where the boundary changes from smooth to fractal. This tangency of the inset and outset of the hilltop saddle cycle, generating a homoclinic tangle, was predicted accurately by a Melnikov analysis [5]. More important than the onset of a fractal boundary is the fact that the whole basin is very rapidly eroded by thick fingers sweeping across the bulk of the catchment domain, and it is this feature that we shall now examine and quantify.

INTEGRITY MEASURES QUANTIFYING BASIN EROSION

Some proposed measures for quantifying the safe basin are summarised in Fig 2.

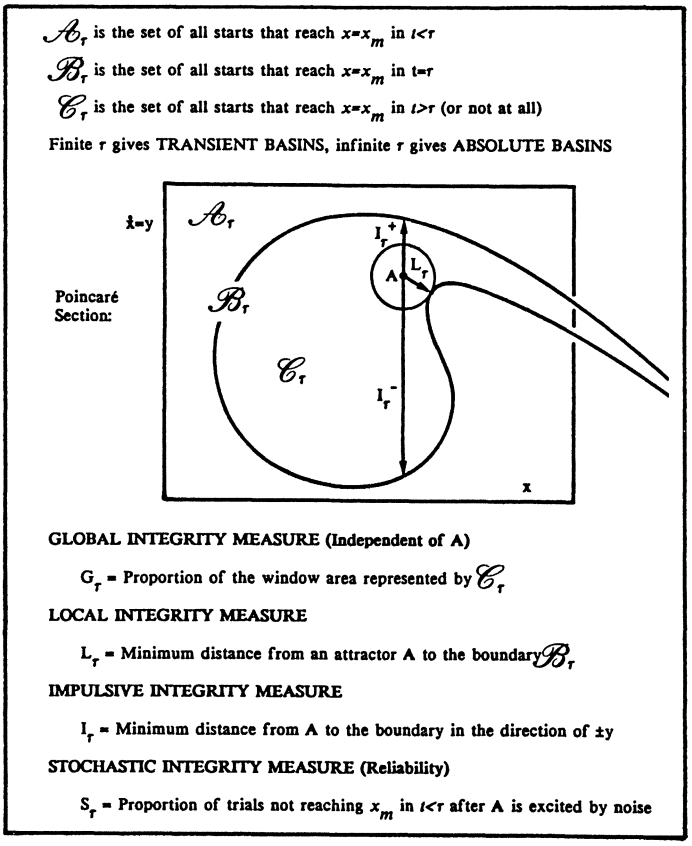

Fig 2. Integrity measures quantifying basin erosion

Here we have focused attention both on the *absolute basins* associated with the infinite time behaviour, and on the *transient basins* associated with a time τ which are of equal interest to the engineer. The value of x_m is an arbitrary measure of escape, here taken as 20: a computer usually overflows shortly after this is exceeded.

Using numerical integrations from a grid of starts in (x,y) space, it is a simple matter to evaluate the first three measures relating to the area, distance to the boundary, and this distance restricted to the ±y directions modelling an impulsive change in velocity. A fourth useful measure is based on superimposed noise excitation: here *reliability* defined in terms of the proportion of runs that survive for time τ under a given noise intensity seems to be the most useful quantification. Integrity diagrams using these measures will be published in a future paper.

LOSS OF GLOBAL INTEGRITY UNDER INCREASING EXCITATION

The most relevant measure will depend on the operating conditions of a system, and we shall see that for vessel capsize it is the *global integrity measure* that should be preferred. This measure has the advantage of requiring no knowledge of the attractors, there often being a large number of, possibly unknown, competing attractors.

The global integrity for $\omega=0.85$ is shown in Fig 3, together with estimates of the fractal dimension of the boundary. These estimates are relatively crude, based on the grid of starts data [6], but confirm that the dimension changes from 1 (smooth) to between 1 and 2 (fractal) as F increases through the Melnikov value of F^M.

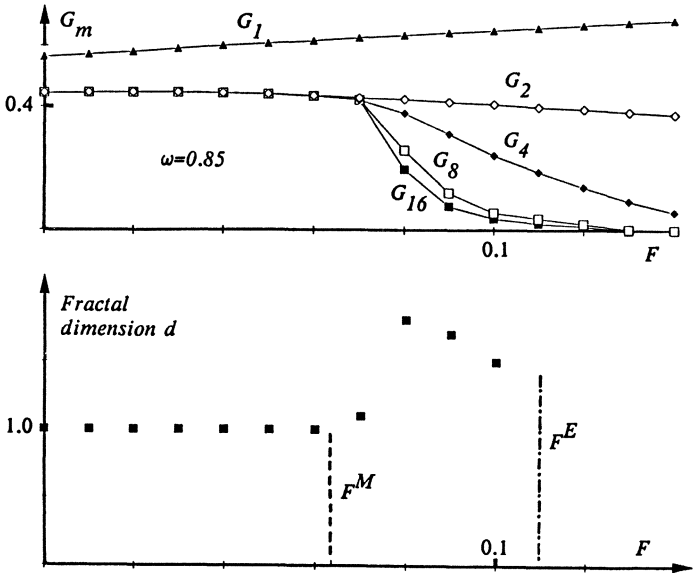

Fig 3. Correlation of global integrity with fractal dimension

In the upper integrity diagram G_m is the proportion of the grid of starts that do not escape within m forcing cycles, for $m=1, 2, 4, 8,$ *and* 16. The curve for G_{16} can be taken as a good estimate of G_∞ . Shortly after F^M there is a dramatic drop in G_{16} together with a significant splitting of the curves due to chaotic transients.

The G_∞ curve is more accurately located in Fig 4, based on computer studies for *60 or more* forcing cycles [3]. Here both scales are normalized, and it can be seen that a very significant loss of area occurs at about *70%* of the crisis forcing magnitude. It may be interesting to explore why the sharp cliff of the integrity diagram occurs at some appreciable distance beyond the homoclinic tangency.

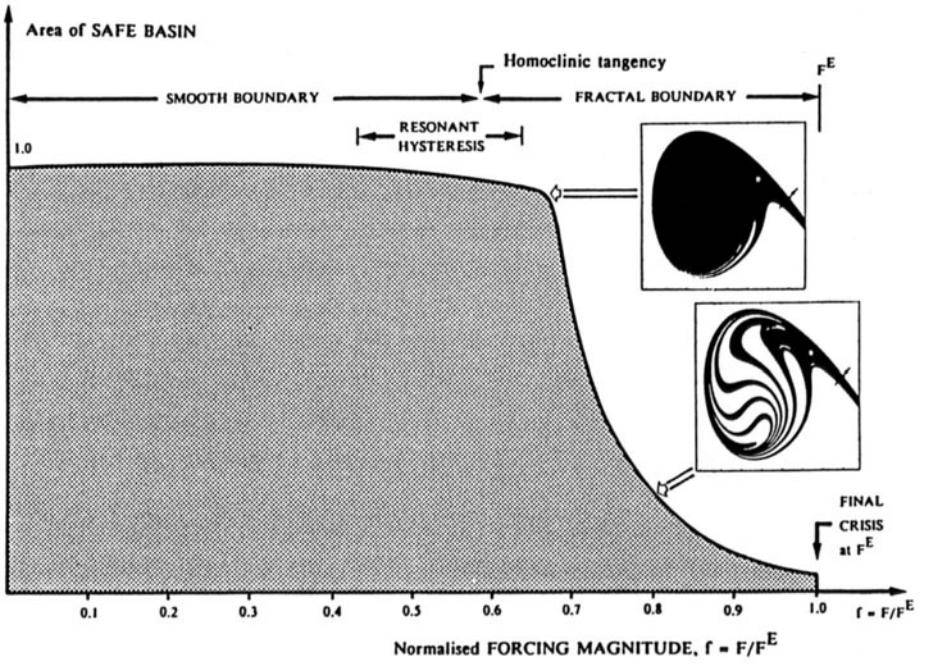

Fig 4. High resolution study of global integrity [3]

The sudden final loss of area at F^E is akin to the sudden loss of *absolute* basin known to occur at a saddle-node bifurcation: such a discontinuity will not occur in any of the *transient* basins, as can be seen in Fig 3.

FRACTAL ESCAPE BOUNDARY IN CONTROL SPACE

The value of $F^S \simeq 0.0725$ where Figs 3 & 4 exhibit their well-defined cliff may be a useful *global safety limit* in a number of practical situations, its variation with ω

giving a global safety boundary, $F^S(\omega)$, in control space. The accurate determination of this safety locus would involve massive computational or experimental effort. To overcome this, it is tempting to make use of the fairly complete central erosion, and make trial runs just from the central ambient resting state $x(t_0)=y(t_0)=0$.

It is thus of interest to compute the transient time map in the (F, ω) control space, starting always at $x=y=0$. This can be viewed as an alternative cross-section through the four-dimensional escape basins residing in the $\{x(t_0), y(t_0), F, \omega\}$ space: and since the phase-space cross-sections are fractal, it follows that the control-space cross-section will likewise be fractal. The computed diagram based on a *100 by 100* grid of (F, ω) starts, is shown in Fig 5, and the fractal dimension of the absolute boundary has been estimated [6] as $d=1.38$. On this figure, black denotes no escape within 32 forcing cycles, grey (dots) denotes escape in between 4 and 32 cycles, while white denotes escape in less than 4 cycles; curve A is a bifurcation locus of saddle-node folds, C is a locus of period-doubling flips (from $n=1$ to $n=2$), and M is the Melnikov estimate of homoclinic tangency [1].

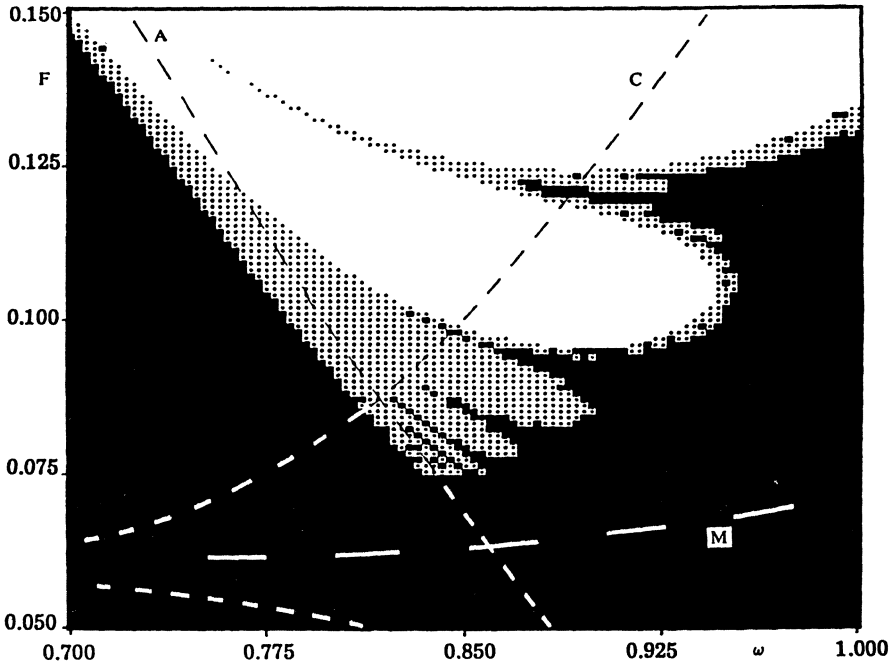

Fig 5. Fractal boundary in control space

Our escape equation corresponds to an archetypal worst-case capsize scenario of a biased boat in regular beam seas. The co-existing harmonic, subharmonic and chaotic attractors undergoing intricate bifurcations, are clearly too complex for routine design work. They are also largely irrelevant, because a boat is unlikely to be in a well-defined steady state, implying that greater attention should be given to the basin of attraction. Our work shows that there is likely to be a sudden and well-defined erosion of the safe basin following a homoclinic tangency, and safety limits should be based on this, rather than on the final instability of a metastable attractor. Liapunov and Melnikov analyses are of limited practical value, so the naval architect most try to assess the safe (F, ω) domain using computer simulations or model tests.

In computations and experiments such transient studies have the advantage of being *not only more relevant, but actually easier to perform:* and considerable savings in time can be made from an inspection of Fig 3 which shows that if a boat does not capsize in *16* forcing cycles, then it is unlikely to capsize at all, since $G_{16} \simeq G_{\infty}$.

The erosion of the central region of the safe phase-space basin means that just a single transient study from the ambient resting equilibrium state might be sufficient to give a good indication of the safe control space domain. So in naval architecture our Fig 5 might be a very useful *transient capsize diagram* [7] showing the allowable sea-states of a boat in terms of the wave magnitude F and the wave frequency ω.

DESIGN AGAINST EARTHQUAKE DAMAGE

An earthquake can often be idealized as just the pulse of periodic loading envisaged here, exciting a structure in its resting state. The Mexican earthquake was remarkably sinusoidal: and even in a less regular event, the excitation reaching a component will be predominantly sinusoidal at the frequency of the main structure. Our fractal control-space diagram is thus relevant to earthquake engineering, especially as our metastable cubic potential would be exhibited by any component with an explosive, shell-like post-buckling characteristic.

CONCLUDING REMARKS

Fractals in phase space have attracted much theoretical attention in recent years [8-10], but their engineering role is largely unexplored: our study suggests that they have important consequences for the integrity of practical systems in noisy environments. Fractals in control space have been investigated for iterated maps, but their occurrence in driven oscillators may be important in a variety of engineering applications [6].

As we have emphasised in our recent book [11], the new and complex phenomena emerging from dynamical systems theory demand that much more effort be expended

to explore the full response of dynamical models of engineering systems. The derivation of the model, which has often been seen as the main task, may in some cases be a relatively trivial part of the whole exercise.

ACKNOWLEDGEMENT: *I am grateful to the Science and Engineering Research Council of Great Britain for a Senior Fellowship which has made this work possible.*

REFERENCES

1. Thompson, J.M.T., Chaotic phenomena triggering the escape from a potential well, *Proc. R. Soc. Lond.* **A 421**, (1989) 195-225.

2. Soliman, M.S. & Thompson, J.M.T., Integrity measures quantifying the erosion of smooth and fractal basins of attraction, *J. Sound Vibration* (In the press, 1989).

3. Thompson, J.M.T. & Ueda, Y., Basin boundary metamorphoses in the canonical escape equation, *Dynamics Stability Syst.* (In the press, 1989).

4. Alexander, N., Production of computational portraits of bounded invariant manifolds, *J. Sound Vibration* (In the press, 1989).

5. Thompson, J.M.T., Bishop. S.R. & Leung, L.M., Fractal basins and chaotic bifurcations prior to escape from a potential well, *Phys. Lett.* **A 121**, (1987) 116-120.

6. Thompson, J.M.T. & Soliman, M.S., Fractal control boundaries of driven oscillators and their relevance to safe engineering design, *Proc. R. Soc. Lond.*, submitted, 1989.

7. Rainey, R.C.T. & Thompson, J.M.T., The transient capsize diagram - a new method of quantifying stability in waves, *Journal of Ship Research*, submitted, 1989.

8. McDonald. S.W., Grebogi, C., Ott, E. & Yorke, J.A., Fractal basin boundaries, *Physica* **D 17**, (1985) 125-153.

9. Moon, F.C., *Chaotic Vibrations*. New York: Wiley 1987.

10. Eschenazi, E., Solari, H.G. & Gilmore, R., Basins of attraction in driven dynamical systems, *Physical Review* **A 39**, (1989) 2609-2627.

11. Thompson, J.M.T. & Stewart, H.B., *Nonlinear Dynamics and Chaos*. Chichester: Wiley 1986.

Calculation of Stability Characteristics through Interpolated Mapping

Benson H. Tongue

Department of Mechanical Engineering
University of California
Berkeley, CA 94720

Abstract

The method of Interpolated Mapping has been demonstrated over the past few years to be a highly advantageous method with which to explore global nonlinear behavior. Such global questions include the determination of the basins of attraction of a system's attractors and fractal dimension calculations for these regions. Such global analyses have focused, by definition, on answering questions regarding system behavior throughout large regions in state space. In addition to analyses of this sort, it is often desirable to consider the response of a given system for small perturbations about a given trajectory. This aspect of the Interpolated Mapping method, that allows a determination of local stability characteristics, has yet to be fully exploited. The present work will present a review of the Interpolated Mapping method and then examine the specific problem of identifying a system's Lyapunov exponents in order to illustrate the method's use in such a transient analysis.

Introduction To Interpolated Mapping

Interpolated Mapping [4-9] serves as a means to determine the phase flow of a dynamical system for any given initial condition without the necessity of direct numerical integration. Figure 1 shows a schematic representation of a typical segment of phase flow that illustrates the technique. As drawn, a set of trajectories corresponding to nine initial conditions are seen to move through the three dimensional phase space made up of X_1, X_2, and t. This could correspond to the evolution in time of a second order differential equation under the action of a time varying forcing, for instance. It is clear that for the time interval shown, the relative orientations of the nine points has changed. Whereas originally they were organized in a rectangular array, they are now displaced from this orientation. However they still retain the essential shape of the original configuration. The four boxes defined by the original array still exist and are still convex. The set of trajectories resemble nothing so much as streamlines in a fluid flow. Adopting this viewpoint, it seems reasonable to say that the position of an initial condition originating in one of the boxes will still be within the image of this box after a given time ΔT has elapsed.

W. Schiehlen (Editor)
Nonlinear Dynamics in Engineering Systems
IUTAM Symposium Stuttgart/Germany 1989

In Interpolated Mapping, a mapping is constructed of just such a set of initial conditions and the numerically determined terminal conditions corresponding to the individual initial conditions are recorded. This information is then used in an interpolation procedure that allows a complete trajectory to be computed for any given initial condition that lies within the confines of the original array. Since there is no overt discretization of phase space, the method allows an infinite number of unique trajectories to be found. For Poincaré analyses the duration of the integration will typically be equal to one period of the forcing function. In an autonomous set of equations, the duration is up to the analyst to determine. For Poincaré maps, a given trajectory can map off of the array in the space of a single mapping due to the finite dimensions of the initial array. For convenience, such points are considered to have no attractor within the array, even though they might eventually return.

The only firm information regarding the system phase flow are initial and final conditions of the original mapping array. A bi-linear interpolation is utilized to determine the terminal behavior of any points that lie within the original array. This procedure is illustrated in Figure 2. The final position of initial condition A is the point B, found by interpolating between the target positions (D_1, D_2, D_3, D_4) of the four surrounding points (C_1, C_2, C_3, C_4).

One can easily extend the trajectory in time by repeatedly applying the map and using further interpolation. It is important to note at this point that the individual segments of a given total trajectory are unique to that particular trajectory. Therefore, even though a finite number of initial conditions were used, an infinite number of trajectories can be generated. This method of Interpolated Mapping is called Bi-Linear Interpolated Cell Mapping (BLICM).

Although this technique does quite well at simulating the dynamics of a given nonlinear system [4,5,7], it has some inherent limitations. One of these difficulties is that it can introduce qualitative distortions in the system's basins of attraction. The reason for these distortions is that the technique relies on the fact that a bi-linear mapping procedure is used to carry the dynamics of the nonlinear system under consideration from an initial time to some future time. This induces slope discontinuities in the phase flow. To address this issue, the Tensor Product Interpolated Cell Map (TPICM) [6] was developed. This method allows a very accurate and smooth approximation to the system phase flow but at the penalty of additional needed computation.

As described above, the Interpolated Mapping methodology clearly considers the behavior of large chunks of phase space. Although necessary for global analyses, such an approach will prove to be computationally inefficient if one is merely interested in local properties. For this case, one must concentrated upon regions of phase space that are close to some nominal trajectory. Lyapunov exponents [1], which measure the exponential rates of divergence or convergence associated with an attractor of a system, represent just such a local property. Periodic attractors are characterized by having only non-positive exponents while chaotic systems will exhibit at least one positive exponent. A calculation of these exponents gives a quantitative measure of the rate at which one loses the ability to predict the system response and can be used to calculate an approximate value of the fractal dimension of the attractor.

Because the individual Lyapunov exponent calculations can vary widely over short time intervals, the exponents are defined as a long time average over the entire attractor. This forces long computer simulations that serve only to give the exponents for a given set of parameters with a particular group of initial conditions. In this paper, the central concept of Interpolated Mapping will be extended to allow a highly efficient calculation of a system's Lyapunov exponents [11].

The system to be examined will be a second order Duffing's equation. The extended method utilizes a modification of the Interpolated Mapping technique to ensure that the only computations undertaken are those that directly affect the Lyapunov calculation.

Predicting Lyapunov Exponents

Because the action of nonlinear differential equations on state space can induce a strong stretching and folding action, the values of locally determined Lyapunov exponents will vary a great deal. In spite of this, the locally determined values can still yield useful information. Since the Lyapunov exponents describe the locally linearized behavior of a system, one can easily show [11] that for a second order system, their sum will be equal to the negative of the linear viscous damping coefficient. One can obviously use this fact as a means of verifying the accuracy of the numerical integration routines.

This system characteristic will be illustrated through a numerical calculation of the Lyapunov exponents for the following Duffing's equation:

$$\ddot{x} + .1\dot{x} - x + x^3 = 3.2\cos(.475t) \tag{7}$$

To obtain the system's Lyapunov exponents, a point that lies on the steady state attractor of the system of interest is selected. Obviously this implies that the simulation has run long enough to have obtained steady state conditions. A vector of magnitude ϵ and arbitrary direction is placed with its base at the point on the trajectory. It is important that ϵ be small so that only localized deformations of phsase space are considered. A second vector, perpendicular to the first and of equal magnitude, is then added. In general, additional vectors would be added in a similar fashion until one has an orthonormal basis for the space in the region of the test point. The test point and the vector set are next integrated forward in time for Δ seconds. The largest local exponent, λ_1 is found from:

$$\lambda_1 = \frac{1}{\Delta t}\ln(\frac{l_f}{\epsilon}) \tag{8}$$

where l_f is the length of the largest vector after integration. This vector will quickly orient itself in the direction of maximum divergence. The second vector, however, is not free to tend toward the second greatest direction of divergence because of the effect of the largest exponent upon its direction. Thus, the second exponent is calculated through the calculation of the sum of the first two exponents, which measures the rate of contraction of a two dimensional trapezoid in state space. This is governed by a similar equation:

$$\lambda_1 + \lambda_2 = \frac{1}{\Delta t}\ln(\frac{A_f}{\epsilon^2}) \tag{9}$$

where A_f is the final area of the space covered by the first two vectors. Subsequent exponent sums would be computed in a similar fashion for higher dimensional systems. The largest vector is then renormalized to a magnitude of ϵ, keeping its direction the same, so that it can continue to converge in the direction of the largest exponent. The remaining vectors are again constructed perpendicular to the first. This process is repeated over a long time interval and the exponents are calculated as a long time average over the steady state motion. This long time average is extremely important, as even very close trajectories leading to periodic orbits can diverge from each other over

short time intervals. Indeed, this phenomenon is what characterizes transient chaos. Physically, the trajectory has to be extended enough to ensure that it visits all the regions of the attractor sufficiently often to accurately reflect the relative degree of visitation that would occur under an infinitely long simulation. It should be noted that this method is similar to that used by Wolf et.al. [11].

The preceding remarks are illustrated in Figure 3, in which the local local behavior of λ_1 and λ_2 for the system given by Equation 7 is plotted as a function of time. For this graph, $\frac{1}{2}(\lambda_1 + \lambda_2) = -.0500$. Figure 5 shows the cumulative averages of λ_1 and λ_2. Note that, as expected, the sum is not changed by averaging. The analytical method derived here would indicate that $\frac{1}{2}(\lambda_1 + \lambda_2) = -.05$, just as expected from the analytical prediction.

Generating Lyapunov Exponents From Interpolated Trajectories

A Lyapunov exponent calculation of a full time series requires a knowledge of the system behavior at all phases of the forcing function, not just at the periodic intervals defined by a Poincaré map. To accomplish this, it is necessary to record the position of each point in the initial condition array, relative to its previous location, at each numerical time step, so that each position can be used to interpolate to the next. Unfortunately, doing this for a large portion of phase space would eliminate any computational efficiency that the basic method displays.

In order to obtain the quantity of transient information necessary to determine the Lyapunov exponents, while preserving the computational advantage of Interpolated Mapping, the following technique is used. An initial condition array is set up, but none of the points are numerically integrated yet. A test point in phase space is selected and numerically integrated until it has converged onto an attractor. Once on an attractor, it is surrounded by four other points, all lying on the initial condition array. Each of these four points are numerically integrated for just one time step in the numerical integration routine, and their final positions are recorded. The test point is then interpolated to its next location and the process is repeated. Each time the point advances a step forward, a test is made to see if the point is surrounded by any existing array points. If it is, then the point is interpolated to its next position and the process continues. Otherwise, another group of surrounding points is created in the manner described above before continuing. The procedure used in finding the exponents by this technique is identical

to the general method except that at each timestep the vectors are interpolated, rather than integrated, to their next positions at some point Δt in the future. In this way, the minimum covering set of array points is utilized that encloses the attractor. This version of Interpolated Mapping will be termed a Sequentially Generated Map.

Because of the transient information recorded, the array can be used to recreate an entire trajectory for the system. Table 1 displays the results of using this approach as well as direct numerical integration. Equation 12 was used in the calculations, with the forcing frequency chosen to equal 0.482, 0.4776, 0.476, and 0.475 to allow different period responses to be studied.

The results show that the exponents found using the Sequentially Generated Mapping are very close to the exponents calculated through exact numerical integration. The practicality of the method is further illustrated by a comparison of CPU times required to complete the calculations. Table 2 displays the CPU time required by a CYBER 855 computer to perform the calculations illustrated above. In each case, 200 forcing periods at 80 time steps per period were used to eliminate the transient behavior. The calculations were then based upon 5000 additional forcing periods.

One can see from Table 2 that the Sequentially Generated Mapping is much less computationally intensive than numerical integration for the periodic cases. Even for the chaotic case, the technique took only about half as long as the direct integration method. Because all of the necessary grid points have been generated by the time 5000 forcing periods have been followed, the savings in computation would of course increase if longer times are examined.

Conclusions

Interpolated Mapping has been shown in a number of previous papers to be a very efficient tool with which to find the global responses of nonlinear systems. In the present paper, a generalization of the method was used to consider the analysis of transient system behavior. Using the Sequentially Generated Mapping procedure, results that were extremely close to those found from numerical integrations were generated at reduced computational costs, thus indicating that the Interpolated Mapping methodology can be profitably extended to the problem of transient analyses.

This work was supported by the National Science Foundation, Grant No. MSM-8451186 with Dr. Elbert Marsh serving as contract monitor.

References

[1.] Benettin, G., Galgani, L., Giorgilli, A. and Strelcyn, J.-M., "Lyapunov Chracteristic Exponents for Smooth Dynamical Systems and for Hamiltonian Systems; A Method for Computing All of Them Part 1: Theory," 1980, *Meccanica*, **15**, No. 1, pp. 9-20.

[2.] Lefschetz, S., 1987, *Differential Equations: Geometric Theory*, Dover Publications, New York.

[3.] Tongue, B.H., 1987, "Characteristics of Numerical Simulations of Chaotic Motions," *ASME Journal of Applied Mechanics*, **54**, No. 3, pp. 695-699.

[4.] Tongue, B.H., 1987, "On the Global Analysis of Nonlinear Systems Through Interpolated Cell Mapping," *Physica* **28D**, No. 3, pp. 401-408.

[5.] Tongue, B.H. and Gu, K., 1988, "Interpolated Cell Mapping of Nonlinear Systems," *ASME Journal of Applied Mechanics*, **55**, No. 2, pp. 461-466.

[6.] Tongue, B.H. and Gu, K., 1988, "A Higher Order Method of Interpolated Cell Mapping," *Journal of Sound and Vibration*, **125**, No. 1, pp. 169-179.

[7.] Tongue, B.H. and Gu, K., 1988, "A Theoretical Basis for Interpolated Cell Mapping," *SIAM Journal on Applied Mathematics*, **48**, No. 5, pp. 1206-1214.

[8.] Tongue, B.H., "A Multiple Map Strategy for Interpolated Mapping," to appear in the *International Journal of Nonlinear Mechanics.*

[9.] Tongue, B.H. and Gu, K., "Adaptive Mesh Stategies for Interpolated Mapping Procedures," to appear in the *International Journal of Engineering Science.*

[10.] Tongue, B.H. and Smith, D. "Determining Lyapunov Exponents by Means of Interpolated Mapping," to appear in the *ASME Journal of Applied Mechanics.*

[11.] Wolf, A., Swift, J.B., Swinney, H.L. and Vastano, J.A., 1985, "Determining Lyapunov Exponents from a Time Series", *Physica*, **16D**, pp. 285-317.

Response Type	Numerically Integrated	Sequentially Generated Mapping
Period 1	-.00860 -.09139	-.00865 -.09135
Period 2	-.04995 -.05004	-.04996 -.05004
Period 4	-.03218 -.06780	-.03287 -.06713
Chaos	.01755 -.11754	.01713 -.11713

Calculated Lyapunov Exponents

Table 1

Response Type	Numerically Integrated	Sequentially Generated Mapping
Period 1	486.1	75.1
Period 2	487.2	77.0
Period 4	486.2	77.6
Chaos	486.9	283.0

Comparison of CPU Requirements

Table 2

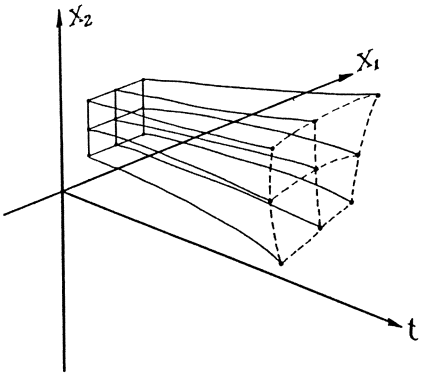

Figure 1: Phase Flow in X_1, X_2, t space

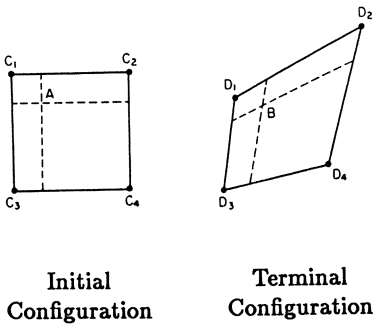

Figure 2: Bi-Linear Mapping

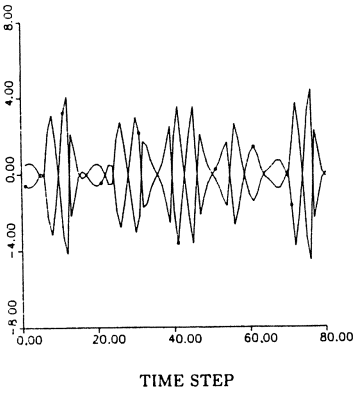

Figure 3: Locally Determined Lyapunov Exponents vs Time Step

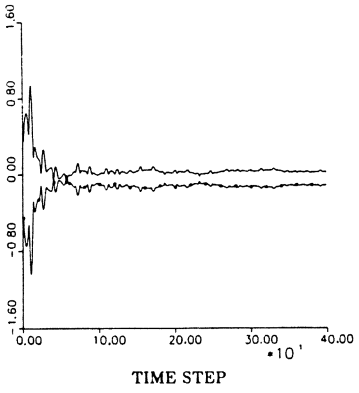

Figure 4: Cumulative Average of Lyapunov Exponents vs Time Step

Decay and Resonance of Coherent States

T. P. Valkering# and E. van Groesen*

Center for Theoretical Physics# and Department of Applied Mathematics*
University of Twente, P.O.Box 217, 7500 AE Enschede, The Netherlands.

Summary

We describe examples of two phenomena: the decay of a nonlinear coherent state under the influence of friction and the resonance of such a state due to a time periodic external forcing. In the latter case a period doubling transition to chaotic motion can be found as function of a parameter in the forcing. Essential is that in each case the state remains spatially coherent. The main features of these phenomena can be described with only two observables: say the amplitude and the phase of the coherent state. Here one method is given to choose these observables properly and to formulate their equations of motion in each case.

Decaying and resonant states

In this paper we consider systems with equations of motion

$$\dot{w} = F_0(w) + F_e(w,t) - D(w). \qquad (1)$$

Here w is an element of the state space whose dimension may be finite or infinite. $F_0(w)$ is a Hamiltonian *autonomous* term, $F_e(w,t)$ is a *time periodic* external forcing and D(w) represents dissipation. The specific form of these terms will be specified later .

As examples for the autonomous Hamiltonian part one may think of a spherical pendulum, a chain of N particles on a ring with nonlinear interaction between nearest neighbours (such as the well-known Toda chain with periodic boundary conditions), or a continous system such as the Korteweg-de Vries equation, which describes one way running waves in many different physical systems. In the latter case the unperturbed part of (1) reads (subscripts denote partial differentiation)

$$u_t = \partial_x (u - 3u^2 - u_{xx}) \qquad (2)$$

which is Hamiltonian indeed with Hamiltonian $\int dx(u^2/2 + u_x^2/2 - u^3)$, and ∂_x is the appropriate anti-symmetric operator.

W. Schiehlen (Editor)
Nonlinear Dynamics in Engineering Systems
IUTAM Symposium Stuttgart/Germany 1989

In all three examples given the autonomous part has special time periodic solutions with common properties, both in appearance and in their analytical 'background' as we will see: we mean the mode rotating with fixed angle to the vertical axis of the pendulum, a travelling 'one hump' density wave running around in ring of particles (cf. [1] for the integrable Toda chain and [2] for nonintegrable chains) and a travelling 'cnoidal' wave in the KdV case [3].

We describe the behaviour of such nonlinear excitations under influence of the extra terms F_e and D in (1) in two different cases. First consider the case of only dissipation: F_e is zero, and take the pendulum with uniform viscous friction as an example. If w = [p,q], p and q denoting momenta and coordinates respectively, the dissipation is given by

$$D(w) = \lambda\ [p,0]. \qquad (3)$$

Choose as initial condition an exact rotating mode. Then obviously the motion decays and goes to equilibrium. Especially, for the friction coefficient λ below a certain treshold we observe numerically that the trajectory remains nearly circular: i.e. at each instant it is near a rotating mode, with slowly decaying amplitude and angular momentum. In fact, if L denotes the angular momentum and $\theta(L)$ the angle with the vertical axis of the rotating mode for a given L, the damped motion is described by $L(t) = L_0 \exp(-\lambda t)$ and $\theta \approx \theta\ (L(t))$ .This may not be very surprising, but a similar phenomenon is found in the Toda chain and in KdV [4,5]: In the former case, again with friction as in (3) and starting with an initial condition of an exact localized wave solution of the autonomous system, the wave decays but remains localized at each instant: if $r_n(t) = r\ (a;\ 2\pi n/N - \omega(a)t)$ describes the coordinate of the n^{th} particle of the density wave of the autonomous system (with 'amplitude parameter' a, particle number N, circular frequency ω), the decaying wave is *approximately* given by the same expression but with the parameter a decreasing as a function of time. In the KdV case the same behaviour is observed for two different types of damping, i.e. if eq. (2) is extended with uniform damping and with a term due to viscosity, given by respectively

$$-\lambda_1 u \quad \text{and} \quad -\lambda_2 u_{xx}. \qquad (4)$$

Next consider a case in which all three terms in (1) are present. In a particle chain (actually with a nonintegrable interaction potential and with two fixed ends instead of an arrangement on a ring) with friction as above it appeared to be possible to choose a time periodic forcing $F_e(w,t\ )$ in such a way that there is an attracting

periodic state which shows a density wave bouncing back and forth beween the two fixed ends [6,7]. Increasing a strength parameter in the forcing a period doubling transition to chaotic motion appeared, whereas the 'one hump' character of the solution was conserved. This means that it remained a strongly localized wave going to and fro between the walls. Thus the spatial coherence was maintained and the chaotic behaviour was observed e.g. in the time intervals between the collisions of the wave with the wall. Note the similarity with a ball moving back and forth between two reflecting walls, the so called Fermi problem, [8] and with a ball dancing on a periodically vertically oscillating table [9].
Transitions to chaos via a period doubling sequence based on a coherent structure of the unperturbed system were observed in continuous systems as well, e.g.in the Nonlinear Schrödinger [10] and in the Sine-Gordon equation [11].

All these phenomena have in common that there seem to be only *a few relevant observables*. The aim of this paper is to describe briefly one way to describe these seemingly different behaviours and to derive equations of motion for the few dominant observables.

Analytical description

Fundamental for this description is that in all cases mentioned, the autonomous system has a *family of periodic solutions* depending on some parameter. In the integrable cases such families come about in the same way. Consider the pendulum. One readily verifies that the rotating mode represents at each time a minimum of the energy for given angular momentum, which is a constant of the motion because of rotational symmetry. Similarly, for KdV the integral $\int dx\, u^2$ is a constant of the motion related to translational symmetry of the system. It is called the wave action. The variational problem: minimize the energy for constant wave action yields the cnoidal solution [12]. In the case of the Toda chain the second constant of the motion is not known explicitly. However, defining the actions as in [1] a one hump wave going around in the chain represents a solution minimizing the energy for a given appropriate action. The period doubling transition discussed above was observed in a nonintegrable chain. Then no second constant of the motion is available. Nevertheless a family of bouncing waves is expected to exist. Using a variational formulation a family of solitary wave solutions can be proven to exist for particles on a ring [2].

In the integrable cases the minimization problem yields the value of the second constant of the motion, call it a, as a function of the energy, or vice versa. So naturally one can parametrize the solution with a. Then also the frequency of the motion depends on a and a solution of the autonomous system is given by

$$w(t) = v(a, \phi) \text{ with } a = a_0 \text{ and } \phi = \omega(a_0)\, t + \phi_0, \qquad (5)$$

a_0 and ϕ_0 being determined by the initial conditions, and $v(a, \phi)$ a 2π periodic function of ϕ.

Essential for the present analysis is that such a family spans *a twodimensional surface* in the phase space of the given system

$$V =\text{def } \{w \mid w = v(a, \phi),\ 0 \leq \phi < 2\pi \text{ and } a \text{ in some range } \}. \qquad (6)$$

This surface is composed of periodic orbits (5) of the unperturbed part of the equation for various values of a_0. Thus V is an invariant surface for this part. One can show [7] that $H_0(v(a, \phi))$ does not depend on ϕ and that for a proper scaling $dH_0/da = \omega(a)$. Thus one can say that *the restriction of the unperturbed part to* V *is a one degree of freedom integrable oscillator* with $[a, \phi]$ as action angle variables.

The experiments described above lead to the observation that in these cases the actual orbit of the full system remains *near the two-dimensional surface* V. This means that one can write

$$w(t) = v(a(t), \phi(t)) + z(t) \qquad (7)$$

with z small. Obviously any solution can be written like (7) but even for a solution near V, z is small only if a and ϕ have the right dependence on time. We now describe briefly how this can be achieved.

Let $T(a,\phi)$ denote the (two-dimensional) tangent space to V at the point $v(a,\phi)$ of V. Let $Y(a,\phi)$ be its complement in the phase space such that

$$(y, J\,x) = 0 \quad \text{for} \quad y \in Y, \quad x \in T \quad \text{and with} \quad J = \begin{matrix} 0 & -Id \\ Id & 0 \end{matrix}. \qquad (8)$$

For a continuos system as KdV, J must be taken as $-\partial x^{-1}$. Now we require

$$(z(t), J\,x(a(t), \phi(t)) \equiv 0 \qquad (9)$$

i.e. $z \in Y$ *for all time.* This requirement serves two purposes: it makes the splitting $w = v(a,\phi) + z$ unique, and it decouples the dynamics of a and ϕ on the one hand and of z on the other in some optimal way

To obtain equations of motion for $[a,\phi]$ and z substitute (7) in the equation of

motion (1) and split it in two parts by projecting on T and Y respectively. Using v_a and v_ϕ (subscripts denote partial differentiation) as the obvious basis for the tangent space T we obtain with (9) , omitting the $O(z^2)$ terms

$$\dot{a}\, v_a + (\dot{\phi} - \omega(a))\, v_\phi = [\, F_e(v,t) - D(v)\,]_T + [\, \{dF_e(v,t) - dD(v)\}\, z\,]_T \quad (*), \quad (10a)$$

$$[\, \dot{z} - (dF_0(v) + dF_e(v,t) - dD(v))\, z\,]_Y = [\, F_e(v,t) - D(v)\,]_Y . \quad (10b)$$

Before we draw conclusions, consider these coupled equations in more detail. The first line of (10a) (referred to as (*)) represents a one degree of freedom driven and damped oscillator with action angle variables a and ϕ. In fact it is precisely the restriction of the system to V (cf [5,6,7] for more details). The second equation (10b) is an inhomogeneous linear equation for z, the inhomogeneous term being the Y-component of the external forcing and the dissipation at the surface V. They are coupled in two ways: both sides of (10b) depend, through v, on a and ϕ, and there is the term linear in z in (10a).

Now we claim that the one degree of freedom (1 dof) oscillator (*) describes the dominant features of the decaying and resonating modes. This is supported by more detailed analysis of experimental data for Toda [4] and KdV [5]. The possible validity of this claim is also supported by the next paragraph.

One interesting question to answer is under what conditions the full system has a trajectory that remains near V and whose dominant features are given by (*). Two conditions seem to be sufficient: i) The zero solution of the homogeneous part of (10b), in which the solution of (*) is substituted, is attracting, and ii) The transversal component of the combined effect of forcing and damping (rhs of (10b)) is much smaller than its tangential component (rhs of (*)). i) causes that z is of the order of this transversal component so that ii) justifies that the linear term in z of the second line of (10a) can be neglected. One consequence is that carefully adjusting the driving term, as in [6], may cause behaviour described by (*). Indeed similar work on the Toda chain, but with a straight sinusoidal term [13], leads to different behaviour.

Comments

In conclusion, we claim that (10) and in particular (*) gives a useful description of the discussed phenomena, but obviously a detailed rigorous analysis, including the effect of the higher order terms, is necessary. Some final remarks are in order. Obviously the 1dof oscillator (*) can show time chaotic behaviour, depending on the chosen driving. In that case one cannot immediately conclude that the full system has a chaotic attractor, let alone that it is low-dimensional. Eq.(10a) is only an *approximate description* of the *projection* of the trajectory on V. The same

holds true if a complete period doubling sequence exists in (10a): One cannot simply conclude that the full system has a pd-sequence too [14].
The above described procedure is one way to introduce 'collective coordinates', that is coordinates which describe the 'bulk features' of the observed motion. Often special solutions are substituted in the equations of motion or in the Lagrangian of the system [3] and assuming several properties of the motion (e.g. slowly varying variables etc.) one ends up with a set ODE´s like here. Sometimes the derivation is purely based on the phenomenology. An interesting example is given in [15]. Our method seems to make optimal use of the Hamiltonian structure of the unperturbed system, via the projection (9) and the use of action-angle variables on V. It seems worthwile to investigate the relation between the several methods.
Finally, the present method seems to be extendable to higher dimensional dominant behaviour: The solution family of the unperturbed system is then for instance a family of two-tori and one can hope to be able to describe and understand 2-dof behaviour. Many interesting experiments in this area are done, as examples we just mention [16,17], presented at this Conference, and [18].

References

1. W.E. Ferguson Jr.; H.Flaschka; D.W. McLaughlin: Nonlinear normal modes for the Toda chain'. J. Comp. Phys. 45 (1982) 157-209.

2. T.P. Valkering: Periodic travelling waves in a non-integrable one-dimensional lattice. Cel. Mech. 28 (1982) 119-131.

3. G.B. Whitham: Linear and nonlinear waves. New York: Wiley 1974

4. G.J. Brinkman;T.P. Valkering: Soliton decay in a Toda chain caused by dissipation. To appear in J. Appl. Math. Phys. ZAMP.

5. E. van Groesen; F van Beckum; T.P. Valkering: Decay of travelling waves in dissipative Poisson systems. Submitted (1989).

6. J.H.J. van Opheusden; T.P. Valkering: Period doubling density waves in a chain. Nonlinearity 2 (1989) 357-371.

7. T.P. Valkering; G. Derks; E. van Groesen: Modelling one degree of freedom behaviour of dissipative Hamiltonian systems with forcing. In: St. Pneumatikos; T. Bountis; Sp. Pneumatikos (eds.): Proc of the. Intern. Conf. on Singular Behaviour and Nonlinear Dynamics, Samos, Greece. World Sc Publ. Corp. 1989.

8. A.J. Lichtenberg; M.A. Lieberman: Regular and Stochastic Motion. New York: Springer 1983.

9. N.B. Tuffilaro; A.M. Albano: Chaotic dynamics of a bouncing ball. Am. J. Phys. 54 (1986) 939-944.

10 K. Nozaki; N. Bekki: Low-dimensional chaos in a driven damped nonlinear Schrödinger equation. Physica 21D (1986) 381-393.

11. M. Taki; K.H. Spatchek; J.C. Fernandez; R. Grauer ; G. Reinisch: Breather dynamics in the nonlinear Schrödinger regime of perturbed Sine-Gordon systems. Physica D (1989) in press..

12. P.D. Lax: Integrals of nonlinear quations of evolution and solitary waves. Comm. Pure Appl. Math. 21 (1968) 467-490.

13. K. Geist; W. Lauterborn: The nonlinear dynamics of the damped and driven Toda chain. Physica D 31 (1988) 103-116.

14. Th. Zeegers; T.P. Valkering: The period doubling sequence of (semi-) symplectic oscillators coupled to a linear one. In preparation.

15. D.K.Campbell; J.F. Schonfeld; C.A. Wingate: Resonance structure in kink-anti-kink interactions in ϕ^4 theory. Physica 9D (1983) 1-32.

16 P.R. Sethna: On symmetry breaking bifurcations: Local and global phenomena. These Proceedings.

17. J. Cusunamo; F.C. Moon: Low-dimensional behaviour in chaotic nonplanar motions of a forced linearly elstic rod: Experiment and theory. These Proceedings.

18. S. Ciliberto; J.P. Gollub. Chaotic mode competition in parametrically forced surface waves. J. Fluid Mech. (1985) 381-398.

Analysis and Simulation of Nonlinear Stochastic Systems

Walter V. Wedig

Institute for Technical Mechanics
University of Karlsruhe, BRD

Abstract

The paper discusses the transition from deterministic to stochastic dynamic systems under external or internal excitations. For this purpose, we apply harmonic excitation models with frequency fluctuations by white noise and derive invariant measures as stationary solutions of associated Fokker-Planck equations. In case of periodic system solutions, the measures degenerate to singular distributions. They become regular for increasing frequency fluctuations. In particular, they determine Lyapunov exponents of systems with generalized parameter fluctuations.

1 Generalized excitation models

In nonlinear dynamics, research is mainly restricted to harmonic excitation models with deterministic amplitudes and frequencies. In nature, however, there are always some noise sources such that parameters of excitation or system models become uncertain. They start to fluctuate around the deterministic mean values and change the system behaviour, correspondingly. The most efficient way to take into account parameter fluctuations is given by the model of white noise $\xi(t) = \dot{W}_t$ which can formally be explained as the time derivative of the Wiener process W_t. The Wiener process is normed and normally distributed with zero mean. It is started with a vanishing initial value and possesses the infinitely increasing square mean $E(W_t^2) = t$. To obtain stationary properties, we apply increments dW_t of the Wiener process. They are normally distributed, as well, and possess the expected values $E(dW_t) = 0$ and $E[(dW_t)^2] = dt$.

To investigate excitation models with frequency fluctuations we start with the following nonlinear process formulation.

$$F_t = \varepsilon \cos \Phi_t, \qquad \dot{\Phi}_t = \omega_e + \sigma \dot{W}_t, \qquad (\Phi_0 = 0). \tag{1}$$

Herein, ε and ω_e are deterministic amplitudes and frequencies of cosine functions. For vanishing noise intensities ($\sigma = 0$), the angular process Φ_t degenerates to $\varphi(t) = \omega_e t$ leading to the harmonic excitation function $f(t) = \varepsilon \cos \omega_e t$, usually applied. However, for increasing frequency fluctuations ($\sigma > 0$), the excitation trajectories become irregular with respect to amplitudes and frequencies such that they have to be analysed by means of measure theory. Appropriately, we apply the spectral measure which is the power spectrum of stationary stochastic processes F_t. Following the analysis, given in [1], the

W. Schiehlen (Editor)
Nonlinear Dynamics in Engineering Systems
IUTAM Symposium Stuttgart/Germany 1989

spectrum $S_f(\omega)$ of the F_t process is derived by means of Ito calculus and finally calculated to

$$S_f(\omega) = \frac{\varepsilon^2\sigma^2(\omega_e^2 + \omega^2 + \sigma^4/4)/2}{(\omega_e^2 - \omega^2 + \sigma^4/4)^2 + \omega^2\sigma^4}, \qquad (-\infty < \omega < +\infty). \tag{2}$$

In figure 1, one finds four typical evaluations of possible frequency distributions (2) in dependence upon the spectral frequencies ω.

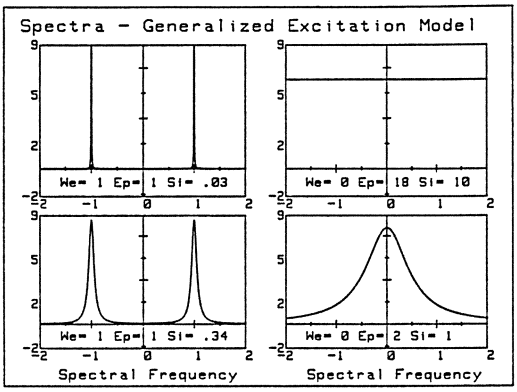

Figure 1: Power spectra of the generalized excitation model

The left side of figure 1 shows a typical band-pass distribution for the data $\omega_e = 1$, $\varepsilon = 1$ and $\sigma = 0.34$. In the limiting case of vanishing noise intensity ($\sigma = 0$), the power spectrum goes over to $S_f(\omega) = \delta(\omega \pm \omega_e)$ which characterizes the frequency concentrations of the harmonic excitation model. On the right-hand side we see a typical low-pass spectrum for $\omega_e = 0$, $\varepsilon = 2$ and $\sigma = 1$. If amplitudes ε and noise intensities σ are simultaneously increasing with $\sigma = \varepsilon\sqrt{2} \to \infty$, we reach the opposite limiting case of the uniformly distributed white noise spectrum $S_f(\omega) = 1$. In this sense, the stationary process (1) covers stochastic excitation models as well as deterministic ones. It allows, therefore, to study the transition between both limiting cases, systems driven by white noise and harmonically excited systems.

2 Chaotic motions of low-pass systems

In the following, we investigate a first application of the generalized fluctuation model. Let us consider a linear low-pass filter with the limiting frequency ω_g under the external excitation defined in (1).

$$\dot{Z}_t + \omega_g Z_t = \varrho \cos\Phi_t, \qquad \dot{\Phi}_t = \omega_e + \sigma\dot{W}_t. \tag{3}$$

Obviously, the dynamic problem (3) is nonlinear. It consists of two scalar first order equations; Z_t is the state process of the filter and Φ_t is the linear angular process. The nonlinearity is introduced by the cosine of the angle process. The system equations (3) are simulated by means of forward differences with the time step Δt.

$$Z_{n+1} = Z_n + (-\omega_g Z_n + \varrho\cos\Phi_n)\Delta t, \qquad n = 0, 1, 2, \ldots, \tag{4}$$

$$\Phi_{n+1} = \Phi_n + \omega_e\Delta t + \sigma R_n\sqrt{\Delta t}, \qquad E(R_n^2) = 1. \tag{5}$$

Herein, R_n is a sequence of independent numbers, normally distributed with zero mean and normed square mean. They are produced by means of linear congruence generators and Box-Muller transformations [2]. The square root $\sqrt{\Delta_t}$ of the time step applied in (5) corresponds to the mean square $E[(dW_t)^2] = dt$ of the stationary Wiener increments.

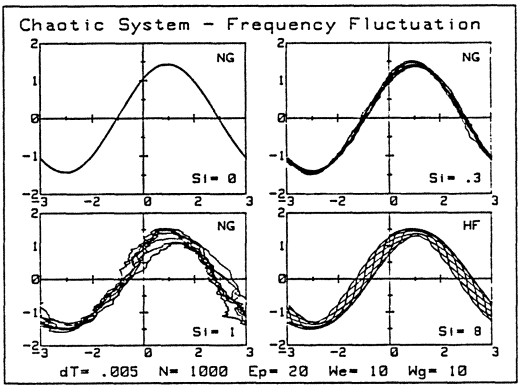

Figure 2: Simulations of periodic and chaotic trajectories

In figure 2, one finds simulation results of the time-discrete systems (4) and (5). They show stationary Z_n solutions over the angular process Φ_n in the range $-\pi \leq \varphi \leq +\pi$. The applied data are $\Delta t = 0.005, \varepsilon = 20, \omega_e = 10$ and $\omega_g = 10$. The first picture (NG) shows periodic solutions of the filter for vanishing frequency fluctuations ($\sigma = 0$). In the next ones (NG), the fluctuation intensities are increased to $\sigma = 0.3$ and $\sigma = 1$. In the fourth picture, the noise generator (NG) is replaced by harmonic frequency fluctuations (HF) of the form $\sigma \cos \pi \omega_e t$ where $\sigma = 8$ is applied. In both cases, we observe a bifurcation of the periodic filter solution. With increasing frequency fluctuations, they bifurcate into chaotic motions with certain variations around the periodic mean solutions. We call them chaotic since all trajectories are simulated in a purely deterministic way. Starting with the same initial values they can be reproduced identically. Differences between narrow-band (HF) and broad-band (NG) fluctuations of the excitation frequencies are only observable in the microstructure of the response trajectories. However, a global description by means of measure theory leads certainly to similar distribution densities in both cases.

We investigate the two-dimensional distribution densities $p(z, \varphi)$ for the broad-band frequency fluctuations, formulated in (3). They are determined by the Fokker-Planck equation, associated to (3). In the stationary case, it has the following form:

$$\frac{1}{2}\sigma^2 \frac{\partial^2}{\partial \varphi^2} p(z,\varphi) - \omega_e \frac{\partial}{\partial \varphi} p(z,\varphi) + \frac{\partial}{\partial z}[(\omega_g z - \varepsilon \cos \varphi) p(z,\varphi)] = 0. \tag{6}$$

Following the analysis, given in [1], the solution of this diffusion equation can be represented by a Fourier series in the angle domain $-\pi \leq \varphi \leq +\pi$ and a Fourier integtral which transforms the density variable z to t, both valid in $-\infty < z, t < +\infty$.

$$p(z,\varphi) = \frac{1}{(2\pi)^2} \int_{-\infty}^{+\infty} \exp(-itz) \sum_{k=0}^{\infty} \frac{1}{k!} (it)^k e_k(\varphi) dt, \tag{7}$$

$$e_k(\varphi) = E(Z_t^k) + \frac{1}{2}\sum_{n=1}^{k} E[Z_t^k \cos n(\varphi - \Phi_t)]. \tag{8}$$

Herein, the coefficient functions $e_k(\varphi)$ are determined by the stationary moments $E(Z_t^k)$, $E(Z_t^k \cos n\Phi_t)$ and $E(Z_t^k \sin n\Phi_t)$ which are easy to calculate from the system equations (3) for all $k, n = 0, 1, 2, \ldots$. Figure 3 shows a three-dimensional evaluation [3] of the calculated density $p(z, \varphi)$ for the data, already applied in the third picture of figure 2. The density is 2π-periodic with respect to the angle variable φ and non-gaussian with respect to z. Naturally, this non-normal form is caused by the nonlinearity of the dynamic system (3). Integrating $p(z, \varphi)$ in the angle range $-\pi \leq \varphi \leq +\pi$ we obtain the density function $p(z)$ of the stationary filter process [1]. In the limiting case $\sigma = \varepsilon\sqrt{2} \to \infty$, it is normally distributed. For $\sigma = 0$, it degenerates to the singular, non-normal cosine distribution of the harmonic response.

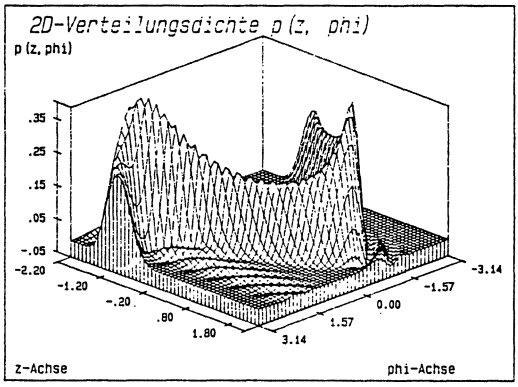

Figure 3: Joint density distribution of filter and angle processes

3 Simulation of Lyapunov exponents

In a second application of the generalized fluctuation model (1) we investigate dynamic systems with time-varying parameters. For this purpose let us consider an oscillator equation of the following form:

$$\ddot{X}_t + 2D\omega_1\dot{X}_t + \omega_1^2(1 + \varepsilon\cos\Phi_t)X_t = 0. \tag{9}$$

Herein, $D > 0$ denotes a dimensionless damping measure and ω_1 is the natural frequency of the oscillator. The parametric excitation has the amplitude ε. The angular process Φ_t is defined in (1). Obviously, $X_t \equiv 0$ is a strong solution of the oscillator. This equilibrium solution is asymptotically stable for $\varepsilon = 0$ and $D > 0$. It is destabilized with increasing amplitudes $\varepsilon > 0$. We investigate the stability of $X_t \equiv 0$ by means of Lyapunov exponents. According to [4], this is performed by introducing the polar coordinates $X_t = A_t \cos\Psi_t$ and $\dot{X}_t = \omega_1 A_t \sin\Psi_t$ which transform the equation (9) into a nonlinear first order system for the phase process Ψ_t and the natural logarithm of the amplitude process A_t.

$$(\log A_t)^{\cdot} = -\omega_1[2D\sin^2\Psi_t + \frac{\varepsilon}{2}\cos\Phi_t \sin 2\Psi_t], \tag{10}$$

$$\dot{\Psi}_t = -\omega_1[1 + D\sin 2\Psi_t + \varepsilon\cos\Phi_t\cos^2\Psi_t]. \tag{11}$$

The phase process Ψ_t is decoupled from the growth behaviour of the amplitude. Moreover, Ψ_t is stationary in the angle range $-\pi \leq \psi \leq +\pi$ describing the rotation of the state processes in the phase plane. The phase process can be simulated by means of forward differences. The simulation of the angle process Φ_t is already explained in (5).

$$\Psi_{n+1} = \Psi_n - \omega_1[1 + D \sin 2\Psi_n + \varepsilon \cos \Phi_n \cos^2 \Psi_n]\Delta t, \tag{12}$$

$$\lambda = -\omega_1 \lim_{N\to\infty} \frac{1}{N} \sum_{n=1}^{N} [2D \sin^2 \Psi_n + \frac{\varepsilon}{2} \cos \Phi_n \sin 2\Psi_n]. \tag{13}$$

Subsequently, the obtained results are inserted into (13) in order to determine the associated Lyapunov exponent λ. The time average (13) represents the discrete version of Oseledec's multiplicative ergodic theorem [5].

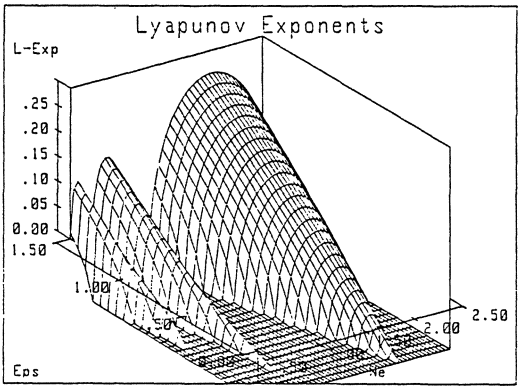

Figure 4: Lyapunov exponents of the Mathieu equation

In figure 4, we show numerical results [6] of the related Lyapunov exponents λ/ω_1 over the parameter range $0 \leq \varepsilon \leq 1.5$ and $0.5 \leq \omega_e \leq 2.5$ for $\sigma = 0$. In this special case of vanishing frequency fluctuations, the angle process Φ_t of the parametric excitation goes over to the deterministic form $\Phi_t = \omega_e t$ of the Mathieu equation. Further data of the applied simulation are $D = 0.1$, $\Delta t = 0.001$ and $N = 100{,}000$. The results of figure 4 verify the well known Mathieu effects with the parameter resonances near $\omega_e = 2\omega_1/p$ for $p = 1, 2, 3, \ldots$ Inside the stability region, the Lyapunov exponents are calculated to $\lambda = -D\omega_1$. These negative values are increasing with increasing amplitudes. They become positive beyond the stability boundaries and reach their maximal values in the center of the instability regions. In particular, we observe a sharp separation between a completely plane Lyapunov exponent distribution in the stability range and a fast growth behaviour of the Lyapunov exponents near the stability boundaries. The sharp separation is smoothed out [6] if we admit frequency fluctuations ($\sigma > 0$) of the harmonic parameter excitation.

4 Invariant measures of the Mathieu equation

In the harmonic case ($\sigma = 0$) of parameter excitations, the Fokker-Planck equation associated to the phase process (11) and to the angle equation, noted in (1), degenerates to a Liouville equation.

$$\omega_e \frac{\partial}{\partial \varphi} p(\varphi,\psi) - \omega_1 \frac{\partial}{\partial \psi}[(1 + D \sin 2\psi + \varepsilon \cos\varphi \cos^2\psi) p(\varphi,\psi)] = 0, \tag{14}$$

$$f(\varphi,\alpha) = \int_{-\pi}^{\pi} \exp(i\alpha\psi) p(\varphi,\psi) d\psi, \qquad -\infty < \alpha < +\infty. \tag{15}$$

It determines the stationary joint invariant measure $p(\varphi,\psi)$ of both processes in the angle range $-\pi \leq \varphi,\psi \leq +\pi$. By means of the Fourier integral (15) the phase variable ψ is transformed into α. This results in a transformed equation of the following form:

$$4\omega_e \frac{\partial}{\partial \varphi} f(\varphi,\alpha) + i\alpha\omega_1 \{2(2 + \varepsilon\cos\varphi) f(\varphi,\alpha) + \varepsilon\cos\varphi [f(\varphi,\alpha+2) + f(\varphi,\alpha-2)] - i2D[f(\varphi,\alpha+2) - f(\varphi,\alpha-2)]\} = 0. \tag{16}$$

The partial differential equation (16) is solved by the exponential function $\exp[i\alpha g(\varphi)]$. Insertion into (16) gives the ordinary differential equation (17) for the determination of the $g(\varphi)$-function.

$$\omega_e g'(\varphi) + \omega_1 [1 + D \sin 2g(\varphi) + \varepsilon \cos\varphi \cos^2 g(\varphi)] = 0, \tag{17}$$

$$f(\varphi,\alpha) = \exp[i\alpha g(\varphi)], \;\rightarrow\; p(\varphi,\psi) = \frac{1}{2\pi}\delta[g(\varphi) - \psi]. \tag{18}$$

Knowing the g-function, we can retransform the α-variable. The final result, noted in (18), is a singular density distribution $p(\varphi,\psi)$ for the joint invariant measure of the two angle processes Φ_t and Ψ_t.

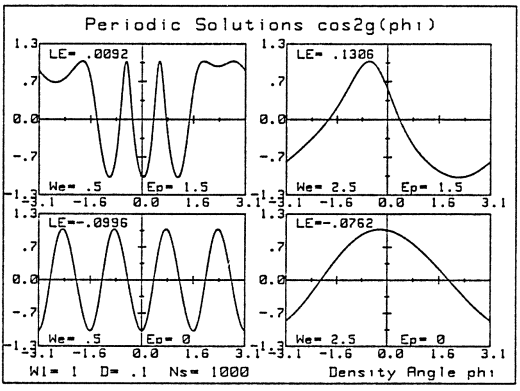

Figure 5: Periodic solutions of $\cos 2g(\varphi)$-functions

The g-solutions of the nonlinear equation (17) are numerically calculated by means of an Euler scheme. Since $p(\psi)$ is periodic in the angle range, we are looking for such solutions that the functions $\sin 2g(\varphi)$ and $\cos 2g(\varphi)$ are periodic in $-\pi \leq \varphi \leq +\pi$. This can be achieved by means of shooting methods. We select those initial values at $\varphi_0 = -\pi$ which coincide with the simulated end values at $\varphi_1 = +\pi$. Hereby, possible initial values are restricted to $0 \leq g_0 \leq \pi/2$ and $-1 \leq \cos 2g_0 \leq +1$, respectively. In figure 5, we give four typical examples of periodic $\cos 2g(\varphi)$-functions. The lower ones are simulated for $\varepsilon = 0$,

$\omega_e = 0.5$ and $\omega_e = 2.5$. The upper ones show periodic solutions for parameter excitations with $\varepsilon = 1.5$ and same ω_e-values, as above. The associated Lyapunov exponents (LE) are now calculable by the expected value (19) defined by $p(\varphi) = 1/2\pi$.

$$\lambda = -\omega_1 \frac{1}{2\pi} \int_{-\pi}^{+\pi} [2D \sin^2 g(\varphi) + \frac{1}{2}\varepsilon \cos\varphi \sin 2g(\varphi)] d\varphi. \tag{19}$$

It follows from the singular density distribution $p(\varphi, \psi)$ after integration with respect to the ψ-variable and corresponds to the time average (13) provided the existence of periodic and continuously differentiable $\cos 2g(\varphi)$-solutions.

5 Invariant measures for multiplicative noise

As already mentioned, the generalized excitation model (1) tends to a broad-band process for infinitely increasing frequency fluctuations and amplitudes. In this limiting case, the parametric excitation in (9) can be replaced by multiplicative white noise.

$$\ddot{X}_t + 2D\omega_1 \dot{X}_t + \omega_1(\omega_1 + \sigma\sqrt{\omega_1}\dot{W}_t)X_t = 0. \tag{20}$$

It can be proofed [6] that both equations (9) and (20) possess the same invariant measures and Lyapunov exponents. In the following, we restrict our interest to the white noise case (20). Introducing polar coordinates we derive the separated phase equation by means of Ito's calculus.

$$d\Psi_t = -\omega_1[1 + (D + \frac{1}{2}\sigma^2 \cos^2 \Psi_t) \sin 2\Psi_t] dt - \sigma\sqrt{\omega_1} \cos^2 \Psi_t dW_t. \tag{21}$$

The phase process is stationary in the angle range $-\pi/2 \leq \psi \leq +\pi/2$. It can be simulated by forward differences and then evaluated in order to estimate associated phase distribution densities $p(\psi)$.

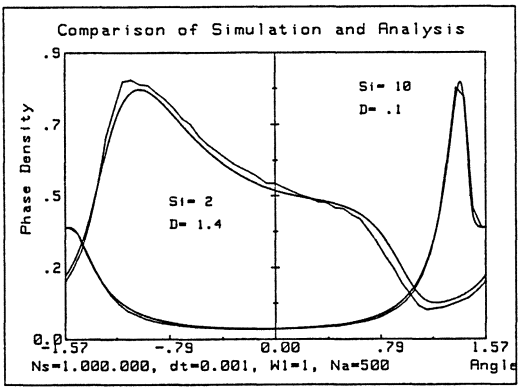

Figure 6: Analytical and simulated phase density solutions

We compare the Monte-Carlo simulation results, shown in figure 6, with corresponding ones derived from the Fokker-Planck equation of (21). Integrated with respect to ψ it takes the following form [7]:

$$\frac{1}{2}\sigma^2 \cos^4\psi p'(\psi) + [1 + (D - \frac{1}{2}\sigma^2 \cos^2\psi)\sin 2\psi]p(\psi) = C, \tag{22}$$

Herein, dash denotes derivation with respect to ψ and C is an integration constant. It has to be calculated by the normalization of the density distribution $p(\psi)$ in $-\pi/2 \leq \psi \leq +\pi/2$. Obviously, the equation (22) is singular at $\psi_0 = \pm\pi/2$. To select a regular solution we introduce backward differences [7] of the form $p'(\psi) = (p_n - p_{n-1})/\Delta\psi$ and solve the equation (22) by means of numerical integration.

$$\begin{gathered} p_n = \frac{\sigma^2 \cos^4\psi_n p_{n-1} + 2\Delta\psi p_0}{\sigma^2 \cos^4\psi_n + 2\Delta\psi[1 + (D - \frac{1}{2}\sigma^2 \cos^2\psi_n)\sin 2\psi_n]} \\ \Delta\psi = \pi/N, \quad -\pi/2 \leq \psi \leq +\pi/2, \quad n = 1, 2, ..., N \end{gathered} \tag{23}$$

This recurrence formula is started with the initial value $p_0 = C$ at the left singularity $-\pi/2$ and ends in the right singularity $+\pi/2$ with the same value $p_N = C$. For sufficiently small step sizes $0 < \Delta\psi << 1$, the denominator in (23) remains positive so that further singularities are avoided. Comparisons with the simulated results of figure 6 show convergence to the desired physical solutions. Finally, the calculated invariant measure $p(\psi)$ can be applied to evaluate the expected value

$$\lambda = -\omega_1 \int_{-\pi/2}^{+\pi/2} [D - (D + \frac{1}{2}\sigma^2 \cos^2\psi)\cos 2\psi]p(\psi)d\psi \tag{24}$$

which is the top Lyapunov exponent of the oscillator (20). Evaluations in form of level lines are given in [6] or in [1].

References

[1] Wedig, W: Vom Chaos zur Ordnung. GAMM-Mitteilungen, Heft 2 (1989) 3-31

[2] Afflerbach, L.; Lehn, J. (Hrsg): Kolloquium über Zufallszahlen und Simulationen (Darmstadt, 1986). B.G. Teubner, Stuttgart 1986

[3] Haßdenteufel, K.D.: Simulation und Lösung linearer Systeme für verallgemeinerte Anregungsmodelle. Diplom Thesis, University of Karlsruhe 1989

[4] Khasminskii, R.Z.: Necessary and sufficient conditions for asymptotic stability of linear stochastic systems. Theor. Prob. and Appls., 12 (1967) 144-147

[5] Oseledec, V.I.: A multiplicative ergodic theorem, Lyapunov characteristic numbers for dynamical systems. Trans. Moscow Math. Soc. 19 (1968) 197-231

[6] Wedig, W.: Stability and bifurcation in stochastic systems. In: Stochastic Systems in Mechanics, Minisymposium 4 of GAMM 89 (ed. by W. Schiehlen, W.Wedig). ZAMM 70, 4/5/6, (1990) T 833

[7] Wedig, W.: Pitchfork and Hopf bifurcations in stochastic systems - effective methods to calculate Lyapunov exponents. To appear in: Effective Stochastic Analysis (ed. by P. Krée, W. Wedig)

Global Analysis of the Loss of Stability of a Special Railway Bogy

G. Xu H. Troger A. Steindl

Institut für Mechanik, Technische Universität Wien,
A-1040 Vienna, Austria

Summary

The nonlinear stability behavior of a special railway bogy is investigated making use of the methods of bifurcation theory. By artificially increasing the degeneracy of the bifurcation problem we are able to treat two local bifurcation problems in one single global problem. These two local problems are, first, the calculation of the subcritical Hopf bifurcation at loss of stability of the steady state motion of the bogy and, second, the calculation of the turning point in the amplitude graph of the limit cycles.

1 Introduction

Experiments ([1]) and every day's ride experience show that the loss of stability of the steady state straight line motion of a rail vehicle at the critical speed V_c is due to a flutter instability. To be more precise, a subcritical Hopf bifurcation occurs (which is explained below). In Fig. 1 a sketch of the experimental results presented in [1] is given. This graph represents the amplitude r of the limit cycle oscillations of the center of mass of a test bogy. In section 4 when the center manifold reduction is discussed it will be explained how it is possible to represent the motion of a complex n-dimensional system by means of a two-dimensional limit cycle oscillation with one frequency.

Let us now consider some of the special features of Fig. 1. The abscissa corresponds to the steady state straight line motion. This motion is asymptotically stable for $V < V_c$. At $V = V_c$ the above mentioned flutter instability occurs. It is called subcritical because the bifurcating limit cycles are unstable. They exist only for $V < V_c$. The amplitude curve of the unstable limit cycles possesses a turning point at the speed $V = V_n$. The existence of the turning point has the consequence that globally, that is at greater amplitudes, also stable limit cycles exist. For $V < V_n$ only the asymptotically stable steady state is present. For $V > V_n$ there exist besides the steady state two limit cycles one stable and one unstable. For two arbitrarily selected velocities V_1 and V_2 the corresponding flows in the phase plane are depicted in Fig. 1, too.

What are the practical conclusions to be drawn from the graph in Fig. 1? First, we note that the stability limit V_c, which is obtained from a linearized stability analysis of the

W. Schiehlen (Editor)
Nonlinear Dynamics in Engineering Systems
IUTAM Symposium Stuttgart/Germany 1989

steady state, is not of great practical importance. This is easy to understand because the domain of attraction of the stable steady state, which is bounded by the unstable limit cycle, is very small in the velocity domain $V_n < V < V_c$. Hence, in this velocity range a sufficiently large perturbation will lead to a stable limit cycle oscillation with amplitude r_2, although a linearized stability analysis still predicts an asymptotically stable steady state. Thus for the practical operation of such a vehicle the stability limit is not given by $V = V_c$ but by $V = V_n$. This poses the question: How can we calculate V_n? There are at least three possibilities which come in mind.

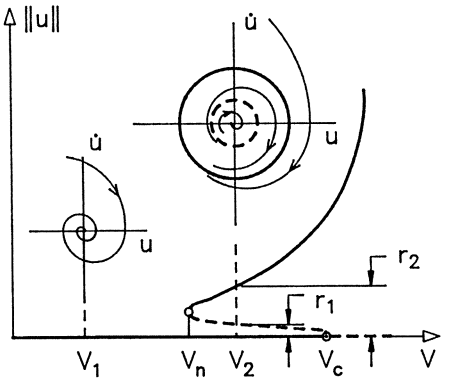

Figure 1: Experimentally obtained limit cycle oscillations of a railway bogy ([1])

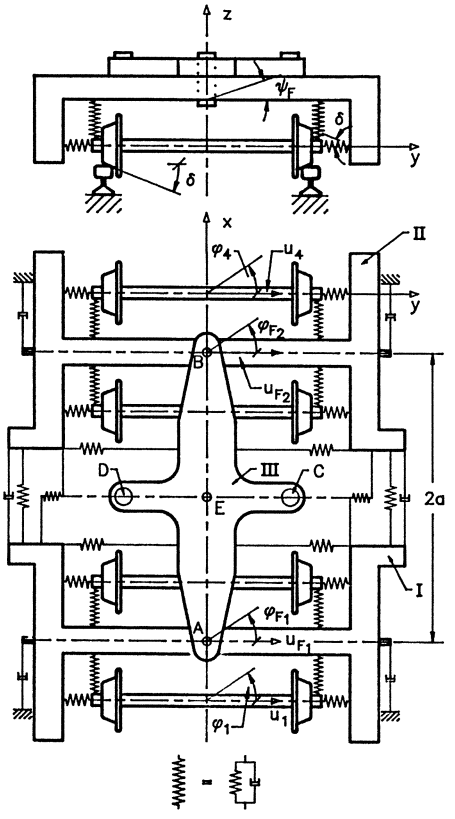

Figure 2: Mechanical model of a special railway bogy with 14 degrees of freedom

The simplest but computationally most expensive method would be by numerical simulation. That is, by integrating the equations of motion numerically for varying initial conditions and checking to which attractor the trajectories converge. This procedure allows to find V_n and also to determine the domain of attraction. However, for a system with many degrees of freedom and several different nonlinear components due to rail-wheel contact, friction, spring and damping characteristics and geometry, numerical simulation is certainly not the best way to handle such a problem, particularly if one wants to study the influence of parameter variations.

A second way to calculate V_n could be by means of a path following method, which would allow to follow the amplitude of the unstable limit cycle ([2]). However, such a method requires to calculate the unstable periodic solution of the full nonlinear system

and to check its stability. Again this is not an easy task computationally for a nonlinear system with many degrees of freedom.

There is still a third method to handle the calculation of V_n by making use of the methods of bifurcation theory ([3–7]). We note that in the graph depicted in Fig. 1 two local bifurcations occur. The first at $V = V_c$, where the steady state loses stability due to a Hopf bifurcation. The second bifurcation occurs at $V = V_n$ where the unstable limit cycle, that is, an unstable periodic solution changes into a stable one. If we treat these two local problems separately we would not gain very much because for the calculation of V_n we had to analyse a periodic state. However, following an idea of *M. Golubitsky* it is possible to calculate the bifurcations at V_c and V_n in one "global" problem simultaneously. Moreover, and this is the most important feature, this problem has still the steady state as its fundamental solution.

This considerable simplification of the problem is achieved by introducing a second parameter in addition to the velocity V and by selecting this parameter in such a way that the bifurcation at V_c becomes more degenerate. To be more precise we want to make the third order terms in the normal form of the Hopf bifurcation vanish. This has the consequence that terms of fifth order must be included in our analysis. These fifth order terms allow us to calculate the amplitude curve with a turning point. The main impact, however, is the application of center manifold theory ([6]) which enables us to reduce the dimension of the n-dimensional system to a two-dimensional bifurcation system. Therefore, the calculation of the value of V_n can be performed (i) still by investigating a steady state and (ii) only having to analyse a two-dimensional system with few nonlinear terms of third and fifth order. This latter goal is achieved by application of normal form theory ([3–7]).

2 Mechanical model and equations of motion

We study the dynamical behavior of a special bogy (Fig. 2) used by the Austrian Railway Company (ÖBB) for special railway freight cars which are able to carry a full size truck. There is a growing interest to shift the transit of goods through Austria from freeways to rails. One of the several possibilities is to carry a whole truck on a rail car. This has the advantage that at the final destination without any loss of time the delivery of the freight is possible. However, due to the existing profiles of the tunnels the height of usual railway freight cars is not admissible and must be decreased. First of all this leads to the requirement that the radius of the wheels of the car must be decreased, too. In order to prevent too high pressures at the wheel-rail contact the number of axles must be increased. This leads to the design of a bogy with four axles instead of the usual two axles. Ride experience of the ÖBB showes, however, that the stability behavior of such a car is made worse in comparison to a conventional car.

For the bogy of Fig. 2 which is an important component of such a car we use a mechanical model with 14 degrees of freedom. The bogy consists of two frames (I,II) which are connected by a balancier (III). Each of the frames has three degrees of freedom expressed by their side motion u_{Fi} and two angles φ_{Fi}, ψ_{Fi} representing rotations about the z- and x-axis, respectively. In vehicle dynamics φ is called yaw angle and ψ roll angle. Each axle has two degrees of freedom u_j, φ_j.

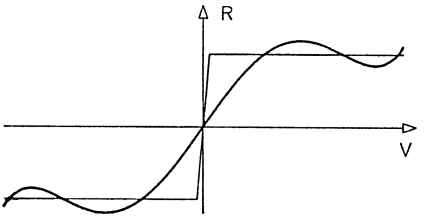

Figure 3: Approximation of the friction force by the fifth order polynomial (3)

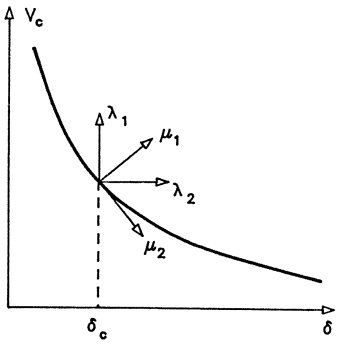

Figure 4: Critical speed V_c in its dependence on the conicity angle δ of the wheels

The motion of the balancier is determined by the motion of the two frames and follows to (Fig. 1)

$$u_B = \frac{u_{F1} + u_{F2}}{2} , \qquad \varphi_B = \frac{u_{F2} - u_{F1}}{2a} . \tag{1}$$

The balancier is fitted to the frames by two pins and friction plates A, B. The car body rests on two friction plates C, D and its position is fixed to the balancier by the pin E.

The friction forces at the contact plates are

$$R(v_r) = \mu T \text{sign}(v_r) . \tag{2}$$

In (2), μ is the friction coefficient, T the vertical load and v_r the relative velocity. We approximate (2) by the fifth order polynomial

$$R(v_r) = c_1 v_r + c_3 v_r^3 + c_5 v_r^5 \tag{3}$$

where the coefficients depend on μ and T (Fig. 3).

The characteristics of the springs and dampers are assumed to be linear except for those springs acting in z-direction. They are progressive or hard springs.

Most important for the success of a theoretical analysis of the dynamics of a road or rail vehicle is the modelling of the ground wheel contact mechanics. We use for it those assumptions made in [8,9,10] leading to nonlinear relationships between the creepages $\xi_x, \xi_y, \xi_\varphi$ and the contact forces T_x, T_y. These assumptions correspond to the theory of Johnson-Vermeulen ([8]).

The equations of motion can be derived in the form of Lagrange's equations as a system of 14 equations of second order

$$\mathbf{B}_0 \ddot{\mathbf{q}} + \mathbf{F}(\mathbf{q}, \dot{\mathbf{q}}) = 0 .$$

We transform these equations to a first order system. It takes the form

$$\mathbf{R}_0 \dot{\mathbf{x}} = \mathbf{N}(\mathbf{x}) \tag{4}$$

where $\mathbf{R}_0$ is a 28×28 matrix with constant elements and $\mathbf{x}, \mathbf{N} \in I\!R^{28}$. The components

of $\mathbf{x}$ are the variables shown in Fig. 2 and their time derivatives. The components of $\mathbf{N}(\mathbf{x})$ are expanded into power series up to and including terms of fifth order. The vector $\mathbf{N}$ takes the form

$$\mathbf{N}(\mathbf{x}) = \mathbf{N}_1\mathbf{x} + \mathbf{N}_3\mathbf{x}^3 + \mathbf{N}_5\mathbf{x}^5 \ .$$

By the notation $\mathbf{x}^3$, for example, we mean a vector containing all possible monomials of third order in the 28 variables. We note that no terms of quadratic and fourth order appear in the equations of motion. Multiplying by $\mathbf{R}_0^{-1}$ in (4) the equations are

$$\dot{\mathbf{x}} = \mathbf{A}(\boldsymbol{\lambda})\mathbf{x} + \mathbf{C}(\boldsymbol{\lambda})\mathbf{x}^3 + \mathbf{Q}(\boldsymbol{\lambda})\mathbf{x}^5 \ . \tag{5}$$

The matrices $\mathbf{A}, \mathbf{C}, \mathbf{Q}$ contain only constant elements. In order to save storage room only those elements which are not equal to zero are stored. The parameter vector $\boldsymbol{\lambda} = (V, \delta)$ has as its components the velocity V and the angle of conicity δ of the wheels (Fig. 2). The angle δ is chosen because its variation will enable us to annihilate the third order terms in the normal form of the bifurcation equations.

3 Critical speed V_c and stability boundary in parameter space

The steady state of the bogy is given by $\mathbf{x}_0 = 0$, which is a solution of (5). The first step of the stability analysis is the calculation of the critical speed V_c. This is performed by increasing V quasistatically and calculating the eigenvalues of $\mathbf{A}$. The angle δ is kept at a prescribed value. For low speed all eigenvalues of $\mathbf{A}(\boldsymbol{\lambda})$ have a negative real part and, therefore, the steady state $\mathbf{x}_0 = 0$ is asymptotically stable. The critical speed V_c is reached when eigenvalues cross the imaginary axis for the first time. In the simplest (generic) cases this will happen either due to a simple zero eigenvalue or due to a purely imaginary pair of eigenvalues. For the bogy always a purely imaginary pair of eigenvalues appears at the stability limit V_c. If, in addition, we vary δ we obtain Fig. 4.

4 Center manifold reduction to a two-dimensional bifurcation system

At $\boldsymbol{\lambda}_c = (V_c, \delta)$ we can reduce the 28-dimensional system (5) to a two-dimensional bifurcation system. We do not explain this step in detail because this is done in [7], chapters 3 and 4. We only mention the necessary calculations. First, for $\boldsymbol{\lambda} = \boldsymbol{\lambda}_c$ a linear transformation of coordinates $x \to By$, is introduced in (5) that transforms the linear part into Jordan form. Those two variables y_1, y_2 which correspond to eigenvalues with zero real part are the active variables and $y_3, \ldots, y_{28}$ are passive variables. Hence, we can write (5) as

$$\begin{aligned}
\dot{y}_1 &= -\omega y_2 + g_{13}(y_1, y_2, \mathbf{y}_s) + g_{15}(y_1, y_2, \mathbf{y}_s) \\
\dot{y}_2 &= \omega y_1 + g_{23}(y_1, y_2, \mathbf{y}_s) + g_{25}(y_1, y_2, \mathbf{y}_s) \\
\dot{\mathbf{y}}_s &= \mathbf{J}_s\mathbf{y}_s + \mathbf{g}_{s3}(y_1, y_2, \mathbf{y}_s) + \mathbf{g}_{s5}(y_1, y_2, \mathbf{y}_s)
\end{aligned} \tag{6}$$

where $\mathbf{y}_s = (y_3, \ldots, y_{28})^T$, $\mathbf{J}_s$ is a 26×26 matrix whose eigenvalues all have a negative real part, $\mathbf{g}_3$ and $\mathbf{g}_5$ contain the nonlinear terms of third and fifth order, respectively. Intuitively speaking one can expect that in a local but finite neighborhood of the bifurcation point the passive variables will decay and only the two active variables will be of relevance. However, it would be a mistake simply to ignore the $\mathbf{y}_s$. The decisive step is to eliminate in (6) the passive variables $\mathbf{y}_s$ from the first two equations, which are the bifurcation equations, in a correct manner. This can be done by expressing the passive variables by the active variables in the form

$$\mathbf{y}_s = \mathbf{H}(y_1, y_2) \tag{7}$$

from $(6)_3$. From the general theory ([6,7]) it follows that

$$\mathbf{H}(y_1, y_2) = O(|y_1|^2 + |y_2|^2) \; . \tag{8}$$

If we were satisfied with bifurcation equations of third order we could set $\mathbf{y}_s \equiv 0$ in $(6)_{1,2}$. This follows from the fact that because of (8), at least fourth order terms would result in $(6)_{1,2}$ after inserting (7). However, for the fifth order terms in any case an influence of the passive variables is given and we have to calculate $\mathbf{H}(y_1, y_2)$ at least up to third order terms. The calculation is performed by series expansion and equating coefficients. From the special form of (6) follows that in (7) only third order terms can be present. After inserting (7) into $(6)_{1,2}$ we obtain

$$\begin{aligned} \dot{y}_1 &= -\omega y_2 + f_{13}(y_1, y_2) + f_{15}(y_1, y_2) + O(|y|^7) \\ \dot{y}_2 &= \omega y_1 + f_{23}(y_1, y_2) + f_{25}(y_1, y_2) + O(|y|^7) \; . \end{aligned} \tag{9}$$

5 Simplification of the bifurcation equations by normal form theory, unfolding and numerical results

By a nonlinear change of variables $y \to z$ we try to annihilate as many nonlinear terms in (9) as possible. If the linear part were not degenerate all nonlinear terms could be removed. However, due to the degeneracy of the linear part resonant terms occur that cannot be eliminated. Despite of that, still a strong simplification can be achieved ([7]). If we further introduce polar coordinates $z_1 = \varepsilon^{1/4} r \cos\varphi$, $z_2 = \varepsilon^{1/4} r \sin\varphi$, (9) takes the form

$$\begin{aligned} \dot{r} &= \varepsilon^{1/2} K_3 r^3 + \varepsilon K_5 r^5 + O(|\varepsilon|^{3/2}) \\ \dot{\varphi} &= \omega + \varepsilon^{1/2} K_2 r^2 + \varepsilon K_4 r^4 + O(|\varepsilon|^{3/2}) \; . \end{aligned} \tag{10}$$

In general $K_3 \neq 0$ in $(10)_1$. This means that the problem is three-determinate. Then locally in the neighborhood of the bifurcation point the third order term determines the behavior of the problem. However, in order to be able to calculate V_n we can use the second parameter δ to make K_3 to vanish. In Fig. 5 K_3 is plotted as function of δ. For $\delta = \delta_c$ we obtain $K_3 = 0$ and the higher degenerate bifurcation equation $(10)_1$ becomes

$$\dot{r} = \varepsilon \bar{K}_5 r^5 \; . \tag{11}$$

A universal unfolding of (11), that is, an embedding of (11) in a parametrized family that includes all qualitative possible solutions requires now two parameters, instead of one for $(10)_1$, and has the form

$$\dot{r} = \varepsilon(\nu_1 r + \nu_2 r^3 + \bar{K}_5 r^5) + O(|\varepsilon|^{3/2}) \; . \tag{12}$$

The mathematical unfolding parameters ν_1 and ν_2 are given by

$$\nu_1 = \frac{1}{\varepsilon}\left.\frac{\partial \alpha_1}{\partial \mu_1}\right|_{\mu_1=\mu_2=0} \mu_1 \,, \qquad \nu_2 = \frac{1}{\varepsilon^{1/2}}\left.\frac{\partial K_3}{\partial \mu_2}\right|_{\mu_1=\mu_2=0} \mu_2 \tag{13}$$

where α_1 is the real part of the critical eigenvalue. Furthermore, the linear relationship between μ_1, μ_2 and $\lambda_1 = V - V_c$, $\lambda_2 = \delta - \delta_c$ can be seen from Fig. 4.

The steady state solutions of (12) allow us to calculate the practically important critical speed V_n by inserting those values of δ, which appear during the life time of a wheel set. Such results are shown in Fig. 6.

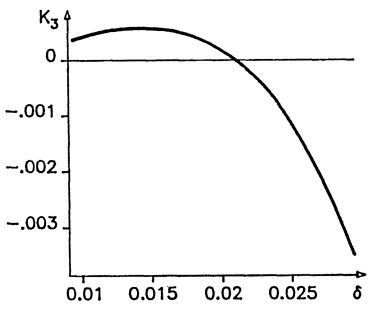

Figure 5: Coefficient K_3 in (10) in its dependence on the conicity angle δ of the wheels

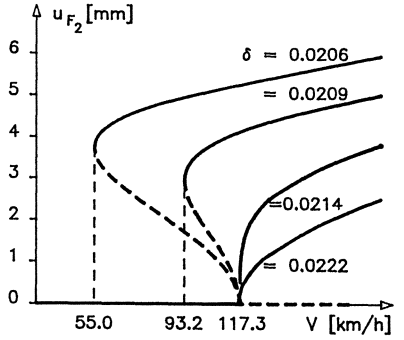

Figure 6: Practical stability limits V_n for some values of the conicity angle δ of the wheels

Acknowledgement

This research project has been partly supported by the "Jubiläumsfonds der Gemeinde Wien".

References

1 Moelle D., R. Gasch, *Nonlinear Bogie Hunting,* Proceedings 7th IAVSD-Symposium (A. H. Wickens ed.) Swets and Zeitlinger B. V., Lisse 1982, 455–467.

2 Seydel R., BIFPACK: *A program package for calculating bifurcations,* State University of New York at Buffalo, 1985.

3 Arnold V. I., *Geometrische Methoden in der Theorie der gewöhnlichen Differentialgleichungen,* VEB-Verlag, Berlin 1987.

4 Golubitsky M., I. Stewart, D. Schaeffer, *Singularities and Groups in Bifurcation Theory,* vol. I and II, Applied Math. Sciences **51** und **69**, Springer-Verlag New York 1985, 1988.

5 Guckenheimer J., Ph. Holmes, *Nonlinear Oscillations, Dynamical Systems, and Bifurcations of Vector Fields,*, Applied Math. Sciences **42**, Springer-Verlag, New York, 1983.

6 Carr J., *Applications of Centre Manifold Theory,* Applied Math. Sciences **35**, Springer-Verlag, New York, Heidelberg, Berlin, 1981.

7 Troger H., A. Steindl, *Introduction into Nonlinear Stability and Bifurcation Theory,* Springer-Verlag, Wien, 1990.

8 Garg V. K., R. V. Dukkipati, *Dynamics of Railway Vehicle Systems,* Academic Press, Toronto, 1984.

9 Jaschinski A., *Analysis and Experimental Verification of Nonlinear Behavior of a Scaled Railway Bogie,* Euromech 229, Stuttgart, 1987.

10 True H., *Bifurcation problems in railway vehicle dynamics,* International Series of Numerical Mathematics, **79**, Birkhäuser Verlag Basel, 1987.

Appendix

The lecture

G. Iooss: A Mathematical Justification of the Steady Ginzburg–Landau Equation

presented at the Symposium has already been published under the following references:

G. Iooss, A. Mielke and Y. Demay: Theory of Steady Ginzburg–Landau Equation in Hydrodynamic Stability Problems. Europ. J. Mech. B / Fluids 8 (1989) 229–268.

G. Iooss and J. Los: Bifurcation of Spatially Quasi–periodic Solutions in Hydrodynamic Stability Problems (submitted to Nonlinearity)

The paper

F.H. Ling and Y.M. Cheung: Bifurcations in a Hard Spring Duffing Oscillator

has not been presented at the Symposium. However, it is published in the proceedings of the Symposium since the authors couldn't attend the Symposium due to reasons out of their own control.

W. Schiehlen, Editor

Bifurcations in a Hard Spring Duffing Oscillator

F.H. Ling[1] and Y.M. Cheung
Department of Physics and Engineering Physics
Stevens Institute of Technology
Hoboken, NJ 07030, U.S.A.

Summary

Tangent and period-doubling bifurcation curves of a hard spring Duffing oscillator are calculated with the shooting method and the continuation technique. From these curves, one observes clearly the route via period-doubling to chaos and the coexistence of multiple solutions. The results are compared with those obtained using harmonic balance method and numerical simulations.

Introduction

The Duffing oscillator and related oscillators with a potential well are among the most frequently studied examples in the chaotic dynamics. They are rather simple in the mathematical description, but still, they possess abundant dynamical behaviours. There are many publications concerning oscillators with a potential well, see Ling [1] and Thompson [2] and references therein. On the contrary, only few papers concern the chaotic dynamics of a hard spring Duffing oscillator, see Fang and Dowell [3] for some numerical simulation results. In the present paper the bifurcations in such an oscillator will be studied in a more systematic way.

Inverse-Symmetry and Harmonic Balance

Many nonlinear oscillators have an inverse symmetry:

$$\ddot{x} + f(x, \dot{x}, t) = 0, \quad f(x, \dot{x}, t) = -f(-x, -\dot{x}, t + \frac{T}{2}), \tag{1}$$

[1]On leave from the Department of Engineering Mechanics, Shanghai Jiao Tong University, Shanghai 200 030, PR China

W. Schiehlen (Editor)
Nonlinear Dynamics in Engineering Systems
IUTAM Symposium Stuttgart/Germany 1989

where T is the period of the exciting force. It is evident (e.g. see Ling [4]) that if $x(t)$ is the solution of (1), then $\bar{x}(t) = -x(t + \frac{T}{2})$ is also a solution. This conclusion does not only apply to a periodic solution, it applies also to a non-periodic solution, e.g., a chaotic solution. Moreover, one distinguishes two different kinds, namely the self-symmetric ones with $x(t) = -x(t + \frac{T}{2}) = \bar{x}(t)$ and the dual ones with $x(t) \neq \bar{x}(t)$. Clearly, the phase portraits of $x(t)$ and $\bar{x}(t)$ are inverse-symmetric each other in the later case.

The Duffing equation belongs obviously to the category (1). In this paper we will study

$$\ddot{x} + \delta\dot{x} + x + x^3 = \gamma \cos \Omega t \tag{2}$$

with $\delta = 0.1$ and γ and Ω of varied values.

Our task is to find bifurcation curves of (2). An obvious choice is to use the harmonic balance method (see e.g. Schmidt and Tondl [5]), which is, however, practically only suitable for the self-symmetric $P1$ solutions.

Suppose that

$$x^* = A\cos(\Omega t - \phi) \tag{3}$$

and substitute (3) into (2), then the approximate $P1$ solution should satisfy

$$[(1 - \Omega^2 + \frac{3}{4}\epsilon A^2)^2 + \delta^2\Omega^2]A^2 = \gamma^2. \tag{4}$$

A bifurcation curve of the periodic solution in the parameter space is in fact an assembly of the parameter combinations, with which the system has critical stable periodic solutions, so we investigate the stability of the periodic solution x^* by adding a perturbation term η

$$x = x^* + \eta. \tag{5}$$

Substituting (5) into (3) leads to the variational equation of (2)

$$\ddot{\eta} + \delta\dot{\eta} + 3x^{*2}\eta = 0, \tag{6}$$

And by substituting (2) into (6) we obtain a Mathieu equation. Apply the harmonic balance method once again to this Mathieu equation, i.e. suppose

$$\eta = u\cos\Omega t + v\sin\Omega t \tag{7}$$

and substitute it into (6), then the condition of non-trivial solution ($u \neq 0, v \neq 0$) leads finally to the equation

$$\Omega^2 = 1 + \frac{3}{2}\epsilon A^2 - \frac{1}{2}\delta^2 \pm [\frac{1}{4}\delta^4 - (1 + \frac{3}{2}\delta A^2)\delta^2 + (\frac{3}{4}\delta A^2)^2]^{1/2}. \tag{8}$$

From (6) and (8) one calculates $P1$ bifurcation curves on the $\gamma \sim \Omega$ plane which are plotted in Fig. 1 with dot lines. There are also numerically calculated bifurcation curves plotted with solid lines in Fig. 1, see next section for details. It is noticed that the harmonic balance results coincide with the numerical (exact) results very well for the out-of-phase $P1$ bifurcation and also for the in-phase $P1$ bifurcation with a not too large exciting amplitude γ.

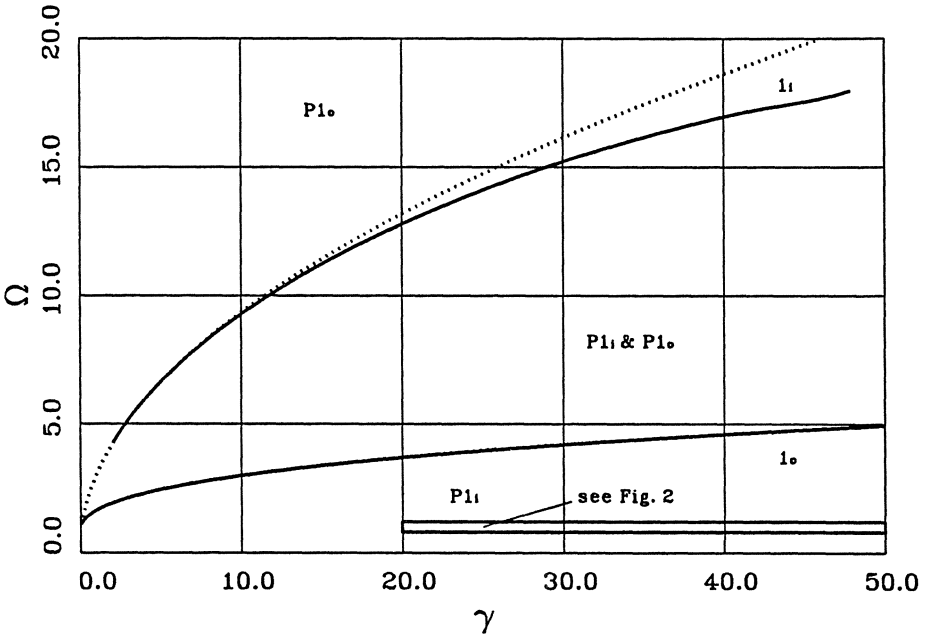

Fig. 1 Bifurcation curves of a hard Duffing oscillator (I)

—— numerical results, ····· harmonic balance results, 1_i — in-phase $P1$ bifurcation curve, $P1_i$ — in-phase $P1$ solution, subscript "o" means out-of-phase

In Fig. 1, the whole parameter plane is devided by the $P1$ bifurcation curves into three regions: the upper region of out-of-phase solution $P1_o$, the lower region of in-phase solution $P1_i$ and the middle region of coexistence of these two. As mentioned above, these $P1$ solutions are self-symmetric. The harmonic balance method can not handle the dual symmetric solutions, but the numerical method can. For this oscillator we find many other bifurcation curves near $\Omega = 1$ as stated in the next section.

Numerical Method

First, we briefly review the numerical method developed by Ling [1]. For a nonlinear periodic system

$$\dot{x} = f(t, x, \alpha), \quad f(t, x, \alpha) = f(t + T, x, \alpha), \tag{9}$$

where α is the parameter of the system, the periodic solution x^* satisfies

$$x^*(0, \alpha) - x^*(T, \alpha) = 0. \tag{10}$$

According to the Floquet theory, the critical periodic solution should also satisfy

$$\dot{\Phi}(t, \alpha) = \frac{\partial f(t, x^*, \alpha)}{\partial x} \Phi(t, \alpha), \quad \Phi(0, \alpha) = I_n, \tag{11}$$

$$\rho[\Phi(T, \alpha)] = 1, \tag{12}$$

where $\Phi(t, \alpha)$ is the fundamental matrix of (9) and $\rho[\cdot]$ denotes the spectral radius.

For a two dimensional system like an one-degree-of-freedom oscillator, the eigenvalues of $\Phi(T, \alpha)$ can be calculated from

$$\lambda^2 - \lambda \ \mathrm{tr}[\Phi(T, \alpha)] + \det[\Phi(T, \alpha)] = 0, \tag{13}$$

and recall the Jacobi identity

$$\det[\Phi(T, \alpha)] = \exp \int_0^T \ \mathrm{tr} \left[\frac{\partial f(t, x, \alpha)}{\partial x} \right] dt, \tag{14}$$

the condition (12) is reduced to

$$1 \mp tr[\Phi(T,\alpha)] + \det[\Phi(T,\alpha)] = 0. \tag{15}$$

In fact, the condition $\lambda = 1$ corresponds to the tangent bifurcation, and $\lambda = -1$ corresponds to the period-doubling bifurcation.

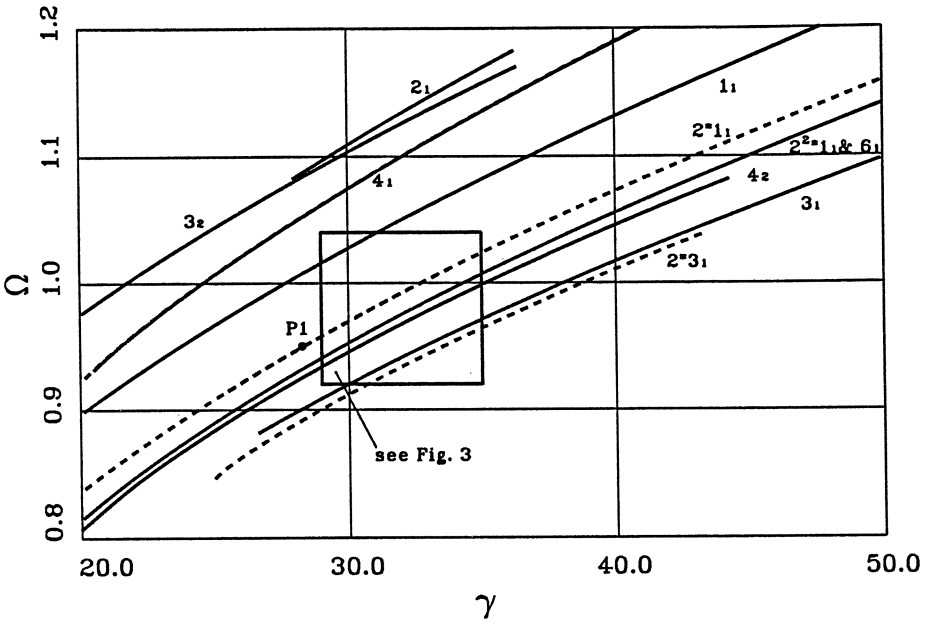

Fig. 2 Bifurcation curves of a hard spring Duffing oscillator (II)

—— tangent bifurcation, – – –– period-doubling bifurcation, $2^2 * 1_1$ — second time period-doubling bifurcation of the first $P1$ solution, $P1$ —periodic, and "chaos" —chaotic solutions found by Fang and Dowell [3]

For our system (2), equations (9), (10), (11) and (15) have the following forms

$$\begin{cases} \dot{x}_1 = x_2, \\ \dot{x}_2 = -\delta x_2 - x_1 - x_1^3 + \gamma \cos \Omega t, \end{cases} \tag{16}$$

$$\begin{cases} x_1(0) - x_1(T) = 0, \\ x_2(0) - x_2(T) = 0, \end{cases} \tag{17}$$

$$\begin{bmatrix} x_3 & x_5 \\ x_4 & x_6 \end{bmatrix}^{\cdot} = \begin{bmatrix} 0 & 1 \\ -(1+3x_1^2) & -\delta \end{bmatrix} \begin{bmatrix} x_3 & x_5 \\ x_4 & x_6 \end{bmatrix}, \quad \begin{bmatrix} x_3 & x_5 \\ x_4 & x_6 \end{bmatrix}_{t=0} = \begin{bmatrix} 1 & 0 \\ 0 & 1 \end{bmatrix}, \tag{18}$$

$$1 \mp [x_3(T) + x_6(T)] + \exp(-\delta T) = 0. \tag{19}$$

Select proper initial conditions and using shooting and continuation techniques we obtain the bifurcation curves from equations (16) to (19) as shown in Figs. 2-4.

In Fig. 2 we find a wide band of dual symmetric $P1$ solutions and several narrow $P3, P4$ and $P6$ bands. There are many tiny periodic bands, however, it is not possible to find all of them. Outside these bands there is the chaotic sea. It is remarkable that the bifurcation curves are almost all parallel one another—a feature we observed also in the driven pendulum [1], which reduces the possible coexistence of different solutions. However, we remember that the whole picture of Fig. 2 is located within the $P1_i$ region, so there is always a coexistence of $P1_i$ solution with other periodic and chaotic solutions.

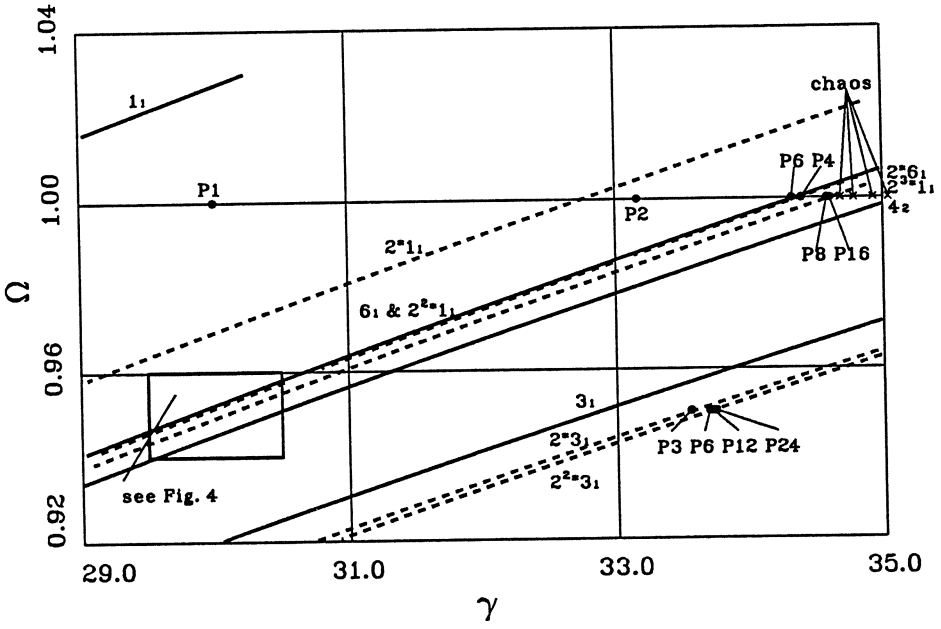

Fig. 3 Bifurcation curves of the hard spring Duffing oscillator (III)
symbol description see Fig. 2

Another remarkable feature is seen from the enlarged pictures, Figs. 3 and 4. There is a $P6$ tangent bifurcation curve almost coincide with the second time period-doubling bifurcation curve of $P1$ (in fact, the bifurcation curve 6_1 is slightly below the bifurcation curve $2^2 * 1_1$), and the whole $P6$ band and its period-doubling extensions are embedded in the $P4$ band, which is the period-doubling extension of the wide $P1$ band. In this region there is a coexistence of $P1_i$ and $P4$ together with $P6$ (or $P12$, $P24$ and so on) solutions.

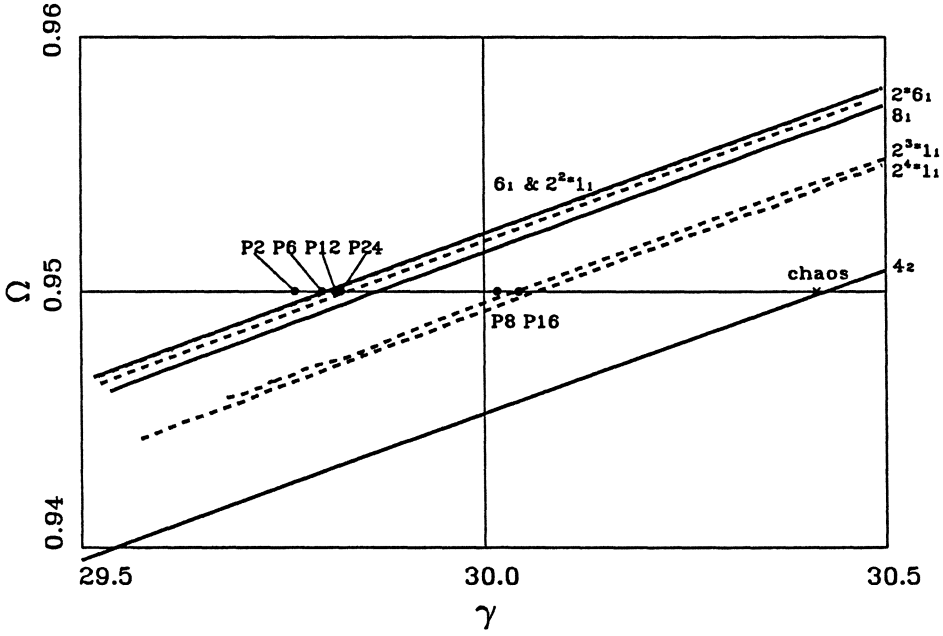

Fig. 4 Bifurcation curves of the hard spring Duffing oscillator (IV)
symbol description see Fig. 2

Concluding Remarks

Bifurcation diagram of the hard spring Duffing oscillator are calculated with numerical method as shown in Figs. 1-4, in which the harmonic balance results and the numerical simulation results are also plotted. The harmonic balance method is a useful tool for treating the self-symmetric $P1$ solution, but also only for this simplest case. It is clear that from the numerically calculated bifurcation diagram one is able to find out the global structure of the distribution of different attractors in the parameter space including the coexistence case. Sparsely distributed periodic and chaotic solutions found by Fang and

Dowell [3] with numerical simulation are all located in the corresponding periodic and chaotic bands of our bifurcation diagram. However, only from these solutions it is difficult to understand the global structure. For example, without the bifurcation diagram one may very likely think that the $P8$ and $P16$ solutions in the middle of Fig. 4 belong to the $P1$ period-doubling sequence, although in fact they belong to a $P8$ period-doubling sequence.

From these diagrams we may conclude that the route to chaos in the hard spring Duffing and similar system is typically through a period-doubling bifurcation of dual symmetric periodic solutions. We do not find the self-symmetric solution undergoes a period-doubling bifurcation in this case. And there is no indication of a quasi-periodic motion as guessed by Fang and Dowell [3]. To our experience, the quasi-periodic motion appears more frequently in driven self-sustained oscillators.

One of the authors (F.H.L.) thanks the hospitality of professor G. Schmidt and the financial support by DE-FG02-87ER13740.

References

1. Ling, F.H.: A numerical study of the distribution of different attractors in the parameter space *Z. Phys. B—Condensed Matter* to appear.

2. Thompson, J.M.T.: Chaotic phenomena triggering the escape from a potential well. *Proc. R. Soc. Lond.* **A 421** (1989) 195-225.

3. Fang, T. and Dowell E.H.: Numerical simulations of periodic and chaotic responses in a stable Duffing system. *Int. J. Non-Linear Mechanics* **22** (1982) 401-425.

4. Ling, F.H.: Numerische Berechnung einiger nichtlinearen Schwingungssysteme. Dissertation Universität Stuttgart 1981.

5. Schmidt, G. and Tondl, A.: Non-Linear Vibrations. Cambridge: Cambridge University Press 1986.